Évolution métallurgique et résistance en fluage à 600°C et 650°C d'aciers à 9-12% Cr

Clara Panait

ParisTech
INSTITUT DES SCIENCES ET TECHNOLOGIES
PARIS INSTITUTE OF TECHNOLOGY

MINES ParisTech

École doctorale №432 : Sciences des Métiers de l'Ingénieur

Doctorat ParisTech

T H È S E

pour obtenir le grade de docteur délivré par

l'École nationale supérieure des mines de Paris

Spécialité « Science et Génie des matériaux »

présentée et soutenue publiquement par

Clara Gabriela PANAIT

le 23 Septembre 2010

Évolution métallurgique et résistance en fluage à 600°C et 650°C d'aciers à 9-12% Cr

Metallurgical evolution and creep strength of 9-12% Cr heat resistant steels at 600°C and 650°C

Directeurs de thèse : **Anne-Françoise GOURGUES-LORENZON**
Jacques BESSON

Jury

M. Vaclav SKLENIČKA, Prof., Academy of Sciences of the Czech Republic	Rapporteur
M. Gunther EGGELER, Prof., Ruhr-Universität Bochum, Germany	Rapporteur
M. Kota SAWADA, Dr. Ing., National Institute for Materials Science, Japan	Examinateur
M. Kazuhiro KIMURA, Dr. Ing., National Institute for Materials Science, Japan	Examinateur
M. Sylvain LECLERCQ, Dr., Chercheur Senior, EdF R&D Les Renardières, France	Examinateur
Mme. Anne-Françoise GOURGUES-LORENZON, Prof., MINES ParisTech	Examinateur
M. Jacques BESSON, Dr., Directeur de recherche CNRS, MINES ParisTech, France	Examinateur
M. Arno FUCHSMANN, Dr. Ing., Vallourec Research Aulnoye, France	Examinateur
M. Eric SCHMIDT, Dr. Ing., Vallourec Research Aulnoye, France	Invité
M. Jean GABREL, Ing., Vallourec Research Aulnoye, France	Invité

MINES ParisTech
Centre des Matèriaux - UMR CNRS 7633
B.P. 87 - 91003 EVRY Cedex

T H È S E

À tous ceux qui, de près ou de loin, ont contribué à la réalisation de ce projet

Résumé

Les aciers martensitiques à 9-12% Cr sont utilisés pour applications à haute température notamment comme composants dans des centrales thermiques de production de l'électricité. Ces composants sont soumis à des phénomènes de fluage, vieillissement thermique, fatigue, oxydation, corrosion. Cette étude vise une meilleure compréhension de l'évolution métallurgique à long terme des aciers martensitiques à 9-12% Cr, ainsi que de son influence sur la résistance en fluage à 600 et 650°C. Le matériau de l'étude est l'acier Grade 92.

La littérature manque de données quantitatives sur la microstructure de l'acier Grade 92 après des temps prolongés d'exposition au fluage ou au vieillissement thermique (temps supérieurs à 10000h) à 600°C et 650°C. Par conséquent, dans un premier temps une expertise d'éprouvettes de fluage testées à 600°C et 650°C pendant des temps allant jusqu'à 50.000h a été réalisée par microscopie électronique en transmission (MET) sur des répliques extractives, microscopie électronique à balayage (MEB) et par diffraction des électrons rétrodiffusés. Cette expertise a révélé une précipitation significative de phase de Laves, une restauration de la matrice et une très faible précipitation de la phase Z-modifiée. Une quantification de l'endommagement et des phases de Laves a été réalisée à partir des micrographies MEB.

La précipitation significative des phases de Laves et la restauration de la matrice semblent être les mécanismes prédominants de l'évolution métallurgique à 600°C et 650°C de l'acier Grade 92. Afin d'étudier séparément l'influence de chacun de ces deux mécanismes sur la résistance au fluage, des essais de fluage ont été réalisés sur des éprouvettes pré-vieillies et sur des éprouvettes pré-fatiguées. Des éprouvettes entaillées ont été également utilisées.

- L'intérêt des éprouvettes pré-vieillies est d'étudier l'influence de grosses phases de Laves sur la résistance au fluage. Le temps à rupture des éprouvettes pré-vieillies est quatre fois plus faible que celui des éprouvettes standard pour les mêmes niveaux de contraintes. Ceci n'est toutefois pas confirmé pour les contraintes les plus faibles.

- Deux essais de fluage ont été réalisés sur des éprouvettes pré-fatiguées à 550°C pour étudier l'effet de l'état de la matrice sur la résistance au fluage. Un temps à rupture deux fois plus faible a été observé à 600°C sur une éprouvette pré-fatiguée comparée à une éprouvette standard pour le même niveau de contrainte. Cet effet n'a pas été observé à 650°C pour les contraintes faibles.

- Des éprouvettes entaillées ont été également utilisées pour étudier l'influence du taux de triaxialité des contraintes sur le développement de l'endommagement par fluage. Pour des temps de fluage comparables, l'endommagement est plus développé dans une éprouvette entaillée que dans une éprouvette lisse.

Un modèle mécanique qui prend en compte l'évolution métallurgique de l'acier a été développé pour estimer la résistance au fluage *à long terme* Le modèle prend également en compte le taux de triaxialité des contraintes. A ce titre, il peut être utilisé pour estimer la durée de vie des composants en service ou pour analyser les composants avec une géométrie complexe qui serait plus sensible au développement de l'endommagement par fluage, du fait d'une triaxialité des contraintes plus élevée.

Abstract

9-12%Cr tempered martensite steels are used for high temperature (400-600°C) especially applications in components of fossil power plants, such as tubes, pipes, heaters. These components are exposed to creep, thermal aging, fatigue, oxidation, corrosion. The development of advanced heat resistant steels with improved long-term creep strength relies on a better understanding of the long-term microstructural evolution and of its influence on the creep strength. This study aims at better understanding of the effect of microstructural evolution on long-term creep strength at 600°C and 650°C of a Grade 92 steel.

There are rather few published data on the microstructure of the Grade 92 steel after long-term creep or thermal aging exposure (times higher than 10,000h) both at 600°C and 650°C. Thus, in a first part, P92 steel specimens that had been creep tested for times up to 50,000h at 600°C and 650°C were investigated using transmission electron microscopy on extractive replicas of precipitates, scanning electron microscopy and electron backscatter diffraction to get data on the microstructure of the Grade 92 steel after long-term exposure. These investigations revealed significant precipitation of Laves phases, recovery of the matrix and little precipitation of modified Z-phase. A quantification of the Laves phases and creep damage were realized by image analysis of scanning electron micrographs.

Significant precipitation of Laves phase and recovery of the matrix seem to be the most prominent microstructural degradation mechanisms. To separately investigate the effect of each of these two mechanisms on creep strength, creep tests were conducted on thermally aged and thermo-mechanically prepared creep specimens. Creep tests were also conducted on notched specimens.

- Thermally aged creep specimens enable to study the effect of large Laves phases on the creep strength. A time to rupture four times lower was observed on the aged creep specimens compared to a standard creep test for same testing conditions. This seems not be confirmed, however, at low stresses.

- Two creep specimens thermo-mechanically prepared by creep-fatigue prestraining at 550°C were used to study the effect of the matrix substructure on the creep strength. A time to rupture twice lower was observed at 600°C (short-term creep) on a thermo-mechanically prepared creep specimen compared to a standard one for the same testing conditions. No such effect was detected at 650°C in the low stress regime.

- Creep tests were also conducted on notched specimens with various notch shapes to study the effect of stress triaxiality on creep damage. In notched specimens higher amounts of creep damage were observed compared to smooth specimens for similar testing time.

A finite element mechanical model coupling microstructural evolution and creep damage was proposed to estimate the long-term creep strength of the Grade 92 steel at 600°C and 650°C. The model taking stress triaxiality into account might also be used to estimate the remaining life of service components and to analyze service components with complex geometry more sensitive to creep damage due to stress triaxiality.

Acknowledgments-Remerciements

First of all, I would like to thank prof. G. Eggeler and prof. V. Sklenička for their acceptance to become a referee of my dissertation. I appreciated their interest in my research work and their efforts in reading my manuscript. I would also like to thank the others members of defense jury : dr. K. Sawada, dr. K. Kimura, dr. S. Leclercq, dr. E. Schmidt and dr. A. Fuchsmann for their participation with valuable comments. I am also grateful for the valuable and interesting discussions we had during various conferences, seminars or working-groups.

This work would not have been possible without the participation and the fruitful support of many wonderful people. Hereafter, I would like to address to them my humble gratitude.

I am very grateful to dr. W. Bendick from SZMF, Germany for his precious help for this phd. work by providing valuable creep specimens which were tested for very long time (up to several years) but also for helpful discussions and advice.

I would like to express my sincere thanks to prof. A. Czyrska-Filemonowicz, A. Zielinska-Lipiec and T. Koziel from AGH University of Science and Technology (Krakow, Poland) for conducting TEM investigations on thin foils and for the knowledge provided about this procedure.

Many thanks to dr. H. Kj. Danielsen for helpful discussions concerning modified Z phase precipitation and TEM investigations.

I will continue my acknowledgments in French since those I would like to thank are French. It is a sort of tribute to the French language and to the French culture I have enjoyed during the last five years.

J'ai toujours voulu faire une thèse de doctorat en pensant à une aventure scientifique extraordinaire, mais j'étais loin de m'imaginer l'aventure humaine et à quel point cette expérience m'a fait grandir. Je voudrais adresser un petit mot de remerciement à ceux qui m'ont accompagnée dans cette belle aventure et qui ont contribué de près ou de loin à ce projet de thèse.

Tout d'abord, je voudrais remercier mes directeurs de thèse Anne-Françoise Gourgues-Lorenzon et Jacques Besson auprès desquels j'ai appris à avoir une démarche scientifique. J'ai eu la change d'être l'un de leur thésards et de profiter de leur compétences scientifiques pointues ainsi que de leur passion pour la recherche et l'excellence.

Je tiens à les remercier pour la grande liberté qu'ils m'ont accordée et pour les enseignements précieux qu'ils m'ont apporté. Ils ont su m'encourager et me conseiller tout au long de ce travail de thèse. Je les remercie sincèrement pour tout ce qu'ils m'ont apporté.

Ce travail de thèse a été réalisée dans le cadre d'une convention CIFRE entre l'Ecole des Mines de Paris et Vallourec&Mannesmann Tubes France ce qui m'a permis de bénéficier

de moyens expérimentaux de deux établissements de recherche: le Centre des Matériaux de l'Ecole des Mines de Paris et le Centre de recherche Vallourec (Vallourec Research Aulnoye).

Je souhaite témoigner ma profonde reconnaissance à Arno Fuchsmann et Jean Gabrel de Vallourec Research Aulnoye (VRA) pour leur soutien permanent tout au long de ce travail de recherche. Les mots ne sont pas suffisants pour vous remercier pour tout ce que vous avez fait pour que ce projet de thèse avance. Merci du fond du cœur, sans vous, cette these ne serait pas ce qu'elle est devenue. Un grand merci pour avoir mis en place une lourde logistique afin de réaliser les différents essais de fluage. Les 110 essais de fluage réalisés au VRA constituent une très bonne base expérimentale et je vous en remercie. De même, je voudrais remercier Bernard Delva, technicien au VRA pour le soin qu'il a porté sur la réalisation de ces essais. Je vous remercie également pour m'avoir encouragée pour aller au working groups COST ainsi qu'au Training School COST. Les échanges avec des nombreux spécialistes lors de ces occasions m'ont beaucoup apporté.

Je remercie chaleureusement Michel Piette, Emmanuel Cini et Eric Schmidt de Vallourec Research Aulnoye pour les différents échanges enrichissants. Je remercie egalement Catherine Grosjean (VRA) pour les calculs Thermo-Calc.

Des gens formidables d'autre laboratoires m'ont abondamment aidé dans mon travail de thèse. Merci à Cristel Caes (CEA) pour mon premier essai de fatigue-fluage réussi. Un grand merci également à Françoise Barcelo (CEA) pour le dépouillement EBSD en joints KS et GT ainsi que pour sa gentillesse et sa disponibilité. Je remercie également Benjamin Fournier (CEA) pour les discussions enrichissantes sur la fatigue des aciers grades 91 et 92 ainsi que sur caractérisation EBSD de ces aciers. Merci à Frédéric Delabrouille (EdF Renardières) pour les observations MET sur des lames minces. Merci également à Charles Petry (EdF Renardières) pour les discussions sur le comportement en fluage des aciers à 9%Cr ainsi que sur la modélisation du comportement en fluage.

J'adresse mes remerciements à Henry Proudhon pour son énorme travail dans la mise en place des mes essais de fatigue-fluage ainsi qu'à Thilo Morgeneyer pour son aide dans la réalisation de ces essais.

Je remercie Abdenour Meddour pour son aide dans la réalisation de mes différents essais. Un grand merci, aussi, à Anne Laurent pour son aide précieuse et sa gentillesse. J'adresse également mes remerciements aux personnel de l'atelier. Je remercie particulièrement Christophe et Jojo pour l'usinage des entailles et la découpe au fil de mes éprouvettes testées en fluage dans les meilleurs délais. Votre aide et bonne volonté m'ont permis de tenir les différentes échéances de ma thèse. Vous me manquerez énormément.

La caractérisation microstructurale et les essais mécanique sont au cœur de mes travaux de thèse. A ce titre, je voudrais témoigner ma gratitude à François Grillon et Maria Betbeder pour m'avoir formée à l'utilisation du MEB, MEB-FEG et de l'EBSD ainsi que pour leur disponibilité et leurs précieux conseils pour l'observation de mes différents échantillons. Je remercie Arnaud Grosjean pour l'initiation à l'utilisation du MET et Mohamed Sennour avec qui j'ai continué ma formation sur le MET. Les résultats de mes observations MET sont d'une grande valeur scientifique. Je vous remercie vivement pour votre aide dans la réalisation de ces observations.

Monsieur A. Pineau, je vous remercie pour tout le temps que vous m'avez consacré. C'était toujours un plaisir de discuter avec vous. Je vous remercie pour les conseils techniques dans la réalisation des essais ainsi que les explications pointues et détaillées sur la métallurgie et, je vous cite, sur la *bonne vieillie mécanique*. Votre enthousiasme et passion pour la recherche

sont une source d'inspiration pour des nombreux doctorants.

Je remercie Grégory Sainte-Luce et Olivier Delhomme pour leur aide et soutien dans les problèmes informatiques.

Je remercie Odile Adam pour son habilité à retrouver n'importe quelle publication scientifique ainsi que pour sa patience à vérifier toutes mes références bibliographiques. J'adore ton franc parler.

Je remercie vivement tous les thésards du Centre des Matériaux, je ne citerai personne de peur d'en oublier. Merci pour le partage, l'entraide, la disponibilité, la présence, l'écoute, les encouragements, la bonne ambiance. Vos marques d'amitié ainsi que les bons moments passés au CdM me manqueront énormément. Je dois adresser un merci particulier à mes collègues de bureau-le B107: Florian (merci pour tous les différents échanges, mais surtout pour l'écoute et les fous rires), Céline (merci pour nos discussions entre filles), Huaidong et Jianqiang (mes chinois préférés, pour vous je visiterai la Chine), Pierre-François et Charlotte (je vous souhaite bon courage pour la fin de vos thèses et tenez-moi au courant de vos résultats de thèse), Mélanie et Auréliane (merci de m'avoir supportée pendant ma dernière année de thèse, vous avez su apprivoiser la bête à coups de gâteaux, chocolats, etc; mais surtout merci pour votre amitié qui m'a énormément aidé à remonter la pente); je voudrais également remercier mon co-pilote préféré auprès duquel j'ai énormément progressé.

Dans ma dernière année de thèse j'ai souvent pensé à ce que Raphaël m'avait dit il y a trois-quatre années. Mes états d'âme au fil de ces trois années se sont passés exactement comme il m'avait dit; à l'époque je ne l'avais pas cru.

J'adresse mes remerciements à l'ensemble de l'équipe administrative pour l'aide dans l'organisation de mes différents réunions, séminaires, workshops, déplacements ainsi que pour l'assistance dans les différentes procédures administratives: Liliane (merci aussi pour nos cours de gym); Konaly (je sais que j'ai été parfois dure avec toi; je te préparerais un bon petit plat pour me faire pardonner :-)), Dolorès et les deux Véro (merci pour votre générosité et votre disponibilité).

Je voudrais remercier l'ensemble des mes professeurs de la Faculté de Mécanique, Galati, Roumanie. Un merci particulier à prof. Mircea Modiga, Alina Dimache et Daniel Olaru prof. Catalina Maier, prof. Mihaela Banu, prof. Catalin Fetecau et prof. Alexandru Epureanu qui ont marqué mon parcours professionnel par leur enseignements.

Je souhaiterais adresser à prof. Nicolae Oancea toute ma reconnaissance pour ses précieux conseils dans mes choix de carrière.

Last but not least, I thank my family for supporting me in all my choices, and, in particular, my brother for his endless encouragements and for taking care of the family so I could focus on my PhD. work. I would also like to thank my grandfather, Manolache, a simple man who had a great career and my grandmother, Neculina, a simple woman who worked all her life for her girls. They taught me the true values of life.

Merci à vous tous,
Clara

General introduction

Problematics

Design of components operating at high temperatures in fossil power plants requires creep data for long-term exposure. The stress level corresponding to a lifetime of 10^5h is generally used as the allowable stress. It is, however, difficult to obtain experimental creep data for more than 10^5h (almost 12 years). Therefore, long-term creep behavior is predicted by numerical extrapolations based on shorter-term experimental creep data.

Most of extrapolation methods lead to an overestimation of long-term creep strength. It was reported in literature that extrapolation of creep data for times lower than 10^4h leads to an overestimation of the long-term creep strength (Abe, 2004). This overestimation is often explained by a degradation of the microstructure during long-term creep exposure, which is not taken into account in the extrapolation methods. However, the effect of the metallurgical evolution such as growth of precipitates, precipitation of new phases or recovery of the matrix on the creep strength is not fully understood.

An objective of this study is to propose a mechanical model coupling damage and metallurgical evolution to estimate the creep strength of the Grade 92 steel after long term creep (times higher than 50,000h) at 600°C and 650°C. To this aim, complementary creep tests were conducted at the mentioned temperatures to better understand the influence of metallurgical evolution on the loss of creep strength and the influence of stress triaxiality on the creep damage development.

Metallurgical evolution of Grade 92 during long-term creep exposure at 600°C and 650°C

As will be shown in this manuscript, there are rather few quantitative data on the microstructure of the Grade 92 steel after long-term creep exposure both at 600°C and 650°C. Also, there is a scatter of data from one study to another concerning the size evolution of precipitates in the Grade 92 steel during creep or thermal aging.

To increase the available database, specimens that have been creep tested for times up to 50,000h at 600°C and 650°C were investigated with regard to their microstructural evolution and creep damage. These investigations aimed at deeper understanding of the microstructural evolution of the Grade 92 steel during long term creep and at identification of major microstructural evolution mechanisms. Available published data on the creep behavior and the microstructure of the Grade 92 after creep are thus reviewed in this manuscript.

Creep tests

The creep rupture behavior of the Grade 92 steel at 600°C and 650°C has largely been studied on smooth specimens. In this study, complementary methods were used to test the creep behavior of the Grade 92 steel such as: thermally aged, thermo-mechanically prepared and notched specimens. The purpose of these complementary tests is two-fold: (i) a better understanding of the microstructural and mechanical features that control creep flow and damage and (ii) an assessment of possible methods to assist alloy design by giving, in a rather short time, indications about the long-term creep behavior of this steel family. The detailed purpose of each of these tests is briefly presented in the following.

Thermally aged and thermo-mechanically prepared specimens intended to separate the metallurgical evolution mechanisms of matrix and precipitation, respectively, and to study their individual influence on the creep behavior. To quantify the effect of each metallurgical mechanism on the loss of creep strength, most of creep tests are iso-stress (same engineering stress on each kind of specimen). The results of these tests were then used to define the internal variables of the creep model, which also takes the metallurgical evolution of the steel during creep into account.

More precisely, the interest of thermally aged creep specimens is to study the influence of large precipitates (mostly Laves phases) on creep flow and creep damage of the T92 steel. The purpose of the creep tests conducted on thermo-mechanically prepared specimens was to estimate the influence of the recovery of the matrix on the creep strength. These specimens were prepared by creep-fatigue cycles at rather low temperature (i.e. 550°C) for a short time (∼11 days) to change the substructure of the matrix without changing the size of precipitates. Due to experimental difficulties only three creep tests were realized on the thermo-mechanically prepared specimens. The results of these tests does not allow to conclude on the effect of the matrix substructure on the loss of long-term creep strength. Thus, for clarity reasons and to facilitate reading of this manuscript all data concerning the creep tests on thermo-mechanically prepared specimens are gathered in *Appendix A*. Details about thermo-mechanical preparation of specimens, results of creep tests as well as investigation of these specimens after creep testing can thus be found in *Appendix A*.

Notched creep specimens were used to accelerate creep damage mechanisms that normally occur in long-term creep only. The presence of a notch increases the stress triaxiality ratio in the minimum cross section of the specimen. For a given engineering stress, the von Mises stress is lower in a notched specimen than in a smooth specimen, leading to a decrease in the strain rate (thus, promoting diffusional creep) and an increase in creep damage due to the high stress triaxiality. Creep damage observed after long term creep (low stresses) in a smooth specimen could possibly be achieved in a notched specimens within a shorter time. In addition, the size of the creep-damaged area, together with accurate assessment of stress and strain fields within the notched creep specimen, allowed damage initiation criterion parameters to be more finely tuned than from a limited set of smooth creep specimens. This requires building a model and identification of corresponding parameters to analyze stress and strain fields in notched creep specimens. In the present study, an existing model was adapted and used together with the finite element simulation method.

About the manuscript

This manuscript is divided into nine chapters and three appendices.

A general literature survey is presented in **chapter I**. This chapter intended to fix the background of this study and to gather available published data related with the present work. The loss of the creep strength loss of the 9-12%Cr steel, improvement of their creep strength and effect of thermal ageing on the creep behaviour of the Grade 91 and Grade 92 steels are discussed from available published data. Quantitative available published data on the microstructure of the Grade 92 steel during long-term creep or thermal ageing at 600°C and 650°C are given in this chapter.

The materials under study- two Grade 92 steels are presented in **chapter II**. General features about their microstructure as well as comments about the alloying elements in the 9-12%Cr tempered martensitic steels are given in this chapter.

In this study creep tests were realized on different kinds of specimens with various geometries (i.e. smooth, notched) and various state of microstructure before creep testing (i.e. thermally aged, thermo-mechanically prepared). The geometry of the smooth and the notched specimens as well as a microstructural characterisation of the thermally aged specimens before creep testing are given in **chapter III**. Details about the thermo-mechanical preparation of specimens is given in the beginning of the *Appendix A*. The data processing of the creep curves is explained in **chapter IV**.

The results of creep tests conducted at 600°C and 650°C are presented in **chapter V** and **chapter VI**, respectively. The creep results were analysed using well known relationships such as Norton power-law and Monkman-Grant equations.

The **chapter VII** is dedicated to investigations of the specimens after creep testing. Great interest was paid to quantitative data regarding the microstructure evolution and creep damage of these specimens. A quantification of creep damage and size of Laves phases was realized for the P92 steel specimens tested for long-term creep at 600°C and 650°C. TEM investigations on extractive replicas of precipitates were also conducted on these specimens. These results are presented in the beginning of **chapter VII**.

Complementary investigations of specimens in Grade 91 steel, also crept for very long time (i.e. 113,431h) which were realized as a first part of the Phd. work is reported in *Appendix B* and *Appendix C* in the form of published articles.

Based on the experimental results a mechanical model was developed in this study. This model is presented in **chapter VII**.

This manuscript ends with the general conclusions of this study.

Introduction Générale

Problématique

Des données sur le comportement à long terme des matériaux sont nécessaires pour le dimensionnement des composants dans les centrales thermiques à production d'électricité. Généralement la contrainte correspondant à une durée de vie de $10^5 h$ est utilisée dans les calculs. Cependant il est industriellement inenvisageable de réaliser des essais de fluage d'une telle durée. Par conséquent, le comportement à long terme est estimé à partir des résultats expérimentaux plus couts.

La plupart des méthodes d'extrapolation mènent à une surestimation de la résistance en fluage. Il a été signalé dans la littérature que l'extrapolation des données inférieures à $10^4 h$ surestime la résistance en fluage à long terme. Cette surestimation est souvent expliquée par la dégradation de la microstructure pendant l'exposition prolongée au fluage, ce qui n'est pas pris en compte dans les méthodes d'extrapolation. Néanmoins, l'effet de l'évolution métallurgique telle que la croissance des précipités, la précipitation de nouvelles phases ou la restauration de la matrice sur la perte de résistance en fluage n'est pas complètement compris.

Un objectif de cette étude est de proposer un modèle mécanique qui prend en compte l'endommagement et l'évolution métallurgique pour estimer la résistance en fluage de l'acier Grade 92 pendant des temps prolongés (temps supérieurs à 50000h). Pour ce faire, des essais de fluage complémentaires ont été réalisés pour mieux comprendre l'impact de l'évolution métallurgique sur la perte de résistance en fluage et l'effet du taux de triaxialité sur le développement de l'endommagement.

Evolution métallurgique de l'acier Grade 92 pendant des temps prolongés d'exposition au fluage à 600°C et 650°C

Comme il sera montré dans ce manuscrit, la littérature manque de données sur la microstructure de l'acier Grade 92 après des temps prolongés d'exposition au fluage à 600°C et 650°C. Il y a également une dispersion dans les valeurs concernant l'évolution de la taille des précipités dans l'acier Grade 92 pendant l'exposition au fluage ou le vieillissement thermique.

Pour enrichir les données publiées existantes, la microstructure et l'endommagement ont été étudiés dans des éprouvettes testées en fluage à 600°C et 650°C pendant des temps allant jusqu'à 50000h. Les objectifs de ces observations ont été de mieux comprendre l'évolution métallurgique de l'acier Grade 92 pendant le fluage et d'identifier les mécanismes prépondérants de l'évolution métallurgique pendant le fluage. Les données disponibles concernant le comportement en fluage ainsi que la microstructure de l'acier Grade 92 pendant le fluage sont revues dans ce manuscrit.

Essais de fluage

Le comportement en fluage de l'acier Grade 92 a été largement étudié sur éprouvettes lisses. Dans le cadre de cette étude des essais complémentaires ont été réalisés pour étudier le comportement en fluage de cet acier, à savoir sur des éprouvettes pré-vieillies, des éprouvettes pré-fatiguées et des éprouvettes entaillées. L'intérêt de ces essais est double: (i) mieux comprendre les éléments microstructuraux et mécaniques contrôlant la déformation

et l'endommagement en fluage et (ii) tester des méthodes complémentaires pouvant être utiles dans le développement de nouvelles nuances d'aciers, du fait qu'elles apporteraient des informations sur le comportement en fluage à long-terme des nouveaux aciers dans un temps relativement plus court. L'intérêt de chaque type d'éprouvette est détaillé brièvement ici.

L'intérêt des éprouvettes pré-vieillies et pré-fatiguées est de séparer l'évolution des précipités de l'évolution de la matrice et d'étudier l'impact séparé de chacune sur le comportement en fluage. Pour pouvoir quantifier l'effet de chaque mécanisme d'évolution métallurgique sur la perte de résistance en fluage, la plupart des essais ont été iso-contraintes (la même contrainte nominale sur chaque type d'éprouvette). Les résultats de ces essais ont été ensuite utilisés pour définir les variables internes du modèle, qui prend également en compte l'évolution métallurgique.

*Plus précisément, l'intérêt des éprouvettes pré-vieillies a été d'étudier l'influence des phases de Laves sur la déformation et l'endommagement en fluage de l'acier T92. L'intérêt des éprouvettes pré-fatiguées a été d'étudier l'influence de la restauration de la matrice sur le comportement en fluage. Ces éprouvettes ont été préparées par des cycles de fatigue-fluage à une température assez basse (550°C) sur une durée courte (∼ 11 jours) pour modifier l'état de la matrice sans changer la nature et la taille des précipités. A cause de difficultés expérimentales, seulement trois essais de fluage ont pu être réalisés sur ce type d'éprouvettes. Les résultats de ces essais ne permettent pas de se prononcer sur un possible effet de l'état de la matrice sur la perte de résistance en fluage. Pour des raisons de clarté et pour faciliter la lecture de ce manuscrit, toutes les données concernant les essais sur les éprouvettes pré-fatiguées ont été regroupées dans l'**Annexe A**. La préparation des ces éprouvettes ainsi que l'investigation des éprouvettes pré-fatiguées après fluage sont présentés en particulier dans l'**Annexe A**.*

Les éprouvettes entaillées ont été utilisées pour accélérer les mécanismes d'endommagement par fluage qui ne sont généralement observés qu'après de temps prolongés d'exposition au fluage. La présence d'une entaille augmente le taux de triaxialité des contraintes dans la zone entaillée de l'éprouvette. Pour un niveau de contrainte nominale donnée, la contrainte équivalente de von Mises est plus faible, ce qui diminue la vitesse de déformation et intensifie le développement de l'endommagement dû à un taux de triaxialité élevé. L'endommagement observé dans une éprouvette lisse après exposition prolongée au fluage (basses contraintes) pourrait probablement être obtenu dans un temps plus court sur une éprouvette entaillée. De plus, la taille de la zone endommagée ainsi que l'état de contrainte et de déformation dans la zone entaillée permettront de mieux ajuster les paramètres du modèle décrivant le développement de l'endommagement à partir du nombre limité d'essais disponibles. Ceci implique la construction d'un modèle et l'identification des paramètres correspondants pour analyser la déformation et l'état des contraintes dans la zone entaillée. Dans le cadre de cette étude, un modèle existant a été utilisé et adapté.

Le manuscrit

*Ce manuscrit est structuré en neuf chapitres et trois annexes. Les matériaux de l'étude: deux aciers Grade 92 sont présentés dans le **chapitre I**. Les éléments de la microstructure ainsi que le rôle des éléments d'alliage dans ces aciers sont présentés dans le **chapitre I**.*

*Une étude bibliographique est présentée dans le **chapitre II**. Afin de préciser le contexte de l'étude et de regrouper toutes les données disponibles dans la littérature en lien avec le travail de cette thèse. La perte de résistance en fluage dans les aciers 9-12%Cr, les solutions pour améliorer leur résistance en fluage ainsi que l'effet du vieillissement thermique sur le*

comportement en fluage des aciers Grade 92 et Grade 91 sont discutés dans ce chapitre à partir des données publiées disponibles. Les données quantitatives disponibles sur la microstructure de l'acier Grade 92 après des temps prolongés d'exposition au fluage sont également présentées dans ce chapitre.

Dans le cadre de cette étude des essais de fluage ont été réalisés sur des éprouvettes avec différentes géométries (lisse, entaillées) et avec différents états de la microstructure avant le fluage (pré-vieillie, pré-fatiguée). La géométrie des éprouvettes lisses et entaillées ainsi que la caractérisation microstructurale des matériaux vieillis sont présentés dans le ***chapitre III****. La préparation des éprouvettes pré-fatiguées est présentée dans l'****Annexe A****. La procédure de dépouillement des courbes de fluage est expliquée dans le* ***chapitre IV****.*

Les résultats des essais de fluage réalisés à 600°C et 650°C sont présentés dans le ***chapitre V*** *et le* ***chapitre VI****, respectivement. Les résultats de ces essais ont été analysés en utilisant des relations bien connues comme la loi de Norton ou l'équation de Monkman-Grant. Le* ***chapitre VII*** *est dédié à l'expertise des éprouvettes après fluage. Une attention particulière à été portée à l'obtention de données quantitatives concernant l'évolution microstructurale et l'endommagement de ces éprouvettes. Une quantification de la taille de phases de Laves et de l'endommagement a été réalisée dans les éprouvettes P92 testées pendant des temps prolongés à 600°C et 650°C. Des observations MET sur des répliques extractives ont également été réalisées sur ces éprouvettes.*

*Une étude complémentaire a été réalisée au début de la thèse sur une éprouvette en acier Grade 91 testée pendant 113431h à 600°C ainsi que sur le même acier à l'état de réception. Les résultats de cette étude sont regroupés dans l'****Annexe B*** *et l'****Annexe C*** *sous la forme de deux articles publiés.*

À partir des résultats expérimentaux, un modèle mécanique a été développé pour décrire le comportement en fluage de l'acier Grade 92 à 600°C et 650°C. Ce modèle est présenté dans le ***chapitre VIII****.*

Contents

List of Figures

List of Tables

Acronyms

- **A**: fracture elongation of crept specimen
- **EBSD**: electron backscatter diffraction (in the SEM)
- **EBSD-IQ**: image quality EBSD map. The lighter the grey level the better the quality of the diffraction pattern
- **EBSD-IPF**: inverse pole figure of sample showing crystal orientation of a particular sample direction
- **EDX=EDS**: energy dispersive X-ray spectrometry
- σ_n: engineering stress
- σ_{VM}: equivalent von Mises stress
- **FEG-SEM**: field emission scanning electron microscopy
- **FE**: finite element
- **OPS**: colloidal silica slurry used for final polishing
- $\dot{\varepsilon}_{ss}$: secondary creep rate
- **SEM**: scanning electron microscopy/microscope
- **SEM-SE**: scanning electron microscopy in secondary electron imaging mode
- **SEM-BSE**: scanning electron microscopy in backscattered imaging electron mode
- **TEM**: transmission electron microscopy/microscope
- t_r: time to rupture
- **Z**: reduction of area of crept specimen (at fracture)

Chapter -I-

General literature survey

Contents

Introduction

Great research efforts are being conducted nowadays for solutions to reduce global warming. Thermal efficiency improvement of fossil power plants is by far the lowest cost method to reduce all emissions including those of CO_2 (Beer, 2007). Increasing thermal efficiency involves more sever thermo-mechanical solicitations for components and advanced alloys with improved long-term creep strength are requested. Thus, development of heat resistant steels with high long-term creep strength is essential for thermal efficiency improvement.

Experience of steels such as Grade 92, presently successfully used for components in power plants can play a key role in the development of new heat resistant steels.

This study aims at a better understanding of both microstructural evolution of the Grade 92 steel during long-term creep exposure at 600°C-650°C and its effect on the creep strength loss. The present study also aims at a modeling various mechanisms involved in the long-term creep behavior of the Grade 92 steel.

High temperature exposure could enhance metallurgical evolution of the steel and consequently affect its creep flow. Thus, models are needed to quantitatively describe the creep behavior of steels during long-term creep exposure at high temperatures.

A literature survey regarding published data mentioning creep behavior or metallurgical evolution of the Grade 92 steel during creep and/or thermal exposure at 600°C and 650°C was conducted. As only few data was found on these issues the literature survey was extended to tempered martensitic ferritic 9-12%Cr steels to better understand the metallurgical evolution of these steels and its influence on their creep behavior.

In the beginning of this chapter a general background of this study is briefly presented. Special attention was focused on microstructural quantitative data of the Grade 92 steel during long-term exposure to creep or aging at 600°C and 650°C which could be further used in the modeling of the creep behavior.

Models describing the precipitate evolution during thermal/ creep exposure and models coupling creep deformation to microstructural parameters are presented in the end of this chapter.

Introduction

D'importants travaux de recherche sont menés partout dans le monde pour prévenir le réchauffement de la planète. Les émissions de centrales thermiques de production d'électricité, parmi lesquelles le CO_2 responsable de réchauffement climatique peuvent être diminuée par une amélioration du rendement thermodynamique de ce type d'installation. Une augmentation du rendement thermodynamique implique des sollicitations thermo-mécanique de plus en plus sévères pour les matériaux des composants, c'est pourquoi des nouveaux alliages plus résistants à haute température sont nécessaires.

L'expérience des aciers déjà utilisés pour applications à haute température, comme l'acier Grade 92, peut jouer un rôle important dans le développement des nouvelles nuances d'aciers avec une résistance au fluage à long terme améliorée.

Cette étude porte sur une meilleure compréhension de l'évolution métallurgique de l'acier Grade 92 pendant des temps prolongés d'exposition au fluage à 600°C et 650°C et son influence sur la perte de résistance au fluage. Cette étude porte aussi sur une modélisation des différents mécanismes impliqués dans le comportement en fluage de l'acier Grade 92.

L'exposition à haute température intensifie l'évolution métallurgique de l'acier ce qui peut diminue sa résistance au fluage. Par conséquent des modelés quantitatifs sont nécessaire pour estimer la résistance au fluage pendant des temps prolongés.

Une étude bibliographique concernant le comportement en fluage à 600°C et 650°C de l'acier Grade 92 et son évolution métallurgique pendant le fluage ou le vieillissement thermique a été réalisée. Comme la littérature manque de données à ces sujets, l'étude bibliographique a été étendue sur la famille des aciers martensitique à 9-12%Cr pour une meilleure compréhension de l'évolution métallurgique des ces aciers et leur influence sur la résistance au fluage.

Le contexte général de cette étude est présenté dans le début de ce chapitre. Des données quantitatives disponibles dans la littérature sur la microstructure de l'acier Grade 92 après exposition au fluage à 600°C et 650°C sont regroupées dans ce chapitre.

Des modèles décrivant l'évolution des précipités pendant l'exposition au fluage ou le vieillissement thermique ou des modèles permettant de lier les paramètres microstructuraux à la déformation sont mentionnés à la fin du ce chapitre.

I.1 General background of the study

In our days, great interest and significant efforts are shown worldwide to energy conservation and environmental protection. As can be seen in figure I.1 fossil fuels such as oil, gas or coal are dominant in the production of electricity in the most of European countries.

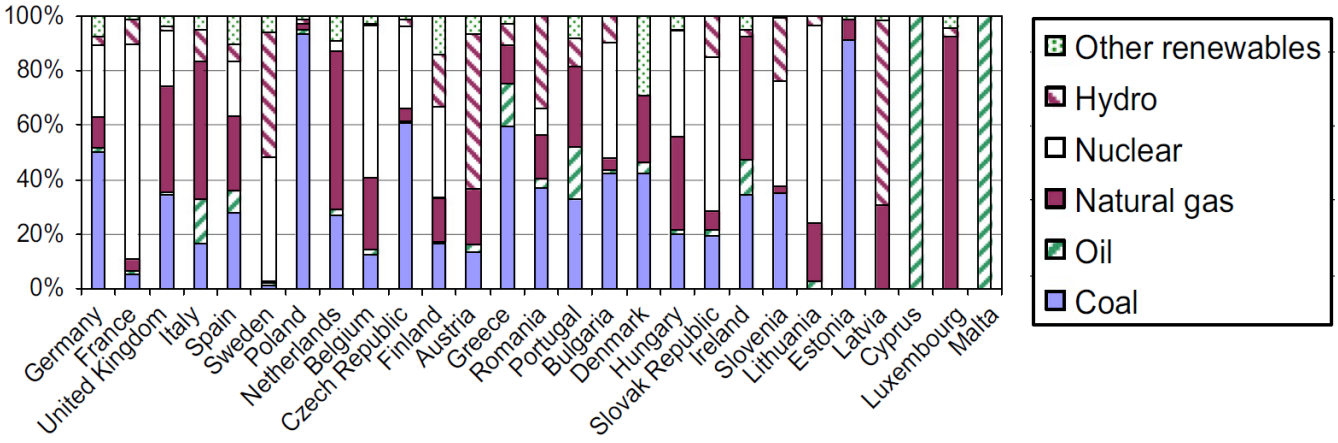

Figure I.1 : Fuel mix power generation by country in 2005 (Graus and Worrell, 2009)

Low emissions together with a more efficient way of fuels consumption are wanted for fossil power plants. There are two main ways for reducing the carbon dioxide (CO_2) emissions from fossil power plants.

The first one consists in capture and storage of CO_2 which can lead to almost zero emission power plants (Oliver, 2008), (Rubin et al., 2007). This involves capture, compression, transport and storage. CO_2 can be stored in oil or gas fields and deep saline aquifers (Vangkilde-Pedersen et al., 2009). Geological sequestration sites are required to be at depths higher than 800m bellow surface or sea bottom while the uppers layers consists of impermeable rocks (Koukouzas and Typou, 2009).

Gas separation membranes, which consist of selective membranes with high permeability for CO_2, 0_2 or H_2, are under development (Czyperek et al., 2009). This technology can allow high purity CO_2 in a readily condensable form.

A solution aims at improvement of thermal efficiency of fossil power plants by increasing steam conditions to higher ranges of temperature and pressure. This imposes more severe

service conditions for heat resistant steels and materials with optimized properties are needed. Figure I.2 shows the evolution of the plant steam operating conditions in the last fifty years together with the research programs conducted for the development of the heat resistant steels. The historical development of the chromium heat resistant steels together with their service temperatures were presented previously, see figure II.1.

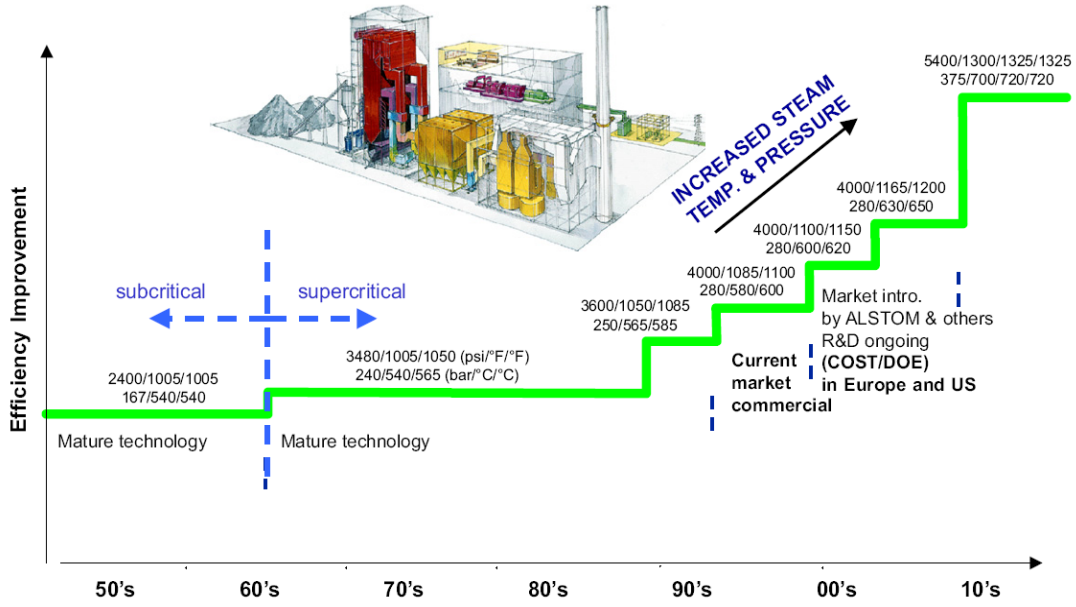

Figure I.2 : Historical and projected future trends in plant steam conditions with relatile indication of efficiency improvement (Perrin and Fishburn, 2008)

Research programs have been simultaneously conducted in the United States (EPRI), Japan (EFDC), and Europe (COST 501 and 522, ECCC, PIPPE). Most results of COST research programs have been reported at a series of COST conferences held in Liège, Belgium, in 1990, 1994, 1998, 2002, 2006 and most recently to be held in 2010.

The COST actions 501 and 522 have developed firstly 9-12% Cr steels with various contents of W and/or Mo and secondary steels with a moderate level of boron (Scarlin et al., 2004). The COST 536 actions aim at the development of 9-12% Cr steels by increasing the boron content.

The ECCC (European Creep Collaborative Committee) generated and provided data packages for the analysis of creep properties of base materials and weldments under study in COST and other programs (Merckling, 2008).

Thermie AD700 is an ambitious project which aims at increasing the steam temperature of USC plants up to 700°/720°C, primarily through the use of nickel base alloys (Millich et al., 1994).

I.2 The creep strength loss of the 9-12%Cr heat resistant steels

The creep strength of the 9-12%Cr heat resistant steels combines provided by the W and Mo atoms in solid solution in the matrix and precipitation-aided strengthening given by both MX type carbo-nitrides (M=V, Nb, Cr; X=N, C) and $M_{23}C_6$ type carbides (M=Cr, Fe, Mo,

W; X=C(B)). High dislocation density before creep testing and fine matrix substructure also contribute to the creep strengthening of these steels.

Microstructural evolution during long-term creep exposure may impair the creep strength of heat resistant steels. The main microstructural degradation mechanisms of the 9-12% Cr steels reported during creep exposure at 600°C and 650°C precipitation of new phases (Laves phases; Z-phases), coarsening of precipitates and recovery of the tempered martensite matrix. One of these mechanisms could be predominant with respect to the other microstructural degradation mechanisms as a function of the steel chemical composition and/or the creep testing conditions.

This section aims at briefly presenting causes of the creep strength loss of the 9-12%Cr heat resistant steels. This is a wide and complex subject and there are rather few published data about it. A fairly complete review of the strengthening mechanisms in 9-12%Cr heat resistant and loss of their creep strength can be found in reference (Maruyama et al., 2001).

In this section the creep strength of some 9-12%Cr heat resistant steels is analyzed together with their microstructural evolution during creep. Only few cases of creep strength loss are considered and complementary data are given in this section compared to these in reference (Maruyama et al., 2001).

I.2.1 11-12%Cr heat resistant steels

A sudden loss of the creep rupture strength is often observed in some 11-12%Cr heat resistant steels compared to that of the 9%Cr heat resistant steels. This is illustrated in figure I.3. The creep strength of the T91 and T92 steels (9%Cr tempered martensitic steels) considered in figure I.3a,b is representative for the creep behavior of the Grade 92 steel and Grade 92 steel, respectively.

The creep behavior of the T122 steel is typical for the 11-12%Cr steels which exhibits a premature loss of the creep strength. T122 steel shows a severe loss of the creep strength after about 10^4h at 600°C (i.e. 873K) and after about 2,000h of creep exposure at 650°C (i.e. 923K). Note that the creep strength of the T122 steel is higher compared to that of T91 and T92 steels for testing time lower than 1,000h both at 600°C and 650°C, for longer testing time the creep strength of the T122 steel decreases and become lower than that of the Grade 91 or Grade 92 steels.

The premature loss of creep strength observed in some 11-12%Cr steels is often explained by the precipitation of modified Z-phase which leads to partial or complete dissolution of MX-type precipitates (Danielsen and Hald, 2006), (Sawada et al., 2007). Thus, the precipitation of this phase could have a detrimental effect on the long term creep strength of the steel since MX-type precipitates are considered to have a significant contribution to the creep strength. The precipitation of modified Z-phase is also observed in 9%Cr heat resistant steels but in lower amount and after longer exposure times compared to that in 11-12%Cr heat resistant steels (Danielsen and Hald, 2007).

TAF650 steel (wt.%: 0.1C-0.55Mn-0.07Si-10.84Cr-0.14Mo-0.55Ni-2.63W-0.19V-0.06Nb-0.016N-0.019B-2.86Co, 1100°C/1h/oil+750°C/2h/air) also shows a pronounced drop in the creep strength after about 3,000h at 650°C (see figure I.4). Quantitative microstructural investigations of the Z6 (σ = 70MPa, t_r=18,870h), Z4(σ = 135MPa, t_r=4,379h) and Z4(σ = 100MPa, t_r=5,888h) specimens quoted in figure I.4 revealed that the subgrain size increases markedly in both head and gauge length of the Z6 specimen compared with Z4 and Z5 specimens (Sklenička et al., 2003).

In addition substantial amount of relatively large particles of $M_{23}C_6$ carbides, Laves phases and Z-phases together with very rare fine particles were observed in the Z6 specimen. It was thus concluded that precipitation and coarsening of Z-phase promote recovery of the tempered

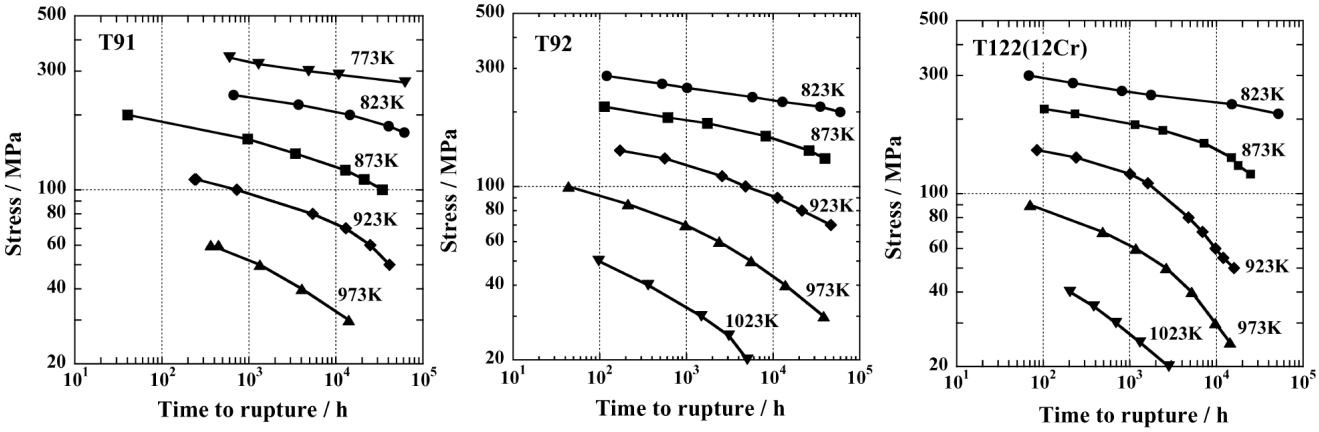

a) b) c)

	C	Si	Mn	P	S	Ni	Cr	Mo	W	Cu
ASME-T91	0.0900	0.29	0.35	0.009	0.002	0.28	8.70	0.90	—	0.032
ASME-T92	0.0980	0.29	0.42	0.007	0.0013	0.13	9.50	0.36	1.74	—
ASME-T122-s	0.1300	0.31	0.60	0.017	0.001	0.36	10.65	0.33	1.87	0.86
ASME-T122-d	0.1100	0.27	0.59	0.015	0.002	0.33	12.10	0.34	1.82	0.82

	V	Nb	Al	B	N	Normalizing	Tempering
ASME-T91	0.22	0.072	0.001	—	0.044	1323K, 10min A.C.	1038K, 30min A.C.
ASME-T92	0.19	0.062	0.009	0.0020	0.0462	1373K, 12min A.C.	1053K, 60min A.C.
ASME-T122-s	0.19	0.050	0.007	0.0024	0.057	1323K, 10min A.C.	1043K, 360min A.C.
ASME-T122-d	0.19	0.060	0.012	0.0030	0.066	1323K, 10min A.C.	1063K, 180min A.C.

d) s and d mean single and dual phase, respectively.

Figure I.3 : Creep rupture strength of the T91 steel (a), T92 steel (b) and T122-d steel (c). d) Chemical composition and heat treatments of the investigated steels (Sawada et al., 2007).

martensite microstructure and results in a decrease in the creep strength (Sklenička et al., 2003). However, no quantitative data on precipitates and subgrains size are reported in reference (Sklenička et al., 2003).

Quantitative microstructural investigations of specimens in TAF650 steel after creep testing at 650°C for times lower than 6,000h were also conducted by (Sawada et al., 1999), specimen referenced [17] in figure I.4. The authors reported an increase in lath width from about 0.4 µm in the as-received state to about 2 µm after about 2×10^7s (i.e. ≈5,600h) of creep exposure at 650°C, 98.1MPa and a decrease in dislocation density from about $1 \times 10^{15}\mathrm{m}^{-2}$ to $2 \times 10^{13}\mathrm{m}^{-2}$ after creep exposure (Sawada et al., 1999).

(Sawada et al., 1999) did not mention the precipitation of modified Z-phase in TAF650 steel after creep exposure; the formation of this phase probably only occurs during longer temperature exposure times than that of the investigated specimens.

Available published data on the precipitation of modified Z-phase in the 9-12%Cr heat resistant steels are gathered in section I.4.4

Quantitative microstructural characterization of a 12%Cr tempered martensite steel (German Grade X20, see chemical composition in table I.18) during long-term aging and creep using interrupted creep tests loaded for 12,456h, 51,072h, 81,984h and 139,971h-ruptured at 550°C under 120MPa revealed that long-term creep mainly affects subgrain coarsening (Aghajani et al., 2009b). An increase in subgrain size, an increase in fraction of low-angle boundaries and a decrease in carbide-induced stabilization of subgrain boundaries were reported to be the dominant degradation mechanisms in this steel (Aghajani et al., 2009b).

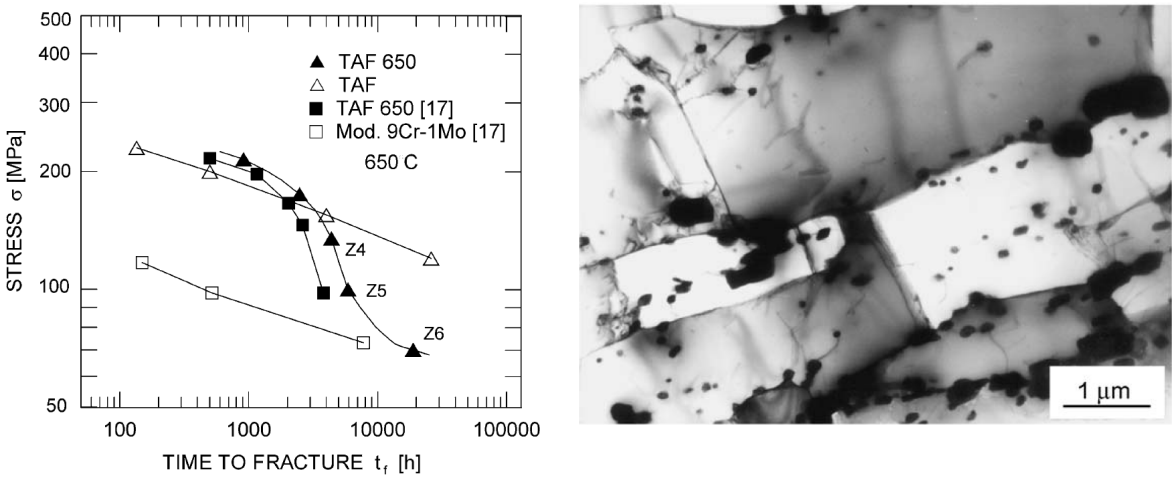

a) **b)**

Figure I.4 : a) Creep rupture strength of the TAF650 steel compared to that of T91 steel, b) Microstructure of the Z6 specimen (gauge) (Sklenička et al., 2003)

I.2.2 9%Cr heat resistant steels

The long-term creep strength loss of 9%Cr heat resistant steels such as Grade 92 and Grade 91 is believed to be due to precipitation of Laves phases (Seung et al., 2006), (Yoshizawa et al., 2009), growth of $M_{23}C_6$ carbides rather than precipitation of modified Z-phase. However, there are rather few quantitative data on the microstructure of the Grade 92 steel after long-term creep exposure (testing time higher than 2×10^4h) both at 600°C and 650°C.

The formation of a completely recovered band free of subgrains along the prior austenitic grain boundaries (PAGBs) was reported to be another possible cause of the creep strength loss of these steels (see figure I.5, Grade 91 steel).

Significant recovery along the PAGBs was related to the precipitation of modified Z-phase which occurs preferentially at PAGBs. Precipitation and growth of modified Z-phase put into solution the MX-type precipitates in the vicinity of PAGBs and thus promoted recovery close to PAGBs (Abe, 2004). The formation of a recovered band is not observed at high stresses, this mechanism is characteristic of low stress and long time creep. However, it has been only scarcely reported so far.

I.3 Improvement of long-term creep strength

This section aims to present some new alloy-design concepts that have been proposed to develop heat resistant steels operating at 650°C. Note that only relatively short-term creep data are available for these new-concept steels and their better creep strength is not confirmed for long-term exposure.

Figure I.6 shows the time to rupture (t_r) and minimum creep rate ($\dot{\varepsilon}_{ss}$) of 9Cr-3W-3Co-VNb-0.05N steel with various carbon contents at 650°C under 140MPa. Lifetime (t_r) and $\dot{\varepsilon}_{ss}$ are independent of the carbon content between 0.05 and 0.15 wt.%. The t_r significantly increases when the carbon content decreases below 0.018wt.%.

The 9Cr-3W-3Co-VNb-0.05N steel with 0.002 wt.%C exhibits a lifetime of about 10^4h at 650°C under 140MPa (see figure I.6) which is almost one hundred times higher than that of the Grade 92 steel under the same testing conditions. The microstructure of this steel consists

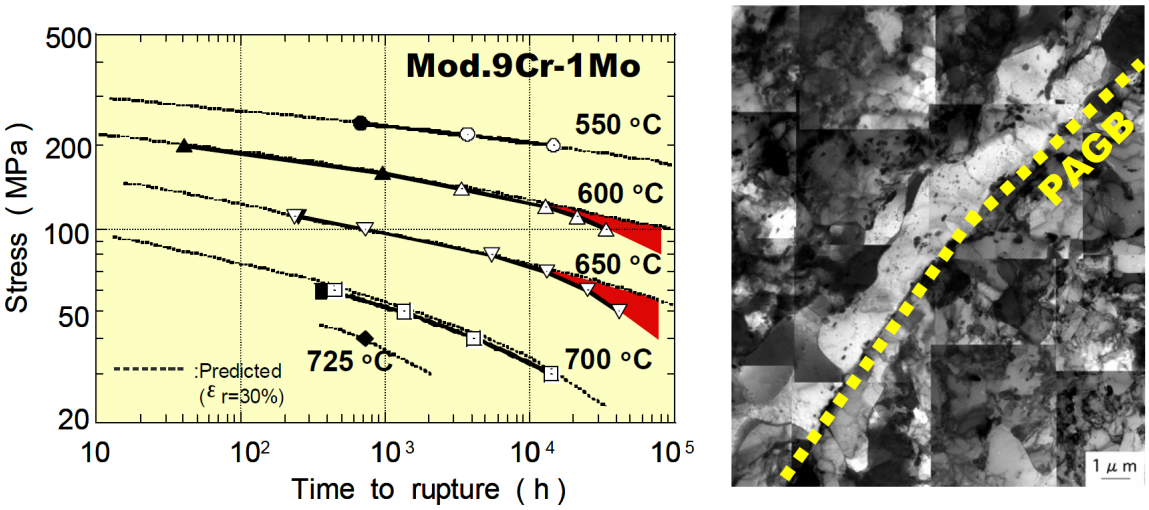

Figure I.5 : a) Creep rupture strength of a Grade 91 steel (T91), b) Completely recovered band in the vicinity of prior austenitic grain boundaries in a Grade 91 steel after 34,141h of creep at 600°C, 100MPa (Abe, 2004), (Kushima et al., 1999), (Kimura et al., 2000)

of a fine dispersion of nano-sized MX-nitrides of vanadium and niobium along boundaries as well as in the matrix without $M_{23}C_6$ carbides.

Note that the high amount of W and Co in these steel provides significant strengthening. Even the 9Cr-3W-3Co-VNb-0.05N steel with carbon content similar (i.e. 0.1 wt.% C) to that in Grade 91 and Grade 92 shows a t_r much higher than that of the Grade 91 and Grade 92 at 650°C under 140MPa.

The superior creep strength of the 9Cr-3W-3Co-VNb-0.05N steel with 0.002 wt.% C was tried to be further improved by increasing the amount of MX-type precipitates. To aim this the nitrogen content was increased up to 0.1 wt.%. Increasing nitrogen content promotes coarsening of the MX nitrides and precipitation of Z phase leading to a decrease in the creep strength, see figure I.7. Precipitation of modified Z-phase occurs for shorter times in the 0.07N and 0.10N steels compared to that in 0.05N steel (Sawada et al., 2004). After tempering large Cr_2N as well as fine MX nitrides were distributed along all kinds of boundaries although the amount of Cr_2N was slight. The coarsening rate of the Cr_2N during exposure at elevated temperature is usually larger than that of MX nitrides (Abe et al., 2007). Coarsening of MX nitrides observed in the 0.07N and 0.10N steels during creep is thought to be mainly due to an effect of Z-phase precipitation, which puts the smaller MX precipitates into solution (Abe et al., 2007).

The premature loss of creep strength observed in some 11-12%Cr heat resistant steels was associated with the growth and/or coarsening of modified Z-phase rather than with the beginning of its precipitation (Sawada et al., 2007). As precipitation of modified Z phase was observed in 0.05N, 0.07N and 0.10N steels after creep exposure at 650°C, these steels could probably exhibit a sudden loss of the creep strength after about 10^4h.

The modified Z-phase is the most stable nitride thus the steels strengthened by MX-type precipitates could be affected by Z-phase precipitates after more or less exposure times.

12%Cr heat resistant steels strengthened by finely dispersed Z-phase could be another new alloy concept for development of high chromium heat resistant steels. This concept is similar to that of finely dispersed nano-size precipitates proposed by (Abe et al., 2007) and it consists

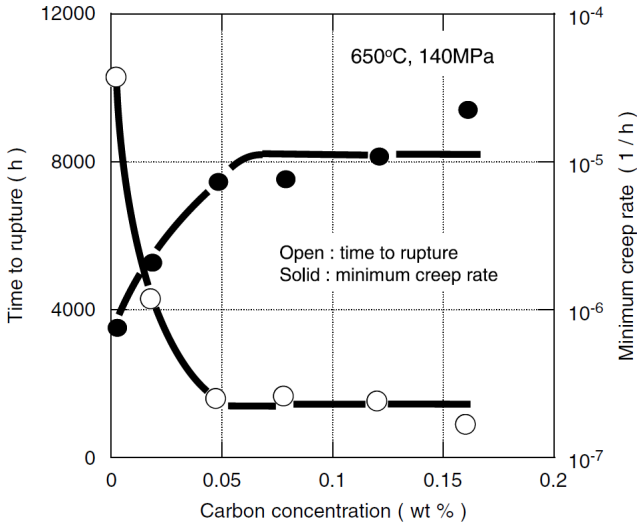

a)

b)

	C	Si	Mn	Cr	W	V	Nb	Co	N (mass %)	B	Normalizing	Tempering
0.002C	0.002	0.29	0.51	9.19	2.96	0.20	0.060	3.09	0.049	0.0070	1100 °C × 0.5 h	800 °C × 1 h
0.018C	0.018	0.29	0.50	9.16	2.91	0.20	0.058	2.94	0.050	0.0058	1100 °C × 0.5 h	800 °C × 1 h
0.047C	0.047	0.30	0.51	9.24	2.90	0.20	0.059	3.07	0.050	0.0063	1100 °C × 0.5 h	800 °C × 1 h
0.078C	0.078	0.31	0.51	9.26	2.93	0.20	0.061	3.08	0.049	0.0064	1100 °C × 0.5 h	800 °C × 1 h
0.12C	0.120	0.30	0.50	9.27	2.93	0.20	0.058	3.08	0.048	0.0065	1100 °C × 0.5 h	800 °C × 1 h
0.16C	0.160	0.30	0.51	9.26	2.94	0.20	0.058	3.08	0.047	0.0061	1100 °C × 0.5 h	800 °C × 1 h

Figure I.6 : a) Time to rupture and minimum creep rate of 9Cr-3W-3Co-VNb-0.05N steel with various carbon contents at 650°C under 140MPa; b) Chemical composition and heat treatment of the studied steels (Abe et al., 2007)

.

of alloys with only MX-type precipitates homogeneously distributed whithin the matrix which transforms into modified Z-phase in a relatively short time (less than 1,000h). This concept implies that each MX-type precipitates transforms into a Z-phase, thus no change in number density or size of precipitates occurs during long term creep exposure. The model alloys used by (Cipolla et al., 2010b) for the study of precipitation and growth of modified Z-phase could be an illustration of this concept.

However, complementary studies are needed to study whether the precipitation strengthening of the small size modified Z-phase is efficient against matrix recovery. Complementary studies are also needed to retarded or to suppress a possible growth of modified Z-phase during long-term creep exposure.

Complementary methods allowing to estimate in a relatively short time the effect of thermal aging on the creep strength could be useful in allow design of new heat resistant steels.

In this study creep tests were conducted on thermally aged specimens, thermo-mechanically prepared specimens and notched specimens to study the effect of microstructural evolution on the creep strength of Grade 92 steel. These tests have shown that typical long-term creep damage and microtexture state could be obtained in a shorter creep testing time.

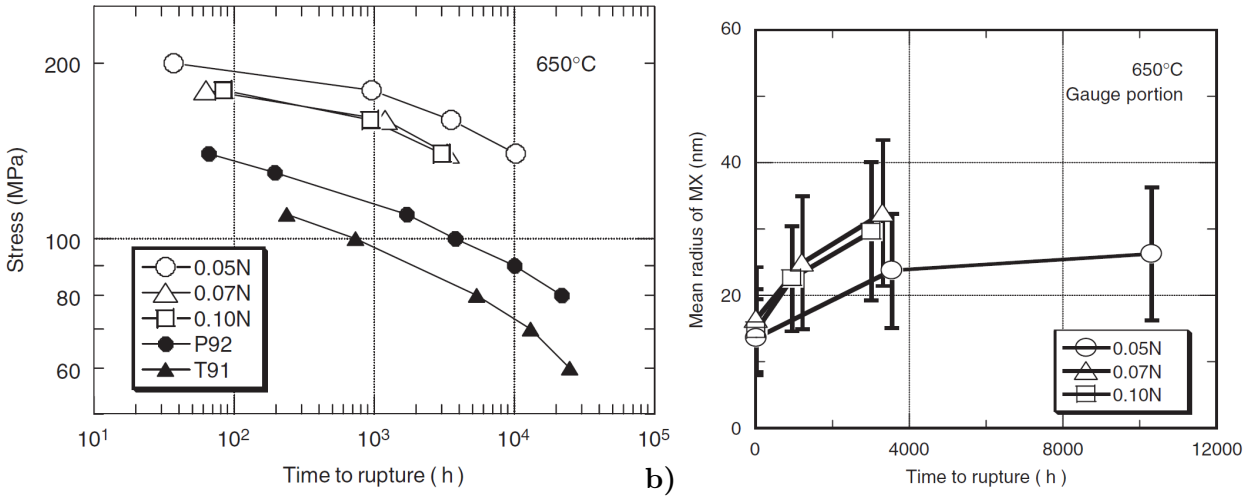

c)

	C	Si	Mn	Cr	W	V	Nb	Co	N (mass %)	B	Normalizing	Tempering
0.05N	0.0020	0.29	0.51	9.19	2.96	0.20	0.060	3.09	0.049	0.0070	1100 °C × 0.5 h	800 °C × 1 h
0.07N	0.0019	0.30	0.50	8.84	3.02	0.20	0.059	3.02	0.074	0.0066	1200 °C × 0.5 h	790 °C × 4 h
0.10N	0.0020	0.29	0.53	8.87	2.90	0.19	0.060	3.03	0.103	0.0062	1200 °C × 0.5 h	790 °C × 4 h

Figure I.7 : a) Time to rupture of 9Cr-3W-3Co-VNb-0.002C steel with various nitrogen contents at 650°C; b) Mean radius of MX nitrides for the 0.05N, 0.07 and 0.10N steel during creep at 650°C; c) Chemical composition and heat treatment of the studied steels (Abe et al., 2007)

.

I.4 Microstructural evolution of the 9-12% Cr heat resistant steels during creep at 600°C and 650°C

The microstructure of Grade 92 steel consists of tempered martensite matrix with a high dislocation density (i.e. $7.5 \pm 0.9 \times 10^{14} \mathrm{m}^{-2}$ (Ennis and Czyrska-Filemonowicz, 2002)) inside subgrains and precipitates (carbides and carbonitrides). Boundaries between prior austenite grains, packets, blocks, laths are mainly decorated with $M_{23}C_6$ carbides (M=Cr, Fe, Mo) while MX carbonitrides (M=V, Nb and X= C, N) precipitate finely and with a high number density within the martensite laths.

Details about the evolution of each kind of precipitates during creep or thermal aging at 600°C and 650°C is discussed in the following sections based on the available published data.

I.4.1 $M_{23}C_6$ carbides

$M_{23}C_6$ carbides precipitate during tempering at all kinds of boundaries (i.e. between prior austenite grains, packets, blocks, laths). The $M_{23}C_6$ carbides are enriched in Cr, they also contain small amounts of Fe, W and Mo.

(Zielińska-Lipiec et al., 1997), (Ennis et al., 2000) reported an increase in the average diameter of the $M_{23}C_6$ carbides from 72±16 nm to 89±12 nm when the tempering temperature is increased from 715°C to 775°C. This increase could not be considered as significant given the uncertainty of the measurements.

I.4.1.1 Chemical composition

Atom probe field ion microscopy (APFIM) analysis revealed the following chemical composition of $M_{23}C_6$ carbides in an as-received P92 steel: (wt. %) 26.4±2.1Fe-50.0±2.4Cr-0.4±0.3Mn-0.3±0.2Ni-3.8±1.0Mo- 11.5±2.3W-0.9±0.4V-6.0±0.9C-0.03±.03B (Hättestrand et al., 1998).

After 10^4h of thermal aging at 600°C of the same P92 steel the chemical composition of carbides becomes: (wt. %) 18.9 ± 0.7Fe-57.0±0.9Cr-1.0 ± 0.2Mn-0.1 ± 0.05Ni-4.2 ± 0.4Mo-12.2 ± 1.0W-0.4 ± 0.1V-6.2 ± 0.4C-0.04 ± .01B (Hättestrand et al., 1998).

An increase in the Cr content and a decrease in the Fe content of $M_{23}C_6$ carbides is reported during creep exposure at 600°C and 650°C in some 9-12% Cr tempered martensitic steels (Lundin et al., 1997), (Ghassemi-Armaki et al., 2009), (Kimura et al., 2002). Similar evolution of $M_{23}C_6$ carbides is expected to happen during creep exposure of the Grade 92 steel. To the author's knowledge except for the APFIM analysis previously mentionned there are no published data on the evolution of average chemical composition of $M_{23}C_6$ carbides during creep exposure at 600°C and 650°C of the Grade 92 steel.

I.4.1.2 Growth during creep or thermal aging at 600°C and 650°C

Due to their small size (average equivalent diameter about 100-120nm) identification of $M_{23}C_6$ carbides can be done using TEM techniques. Usually combination of energy-filtered TEM (EFTEM), energy-dispersive X-ray spectrometry (EDS) and image analysis are carried out for size evaluation of $M_{23}C_6$ carbides.

In table I.1 are summarized published data on the size of $M_{23}C_6$ carbides in Grade 92 steels during creep or thermal exposure at 600°C and 650°C for various amounts of time.

For similar exposure time to creep or aging there is a discrepancy between the size of $M_{23}C_6$ carbides published by different studies. This is probably because of the limited sample area and limited number of particles which can be investigated using TEM techniques.

Table I.1 : Average equivalent diameter (D) of $M_{23}C_6$ carbides in Grade 92 steels during creep or thermal aging at 600°C and 650°C

Testing conditions	Time [h]	D [nm] of $M_{23}C_6$	Chemical composition (wt.%) & heat treatment of Gr. 92 steel under study	Observations
600°C, creep	As-received 1,500 10,000 33,000 ≃57,000	89±13 119±8 125±10 131±12 ≃ 170	0.124C-0.02Si-0.47Mn-0.011P-0.006P-9.07Cr-0.46Mo-1.78W-0.19V-0.063Nb-0.003B-0.043N-0.06Ni-0.002Al; 2h/1070°C+12h/775°C air cooling. (Ennis et al., 2000), (Ennis and Czyrska-Filemonowicz, 2002)	-The levels of stress corresponding to the investigated crept specimens are not mentioned - TEM investigations on thin foils
600°C, aging	As-received 1,000h 3,000h 10,000h 26,000h	84.1±6.8 83.9±11 88.4±9.1 81.8±8.3 95.5±8.6	0.11C-0.04Si-0.46Mn-0.008P-8.96Cr-0.47Mo-1.84W-0.20V-0.07Nb-0.001B-0.05N-0.06Ni; annealed+2h/770°C air cooling (Gustafson and Hättestrand, 2002)	- EFTEM investigations
650°C, aging	1,000h 3,000h 10,000h 26,000h	104 ±16 104 ±8.7 124 ±16 132 ±13	0.11C-0.04Si-0.46Mn-0.008P-8.96Cr-0.47Mo-1.84W-0.20V-0.07Nb-0.001B-0.05N-0.06Ni; annealed+2h/770°C air cooling (Gustafson and Hättestrand, 2002)	- EFTEM investigations
600°C, creep	As-received ≃59,000	≃90 100	not mentioned (Hald and Korcakova, 2003)	stress levels are not mentioned; values picked from figures

I.4.1.3 Effect of stress

Applied stress and/or strain seem to enhance growth of $M_{23}C_6$ carbides. The size of $M_{23}C_6$ carbides measured in the gauge portion of the crept specimen is slightly higher than that measured in the head of the crept specimens, see figure I.8. This is also observed by (Hättestrand and Andrén, 2001).

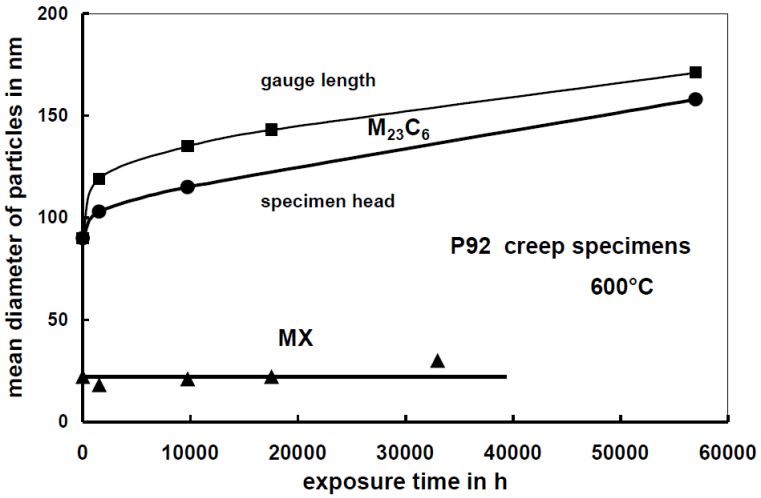

Figure I.8 : Evolution of average equivalent diameter (D) of $M_{23}C_6$ carbides in the Grade 92 steel during creep exposure at 600°C, (Ennis and Czyrska-Filemonowicz, 2002), (Czyrska-Filemonowicz et al., 2006)

The size of $M_{23}C_6$ carbides in the gauge part in figure I.8 corresponds to the values given in table I.1 for the references (Ennis and Czyrska-Filemonowicz, 2002), (Ennis et al., 2000).

I.4.1.4 Effect of alloy elements

Higher tungsten content of steel seems to limit the growth rate of $M_{23}C_6$ carbides. The size of $M_{23}C_6$ carbides is smaller and the growth rate during thermal exposure decreases when the tungsten content of the steel Fe-0.1C-9Cr-0.5Mn-0.3Si (%wt.) is increased from 0 to 4 wt.%, see figure I.9. The effect of tungsten on the growth of $M_{23}C_6$ carbides is not fully understood and there are no complementary published data on this issue.

The decrease in growth rate of $M_{23}C_6$ carbides with the increase of tungsten content in the steel can be explained by the precipitation of Laves phases which depletes the matrix in W and other elements which could be otherwise available to the growth of $M_{23}C_6$ carbides.

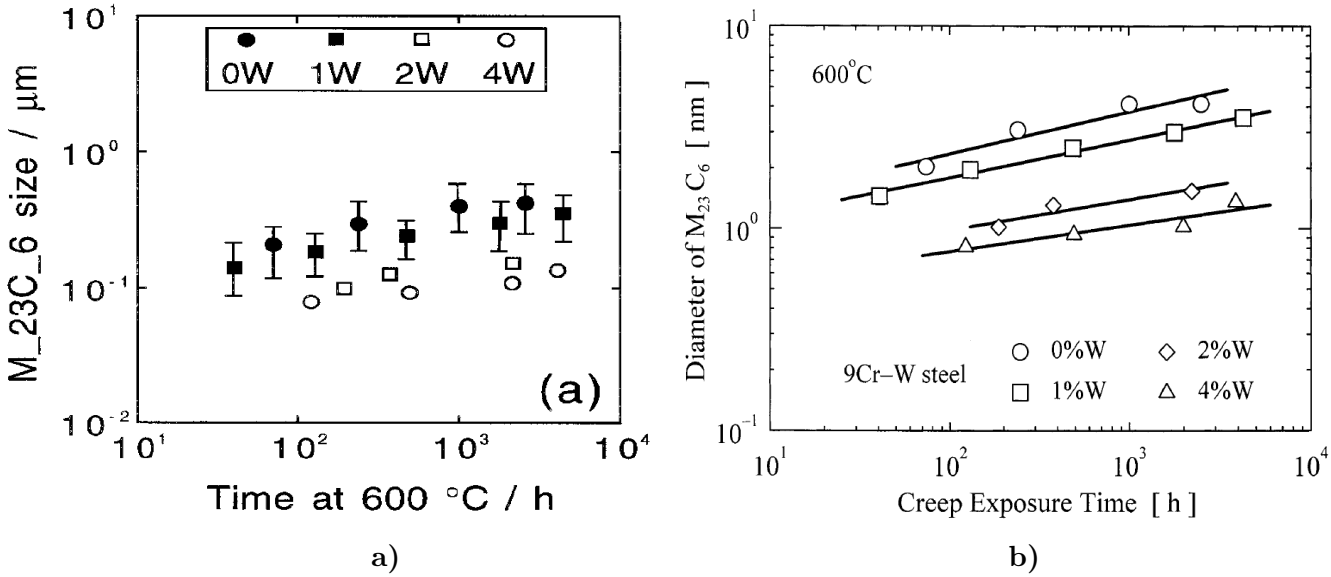

a) b)

Figure I.9 : Size of $M_{23}C_6$ carbides as a function of the exposure time at 600°C and of the tungsten content of the steel a) (Bhadeshia, 2001), b) (Maruyama et al., 2001)

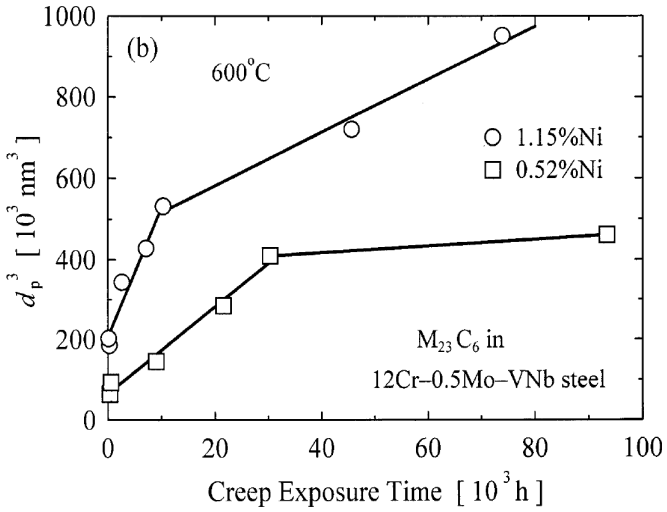

Figure I.10 : Size of $M_{23}C_6$ carbides as a function of the nickel content in 12Cr-0.5Mo-VNb steels at 600°C (Maruyama et al., 2001)

The scale in figure I.9b is most probably wrong, also the results in figure I.9b seem to be similar to these in figure I.9a. Thus, the results in figure I.9b most be used with caution.

Reducing nickel content in the 12Cr-0.5Mo-VNb steels slows down the growth rate of $M_{23}C_6$ carbides. Nickel content of the steel seem to influence the size of $M_{23}C_6$ carbides in the as-received conditions. The effect of nickel on the behavior of carbides during aging is not fully understood.

Boron seems to stabilize the growth of $M_{23}C_6$ carbides. The $M_{23}C_6$ carbides show a high growth rate in the Grade 91 steel during creep exposure at 600°C while in the Grade 92 steel these are relatively stable (Hald and Korcakova, 2003), (Hald, 2008). This is attributed to

the B content in the Grade 92 steel.

Published data concerning the effect of boron on the microstructural stability of the steels was discussed in the section II.3.

I.4.2 Laves phases

Laves phases in 9-12%Cr steels are intermetallic $(Fe,Cr)_2(Mo,W)$ phases. The precipitation of Laves phases only occurs during creep or isothermal aging. Laves phases are precipitating at all kinds of boundaries (i.e. prior austenite grains, blocks, packets, martensite laths).

Laves phase precipitation is not observed during the tempering heat treatment standardized by ASME (770°C, 2h).

The precipitation of Laves phase causes the depletion of W and Mo in solid solution in the matrix. Hence, the contribution of W and Mo to strengthening is partially lost and a decrease in the creep strength of the steel can appear.

Laves phases in Grade 92 steel are relatively large particles, their size can reach the width of martensite laths, as can be seen in the TEM micrograph in figure I.11a.

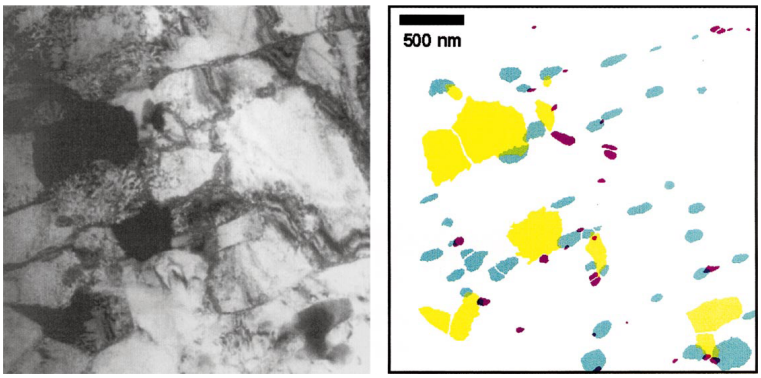

Figure I.11 : (left) Bright field TEM micrograph of P92 steel after aging (600°C, t=1,000 h); (right) the corresponding elements distribution: vanadium (red), chromium (blue), tungsten (yellow) showing MX precipitates (red), $M_{23}C_6$ carbides (blue), Laves phases (yellow) (Andrén, 2001)

Due to their relatively large size Laves phases could act as nucleation sites of creep cavities and thus reduce the long-term creep strength. However, so far, the effect of presence of Laves phase particles on the creep properties of the steel is not fully understood.

I.4.2.1 Chemical composition

Small amounts of carbon (0.8 at.%), silicon (3.7 at.%) and phosphorus (0.7 at.%) were revealed by APFIM techniques in the chemical composition of Laves phases in a 10.5 Cr steel (10.6Cr-0.11C-1.03Mo-1.01W-0.2V-0.04Nb-0.56Ni-0.06N-0.002B-0.11Si-0.5Mn-0.006P-0.005S) that had been creep tested for nearly 1,500h at 600°C (Lundin, 1996).

The chemical composition of Laves phases does not seem to evolve significantly during thermal or creep exposure (Aghajani et al., 2009a), (Hättestrand et al., 1998).

I.4.2.2 Precipitation and growth mechanisms

The precipitation and growth mechanisms of Laves phases in the Cr bearing tempered martensitic ferritic steel are not fully understood and various studies were conducted on this

issue. These mechanisms are apparently strongly depending on the chemical composition of the steel.

Silicon seems to play a key role in the nucleation and growth of Laves phases. (Hosoi et al., 1986) observed that reduction of the Si content of a 9%Cr steel (9.22Cr-2.25Mo-1.2Mn-0.78Ni-0.09V-0.04C-Si) slows down the precipitation of Laves phases. Moreover, no Laves phases are observed in this 9%Cr steel with negligible amount of Si.

(Aghajani et al., 2009a) reported that Laves phase particles do not reach thermodynamic equilibrium during almost 140,000h of creep exposure at 550°C of a 12%Cr steel (German grade X20). This was explained by the slow diffusion of silicon in the steel matrix (Aghajani et al., 2009a).

(Lundin, 1996) suggested that enrichment in phosphorous and silicon at the interface between carbides and matrix could favour the nucleation of Laves phases.

(Cui et al., 2001) observed that the size of Laves phases in 10Cr-6W-3Co steels are higher than that in the 10Cr-6W steel without Co for similar testing conditions. This suggests an influence of Co on the growth of Laves phases at least in the 10Cr-6W steels.

Copper seems to accelerate the nucleation of Laves phases. A higher amount of Laves phases is observed in the P122 steel (11Cr, 0.8 Cu wt.%) compared to P92 steel after 1,000h of aging at 600°C. (Hättestrand et al., 1998) suggested that small copper precipitates might be suitable nucleation sites for Laves phases.

The alloy elements in steels affect the solvus temperature of Laves phase, this could explain the influence of different elements on the precipitation and growth of Laves phases. When creep or aging temperature is close to solvus temperature the nucleation of Laves phases is difficult and low number of Laves phases will nucleate and will grow rapidly. (Murata et al., 2005) established a diagram of solvus temperature of Laves phases as a function of Mo and W content of the steel.

I.4.2.3 Growth during creep or thermal aging at 600°C and 650°C

Figure I.12 shows the corected mean diameter of Laves phases as a function of aging time at 600°C and 650°C realized both using EFTEM and FEGSEM. The corrected mean diameter takes into account the truncation of particle and it was evaluated using the following formula (Korcakova et al., 2001) under the assumption that all particles are spherical.

$$d_{corr} = \frac{4}{\pi} d_{obs} \simeq 1.27 d_{obs} \tag{I.1}$$

Significant growth of Laves phases is observed in the first 10^4h of thermal exposure both at 600°C and 650°C, see figure I.12. A higher temperature enhance their growth, larger sizes are observed after exposure at 650°C compared to 600°C for similar exposure times. The significant influence of temperature on the growth of Laves phase could possibly explained by the boundary diffusion of W which is accelerated by increase of temperature (Cermak et al., 1995).

The corrected mean diameters of Laves phase measured by EFTEM and given in figure I.12 are in good agreement with those measured by (Hättestrand and Andrén, 2001) using the same technique (EFTEM).

The results in figure I.12 show no significant influence of stress on the growth of Laves phases. This is consistent with results obtained in a P91 steel specimen that had been creep tested at 600C° for 113,431h and reported in (Panait et al., 2009).

At 600°C, the corrected mean diameter of Laves phase determined by FEGSEM (figure I.12a) is 20% smaller than the values measured by EFTEM. At 650°C the difference between the values measured by the two techniques is much higher, the corrected mean diameter of

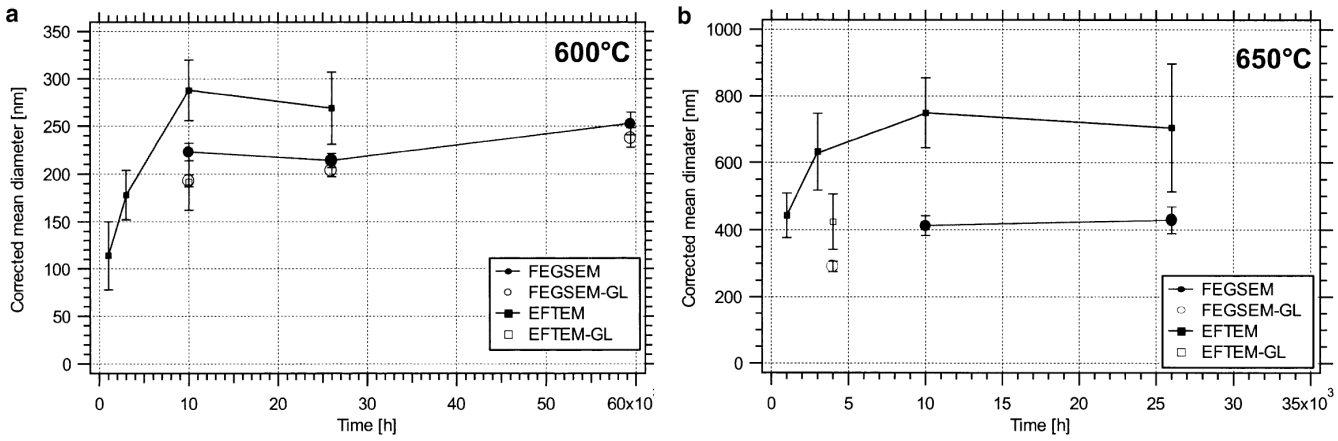

a) b)

Figure I.12 : Corrected mean diameter of Laves phase as a function of exposure time at 600°C(a) and at 650°C(b); (empty symbols-creep; full symbols-isothermal aging) (Korcakova et al., 2001)

Laves phase during exposure at 650°C determined by EFTEM is 60% higher than the values determinated by FEGSEM, figure I.12b.

The discrepancy between FEGSEM and EFTEM results in figure I.12 can be explained as follows. The size parameters of particles such as: the corrected mean diameter or the average diameter, volume fraction, density are evaluated from FEGSEM or EFTEM images by statistical methods. Hence, better statistics are achieved if the number of particles is higher. Errors bars are calculated from the number of analyzed particles and the distribution of measured values. As can be seen in figure I.12 error bars corresponding to the EFTEM measurements are higher than those corresponding to FEGSEM measurements.

At 650°C, the Laves phase particles are so large that the thin foils used for EFTEM observations contain only few Laves phase particles per image. This causes non-random sampling which is reflected by the large errors bars. Using FEGSEM images, it is possible to sample larger areas and obtain more particles per image and better statistics of measured values.

To conclude, for the evaluation of relatively large particles (d_{obs}>200 nm) SEM images are recommended (Korcakova et al., 2001).

(Hättestrand and Andrén, 2001) also pointed out the low accuracy and uncertainty of the size measurements of Laves phases using EFTEM. This is more problematic for the material aged at 650°C for which the Laves phases are larger and the number of particles sampled is very low.

After 10^3h of creep exposure at 650°C a coarsening of Laves phases is observed in various 9-12% Cr tempered martensitic ferritic steels. This is indicated by a decrease in the number of Laves phases particles and an increase in their average equivalent diameter, see figure I.13.

On the basis of the results shown in figure I.12, it can be concluded that after an initial fast growth in the first 10^4h of exposure at 600°C and 650°C, no significant growth of Laves phase particles seem to occur.

NF616 is the Japanese denomination of the Grade 92 steel. The results in figure I.13 show quantitative results on Laves phases after 1h of creep exposure at 650°C in all investigated steels. This is relatively surprising and authors do not comment these results. No study reports precipitation of Laves phase after such a short time creep exposure.

a)

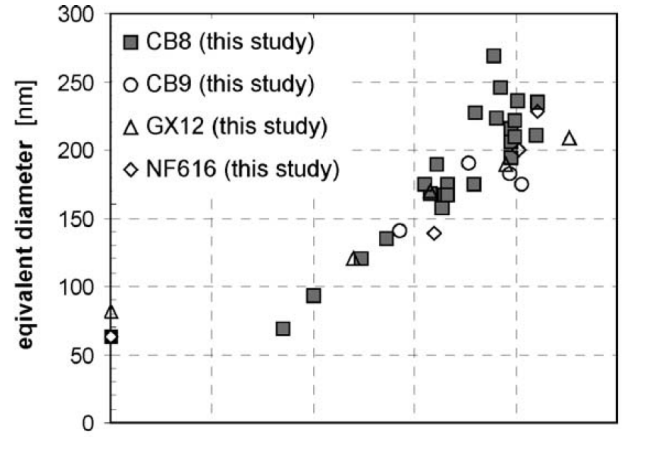

b)

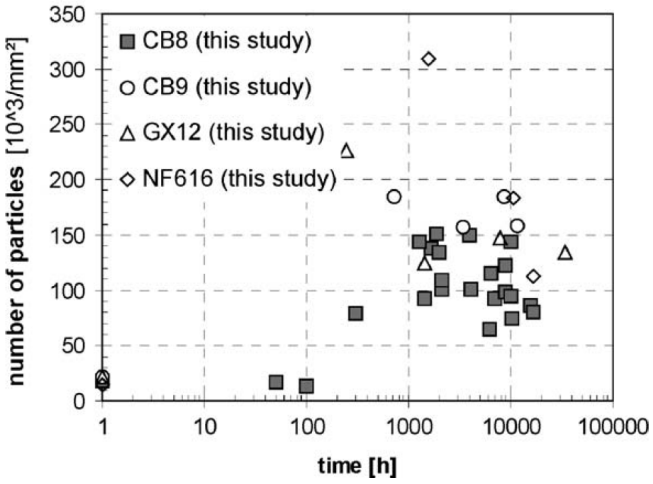

Chemical composition (mass %)

	GX12[a]	NF616 (P92)[b]	CB2[a]	CB8[a]	CB9[a]
C	0.13	0.106	0.11	0.17	0.17
Si	0.33	0.04	0.28	0.27	
Mn	0.52	0.46	0.85	0.2	0.20
P	0.012	0.008	0.013	0.009	
S	0.004	0.001	0.0074	0.006	
Al	0.006	0.007	0.004	0.026	
Cr	10.5	8.96	9.14	10.86	10.90
Mo	1.03	0.47	1.44	1.42	1.47
Co	–	–	–	2.94	5.91
Ni	0.86	0.06	0.22	0.15	0.16
V	0.23	0.2	0.19	0.21	0.20
Nb	0.066	0.069	0.062	0.061	0.06
N	0.049	0.051	0.021	0.024	0.0200
W	1.01	1.84	–	–	–
B	–	0.001	0.0112	0.0106	0.0105

[a] Cast material.
[b] Pipe material.

Figure I.13 : Size (a) and number (b) of Laves phases particles in some 9-12% Cr tempered martensitic ferritic steels during creep exposure at 600°C (gauge length) (Dimmler et al., 2003)

The values for the equivalent diameter of Laves phase in the Grade 92 steel (NF616 steel in figure I.13) after 10^4h of creep at 600°C reported by (Dimmler et al., 2003) are similar to those reported by (Korcakova et al., 2001), see figure I.13 compared with figure I.12.

Despite the significant precipitation of Laves phases some amounts of tungsten remains in matrix contributing to strengthening of the steel. In table I.2 are reported the matrix content of tungsten measured by APFIM in Grade 92 steel after various aging conditions. The volume fraction of Laves phases in table I.2 was estimated under the assumption that all tungsten that is not dissolved in the matrix is present in Laves phase particles with a content of 22 at.% (Hättestrand and Andrén, 2001).

(Dimmler et al., 2003) reported an area fraction of Laves phases of about 0.9% and of about 1.1% in a P92 steel after 1,000h and 10,000h of creep exposure at 650°C, respectively. The area fraction was estimated by image analysis of FEGSEM micrographs with a magnification of $\times 10,000$. Note that area fraction determined this manner could depend on the magnification of the micrograph and inhomogeneities in the material microstructure.

The results reported by (Dimmler et al., 2003) are different from those reported by (Hättestrand and Andrén, 2001) and represented in table I.2.

Figure I.14 shows the amount of precipitated tungsten during thermal exposure. The

Table I.2 : Measured matrix content of tungsten and calculated volume fraction of Laves phases in different material conditions of steel P92 (Hättestrand and Andrén, 2001)

	W (at.%)	Vol. fraction Laves phase (%)
Unaged material	0.58	-
Aged 1,000h, 600°C	0.43	0.20
Aged 10,000h, 600°C	0.23	0.98
Aged 26,000h, 600°C	0.28	0.78
Aged 1,000h, 650°C	0.39	0.35
Aged 10,000h, 650°C	0.30	0.70
Aged 26,000h, 650°C	0.31	0.66

lines in figure I.14 represents values predicted by a model developed by (Hald, 1996). Details about this model can be found in reference (Hald, 1996). Note that for exposure times lower than 10^4h there is no significant difference in the amount of precipitated tungsten at 600°C compared to that at 650°C, given the scatter in experimental measurements in figure I.14.

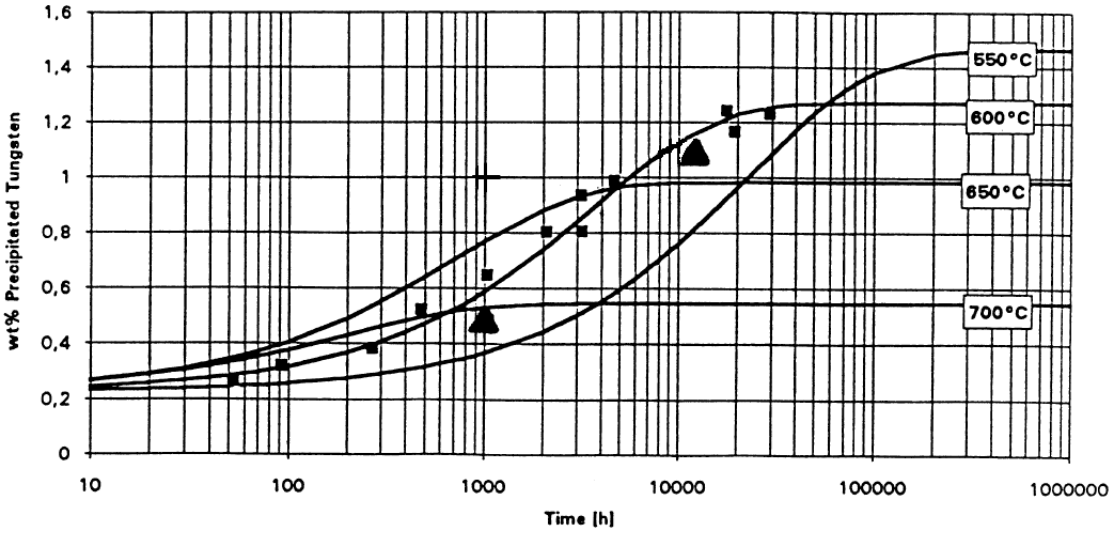

Figure I.14 : Calculated amount of tungsten precipitated in steel P92. Squares are measured values at 600°C at Nippon Steel used to calibrate the model and triangles are measured values in a different study (Hättestrand et al., 1998)

I.4.2.4 Effect on the creep properties

(Seung et al., 2006) reported that Laves phases over a critical size (average diameter of 130nm) triggers cavity nucleation at boundaries and consequently intergranular fracture. (Seung et al., 2006) reported also a hardness drop in the head of crept specimens after less than 1,000h at 650°C and after approximately 6,000h at 600°C. The hardness drop was associated with coarsening of Laves phases (Seung et al., 2006).

The mechanical properties (tensile, creep) of a 12Cr-2W steel (12.4Cr-2W-0.85Cu-0.35Ni-0.35Mo-0.2V-0.047Nb-0.052N %wt.) did not significantly change after one year and after three years service exposure (570°C, pressure of 19,2 MPa). After service exposure precipitation of Laves phases with a needle morphology was observed without influence on

the mechanical properties of the steel (Miyata et al., 2000). A conclusion of that study was that the service temperature and pressure were not high enough to allow growth of Laves phase (Miyata et al., 2000).

I.4.3 MX-type precipitates

MX carbonitrides (M=Nb, V, Cr; X=C, N) precipitate within martensite laths during tempering. MX-type precipitates represent obstacles to the movement of dislocations and they are believed to have the most significant precipitation strengthening contribution.

The size of MX carbonitrides is of about 20...40 nm and they are very stable against growth during exposure below 650°C. Due to their small size, these precipitates can only be studied using TEM techniques or indirect methods such as small angle scattering and diffraction measurements.

I.4.3.1 Precipitation mechanisms

There are no published data dedicated to the precipitation mechanisms of the MX-type precipitation in Grade 92 steel. These mechanisms were studied in a P91 steel (Suzuki et al., 2003), (Yoshino et al., 2005) and they are presented briefly below.

After austenitization of the P91 steel, two types of MX are observed: large MX with a content of Nb < 70 wt.% and fine MX homogeneously distributed with a high content of Nb >70 wt.% (Suzuki et al., 2003). Location of the MX is not precisely indicated, it is supposed that the large MX are located at the austenite grain boundaries and that the fine MX very rich in Nb are located whithin the grains.

After tempering the large MX with low Nb content are dissolved, only MX enriched in Nb and MX enriched in V are observed. The Nb content of the larger MX after austenitization is lower than the content in Nb of the Nb (C, N) observed after tempering. These observations indicate a dissolution of the large MX (<70 %wt. Nb) which makes available the elements for the formation of the two types of MX. The formation of the two types of MX is explained by a miscibility gap in the Cr-V-Nb system (Suzuki et al., 2003).

Dislocations are nucleation sites for the MX-particles (Yoshino et al., 2005). Annihilation of dislocations due to the recovery of the matrix during tempering can involve the dissolution of the MX which had nucleated on the dislocation. Recent studies confirm the dissolution and the final precipitation of MX of type Nb (C, N) and of VN type during tempering (Tamura et al., 2001), (Tamura et al., 2004).

I.4.3.2 Effect of heat treatment

The tempering temperature does not significantly affect the size of MX-type precipitates. The average diameter of the MX increases from 14±1nm to 16±1nm when the tempering temperature increases from 715 to 835°C, respectively (Ennis et al., 1997), (Ennis et al., 2000). In these studies the austenitization was conducted at 1070°C for 2h.

The creep strength of a P92 steel is significantly improved (see table I.3) after an alternative heat treatment consisting in an austenization at a higher temperature (i.e. 1150°C, 1h) followed by double tempering at 660°C during 3h. The better creep strength of the steel after this alternative heat treatment is attributed to a finer distribution of the MX-type precipitates compared to that obtained after a conventional heat treatment (Yescas and Morris, 2005). A high density of MX-type precipitates is obtained after double tempering, due partially to the high austenitization temperature. Remarkable is also the fact that the rupture time and the hardness of steel are improved without deteriorating its ductility, see table I.3.

Table I.3 : Creep strength after double tempering (Yescas and Morris, 2005)

Temp.	Stress	Alternative		Conventional	
	[MPa]	Duration [h]	Z[%]	Duration [h]	Z[%]
600°C	172	17,235	ub	2,722	66
	156	17,144	ub	8,222	45
650°C	110	6,179	35	1,734	35
	92	12,089	27	6,109	15

ub = unbroken specimens

It is to be noticed that the size of precipitates before creep of the double tempered P92 steel is higher than the size of precipitates after the conventionally heat treated. (Yescas and Morris, 2005) mention the existence of Sigma phase, Chi phase with a chemical composition close to that of Laves phases. Except for the chemical composition, the authors give no other complementary information on these phases. The formation of Sigma and Chi phase in the P92 steel before or after creep exposure is not reported by any other study.

Other non conventional heat treatments were studied in order to improve the creep strength of the 9-12% Cr heat resistant steels. For example, a 9Cr-3W-3Mo-MnVNb steel heat treated in a magnetic field shows a rupture time three times higher than the one conventionally heat treated (1100°C, 10min + 770°C, 4h) steel (Okubo et al., 2004).

The martensite transformation in a magnetic field increases the density of nucleation sites for precipitates during tempering, thus a finer and more uniform distribution of precipitates is obtained; the growth of precipitates during tempering is also slowed down (Okubo et al., 2004).

I.4.3.3 Growth during creep or thermal aging at 600°C and 650°C

(Ennis et al., 2000) reported an increase in the average equivalent diameter of MX-type precipitates from 16±1 (in as-received conditions) to 30±3 after 33,000h of creep at 600°C.

On the contrary, (Hald and Korcakova, 2003) reported an average diameter for the MX-type precipitates of about 40 nm in the as received steel without significant changes during creep exposure both at 600°C and 650°C.

(Gustafson and Hättestrand, 2002) reported also an average diameter for the MX-type precipitates of about 30-40nm in the as-received conditions without no significant changes during thermal aging both at 600°C and 650°C for times up to 26,000h.

No significant change was found in the size of MX-type precipitates in a P91 steel during creep and during thermal ageing at 600°C for more than 100,000h (Panait et al., 2010b).

From the results presented above, it can be concluded that MX-type precipitates are very stable against growth during long-term exposure at temperatures below 650°C.

A significant growth of MX-type precipitates is observed during exposure at 750°C (Sawada et al., 2001).

I.4.4 Modified Z-phase

I.4.4.1 Crystal structure and chemical composition

Modified Z-phase is a complex (Cr, Fe)(Nb, V)N nitrides with a chemical composition in metallic elements of $\sim$ 50 at.% (Cr+Fe) and $\sim$ 50 at.% (Nb+V) (Danielsen and Hald, 2006). Its precipitation occurs during relatively long-term thermal exposure.

The Z phase precipitation was reported for the first time in austenitic steels (Binder, 1950). In most of austenitic steels Z phase precipitation occurs during tempering. In these steels Z phase is finely and homogeneously distributed thus having a strengthening effect. (Soumail, 2001) realized a comprehensive literature survey of Z phase in austenitic steels. The crystal structure of Z phase in austenitic steels is represented in figure I.15a.

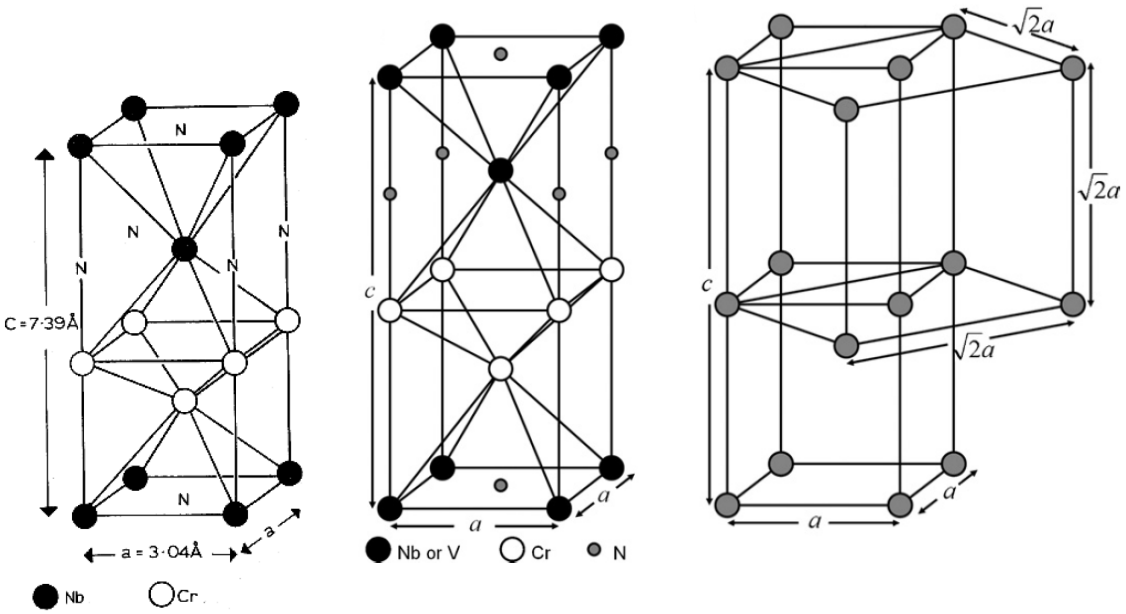

Figure I.15 : a) Crystal structure of Z phase (as firstly observed in austenitic steels) (Jack and Jack, 1972); b) Crystal structure of modified Z phase with a=0.286nm and c=0.739nm (observed in 9-12% Cr tempered martensitic ferritic steels) (Danielsen and Hald, 2006); c) Hybrid crystal structure of modified Z-phase (Danielsen et al., 2006), (Vodarek et al., 2006)

In the Z phase observed in the 9-12% Cr heat resistant steels half of the Nb atoms are replaced by V atoms and the lattice parameter a is smaller, see figure I.15b. From these two differences the term of *modified Z phase* is used to distinguish the Z phase observed in the 9-12% Cr heat resistant steels from that observed in the austenitic steels.

A NaCl-type cubic structure (similar to that observed for the MX-type precipitates) coexisting with a tetragonal structure was also observed for the modified Z-phase (Danielsen et al., 2006), (Vodarek et al., 2006). Figure I.15c shows this complex crystal structure. The cubic structure is predominant in the specimens exposed for relatively short-term while the tetragonal structure becomes predominant for longer exposure times (Danielsen et al., 2006). This observation leaded to the assumption that the cubic structure is metastable compared to the tetragonal crystal structure of modified Z-phase (Danielsen et al., 2006).

I.4.4.2 Precipitation mechanims

The chemical composition of the modified Z phase is close to that of the MX-type precipitates. Precipitation of modified Z-phase occurs only during thermal exposure at the expense of MX-type precipitates, leading to partial or complete dissolution of those precipitates and supression of the MX-induced precipitation strengthening. Thus the precipitation of modified Z-phase could impair the creep strength of the steel.

Better understanding of the precipitation mechanisms of modified Z phase could reveal interesting insights of delaying its formation and/or controlling its formation throughout small-size particles and thus reduce its detrimental effect on the creep strength. Recently, significant progress have been accomplished in understanding the modified Z-phase precipitation.

In the 12CrMoVNb steel, modified Z phase particles were often observed closely associated with primary NbX particles (i.e. primary NbC, MX-type precipitates) which gradually dissolve with increasing creep exposure time (Strang and Vodarek, 1996). Thus it was suggested that modified Z phase precipitates at or close to the NbX/matrix interface using V and Nb available in the matrix (Strang and Vodarek, 1996).

(Golpayegani et al., 2008) also investigated the precipitation of modified Z phase using EFTEM and concluded that vanadium nitrides (VN) could provide the most suitable nucleation site for this phase, given the small misfit between the (001) planes of VN and Z-phase. (Golpayegani et al., 2008) also highlighted the role of Nb in the nucleation and growth of Z-phase supported by observation of niobium carbides (NbC) close to nucleation sites of this phase. (Cipolla et al., 2010a) confirms the role of Nb in Z-phase formation in a 12% Cr steel.

(Danielsen and Hald, 2009) proposed two mechanisms for the nucleation of modified Z-phase: (i) nucleation on an existing MX-type precipitate and (ii) transformation of an existing MX-type precipitate into modified Z-phase by Cr diffusion from the steel matrix into the MX. These two mechanisms are illustrated in figure I.16.

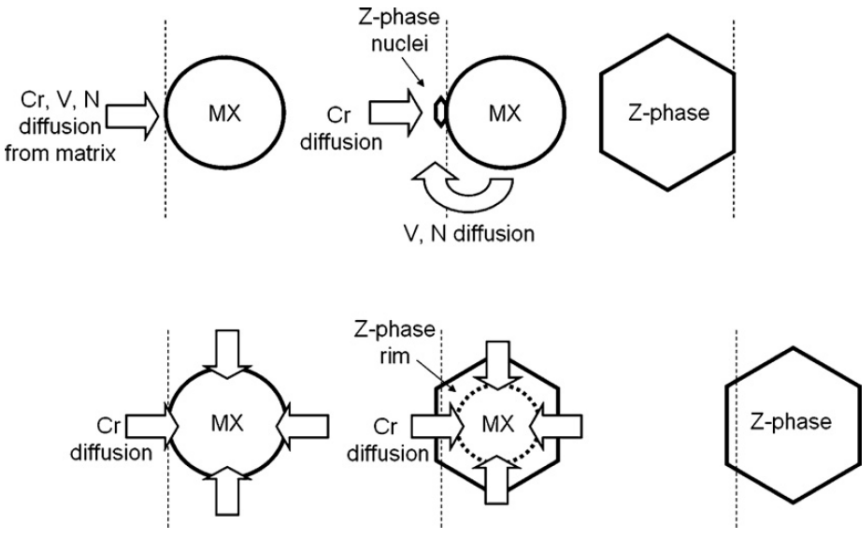

Figure I.16 : Formation of Z-phase by nucleation on MX (top) and by transformation from MX to Z-phase (bottom) (Danielsen and Hald, 2009)

Nucleation on an existing MX-type precipitate requires V, Nb and N available in the steel matrix in order to form nucleus on the MX-type precipitate. After tempering heat treatment these elements are mostly trapped in MX-type precipitates and thus nucleation of modified Z-phases is very difficult (Danielsen and Hald, 2009). This mechanism could explain the relatively long time needed for precipitation of this phase. Once the modified Z-phase has nucleated it grows by consumption of the MX-particles next to it by diffusion in the matrix. The interface of the MX/Z-phase will remain until complete dissolution of the MX-type precipitate.

The hybrid crystal structure of modified Z-phases observed in some 9-12% Cr heat

resistant steels could be explained by the mechanism of direct transformation of an existing MX-type precipitate. Cr diffusion into V-rich MX precipitate together with a rearrangement of atoms into VN and Cr layers leads to the transformation of the MX-type precipitate into Z-phase. Cr diffusion gradually changes the chemical composition from (V,Nb)N (i.e. MX precipitate) to Cr(V,Nb)N (Z-phase). A rearrangement of atoms into VN and Cr layers was supposed to lead to the well-known tetragonal crystal structure (Danielsen and Hald, 2009).

The two mechanisms proposed by (Danielsen and Hald, 2009) and illustrated in figure I.16 are supported both by EDX-TEM analysis and electron diffraction (in TEM) of hybrid particles (i.e. modified Z phase not completely formed) showing core/rim composition where the rim is Cr-rich or Z-phase. Diffraction patterns reveals both cubic and tetragonal crystal structure in these hybrid Z-phase. Occasionally, interfaces between Z-phase and MX-type precipitate could be distinguished.

The mechanism of the conversion of MX-type precipitate into Z-phase was confirmed using model alloys designed to rapidly precipitate Z-phases. To this aim the Cr content was 12% to promote Z-phase precipitation; the Nb, V and Ni contents were similar to industrial 9-12% Cr; C content was limited to 45ppm to avoid formation of $M_{23}C_6$ carbides; W and Mo were excluded to avoid precipitation of Laves phases during thermal exposure (Cipolla et al., 2010b).

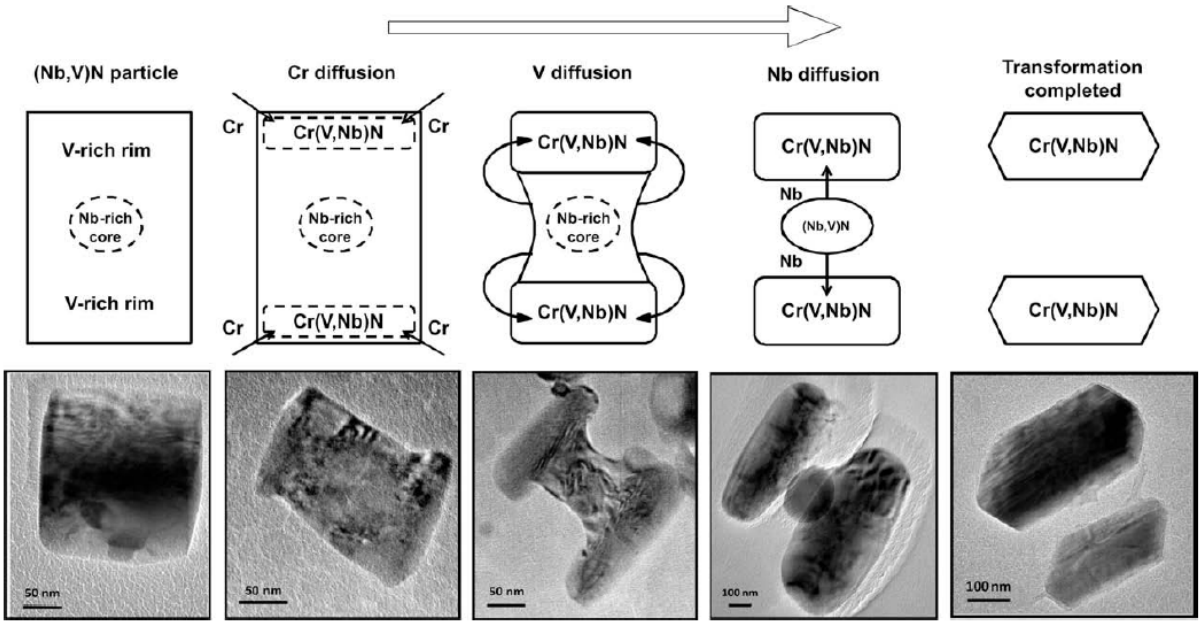

Figure I.17 : Formation of two parallel Z-phases. The pictures are taken by the following samples, starting from the left: as-treated material, 650°C/300h, 650°C/1000h, 650°C/1000h 650°C/10,000h samples (Cipolla et al., 2010b).

Another less straightforward formation mechanism of modified Z-phase was revealed using model alloys. Several Cr-rich areas form on MX particles with Nb-rich core by incorporation of Cr from the matrix, see figure I.17. Once the Cr-rich region are formed the Z-phases grows by consumption of V, Nb and N from the host precipitate until the complete dissolution of the ”core” leaving several Z-phase particles.

I.4.4.3 Effect of alloy elements on precipitation of modified Z-phase

Precitation of modified Z phase might impair the creep strength of the steel since it is associated with the dissolution of fine MX-type precipitates.

Note that the simple observation of low amounts of modified Z phase is not associated with a degradation of creep strength. The precipitation of this phase becomes dangerous for the steel creep strength, only once it is accompanied by significant dissolution of MX-type precipitates.

The precipitation of modified Z phase is strongly dependent on the chemical composition of the steel and consequently its effect on the loss creep strength is different from one steel to another.

Some alloy elements such as Cr, Nb, N seem to have a major influence on the precipitation and growth of modified Z-phases. The published available data on these issues are summarized in the following sections.

a) Effect of Chromium

The chromium content of the steel seems to have the most significant influence on the precipitation and growth of modified Z phase. Precipitation of this phase occurs more intensely in the 12%Cr steels compared to that in 9%Cr steels, see figure I.18. Moreover, the precipitation of modified Z phase has been held responsible for the sudden creep strength loss of some 11-12%Cr commercial steels.

The amounts of modified Z phases observed in various 9-12% Cr tempered martensitic ferritic steels after creep exposure evaluated by (Danielsen and Hald, 2007) are shown in figure I.18. The criteria of classification as *low*, *medium* and *high* in figure I.18 are not mentioned and no quantitative data related to the results in figure I.18 were given.

Steel grade	Exposure	Observed Z-phase quantity
P91	8 000 h/650 °C	Very low
X20	150 000 h/600 °C	Low
E911	10 000 h/650 °C	Low
P92	31 000 h/650 °C	Low
P122	10 000 h/650 °C	Medium
AXM	43 000 h/600 °C	Medium
FN5	8 000 h/650 °C	Medium
HCM12	85 000 h/585 °C	Medium
VM12	16 000 h/625 °C	High
TB12	10 000 h/650 °C	High
T122	12 000 h/660 °C	High
NF12	17 000 h/650 °C	High

a)

	P91	E911	P92	AXM	HCM12	P122	T122	NF12	FN5	TB12	VM12	X20
C	0.10	0.11	0.11	0.11	0.10	0.11	0.09	0.085	0.11	0.113	0.12	0.19
N	0.053	0.065	0.049	0.05	0.025	0.053	0.0609	0.045	0.027	0.055	0.078	0.025
Si	0.36	0.18	0.17	0.08	0.18	0.02	0.25	0.25	0.06	0.01	0.48	0.23
Mn	0.37	0.46	0.43	0.42	0.51	0.56	0.60	0.44	0.55	0.51	0.37	0.49
Cr	8.30	8.61	9.27	10.48	12.20	11.0	12.20	11.60	11.20	11.33	11.61	11.5
Mo	0.95	0.92	0.48	1.04	1.00	0.42	0.35	0.14	0.26	0.5	0.28	0.91
W	–	0.995	1.701	0.99	0.99	1.94	1.97	2.68	2.63	1.98	1.58	–
Ni	0.15	0.21	0.25	0.77	0.01	0.32	0.18	0.17	0.40	0.96	0.31	0.66
Nb	0.07	0.089	0.067	0.043	0.05	0.05	0.06	0.08	0.065	0.082	0.044	–
V	0.21	0.19	0.197	0.18	0.24	0.19	0.25	0.20	0.22	0.18	0.251	0.31
Cu	–	–	–	0.04	–	0.87	0.43	0.01	–	0.06	0.06	0.054
Al	0.15	0.013	0.005	0.008	–	0.012	0.004	–	–	0.004	–	0.016
B	–	–	0.0026	0.0002	–	0.0011	0.0021	0.0026	0.0010	–	0.0045	–
Co	–	–	–	–	–	–	–	2.48	2.66	–	1.56	0.021
Heat treatment	1050 °C/ 1 h 780 °C/ 1 h	1060 °C/ 1 h 770 °C/ 2 h	1060 °C/ 1 h 770 °C/ 2 h	1070 °C/17 h 570 °C/22 h 700 ° C/24 h	1050 °C/ 1 h 800 °C/ 1 h	1050 °C/ 1 h 770 °C/ 3 h	1050 °C/ 0.2 h 790 °C/ 3 h	1100 °C/ 0.2 h 760 °C/ 1 h	1100 °C/4 h 570 °C/8 h 715 °C/24 h	1080 °C/ 2.5 h 775 °C/ 2 h	1060 °C/ 0.5 h 780 °C/ 2 h	1050 °C/ 1 h 750 °C/ 2 h
Exposure	8 000 h 650 °C	10 000 h 650 °C	31 000 h 650 °C	43 000 h 600 °C	85 000 h 585 °C	10 000 h 650 °C	12 000 h 660 °C	17 000 h 650 °C	8 000 h 650 °C	10 000 h 650 °C	16 000 h 625 °C	150 000 h 600 °C

b)

Figure I.18 : a) Amounts of modified Z phases in various 9-12% Cr tempered martensitic ferritic steels after creep exposure at 600°C and 650°C; b) Chemical composition of studied 9-12% Cr tempered martensitic ferritic steels steels (Danielsen and Hald, 2007)

(Sawada et al., 2007) established time-temperature-precipitation (TTP) diagram of modified Z-phase observed in crept specimens of some 9-12%Cr heat-resistant steels, see figure I.19.

Note that TTP diagrams show the shortest testing time of specimens in which modified Z-phase were observed and this not correspond to the sudden loss of the creep strength observed

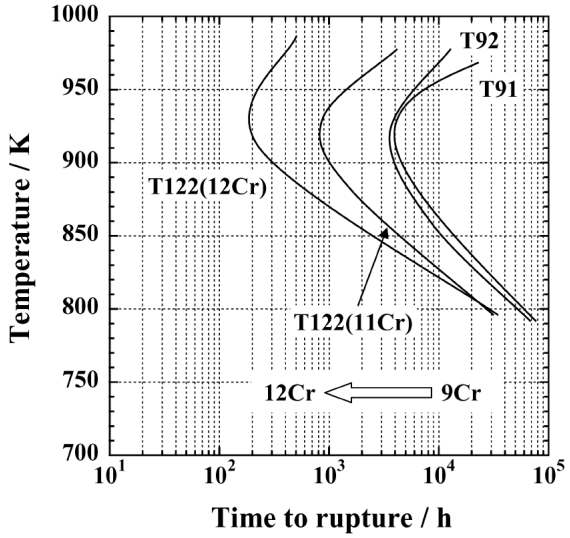

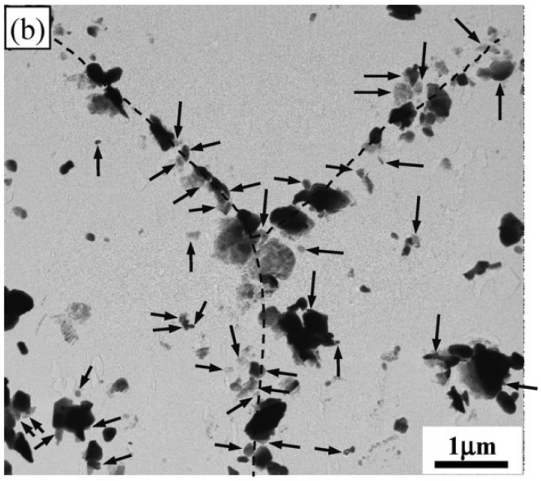

a) b)

	C	Si	Mn	P	S	Ni	Cr	Mo	W	Cu
ASME-T91	0.0900	0.29	0.35	0.009	0.002	0.28	8.70	0.90	–	0.032
ASME-T92	0.0980	0.29	0.42	0.007	0.0013	0.13	9.50	0.36	1.74	–
ASME-T122-s	0.1300	0.31	0.60	0.017	0.001	0.36	10.65	0.33	1.87	0.86
ASME-T122-d	0.1100	0.27	0.59	0.015	0.002	0.33	12.10	0.34	1.82	0.82

	V	Nb	Al	B	N	Normalizing	Tempering
ASME-T91	0.22	0.072	0.001	–	0.044	1323K, 10min A.C.	1038K, 30min A.C.
ASME-T92	0.19	0.062	0.009	0.0020	0.0462	1373K, 12min A.C.	1053K, 60min A.C.
ASME-T122-s	0.19	0.050	0.007	0.0024	0.057	1323K, 10min A.C.	1043K, 360min A.C.
ASME-T122-d	0.19	0.060	0.012	0.0030	0.066	1323K, 10min A.C.	1063K, 180min A.C.

c) s and d mean single and dual phase, respectively.

Figure I.19 : a) Time-temperature-precipitation (TTP) of Z phases in various 9-12% Cr heat resistant steels; b) Microstructure of the T122(12%Cr) steel after 24,656h of creep at 600°C (TEM micrograph on extractive replica); Arrows shows Z phase particles (Sawada et al., 2007); c) Chemical composition and heat treatments of investigated steels.

in some 12%Cr heat resistant steels, (Sawada et al., 2007). In addition, these diagrams gives no information about the amounts of observed modified Z-phase.

For example the creep strength of the T122 (12Cr) steel suddenly drops after about 10^4h at 600°C (see figure I.3) while ed Z-phase starts to precipitate after less than 10^3h at 600°C, see figure I.19a. However, the high density of Z-phase observed in this steel after 24,656h of creep at 600°C (figure I.19b) could explain the significant loss of the creep strength of this steel.

Note also that the results of given in figure I.18 and the TTP diagrams established by (Sawada et al., 2007) give no indication on the number density or size of observed Z-phase. Probably it is difficult to determine a number density of modified Z-phase as this phase precipitates preferentially to the prior austenite grain boundaries (Cipolla et al., 2010b), (Sawada et al., 2007).

In addition to the results given in figures I.18 and I.19 concerning precipitation of modified Z-phase in the Grade 92 steel, (Hättestrand and Andrén, 2001) observed Z-phase in a Grade 92 steel after 26,000h of thermal aging at 600°C.

(Sawada et al., 2006) investigated the precipitation of modified Z-phase in a T92 steel specimen that had been creep tested at 600°C under 130MPa for 39,539h and reported a

mean diameter of 155.3nm and a number density of about $1.5 \times 10^{11} m^{-2}$.

b) Effect of niobium

Nb has a high influence on the precipitation of modified Z phase. In Nb-free steel the number of modified Z phase particles is extremely low and the precipitation of this phase is observed after very long exposure times

In the X20 (11.5Cr-0.91Mo-0.66Ni-0.49Mn-0.31V6-0.23Si-0.19C-0.025N-AlCo wt.%, 1050°C, 1h + 750°C, 2h) without Nb, precipitation of modified Z phase (CrVN) occurs after very long time exposure (i.e. 150,000h at 600°C). The number density of these phases is very small and large amounts of MX precipitates are still observed in the steel. (Danielsen and Hald, 2006) are the first to report the modified Z phase without Nb atoms.

c) Effect of nickel

Nickel enhances the precipitation of modified Z phase. In steels with higher nickel content modified Z phases are observed after shorter time exposures. For example, in the 12CrMoVNb (11.2Cr-0.61Mo-0.52Ni-0.28V-0.29Nb-0.28Si-0.16C-0.074N wt.%, 1150°C, ?h + 650°C, 6h) steel with 0.52% Ni, the modified Z phase is observed after 22,052h of creep at 600°C and in the same steel but with a 1.15% Ni, modified Z phase is observed after 7,247 h of creep at 600°C. In the 12CrMoVNb steel with 0.52% Ni and with 1.15% Ni the modified Z phase is observed after 79,171 h and after 17,875 h of creep at 550°C, respectively (Vodarek and Strang, 2000), (Golpayegani and Andrén, 2006). Note that the Nb content of these steels is relatively high reported to the usual amount in 9-12%Cr heat resistant steels (i.e. about 0.05Nb wt.%).

The effect of nickel on the mechanism of modified Z phase precipitation is not fully clarified. The chemical composition of modified Z phase does not change during creep and it depends on the temperature at which precipitation of this phase occurs. The Nb content of the modified Z phase increases with the nickel content of the steel (Vodarek and Strang, 2006)

d) Effect of nitrogen

Increasing nitrogen content from about 0.05 to 0.10 promoted the growth of MX-type precipitates and precipitation of modified Z-phase leading to a loss in the creep strength, see figure I.7.

I.4.5 Evolution of the tempered martensite matrix

There are rather few data on the matrix substructure (i.e. dislocation density, subgrains) evolution during creep/thermal aging at 600°C or/and 650°C. The matrix substructure is often characterized using TEM on thin foils or EBSD techniques.

ESBD technique has been successfully applied to evaluate the matrix substructure and creep damage of the high chromium steels during creep/thermal aging.

EBSD investigations conducted on interrupted creep specimens in a chromium steel (0.15C-0.03Si-0.64Mn- 0.69Ni-10Cr-0.99Mo-0.19V-1.01W-0.05Nb-0.04N, wt. %) after various creep lifetime fractions suggested an increase in block width with increasing creep time fracture (Fujiyama et al., 2009). The block width was calculated from EBSD-IPF maps as the ratio of block area to the longest length of the block. (Fujiyama et al., 2009) suggested that these values were more easily obtained through EBSD method compared to

TEM observations. (Fujiyama et al., 2009) also suggested a greater increase in block width near grain boundaries than inside parent austenite grain.

However, possible sampling effects due to the complex three-dimensional shape of blocks were not addressed in this paper. In addition, block boundaries are high-angle boundaries that are often decorated with a high density of precipitates, so that their mobility is expected to be rather low.

(Sonderegger et al., 2007), (Sonderegger et al., 2008) developed an extended model combining classical transformation models K-S and N-W to process EBSD data. Using this model an increase in the lath width (respectively subgrain diameter) from about 0.75μm to about 1.2μm (respectively from about 0.75μm to about 1.6μm) was revealed in a 0.17C-10.86Cr-1.42Mo-0.21V-0.061Nb-0.024W-0.01B-2.94Co-0.22Si wt.%) during creep exposure at 650°C for about 16,000h, (Sonderegger et al., 2008).

The dislocation density could be evaluated using the linear intercept method, which consists in overlapping a grid of horizontal and vertical lines on subgrains and counting the intersections of dislocations with grid lines. The number of vertical and horizontal grid lines is adjusted in relation with the size and shape of subgrains in a such way to keep a constant grid spacing. This method is generally used to evaluate dislocation density, see for instance ref. (Pešička et al., 2003), (Pešička et al., 2010), (Ennis et al., 1997), (Zielińska-Lipiec et al., 1997).

The dislocation density decreases and the average subgrain size increases with the tempering temperature, see table I.4. The values of dislocation density in table I.4 were determined using the linear intercept method on TEM thin foils. The mean subgrain width was measured perpendicularly to the long axis of the martensite lath.

Table I.4 : Dislocation density and subgrain width in the P92 steel as a function of heat treatment or creep at 600°C, (Ennis et al., 2000), (Ennis and Czyrska-Filemonowicz, 2002)

T_{aust}[°C] (2h)	T_{temp}[°C] (2h)	Creep test	Dislocation density $10^{14}m^{-2}$	Subgrain width [µm]
970	775	...	8.7 ± 1.2	0.38 ± 0.1
1070	715	...	9.0 ± 1.0	0.37 ± 0.1
1070	775	...	7.5 ± 0.9	0.42 ± 0.1
1070	835	...	2.3 ± 0.6	0.50 ± 0.1
1145	775	...	...	0.58 ± 0.1
1070	775	600°C/1,500h	5.3 ± 0.6	0.70 ± 0.1
1070	775	600°C/10,000h	2.5 ± 0.5	1.4 ± 0.1
1070	775	600°C/33,00h	1.5 ± 0.4	1.5 ± 0.1

*the levels of stress of investigated crept specimens are not mentioned

High resolution EBSD measurements were performed with a step size of 10nm by (Tak et al., 2009). These measurements revealed microstructural features which are generally observed using TEM techniques, see figure I.20.Similar findings were reported by (Panait et al., 2010b) in a P91 steel creep tested for 113,431h at 600°C (EBSD measurements conducted with a step size of 40nm).

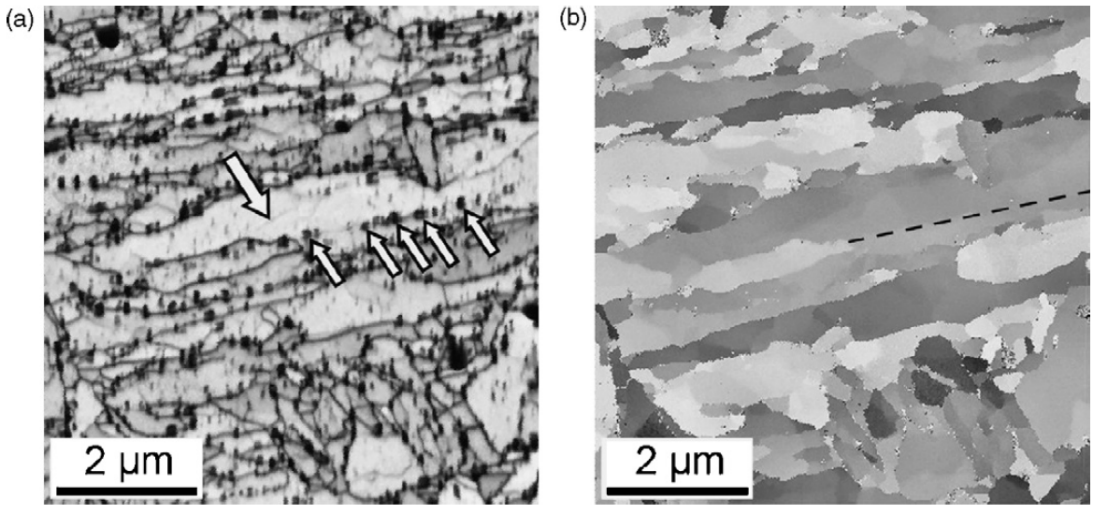

Figure I.20 : High resolution EBSD maps (step size of 10nm) of an X20 steel after creep exposure at 650°C (100MPa interrupted after 7% strain). a) EBSD Image Quality map b) Inverse pole figure (IPF) (Tak et al., 2009)

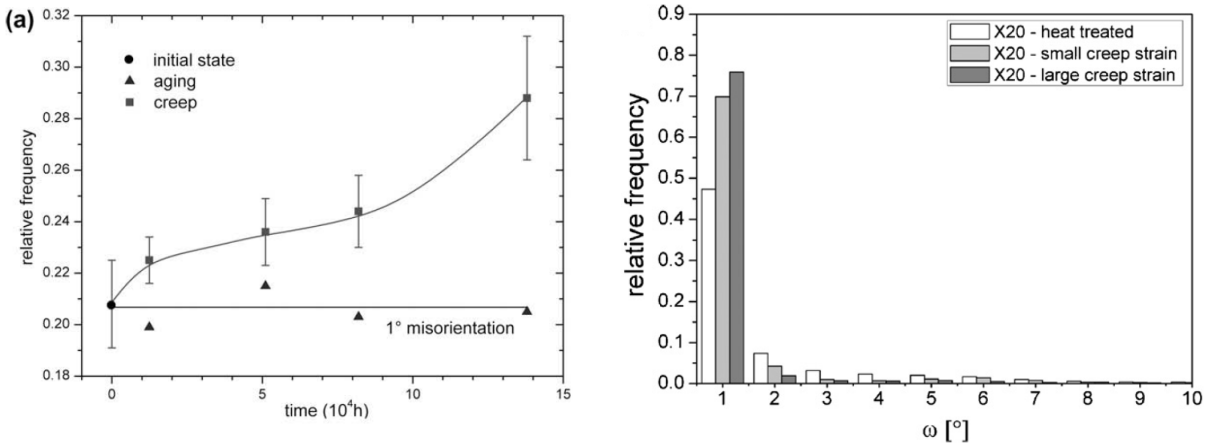

a) **b)**

Figure I.21 : a) Amount of boundaries of 1° determined by EBSD techniques in X20 steel specimens of interrupted creep at 550°C, 120MPa (Aghajani et al., 2009b); b) Relative frequency of the misorientation angles between individual crystallines in 50 µm × 50 µm fields size (EBSD maps with a step size of 80nm) in the X20 steel in the as-received state and after small and high strain creep exposure (Tak et al., 2009)

More precisely presence of subgrains and small carbides are revealed in the EBSD-IQ maps, I.20a. In combination with the cristallographic information provided in the IPF-EBSD map (figure I.20b) it is possible to relate the presence of carbides to the local grain boundary character (i.e. low angle, high angle) on which they are located. Moreover, figure I.20a shows that not only presence of precipitates but also presence of dislocations yield IQ contrast (one apparent line defect is highlighted by an arrow pointing down).

Figure I.21b shows the relative frequency of the misorientation angles between adjacent micrograins determined by the means of EBSD techniques in the German grade X20 in

the as-received state, after small creep strain at lower temperature(600°C, 100MPa, 1.2% strain) and after large creep strain at a higher temperature (650°C, 100MPa, 7% strain). Figure I.21b shows that the frequency of the misorientation angles of 1° increases with strain. This result was confirmed by (Aghajani et al., 2009b) which conducted the same analysis after interrupted creep tests of an X20 steel loaded for 12,456h (0.5% strain); 51,072h (1% strain); 81,984h (1.2% strain) and 139,971h (11.9% strain), see figure I.21a. However, (Tak et al., 2009) concluded that the decrease in creep rate during the primary creep stage in tempered martensite ferritic steels is not directly related to an increaseing frequency of the 1° boundaries.

I.5 The effect of long-term isothermal aging on the creep behaviour of 9-12%Cr heat resistant steels

There are rather few published data available on the effect of thermal aging on the creep strength loss. Some data were found concerning 9% Cr heat resistant steels such as Grade 91 and 92 steels while a lack of data is observed for the 12%Cr heat resistant steels. However, the few available data are incomplete and they do not allow full understand or quantification of the effect of thermal aging on the creep strength.

(Sklenička et al., 2003) reported interesting findings concerning the creep behaviour of the P91 steel and P92 steel both isothermally aged at 650°C for 10^4h prior to creep testing at 600°C. Figures I.22 and I.23 show the results of standard constant tensile load creep tests conducted at 600°C under levels of stress ranging from 100MPa to 250MPa on the P91 steel and P92 steel in their as-received state and after long-term isothermal aging (650°C, 10^4h).

Results in figures I.22 and I.23 show that the lifetime (respectively secondary creep rate, $\dot{\varepsilon}_{ss}$) of the aged steels is markedly shorter (respectively higher) than that of the steels in as-received state for a given level of applied stress. The difference between the lifetimes (respectively $\dot{\varepsilon}_{ss}$) of the aged steel and that of the as-received steel seems to be independent of the level of applied stress in the case of the P91 steel while this difference increases with decreasing the applied stress for the P92 steel (Sklenička et al., 2003).

Note that the levels of applied stress investigated in figure I.23 correspond to the high stresses region of the Grade 92 steel and decreasing further the applied stress might increase more the difference between the lifetimes (or $\dot{\varepsilon}_{ss}$) of the as-received P92 steel and aged P92 steel compared to these in figure I.23.

No microstructural characterization is available for aged P91 and P92 steel before and after creep testing. Most probably significant precipitation of Laves phases occurred during long-term isothermal aging in both steels. This is not mentioned in reference (Sklenička et al., 2003).

The different effect of stress on the creep behaviour of aged P91 steel compared to that of aged P92 steel could be an indication of a different effect of Fe_2Mo-type Laves phases precipitation (occurring in the P91 steel) on the creep behaviour compared to that of Fe_2W-type Laves phases occurring in the P92 steel.

APFIM analysis revealed that 0.3 wt.% of W remains in solid solution in the matrix of the P92 steel after aging at 650°C for 10^4h which might be beneficial against creep deformation (i.e. decrease in the $\dot{\varepsilon}_{ss}$) when the applied stress is low enough. No such data are available for the P91 steel after 10^4h of aging at 650°C.

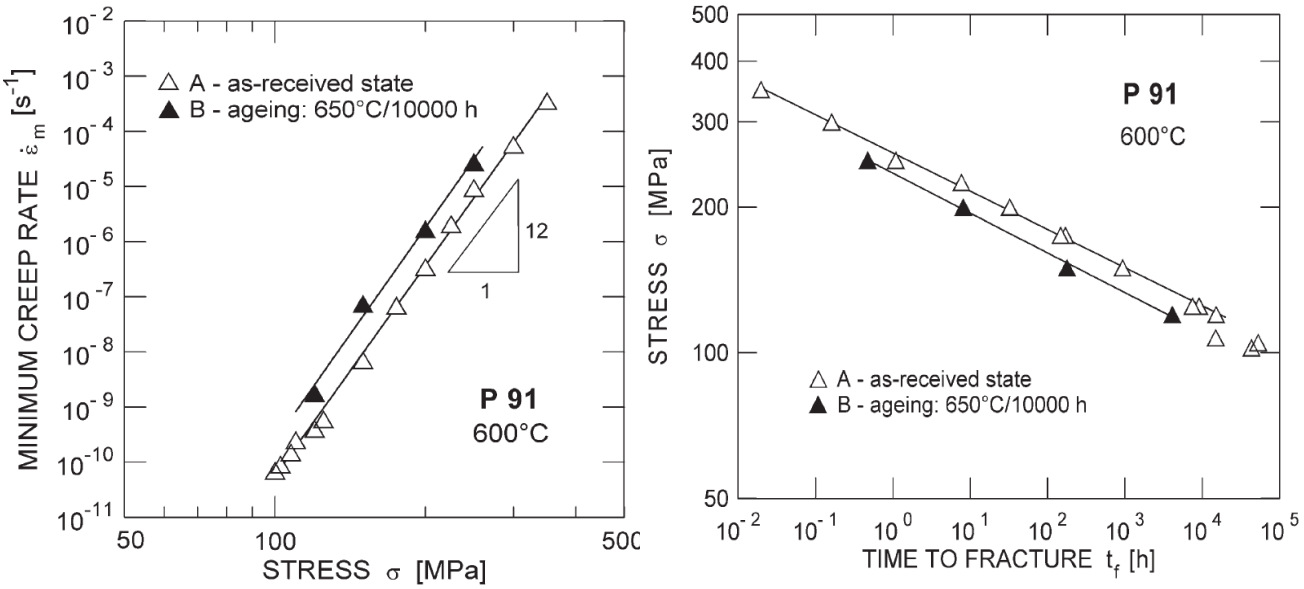

a) b)

Figure I.22 : Stress dependence of the minimum creep rate ($\dot{\varepsilon}_{ss}$) and time to fracture for the P91 steel both in the as-received state and thermally aged (650°C, 10^4h) (Sklenička et al., 2003)

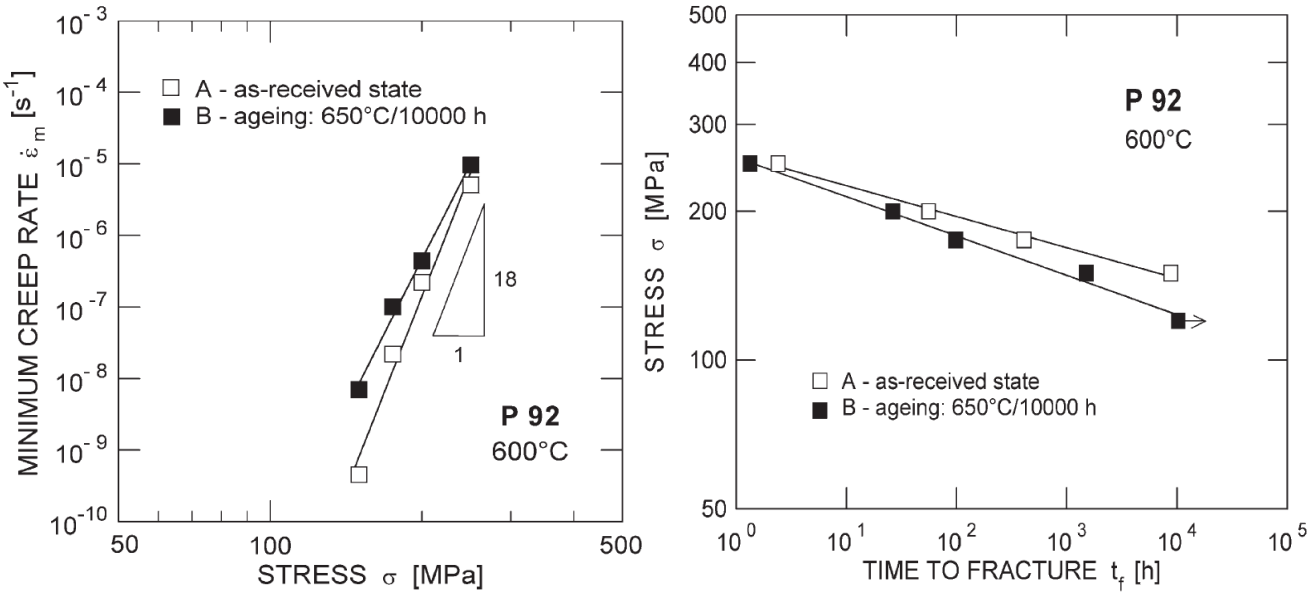

a) b)

Figure I.23 : Stress dependence of the minimum creep rate ($\dot{\varepsilon}_{ss}$) and time to fracture for the P91 steel both in the as-received state and thermally aged (650°C, 10^4h) (Sklenička et al., 2003)

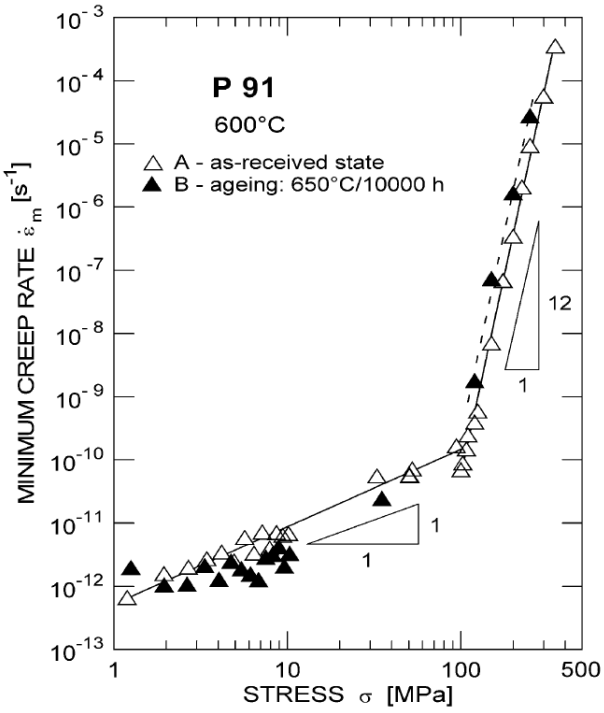

Figure I.24 : Stress dependence of the minimum creep rate ($\dot{\varepsilon}_{ss}$) for the P91 steel both in the as-received state and thermally aged (650°C, 10^4h) (Skleničkа et al., 2003)

Creep tests conducted using helicoidal spring, which allow testing levels of stress lower than 10MPa revealed that the $\dot{\varepsilon}_{ss}$ of the aged P91 steel is slightly lower than that of the as-received P91 steel, see figure I.24.

A slope change is observed in the $\dot{\varepsilon}_{ss}$ versus stress σ of the P91 steel both in as-received state and long-term aged (see figure I.24). This slope change could be due to a change in the dominant deformation mechanism from dislocation creep (high stresses) to diffusional creep (low stresses).

Indeed, a values of 1 for the exponent n in the Norton law (i.e. $\dot{\varepsilon}_{ss} = A\sigma^n$) indicates the diffusional creep. Note that diffusional creep is observed for levels of stress lower than 10MPa. These levels of stress can be tested using helicoidal springs. No such tests were conducted for the Grade 92 steel.

Note that the aging temperature (i.e. 650°C) is different from that of creep testing (i.e. 600°C) and the underlying microstructural evolution during thermal exposure at 650°C could be different from that during creep at 600°C. More precisely, the effect of Laves phase precipitation on the long-term creep behaviour of the P92 steel at 600°C could not be quantified from the results in figure I.23. To this aim creep tests were conducted in this study at both 600°C and 650°C on T92 steel thermally aged for 10^4h at the same temperature as the creep tests. Furthermore microstructural investigations were conducted on the aged T92 steel before and after creep testing to better understand the effect of thermal aging on the loss of creep strength.

Long-term aging at 650°C significantly decreases the creep strength at 650°C of both Grade 91 and Grade 92 steel compared to long-term aging at 600°C, see figure I.25. Note that long-term aging at 600°C doe not significantly affect creep strength of the T91 steel at least at 120MPa, 650°C. No complementary information are available related to the results in figure I.25. No microstructural characterization is given in reference (Masuyama, 1998).

I.6 Modeling microstructural evolution during high temperature exposure

Equations, models that have been used in previous studies to describe the evolution of the microstructural features (i.e. precipitates, subgrains, dislocation density) during creep or thermal exposure are summarized in this chapter. Special attention was focused in finding relationships linking stress or strain to evolution of microstructure features, in order to include

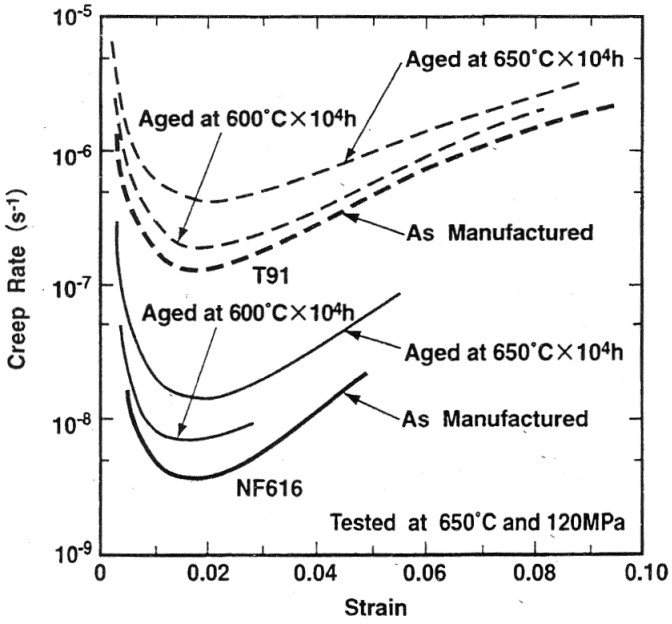

Figure I.25 : Comparison of the creep rate versus strain behaviours of T91 steel and NF616 (Grade 92 steel) (Masuyama, 1998)

relevant equations into the constitutive equations of the mechanical model to be developed in the present study.

I.6.1 Evolution of precipitates

Coarsening of precipitates during thermal exposure is often described using the well-known Ostwald ripening equation or Livshitz-Slyozov-Wagner equation (Lifshitz and Slyozov, 1961):

$$d^n - d_0^n = K_d t \tag{I.2}$$

where d is the precipitate diameter at time t and d_0 is the precipitate diameter at time 0 (i.e. before temperature exposure). K_d is the coarsening rate.

n=3 is often used to model precipitate coarsening in 9-12%Cr heat resistant steel during creep or thermal exposure.

K_d could be expressed as:

$$K_d = K_0 t \exp\left(-\frac{Q_d}{RT}\right) \tag{I.3}$$

where Q_d is the activation energy for particle coarsening, R is the gas constant, T is the temperature and K_0 is a constant.

The value of K_d is usually determined by fitting parameters of equation I.2 to the size of precipitates evaluated using SEM or TEM techniques. For example (Aghajani et al., 2009b) reported $K_d = 1.37 \times 10^{-29}$ m^3/s for coarsening of $M_{23}C_6$ carbides in a 12%Cr steel (German grade X20) during almost 140,000h of creep exposure at 550°C.

(Korcakova et al., 2001) found $K_d = 3.5 \times 10^{-29}$ m^3/s and $K_d = 15 \times 10^{-29}$ m^3/s for the coarsening rate of Laves phases in the P92 steel during exposure at 600°C and 650°C, respectively using the following expression of the Ostwald ripening equation

$$d^n - d_0^n = K_d \left(t - t_0\right) \tag{I.4}$$

with $t_0 = 10^4$h and the value of d_0 corresponding to the average equivalent diameter of Laves phases after 10^4h of aging (i.e. $d_0 = 193$nm (600°C) and $d_0 = 413$nm (650°C)).

The following formula was developed for the coarsening rate (K_d) in a multicomponent system of β precipitates in a α matrix (Agren et al., 2000).

$$K_d = \frac{8}{9} \frac{\gamma V_m^\beta}{\sum\limits_{i=1}^{C} \frac{\left(x_i^\beta - x_i^{\alpha/\beta}\right)^2}{x_i^{\alpha/\beta} D_i / RT}} \tag{I.5}$$

where γ is the interfacial energy and V_m^β is the molar volume of the precipitate phase. D_i is the diffusion coefficient of element i in the matrix, x_i^β is the mole fraction of element i in the precipitate and $x_i^{\beta/\alpha}$ is the mole fraction of element i at the precipitate/matrix interface.

Calculations of K_d using formula I.5 indicated that the values of solubility of alloy elements in precipitates and matrix have more significant influence on coarsening of precipitates than their diffusivities (Hald and Korcakova, 2003).

Precipitates evolution (i.e. growth, coarsening) could also be described by a time-dependent volume fraction (f) equation (Johnson-Mehl-Avrami equation):

$$f\left(t\right) = C_{JMA} \left(1 - \exp\left(-\frac{t}{t_0}\right)^n\right) \tag{I.6}$$

where t_0 is a time constant and n is a time exponent. A time exponent n=1.5 indicates a one-time nucleation process and the further growth of a constant number of precipitates.

The main precipitates in 9-12%Cr tempered martensitic ferritc steels are $M_{23}C_6$ carbides located at all kinds of boundaries and MX-type precipitates homogeneously distributed in the martensite laths. Precipitates are obstacles against movement of subgrain boundaries and dislocations, thus contributing to creep strength. (Kostka et al., 2007) highlighted the beneficial contribution of carbides located at boundaries on stabilization of the matrix substructure. Therefore the creep strength is controlled by the stability of precipitates. The direct contribution of precipitates to creep strength is usualy described by the Orowan stress (σ_{Or}):

$$\sigma_{Or} = 3.32 G b \frac{\sqrt{f_p}}{d_p} \tag{I.7}$$

where G is the shear modulus, b is the Burgers vector, f_p is the precipitate volume fraction and d_p is the mean precipitate diameter.

Equation I.7 expresses the fact that the effect of precipitates on strength depends on their size and volume fraction. Growth of precipitates during thermal/creep exposure decreases the strength.

A definition of the Orowan stress (equation I.8) involving the average spacing of precipitates (λ_p) was used by (Maruyama et al., 2001) to evaluate the contribution of each kind of precipitate in 9-12%Cr tempered martensitic ferritic steels, see table I.5.

$$\sigma_{or} = 0.8\frac{MGb}{\lambda_p} \tag{I.8}$$

where M is the Taylor factor (=3).

Table I.5 : Volume fraction, diameter and spacing of each kind of precipitate in high chromium ferritic steels, together with Orowan stress estimated from the values of interparticle spacing (Maruyama et al., 2001)

Particle	Volume fraction V[%]	Diameter d_p[nm]	Spacing λ_p[nm]	Orowan stress σ_{Or}[MPa]
Fe_2M	1.5	70	410	95
$M_{23}C_6$	2	50	260	150
MX	0.2	20	320	120

Fe_2M are probably Laves phases

The volume fraction (V), diameter (d_p) and spacing λ_p of each kind of precipitate in table I.5 were estimated by (Maruyama et al., 2001) based on experimental data reported in the literature (Hättestrand et al., 1998), (Hald and Straub, 1998), (Strang and Vodarek, 1998).

Note that the values of V, d_p, λ_p in table I.5 were estimated on various ferritic tempered martensitic steels and tested under various conditions (i.e. temperature, levels of stress, exposure time are different from one study to another). Note also that the sizes of MX and $M_{23}C_6$ carbides are almost twice lower compared to those reported in the Grade 92 steel in other studies (see for instance table I.1).

In the modeling of the creep behavior creep damage due to coarsening of particles (D_p) was defined by (Dyson, 2000) as:

$$\dot{D}_p = \frac{k_p}{3}\left(1 - D_p\right) \tag{I.9}$$

where k_p has the same definition as the parameter K_d (equation I.3).

Creep damage due to coarsening of particles (D_p) together with others damage variables are then related with the strain rate.

For example (Yin and Faulkner, 2005), (Yin and Faulkner, 2006) related the damage due to particles growth ($\dot{D}_p$) to the strain rate to model the creep behavior of the Grade 92 steel and E911 steel as follows:

$$\dot{\varepsilon} = \dot{\varepsilon}_0 \sinh\left[\frac{\sigma\,(1-H)}{\sigma_0\,(1-D_p)}\right] \tag{I.10}$$

where H is a dimensionless parameter used to model primary creep.

I.6.2 Evolution of subgrains

(Qin et al., 2003) proposed the following relationship between the subgrain size evolution fonction and the applied stress (σ):

$$\log\lambda = \log\lambda_\infty + \log\left(\lambda_0/\lambda_\infty\right)\exp\left(-\varepsilon/k(\sigma)\right) \tag{I.11}$$

where λ represents the subgrain size, λ_0 is the subgrain size before creep exposure, $\lambda_\infty = 10\,[Gb/\sigma]$ is the steady-state subgrain size (Qin et al., 2003), (Blum and Götz, 1999) where G is the shear modulus, b is the Burgers vector, ε is the cumulat strain and $k\,(\sigma) \approx 0.12$ is a growth constant.

Equation I.11 suggests that subgrain growth requires strain. Subgrain growth in P91 and German grade X20 steels during more than 10^5h of creep at 600°C and 550°C respectively were fairly well described by equation I.11 (Panait et al., 2010b), (Aghajani et al., 2009b).

(Sawada et al., 1998b) established the following relationship between the subgrain size evolution and strain:

$$\frac{\lambda_s - \lambda_{so}}{\lambda_s^* - \lambda_{so}} = a\varepsilon \tag{I.12}$$

where λ_{so} and λ_s are respectively the initial and steady-state values of subgrain width, and a is a constant independent of the creep conditions and materials tested.

The linear relation between $(\lambda_s - \lambda_{so})\,/\,(\lambda_s^* - \lambda_{so})$ is confirmed by recent studies (Sawada et al., 2010).

I.6.3 Evolution of dislocation density

Dislocations whithin subgrains (i.e. mobile dislocations) are carriers of plastic deformation under creep conditions and the creep rate ($\dot{\varepsilon}$) is a function of the mean dislocation velocity (v) and the density of mobile dislocations (ρ) as follows (Hald, 2008):

$$\sigma^* = \frac{M\dot{\varepsilon}}{\rho b B} \tag{I.13}$$

where σ^* is the backstress due to solid solution strengthening; $\dot{\varepsilon}$ is the minimum creep rate and B is the mobility of dislocations.

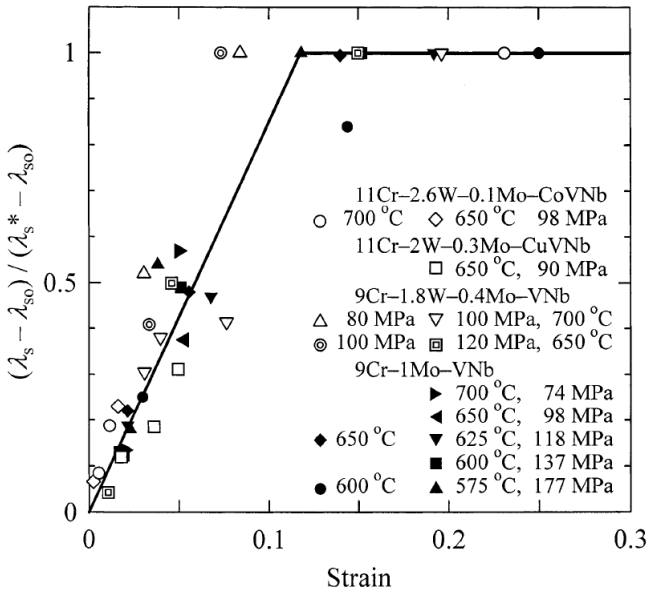

Figure I.26 : Evolution of subgrains width as a function of creep strain (Sawada et al., 1998b), (Sawada et al., 1998a), (Maruyama et al., 2001)

I.7 Summary

This chapter does not claim to give a detailed literature survey of creep resistant tempered martensitic steels. This chapter intended both to fix the background of this study and to highlight the most relevant findings related to this PhD. work.

Available published data on the microstructure of the Grade 92 steel during creep and/or thermal aging exposure at 600°C and 650°C were presented in this chapter. These data are summarized in table I.6. However, a scatter of data can be observed from one study to another. Also, there are rather few quantitative data concerning the microstructure of the Grade 92 steel during creep and/or thermal aging exposure for times higher than 20,000-30,000h both at 600°C and 650°C. Thus, microstructural investigations were conducted in this PhD. study on P92 steel specimens that have been creep tested for times up to 50,000h at 600°C.

Microstructural evolution as well as creep damage developement occur during long-term creep exposure at 600°C and 650°C in the 9-12%Cr heat resistant steels. The effect of microstructural evolution on the creep strength is not fully understood.

A sudden loss of the creep strength is observed in some 11-12% heat resistant steels compared to 9% Cr heat resistant steels. This was explained by a more intense (i.e. shorter time, higher amounts) modified Z-phase precipitation in 11-12% Cr steels compared to that in 9% Cr. However, there is a lack of quantitative data on this phase and it is difficult to estimate what *high* and *low* amounts mean.

The detrimental effect of modified Z-phase precipitation on creep strength consists in dissolution of finely distributed MX-type precipitates and thus promoting matrix recovery.

Note that the sudden loss of the creep strength observed in some 11-12% Cr steel does not correspond to the beginning of the modified Z-phase precipitation (Sawada et al., 2007). Most probably the creep strength significantly decreases when high amount of MX-type precipitates are put into solution by the precipitation and/or growth of modified Z-phase.

Modified Z-phase precipitation is also reported in the Grade 92 steel but for exposure

times lower than 40,000h at 600°C and it is considered as low in this steel.

The creep strength loss of the 9% Cr heat resistant tempered martensitic steels seems to be due to one or several of the following metallurgical evolution mechanisms: growth of $M_{23}C_6$ carbides, significant precipitation of Laves phases and recovery of the matrix rather then modified Z-phase precitation.

The influence of both precipitation of Laves phase and recovery of the matrix on the creep strength are not fully understood. Moreover the effect of these two mechanisms on the creep strength has never been studied separately.

Some attempts were done by (Sklenička et al., 2003) which conducted creep tests on thermally aged specimens in order to study the effect of long-term aging on the creep strength (most probably the effect of Laves phases). However the aging heat treatment was realized at a higher temperature (i.e. 650°C) than that of creep testing (i.e. 600°C) and there is no microstructural characterization.

In this study complementary creep tests were conducted to better understand the influence of each metallurgical mechanism on the creep behavior of the Grade 92 steel. Thermally aged and thermo-mechanically prepared specimens were used to separate the metallurgical mechanisms and to study their individual influence on the creep strength. To quantify the effect of each metallurgical mechanism on the loss of creep strength, most of creep tests are iso-stress (same stress on each kind of specimen). The results of these tests were then used to define internal variables of a mechanical model coupling creep damage and metallurgical evolution of the steel during creep.

The interest of thermally aged creep specimens is to study the influence of large precipitates (mostly Laves phases) on creep flow and creep damage of the T92 steel. The purpose of the creep tests conducted on thermo-mechanically prepared specimens was to estimate the influence of the recovery of the matrix on the creep strength. Creep tests were also conducted on notched specimens to study the influence of stress triaxiality on creep damage development.

Résumé

Ce chapitre ne prétend pas donner une étude bibliographique complète sur les aciers martensitiques au chrome. Les objectifs de ce chapitre ont été d'une part de fixer le contexte de l'étude et d'autre part de mentionner les résultats les plus significatifs disponibles dans la littérature en relation avec les travaux de cette thèse.

Les données quantitatives disponibles dans la littérature sur la microstructure de l'acier Grade 92 pendant l'exposition au fluage ou le vieillissement thermique à 600°C et 650°C ont été présentées dans ce chapitre. Ces données sont synthétisées dans le tableau I.6. Concernant l'évolution de la taille des précipités pendant le fluage ou le vieillissement de l'acier Grade 92, il y a des écarts assez importants entre les valeurs déterminées par différentes études. De plus, il n'y a pas beaucoup de données sur la microstructure de l'acier Grade 92 après des temps d'exposition au fluage ou au vieillissement supérieurs à 20000-30000h. Par conséquent, une caractérisation microstructurale des éprouvettes déjà testées en fluage à 600°C et 650°C pour des temps allant jusqu'à 50000h a été réalisée dans cette thèse.

Pendant des temps prolongés d'exposition au fluage il y a une évolution métallurgique de l'acier et un développement de l'endommagement. L'influence de cette évolution de la microstructure sur la résistance au fluage n'est pas complément comprise.

Une perte significative de la résistance au fluage est observée après de temps assez courts dans les aciers à 11-12%Cr comparé aux aciers à 9%Cr. Ceci est expliqué par une précipitation de la phase Z modifiée plus intense dans les aciers 11-12%Cr comparés aux

aciers à 9%Cr. Cependant, il n'y a pas assez de données quantitatives sur la phase Z modifiée et il est difficile d'évaluer quantitativement la classification en "low" and "high" faite par (Danielsen and Hald, 2007).

La précipitation de la phase Z modifiée met en solution les précipités de type MX ce qui peut dégrader la résistance au fluage de l'acier. À noter que la perte significative de la résistance au fluage dans les aciers à 11-12%Cr ne correspond pas au début de la précipitation de la phase Z modifiée (Sawada et al., 2007). Plus probablement, la précipitation de cette phase devient dangereuse pour la résistance au fluage quand elle est accompagnée d'une significative mise en solution des précipités de type MX.

La précipitation de la phase Z-modifiée est observée également dans l'acier Grade 92 après de temps d'exposition inférieurs à 40000h à 600°C et elle est considérée étant faible.

La perte de résistance au fluage des aciers à 9%Cr semble être plutôt due à des mécanismes comme la croissance des carbures $M_{23}C_6$, la précipitation significative des phases de Laves et la restauration de la matrice qu'à la précipitation de la phase Z-modifiée.

Les effets de la précipitation des phases de Laves et de la restauration de la matrice sur la perte de résistance au fluage ne sont pas complètement compris. De plus, l'effet de ces deux mécanismes n'a jamais été étudié séparément.

Des essais de fluage sur des éprouvettes pré-vieillies ont été réalisés par (Sklenička et al., 2003) pour étudier l'effet du vieillissement thermique (probablement l'effet des phases de Laves) sur la résistance au fluage. Cependant, la température du vieillissement thermique (i.e. 650°C) subi par les éprouvettes est supérieure à celle des essais de fluage (i.e. 600°C). Il n'y a pas de caractérisation microstructurale des éprouvettes pré-vieillies après fluage.

Dans la présente étude des essais de fluage complémentaires ont été réalisés pour mieux comprendre l'effet de chaque mécanisme de l'évolution métallurgique sur la résistance au fluage de l'acier Grade 92. Pour ce faire, des éprouvettes pré-vieillies et des éprouvettes pré-fatiguées ont été utilisées pour les essais de fluage. Pour quantifier l'effet de chaque mécanisme sur la résistance au fluage, la plupart des essais de fluage sont iso-contraintes (le même niveau de contrainte sur chaque type d'éprouvette). Les résultats de ces essais seront utilisés pour définir des variables internes dans le modèle mécanique qui sera construit par la suite.

L'intérêt des éprouvettes pré-vieilles et des éprouvettes pré-fatiguées sera d'étudier l'effet des phases de Laves et de l'état de la matrice sur le comportement en fluage, respectivement.

Des essais de fluage ont été également réalisés sur des éprouvettes entaillées pour étudier l'influence du taux de traixialité des contraintes sur le développement de l'endommagement par fluage.

Table I.6 : Microstructural evolution of the Grade 92 steel during creep or thermal exposure at 600°C and 650°C (literature survey)

Microstructural feature	Strengthening effect	Type of evolution	Quantitative results	Characterization technique	References
Matrix	-substructure strengthening	-decrease in dislocation density -subgrains growth - recrystallization	-dislocation density is reduced by 75% after 10^4h of creep at 600°C compared to that of the as-received steel; -subgrain size increases from 0.42 µm (in the as-received state) to 1.5 µm during 33,000h of creep at 600°C	-TEM on thin foils -EBSD	(Ennis et al., 1997), (Ennis et al., 2000), (Czyrska-Filemonowicz et al., 2006)
MX	-precipitate strengthening contribution -obstacles against dislocation motion	-can be dissolved by precipitation of modified Z-phase -posible growth	-EqD of about 20-40 nm with no significant evolution during exposure at 600°C and 650°C -very stable against growth and coarsening for temperatures lower than 650°C	TEM on extractive replicas or thin foils	(Ennis et al., 2000), (Sawada et al., 2001), (Ennis et al., 1997), (Gustafson and Hättestrand, 2002)
$M_{23}C_6$ carbides	-precipitate strengthening contribution -obstacles against boundaries motion	-growth	-E_qD increases from 90 nm to 120 nm in the first 10^4h creep exposure at 600°C - after 6×10^4h of creep exposure at 600°C their size is 50% higher than that in the as received steel -see table I.1 -enhanced by stress (see figure I.8)	-TEM on extractive replicas or thin foils	(Ennis and Czyrska-Filemonowicz, 2002), (Ennis et al., 2000), (Gustafson and Hättestrand, 2002)
Laves phases	-might reduce the solid solution strengthening due to W and Mo atoms in the matrix	-precipitaton during creep or thermal exposure -high growth and coarsening rates	the EqD increases from 0 to 250 nm and from 0 to 400 nm in the first 10^4h of creep exposure at 600°C and 650°C, respectively (figures I.12 and I.13)	-TEM tecniques -SEM techniques (recommended)	(Hald and Korcakova, 2003), (Korcakova et al., 2001), (Dimmler et al., 2003)
Modified Z-phase	-might reduce the precipitation strengthening du MX-type precipitates	-precipitation during long-term creep or thermal exposure at the expense of MX-type precipitates	-EqD of 155 nm after 39,539h of creep at 600°C, 130MPa (Sawada et al., 2006) -low precipitation (see figure I.18) -lack of quantitative data	-TEM on extractive replicas or thin foils	(Danielsen and Hald, 2007), (Sawada et al., 2007), (Hättestrand and Andrén, 2001)

EqD-averange equivalent diameter

Chapter -II-

General presentation of the materials under study

Contents

II.1 Introduction

This chapter aims to present the materials under study- two Grade 92 steels. Their chemical composition, heat treatments as well as principal microstructural features are presented. Results of tensile tests conducted at room temperature, 600°C and 650°C are also presented in this chapter.

Introduction

Ce chapitre porte sur la présentation des matériaux de l'étude: deux aciers Grade 92. Les compositions chimique, les traitements thermique ainsi que leurs microstructure sont présentés. Les résultats des essais de traction à température ambiante, à 600°C et 650°C sont également présentés dans ce chapitre.

II.2 Heat treatments and chemical composition

The T92 steel was supplied by *Vallourec&Mannesmann*, France as a tube of 48.3mm in outside diameter and 11.2 mm in wall thickness. The tube was produced by continuous hot rolling and delivered in the austenitized and tempered conditions. Heat treatment and chemical composition of the T92 steel tube are given in table II.1.

Specimens cut off from this T92 steel tube were used for mechanical tests (i.e. creep, creep-fatigue and tensile) conducted in this study. There specimens were machined along the tube axis at mid-thickness.

Table II.1 : Chemical composition and heat treatments of T92 steel

	C	Si	Mn	P	S	Al	Cr	Ni	Mo	V	Nb	W	N	B
wt.[%]	0.12	0.2	0.50	0.015	0.002	0.001	8.79	0.15	0.38	0.20	0.056	1.67	0.046	0.0026

Heat treatment: 1070°C, 1h +770°C, 2h; air cooling

Exceptionally long-term crept specimens tested at 600°C and 650°C for times up to 50,000h were provided by Salzgitter Mannesmann Forschung GmbH (SZMF), Germany. These creep specimens were cut out of a P92 steel pipe 323.9mm in outside diameter and 25mm in wall thickness, the chemical composition and heat treatment are given in table II.2. A piece of the same P92 steel in as-received condition from the same pipe as the crept specimens was also provided. As-received P92 steel and long-term crept specimens in P92 steel were investigated with regard to microstructural evolution and creep damage using scanning electron microscopy (SEM) and transmission electron microscopy as well as electron backscatter diffraction (in SEM). Results of these investigations as well as details about testing conditions of the crept specimens will be given in the next chapters.

Table II.2 : Chemical composition and heat treatment of P92 steel (data from SZMF, Germany)

	C	Si	Mn	P	S	Al	Cr	Ni	Mo	V	Nb	W	N	B
wt.[%]	0.12	0.16	0.42	0.012	0.001	0.005	9.32	0.24	0.49	0.20	0.055	1.75	0.049	0.0012

Heat treatment: 1060°C, 1h +770°C, 2h; air cooling

T92 and P92 steels have similar chemical compositions but different thermo-mechanical processing routes, owing to the fact that the product shape are different.

The T92 and P92 steels under study, both belong to ASME Grade 92 steel. Grade 92 is the result of research efforts conducted for the improvement of Cr-bearing heat resistant steels.

Figure II.1 shows the chemical composition evolution of the main Cr-bearing heat resistant steels developed in the last decades. Grade 92 steel was developed in the early 1990s from the experience of the Grade 91 (9Cr-1Mo-0.2V-Nb) steel. Compared with the Grade 91, the chemical composition of the Grade 92 was improved by both addition of W which increases solid solution strengthening and addition of up to 0.006 wt.%B.

a)

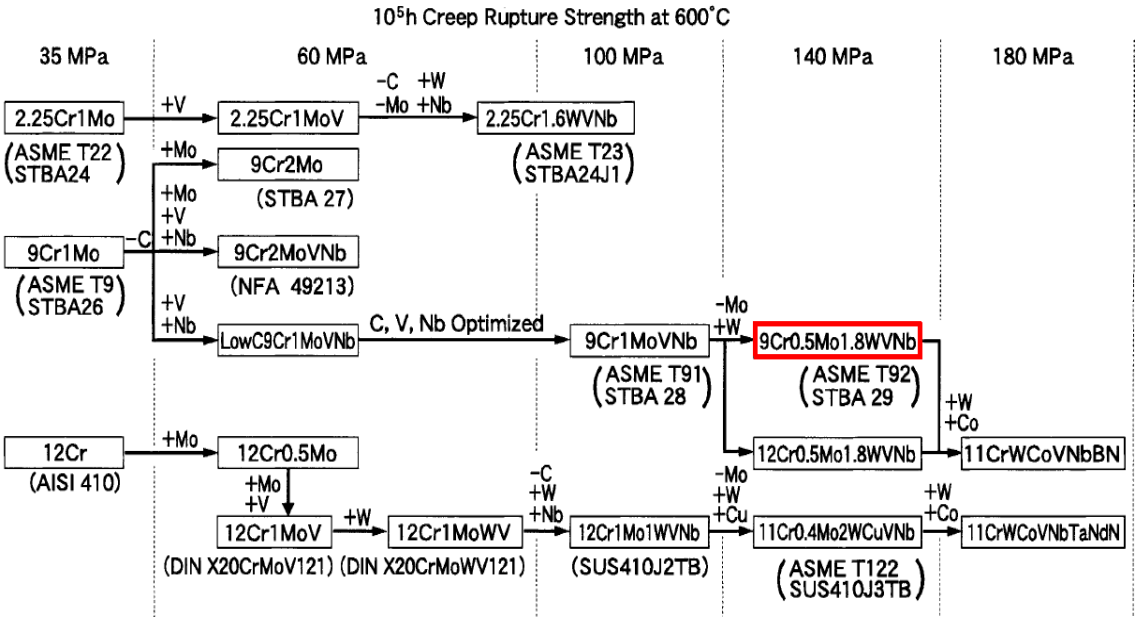

b)

	Steels	Specification ASME	Specification JIS	C	Si	Mn	Cr	Mo	W	Co	V	Nb	B	N	Others
2%Cr	2.25Cr1Mo	T/P22	STBA24	0.12	0.3	0.45	2.25	1.0	—	—	—	—	—	—	—
	2.25Cr1.6WVNb	T/P23	STBA24J1	0.06	0.2	0.45	2.25	0.1	1.6	—	0.25	0.05	0.003	—	—
9%Cr	9Cr1Mo	T/P9	STBA26	0.12	0.6	0.45	9.0	1.0	—	—	—	—	—	—	—
	9Cr2Mo	—	STBA27	0.07	0.3	0.45	9.0	2.0	—	—	—	—	—	—	—
	9Cr1MoVNb	T/P91	STBA28	0.10	0.4	0.45	9.0	1.0	—	—	0.20	0.08	—	0.05	—
	9Cr0.5Mo2WVNb	T/P92	STBA29	0.07	0.06	0.45	9.0	0.5	1.8	—	0.20	0.05	0.004	0.06	—
	9Cr1Mo1WVNb	T/P911	—	0.11	0.3	0.45	9.0	1.0	1.0	—	0.20	0.08	0.003	0.06	—
	LowC9Cr1MoVNb	—	—	0.06	0.5	0.60	9.0	1.0	—	—	0.25	0.40	0.005	—	—
	9Cr2MoVNb	(NFA49213)		0.10	0.4	0.10	9.0	2.0	—	—	0.30	0.40	—	—	—
12%Cr	12Cr1MoV	(DIN X20CrMoV121)		0.20	0.4	0.60	12.0	1.0	—	—	0.25	—	—	—	0.5Ni
	12Cr1MoWV	(DIN X20CrMoWV121)		0.20	0.4	0.60	12.0	1.0	0.5	—	0.25	—	—	—	0.5Ni
	12Cr1Mo1WVNb	—	SUS410J2TB	0.10	0.3	0.55	12.0	1.0	1.0	—	0.25	0.05	—	0.03	—
	12Cr0.4Mo2WCuVNb	T/P122	SUS410J3TB	0.11	0.1	0.60	12.0	0.4	2.0	—	0.20	0.05	0.003	0.06	1.0Cu
	11Cr2.6W2.5CoVNbBN	—	—	0.08	0.2	0.50	11.0	0.2	2.6	2.5	0.20	0.07	0.004	0.05	—
	11Cr3W3CoVNbTaNdN	—	—	0.10	0.3	0.20	11.0	—	3.0	3.0	0.20	0.07	—	0.04	0.07Ta, 0.04Nd

Figure II.1 : a) Development progress of Cr-bearing heat resistant steels for boilers; b) Chemical composition evolution of Cr-bearing heat resistant steels developed in the last decades (Masuyama, 2001)

II.3 Role of alloy elements

Alloy elements in steels are of a great importance for their mechanical properties. Thus, the role of alloy elements in Cr-bearing heat resistant steels is discussed in the following based on a literature survey.

II.3.1 Chromium

Figure II.2 represents the equilibrium Fe-Cr phase diagram. Chromium is an α- (ferrite) forming alloy element. For Cr contents below 10.5% the Fe-Cr binary diagram allows a two phase ($\alpha + \gamma$) and an austenite (γ) region. For Cr contents higher than 11.5 % only the α domain exists. In this case the steel has no solid state equilibrium phase transformation and remains ferritic (α phase) at all temperatures. For Cr contents between 10.5 et 11.5%, and for a narrow temperature range, the α and γ phases coexist forming a two-phase structure.

The γ domain is strongly reduced by chromium addition, figure II.2. This drawback is compensated by the addition of γ - forming alloying elements. Chromium as alloy element brings good oxidation and corrosion properties to the steel. Cr improves also the hardenability of the steel.

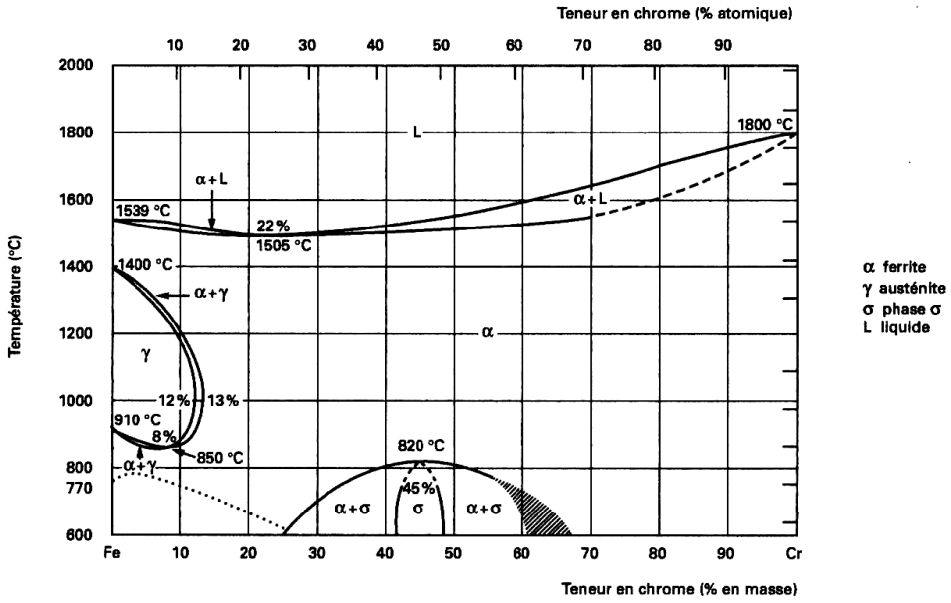

Figure II.2 : Binary Fe-Cr equilibrium phase diagram (Massabki, 1986)

In the 9-12% Cr heat resistant steels, chromium reacts with carbon and form $M_{23}C_6$ carbides during tempering. In steels with high content in nitrogen, formation of M_2X type nitrides rich in chromium is observed. Liu and Fujita (Liu and Fujita, 1989) found that the volume fraction of Cr_2N precipitates increases with Cr content of the steel (9.9...12.9%Cr).

Chromium seems to have an influence on the precipitation of modified Z phase. In the 11-12% Cr heat resistant steels the precipitation of modified Z phase is more intense than in the 9-10% Cr steels (Danielsen and Hald, 2007), (Danielsen and Hald, 2006).

II.3.2 Carbon and nitrogen

Carbon and nitrogen are strong γ- forming elements. Carbon strongly expands the γ domain. In small amount its effect is 30 times higher than the nickel effect, see figures II.3a and II.3b.

Carbon strongly influences on the hardenability of the steel. The carbon content is limited to low values to ensure good corrosion and welding properties of the steel.

The solubility of carbon and nitrogen is very low in ferrite, so those elements will form carbides and carbonitrides.

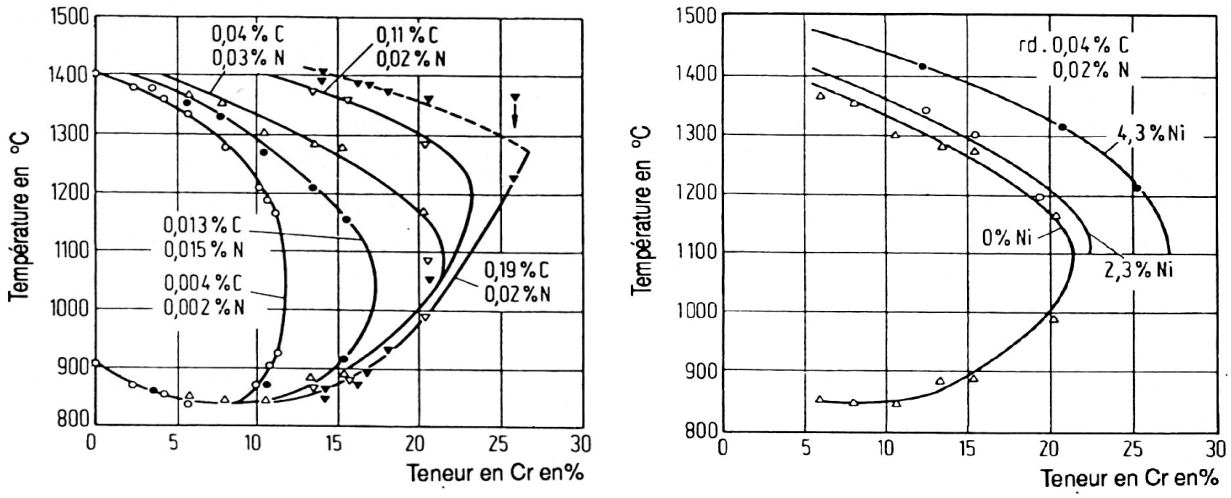

a) b)

Figure II.3 : Influence of the carbon (a) and carbon, nickel and nitrogen (b) content on the γ domain (Massabki, 1986)

II.3.3 Molybdenum and Tungsten

Molybdenum and tungsten have a solid solution strengthening effect. In Fe-Mo and Fe-W alloys there is a precipitation of Laves phases ($Fe_2(Mo,W)$) during creep or thermal aging which depletes the solid solution in W and Mo. For this reason the W and Mo contents are limited to 2 wt. % and 1 wt. % respectively (Klueh et al., 2002). Figure II.4 shows the influence of W content on the creep rupture strength of the P92 steel.

Higher W and/or Mo contents will increase creep strength for short-term (see figure II.4) but it will enhance the Laves phases precipitation and the long-term creep strength will significantly decrease (Foldyna et al., 2001), (Hasegawa et al., 2001b). Creep strength degradation by precipitation of Laves phases can be explained by formation of areas free of W and/or Mo atoms where creep strain can localize.

Improvement of the Grade 92 steel creep strength compared to Grade 91 steel by substituting W for Mo can be attributed to the lower diffusivity of W (Miyata and Sawaragi, 2001) in the Grade 92 steel. The better creep strength of the Grade 92 steel can be also explained by a finer size and a lower coarsening rate of Laves phases in the Grade 92 compared to Laves phases in the Grade 91 steel for comparable high temperatures exposure time (Hald and Korcakova, 2003), (Hasegawa et al., 2001a).

There seems to be little difference between the intrinsic effect of the addition of W on solid solution strengthening compared to that of Mo because the mobility of dislocations in Fe-W alloys was reported to be similar to that in Fe-Mo alloys (Terada et al., 2002).

Due to its slow diffusivity, W can also slow down the recovery of tempered martensitic matrix during creep exposure (Sawada et al., 1999).

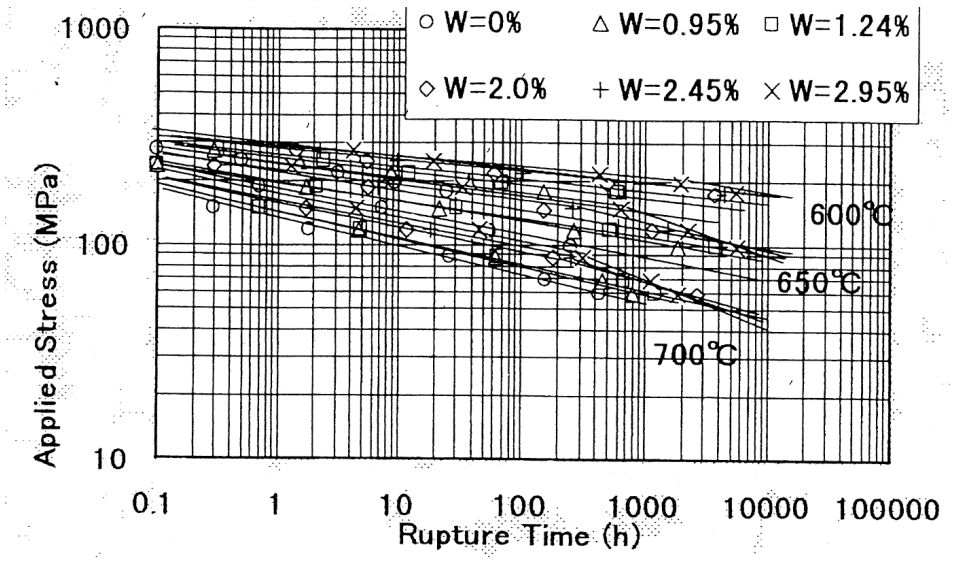

Figure II.4 : Influence of W content on the creep rupture strength of the P92 steel, (Hasegawa et al., 2001b)

II.3.4 Vanadium, niobium, tantalum, titanium

Vanadium, niobium, tantalum and titanium form carbides, nitrides and carbonitrides of MX-type (M=V, Nb, Ta, Ti; X=C,N) precipitates. MX-type precipitates form during tempering and have an average equivalent diameter of about 20-40nm. They are finely dispersed within the martensitic laths yielding a precipitation strengthening effect.

Three types of MX-type precipitates are found in the T92 steel, details about their chemical composition, size and shape are presented the next section: *General features of the microstructure.*

Steels alloyed with tantalum show better creep strength than steels alloyed with niobium and/or vanadium (Klueh et al., 2002). The effect of tantalum on creep properties of the steel is still controversial; there are studies which show that MX (M=Ta) particles are more stable that MX (M=Nb, V) at high temperatures (Taneike et al., 2001); other studies reveal that 75-90% of tantalum content remains dissolved in the matrix after aging or creep exposure thus maintaining solid solution strengthening (Tamura et al., 2000), (Jayaram and Klueh, 1998).

II.3.5 Boron

Cr-bearing heat resistant steels containing boron show a remarkable long-term creep strength (Kager et al., 2006). The effect of boron on the microstructural evolution is not fully understood. For instance, (Karlsson and Nordén, 1988b), (Karlsson and Nordén, 1988a) reported a segregation of boron at boundaries which seems to slow down the growth of $M_{23}C_6$ carbides during creep or thermal aging.

(Lundin and Richarz, 1995) reported an homogeneously distribution of boron within the $M_{23}C_6$ carbides in a 9%Cr steel doped with 80 ppm B and no interfacial segregation was detected by the means of atom probe fiels ion microscopy (APFIM). This observation was confirmed later (Lundin et al., 1997).

In the P122 (11Cr-1.94W-0.87Cu-0.56Mn-0.42Mo-0.32Ni-0.19V-0.11C-0.05N-0.02Si-0.13P-0.001B) steel boron was located within $M_{23}C_6$ carbides close to the interface between

the carbide and the matrix, while in the P92 steel the boron was homogeneusly distributed (Hättestrand et al., 1998) within $M_{23}C_6$ carbides. The authors do not give complementary information about this diference.

Some others studies reported (Horiuchi et al., 2002), (Abe, 2009), (Kauffmann and et al., 2006), that the boron content is four times higher in the $M_{23}C_6$ carbides localized at prior austenite grain boundaries compared to that in $M_{23}C_6$ carbides inside grains.

Atom probe field ion microscopy used for chemical analyses of precipitates in a 0.17C-9.3Cr-1.55Mo-0.27V-0.015N-0.01B (%wt.) tempered martensitic steel in as-received and crept conditions showed that boron was distributed uniformly within all the precipitates and boron was not segregated to precipitates-matrix interface (Hofer et al., 2002). A substantial amount of boron was detected in the matrix in as-received and crept conditions. Little boron segregation was observed in addition to phosphorus segregation along interface of $M_{23}C_6$ carbides with matrix (Hofer et al., 2002).

Experimental published data on the spatial distribution of boron in heat resistant steels and interpretation of boron effect on the microstructural evolution are different from a study to another. This is probably due to the difficulty of studying light elements such as boron, the accuracy of experimental technique, or probably because the influence of boron on the microstructure depends on the B/C ratio and/or B/N ratio of the steel.

The amount of boron increase with the nominal boron concentration of the steel (Hättestrand and Andrén, 1999), (Andrén, 2001). Figure II.5a shows the amount of boron inside M_23C_6 carbides in several 9-12% Cr steels determined by APFIM technique.

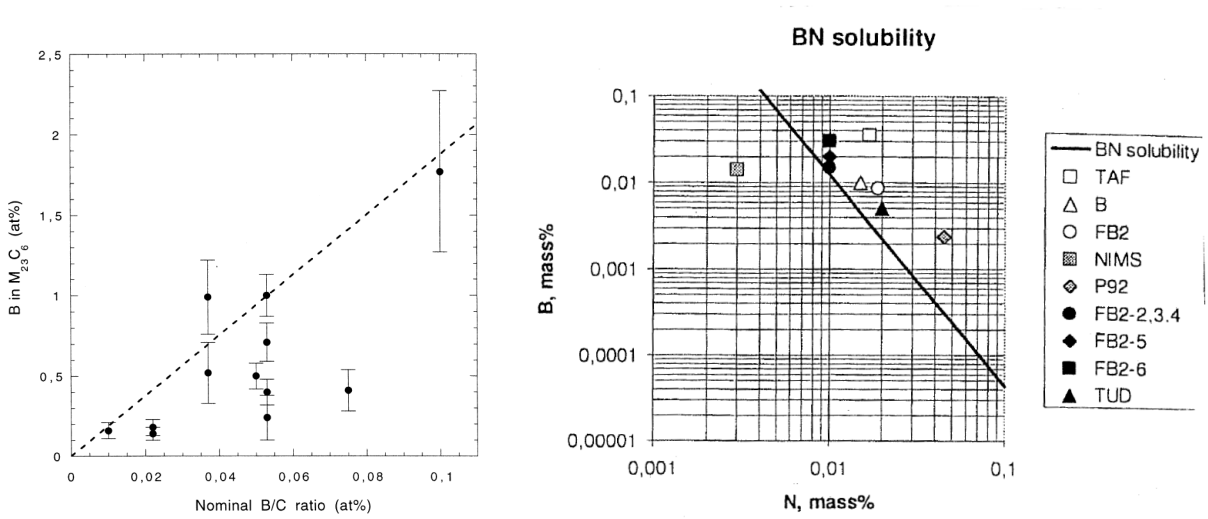

a) b)

Figure II.5 : a) Content of boron in $M_{23}C_6$ carbides in various 9-12%Cr steels (Hättestrand and Andrén, 1999), (Andrén, 2001); b) BN solubility at 1150°C according to NIMS (Hald, 2006)-initially in (Nowakowski, 2000)

Nevertheless, the amount of boron is limited to small amount, few ppm, in order to avoid the formation of large BN inclusions (average equivalent diameter of 1-5μm) (Sakuraya et al., 2004). Diagrams of boron solubility were established in NIMS en function of both nitrogen and boron content of the steel, see figure II.5b. The steels indicated in figure II.5b are 9-11%Cr heat resistant steels with various boron contents developed in the COST Actions (i.e. 501, 522, 536). For more details about these steels, see for instance (Hald, 2006).

To conclude, advanced studies are needed both to better understand the effect of boron

on the microstructure and to avoid formation of precipitates such as BN, (Mo, Nb)- rich borides which may decrease the beneficial effect of boron.

II.3.6 Nickel, manganese and cobalt

Nickel, manganese and cobalt are γ- forming elements. They are added in 9-12% Cr heat resistant steels to avoid the formation of δ ferrite. Nickel and manganese have the drawback of reducing the Ac_1 temperature and thus limiting the tempering temperature to avoid formation of reverse austenite. This is not true for cobalt.

(Vodarek and Strang, 1998), (Strang and Vodarek, 1998) observed that nickel influences the growth of $M_{23}C_6$ carbides. They also observed that nickel favours the precipitation of M_6X particles. The growth rate of M_6X and $M_{23}C_6$ precipitates increases with the nickel content (0.32-1.28% wt.) in 12Cr-0.6Mo-0.7Mn-0.2Si-0.2V-0.13C (% wt.) steels, (Vodarek and Strang, 1998), (Strang and Vodarek, 1998).

Nickel enhances the precipitation of modified Z phase. In steels with high nickel content modified Z phases are observed after shorter time exposures. For example, in the 12CrMoVNb steel with 0.52% Ni, the modified Z phase is observed after 22,052 h of creep at 600°C and in the same steel but with a 1.15% Ni, modified Z phase is observed after 7,247 h of creep at 600°C. In the 12CrMoVNb steel with 0.52% Ni and with 1.15% Ni the modified Z phase is observed after 79,171 h and after 17,875 h of creep at 550°C, respectively (Strang and Vodarek, 1998), (Vodarek and Strang, 2000), (Weinert, 2002).

The effect of nickel on the mechanism of modified Z phase precipitation is not fully clarified. The chemical composition of modified Z phase does not change during creep and it depends on the temperature at which precipitation of this phase occurs. The Nb content of the modified Z phase increases with the nickel content of the steel (Vodarek and Strang, 2006).

II.4 Inclusions

Inclusions are large particles with an average equivalent diameter going from 0.5 to 5 μm and they are mainly due to steelmaking process.

Figure II.6 shows the EDS spectra of main inclusions found in the T92 steel, they were identified on fracture surfaces of tensile and crept specimens. Specimens fractured in a ductile manner and fracture surfaces were characterized by dimples. It is to be mentioned that identification of inclusions on fracture surface is difficult due to the dimple geometry and localization of the EDS detector inside MEB-FEG.

X-ray dispersive wave length spectroscopy analysis, using Castaing electron microprobe revealed very low amounts of inclusions in a Grade 91 steel (Gaffard, 2004), (Vivier, 2009). Optical and MEB observations carried out on the T92 steel confirm a very low inclusion content. As inclusions play a negligible role on the creep strength loss or creep cavitation process, no quantification or detailed study on inclusions in the T92 steel was carried out.

II.5 General features of the microstructure

The microstructure of Grade 92 steel consists of a tempered martensite matrix and precipiates mainly of $M_{23}C_6$ and MX types. The microstructure of Grade 92 steel in the as-received conditions is also characterized by high dislocation density inside sub-grains, W and Mo atoms in solid solution.

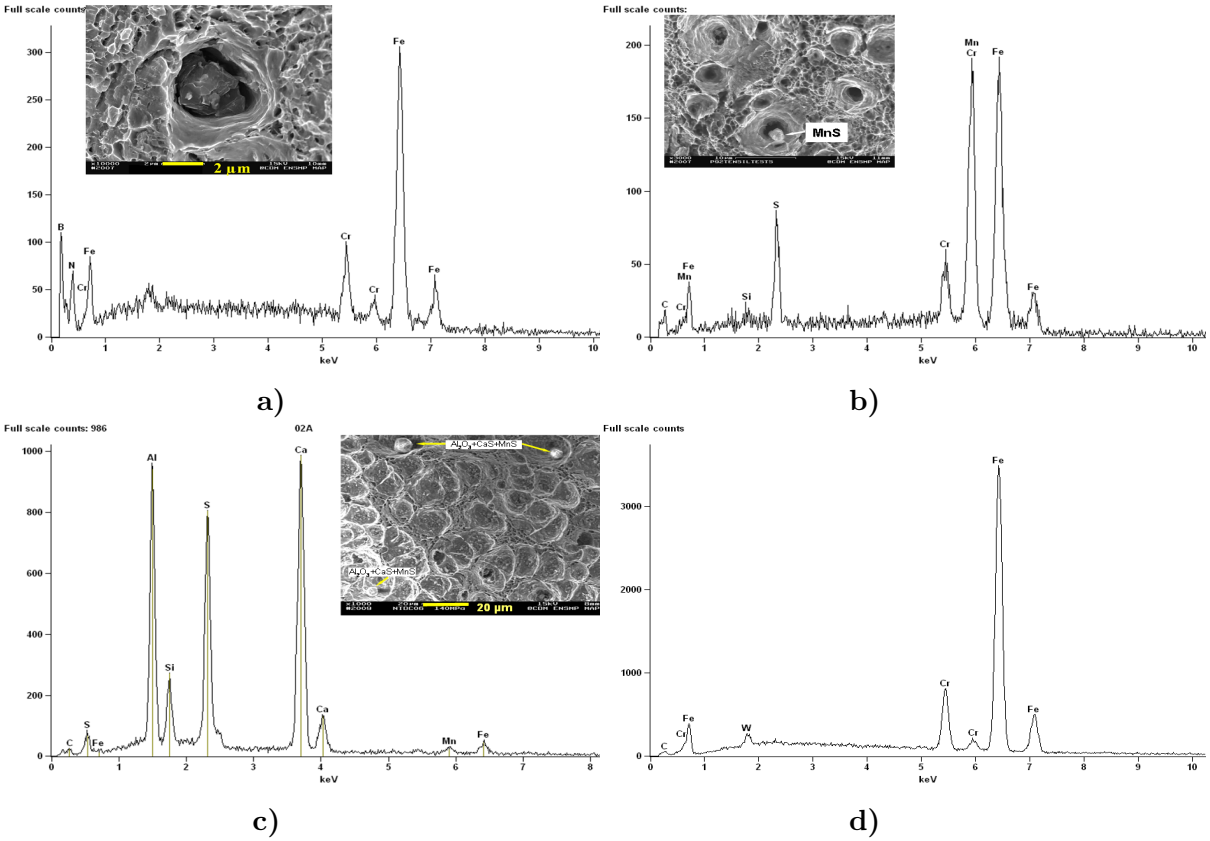

Figure II.6 : EDS spectra of typical inclusions identified on fracture surface of T92 steel tensile or crept specimens compared with a EDS spectrum from the matrix (d)
a) BN; b) MnS; c) Al_2O_3+CaS+MnS

II.5.1 Microtexture

The microtexture of the as-received T92 steel consists of a tempered lath martensite arranged in packets (group of lath with same morphological orientation) subdivided into blocks (the group of laths of close crystal orientations, one or two variants) inside prior austenite grains (Morito et al., 2003), (Morito et al., 2006).

Figure II.7a shows a schematic illustration of the lath martensitic structure. Due to their very small size, individual martensite laths can not be observed on optical, MEB or FEG-SEM micrographs, TEM observations on thin foils are required. Block and packet boundaries are decorated with precipitates and they can be easily distinguished after etching, even with light microscopy or SEM imaging, see figure II.10. In figures II.10b and II.10d are underlined some block and packet boundaries in the T92 steel in the as-received conditions after a Villela etching.

Figure II.9 shows the microtexture of the as-received T92 steel. Inverse Pole Figure (IPF) with orientation of sample normal in the crystal frame as key colour in figure II.9 shows the packets (same morphological orientation) and blocks (one color per block, in general) in as-received the T92 steel martensitic microstructure. Figure II.8 shows the distribution of misorientation angles between the small grains (blocks and packets) of EBSD maps of figure II.9. The histogram of figure II.8 is typical of that of martensite variants (Gourgues et al., 2000), (Morito et al., 2003) .

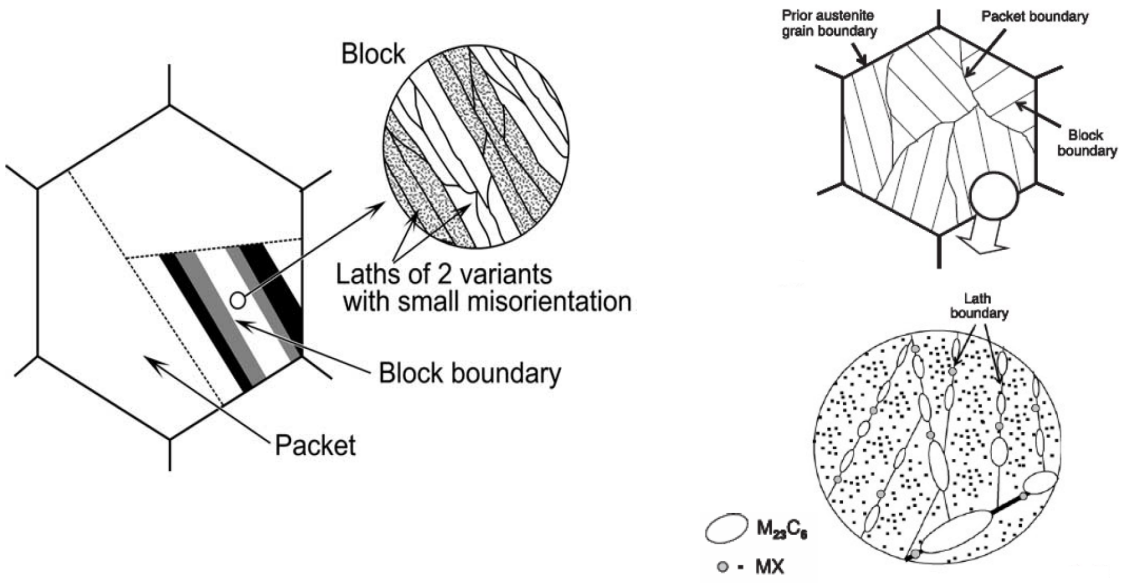

Figure II.7 : Schematic illustration of tempered matensitic microstructure (a) (Morito et al., 2003) and distribution of precipitates (b) (Abe, 2006) in 9-12% Cr heat resistant steels

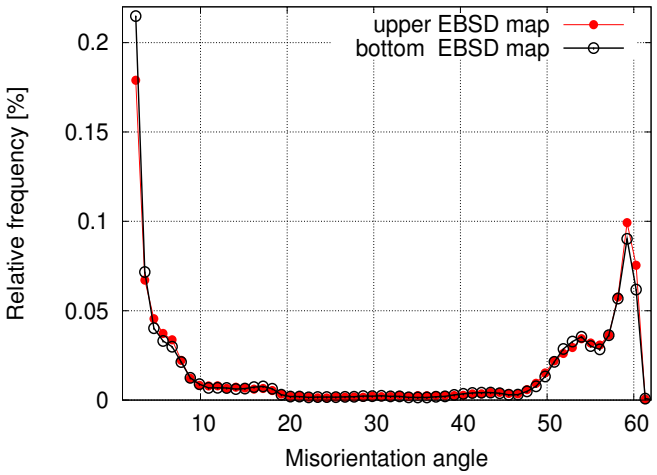

Figure II.8 : Misorientation angle histogram between grains corresponding to the EBSD maps (as-received T92 steel) in figure II.9

In order to a sample large area of the as-received T92 steel and to get representative data on its microtexture, two EBSD maps were acquired closely due to experimental reasons. The acquisition files corresponding to the two EBSD maps in figure II.9 were processed separately.

EBSD investigations were also conducted in the as-received P92 steel. No significant difference was observed in both EBSD maps and corresponding histograms of misorientation angles of P92 steel compared to these in figures II.9 and II.8.

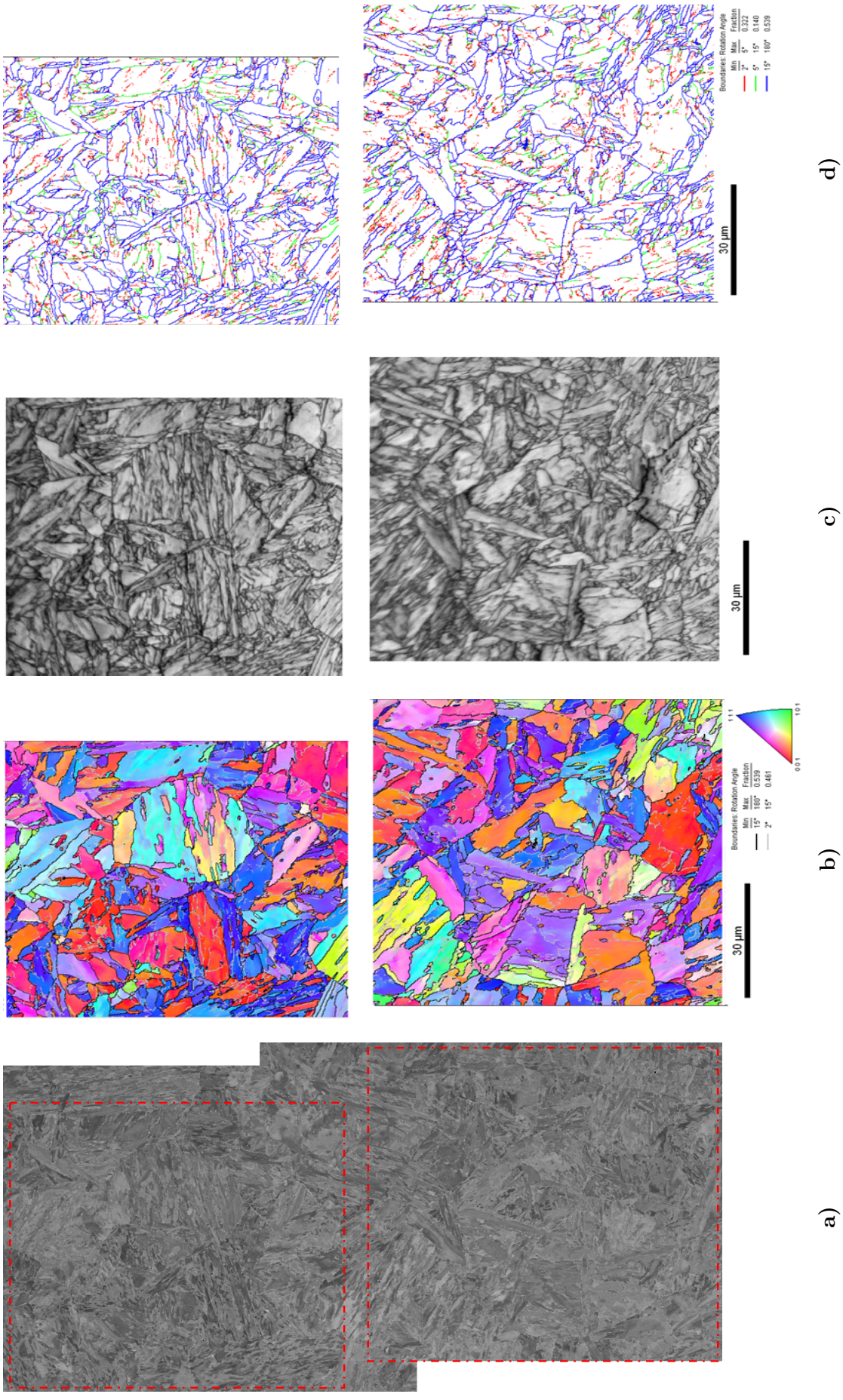

Figure II.9 : Microtexture of as-received T92 steel a) SEM-BSE image; b) Inverse Pole Figure (IPF) with orientation of sample normal in the crystal frame as key color; c) EBSD Image Quality map (IQ); d) EBSD boundaries map (key color after misorientation angles)

II.5.2 Precipitates

The precipitates in the as-received Grade 92 steel are mainly of $M_{23}C_6$ and MX types.

II.5.2.1 $M_{23}C_6$ carbides

$M_{23}C_6$ carbides precipitate during tempering mainly on boundaries (prior austenite grains, packets, blocks, laths). $M_{23}C_6$ is the most stable carbide and will replace nearly all other metastable carbides during tempering. An example of a precipitation sequence of carbides during tempering at 1053K in a 12% Cr steel could be:

$M_3C \rightarrow M_{23}C_6 + M_2X \rightarrow M_{23}C_6 + MX$ (Janovec et al., 1994), (Hald and Straub, 1998)

or

$M_3C \rightarrow M_7C_3 + M_2X \rightarrow M_{23}C_6 + MX$ (Danielsen, 2007)

$M_{23}C_6$ carbides have a cubic crystal structure and consists mainly of Cr, Fe and C, with small contents of Mo, W, Mn and B. A TEM-EDX spectrum of $M_{23}C_6$ carbides obtained on carbon extractive replicas of precipitates of as-received T92 steel is shown in figure II.11. The Cu peak in all TEM-EDX spectra cames from the copper grids on which extractive replicas were fixed. The following average chemical composition of $M_{23}C_6$ carbides was established from the TEM-EDX analysis of 70 precipitates investigated: 61.84Cr-27.98Fe-3.85W-2.24Mo-3.79Mn-0.3V (% at.).

The average diameter of the $M_{23}C_6$ carbides increases from 72 to 89 nm when the tempering temperature is increased from 715 to 775°C (Ennis et al., 2000), (**?**). Taking into account the uncertainty of measurements, this increase is not very significant. Tempering temperatures higher than 775°C do not yield an average diameter of $M_{23}C_6$ carbides higher than 89 nm.

Quantification of $M_{23}C_6$ carbides sizes on TEM micrographs of extractive replicas confirmed an average equivalent diameter of 90-100nm in the as-received T92 steel.

II.5.2.2 MX-type precipitates

MX-type precipitates have an average equivalent diameter of 20-40nm and they can be divided in two groups, NbC (enriched in Nb) and VN (enriched in V). Typical TEM-EDX spectra for NbC and VN precipitates are shown in figure II.12a and II.12b, respectively. The formation of the two types of MX is explained by the miscibility gap in the Cr-V-Nb system (Suzuki et al., 2003). More details about the precipitation mechanism of MX-type precipitates during tempering were given by (Yoshino et al., 2005), (Tamura et al., 2001), (Tamura et al., 2004).

MX particles with a more complex shape ("V-wings") are also observed in low quantities in chromium heat resistant steels (Yamada et al., 2001), (Tokuno et al., 1991), (Hamada et al., 1995). The TEM micrograph in figure II.10f shows this kind of MX precipitate found in the as-received T92 steel. The V-wings are forming by secondary precipitation of VN on Nb(C,N) during tempering. The Nb(C,N) surrounded by a region enriched in V are nucleation sites for V-wings. The size of the "wings" seems to be influenced by the nitrogen content of the steel (Tokuno et al., 1991).

As NbC remains undissolved throughout the heat treatment, they are also called primary MX, while VN are called secondary MX. The primary MX, NbC, precipitates at high temperatures at austenite grain boundaries. They did not dissolve during austenization thus preventing from $\gamma-$ grain growth. NbC precipitates usually appear as round shaped particles of various sizes.

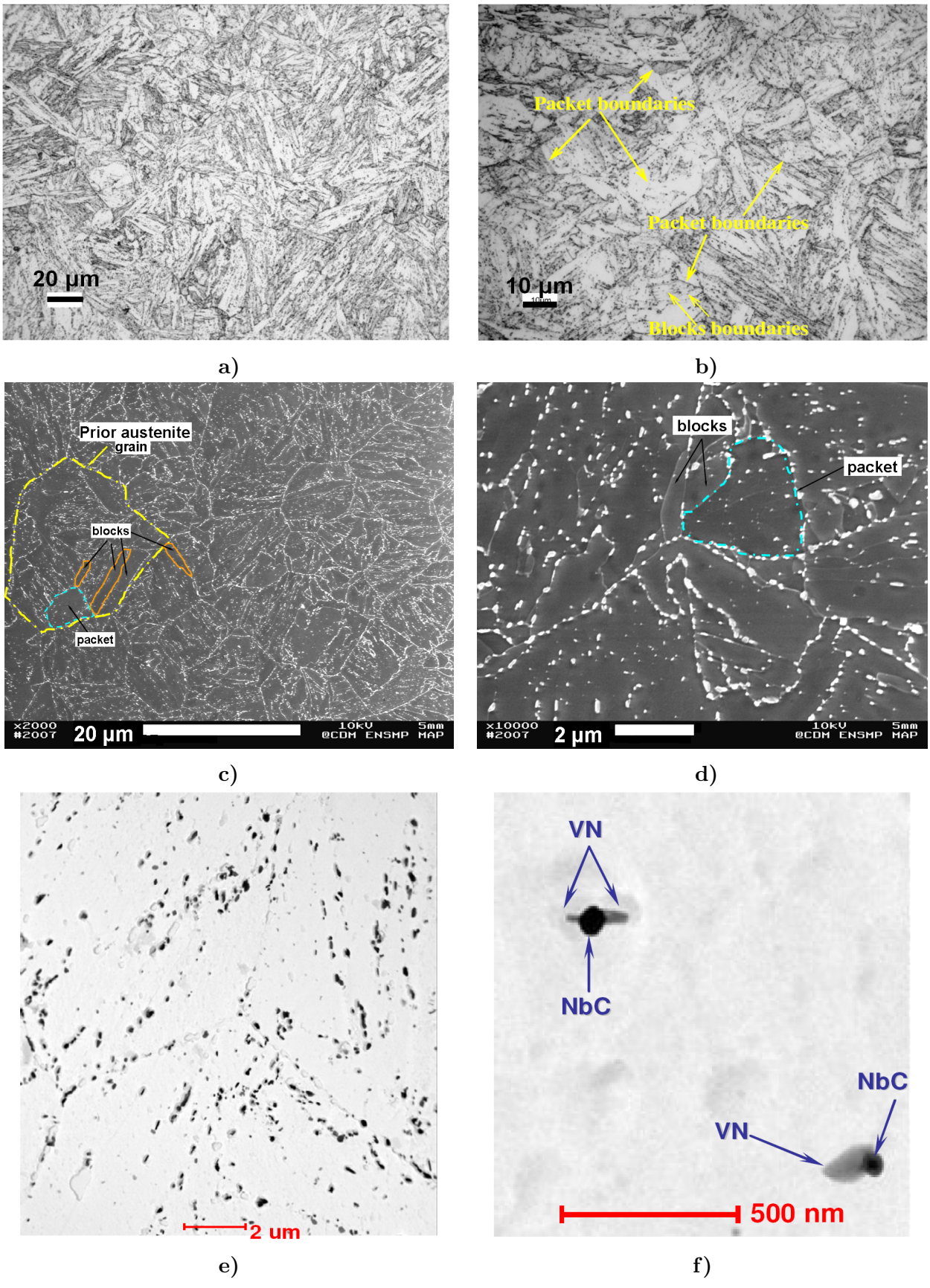

Figure II.10 : Microstructure of the as-received T92 steel. a), b) light micrographs after Villela etching ; c), d) FEG-SEM micrographs after Villela etching; e), f) TEM micrographs of extractive replicas

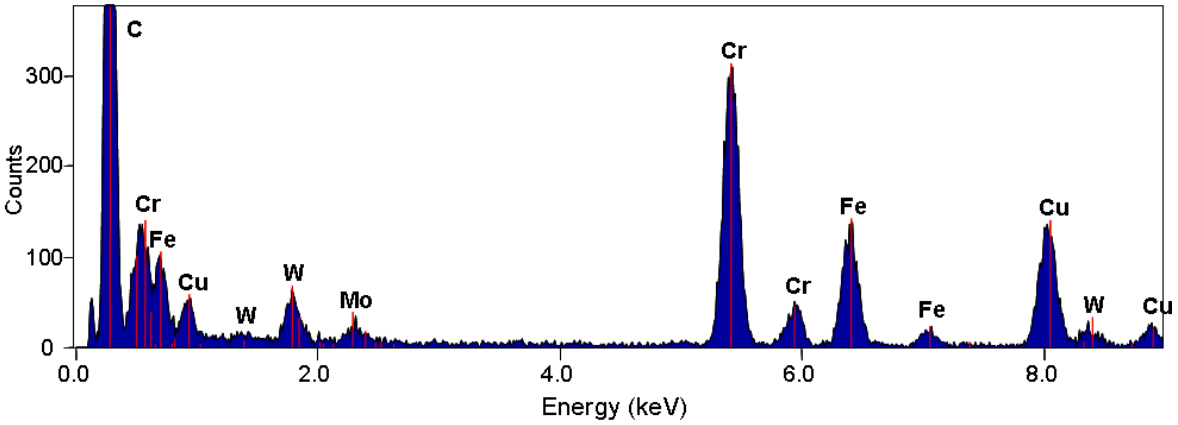

Figure II.11 : Typical TEM-EDX spectra of $M_{23}C_6$ carbides in the as-received T92 steel obtained on carbon extractive replicas

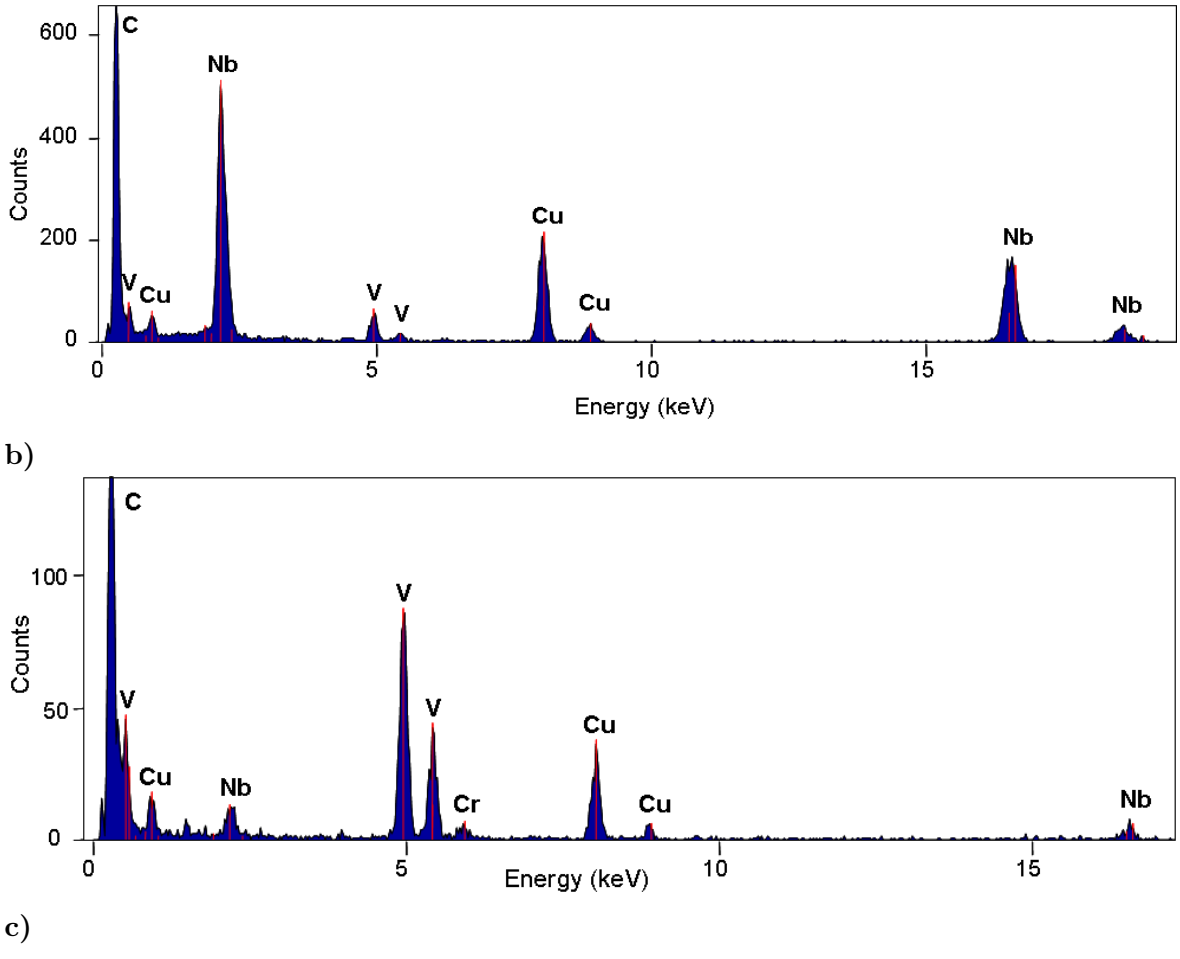

Figure II.12 : Typical TEM-EDX spectra of NbC precipitates (a) and VN precipitates (b) in the as-received T92 steel obtained on carbon extractive replicas

The secondary MX, VN, precipitate homogeneously inside martensite laths during tempering. Dislocations are nucleation sites for this type of MX (Yoshino et al., 2005). Dislocations annihilation due to matrix recovery during tempering can involve the dissolution

of the MX which had nucleated at these dislocations (Yoshino et al., 2005).

MX precipitates have a cubic NaCl crystal structure and the following orientation relationships between MX and the matrix are established:

$$\{100\}_{\alpha-Fe} \parallel \{100\}_{VN} \text{ and } \langle 011\rangle_{\alpha-Fe} \parallel \langle 010\rangle_{VN} \qquad \text{(Sawada et al., 2003)}$$

Due to their fine and homogeneous distribution inside martensite lath, MX-type precipitates can pin dislocations and thus contribute to creep strength of the steel. Precipitation strengthening of MX-type precipitates is believed to be the most efficient high temperature strengthening mechanism (Abe et al., 2007), (Maruyama et al., 2001).

In order to further increase the creep strength of heat resistant steels non-conventional heat treatments are under study in order to improve the MX distribution. Compared to the MX distribution after a conventional heat treatment, a higher density of MX is observed after a double tempering (Yescas and Morris, 2005) or after heat treatments in a magnetic field (Okubo et al., 2004). The martensite transformation in a magnetic field increases the density of nucleation sites for precipitates during tempering, thus a finer and more uniform distribution of precipitates is obtained and the growth of precipitates during tempering is slowed down (Okubo et al., 2004).

II.6 Tensile properties

Tensile tests were conducted in air, at 600°C and 650°C under various values for the strain rate, $\dot{\varepsilon}$. The tensile specimens with 3 mm diameter and 15 mm gauge length (figure II.13) were machined along the T92 steel tube axis at mid-thickness.

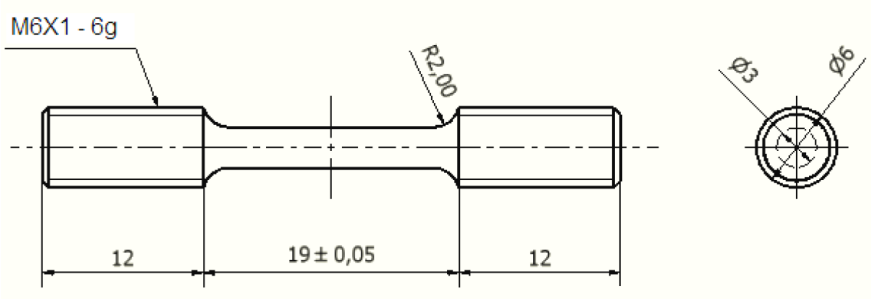

Figure II.13 : Geometry of tensile specimens

The tensile elongation curves obtained at 20°C, 600°C and 650°C under an initial strain rates of $10^{-3}s^{-1}$ and $10^{-5}s^{-1}$ are given in figure II.14a and figure II.14b, respectivelly. The tensile strength and 0.2% proof stress decrease with increasing temperature.

In table II.3 are summarized the results of tensile tests conducted at 20°C, 600°C and 650°C. The tensile properties are in good agreement with the specification of the Grade 92 steel (V & M, 2000).

Higher values of reduction of area are observed after testing at 600°C and 650°C compared to these after testing at 20°C.

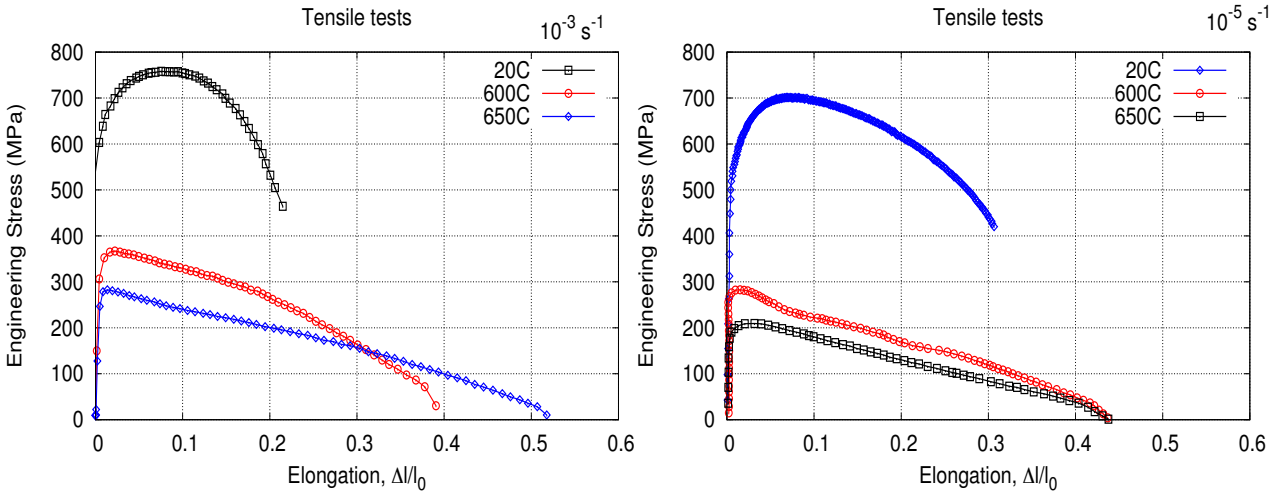

a) **b)**

Figure II.14 : Tensile curves of the T92 steel at 20°C, 600°C and 650°C. a) tensile tests conducted with a strain rate $\dot{\varepsilon} = 10^{-3}s^{-1}$ b) tensile tests conducted with a strain rate $\dot{\varepsilon} = 10^{-3}s^{-1}$

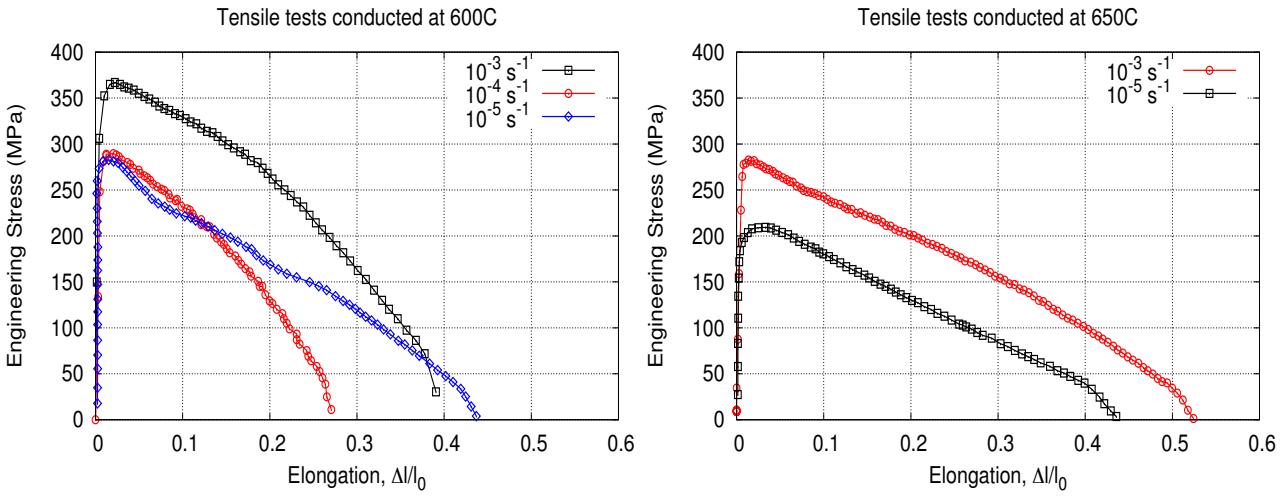

a) b)

Figure II.15 : Tensile properties of the T92 steel at 600°C (a) and 650°C (b) as a function of the strain rate

The structure instability (necking of the specimen) is observed at relatively low values of elongation (see table II.3). The value of elongation at which structure instability occurs are almost four times lower at 600°C and 650°C compared to these at room temperature.

Figures II.15 and II.16 show the evolution of tensile strength and 0.2% proof stress as a function of strain rate 20°C, 600°C and 650°C. The tensile strength and 0.2% proof stress decrease with the strain rate, figure II.15.

For all specimens the rupture is ductile and the fracture surface is characterized by

Table II.3 : Tensile properties of the T92 steel

Temp. °C	Initial strain rate [s^{-1}]	0.2% proof stress [MPa]	Tensile strength, Rm [MPa]	Max. uniform elongation [%]	Reduction of area [%]
20	$10^{-3}s^{-1}$	638	758	8	66
	$10^{-5}s^{-1}$	624	700	8.7	75
600	$10^{-3}s^{-1}$	367	367	2.2	95
	$10^{-4}s^{-1}$	290	290	1.7	93
	$10^{-5}s^{-1}$	281	283	1.6	93
650	$10^{-3}s^{-1}$	282	283	1.3	94
	$10^{-5}s^{-1}$	208	209	2.6	87

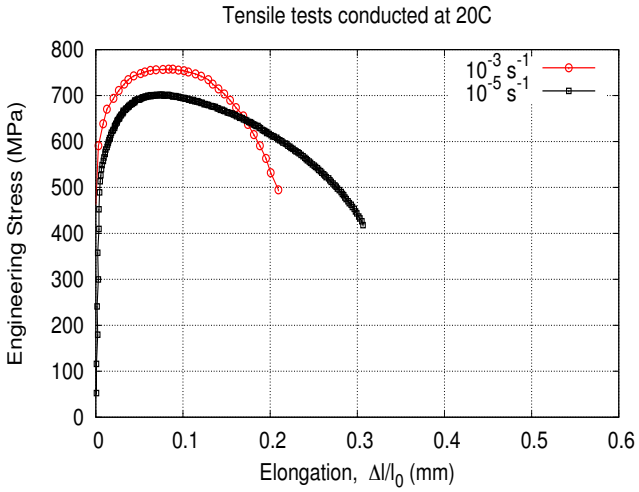

Figure II.16 : Tensile properties of the T92 steel at 20°C as a function of the strain rate

dimples. Occasionally on fracture surfaces inclusions of MnS, CaS and Al_2O_3 are observed. These inclusions were identified by EDS analysis on FEG-SEM. On the fracture surface of the specimen tested at 20°C, BN were observed.

II.7 Summary

The aim of this chapter was to present the materials under study, namely, T92 steel and P92 steels. The chemical composition and heat treatments of these two steels are in good agreement with the specifications of ASME Grade 92. The role of alloy elements in the Grade 92 steel as well as their influence on the microstructural evolution during creep or thermal exposure at 600°C and 650°C were discussed based on available published data.

Specimens in T92 steel were used for mechanical tests (i.e. creep, creep-fatigue, tensile) conducted in this study. These specimens were machined along the T92 steel tube axis at mid-thickness. All creep tests were conducted at *Vallourec Research Aulnoye (VRA), France.* Tensile and creep-fatigue tests were conducted at *Centre des Matériaux, MINES ParisTech, France*

Specimens in P92 steel already tested for long-term creep (times lower than 50,000h) at 600°C and 650°C were investigated in this study. These crept specimens were delivered

by *Salzgitter Mannesmann Forschung GmbH (SZMF), Germany* and they are particularly interesting for this Phd. study which focuses on a better understanding and modeling of long-term creep strength loss at 600°C and 650°C. The interest of long-term crept specimens in P92 steel consists in (i) their testing time which could not be achieved during the duration of this Phd. project; (ii) they could provide data on the microstructure and creep damage of the P92 steel after long-term creep exposure at 600°C and 650°C and (iii) the creep data of these specimens could be used in the modeling part of this study as they are complementary to the creep results obtained in this study.

The microstructure of both T92 steel and P92 steel in the as-received conditions was investigated using light microscopy, SEM, FEG-SEM, EBSD and TEM on extractive replicas of precipitates. The microstructural investigations were conducted on longitudinal sections of tube in T92 steel and respectively of pipe in P92 steel to be further comparable with the investigations of specimens after creep testing.

EBSD investigations revealed a microtexture composed of prior austenite grains with packets and several blocks per packets which is typical to tempered martensite. No significant difference was observed in EBSD maps of T92 steel compared to these of P92 steel. Thus it can be concluded that the microtexture of the two steel is similar.

Two types of precipitates were observed by TEM observations conducted on extractive replicas in the P92 steel and T92 steel in as-received conditions. The $M_{23}C_6$ carbides with an average diameter of 90-120nm located mainly at all kinds of boundaries and MX-type precipitates with an average diameter of 20-40nm homogeneously distributed within the martensite laths. Most of MX-type precipitates are VN with a plate-like shape. Small amounts of NbC with a round-shape are observed mainly on prior austenite grain boundaries and low amounts of MX-type precipitates with a more complex shape (so called *V-wings*) are observed inside martensite laths.

TEM investigations conducted on extractive replicas revealed no significant difference between the nature and size of precipitates in the as-received T92 steel compared to these in as-received P92 steel.

No significant difference was observed in the microstructure, both microtexture and precipitates, of the two steels under study even their different product shape. Thus the microstructural evolution during creep or thermal aging exposure could be considered similar.

No Laves phases were observed in T92 steel and P92 steel in as-received conditions using TEM on extractive replicas of precipitates and SEM in backscatter electron mode (BSE).

Hardness measurements with a 500g load conducted on the longitudinal axis at mid-thickness revealed a hardness of $231\pm3HV_{0.5}$ for the as-received T92 steel and $237\pm5HV_{0.5}$ for the as-received P92 steel. The results of tensile tests conducted on T92 steel under various initial strain rate were presented in this chapter. At room temperature the 0.2% proof stress was of about 620-640MPa. Tensile tests conducted at 600°C and 650°C revealed a significant influence of the initial strain rates on the 0.2% proof stress (Rp_{02}). At 600°C it was found Rp_{02} =∼370MPa and Rp_{02} =∼ 280MPa for initial strain rates of $\dot{\varepsilon} = 10^{-3}s^{-1}$ and $\dot{\varepsilon} = 10^{-5}s^{-1}$, respectively. Tensile tests conducted at 650°C revealed Rp_{02} =∼280MPa and Rp_{02} =∼210MPa for initial strain rates of $\dot{\varepsilon} = 10^{-3}s^{-1}$ and $\dot{\varepsilon} = 10^{-5}s^{-1}$, respectively.

Résumé

Ce chapitre porte sur la présentation et la caractérisation microstructurale des matériaux de l'étude, à savoir l'acier T92 et l'acier P92, à l'état de réception.

La composition chimique et les traitement thermiques de ces aciers sont conformes aux spécifications ASME pour le Grade 92. Le rôle des éléments d'alliage dans la composition de l'acier Grade 92 ainsi que leur influence sur l'évolution métallurgique de l'acier pendant le fluage ou le vieillissement thermique à 600°C et 650°C ont été discutés à partir des données trouvées dans la littérature.

Dans cette étude, tous les essais (traction, fluage, fatigue-fluage) ont été réalisés sur des éprouvettes en acier T92. L'acier T92 a été reçu sous la forme d'un tube ayant un diamètre extérieur de 48.3mm et une épaisseur de 11.2mm. Les éprouvettes ont été usinées dans le sens longitudinal du tube à mi-épaisseur. Tous les essais de fluage ont été réalisés chez Vallourec Research Aulnoye (VRA), France. Les essais de traction et de fatigue-fluage ont été réalisés au Centre des Matériaux, MINES ParisTech, France

Une expertise des éprouvettes de fluage en acier P92 déjà testées en fluage à 600°C et 650°C pendant des temps prolongés a été menée dans cette étude. Ces éprouvettes ont été fournies par Salzgitter Mannesmann Forschung GmbH (SZMF), Allemagne et elles sont très intéressantes au vu des objectifs de cette étude qui portent sur une meilleure compréhension de la perte de résistance en fluage à long terme et sur la modélisation du comportement en fluage. L'intérêt de ces éprouvettes réside dans: (i) leurs temps à rupture très prolongés, durées qui n'auraient pas pu être atteintes dans le cadre de cette thèse; (ii) dans les données qu'elles peuvent fournir sur la microstructure et l'endommagement de l'acier P92 après des temps prolongés d'exposition au fluage à 600°C et 650°C; (iii) leur résultats de fluage (contrainte, temps à rupture, courbes de fluage) qui correspondent à des niveaux des contraintes plus faibles que ceux utilisés pour les essais de fluage réalisés dans cette étude. Ceci sera utile dans la modélisation du comportement en fluage de l'acier Grade 92.

La microstructure de l'acier T92 et de l'acier P92 à l'état de réception a été caractérisée par microscopie optique, microscopie électronique à balayage (MEB) et en transmission (MET) sur répliques extractives. La caractérisation microstructurale a été réalisée dans une section longitudinale des tubes pour être comparable avec la caractérisation des éprouvettes après fluage.

Les observations EBSD ont révélé des anciens grains austenitique avec des paquets et plusieurs blocs par paquet, ce qui correspond à une martensite revenue. Les cartographies EBSD montrent une microtexture similaire pour les deux aciers.

A l'état de réception, les précipités dans les aciers T92 et P92 peuvent être divisés en deux catégories: les carbures $M_{23}C_6$ avec une taille de 90-120nm localisés principalement aux niveaux des joints et des carbonitrures MX avec une taille de 20-40nm distribués d'une façon homogène dans les lattes de martensite. La plupart des précipités MX sont des nitrures de vanadium (VN) avec une morphologie en plaquettes. De carbures de niobium (NbC) avec une forme sphérique sont observées dans les ancien joints austenitiques. Des précipités MX avec une morphologie plus complexe (V-wings) composé d'un "cœur" en NbC avec des "ailes" en VN sont aussi observés en faible quantité dans les lattes de martensite.

Les observations MET sur des répliques extractives de précipités n'ont montré aucune différence entre la nature et la taille de précipités entre les deux aciers. Il peut donc être supposé que les évolution métallurgiques de ces deux aciers pendant le fluage sont à priori comparables.

Les observations MET sur répliques extractives ainsi que les observations MEB en mode électrons retro-diffusés n'ont pas révélé l'existence des phases de Laves dans les aciers T92 et P92 à l'état de réception.

Les mesures de dureté effectuées avec une masse de 500g dans une section longitudinale du tube à mi-épaisseur ont montré une dureté de 231$\pm 3 HV_{0.5}$ *pour l'acier T92 et une dureté de 237*$\pm 5 HV_{0.5}$ *pour l'acier P92.*

Des essais de traction ont été effectués sur l'acier T92 à température ambiante, à 600°C et à 650°C avec différentes vitesses de déformation initiale. Une limite d'élasticité (Rp_{02}*) de 620-640MPa a été mesurée à température ambiante. A haute température la vitesse de déformation a une influence significative sur les propriétés en traction de l'acier. A 600°C des valeurs de* Rp_{02} *=∼370MPa et* Rp_{02} *=∼280MPa ont été trouvées pour des vitesses de déformation de* $\dot{\varepsilon} = 10^{-3} s^{-1}$ *et* $\dot{\varepsilon} = 10^{-5} s^{-1}$*, respectivement. A 650°C,* Rp_{02} *=∼280MPa et* Rp_{02} *=∼210MPa pour des vitesses de deformation de* $\dot{\varepsilon} = 10^{-3} s^{-1}$ *et* $\dot{\varepsilon} = 10^{-5} s^{-1}$*, respectivement.*

Chapter -III-

Preparation of creep specimens

Contents

Introduction

In the present study several types of creep specimens were used. Creep tests were conducted both on as-received T92 steel, on thermally aged T92 steel and on thermo-mechanically prepared T92 steel. The creep specimen types used in this study are listed below.

Creep specimens with an as-received T92 steel microstructure before testing:

1. Smooth creep specimens
2. Notched creep specimens
   - NTDC1.2
   - NTDC0.6
   - NTDC0.6M
   - NTDV

Creep specimens with a modified T92 steel microstructure before testing:

3. Thermally aged at 600°C for 10^4h (smooth geometry)
4. Thermally aged at 650°C for 10^4h (smooth geometry)
5. Thermo-mechanically prepared (modified smooth geometry)

The purpose of this chapter is to give a complete description of creep specimens and details about their preparation. Microstructural characterization of T92 steel thermally aged at 600°C and 650°C for 10^4h is also given.

Due to experimental difficulties only three creep tests were conducted on thermo-mechanically prepared specimens. All data concerning these specimens were gathered in *Appendix A* to facilitate the lecture of this manuscript

A microstructural characterization of the thermo-mechanically prepared T92 steel specimens before creep testing as well as details about their preparation can be found in *Appendix A*.

Introduction

Dans cette étude des essais de fluage ont été réalisés sur plusieurs type d'éprouvettes à la fois avec des géométries différents et à la fois avec des état différents de la microstructure avant fluage (acier T92 à l'état de réception, acier T92 vieilli thermiquement, acier T92 après fatigue-fluage). Les éprouvettes des fluage utilisées dans cette étude sont listées ci-dessous:

Éprouvettes avec une microstructure acier T92 à l'état de réception avant fluage:

1. *Éprouvettes lisses*
2. *Éprouvettes entaillées*

- *NTDC1.2*
- *NTDC0.6*
- *NTDC0.6M*
- *NTDV*

Éprouvettes avec une microstructure acier T92 modifiée avant fluage:

3. *pré-vieillie à 600°C pendant $10^4 h$ (géométrie éprouvettes lisse)*
4. *pré-vieillie à 650°C pendant $10^4 h$ (géométrie éprouvettes lisse)*
5. *pré-fatiguée (géométrie modifiée éprouvettes lisse)*

Dans ce chapitre sont présentés les éprouvettes de fluage utilisées dans cette étude ainsi que des détailles sur leur préparation. La caractérisation microstructurale de l'acier T92 après vieillissement à 600°C et à 650°C pendant $10^4 h$ est également présentée dans ce chapitre.

A cause des difficultés expérimentales, seulement quatre éprouvettes pré-fatiguées ont pu être préparées. Pour faciliter la lecture de ce manuscrit, toutes les données concernant les éprouvettes pré-fatiguées sont regroupées dans l'annexe A. Une caractérisation de la microstructure des éprouvettes pré-fatiguées avant fluage ainsi que des détailles sur la préparation de ces éprouvettes peuvent sont donnés dans l'annexe A.

III.1 Smooth creep specimens

Creep tests on smooth specimen are reference tests. The interest of these tests was to compare the creep strength of the studied T92 steel with creep data available in literature for the Grade 92 steel family (Bendick and Gabrel, 2005), which only address smooth specimens.

Another purpose of creep tests on smooth specimens was to have reference samples for microstructural investigations to be further compared to thermally aged T92 steel or thermo-mechanically prepared T92 steel creep tested in same conditions.

III.1.1 Geometry of smooth specimen

In figure III.1 is represented the geometry of the creep smooth specimens. They were machined from the T92 steel tube along the tube axis.

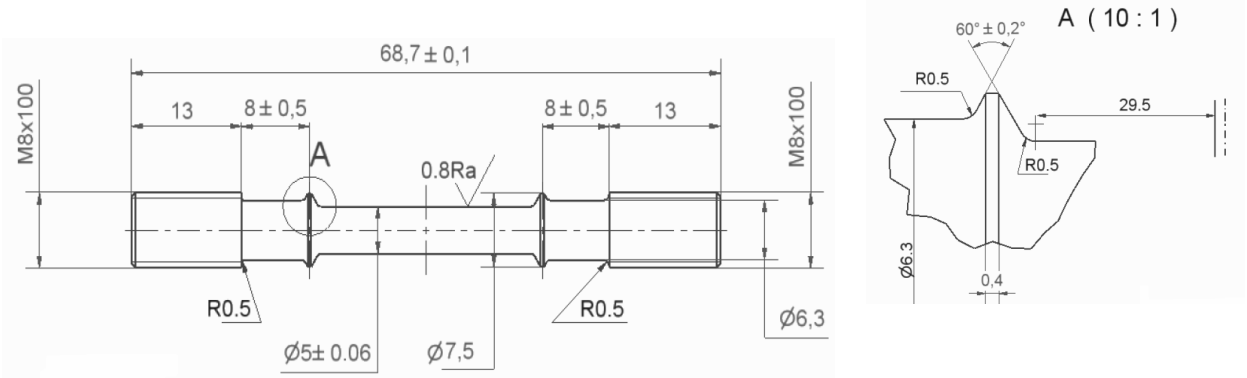

Figure III.1 : Geometry of the smooth creep specimens

III.1.2 Creep elongation on a smooth specimen

Elongation of the specimens during the creep tests has been measured by using an in situ extensometer. The engineering strain was calculated using the formula III.1:

$$\varepsilon = \frac{L - L_0}{L_0} \tag{III.1}$$

where $L - L_0$ is measured using the extensometer during creep and L_0 is the reference length before creep. An illustration of these two parameters is given in figure III.2.

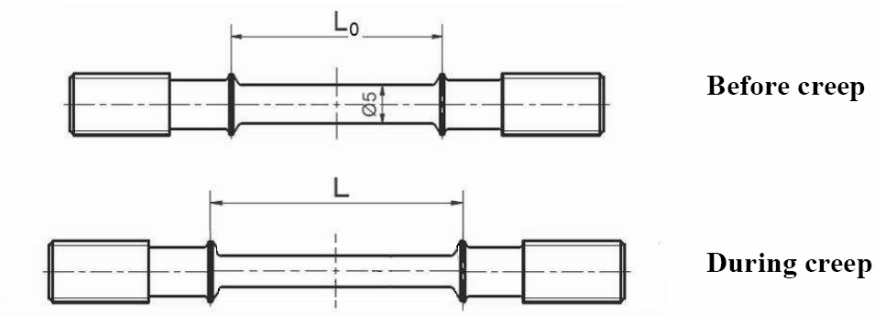

Figure III.2 : Deformation of a smooth specimen during a creep test

III.2 Notched creep specimens

Notched creep specimens are used to promote creep damage mechanisms that normally occurs in long-term creep only. The presence of a notch increases the stress triaxiality ratio in the minimum cross section of the specimen.

The presence of a notch induces a stress concentration and changes the stress state from uniaxial to multiaxial. For a given axial engineering stress (i.e. load divided by the minimum area), the von Mises equivalent stress is lower in a notched specimen than in a smooth specimen, leading to a lower strain rate (thus, promoting diffusional creep) and an increase in creep damage due to the rather high hydrostatic stress.

Both mechanisms and levels of damage observed after long-term creep (low stresses) on smooth specimens could possibly be observed in a notched specimen in a shorter time. In addition, due to gradient in stress and strain fields induced by the notch, the size of the creep-damaged area, together with accurate assessment of stress and strain fields within the notched creep specimen, allow damage initiation criterion parameters to be more finely tuned than from a limited set of smooth creep specimens.

III.2.1 Geometry of notched specimens

Creep damage development varies with the notch shape and notch radius. The choice of the notches geometries used in this study was based on previous works dealing with the creep behaviour of notched specimens (Gaffard et al., 2005b), (Jiang et al., 2006), (Hayhurst et al., 2008).

(Jiang et al., 2006) performed numerical calculations to study the influence of the notch shape on the distribution of creep damage. For the V-type notched specimens the maximum creep damage always happens at the notch root. The notch angle of the V-type notch influences the stress distribution without no influence on the localization of the maximum creep damage. The distance between maximum creep damage and notch root increases with increasing the notch radius of the C-type notches.

For this study a V-type notch and C-type notches with a radius of 1.2 mm and a radius of 0.6 mm were chosen. In figure III.3 are represented the geometries of the notched creep specimens. A simple analysis of NTDC1.2 and NTDC0.6 specimen deformation showed that the notch of the NTDC0.6 specimen was not deep enough. The geometry of the NTDC0.6 specimen was thus changed into NTD0.6M after a few tests.

The purpose of double notched specimens was to better understand creep fracture. After testing the unbroken notch is expected to provide information about initiation and propagation of rupture or creep damage preceding rupture.

III.2.2 Calculation of creep elongation on a notched specimen

The so-called creep elongation of notched specimens has been measured with an extensometer having the same L_0 reference length as for smooth specimens. It was assumed that only the notched area of the specimen deforms (figure III.4). Indeed engineering stress in the maximum section of the notched specimens is much lower than the engineering stress in the notched area. Table III.1 gives the values of the engineering stress in the minimum and maximum section of the notched specimen. An illustration of parameters in table III.1 is given in figure III.4.

Table III.1 : Creep test parameters used with notched specimens

Geometry	$2\delta_0$ [mm]	Minimum diameter ϕ_{min}[mm]	Load F [N]	Engineering Stress [MPa] $\left(\frac{F}{S_{\phi_{min}}}\right)$	$\left(\frac{F}{S_{\phi_{max}}}\right)$ [MPa]
NTDC0.6	2.36	4	2638	210	134.4
	2.36	4	1758	140	89.6
NTDC0.6M	2.4	3	1625	230	82.8
	2.4	3	1484	210	75.6
NTDC1.2	4.72	3	1484	210	75.6
	4.72	3	989	140	50.4
NTDV	2.3	3	1625	230	82.8
	2.3	3	1342	190	68.4
	2.3	3	671	95	35.2

The previous assumption reads:

$$L - L_0 = 2\left(\delta - \delta_0\right) \tag{III.2}$$

The average elongation of a notched specimen could be calculated using the following formula III.3

$$\varepsilon = \frac{L - L_0}{2\delta_0} \tag{III.3}$$

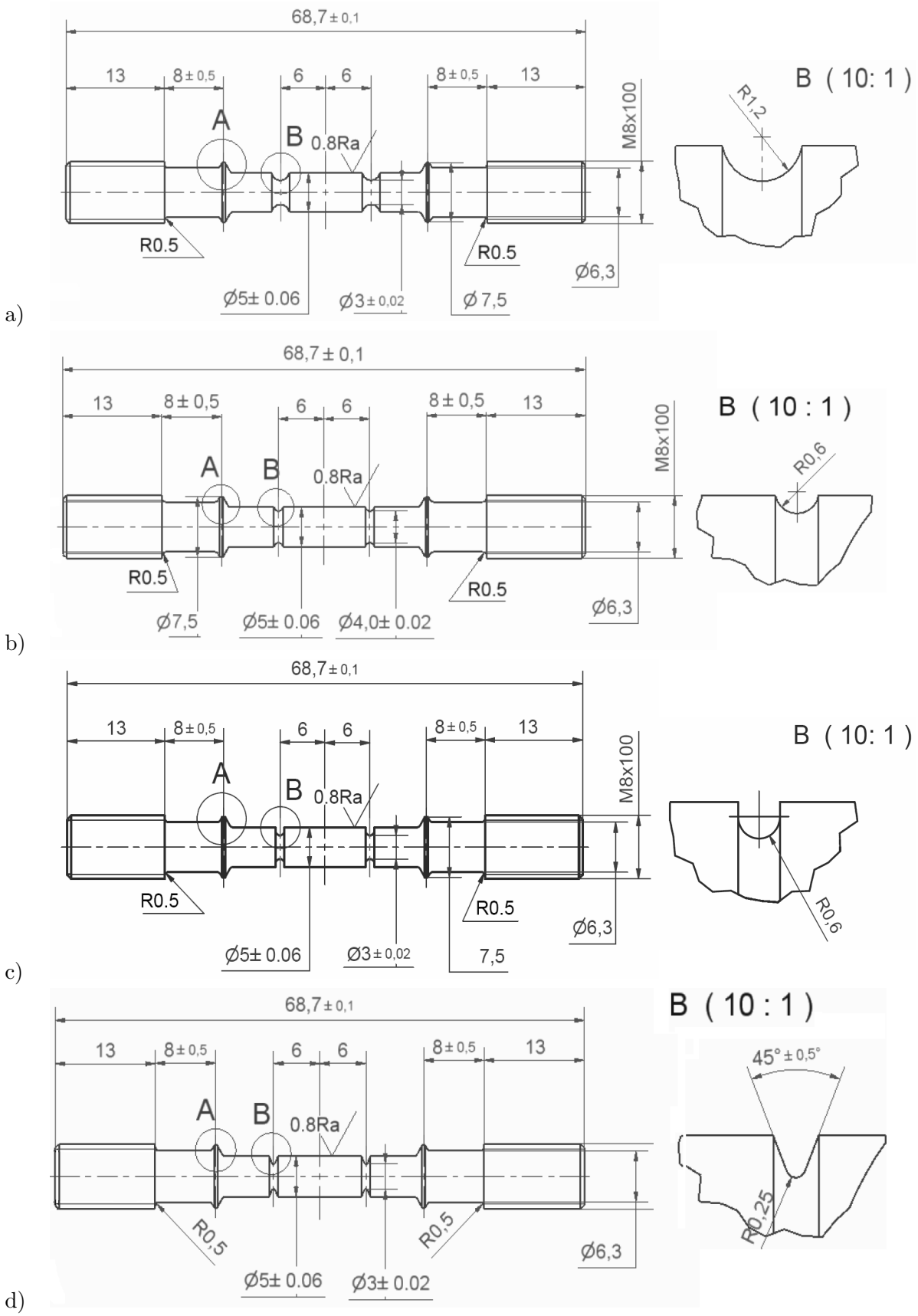

Figure III.3 : Geometry of the notched creep specimens
a) NTDC1.2; b) NTDC0.6; c) NTDC0.6M; d) NTDV

where $L - L_0$ is measured by the extensometer during the creep test and $2\delta_0$ is given in table III.1 for each notched geometry.

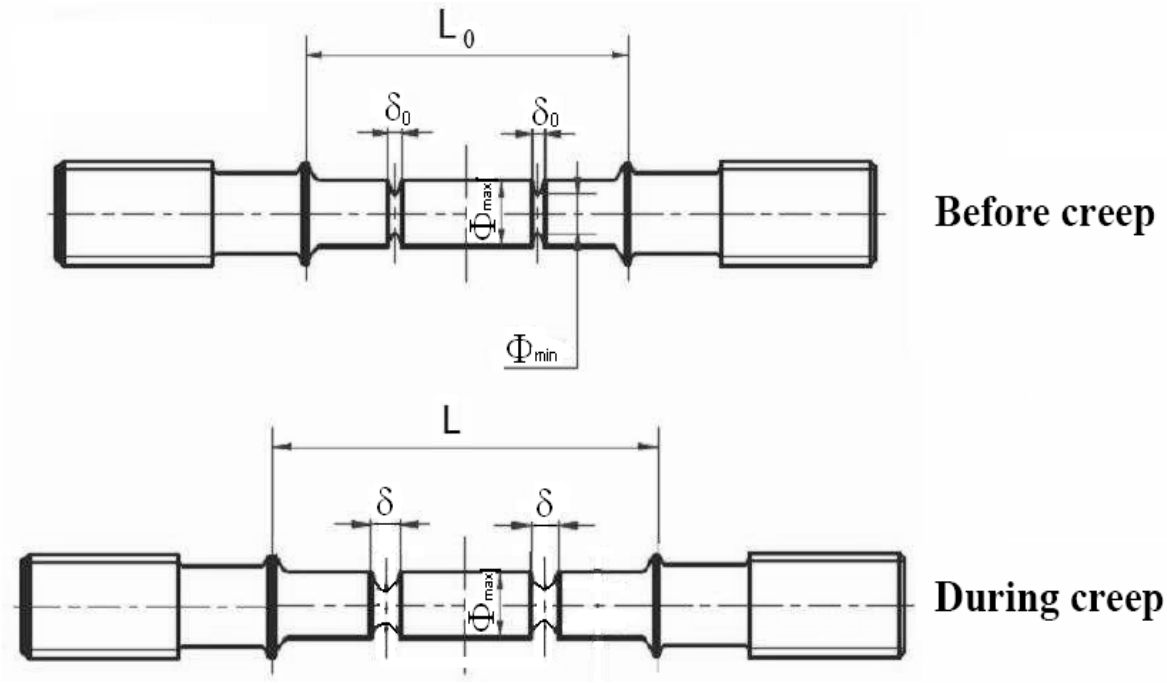

Figure III.4 : Deformation of a notched specimen during creep test

III.3 Thermally aged creep specimens: microstructural characterization

Introduction

Laves phase precipitation occurs during creep or thermal aging. Quantitative data on the size evolution of Laves phases show a relatively high growth rate during the first 10^4h of exposure at 600°C and 650°C (Dimmler et al., 2003), (Korcakova et al., 2001). In order to quantify the effect of large Laves phases on the creep strength of the T92 steel, smooth creep specimens were machined from bulk T92 steel aged at 600°C and 650°C for 10^4h. Blanks with 12mm×12mm cross section and a length of 75mm were cut from the T92 steel tube and thermally aged in induction furnaces at 600°C and 650°C for 10^4h. The temperature during aging heat treatments was controlled with thermocouples welded on the samples and never exceeded ±2° C from the imposed temperature.

The oxidation layer due to aging heat treatments was completely removed by machining of the thermally aged creep specimens from the aged T92 steel samples The geometry of the thermally aged creep specimens is the same as that of the smooth specimens used for the reference creep tests conducted on the as received T92 steel (see figure III.1). Aging heat treatments, machining and creep tests were conducted by CEV, Aulnoye-Aymeries. All microstructural investigations were conducted at Centre des Matériaux, MINES ParisTech.

Two kinds of specimens of Grade 92 steel exposed for $\simeq 10^4$h both at 600°C and 650°C were available: thermally aged blanks (T92 steel) and crept specimens of P92 steel tested for 9,497h and 9,210h at 600°C and 650°C respectively. The chemical composition of Laves phases was investigated on P92 steel crept at 600°C only. Hardness measurements and SEM analysis were conducted on both T92 steel and P92 steel. The purpose of the SEM analysis on both thermally aged and crept specimens was to investigated whether the stress or deformation influences the precipitation or growth of Laves phases.

This section presents results of SEM and EBSD investigations conducted on the thermally aged T92 steel. The purpose of SEM investigations was to determine the size of Laves phases after aging at 600°C and 650°C. EBSD investigations were conducted in order to check whether aging heat treatments induced a significant change of the matrix microtexture.

SEM and EBSD investigations were conducted on aged samples after a final mechanical-chemical polishing with colloidal silica. SEM investigations were also conducted on Villela etched samples.

III.3.1 Chemical composition of Laves phases

The chemical composition of Laves phases cannot be precisely determined by EDS coupled with SEM on bulk material due to their relatively small size (average equivalent diameter <1 µm). The chemical composition of precipitates can be precisely determined by Dispersive X-ray Spectroscopy (EDX) coupled with TEM. TEM investigations were conducted on extractive replicas of precipitates from P92 steel creep specimens tested at 600°C and 650°C. Figure III.5 shows a typical EDX spectrum for Laves phase in P92 steel after $\simeq 10^4$h of creep at 600°C.

EDX analysis of almost forty Laves phases in a P92 steel specimen (gauge length) creep tested for 9,497h at 600°C, 160MPa revealed the following chemical composition (wt.%): 50-57% W, 25-27%Fe, 8-11%Mo, 5-7%Cr, 5-8%Si, 0.45-0.7%Mn, which is consistent with published data.

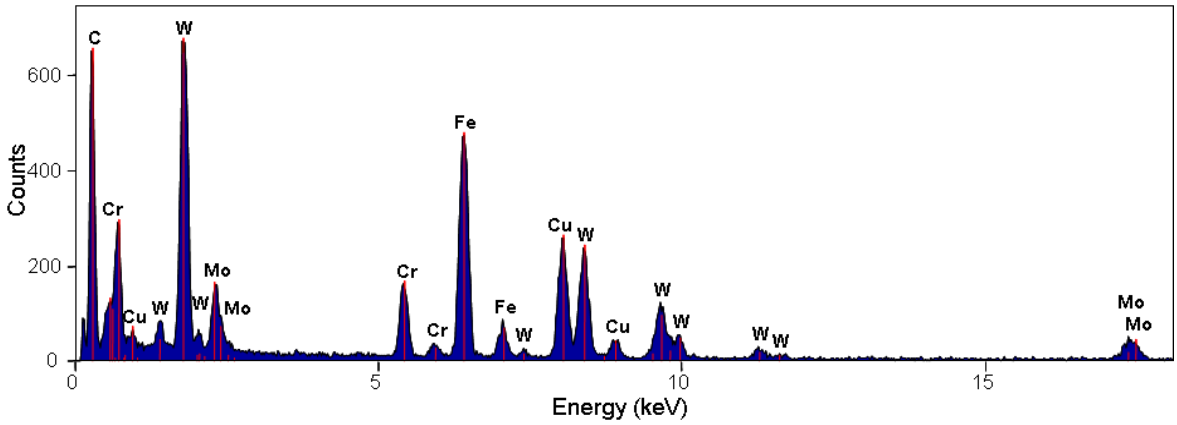

Figure III.5 : Typical TEM-EDX spectrum for Laves phases obtain on extractive replicas of precipitates

No significant further change in chemical composition of Laves phases was observed in P92 steel creep specimens tested for longer times both at 600°C and 650°C.

III.3.2 Evolution of hardness

Vickers hardness measurements with a 500g load were conducted on both as-received and aged steels and the results are summarized in table III.2. Hardness measurements were conducted in a plane parallel to the axis of the tube in the middle of the wall thickness, in order to be further comparable to the investigations of longitudinal cross sections of creep specimens after testing.

Table III.2 : Hardness measurements on thermally aged T92 steels

Hardness [$HV0.5$]	As-received T92 steel	T92 steel aged at 600°C for 10^4h	T92 steel aged at 650°C for 10^4h
Minimum	221	226	225
Average	231	236	232
Maximum	236	243	239
Standard deviation	3.3	4.2	3.6
Number of measurements	60	60	73

After aging at 600°C, no significant change in hardness was observed compared with the hardness of the T92 steel in the as-received condition. This is consistent with hardness measurements conducted on the head (only exposed to thermal aging during the test) of P92 steel creep specimens tested for longer times at 600°C, as it will be shown later. Even after almost 50,000h of thermal exposure at 600°C there is no change in hardness despite extensive precipitation of Laves phases.

III.3.3 Size distribution of Laves phases (SEM investigations)

Due their chemical composition, enriched in heavy elements such as W and Mo, Laves phases have a high average atomic number compared to that of the matrix, so that they can be easily revealed as bright precipitates in a dark matrix using SEM in BSE imaging mode. Using this

kind of images, a quantification of Laves phases can then be made by image analysis. This experimental procedure is limited by the spatial resolution of the SEM but it offers good results for precipitates with a diameter of about 100nm or higher.

Image analysis was performed using Matlab image processing toolbox in which an image processing treatment was implemented. For each specimens approximately 40 SEM-BSE images were used and thousands of particles were quantified. Equivalent circle diameters determined from binarized images showed a lognormal distribution.

Laves phases are relatively large particles, with an average diameter larger than 250 nm and for a correct evaluation of their size, SEM techniques were recommended because it allows to sample larger areas, obtain more particles per image and a better statistic of measured values compared to TEM techniques (Korcakova et al., 2001).

In literature, the mean diameter of Laves phases in aged samples at 600°C measured on FEGSEM was found to be smaller by approximately 20% than these measured using EFTEM (Korcakova et al., 2001). In samples aged at 650°C a higher discrepancy is found between the values evaluated using the two techniques. The discrepancy is explained by an almost ten times higher number of precipitates on FEGSEM images compare to EFTEM images (Korcakova et al., 2001).

III.3.3.1 T92 steel aged at 600°C for 10^4h

Figure III.6 shows the microstructure of the T92 steel aged at 600°C for 10^4h after a colloidal silica polishing (figure III.6a) and after Villela etching (figure III.6b) of the same area. After SEM observations of the colloidal silica polished sample a slight Villela etching was applied in order to keep most of the precipitates observed previously and to reveal more features of the aged microstructure.

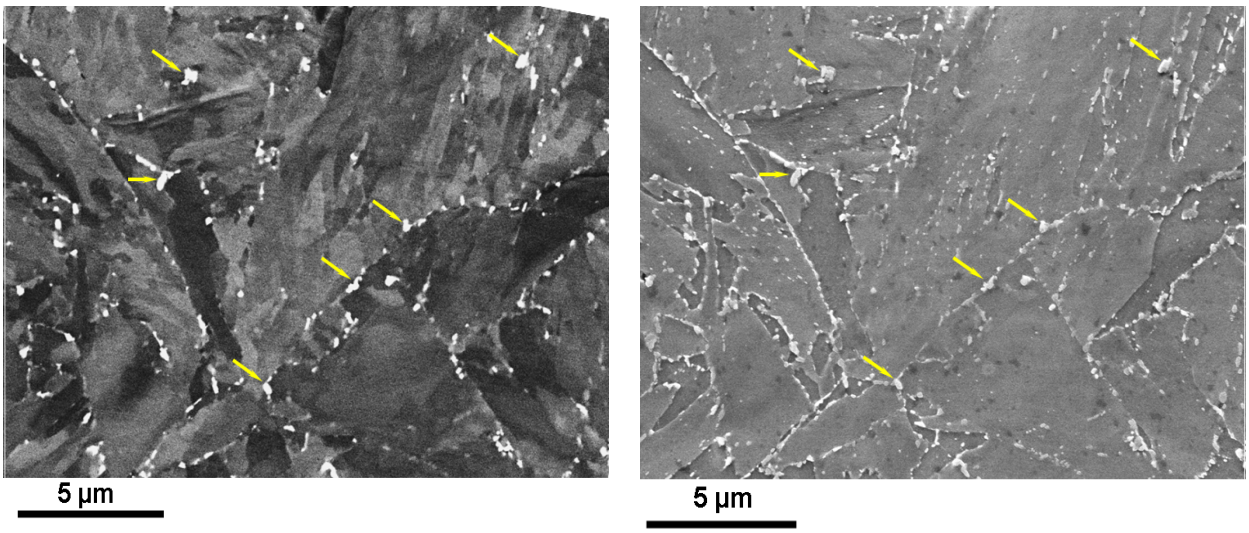

Figure III.6 : Microstructure of the T92 steel after aging at 600°C for 10^4h; after a colloidal silica polishing, BSE mode (a) and after Villela etching, SE mode (b) of the same sample area.

Compared to the microstructure of the as received T92 steel, an increase in the area fraction of precipitates is observed after aging at 600°C for 10^4h, figure III.6. Most of the large precipitates observed after aging are Laves phases, bright precipitates in figure III.6a, as can be seen by comparing the two SEM micrographs of the same sample area. For the sake of

illustration some of these precipitates are arrowed on the two micrographs. Precipitates that are clearly visible in figure III.6b and not in figure III.6a are most probably $M_{23}C_6$ already found in the as-received material.

The size distribution of Laves phases after aging at 600°C for 10^4h was determined by image analysis of SEM-BSE images with a magnification of ×2000, see figure III.7b. Figure III.7a shows a typical SEM-BSE image used for the quantification of Laves phases, 40 such images were processed by image analysis techniques.

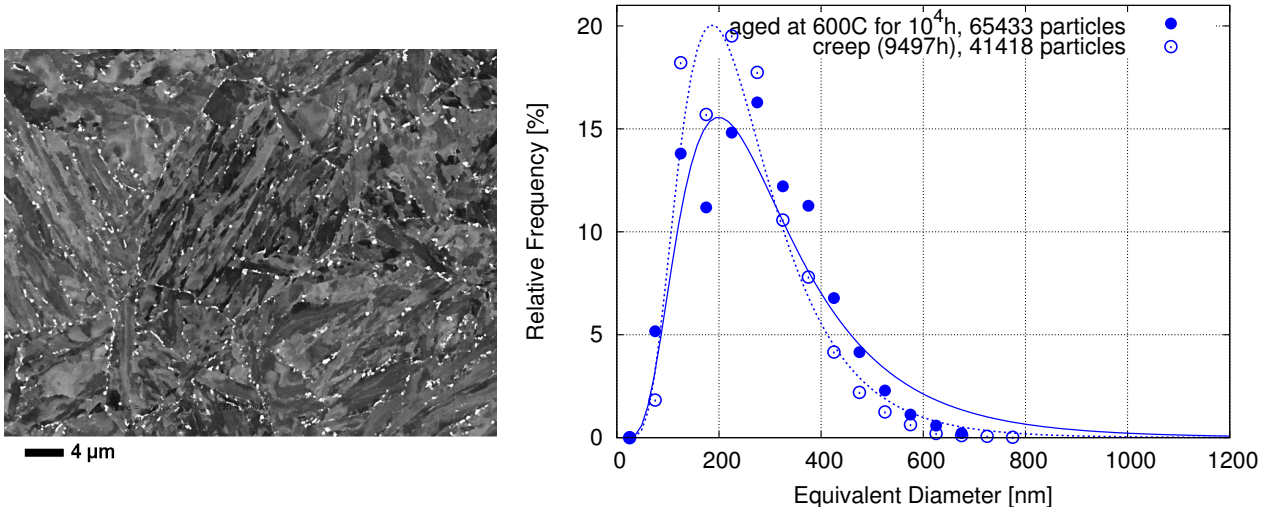

a) **b)**

Figure III.7 : a) Typical BSE-SEM image used for image analysis processing, showing Laves phases as bright precipitates (T92 steel aged at 600°C); b) Size distribution of Laves phases after aging at 600°C for 10^4h (T92 steel) and after almost 10^4h of creep at 600°C (P92 steel). Experimental results (symbols) compared with a lognormal fit (line)

In figure III.7b are represented the size distribution of Laves phases after thermal aging at 600°C for 10^4h and the size distribution of Laves phases in the gauge part of a P92 steel crept specimen tested at the same temperature for almost 10^4h, determined using the same experimental procedure.

There is no significant difference between the size of Laves phases after 10^4h of thermal aging compared to the size after creep exposure for almost the same time, see figure III.7b. Stress and/or deformation during the creep test does not seem to have an influence on the growth of Laves phases, at least after 10^4h of exposure.

The slight difference between the size of Laves phases after thermal aging and after creep in figure III.7b is due to the scatter of data. The size distribution of Laves phases determined both after aging and after creep show an average equivalent diameter of about 200nm. This is consistent with published data on the size of Laves phase in the Grade 92 steel after 10^4h of aging or creep exposure at 600°C, see figures I.12 and I.13.

A possible influence of stress and/or strain on the precipitation or growth of Laves phase in the Grade 92 steel is not reported in the literature at least for exposure times of about 10^4h both at 600°C and 650°C. (Korcakova et al., 2001) reported an corrected mean diameter of about 190 nm and of about 220 nm in a creep deformed sample and in a thermally aged sample at 600°C for 10^4h, respectively (see figure I.12). Note the significant uncertainty of measurements which does not allow to evaluate the influence of stress or strain in the growth of Laves phase, see figure I.12. The differences in size of Laves phase in the creep deformed sample compared to that in the thermally aged one could be due to a scatter of measurements.

Moreover, for higher exposure times the scatter between the size of Laves phases in the creep deformed specimen and the thermally aged ones is less pronounced and the authors do not comment on a possible effect of stress and/or strain on the growth of Laves phases.

III.3.3.2 T92 steel aged at 650°C for 10^4h

The size distribution of Laves phases in the T92 steel aged at 650°C for 10^4h determined by image analysis of forty SEM-BSE images is given in figure III.8b. In figure III.8b are also represented the size distribution of Laves phases in a P92 steel after almost 10^4h of creep exposure at 650°C.

Figure III.8a represents a typical SEM-BSE image used for image analysis processing showing the microstructure of the T92 steel aged at 650°C after colloidal silica polishing with Laves phases as bright precipitates.

There is no significant difference between the size distribution of Laves phases after aging at 650°C for 10^4h (T92 steel) and after almost 10^4h of creep at 650°C (P92 steel), figure III.8, indicating that stress does not seem to have a significant influence on the size distribution of Laves phases.

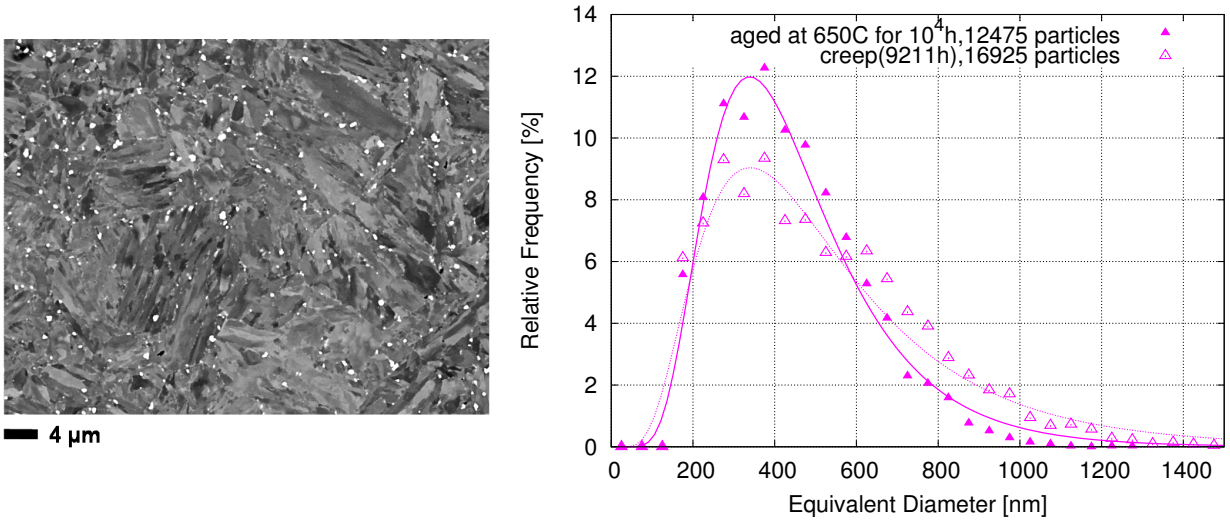

a) **b)**

Figure III.8 : a) Typical BSE-SEM image used for image analysis processing, showing Laves phases as bright precipitates (T92 steel aged at 650°C); b) Size distribution of Laves phases after aging at 650°C for 10^4h (T92 steel) and after almost 10^4h of creep at 650°C (P92 steel). Experimental results (symbols) compared with a lognormal fit (line)

III.3.4 Characterization of the microtexture after aging (EBSD investigations)

The purpose of aging heat treatments at 600°C and 650°C was to precipitate large Laves phases without significantly changing the substructure of the steel matrix. EBSD investigations were conducted in order to investigate the substructure of the T92 steels after thermal aging.

In order to get a representative characterization of microtexture of the T92 steel after thermal aging, microtextural information was obtained on relatively large areas of the aged samples. Because of too large acquisition files and due to difficulties to process them, the EBSD maps in figure III.9 (respectively figure III.12) were acquired in two steps (two

acquisitions files). Each acquisition file was indexed and processed separately. The white line on IPF images in figure III.9 (respectively figure III.12) indicates were the two EBSD maps were put together after processing. EBSD investigations were conducted with a step size of 0.15 µm.

III.3.4.1 T92 steel aged at 600°C for 10^4h

A lower Image Quality index is observed in upper EBSD map in figure III.9, this was probably due to an instability of the electron beam during the second part of the acquisition of the diffraction patterns; this had probably very little influence on the Euler angles of the EBSD map.

EBSD maps in figure III.9 reveals no significant change in the substructure of the T92 steel steel after aging at 600°C for 10^4h, see figure III.9. The Inverse pole figure (IPF) and image quality (IQ) maps show a typical martensitic structure with blocks and packets after aging. This is confirmed by the histogram of misorientation angles corresponding to the EBSD maps of figure III.9, which shows a typical distribution of boundaries between martensite variants (Gourgues et al., 2000), see figure III.10. There is no significant difference between the histograms of misorientation angles of the upper and lower EBSD maps in figure III.9.

In figure III.11 are represented the histograms of misorientation angles in the as-received T92 steel (corresponding to the EBSD maps in figure II.9) and in the T92 steel aged at 600°C for 10^4h (corresponding to the EBSD maps in figure III.9). Only a slight decrease in the amount of low angle boundaries is observed after aging compared to as-received state.

III.3.4.2 T92 steel aged at 650°C for 10^4h

The EBSD maps realized on the T92 steel after aging at 650°C for 10^4h show a martensitic substructure organized in blocks and packets, figure III.12.

Figure III.13 shows the histograms of misorientation angles between neighbouring grains corresponding to the two EBSD maps of figure III.12 (i.e. upper and lower). There is no significant difference between the two histograms and they show a typical distribution between martensite variants.

A slight decrease of low angle frequency is observed after aging at 650°C for 10^4h when comparing with the histograms of misorientation angles boundaries of the as-received T92 steel and T92 steel aged at 650°C, see figure III.14.

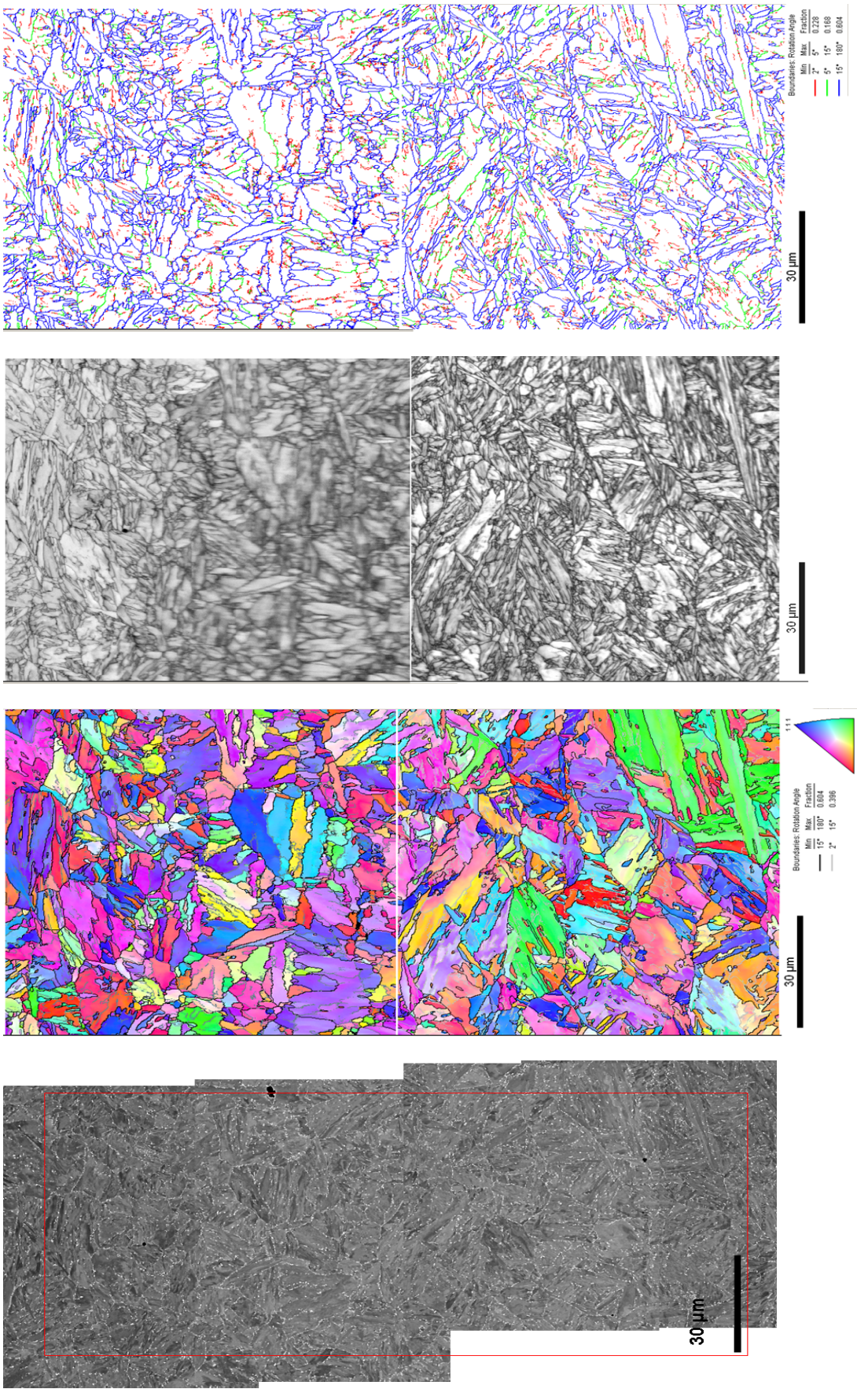

Figure III.9 : Microtexture of the T92 steel aged at 600°C for 10^4h. a) SEM-BSE image; b) Inverse Pole Figure (IPF) with orientation of sample normal in the crystal frame as color key; c) EBSD Image Quality map (IQ); d) EBSD boundary map

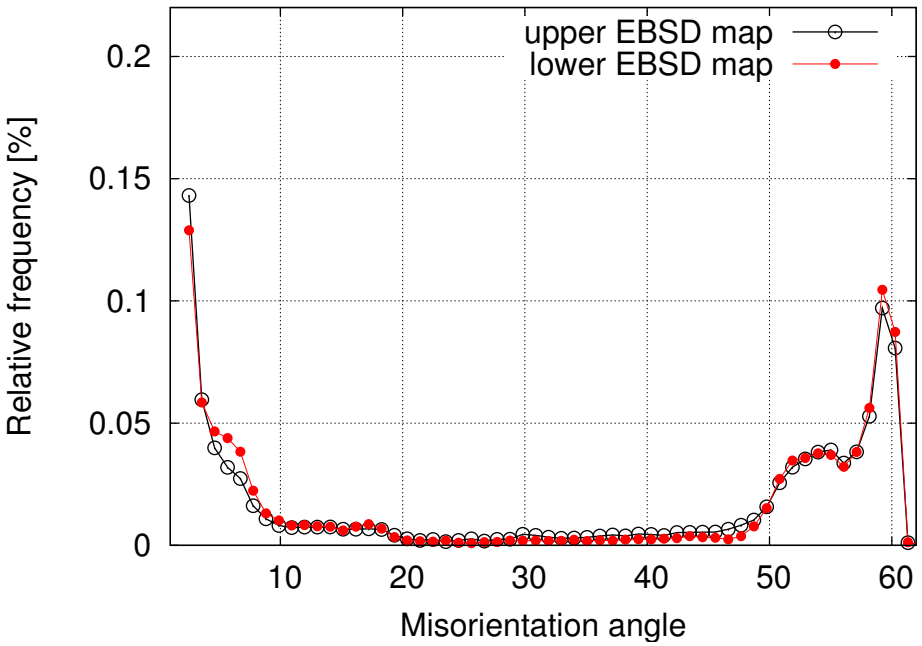

Figure III.10 : Misorientation angle (°) distribution between grains corresponding to the EBSD map (T92 steel aged at 600°C for 10^4h) of figure III.9

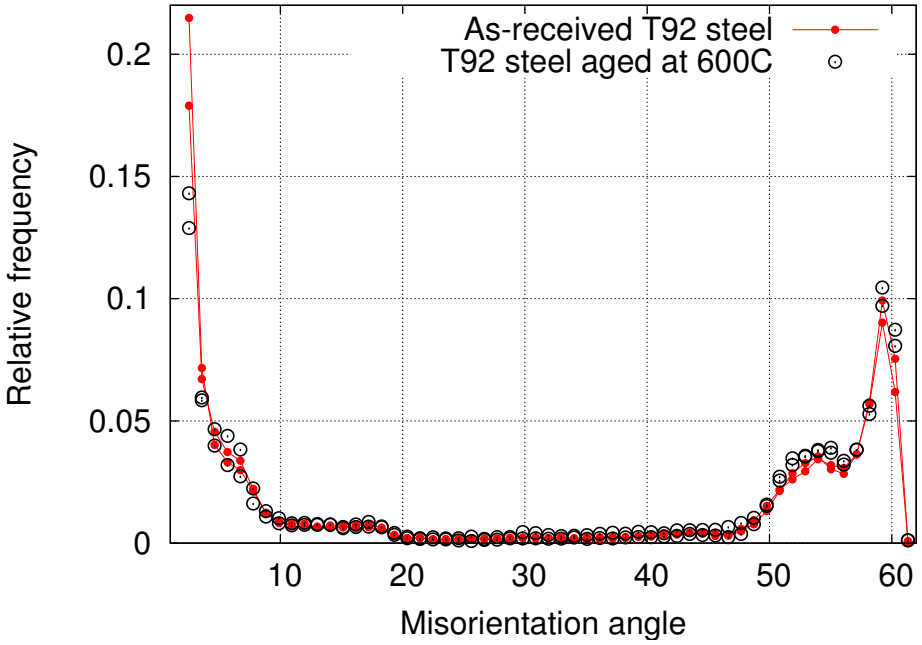

Figure III.11 : Comparison between misorientation angles in as-received T92 steel (EBSD maps in figure II.9) and misorientation angles in T92 steel aged at 600°C for 10^4 h (EBSD maps in figure III.9)

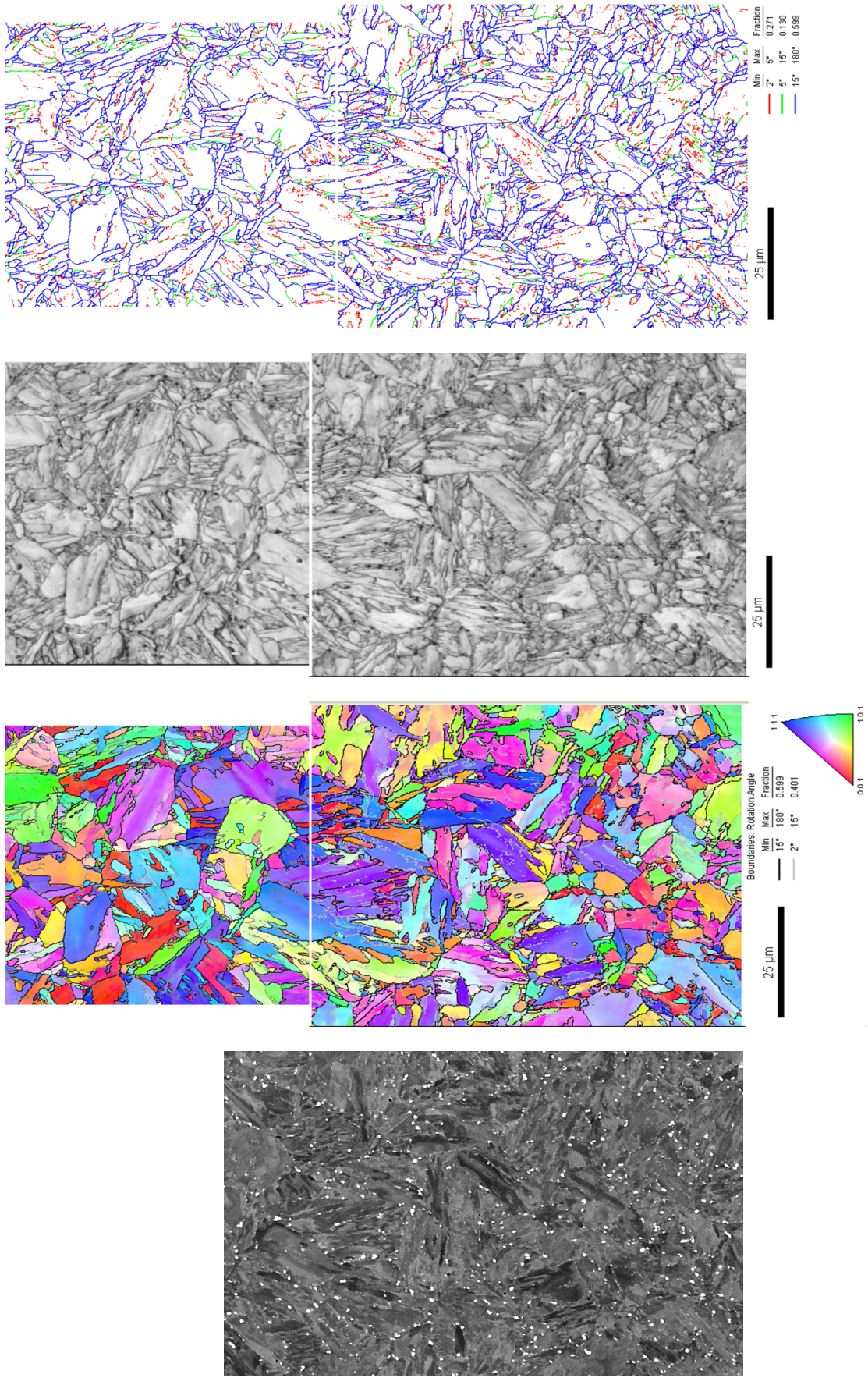

Figure III.12 : Microtexture of the T92 steel aged at 650°C for 10^4h. a) SEM-BSE image; b) Inverse Pole Figure (IPF) with orientation of sample normal in the crystal frame as color key; c) EBSD Image Quality map (IQ); d) EBSD boundary map

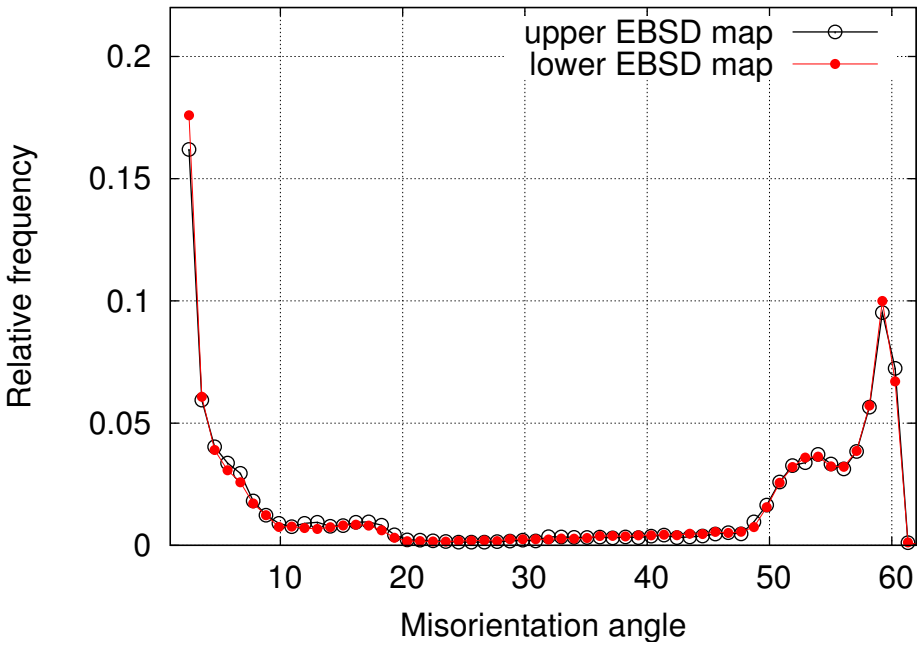

Figure III.13 : Misorientation angles (°) between grains corresponding to the EBSD map (T92 steel aged at 650°C for 10^4h) of figure III.12

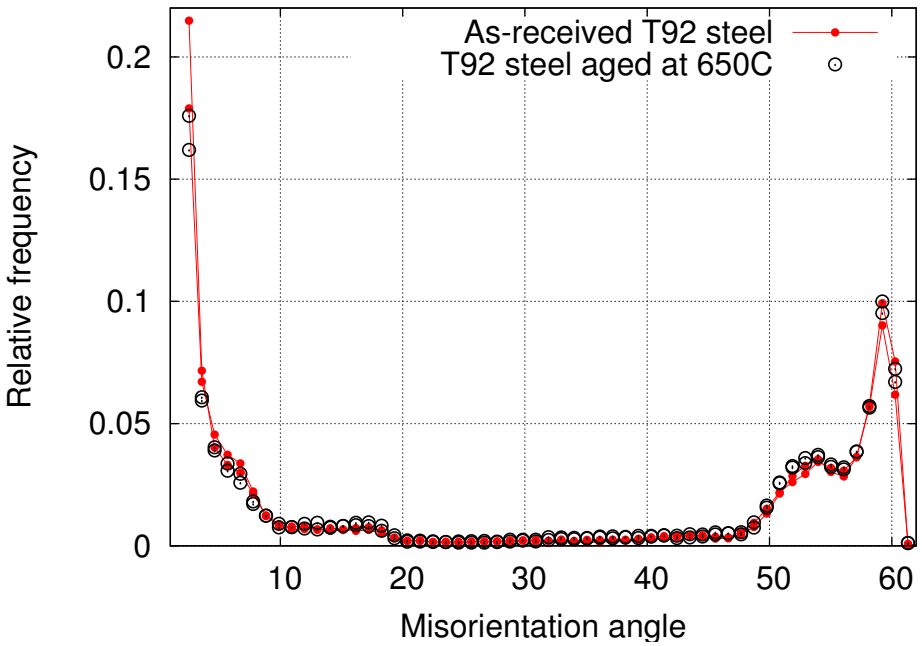

Figure III.14 : Comparison between misorientation angles between in as-received T92 steel (EBSD maps in figure II.9) and misorientation angles in T92 steel aged at 650°C for 10^4 h (EBSD maps in figure III.12)

III.3.4.3 Analysis of K-S and G-T boundaries

EBSD maps together with the misorientation angle distribution between neighboring grains revealed no significant change in the microtexture of the T92 steel after aging both at 600°C and 650°C for 10^4h. A complementary EBSD data processing was realized in collaboration with F. Barcelo at CEA Saclay, using their *in-house* developed procedure.

Table III.3 : Analysis of boundaries respecting the K-S and G-T relationships in EBSD map

EBSD map	**T92 steel** As-received	**T92 steel** Ther. aged at 600°C, 10^4h		**T92 steel** Ther. aged at 650°C, 10^4h	
Size of area	µm × µm	µm × µm	µm × µm	µm × µm	µm × µm
Step size	0.15 µm	0.15 µm	0.15 µm	0.15 µm	0.15 µm
Observations	figure II.9 upper map	figure III.9 upper map	figure III.9 lower map	figure III.12 upper map	figure III.12 lower map
Fraction of G-T (K-S) boundaries in EBSD maps					
G-T type boundary					
⟨433⟩ 60.2 G-T	26.4	24.6	26.6	24.4	23.7
⟨111⟩ 49.6 G-T	1.16	0.77	1.08	1.08	0.66
⟨331⟩ 50. G-T	2.16	2.92	2.82	3.42	2.69
⟨433⟩ 50.2 G-T	1.72	1.53	1.96	2.13	2.00
⟨332⟩ 50.8 G-T	3.87	3.54	4.43	3.88	3.69
⟨110⟩ 60. G-T	5.06	4.99	5.21	4.68	4.93
⟨331⟩ 51.9 G-T	3.61	5.07	5.17	4.88	4.11
⟨110⟩ 54.3 G-T	4.94	5.92	5.63	4.87	5.19
⟨331⟩ 55.6 G-T	3.58	4.71	4.58	4.96	3.78
⟨441⟩ 57.5 G-T	4.02	4.44	4.98	4.7	4.16
K-S type boundary					
⟨111⟩ 60. K-S	1.49	0.91	0.77	1.18	1.23
⟨432⟩ 57.2 K-S	2.1	1.47	1.73	1.89	2.15
⟨331⟩ 57.2 K-S	4.79	5.83	6.16	6.31	5.06
⟨221⟩ 51.7 K-S	3.39	3.9	4.57	4.16	4.21
⟨322⟩ 50.5 K-S	0.9	1.01	1.09	0.95	1.24
⟨431⟩ 50.5 K-S	0.62	0.99	0.68	1.01	0.94
⟨111⟩ 49.5 K-S	0.04	0.58	0.04	0.08	0.02
⟨221⟩ 47. K-S	0.8	0.66	0.07	0.66	0.48
⟨110⟩ 49.5 K-S	0.1	0.13	0.07	0.11	0.20
⟨110⟩ 60. K-S	5.06	4.99	5.21	4.68	4.93

In order to check the absence of any recrystallization during aging heat treatments, the misorientation relationships between neighboring grains were quantitatively compared to *reference* relationships calculated assuming exact (K-S) or exact (G-T) orientation relationships (ORs) between martensite and parent austenite. Although these ORs are not strictly obeyed in this steel family, they could allow easy detection of recrystallized grains, which do not have any ORs with parent austenite. Here although the G-T ORs seem to better describe the boundaries in the microstructure (see table III.3), such analysis is only used for comparison purposes.

No significant change is observed in the area fraction of boundaries respecting the K-S and G-T ORs in the T92 steel aged both at 650°C and at 650°C for 10^4h compared to these in the as-received T92 steel, indicating that no recrystallisation should have occured during aging heat treatments.

III.3.5 Summary

This section presented the microstructure of the thermally aged creep specimens before testing. The purpose of the heat treatments at 600°C and 650°C for 10^4h was to obtain a microstructure with large Laves phases for the T92 steel in order to quantify the influence of these phases on the loss of creep strength. Microstructural investigations were conducted on the aged T92 steels and the mains result listed below show that the objective was fulfilled:

- no significant change in hardness was observed after aging at 600°C and 650°C for 10^4h (see table III.2)
- the size distribution of Laves phases determined by analysis of SEM-BSE images showed an average equivalent diameter of $\sim$ 200nm and $\sim$ 300nm after aging at 600°C and 650°C, for 10^4h respectively (see figures III.7b and III.8b). This is consistent with literature data (Dimmler et al., 2003), (Korcakova et al., 2001).
- stress and/or strain during creep test does not seem to have a significant influence on the size distribution of Laves phases after 10^4h, no significant difference is observed between size distribution of Laves phases in crept specimens and thermally aged specimens for comparable time exposure (see figure III.7 and III.8).

  No clear indication of a possible effect of stress and/or strain on the growth of Laves phases in Grade 92 steel during exposure at both 600°C and 650°C can be found in the literature, at least for exposure times of about 10^4h.
- EBSD investigations revealed no significant change in the microtexture of the aged T92 steels (see figure III.9 and III.12). At the author's knowledge there are no EBSD investigations conducted on the Grade 92 steel after creep or thermal exposure. However, published EBSD results revealed no significant change in the microtexture of various 9-12% Cr tempered martensitic steel during thermal exposure at 550°C-650°C (Aghajani et al., 2009b), (Tak et al., 2009).

Five creep tests were conducted at 600°C on specimens thermally aged at 600°C for 10 10^4h and five creep tests were realized at 650°C on creep specimens on thermally aged 650°C C for 10^4h. The results of these creep tests will be given in the following chapters.

III.4 Summary

In the present study creep tests were conducted on smooth, notched, thermally aged and thermo-mechanically prepared specimens. This chapter presented the geometry of both smooth and notched specimens together with a microstructural characterization of the thermally aged specimens before testing. Details about thermo-mechanical preparation of specimens as well as the results of creep tests conducted on this kind of specimens are gathered in *Appendix A*.

Creep tests conducted on smooth specimens are reference tests. The purpose of these tests is to compare the creep behavior of the T92 steel under study with available creep data for the Grade 92 steel. These tests provide also reference crept specimens for microstructural investigations which could be further compared with those of the other kinds of specimens (i.e. notched, thermally aged and thermo-mechanically prepared specimens) after creep testing.

The notched specimens were used to study the influence of stress triaxiality on the creep damage development. Three different notch geometries were used to obtain different distribution of stress state during creep testing from a notched specimen to another. The geometries of the notched specimens were given in figure III.3.

The purpose of the thermally aged specimens was to study the effect of large Laves phases on the creep behavior of the T92 steel. Previous studies (see for instance (Dimmler et al., 2003), (Korcakova et al., 2001)) reported a relatively large size of Laves phase during the first 10^4h of exposure both at 600°C and 650°C without no significant change in size for longer exposure times. Thus blanks were thermally aged for 10^4h both at 600°C and 650°C and than machined into creep specimens with same geometry as that of the reference creep test.

A microstructural characterization of the T92 steel aged at 600°C and 650°C was realized and the main results were summarized previously. No change in the microtexture was observed using EBSD techniques and the size of Laves phase evaluated using analysis of SEM-BSE images are comparable with published data. No change in hardness occurred during aging heat treatments.

The purpose of the thermo-mechanically prepared specimens was to study the influence of the matrix substructure on the creep behavior of the T92 steel. Due to experimental difficulties only three creep tests were conducted on this kind of specimens. Such a low number of tests does not permit to correctly evaluate the influence of matrix substructure on the creep behavior. However, this is an original complementary method to test the creep behavior of steels which is worth of consideration.

Résumé

Dans le cadre de cette étude, des essais de fluage on été réalisés à 600°C et 650°C sur plusieurs types d'éprouvettes, à savoir lisses, entaillées, pré-vieillies et pré-fatiguées. Ce chapitre porte sur la présentation des éprouvettes lisses et entaillées ainsi que sur la caractérisation microstructurale des éprouvettes pré-vieillies. La préparation des éprouvettes pré-fatiguées ainsi que les résultats des essais de fluage sur ces types d'éprouvettes sont donnés dans l'annexe A.

Les essais de fluage sur éprouvettes lisses sont des essais de référence. L'objectif de ces essais est de comparer le comportement en fluage de l'acier T92, le matériau de l'étude, avec les données disponibles dans la littérature concernant le fluage de l'acier Grade 92. Aussi, ces essais donnent des échantillons de référence de la microstructure de l'acier T92 après fluage dans de conditions conventionnelles qui seront ensuite comparés avec ceux des autres

type d'éprouvettes non-conventionnelles (entaillées, pré-vieillies et pré-fatiguées) après fluage dans des conditions similaires de temps ou de contrainte nominale.

Les éprouvettes entaillées sont utilisées pour étudier l'effet de la triaxialité des contraintes sur l'endommagement par fluage. La triaxialité des contraintes pendant le fluage dans une éprouvette entaillée dépend de la géométrie de l'entaille et par conséquent trois géométries d'éprouvettes entaillées ont été utilisées (figure III.3) pour varier l'état des contraintes pendant le fluage d'une éprouvette à l'autre.

L'objectif des éprouvettes pré-vieillies est d'étudier l'influence de phases de Laves grossières sur le comportement en fluage de l'acier T92. Des études (Dimmler et al., 2003), (Korcakova et al., 2001) ont montré une croissance significative des phases de Laves dans les premières $10^4 h$ *d'exposition à* $600°C$ *et* $650°C$ *sans modification significative de taille pour des temps plus prolongés. Par conséquent des éprouvettes lisses avec la même géométrie que celles pour les essais de fluage de référence ont été usinées à partir des ebauces en acier T92 vieillies thermiquement à* $600°C$ *et* $650°C$ *pendant* $10^4 h$.

Une caractérisation microstructurale de l'acier T92 après vieillissement à été réalisée et les résultats ont été résumés à la fin de la section précédente. Les observations EBSD n'ont pas révélé de changement significatif dans la microtexture de l'acier après vieillissement. La distribution de taille de phases de Laves a été mesurée à partir des micrographies MEB à l'aide des techniques d'analyse d'image, elle est similaire aux données de la littérature. La dureté de l'acier T92 après les traitements de vieillissement thermique est similaire à celle de l'acier T92 à l'état de réception.

L'intérêt des éprouvettes pré-fatiguées est d'étudier l'influence de l'état de la matrice sur le comportement en fluage de l'acier T92. A cause des difficultés expérimentales liées à la préparation des éprouvettes pré-fatiguées, seulement trois essais de fluage ont pu être réalisés sur ce type d'éprouvette. Le nombre très faible de ces essais ne permet pas d'évaluer correctement l'influence de l'état de la matrice sur le comportement en fluage. Pourtant, l'utilisation des éprouvettes pré-fatiguées est une méthode originale qui mérite d'être considérée comme méthode complémentaire pour tester la résistance au fluage des aciers.

Chapter -IV-

Creep data processing

Contents

IV.1 Creep curve

A creep curve represents the evolution of elongation as a function of time for a given constant load. Three stages can be identified on typical creep curves (elongation versus time):

- **Primary creep stage**, in which the elongation rate increases with time. This stage is mainly due to glide and annihilation of dislocations related to the martensitic transformation and tempering mechanisms.
- **Secondary creep stage**: elongation shows an almost linear relationship with time and the strain rate is almost constant. During secondary creep there is a competition between recovery and hardening of the matrix.
- **Tertiary creep stage** corresponds to an acceleration of strain rate due to necking of the specimen and/or creep damage development and/or to metallurgical evolution.

IV.2 Creep data processing for smooth specimens

A decomposition of the first part of the creep curves into the primary stage and secondary stage was assumed for data processing of creep tests. The primary creep stage can be estimated using the following function:

$$\varepsilon^I(t) = E_0 + Q\left(1 - \exp\left(-\frac{t}{\tau}\right)\right) \tag{IV.1}$$

where t is time; E_0 is the instantaneous elastic/plastic strain which appears on the creep curve due to loading; Q represents the strain at the end of the primary stage and τ represents the characteristic time of the primary stage.

The deformation in the secondary creep stage can be described by a linear dependence between strain rate and time as follows:

$$\varepsilon^{II}(t) = \dot{\varepsilon}_{ss} t \tag{IV.2}$$

where $\dot{\varepsilon}_{ss}$ is the strain rate during the secondary stage. It is also called secondary creep rate.

Beside time to rupture, $\dot{\varepsilon}_{ss}$ is the most used parameter to characterize the creep behavior of a material under various levels of stress. Moreover $\dot{\varepsilon}_{ss}$ is often used in models and design applications, thus a good estimation of the $\dot{\varepsilon}_{ss}$ is of great importance.

$$\varepsilon(t) = \varepsilon^I(t) + \varepsilon^{II}(t) = E_0 + Q\left(1 - \exp\left(-\frac{t}{\tau}\right)\right) + \dot{\varepsilon}_{ss} t \tag{IV.3}$$

To get a continuous function, the engineering stain was modeled as the sum of the primary and secondary creep strain (equation IV.3). In fact, in almost all the considered part of the creep curve, either $\varepsilon^I \ll \varepsilon^{II}$ or $\varepsilon^{II} \ll \varepsilon^I$ so that the total strain rate is due to either the primary or the secondary creep rate.

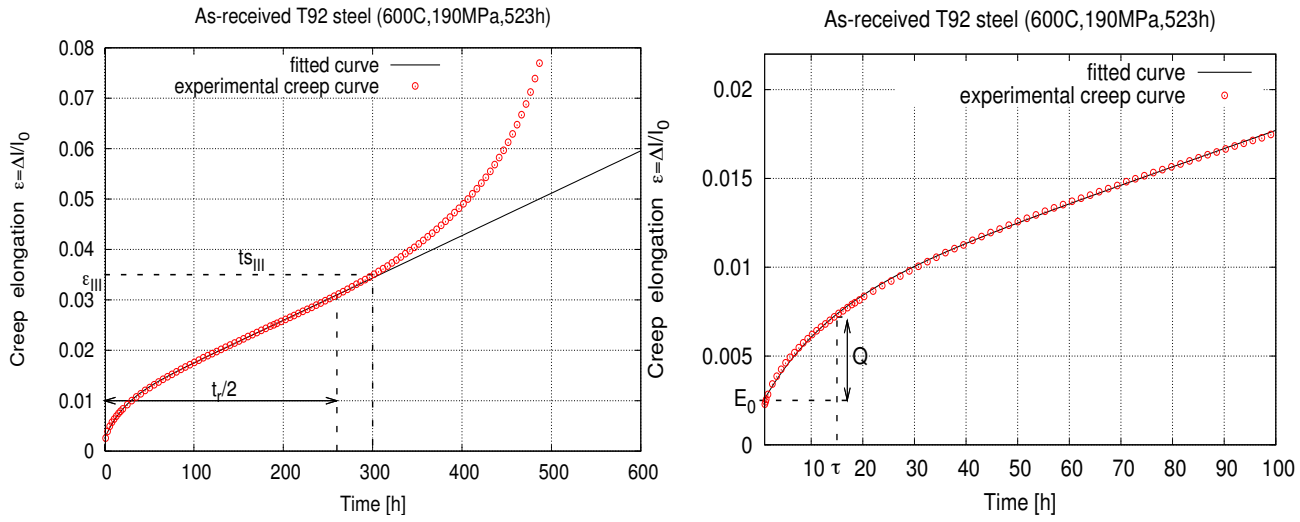

Figure IV.1 : Data processing of creep curves (a) Experimental creep curve for the test conducted at 600°C, 190MPa on as-received T92 steel and the adjusted curve using equation IV.3; (b) closer view of the begining of the curve together with a representation of equation IV.3 parameters

The $\dot{\varepsilon}_{ss}$ was estimated by adjusting equation IV.3 to the the first half of the experimental creep curves (i.e. $t \in [0, t_r/2]$, where t_r is the time to rupture of the specimen).

To illustrate the procedure, the experimental creep curve for a test conducted at 600°C under an engineering stress (σ_n) of 190MPa on T92 steel together with the adjusted curve using equation IV.3 are represented in figure IV.1a. In figure IV.1b shows a representation of the equation IV.3 parameters (constants).

The end of the linear part of the experimental creep curve is considered as the beginning of the tertiary creep stage. The time (ts_{III}) and the elongation (ε_{III}) at the beginning of the tertiary stage were also defined using equation IV.3 and corresponds to the point where the difference between the adjusted curve and experimental creep curve is equal to 0.0001.

Another method to estimate the $\dot{\varepsilon}_{ss}$ is to plot the strain rate versus time during creep test. The minimum value of the strain rate in these kind of plots represents the $\dot{\varepsilon}_{ss}$. The drawback of this method is the scatter of values due to acquisition system, anyway the first method, consisting of adjusting the equation IV.3 to determine the slope of the experimental creep curve is believed to be more appropriate to better estimate the $\dot{\varepsilon}_{ss}$.

The evolution of the strain rate during creep tests is also presented in the next two chapters in addition to creep curves. The strain rate during creep test was calculated using the following formula:

$$\dot{\varepsilon} = \frac{\varepsilon(t_{i+1}) - \varepsilon(t_i)}{t_{i+1} - t_i} \tag{IV.4}$$

where $\dot{\varepsilon}$ is the strain rate; $\varepsilon(t_{i+1})$ and $\varepsilon(t_i)$ are the elongation at acquisition time t_{i+1} and t_i respectively.

IV.3 Creep data processing for notched specimens

The presence of notches induces a non-uniformity of stress fields (respectively strain fields) which varies with time (stress redistribution) in the notched area of specimens during creep testing. Thus, an assessment of reference stresses such as axial stress (σ_{22}) and von Mises equivalent stress (σ_{VM}) had to be considered to compare the results of creep tests on smooth and notched specimens. The determination of maximum value and spatial distribution of stress was aimed using finite element simulations.

Constitutive equations corresponding to the damage-free model (conform chapter VIII.2) were used for FE simulations. Note that model without damage overestimates the lifetime of notched specimens. The lifetime of the specimens predicted by damage-free model are given in figures VIII.16 and VIII.17, chapter VIII.2.

Because of the axisymmetry of notched specimens FE simulations were conducted only on a quart of each kind of these specimens. In figure is shown the notched area of the specimens meshing used for FE simulations.

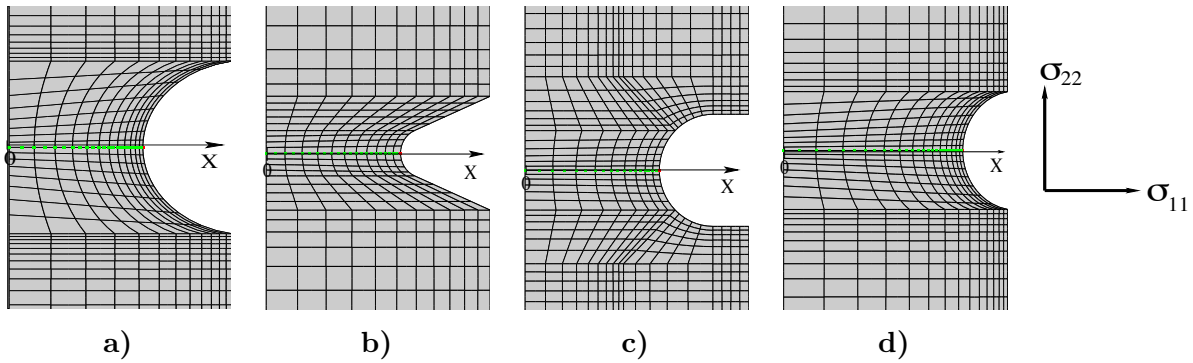

Figure IV.2 : Mesh of notched specimens a) NTDC1.2; b) NTDV; c) NTDC0.6M; d) NTDC0.6

The evolution of stress fields in the symmetry plane of the notched area, as a function of both the distance from the specimens axis and the notch opening were considered for data processing of creep curves on notched specimens.

Influence of the notch geometry on the localization of the maximum value of both σ_{22} and σ_{VM} were also analyzed.

Chapter -V-

Results of creep tests conducted at 600°C

Contents

Introduction

This chapter aims to present the results of creep tests conducted at 600°C on smooth, notched and thermally aged specimens. These specimens together with a microstructural characterization of the thermally aged specimens were presented in chapter III.

In the present study creep tests were conducted on thermo-mechanically prepared specimens. Details about their preparation together with the results of creep tests conducted on this kind of specimens and investigation of specimens after creep testing are gathered in *Appendix A* of the present study.

One creep test was conducted at 600°C under a load of 170MPa on a specimen thermo-mechanically prepared at 550°C (for more details see *Appendix A*). However, the level of stress and lifetime of this creep test is mentioned in this chapter for comparison reasons.

The purpose of creep tests is briefly recalled in the following.

The purpose of creep tests on smooth specimens was to compare the creep strength of the studied T92 steel to available published data on Grade 92 steel, see for instance references (V & M, 2000), (Bendick and Gabrel, 2005), (Vaillant et al., 2008), (Petry and Lindet, 2009), (Ennis et al., 1997).

The purpose of notched specimens was to study the effect of stress triaxiality on creep damage developement.

Thermally aged and thermo-mechanically prepared specimens were used to study the effect of the large Laves phases and the matrix substructure on the creep strength loss, respectively. On these kinds of creep specimens same levels of stresses as on standard smooth specimens were used in order to quantify the effect of the microstructure state on creep strength.

In addition to creep tests conducted at 600°C on the investigated T92 steel, P92 steel specimens creep tested for times up to 50,000h at 600°C were provided by *Salzgitter Mannesmann Forschung (SZMF), Germany*. The creep curves of these specimens are also reported in this chapter.

General remarks:

The data processing of creep curves was presented in chapter IV. In all tables of this chapter, σ_n is the engineering stress in MPa; t_r is the time to rupture in hours; Z and A are respectively the reduction of area and elongation at rupture of crept specimens after testing. $\dot{\varepsilon}_{ss}$ is the secondary creep rate, which was estimated by fitting equation IV.3 to the half of the experimental creep curves as explained in chapter IV. The adjusted values of Q, E_0 and τ are also given.

Introduction

Dans ce chapitre sont présentés les résultats des essais de fluage réalisés à 600°C sur des éprouvettes lisses, éprouvettes entaillées et éprouvettes pré-vieillies. La géométrie de ces éprouvettes ainsi qu'une caractérisation de la microstructure des éprouvettes pré-vieillies ont été présentées dans le chapitre III.

Dans cette thèse des essais de fluage ont également été réalisés sur éprouvettes pré-fatiguées. La préparation de ces éprouvettes ainsi que les résultats des essais de fluage sur ce type d'éprouvette sont regroupés dans l'annexe A.

Un essai de fluage a été réalisé à 600°C sur une éprouvette pré-fatiguée à 550°C (voir l'annexe A pour plus de détails). Dans ce chapitre, le résultat de cet essai (contrainte et temps à rupture) est comparé avec l'ensemble des résultats des essais de fluage à 600°C.

L'objectif des essais de fluage sur éprouvettes lisses est de comparer la résistance au fluage du matériau de l'étude - l'acier T92 avec des données disponibles dans la littérature pour l'acier Grade 92, dans des références comme: (V & M, 2000), (Bendick and Gabrel, 2005), (Vaillant et al., 2008), (Petry and Lindet, 2009), (Ennis et al., 1997)

Les intérêts des essais de fluage sur éprouvettes pré-vieillies et éprouvettes pré-fatiguées sont d'étudier l'influence de large phases de Laves et l'influence de la restauration de la matrice sur le comportement en fluage. Les niveaux des contraintes utilisés sur ce type d'essais sont les mêmes que ceux utilisés pour les essais de référence sur éprouvettes lisses pour pouvoir quantifier l'influence de l'état de la microstructure sur le comportement en fluage.

En plus des essais de fluage réalisés sur l'acier T92, quatre éprouvettes en acier P92 déjà testées en fluage à 600°C pour des temps allant jusqu'à 50,000h ont été délivrés par Salzgitter Mannesmann Forschung (SZMF), Germany. Les courbes de fluage ainsi que les résultats des essais correspondants aux éprouvettes en acier P92 sont présentés dans ce chapitre.

Remarques générales

Le dépouillement des courbes de fluage a été présenté dans le chapitre IV. Dans chacun des tableaux de ce chapitre σ_n est la contrainte nominale en MPa, t_r est le temps à rupture en heures; Z et A sont la réduction de l'aire et l'élongation de l'éprouvette après rupture. $\dot{\varepsilon}_{ss}$ est la vitesse de fluage secondaire déterminée par l'ajustement de l'équation IV.3 sur la première partie de la courbe expérimentale, comme il a été expliqué dans le chapitre IV. Les valeurs des paramètres Q, E_0 et τ après ajustement sont représentées dans les tableaux.

V.1 Smooth creep specimens

V.1.1 T92 steel creep specimens

Table V.1 presents the results of the creep tests conducted at 600°C on T92 steel smooth specimens. The creep curves from these tests are given in figure V.1.

The results in table V.1 show that the elongation at the end of the primary creep stage, the sum of E_0 and Q is almost constant of about 0.009±0.0003.

The values of $\dot{\varepsilon}_{ss}$ estimated by using equation IV.3 is consistent with $\dot{\varepsilon}_{ss}$ shown by ploting the evolution of the strain rate during creep tests (see table V.1 and figure V.2).

The tertiary creep stage is onset at an elongation of about 0.03 for all creep tests, independently of the applied stress level. This indicates a structure instability leading to necking of the specimen. The relatively high values of elongation at rupture (A) and reduction of area (Z) also indicate that failure of these specimens occurs by extensive necking.

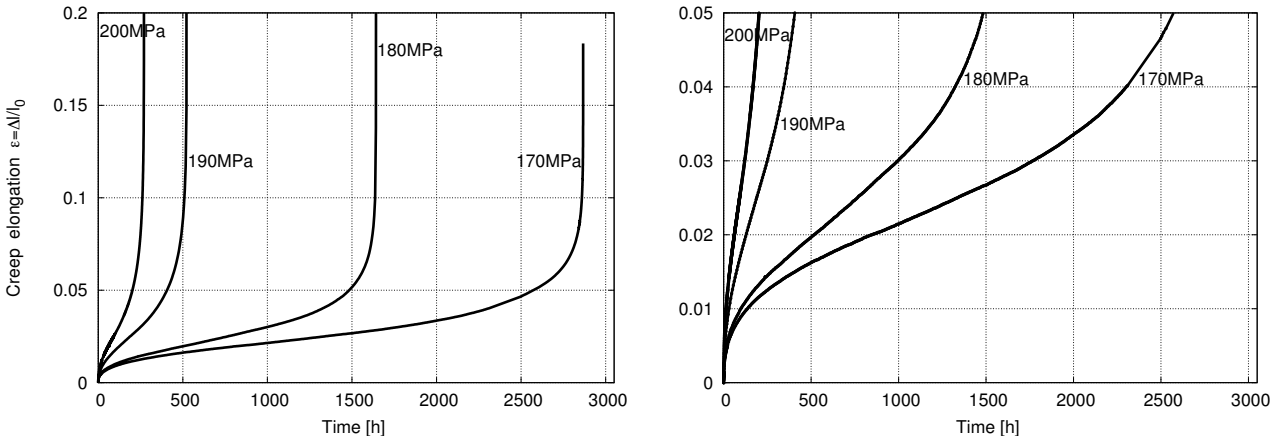

Figure V.1 : a) Creep curves for creep tests conducted on smooth specimens at 600°C on T92 steel; b) same as a), close-up view of the begining of the creep curves

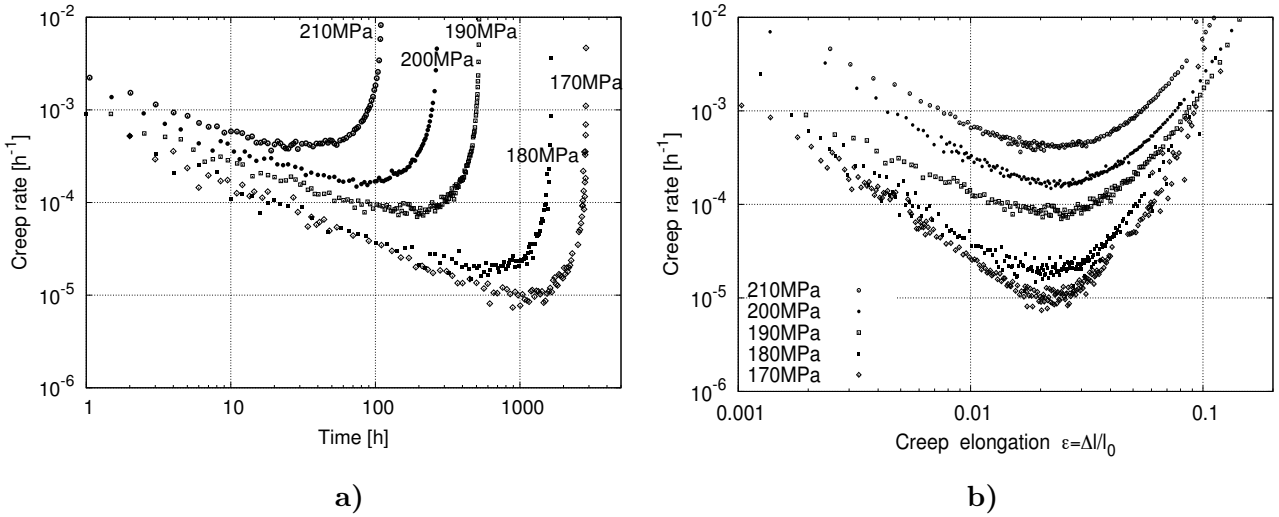

Figure V.2 : Strain rate for creep tests conducted on smooth specimens at 600°C on T92 steel as a function of time (a) and elongation (b)

Table V.1 : Results of creep tests conducted at 600°C on T92 steel smooth specimens

Temp. Steel	σ_n [MPa]	t_r [h]	A [%]	Z [%]	E_0	Q	τ [h]	ts_{III} [h]	ε_{III}	$\dot{\varepsilon}_{ss}$ [h^{-1}]
600°C T92 steel	210	112	28.7	89	0.0015	0.0073	2.9	60	0.036	43.77×10^{-5}
	200	270	29.8	90	0.0014	0.0078	7.8	141	0.034	17.38×10^{-5}
	190	523	28.4	85	0.0014	0.0074	15.2	287	0.034	8.58×10^{-5}
	180	1,642	23.2	84	0.0011	0.0077	29.3	1,133	0.033	2.15×10^{-5}
	170	2,867	21	78	0.0010	0.0083	95.0	1,718	0.029	1.07×10^{-5}

The analysis of the creep curves of the tests conducted on the T92 steel at 600°C reveals that the tertiary stage represents 30% to 50% of the life time of the specimen (see table V.1).

Figure V.2a shows that the minimum strain rate is achieved after almost 30% of the creep test duration. The so-called secondary creep stage is thus only a small part of the creep lifetime.

V.1.2 Long term creep data (P92 steel creep specimens provided by SZMF)

The creep curves of the long-term crept specimens provided by SZMF are given in figure V.3. The creep tests were conducted at SZMF before the beginning of this study.

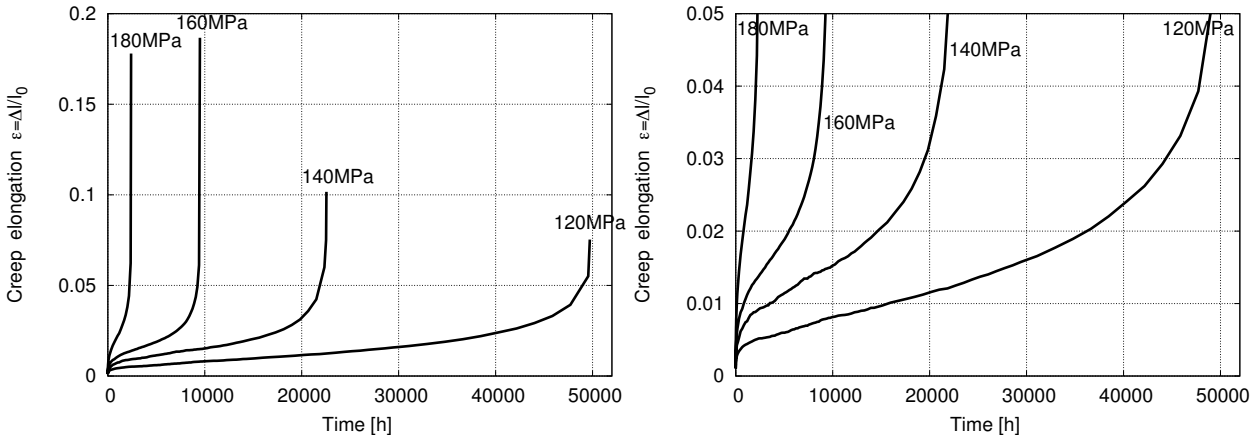

Figure V.3 : a) Creep curves of P92 steel specimens tested for long-term at 600°C (data from SZMF); b) same as a), close-up view of the begining of the creep curves

The creep data of P92 crept specimens are very useful for the modelling part of this study due to their exceptionally high time to rupture. It is to be noticed that the long term creep specimens were chosen to be located well within the stress vs. creep lifetime curve established by ECCC for the Grade 92 steel. So, it is believed that these creep specimens are representative for the creep behaviour of the Grade 92 steel.

A low ductility (low values of both Z and A) is observed for specimens tested for times higher than 10^4h compared to crept specimens tested for shorter times, both of P92 steel and T92 steel. The instantaneous plastic deformation due to loading, E_0 increases when the applied stress is increased, table V.2.

Table V.2 : P92 steel creep specimens tested at 600°C (provided by SZMF, Germany)

Temp. Steel	σ_n [MPa]	t_r [h]	A [%]	Z [%]	E_0	Q	τ [h]	ts_{III} [h]	ε_{III}	$\dot{\varepsilon}_{ss}$ [h^{-1}]
600°C P92 steel	180	2,399	17.9	74	0.0031	0.00680	42.5	1,617	0.031	1.22×10^{-5}
	160	9,497	18.7	68	0.0027	0.0060	197.4	5,876	0.021	2.05×10^{-6}
	140	22,547	10.2	27	0.0022	0.0049	370.5	13,258	0.018	8.37×10^{-7}
	120	49,721	7.5	16	0.0017	0.0025	319.6	25,560	0.014	3.70×10^{-7}

The creep test conducted on the P92 steel under 180MPa shows an elongation at the end of the primary creep stage (the addition of E_0 and Q) of 0.01 which is comparable with the values of elongation found for the T92 steel at the end of primary stage, see table V.1. The

results in table V.2 show that the primary creep stage of long-term creep tests ($t_r > 10^4$h) ends for values of elongation of ~ 0.005 (120MPa) and ~ 0.007 (140MPa).

The creep test conducted under 180MPa revealed a similar t_r as the T92 steel tested under the same load. Thus creep behavior at 600°C of the P92 steel could be considered similar to that of the T92 steel.

The values of $\dot{\varepsilon}_{ss}$ estimated from data processing of creep curve using equation IV.3 corresponds to the minimum values of the strain rate shown in figure V.4.

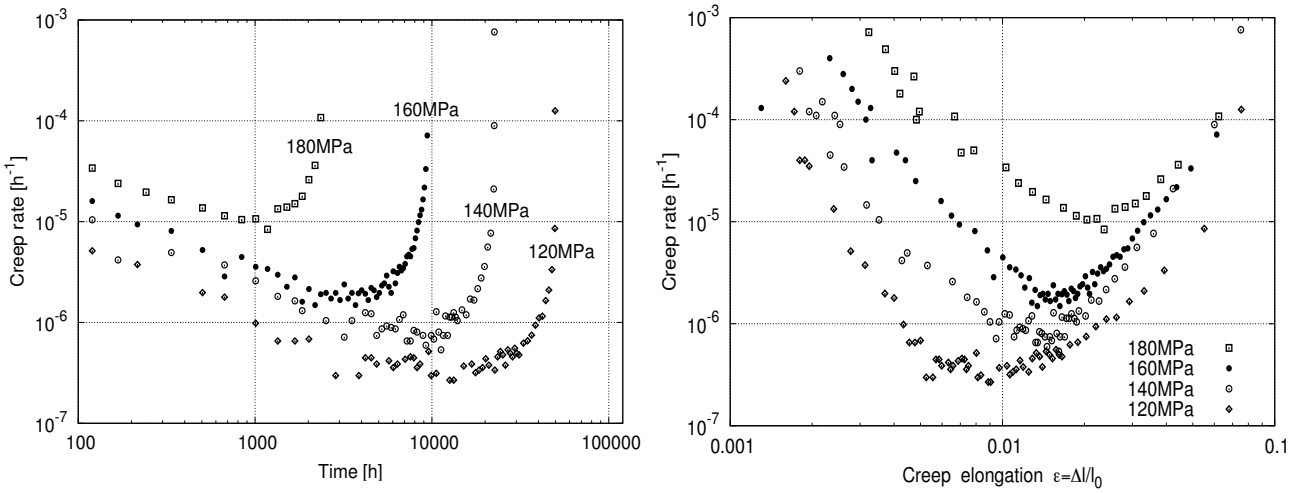

Figure V.4 : Strain rate of P92 steel specimens tested for long-term at 600°C as a function of time (a) and elongation (b)

As observed for creep tests conducted on the T92 steel, the beginning of the tertiary creep stage on the test conducted on P92 steel at 180MPa occurs at an elongation of about 0.03, which corresponds to the values observed from the creep tests conducted on T92 steel indicating that this P92 steel specimen failed like the T92 specimens, most probably by necking. The beginning of the tertiary stage of the other tests conducted on the P92 steel occurs at lower elongation values. Remarkably, the tertiary stage of the test conducted under a load of 120MPa starts at an elongation of about 0.01, see figure V.4b.

The low values of elongation at the beginning of the tertiary stage together with low values of Z for the specimens tested for long-term compared to these tested for short term ($t_r < 10^4$h), indicates that there is a difference between the failure of short term crept specimens and failure of long term crept specimens. The failure of long-term crept specimens can be due partly to creep damage development, the onset of tertiary stage could be due to nucleation and growth of cavities by a diffusion assisted mechanism.

For the long-term creep tests, and besides creep damage development, metallurgical evolution of the steel during test should be also considered in the understanding of the creep strength loss or failure. Metallurgical evolution of the steel could decrease the creep strength of the steel, precipitation of new phases could decrease the amount of atoms in solid solution in the matrix or precipitates which are obstacle to dislocations glide.

To separately assess development of damage and metallurgical evolution of crept specimens, P92 steel crept specimens together with some T92 crept specimens were investigated using appropriate techniques such as SEM, TEM, EBSD (see chapter VII).

V.2 Thermally aged creep specimens

A characterization of the microstructure of the T92 steel after aging at 600°C for 10^4h was presented in chapter III. The geometry of the thermally aged specimens is the same as the geometry of the smooth specimens used for reference creep tests on T92 steel, for more details about specimens preparation see chapter III.

The results of creep tests conducted at 600°C on specimens thermally aged at 600°C for 10^4h are given in table V.3. The creep curves of these tests are given in figure V.5. In figure V.5 are also represented the creep curves of the as-received T92 steel tested under 180MPa and 170MPa.

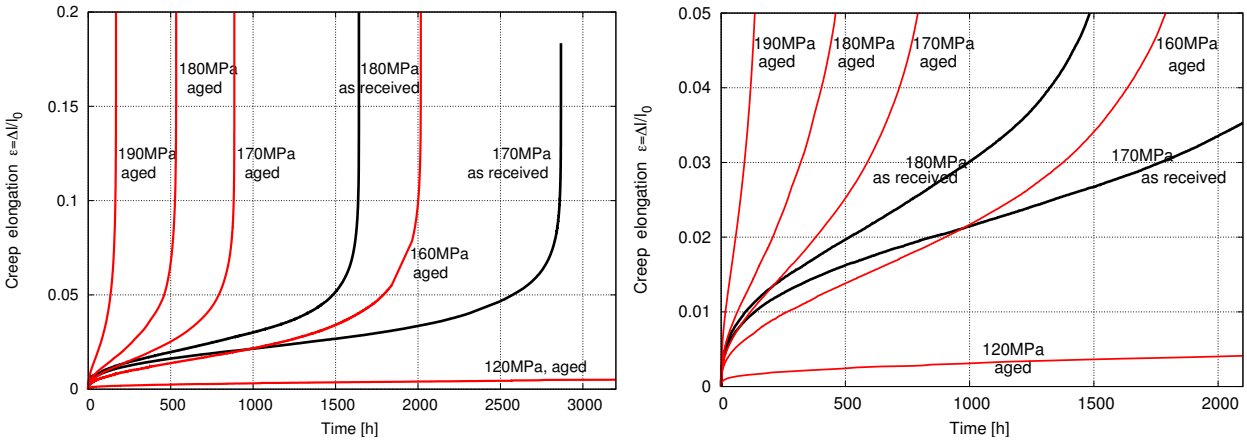

Figure V.5 : a) Creep curves for tests conducted at 600°C on T92 steel thermally aged at 600°C for 10^4h; b) same as a), close-up view of the begining of the curves; the creep test under 120MPa on thermally aged specimen is still in progress

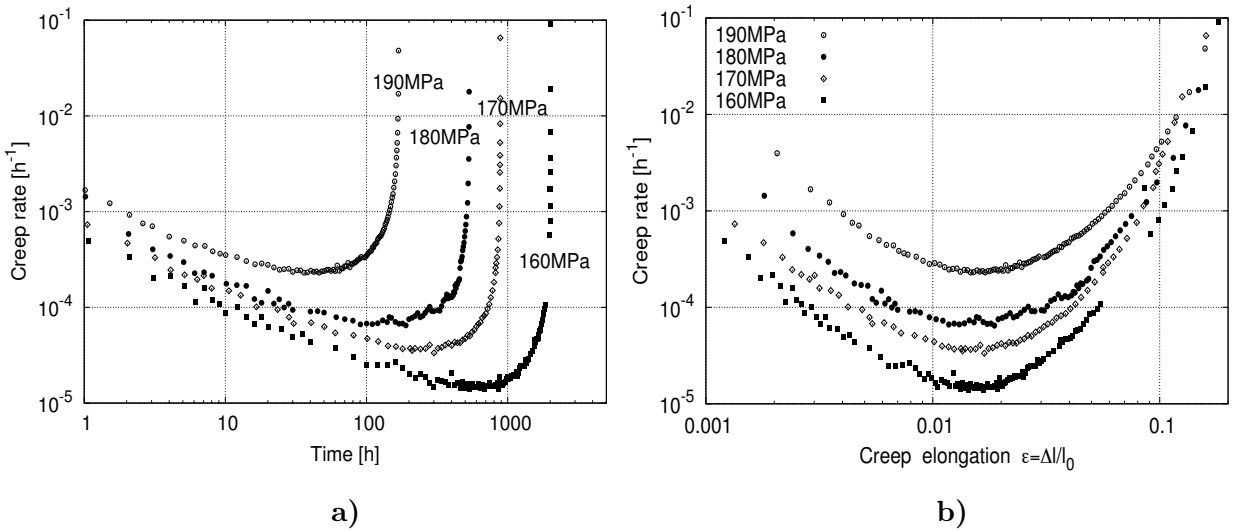

Figure V.6 : Strain rate of T92 steel thermally aged at 600°C during subsequent creep at 600°C as a function of time (a) and elongation (b)

As can be seen in figure V.5, after aging at 600°C for 10^4h the T92 seel shows a higher secondary creep strain rate ($\dot{\varepsilon}_{ss}$) and a lower time to rupture (divided by about 3) compared to as received steel for the same testing conditions. The increase in $\dot{\varepsilon}_{ss}$ after aging can be explained by the matrix depletion of W and Mo atoms by Laves phase precipitation during ageing heat treatment which reduces the solid solution strengthening.

The values of $\dot{\varepsilon}_{ss}$ of the aged T92 steel was estimated, as for creep tests conducted on as-received specimens, by fitting equation IV.3 to half of the experimental creep curves and the identified parameters are given in table V.3.

Table V.3 : Results of creep tests conducted at 600°C on specimens thermally aged at 600°C for 10^4h

Temp.	σ_n [MPa]	t_r [h]	A [%]	Z [%]	E_0	Q	τ [h]	ts_{III} [h]	ε_{III}	$\dot{\varepsilon}_{ss}$ [h^{-1}]
600°C	190	169	26,7	87	0.0003	0.00507	2.1	84	0.026	$25{,}3\times10^{-5}$
	180	534	26,2	87	0.0002	0.00455	7.3	251	0.023	7.33×10^{-5}
	170	886	21,6	82	0.0002	0.00478	11.5	474	0.024	$3{,}95\times10^{-5}$
	160	2016	24,1	82	0.0001	0.00460	44.8	1,060	0.023	1.60×10^{-5}
	120	in progress			0.0001	0.00181	103.0	in progress		8.73×10^{-7}

Thermal aging does not seems to have a significant influence on the short-term creep ductility of the T92 steel. There is no significant difference between the reduction of area (Z) and the elongation (A) of the thermally aged T92 steel specimens and as received T92 steel specimens creep tested for the same levels of σ_n, see table V.3 compared with table V.1.

The analysis of creep curves revealed that the beginning of the tertiary stage occurs at lower values of elongation on thermally aged T92 steel compared to as-received T92 steel for same levels of σ_n, see tables V.3 and V.1.

The tertiary creep stage of tests conducted on thermally aged specimens represents almost 50% of test duration, see table V.3 and figure V.6a.

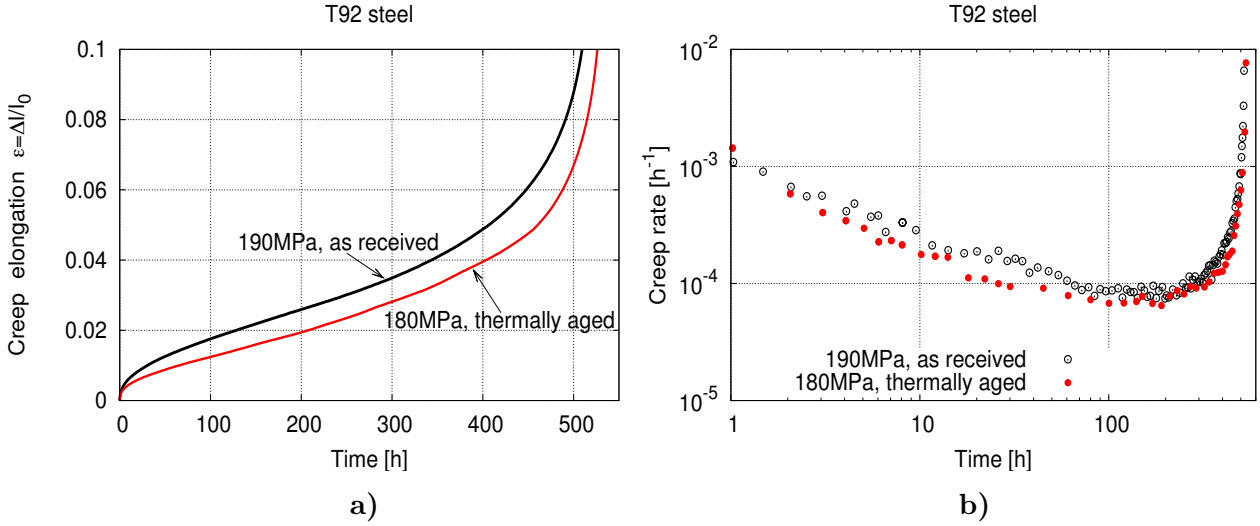

Figure V.7 : a) Creep curves of the as-received T92 steel under 190MPa and of the T92 steel thermally aged (600°C, 10^4h) under 180MPa; b) strain rate evolution during the two creep tests

Creep test conducted under 180MPa on thermally aged specimen reveals similar t_r to that

of the test conducted under 190MPa on as-received T92 steel. The creep curves of two tests are given in figure V.7a. The strain rate evolution during creep tests (figure V.7b) show no significant difference between the two tests. One may say that aging at 600°C induces a loss of the creep strength of about 10MPa, at least for high stressess ($\sigma > 160$MPa).

The creep strength of the thermally aged T92 steel should be still higher than the creep strength of a steel with similar chemical composition as the T92 steel but without W, because some amount of the W content remains in solid solution after aging (Hald, 1996). For example, for same testing conditions (600°C, 160MPa) a lower t_r (about 1,000h) and a higher $\dot{\varepsilon}_{ss}$ (about 4×10^{-5}h^{-1} (Kimura et al., 2009)) are obtained for the Grade 91 steel (9Cr-1Mo-VNb) compared to the thermally aged T92 steel.

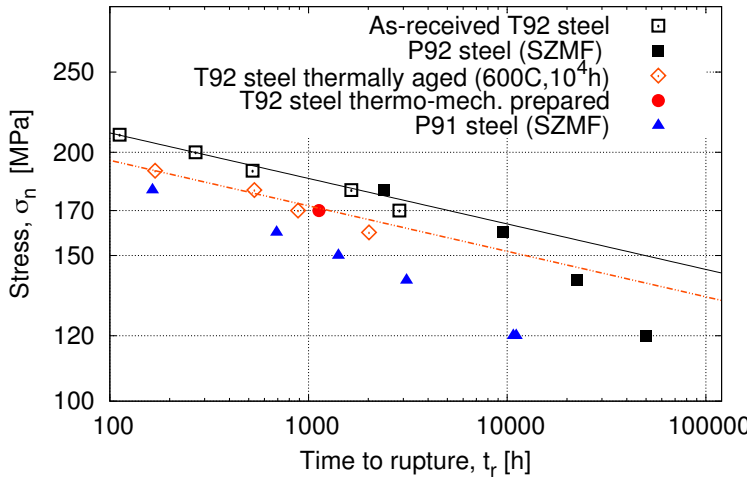

Figure V.8 : Creep rupture data at 600°C of the T92 steel, T92 steel thermally aged at 600°C, P92 steel and P91 steel

In figure V.8 are represented the stress and the time to rupture of the creep tests conducted in this study on the T92 steel and on the thermally aged T92 steel, together with results of creep tests conducted at 600°C on three different P91 steels. The chemical composition and the heat treatments of the three P91 steels correspond to the specifications of the EN 10216 Standard. The results of creep tests conducted on Grade 91 steel were delivered by SZMF and corresponds with published data (V & M, 2002), (Kimura et al., 2009), (Haney et al., 2009), (Sklenička et al., 2003) on the creep rupture behavior of Grade 91 steel at 600°C.

Figure V.8 shows than even after aging at 600°C for 10^4h the creep strength of the Grade 92 steel is still better than the creep strength of the Grade 91 steel, at least for testing time lower than 3,000h.

Steels alloyed with W, loss their creep strength by precipitation of Laves phases (Seung et al., 2006), but they show a higher creep strength compared to steel without W. W should be regarded as a good alloying element to improve the creep strength of steels despite Laves phase precipitation. The effect of W content of steels on the creep strength was discussed in chapter II.

For high stresses (σ_n >160MPa), a $\dot{\varepsilon}_{ss}$ three times higher is observed on the thermally aged T92 steel compared to as-received T92 steel. In order to determine the $\dot{\varepsilon}_{ss}$ of the thermally aged T92 steel at low stresses, a creep test is in progress under σ_n =120MPa. This stress level was chosen for this test because of both availability of the creep curve of the P92 steel tested at 120MPa for 49,721h and for comparison purposes.

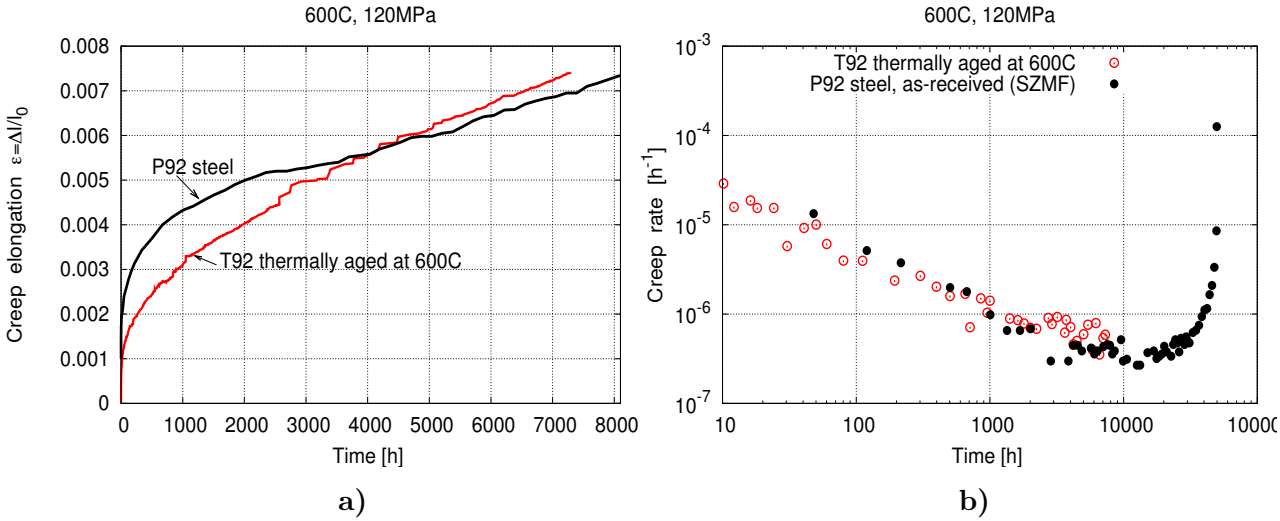

Figure V.9 : Creep curves (a) and creep rate (b) for the P92 steel tested at 120MPa, 600°C for 49,721h and T92 steel thermlally aged at 600°C, 10^4h under testing at 120MPa, 600°C (test in progress)

Figure V.9 shows the creep curve (a) and the creep rate (b) of the P92 steel tested at 120MPa, together with the available part of the creep curve of the running test on thermally aged T92 steel. The slight scatter between the creep curves in figure V.9a can be due to the different geometries of the specimens and testing machines. The available data on running test show a similar creep rate for the thermally aged T92 steel and the P92 steel tested at 120MPa, figure V.9b. The short duration of the test at present (test is running) does not allow a good estimation of the $\dot{\varepsilon}_{ss}$ of thermally aged steel under a load of 120MPa. The creep rate of the P92 steel under 120MPa (figure V.9b) shows that at least 5,000h of testing are needed to reach the minimum creep rate.

The progress of the creep test on thermally aged T92 steel under 120MPa will enable to check whether the $\dot{\varepsilon}_{ss}$ of a long-term creep test (t_r>30,000-40,000h) is given by a steel thermally aged in the first part of the test.

There no available published data on creep behavior at 600°C of Grade 92 steel after 10^4h of thermal aging at 600°C. (Sklenička et al., 2003) reported creep results at 600°C on a P92 steel thermally aged at 650°C for 10^4h. These results were given in figure I.22, chapter I. The creep results at 600°C on thermally aged T92 steel obtained in the present study could not be compared with the results of (Sklenička et al., 2003) because of the different aging temperature.

V.3 Simple analysis of the creep flow of Grade 92 steel at 600°C

This section aims at a simple analysis of the stress dependence of secondary creep rate ($\dot{\varepsilon}_{ss}$) and time to rupture (t_r) for the as-received and the thermally aged T92 steel creep tested in this study, together with the results provided by SZMF for the P92 steel and literature data. Simple laws and relationships, usually used to model creep data such as Monkman-Grant relationship, Norton flow rule are applied to the creep results of this study.

Symbols in figure V.10 represent the $\dot{\varepsilon}_{ss}$ estimated using the procedure presented in chapter IV and errors bars in figure V.10 represent the minimum and the maximum values of $\dot{\varepsilon}_{ss}$ derived from the plots of the strain rate in secondary stage creep, such as figures V.2, V.4, V.6.

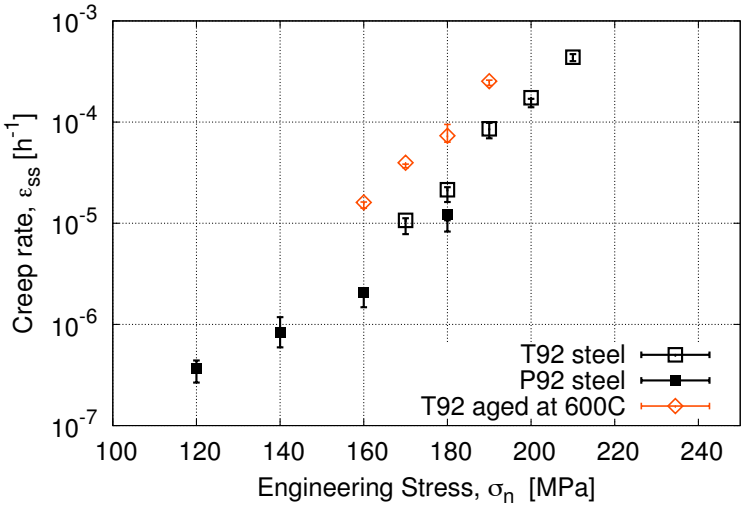

Figure V.10 : Secondary creep rate of creep tests conducted at 600°C; symbols represent values estimated using equation IV.3 and error bars show the minimum and the maximum values of strain rate during secondary creep stage

Figure V.10 shows that the values of $\dot{\varepsilon}_{ss}$ estimated using the two methods are similar. Estimation of $\dot{\varepsilon}_{ss}$ using equation IV.3 is an analytical and reliable method which avoids the scatter of strain rate values during creep test. The values of $\dot{\varepsilon}_{ss}$ estimated using equation IV.3 are considered for the further analysis of the creep behaviour.

V.3.1 Creep rupture behavior at 600°C of Grade 92 steel

A high reduction of area (Z) is observed for specimens with $t_r < 10^4$h for both T92 steel and P92 steel, furthermore these specimens show a higher secondary creep rate ($\dot{\varepsilon}_{ss}$) compared to long-term crept specimens ($t_r > 10^4$h), suggesting that necking of the specimen lead to the final rupture.

Thermally aged specimens (600°C for 10^4h) show Z and $\dot{\varepsilon}_{ss}$ similar to those of the as received T92 steel, at least for specimens with a testing time lower than 2,000h (figure V.11), suggesting that the thermally aged specimens failed as the short-term specimens of as-received material.

The results of creep tests on smooth specimens in as-received T92 steel and creep rupture data of the P92 steel correspond to published data on the creep behaviour at 600°C of the Grade 92 steel, figure V.12. Thus, the creep behaviour of the investigated T92 steel can be considered as being representative for the creep behaviour of the Grade 92 steel at 600°C, moreover the creep results of T92 steel and P92 steel are on the line established by ECCC for the Grade 92 steel at 600°C. The ECCC regression line was taken from the reference (Yoshizawa et al., 2009).

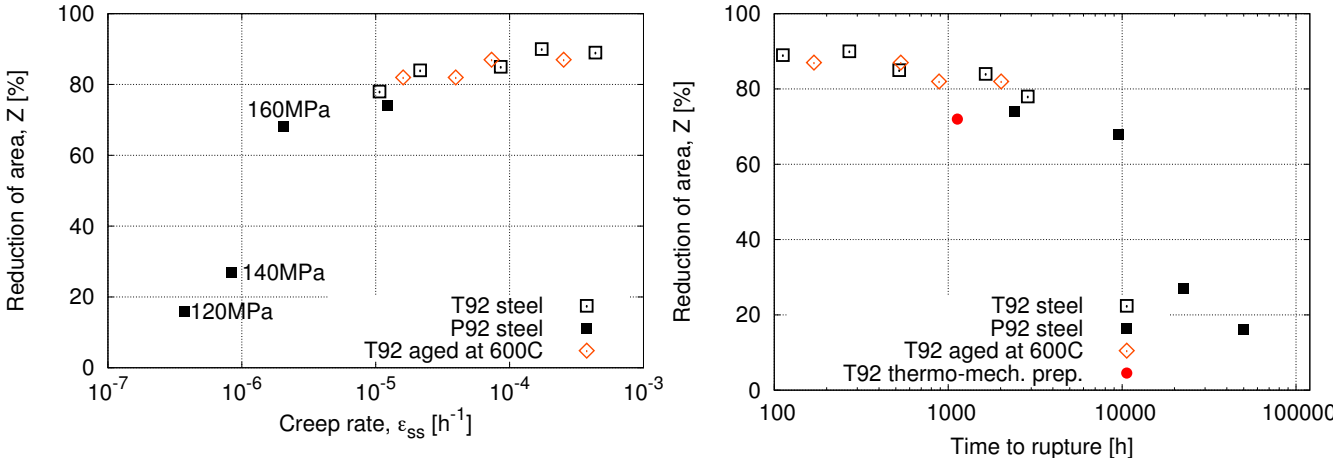

a) b)

Figure V.11 : Reduction of area (Z) as a function of secondary creep rate (a) and time to rupture (b) for specimens creep tested at 600°C

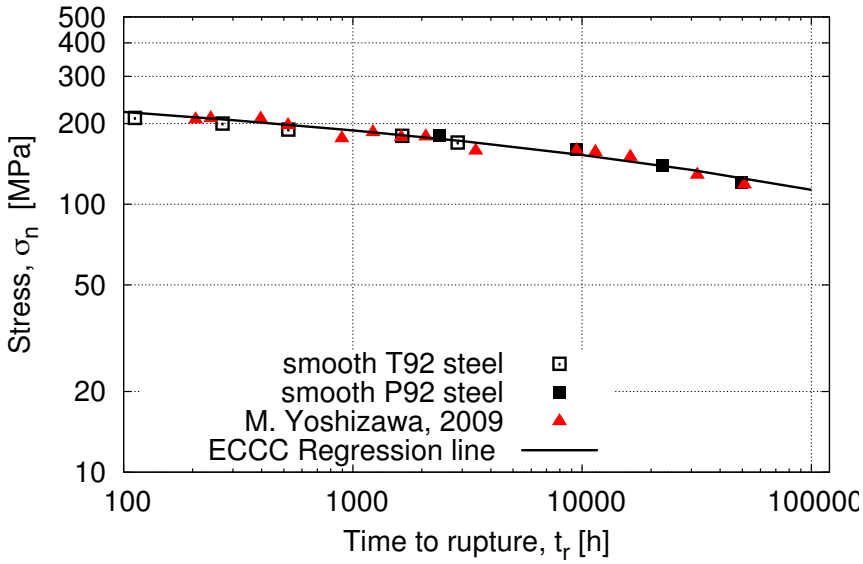

Figure V.12 : Creep rupture data at 600°C of the T92 steel and P92 steel, investigated in this study compared to published data on the creep rupture behaviour of the Grade 92 steel

V.3.2 Monkman-Grant relationship

Among the methods of extrapolating the long-term creep data from short-term data, Monkman-Grant relation is a simple method which states that there is a power-law relationship between the $\dot{\varepsilon}_{ss}$ and t_r, equation V.1.

$$t_r \times (\dot{\varepsilon}_{ss})^m = C \tag{V.1}$$

A first adjustment of the Monkman-Grant relationship to the creep results (i.e. $\dot{\varepsilon}_{ss}$ and t_r) of both T92 steel and P92 steel revealed m=1.19 and $C = 0.133$ h$^{-0.19}$ (see figure V.13a).

Because the value of m was found close to 1, a second adjustment of the Monkman-Grant relationship with $m = 1$ (i.e. $t_r \times \dot{\varepsilon}_{ss} = C_2$) was done on the creep data of both T92 and P92 steel and revealed $C_2 = 0.03$.

The value of C_2 found after the second adjustment is close to $\frac{1}{18}$, thus the Monkman-Grant relationship with $C = \frac{1}{18}$ and $m = 1$ is also plotted in figure V.13a. As it will be shown in the next section, the $\frac{1}{18}$ represents the slope of the stress versus $\dot{\varepsilon}_{ss}$ for high stress regime identified using the Norton-power law.

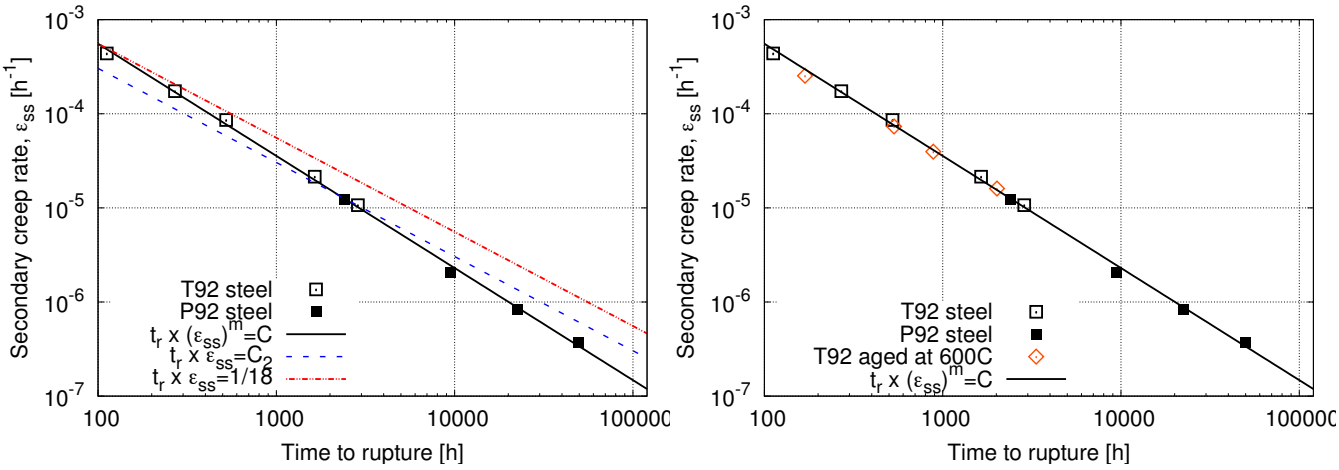

Figure V.13 : Monkman-Grant relationship for creep tests conducted at 600°C on smooth specimens a) T92 and P92 steel; b) T92 steel, P92 steel and T92 steel thermally aged (600°C, 10^4h)

The Monkman-Grant relation with $C = 0.133$ and $m = 1.19$ reproduces the best the creep results of both T92 steel and P92 steel, compared with the other two adjustments.

The Monkman-Grant relationship (equation V.1 was adjusted on the creep data of T92 steel and P92 steel. In figure V.13b the $\dot{\varepsilon}_{ss}$ and t_r of creep tests conducted on thermally aged T92 steel are added to the creep results of T92 steel, P92 steel and the adjusted Monkman-Grant relationship (i.e. $C = 0.133$ and $m = 1.19$). The creep data of the thermally aged T92 steel are also quite well represented by the Monkman-Grant relationship.

V.3.3 Norton flow rule

The secondary creep rate, $\dot{\varepsilon}_{ss}$, determined from elongation-time creep curves is plotted as a function of engineering stress in figure V.14a. Two regions can be distinguished: high stresses ($\sigma > 160$MPa) and low stresses ($\sigma < 160$MPa). The stress dependence of $\dot{\varepsilon}_{ss}$ can be modeled by a typical Norton power-law, defined by equation V.2 where A and n are constants depending on temperature. In equation V.2, σ_0 was chosen arbitrarily equal to 100MPa. For the creep results of this study it was found $A = 5.18 \times 10^{-10}$h^{-1} and $n = 18$ for high stresses and $A = 1.19 \times 10^{-7}$h^{-1} and $n = 6$ for low stresses.

$$\dot{\varepsilon}_{ss} = A \left(\frac{\sigma}{\sigma_0} \right)^n \tag{V.2}$$

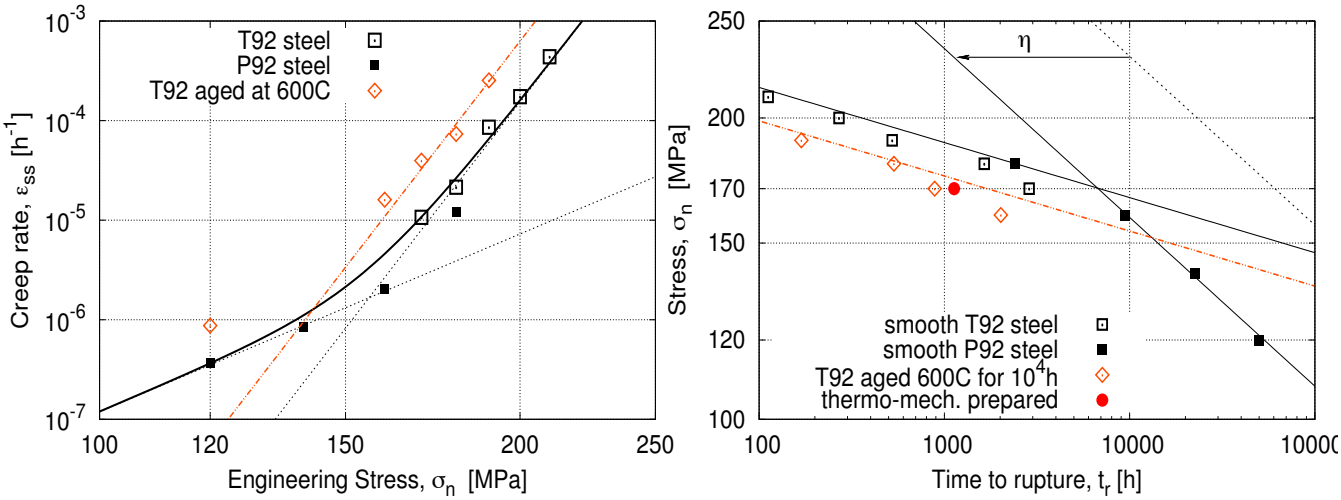

a) **b)**

Figure V.14 : Secondary creep rate (a) and time to rupture (b) as a function of engineering stress for creep tests conducted at 600°C on smooth specimens (as-received, thermally aged (600°C, 10^4h) and thermo-mechanically prepared specimen)

A clear change in slope is observed from the $\dot{\varepsilon}_{ss}$ versus t_r, figure V.14a. This slope change is often associated to a transition of dominant deformation mechanism from power-law creep or dislocation creep (high stresses) to viscous creep (low stresses), but no clear evidence of viscous creep in the Grade 92 steel was reported.

For the power-law creep several mechanisms were proposed such as interaction between dislocation and precipitates (Cadek et al., 1997). (Sklenička et al., 2003) suggested that creep behavior in the power-law creep is controlled by the rearrangement of dislocations and subgrain coarsening.

In viscous creep, deformation is controlled by diffusion processes, such as migration of vacancies rather than dislocation glide. Two main mechanisms are proposed for the viscous creep Nabarro-Herring (diffusion through the bulk of the grain) and/or Coble (diffusion is mainly along grain boundaries).

Theoretically a Norton law exponent of about 4-5 is characteristic to dislocation creep and a Norton law exponent of 1 is characteristic to diffusional creep. These theoretical interpretations of the Norton law exponents were established for pure metals.

Norton law exponents of 18 and 6 found for the creep results of this study are relatively high compared to theoretical values but corresponds to published data (Ennis et al., 1997), (Sklenička et al., 2003) on the creep behavior of the P92 steel at 600°C. The exponents of 18 ad 6 gives no indication about the predominant deformation mechanisms for high stresses and low stresses respectively.

(Kloc and Sklenička, 1997) evidenced the viscous creep in a P91 steel using helicoid springs which allowed an estimation of $\dot{\varepsilon}_{ss}$ for stress levels below 20MPa. These creep tests could be modeled by a Norton law with an exponent $n = 1$, indicating diffusional creep. Probably the three creep tests conducted under $\sigma < 160$MPa do not allow a good estimation of the Norton law exponent for the low stresses regim. There are no available published data on the creep flow at 600°C of the Grade 92 steel for levels of stress bellow 90MPa.

Given the slope change in figure V.14a any extrapolation from the high stresses regim to low stresses may lead to underestimation of the $\dot{\varepsilon}_{ss}$. It has been shown that extrapolation of short-term creep data (e.g. for lifetime lower than 10^4h hours) can lead to an overestimation

of the creep strength after long term creep (Dimmler et al., 2008), (Bendick and Gabrel, 2005), (Abe, 2004). Thus, the region of stresses where $\dot{\varepsilon}_{ss}$ shows a significant slope change is of great interest.

A Norton-type law with $A = 21 \times 10^{-10}\text{h}^{-1}$ and $n = 18$ well represents the creep results ($\dot{\varepsilon}_{ss}$, t_r) of thermally aged T92 steel. The value of the constant A identified for the thermally aged T92 steel is four times higher than that of the as-received steel, this express well the factor found between the $\dot{\varepsilon}_{ss}$ of the thermally aged T92 steel compared to that of the as-received T92 steel both tested under same levels of stress (sse table V.1 compared with table V.3).

Equation V.3 allows the estimation of the t_r of creep tests once the values of A and n of the Norton flow rule were identified.

$$\sigma = \sigma_0 \left(nAt_r\right)^{-1/n} \tag{V.3}$$

The equation V.3 is obtained by considering the volume conservation of the specimen during test and by integrating the Norton flow rule. A complete demonstration of the equation is given in (Vivier, 2009), (Hoff, 1953). However, equation V.3 could be simply deducted from both Monkman-Grant relationship assuming that $C = \frac{1}{n}$ and $m = 1$ as follows.

$$t_r \times \dot{\varepsilon}_{ss} = \frac{1}{n} \tag{V.4}$$

From the Monkman-Grant relationhip (equation V.1 or V.4) $\dot{\varepsilon}_{ss}$ can be expressed as:

$$\dot{\varepsilon}_{ss} = \frac{1}{nt_r} \tag{V.5}$$

Replacing $\dot{\varepsilon}_{ss}$ given by equation V.5 in the Norton flow rule, a relationship between t_r and σ is obtained as follows:

$$\frac{1}{nt_r} = A\left(\frac{\sigma}{\sigma_0}\right)^n \tag{V.6}$$

this can be written as

$$nt_r = \frac{1}{A}\left(\frac{\sigma_0}{\sigma}\right)^n \Rightarrow t_r^{\frac{1}{n}} = \left(\frac{1}{An}\right)^{\frac{1}{n}} \frac{\sigma_0}{\sigma} \Rightarrow \sigma = \sigma_0 \left(nAt_r\right)^{-1/n} \tag{V.7}$$

A good estimation of the t_r of short-term creep tests is obtained using equation V.3 with A and n identified for the high stresses regime. Equation V.3 with A and n identified for the low stresses region ovestimates the t_r of long-term creep tests, dotted line in figure V.14b. To get a good representation of the experimental results, the values estimated with equation V.3 had to be adjusted by a factor $\eta = 9$ as follows:

$$\sigma = \sigma_0 \left(n_{Ls} A_{Ls} t_r \eta\right)^{-1/n_{Ls}} \tag{V.8}$$

Time to fracture (t_r) of long term crept specimens, estimated from the $\dot{\varepsilon}_{ss}$ of the specimens is nine times higher than the experimental results. This indicates the existence of some other mechanism leading to fracture. Creep damage development (cavities) could explain fracture of specimens well before the structure instability (i.e. necking of specimen). Nucleation and growth of cavities decrease the lifetime of specimen by reducing the effective section of the specimen. η could express the influence of creep damage on lifetime of the specimens.

Equation V.3 gives also a rather good estimation of the t_r of thermally aged specimens, which were only tested for short-term creep.

V.4 Notched creep specimens

V.4.1 Creep curves

The geometry of the four notched creep specimens was presented in chapter III, figure III.3. The engineering stress (σ_n) on the notched specimens corresponds to the engineering stress in the notched area. The minimum cross section of the notched specimens was considered for the calculation of applied σ_n (for more details see chapter III).

The results of creep tests conducted at 600°C on notched specimens are presented in table V.4. The creep curves (notch opening vs time) corresponding to these tests are represented in figures V.17 and V.16.

Table V.4 : Results of creep tests conducted at 600°C on T92 steel notched specimen

Temp.	Geometry of specimen	σ_n [MPa]	t_r [h]	Z [%]	Observations
600°C	NTDC0.6	210	4,074	9	
		170	(6,193)	-	interrupted before rupture
600°C	NTDC0.6M	310	114	56	
		240	2,202	16	
		230	4,844	19	
600°C	NTDC1.2	280	90	69	
		270	138	72	
		230	842	57	notch accidentally broken during removal
		210	2,957	24	
		170	(14,137)	-	interrupted before rupture
600°C	NTDV	350	43	59	
		330	135	49	
		320	192	47	
		310	598	27	
		260	1,568	22	
		230	2,451	6	both notches broken during testing
		210	4,063	8	
		190	8,199	3	

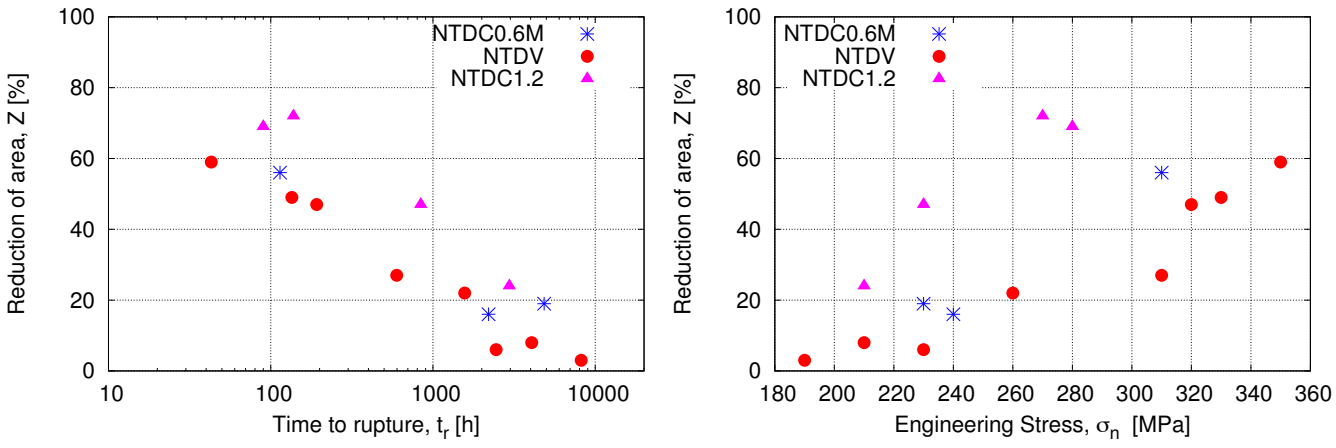

a) b)

Figure V.15 : Reduction of area (Z) as a function of time to rupture (a) and engineering stress (b) for notched specimens creep tested at 600°C

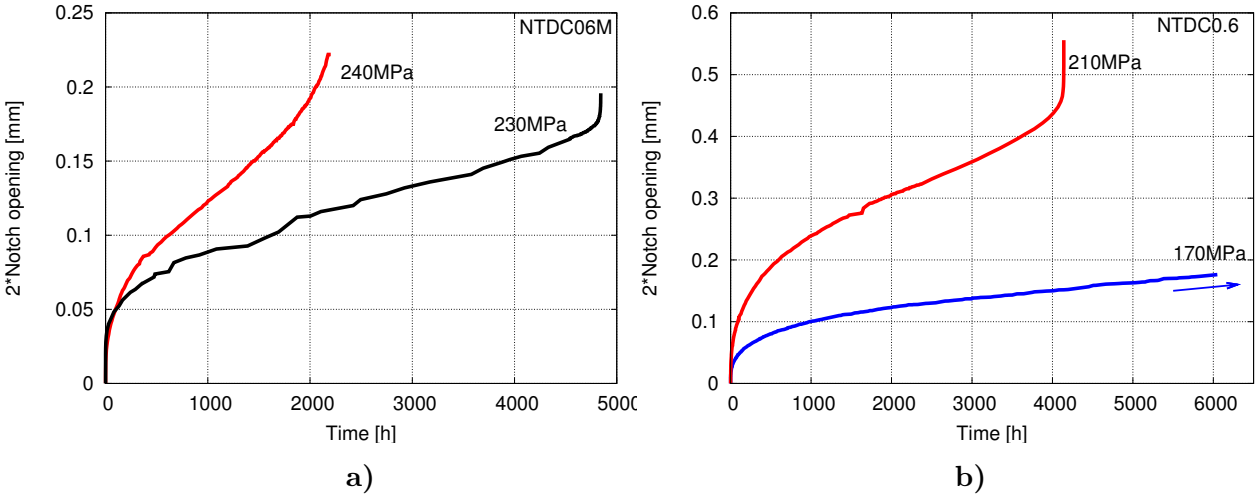

Figure V.16 : Creep curves of tests conducted at 600°C on NTDC0.6M (a) and NTDC0.6 (b) notched specimens. Arrow indicates that the creep tests was interrupted before fracture

Occasionally, both notches broken during creep testing of some notched specimens, they are indicated in table V.4.

Notched specimens creep tested for times higher than 2,000h showed very low values of reduction of area (Z) while the notched specimens creep tested for times lower than 200h showed relatively high values of Z, see table V.4 and figure V.15.

The fracture of some notched specimens probably occurred suddenly and the last part of the creep curves could not be recorded (see creep curves of the NTDC1.2 and NTDV specimens under 210MPa and 260MPa respectively, figure V.17c, d).

For a given engineering stress (σ_n) the time to rupture (t_r) is much higher on a notched specimen compared to a smooth one. From the results published by (Gaffard, 2004) it was estimated that the fracture time, t_r, for notched specimen is about three times higher than for a smooth one for the Grade 91 steel. The first creep tests were launched at 170 MPa, in order to get a t_r of about 10^4h on notched specimens, giving that for these stress levels a t_r of about 3,000h was obtained on smooth specimens.

Because the notched specimens tested at 170 MPa showed a slow evolution of strain with time, the next creep tests were launched at higher stresses: 230MPa, 210MPa at 600°C in order to reduce the fracture time and to ensure that a significant number of notched creep specimens could be examined after fracture during the present study.

For the same engineering stress, the creep rate of NTDC1.2 specimen was expected to be higher than that of the NTDC0.6 specimen because of a higher notch radius in the NTDC1.2 specimen. Creep tests on NTDC1.2 and NTDC0.6 specimens under 170MPa and 210MPa showed the contrary. A simple analysis of deformation of the NTDC1.2 and NTDC0.6 specimens showed that the notch of the NTDC0.6 specimen was not deep enough. The geometry of the NTDC0.6 specimen was thus changed into NTD0.6M for the next tests, see figure III.3b compared to figure III.3c.

Because of a limited number of available testing machines, the creep tests under σ_n=170MPa conducted on NTDC1.2 and NTDC0.6 notched specimens were interrupted after 14,137h and 6,193h of testing and replaced by other tests. In fact fracture of the NTDC0.6 would not have occured during this project but maybe years after its completion. Note that the NTDC1.2 specimen under 170MPa was interrupted in beginning of the tertiary creep stage (see figure V.17e) and both of notches are not broken.

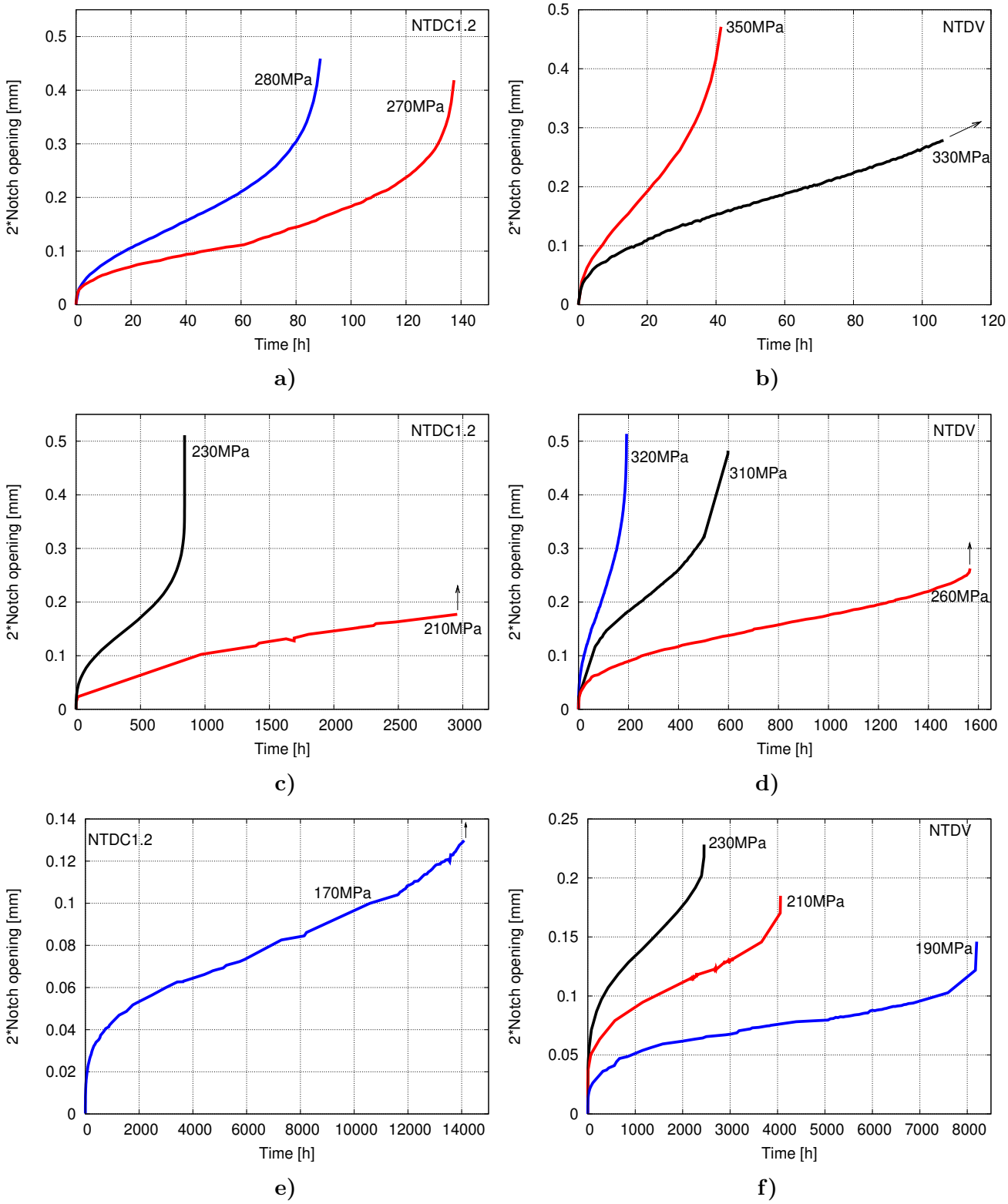

Figure V.17 : Creep curves of tests conducted at 600°C on NTDC1.2 notched specimens (a, c, e) and NTDV notched specimens (b, d, f). Arrows indicate that the creep tests were interrupted before fracture or the record of last part of test is missing

V.4.2 Analysis of creep curves

The creep curves of the notched specimens gives a notch opening, which cannot be simply linked to a strain rate. In the notched area the stress state is complex and the equivalent von Mises stress (σ_{VM}) varies within the section of the notched area.

The interest of notched specimens consists in reducing the σ_{VM} stress and increasing of the principal stress (σ_{22}) and thus promoting creep damage development. The purpose of the creep tests on notched specimens was to study the influence of stress triaxiality on creep damage development.

In figures V.18, V.19, V.20 and V.21 are represented the distribution σ_{VM} and σ_{22} in the notched area of specimens for some levels of σ_n used in this study as a fonction of the notch opening. The stress distributions in figures V.18, V.19, V.20 and V.21 were estimated by finite element (FE) simulations as explained in chapter IV.

In order to evaluate the evolution of the σ_{VM} and σ_{22} stresses during creep testing, the levels of σ_{VM} and σ_{22} were estimated for various levels of notch opening related with the experimental creep curves in figures V.17 and V.16. Note that the notch opening of both notches was experimentally measured in figures V.17 and V.16 while the stress distribution in figures V.18, V.19, V.20 and V.21 was estimated for one notch.

Figure V.19 shows the distribution of the σ_{VM} and σ_{22} stresses in the NTDC 1.2 notched specimens under some levels of σ_n used in this study. For same engineering stress (σ_n) e.g. 210MPa and 230MPa the σ_{VM} stress is higher in the center of the NTDC1.2 specimens compared to NTDV specimens, which explains the higher creep rate of the NTDC1.2 specimen compared to NTDV specimens, see creep curves in figure V.17.

A redistribution of the σ_{22} stress is observed during the creep test of notched specimens. This is more obviously evidenced in the NTDC1.2 specimens. In the first part of the creep test, roughly for notch opening (δ) lower than 0.05mm, the σ_{22} stress is higher close to the notch root, in the second part of the test the σ_{22} stress is higher in the center of the notched area. Creep damage is expected to develop preferentially in the center of the NTDC1.2 specimen because of the highest levels of σ_{22} stress after stress redistribution.

The redistribution of the σ_{22} stress also occurs in the other notched specimens, but on a smaller area e.g. 0.2 mm from the notch root in the NTDV and 0.4mm from the notch root in the NTDC0.6M and NTDC0.6 specimens. For example in the NTDV specimen in the first part of the creep test, the σ_{22} stress is maximum close to the notch root and in the second part of the test the σ_{22} stress is maximum at a distance of about 0.1 mm from the notch root (see figure V.18). Creep damage is expected to develop preferentially at a distance of about 0.1 mm from the notch root in NTDV specimens.

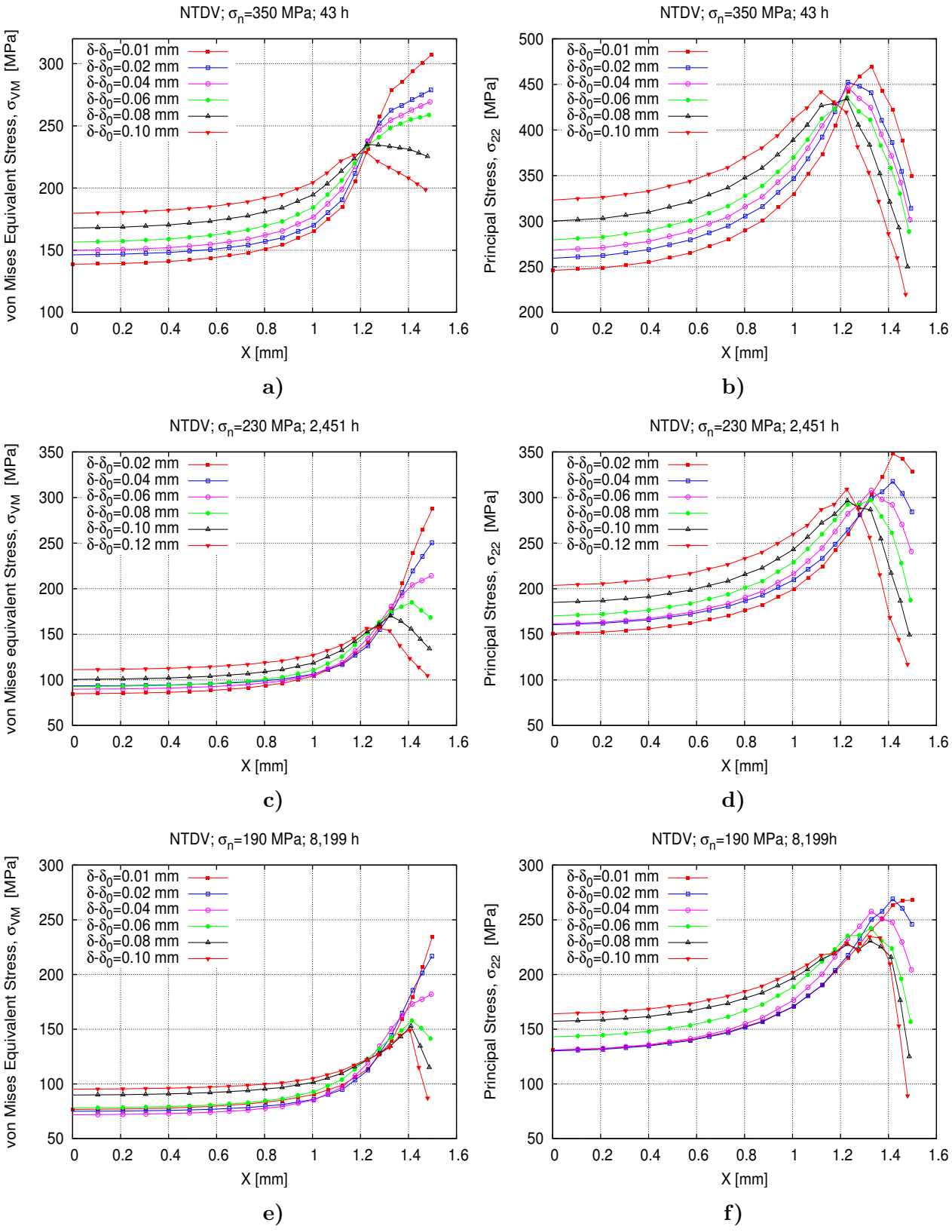

Figure V.18 : Distribution of von Mises equivalent stress (σ_{VM}) and principal stress (σ_{22}) in the NTDV notched specimens during creep testing as a function of the notch opening (δ). X=distance to specimen axis; a), b) σ_n = 350MPa, t_r = 43h; c), d) σ_n = 230MPa, $t_r = 2,451$h; e), f) σ_n = 190MPa, $t_r = 8,199$h

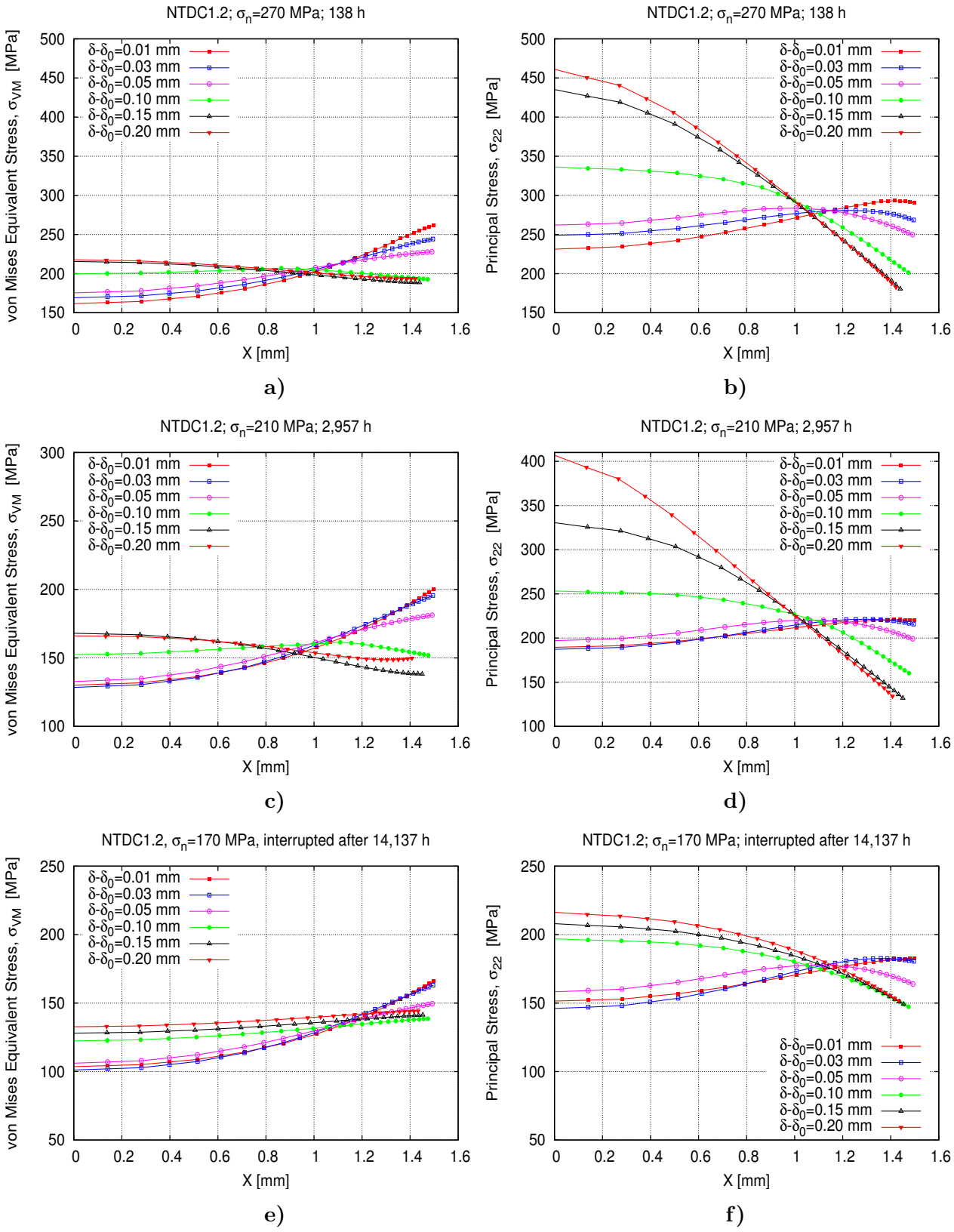

Figure V.19 : Distribution of von Mises equivalent stress (σ_{VM}) and principal stress (σ_{22}) in the NTDC1.2 notched specimens during creep testing as function of the notch opening (δ). X=distance to specimen axis; a), b) σ_n = 270MPa, t_r = 138h; c), d) σ_n = 210MPa, $t_r = 2,957$h; e), f) σ_n = 170MPa, interrupted after 14,137h

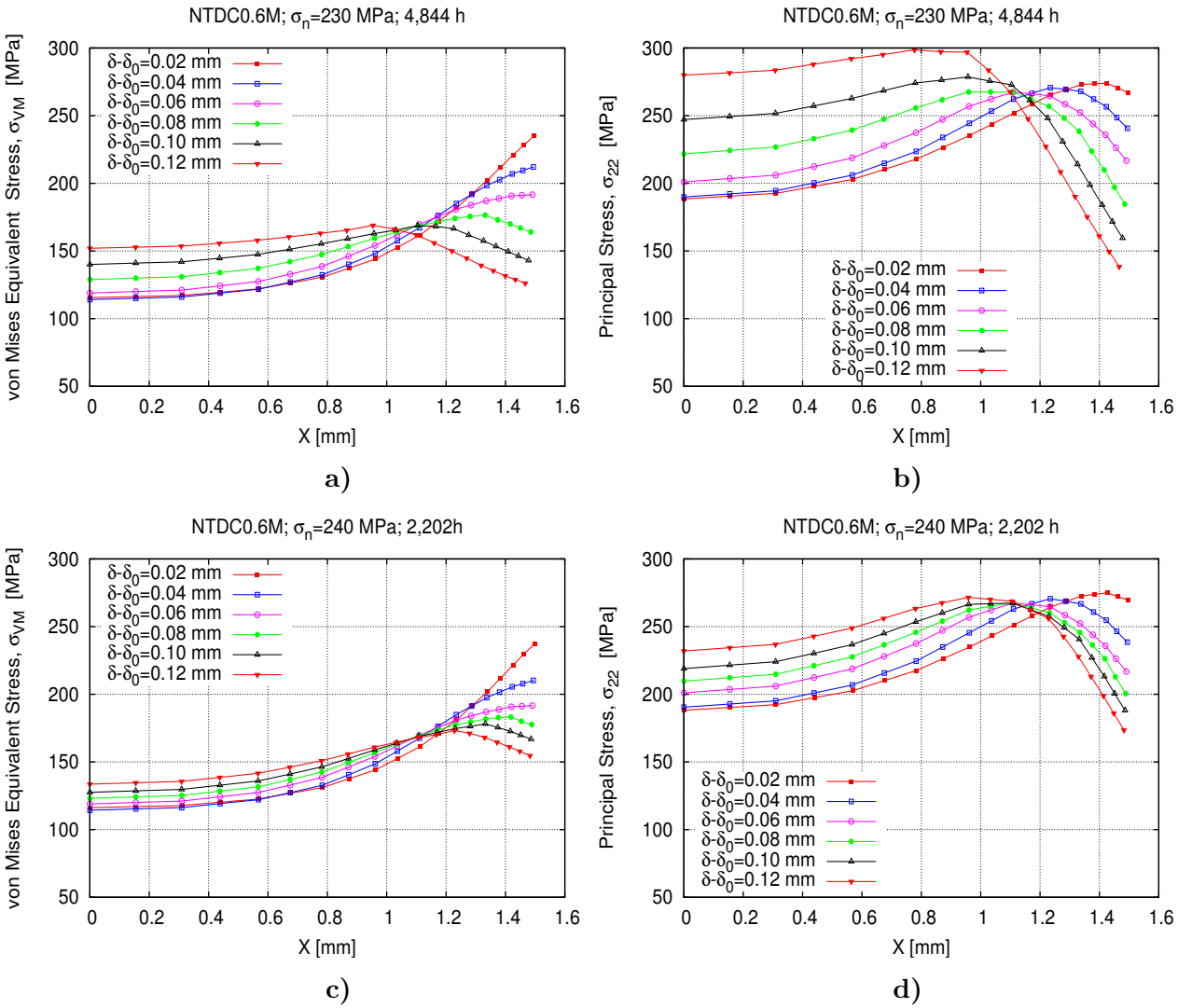

Figure V.20 : Distribution of von Mises equivalent stress (σ_{VM}) and principal stress (σ_{22}) in the NTDC0.6M notched specimens during creep testing as a function of the notch opening (δ). X=distance to specimen axis; a), b) $\sigma_n = 230$MPa, $t_r = 4,844$h; c), d) $\sigma_n = 240$MPa, $t_r = 2,202$h

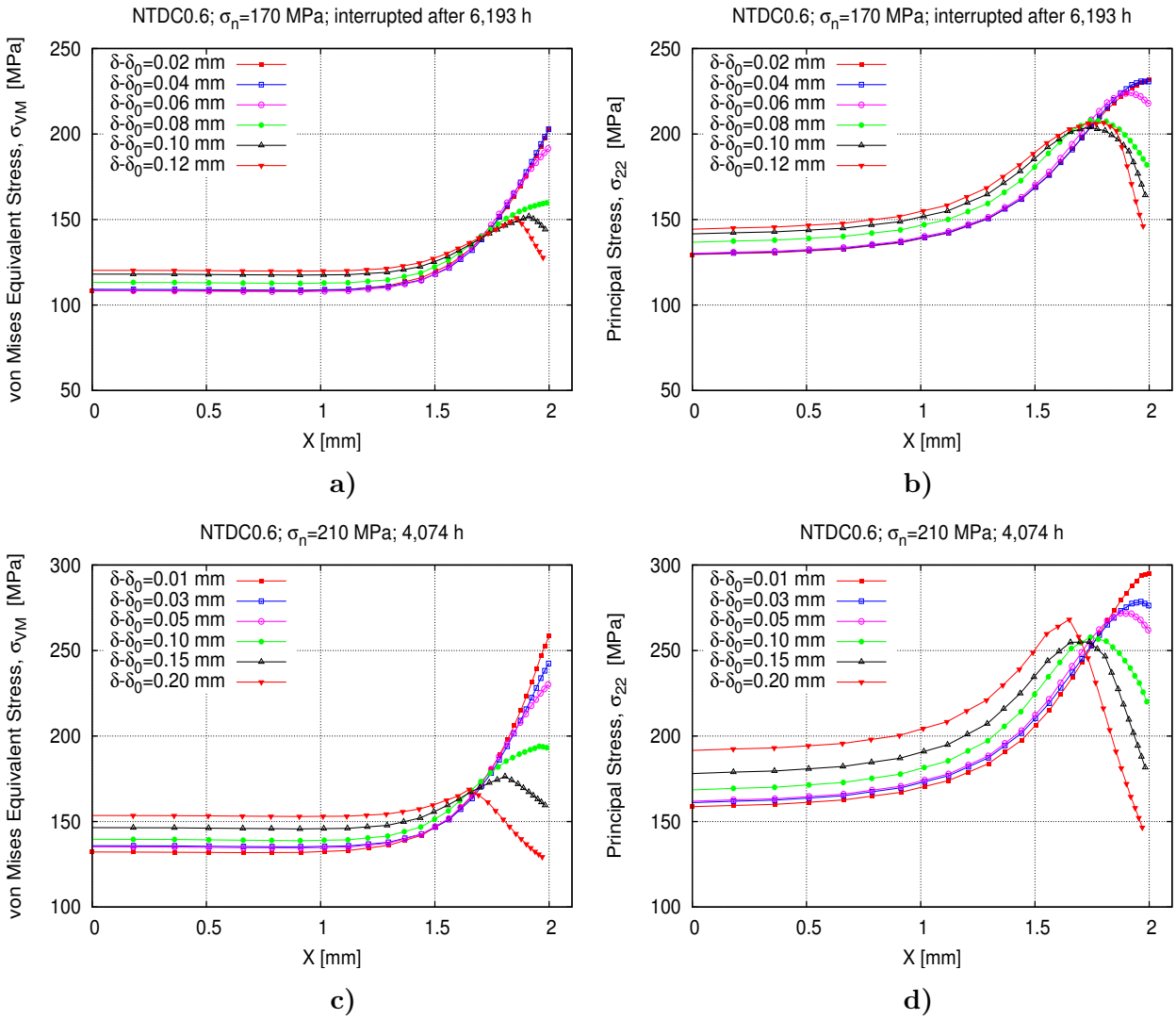

Figure V.21 : Distribution of von Mises equivalent stress (σ_{VM}) and principal stress (σ_{22}) in the NTDC0.6 notched specimens during creep testing as a function of the notch opening (δ). X=distance to specimen axis. a), b) σ_n = 170MPa, interrupted after 6,193h; c), d) σ_n = 210MPa, $t_r = 4,074$h

Figure V.22 shows time to rupture (t_r) of smooth and notched specimens versus engineering stress (σ_n) and von Mises stress (σ_{VM}). In figure V.23 the maximum value of the σ_{VM} after stress redistribution was considered. More precisely, the maximum value of the σ_{VM} corresponding to $\delta = 0.08$mm for both NTDV and NTDC0.6M specimens (figures V.20 and V.18) and $\delta = 0.10$mm for the NTDC1.2 specimen (figure V.19). In smooth specimens the σ_{VM} is almost the same as the σ_n before necking of the specimen.

For a given σ_n, a higher time to rupture (t_r) is observed on the notched specimens compared to smooth ones (figure V.22). For same levels of σ_{VM} the t_r of notched specimens is similar to that of the smooth ones (figure V.23).

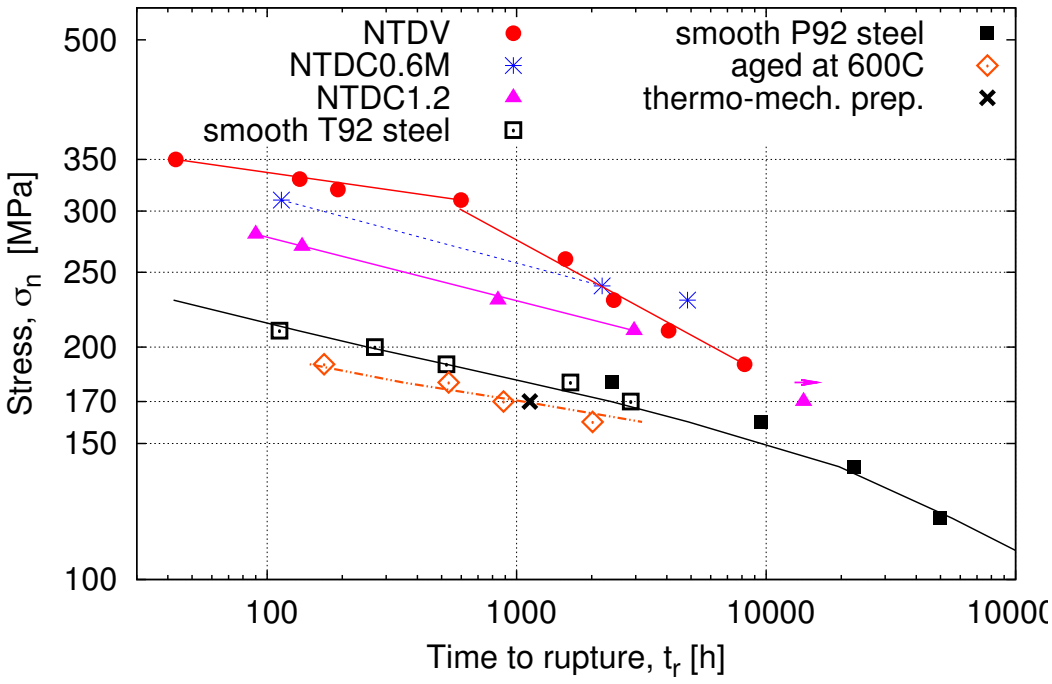

Figure V.22 : Creep rupture data of all tests conducted at 600°C as a function of engineering stress, σ_n

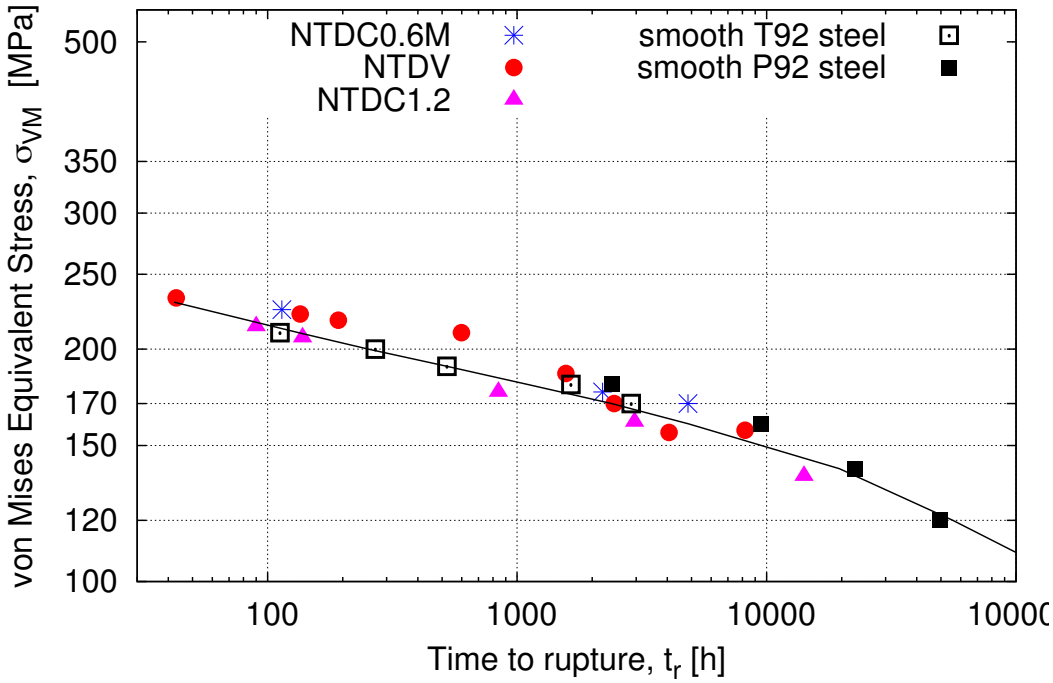

Figure V.23 : Creep rupture data of the smooth and notched specimens as a function von Mises equivalent stress, σ_{VM}

V.5 Summary

In table V.5 are summarized the results of all creep tests conducted at 600°C on various types of specimens. These results are plotted in figure V.22. For visibility reasons the results of creep tests conducted on NTDC0.6 notched specimens are not represented in figure V.22. The creep tests conducted in this study required a significant experimental capacity, in table V.5 are indicated the accumulated time testing machine represents the testing time of all the indicated specimen type.

Table V.5 : Summary of all creep tests conducted at 600°C

Creep specimen	Levels of stress σ, σ_n [MPa]	Nb. of tests	Accumulated time for all specimens [h]	Observations
T92 steel, smooth	170-210	5	5,414	
P92 steel, smooth	120-180	4	84,164	data provided by SZMF
T92 steel thermally aged	160-190	4	3,605	
(600°C, 10^4h)	120	1	3600	in progress
thermo-mech. prepared at 550°C	170	1	1,129	no creep curve available
NTDC0.6	170-210	2	10,267	one test interrupted before rupture
NTDC0.6M	230-240	3	7,160	
NTDC1.2	170-230	5	18,164	one test interrupted before rupture
NTDV	190-230	8	17,249	
TOTAL	-	24	67,992	lifetime of the P92 crept specimens was not added

Creep tests on smooth specimens (T92 steel and P92 steel altogether) showed a slope change in the secondary creep rate ($\dot{\varepsilon}_{ss}$) in the stress range 140-160MPa. This was also reported by others studies (Ennis et al., 1997), (Sklenička et al., 2003), (Dimmler et al., 2008). It was suggested that the slope change of $\dot{\varepsilon}_{ss}$ is due to a change in the dominant creep deformation mechanism, a transition from power law creep to viscous creep (Kloc and Sklenička, 2004). The mechanisms of the viscous creep in the precipitation strengthened steels such as Grade 92 steel are not fully understood and no clear evidence about the viscous creep is reported.

A different creep behavior is observed for short-term ($t_r < 10^4$h) creep tests compared with long-term ($t_r > 10^4$h) creep tests. The specimens tested for short-term creep show higher ductility (high elongation at rupture and high reduction of area) compared to specimens tested for long-term creep. The tertiary creep stage of short-term crept specimens is onset for values of elongation higher than that of the long-term crept specimens.

The creep results obtained with as-received T92 steel and creep data provided by SZMF for P92 steel were analyzed using Monkman-Grant relationship and Norton power law equation. A good representation of the creep results is obtained Monkman-Grant relationship (see figure V.13). The exponents of the Norton flow rule were identified to be 18 for high stress ($\sigma > 160$MPa) and 6 for low stress ($\sigma < 160$MPa). This is in agreement with published data on the creep behavior of the Grade 92 steel at 600°C (Ennis et al., 1997), (Dimmler et al., 2008).

A simple equation (equation V.3) derived from both Monkman-Grant relationship and Norton power-law gives a rather good estimation of lifetime of the short-term creep specimens. However this equation overestimates the lifetime of long-term crept specimens.

After a thermal aging at 600°C for 10^4h the T92 steel show a higher creep rate and a lower t_r (divided by three) compared to the as received T92 steel for the same testing conditions. The creep strength loss of the aged T92 steel is probably due to a significant precipitation of Laves phases during aging heat treatment (as suggested by both literature data in chapter I

and the microstructural characterization of the aged T92 steel at 600°C in chapter III).

For a given engineering stress (σ_n) the t_r of a notched specimen is higher compared to that of a smooth one. For the same level of σ_{VM} similar values of t_r is obtained on smooth and notched specimens (see figure V.23). Two slopes were observed on the stress versus lifetime curve of NTDV notched specimens.

The stress state in the notched specimens during creep testing was evaluated using FE simulations as explained in chapter IV. From the distribution of the principal stress (σ_{22}) in the notched area, creep damage is expected to develop preferentially in the center of the NTDC1.2 specimen and close to the notch root in the NTDV and NTDC0.6M specimens.

The creep specimen thermo-mechanically prepared at 550°C showed a value of t_r three times lower compared to that of the as-received T92 steel for the same level of σ_n. No creep curve was available for the creep test conducted on the thermo-mechanically prepared specimen so that no comments can be made on the creep flow.

The purpose of creep tests conducted on specimens with various microstructures before testing was to quantify the effect of the matrix substructure and large Laves phases on creep strength. The creep tests conducted under a load of 170MPa, revealed the following results:

- t_r=2,867h on a standard creep test with an as-received T92 steel microstructure before testing.
- t_r= 886h (i.e. more than 3.2 times lower) on a thermally aged (600°C for 10^4h) specimen. This is related to a higher secondary creep rate ($\dot{\varepsilon}_{ss}$) after aging. The aged T92 steel probably shows lower solid solution strengthening compared to the as-received T92 steel due to the precipitation of Laves phases during aging, which reduces the amount of W and Mo atoms in solid solution.
- t_r= 1,129h (i.e. ∼2.5 times lower than for as-received steel) on specimen thermo-mechanically prepared at 550°C.

Résumé

Une synthèse des essais de fluage réalisés à 600°C sur les différents type d'éprouvettes est représentée dans le tableau V.5. Les résultats de ces essais (contrainte, temps à rupture) sont représentés dans la figure V.22. Pour des raisons de visibilité les résultats des essais sur les éprouvettes entaillées NTDC0.6 ne sont pas représentés dans la figure V.22. Les essais de fluage réalisés dans le cadre de cette thèse ont demandé une forte mobilisation de ressources expérimentales. Dans le tableau V.5 le temps machine cumulé (Accumulated time for all specimens dans le tableau V.5) signifie la somme des temps à rupture sur chaque type d'éprouvette indiquée.

Les résultats des essais de fluage sur éprouvettes lisses (en acier P92 et en acier T92) montrent un changement de pente dans la vitesse de fluage secondaire pour des niveaux de contraintes de 140-160MPa. Ceci a aussi été signalé dans d'autres études, comme (Ennis et al., 1997), (Sklenička et al., 2003), (Dimmler et al., 2008). Il a été suggéré que ce changement de pente est lié à un changement dans le mécanisme de déformation prédominant, une transition du fluage dislocations vers le fluage diffusionnel. Les mécanismes du fluage diffusionnel ne sont pas complètement compris dans les aciers à durcissement par précipitation comme l'acier Grade 92. Il n'y a pas de données publiées concernant le fluage diffusionnel dans l'acier Grade 92.

Les éprouvettes de fluage testées pendant des temps courts ($t_r < 10^4 h$) montrent une ductilité (réduction de l'aire, allongement à la rupture) élevée comparée à celle des éprouvettes testées pendant des temps longs ($t_r > 10^4 h$). Sur les éprouvettes court terme le début du fluage tertiaire est observé pour de valeurs de l'allongement plus élevées que sur les éprouvettes testées pendant des temps longs.

Les résultats des essais de fluage réalisés sur les éprouvettes lisses en acier T92 et les données fournies pour les éprouvettes long terme en acier P92 ont été analysés en utilisant la relation de Monkman-Grant et la loi de Norton. Une bonne représentation des résultats est obtenue avec la relation de Monkman-Grant (figure V.13). L'ajustement de la loi de Norton a révélé un exposant 18 pour les contraintes élevée ($\sigma > 160 MPa$) et un exposant 6 pour les faibles contraintes ($\sigma < 160 MPa$). Les valeurs de l'exposant de la loi de Norton sont en bon accord avec les valeurs publiées dans la littérature pour l'acier Grade 92 (Ennis et al., 1997), (Dimmler et al., 2008).

Une équation simple obtenue à partir de la relation de Monkman-Grant et de la loi de Norton permet une assez bonne estimation de la durée de vie des éprouvettes testées pendant des temps courts de fluage. Cette équation surestime cependant la durée de vie des éprouvettes long terme.

Après un vieillissement thermique statique à 600°C pendant $10^4 h$, la vitesse de fluage de l'acier T92 augmente et sa durée de vie diminue d'environ un facteur trois comparé à l'acier T92 à l'état de réception testé dans les mêmes conditions. Cette perte de résistance en fluage est probablement liée à la précipitation des phases de Laves pendant le traitement de vieillissement thermique (suggéré par les données bibliographies regroupées dans le chapitre I et la caractérisation microstructurale de l'acier T92 après vieillissement thermique à 600°C, donnée dans le chapitre III).

Pour une même valeur de la contrainte nominale (σ_n), le temps à rupture (t_r) est beaucoup plus élevé sur une éprouvette entaillée que une éprouvette lisse. Pour la même valeur de la contrainte équivalente de von Mises (σ_{VM}), les temps à rupture sur les deux types d'éprouvettes sont comparables (figure V.23). La courbe temps à rupture en fonction de la contrainte des éprouvettes entaillées NTDV présente deux pentes.

L'état des contraintes dans les éprouvettes entaillées pendant le fluage a été estimé par des simulations par éléments finis, comme été présenté dans le chapitre IV. La distribution de la contrainte principale (σ_{22}) dans la zone entaillée suggère un développement préférentiel de l'endommagement par fluage près du rayon de l'entaille dans les éprouvettes NTDV et NTDC0.6M et dans le centre de l'éprouvette NTDC1.2.

L'éprouvette pré-fatiguée à 550°C et testée en fluage à 600°C montre une durée de vie (t_r) trois fois plus faible qu'une éprouvette en acier T92 à l'état de réception testé en fluage pour le même niveau de contrainte nominale. La courbe de fluage pour l'éprouvette pré-fatiguée n'est pas disponible, par conséquent la déformation en fluage de cette éprouvette n'a pas pu être étudié.

L'intérêt des essais de fluage sur des éprouvettes avec des microstructures différentes avant le fluage a été d'étudier et de quantifier l'influence des phases de Laves et de l'état de la matrice sur le comportement en fluage. Les essais de fluage réalisés en utilisant une contrainte de 170MPa ont révélé les résultats suivants:

- *t_r=2867h sur une éprouvette lisse en acier T92 à l'état de réception avant fluage;*
- *t_r= 886h (environ 3,2 fois plus faible) sur une éprouvette lisse en acier T92 vieilli thermiquement (600°C for $10^4 h$) avant fluage. Ceci est lié à une vitesse de fluage secondaire plus élevée sur l'acier vieilli. Le durcissement par solution solide de l'acier*

vieilli est probablement diminué par la précipitation des phases de Laves pendant le traitement thermique de vieillissement;

- $t_r = 1129h$ *(environ 2,5 fois plus faible que l'acier T92) sur une éprouvette pré-fatiguée à 550°C.*

Chapter -VI-

Results of creep tests conducted at 650°C

Contents

Introduction

This chapter aims to present the results of creep tests conducted at 650°C. Testing temperature was increased to enhance the creep deformation mechanisms and to study the effect of the microstructural evolution on the creep strength loss at higher temperature. Because of a higher temperature the kinetics of Laves phase precipitation might be diferent from these at 600°C.

The same approach and same kinds of creep specimens were used as for creep tests conducted at 600°C. The purpose of each kind of creep specimen is recalled briefly in the following.

Creep tests on smooth specimens are reference tests. The objectives of these creep tests are: (i) to compare the creep behaviour of the T92 steel studied here with the available published creep data at 650°C for Grade 92 steel, see for instance references (V & M, 2000), (Bendick and Gabrel, 2005), (Vaillant et al., 2008), (Petry and Lindet, 2009), (Ennis et al., 1997); (ii) to get reference samples of the as-received T92 steel creep tested for microstructural investigations which could be further compared with thermally aged or thermo-mechanically prepared T92 steel after creep testing in similar conditions.

The purpose of the thermally aged creep specimens is to study the influence of large Laves phases on the creep strength loss and the purpose of the thermo-mechanically prepared prepared specimens was to study the effect of the matrix substructure state on the creep strength loss.

Two different thermo-mechanically prepared specimens were creep tested at 650°C both under a load of 95 MPa. These two specimens were thermo-mechanically prepared in same conditions of strain (i.e. same shape and number of creep-fatigue cycles) but at two different temperatures (i.e. 550°C and 600°C). More details about the sample preparation of these two specimens can be found in *Appendix A* of the present study.

The specimen thermo-mechanically prepared at 550°C creep tested at 650°C, 95 MPa revealed a lifetime of 4,659h while the specimen thermo-mechanically prepared at 600°C creep tested in same conditions revealed a lifetime of 3,210h. Details about these creep results can be also found in *Appendix A*.

The creep results (σ and t_r) on the two thermo-mechanically prepared specimens are not represented in figures of this chapter, as done for creep tests at 600°C, because they are similar to these of the as-received T92 steel (σ_n = 95MPa, $t_r = 4,480$) and the NTDV notched specimen (σ_n = 95MPa, interrupted after 4,480h). This would be illegible on the graphs of this chapter.

Creep tests on notched specimens were also conducted at 650°C. The purpose of notched specimens is to study the effect of stress triaxiality on the creep damage development.

Four P92 steel specimens that have been creep tested for times up to 33,300h at 650°C were provided by SZMF, Germany. These crept specimens came from the same pipe as the long term crept specimens tested at 600°C. It is to be noticed that the long term creep specimens are located well within the stress vs. creep lifetime curve established by ECCC for the Grade 92 steel. So, it is believed that these crept specimens are representative for the creep behaviour at 650°C of the Grade 92 steels.

General remark:

In all the tables of this chapter, σ_n is the engineering stress in MPa; t_r is the time to rupture in hours; Z and A are the reduction of area and elongation at rupture of crept specimens after testing. $\dot{\varepsilon}_{ss}$ is the secondary creep rate, which was estimated by fitting equation IV.3 to the half of the experimental creep curves as explained in chapter IV. The

adjusted values of Q, E_0 and τ are also given.

Introduction

Ce chapitre présente les résultats des essais de fluage réalisés à 650°C sur éprouvettes lisses, éprouvettes entaillées et éprouvettes pré-vieilles. Les essais de fluage à 650°C ont été réalisé afin d'accélérer les mécanismes de déformation en fluage et d'étudier l'impact de l'évolution métallurgique sur le comportement en fluage à une température plus élevée. A 650°C, la cinétique de précipitation des phases de Laves est probablement différent de celle à 600°C.

La même approche et le même type d'éprouvette ont été utilisé, que pour les essais de fluage à 600°C. Les objectifs des essais de fluage sont rappelés brièvement.

Les essais de fluage sur éprouvettes lisses sont des essais de référence. Les objectifs de ces essais sont: (i) de comparer la résistance en fluage de l'acier T92 étudié avec des données bibliographiques et (ii) d'avoir des échantillons de référence du matériau à l'état de réception testés en fluage dans des conditions standards, pour être ensuite comparés aux éprouvettes pré-vieillies et éprouvettes pré-fatiguées testées en fluage dans de conditions similaires.

L'objectif des éprouvettes pré-vieilles est d'étudier l'influence des phases de Laves sur le comportement en fluage et l'intérêt des éprouvettes pré-fatiguées est d'étudier l'influence de l'état de la matrice sur le comportement en fluage.

Deux éprouvettes pré-fatiguées différentes ont été testées en fluage à 650°C, σ_n =95MPa. Ces deux éprouvettes ont été préparées par des essais de fatigue-fluage dans les mêmes conditions de déformation mais à deux températures différentes (i.e. 550°C et 600°C). La préparation de ces éprouvettes est présentée dans l'annexe A.

Les durées de vie des éprouvettes pré-fatiguées testées en fluage à 650°C, σ_n =95MPa ont été de 4,659h (pré-fatiguée à 550°C) et de 3,219h (pré-fatiguée à 600°C). Les détails sur ces deux essais de fluage peuvent être trouvés dans l'annexe A.

Les résultats des essais de fluage sur les éprouvettes pré-fatiguées (σ et t_r) ne sont pas représentés dans les figures de ce chapitre comme c'était le cas pour les résultats des essais à 600°C. Les résultats de ces deux essais sont similaires avec ceux obtenus sur l'acier T92 (σ_n =95MPa, t_r =4,480h) et sur une éprouvette entaillée NTDV (i.e. σ_n =95MPa, interrompu après 4,656h). Par conséquent, la représentation de la contrainte (σ) et de la durée de vie (t_r) des éprouvettes pré-fatiguées aurait rendu illisible les graphiques représentant l'ensemble des résultats de fluage à 650°C.

L'intérêt des essais de fluage sur éprouvettes entaillées est d'étudier l'effet du taux de triaxialité de contraintes sur le développement de l'endommage par fluage.

Quatre éprouvettes en acier P92 déjà testées en fluage à 650°C pour des temps allant jusqu'à 33,308h ont été fournies par SZMF, Germany. Ces éprouvettes proviennent du même tube que les éprouvettes testées pendant des temps prolongés à 600°C. La contrainte et le temps à rupture de ces éprouvettes sont localisés sur la courbe maîtresse établie par l'ECCC pour l'acier Grade 92. Donc, ces éprouvettes peuvent être considérées comme représentatives pour le comportement en fluage de l'acier Grade 92.

Remarques générales

Le dépouillement des courbes de fluage a été présenté dans le chapitre IV. Dans tous les tableaux de ce chapitre, σ_n est la contrainte nominale en MPa, t_r est le temps à rupture en heures; Z et A sont la réduction de l'aire et l'élongation de l'éprouvette après rupture. $\dot{\varepsilon}_{ss}$ est la vitesse de fluage secondaire déterminée par l'ajustement de l'équation IV.3 sur la première partie de la courbe expérimentale, comme il a été expliqué dans le chapitre IV. Les valeurs des paramètres Q, E_0 et τ après ajustement sont représentées dans les tableaux.

VI.1 Smooth creep specimens

VI.1.1 Creep specimens from as-received T92 steel

Five creep tests were conducted at 650°C on smooth creep specimens from the as-received T92 steel under stress range 95-150MPa. The corresponding creep curves of four tests are given in figure VI.1. For visibility reasons the creep curve of the test conducted under 140MPa was not represented, with the scale used in figure VI.1 this creep curve is overlapped on the creep curve of test conducted under 150MPa.

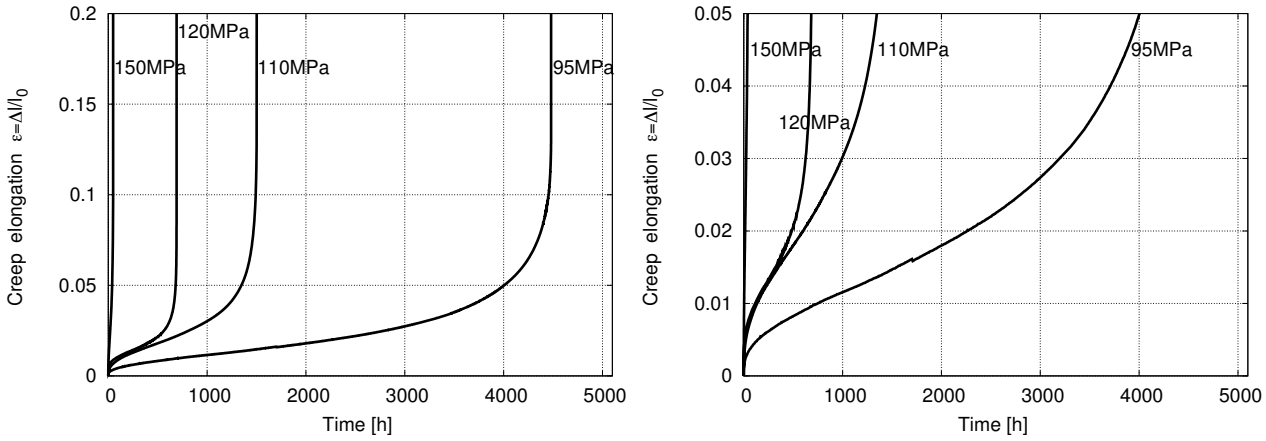

Figure VI.1 : a) Creep curves for tests conducted on smooth specimens at 650°C on as-received T92 steel; b) same as a), close-up view of the begining of the curves

Table VI.1 : Results of creep tests conducted at 650°C on T92 steel smooth specimens

Steel	σ_n [MPa]	t_r [h]	A [%]	Z [%]	E_0	Q	τ [h]	ts_{III} [h]	ε_{III}	$\dot{\varepsilon}_{ss}$ [h^{-1}]
650°C T92 steel	150	50	26.3	92	0.0001	0.00689	0.8	26	0.032	95.66×10^{-5}
	140	67	17.8	88	0.0007	0.00749	1.9	33	0.036	82.78×10^{-5}
	120	691	26.1	84	0.0009	0.00497	11.4	403	0.016	2.48×10^{-5}
	110	1,502	22.9	77	0.0012	0.00619	34.9	782	0.024	2.11×10^{-5}
	95	4,480	14.9	35	0.0010	0.00393	91.2	2,102	0.018	0.65×10^{-5}

The creep tests conducted under 120MPa and 110MPa show almost the same value of $\dot{\varepsilon}_{ss}$ although different times to rupture. The creep curves of these tests in figure VI.1 show similar deformation of specimens in the first part of the tests and an earlier tertiary creep stage on the specimen under 120MPa compared to that under 110MPa. However, note that creep tests are characterized by an experimental scatter (see also the result on the P92 steel creep tested under 110MPa in table VI.2).

The tertiary creep stage is onset at values of elongation of about 0.03 on short-term creep tests ($t_r < 10^2$h) and they show a significant reduction of area (Z) and a high elongation at rupture (A). This was also observed on the specimens creep tested at 600°C in the high stress regime ($\sigma > 160$MPa, $t_r < 10^3$h).

Except for creep test conducted under $\sigma = 120$MPa the primary creep stage seems to end at values of elongation (the sum of E_0 and Q in table VI.1) between 0.007-0.008 for high stresses ($\sigma > 110$MPa).

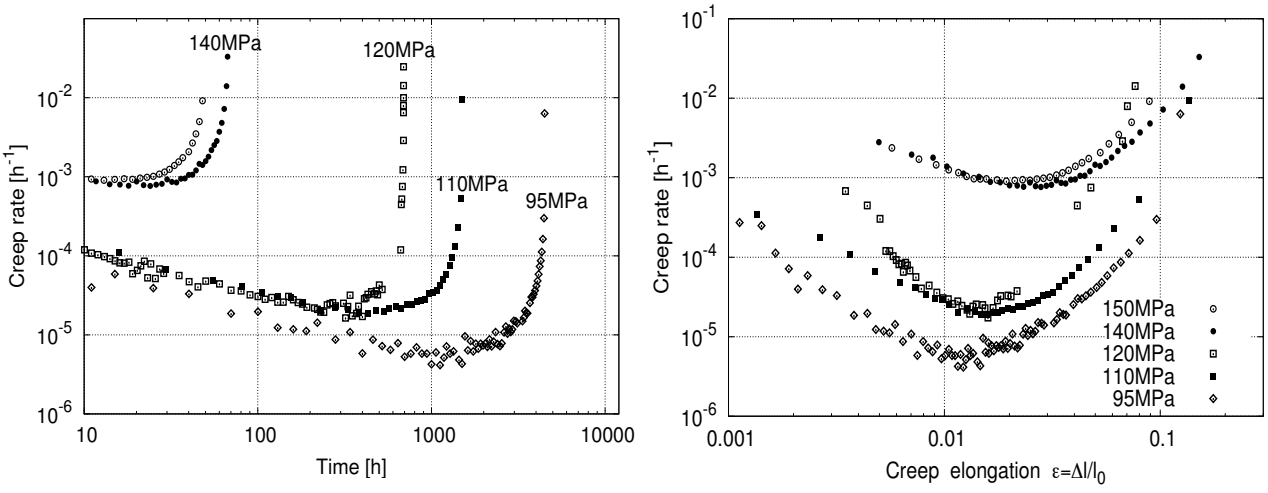

a) b)

Figure VI.2 : Creep rate of T92 steel specimens tested at 650°C as a function of time (a) and elongation (b)

The specimen tested at 95MPa for 4,480h shows a relatively low ductility compared to specimens tested at higher levels of stress, see table VI.1. The values of A and Z are similar to those observed on the P92 steel creep tested at 600°C for long-term, see table V.2. On this specimen (i.e. 95MPa, 4,480h) secondary and tertiary creep stages are onset at values of elongation much lower than those of creep tests conducted at $\sigma_n > 110$MPa. This is typical for creep tests conducted under low stresses.

Analysis of creep curves reveals that the tertiary creep stage represents about the half of the specimen lifetime, see table VI.1.

Temperature does not seem to have a significant influence on the failure nature of specimens creep tested at high stresses, similar values of A and Z are observed on specimens both tested at 600°C ($\sigma_n > 160$MPa) and 650°C ($\sigma_n > 110$MPa).

For a given (short-term) lifetime, increasing the testing temperature by 50°C leads to a loss of the creep strength of about 70MPa.

VI.1.2 Long term creep data (P92 steel creep specimens provided by SZMF)

The creep curves corresponding to the four P92 steel crept specimens tested at 650°C, provided by Salzgitter Mannesmann Forschung, Germany (SZMF) are plotted in figure VI.3. The engineering stress (σ_n), time to rupture (t_r), elongation at rupture (A) and reduction of area (Z) of the P92 steel crept specimens together with $\dot{\varepsilon}_{ss}$ estimated by data processing of creep curves are given in table VI.2.

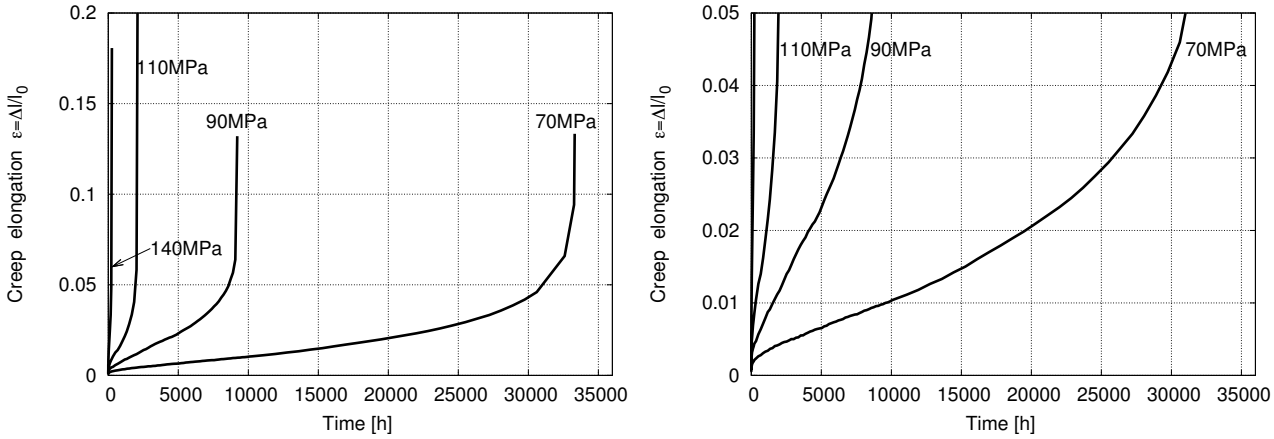

Figure VI.3 : a) Creep curves for creep tests conducted on smooth specimens at 650°C on P92 steel (provided by SZMF); b) same as a), close-up view of the begining of the curves

Table VI.2 : P92 steel creep specimens tested at 650°C (data from SZMF, Germany)

	σ_n [MPa]	t_r [h]	A [%]	Z [%]	E_0	Q	τ [h]	ts_{III} [h]	ε_{III}	$\dot{\varepsilon}_{ss}$ [h^{-1}]
650°C P92 steel	140	256	18.1	74	0.00254	0.00614	5.35	140	0.030	14.40×10^{-5}
	110	2,092	21.0	74	0.00245	0.00330	34.9	1017	0.019	1.28×10^{-5}
	90	9,211	13.2	43	0.00162	0.00210	34.9	5900	0.027	3.97×10^{-6}
	70	33,308	13.3	20	0.00092	0.00168	238.3	14293	0.014	0.79×10^{-6}

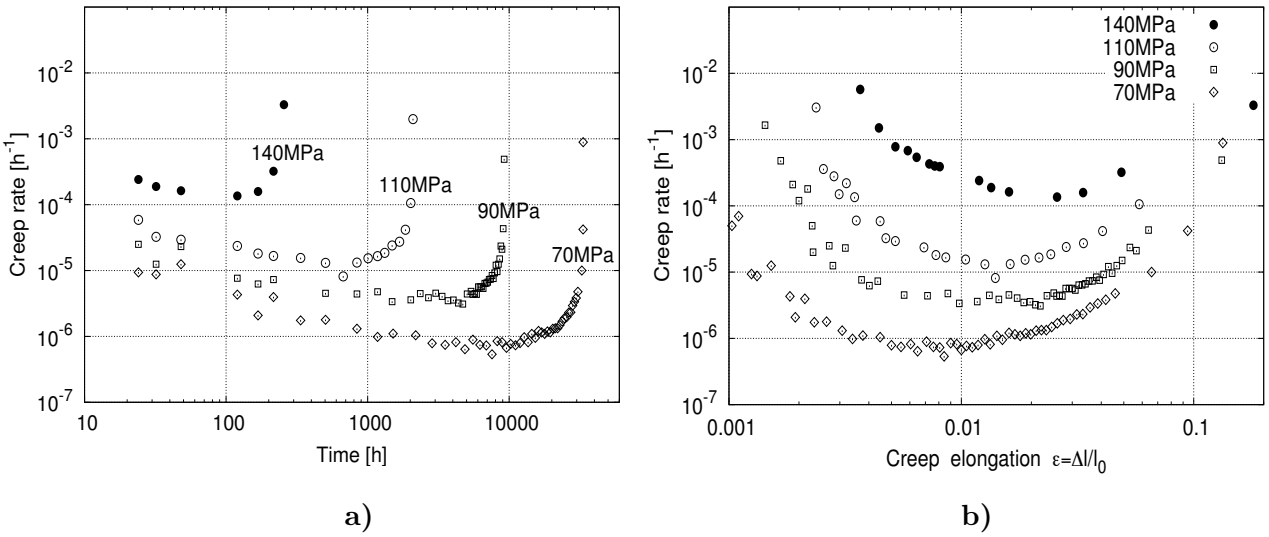

Figure VI.4 : Creep rate of P92 steel tested at 650°C as function of time (a) and elongation (b)

P92 steel and T92 steel tested under 110MPa show similar lifetime. The P92 steel specimen tested under 140MPa shows a t_r five times higher than that of the T92 steel tested under the same engineering stress, see tables VI.4 and VI.2. Although the creep flow of the

T92 steel and P92 steel can be considered to be similar taking account the well-known scatter of creep results.

As observed from the results of creep tests conducted on T92 steel, the P92 steel specimens tested for high stresses ($\sigma > 110$MPa) show a high fracture elongation (A) and a high reduction of area (Z).

The P92 steel specimen with the highest t_r show an extremely low elongation at the end of primary creep stage and at the beginning of the tertiary creep stage, see table VI.2. These values are lower than those of the P92 steel specimen creep tested for almost 50,000h at 600°C. All these elements indicate that failure of this specimen is due to some other mechanisms than high deformation of the specimen followed by necking.

Half of the P92 steel specimens lifetime represents the tertiary creep stage.

VI.2 Thermally aged creep specimens

A microstructural characterization of the T92 steel after aging at 650°C for 10^4h is given in chapter III.

Four creep tests were conducted at 650°C on the thermally aged specimens and one test is in progress. The corresponding creep curves of these tests are represented in figure VI.5a. For comparison reasons in figure VI.5 are also represented the creep curves of the as-received T92 steel tested under 110MPa (figure VI.5a) and 95MPa (figure VI.5b).

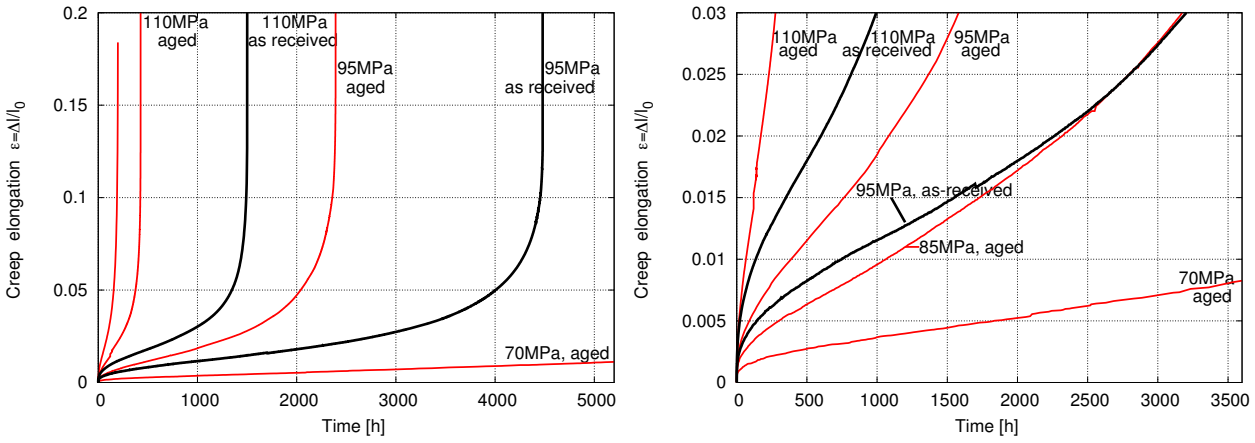

Figure VI.5 : a) Creep curves for tests conducted at 650°C on T92 steel thermally aged at 650°C for 10^4h; b) same as a) close-up view of the begining of the curves

As can be seen in figure VI.5b there is no significant difference between the creep curve of the test conducted under 85MPa on thermally aged specimen and that of the as-received T92 steel creep tested under 95MPa.

Similar t_r, $\dot{\varepsilon}_{ss}$ and values of elongation at the onset of the tertiary creep stage are observed from the creep curves of the tests conducted on the as-received T92 steel under 95MPa and on thermally aged specimen under 85MPa, see table VI.3 compared with table VI.1. This may indicates that ageing at 650°C for 10^4h induces a loss of the creep strength of about 10%. This is probably valid only for the low stresses ($\sigma < 110$MPa).

Creep tests conducted on thermally aged specimens revealed a lower lifetime (t_r) and a higher $\dot{\varepsilon}_{ss}$ compared to the as-received T92 steel for same testing conditions. The difference

Table VI.3 : Results of creep tests conducted at 650°C on specimens thermally aged at 650°C for 10^4h

Temp.	σ_n [MPa]	t_r [h]	A [%]	Z [%]	E_0	Q	τ [h]	ts_{III} [h]	ε_{III}	$\dot{\varepsilon}_{ss}$ [h^{-1}]
650°C	120	199	33,.7	88	0.00081	0.00507	3.4	94	0.026	$21{,}1\times10^{-5}$
	110	427	20.6	80	0.00016	0.00353	3.7	270	0.030	9.43×10^{-5}
	95	2,392	19.8	65	0.00031	0.00381	22.7	1,098	0.020	1.45×10^{-5}
	85	4,434			0.00087	0.00163	29.3	2,074	0.017	0.73×10^{-5}
	70	in progress			0.00052	0.00122	57.0	in progress		1.73×10^{-6}

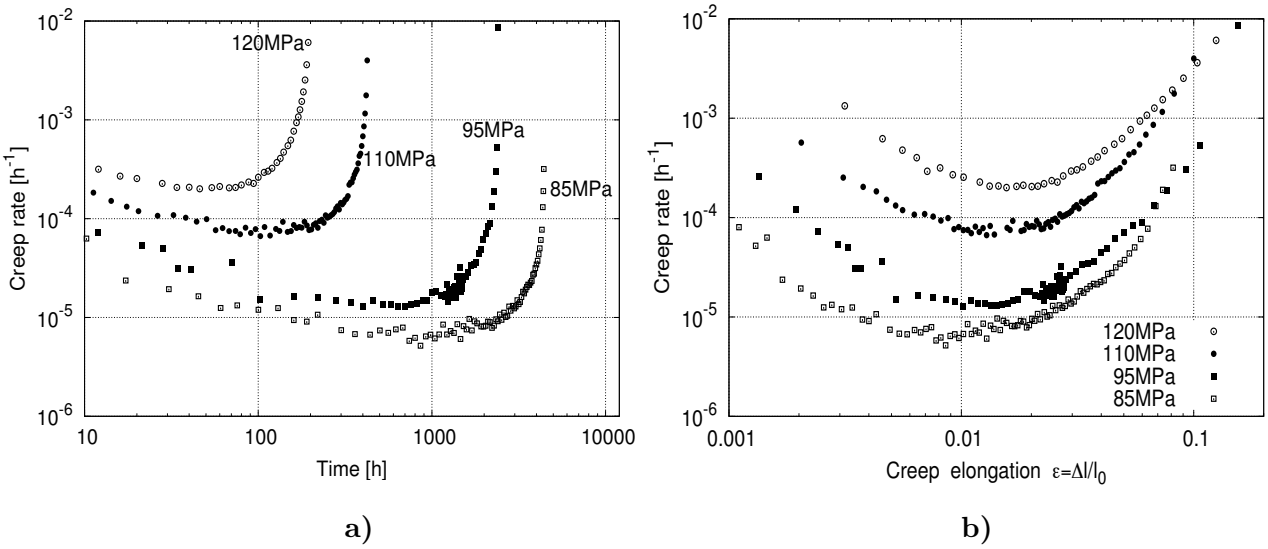

Figure VI.6 : Strain rate during creep of T92 steel thermally aged at 650°C

between $\dot{\varepsilon}_{ss}$ of the as-received T92 steel and the aged T92 steel depends on the level of applied stress. In the high stresses region ($\sigma > 110$MPa) the $\dot{\varepsilon}_{ss}$ of the aged steel is 3-4 times higher than that of as-received steel and in the low stresses region ($\sigma < 110$MPa), the $\dot{\varepsilon}_{ss}$ is only twice higher than that of the as-received T92 steel for same σ_n, see table VI.3 compared with table VI.1.

The increase in $\dot{\varepsilon}_{ss}$ after ageing can be explained by the precipitation of Laves phases (enriched in W). Laves phases precipitation deplets the matrix of W and Mo atoms in solid solution.

In figure VI.7 are compared the creep rupture data at 650°C of the T92 steel after ageing at 650°C for 10^4h and various P91 steels. Grade 91 steel has similar chemical composition to that of Grade 92 steel but without W. The creep rupture data of the P91 steel in figure VI.7 were delivered by SZMF and corresponds to published data on the creep behaviour of the Grade 91 steel at 650°C, see for instance (V & M, 2002), (Yoshizawa et al., 2009). The chemical composition and the heat treatments of the P91 steel creep tested in figure VI.7 are in agreement to specifications of the EN 10216 Standard.

The higher creep strength of aged T92 steel compared to that of P91 steel can be explained by the fact that after ageing some amount of W is still en solid solution and contribute to the creep strength of the steel. (Hald, 1996) reported that only 1% of W precipitated after ageing at 650°C for 10^4h of Grade 92 steel.

The creep test conducted under 95MPa on thermally aged T92 steel revealed a $\dot{\varepsilon}_{ss}$ twice

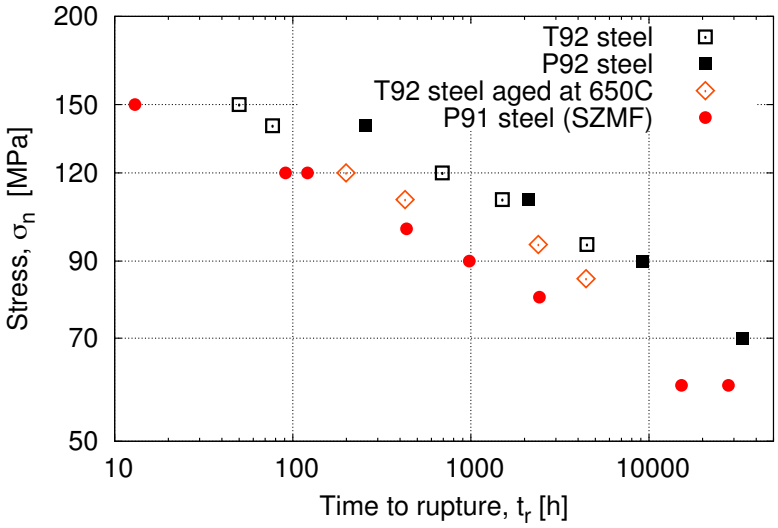

Figure VI.7 : Creep rupture data at 650°C of the T92 steel, T92 steel thermally aged at 600°C, P92 steel and P91 steel

higher than that of the as-received T92 steel creep tested under the same load. In order to estimate the $\dot{\varepsilon}_{ss}$ of the aged T92 steel at lower levels of stress a creep test is in progress under 70MPa. Figure VI.8 shows the first 1,000h of the creep curve of aged T92 steel under 70MPa together with the creep curve of the P92 steel tested under 70MPa for 33,308h. The first 1,000h of the running creep test shows no significant difference between the deformation of both steels.

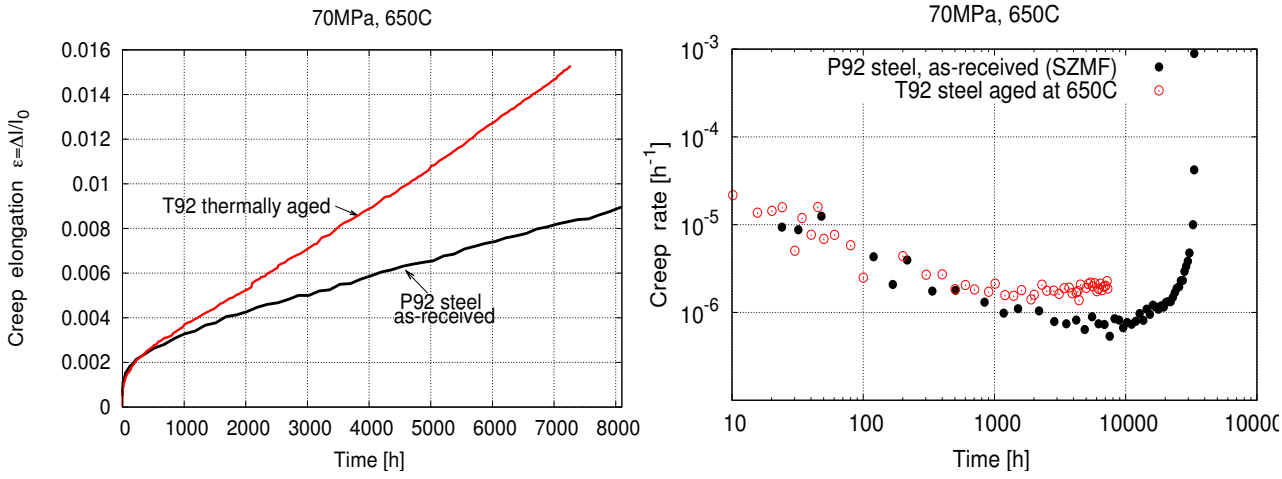

Figure VI.8 : Creep curve (a) and creep rate (b) for the P92 steel tested at 70MPa, 650°C for 33,308h and T92 steel thermally aged at 650°C for 10^4h tested at 70MPa, 650°C (test in progress)

The progress of the creep test under 70MPa on the thermally aged T92 will enable to determine whether the $\dot{\varepsilon}_{ss}$ of a long term creep test (testing time higher that 30,000h) is given

by a thermally aged steel in the first part of test.

Thermal ageing at 650°C for 10^4h does not seem to have a significant influence on the ductility of the T92 steel. Reduction of area (Z) of thermally aged crept specimens is similar to that of crept specimens in as-received T92 steel, see table VI.3 compared with table VI.1.

VI.3 Simple analysis of the creep flow of Grade 92 steel at 650°C

In this section the creep results of as-received T92 steel, T92 steel thermally aged at 650°C and P92 steel are analyzed using simple models, equations, relations usually used to model or to characterize the creep behaviour of steels. The same simple analysis is realized here as for creep data at 600°C.

VI.3.1 Creep rupture behavior at 650°C of the Grade 92 steel

Specimens in as-received T92 steel and aged T92 steel tested for short-term creep (t_r<1,000h) show a significant reduction of area (Z) compared to the crept specimens tested for long-term (t_r>1,000h), figure VI.9. Crept specimens tested for short-term correspond to levels of stress higher than 110MPa and the long term crept specimens to levels of stress below 110MPa.

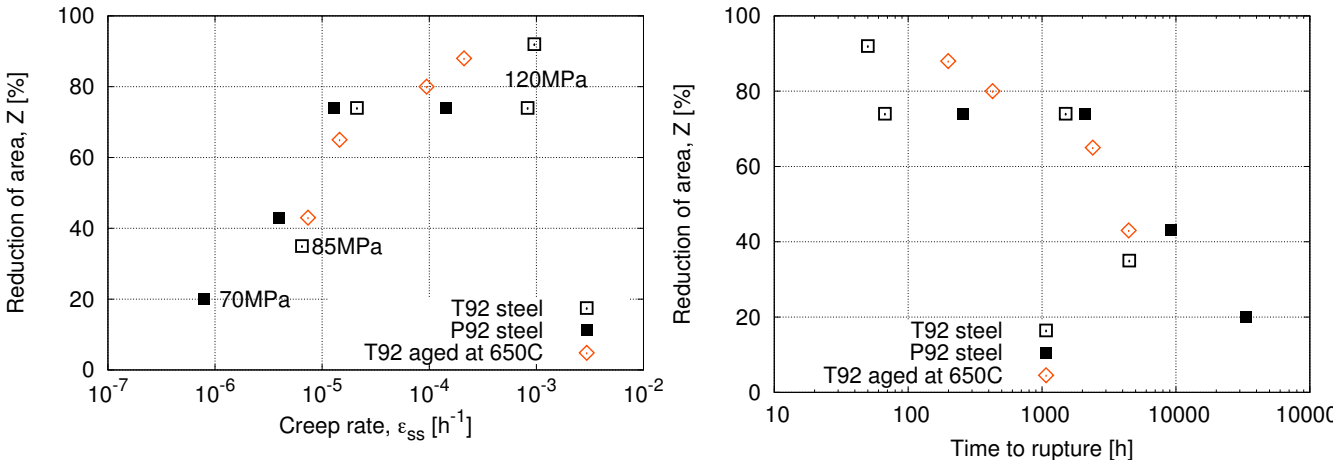

Figure VI.9 : Reduction of area (Z) as a function of secondary creep rate (a) and time to rupture (b) for specimens creep tested at 650°C

The results of creep tests conducted at 650°C on as-received T92 steel correspond to creep rupture data available in literature for P92 steel, figure VI.10. The rupture data of the P92 crept specimens are on the mean line established by ECCC for the Grade 92 steel at 650°C while the creep rupture results of the investigated T92 steel are slightly below the ECCC mean line. The ECCC mean line in figure VI.10 comes from reference (Yoshizawa et al., 2009).

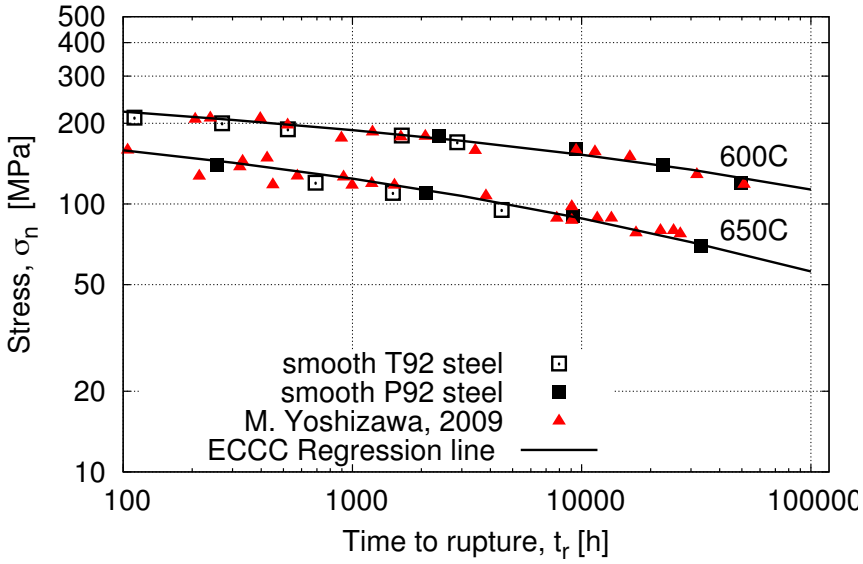

Figure VI.10 : Creep rupture data at 600°C and 650°C of the T92 steel and P92 steel compared to published data on the creep rupture behaviour of the Grade 92 steel

VI.3.2 Monkman-Grant relationship

Adjustment of the Monkman-Grant relationship (equation VI.1) to the creep results at 650°C revealed $m = 1.09$ and $C = 0.06\text{h}^{-1.09}$, figure VI.11a. These values are sligthly different compared to those adjusted for creep tests conducted at 600°C. As explained for creep results at 600°C, the Monkman-Grant relationship with $m = 1$ and two values for the constant C (i.e. $C = C_2 = 0.03$ and $C = \frac{1}{18}$) are also represented in figure VI.11a.

$$t_r \times (\dot{\varepsilon}_{ss})^m = C \tag{VI.1}$$

The two graphs in figure VI.11 are the same, the only difference is that in figure VI.11b were added the $\dot{\varepsilon}_{ss}$ and t_r of the T92 steel thermally aged at 650°C.

VI.3.3 Norton flow rule

In figure VI.12 are represented the $\dot{\varepsilon}_{ss}$ and σ of the creep tests conducted at 650°C on as-received T92 steel, thermally aged T92 steel and P92 steel. Two regions can be distinguished namely high stresses ($\sigma > 110$MPa) and low stresses ($\sigma < 110$MPa). For each region, the dependence of $\dot{\varepsilon}_{ss}$ on σ can be described by a Norton power-law equation (VI.2).

$$\dot{\varepsilon}_{ss} = A \left(\frac{\sigma}{\sigma_0} \right)^n \tag{VI.2}$$

In equation VI.2, σ_0 was chosen arbitrary to 100MPa. For the high stresses region it was found $A = 1.07 \times 10^{-6}\text{h}^{-1}$ and $n = 18$ and for low stresses region it was found $A = 9.78 \times 10^{-6}\text{h}^{-1}$ and $n = 6$. The lines in figure VI.12a represent the adjusted Norton power-law equation.

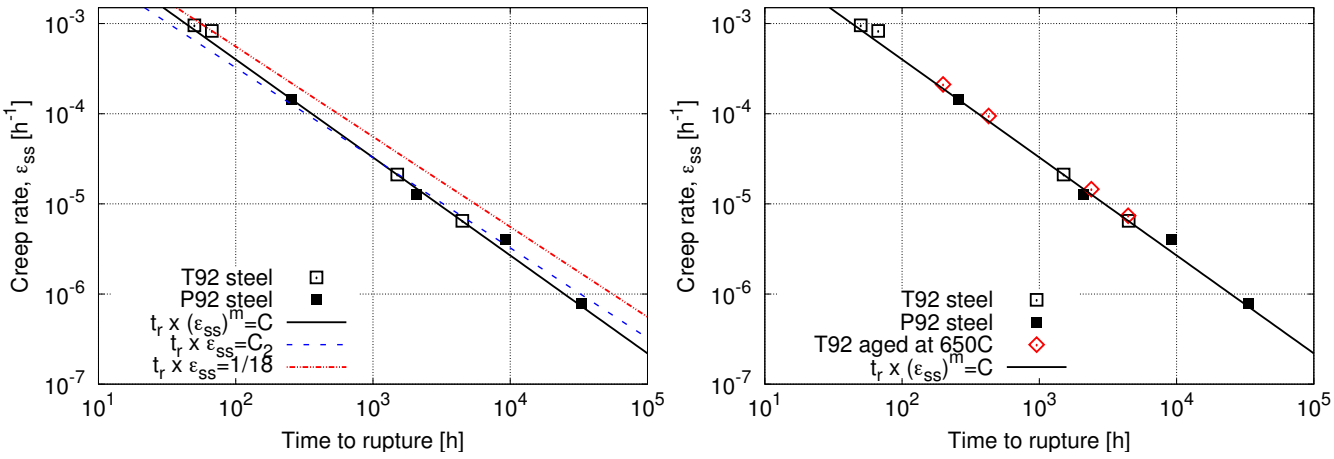

Figure VI.11 : a) Monkman-Grant relationship for creep tests conducted at 650°C on smooth specimens. a) T92 and P92 steel; b) as-received T92 steel, T92 steel thermally aged at 650°C for 10^4h and P92 steel

The Norton power-law exponents are identical to those found for creep data at 600°C. The value of parameter A are much higher at 650°C compared to those found at 600°C in both high stress and low stress regions.

A Norton power-law with $A = 4.06 \times 10^{-6}\text{h}^{-1}$ and $n = 18$ represents well the the creep tests conducted on T92 steel thermally aged at 650°C for 10^4h in the high stress regime. A constant $A = 19.6 \times 10^{-6}\text{h}^{-1}$ and $n = 6$ were found for the thermally aged T92 steel creep tested under low stresses.

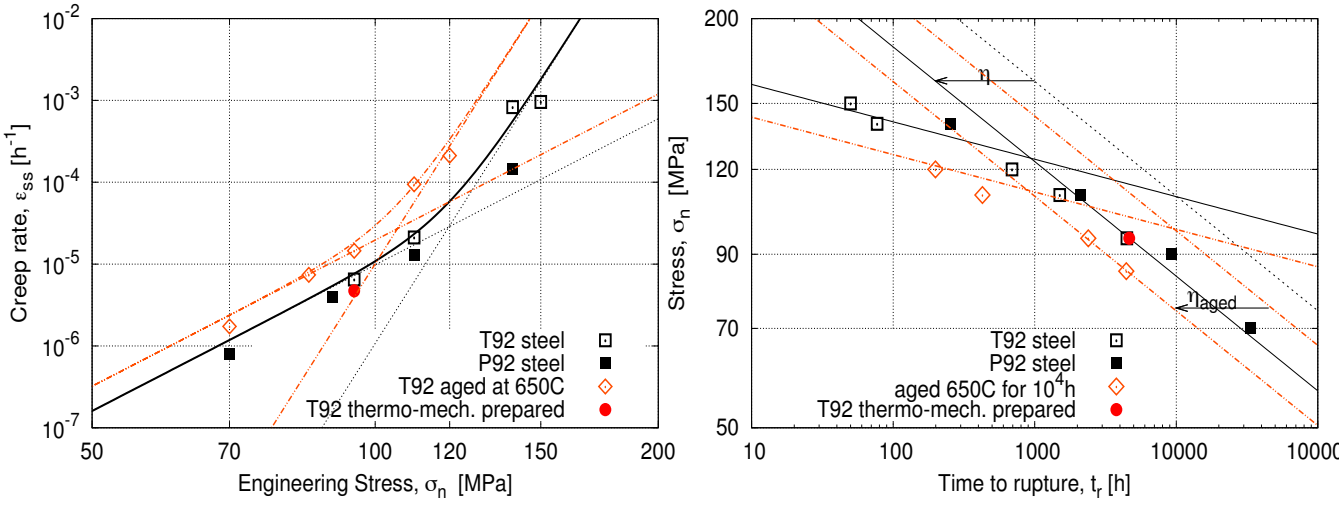

Figure VI.12 : Secondary creep rate (a) and time to rupture (b) as a function of engineering stress for creep tests conducted at 650°C on smooth and thermally aged at 650°C specimens

Once the dependence of $\dot{\varepsilon}_{ss}$ on stress known, lifetime (t_r) of the specimens for a given level of stress can be estimated with the following formula (see chapter V):

$$\sigma = \sigma_0 \left(nAt_r\right)^{-1/n} \tag{VI.3}$$

The formula VI.3 gives a quite good estimation of the of the t_r of both as-received and thermally aged T92 steel at 650°C in the high stress region ($\sigma > 110$MPa), in the same way the t_r of creep tests conducted under low stresses is overestimated, dotted lines in figure VI.12b.

The fact that equation VI.3 gives a well estimation of the t_r of short-term specimens but overestimates the t_r of long-term creep specimens indicates once again that the failure nature of short-term specimens is different from the failure of long-term specimens. To get a good representation of creep rupture results at low stresses, the estimated t_r by equation VI.3 had to be adjusted with a factor $\eta = 5$ both for as-received T92 steel and aged T92 steel. The value of η could express the creep damage development which decreases the lifetime of specimens.

The slope change in $\dot{\varepsilon}_{ss}$ is often associated with a change in the dominant deformation mechanism, a transition from the dislocation creep to diffusional creep. At high stresses the dominant deformation mechanism is probably the dislocation creep. Norton law exponent $n = 18$ identified for high stresses is relatively high, compared to theoretically values, e.g. 4-5 of Norton exponent characteristic to dislocation creep. This is probably because the thermo-mechanical history of this steel involves development of internal stresses.

Dominant diffusional creep occurs at levels of stress much lower than the levels investigated in this study. The Norton law exponent $n = 6$ identified for low stresses does not indicate the diffusional creep. However, based on the work of (Kloc and Sklenička, 1997) which evidenced the diffusional creep in a P91 steel, it can be assumed that the creep results at low stresses of this study are indicating the beginning of transition to diffusional creep.

VI.4 Notched creep specimens

The geometries of the four notched specimens were given in chapter III, figure III.3. The results of creep tests conducted on notched specimens are given in table VI.4. The corresponding creep curves (notch opening versus time) of these tests are represented in figure VI.14.

For a given engineering stress (σ_n), the t_r is higher of a notched specimens compared to a smooth one because of a lower von Mises equivalent stress in the notched specimen.

The first creep test at 650°C was realized under 95MPa on NTDV specimen. Because this specimen showed relatively low creep rate, the next creep tests were lunched at higher levels of stress, e.g. 130MPa and 140MPa. Due to availability of testing machines the creep test on NTDV under $\sigma_n = 95$MPa was interrupted after 4,480h.

Table VI.4 : Results of creep tests conducted at 650°C on T92 steel notched specimens

	Geometry of specimen	σ_n [MPa]	t_r [h]	Z [%]	Observations
650°C	NTDC0.6	140	1,212	11	
650°C	NTDC0.6M	140	1,027	14	no creep curve available
		130	1,593	13	
650°C	NTDC1.2	140	860	24	notch accidentally broken during removal
		130	1,708	25	
650°C	NTDV	150	1,048	16	
		140	1,700	6	
		95	(4,656)	-	test interrupted before fracture

Notched specimens creep tested for times higher than 1,000h showed relatively low values of reduction of area (Z). These values are similar to these observed in the notched specimens creep tested at 600°C for times higher than 2,000h, see figure VI.13 and table VI.4.

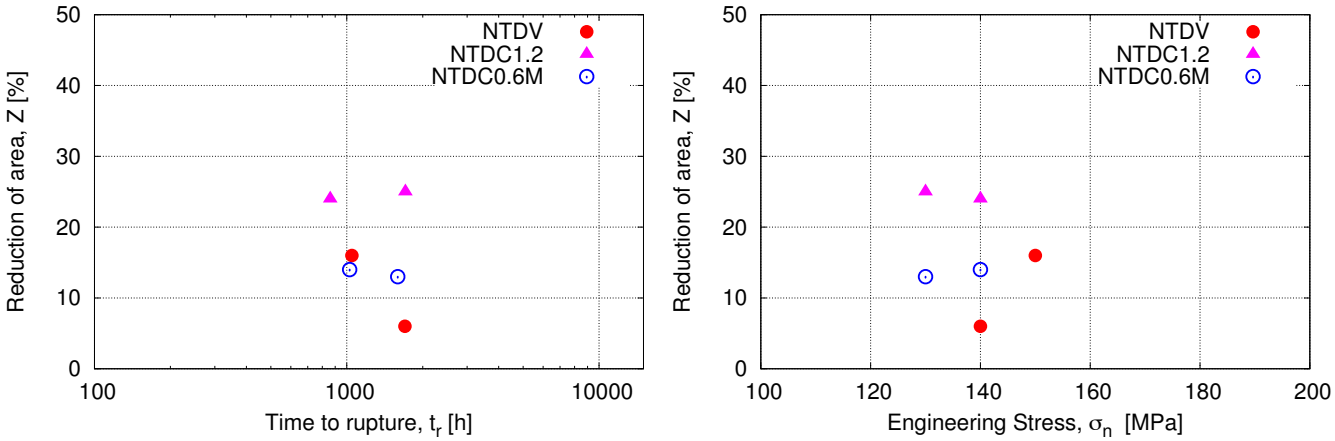

a) b)

Figure VI.13 : Reduction of area (Z) as a function of time to rupture (a) and engineering stress (b) for notched specimens creep tested at 650°C

In figures VI.15, VI.16, VI.17 and VI.18 are given the distribution of the σ_{22} and σ_{VM} in the notched specimens for the levels of σ_n used in this study. The stress distribution was estimated by finite element (FE) simulations as it was explained in chapter IV.

As previously shown and discussed, from the distribution of σ_{22} in the notched area (figures VI.15, VI.16, VI.17 and VI.18), creep damage is expected to develop preferentially close to notch root of NTDV, NTDC 0.6M, NTDC0.6 and in the center of the NTDC1.2 specimen. In all the notched specimens the levels of the σ_{VM} are much lower than the applied σ_n.

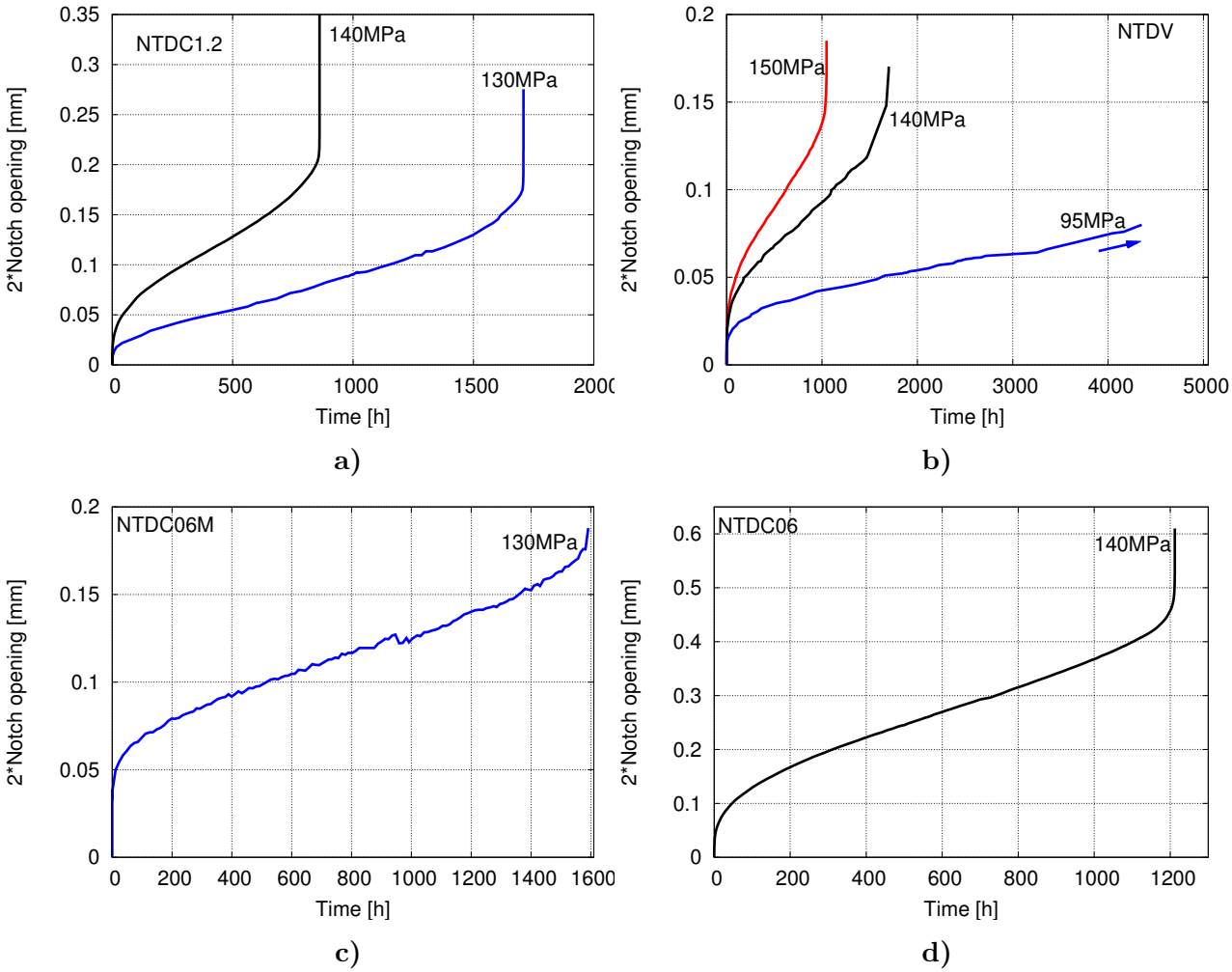

Figure VI.14 : Creep curves of tests conducted at 650°C on notched specimens; a) NTDC1.2; b) NTDV; c) NTDC0.6M; d) NTDC0.6

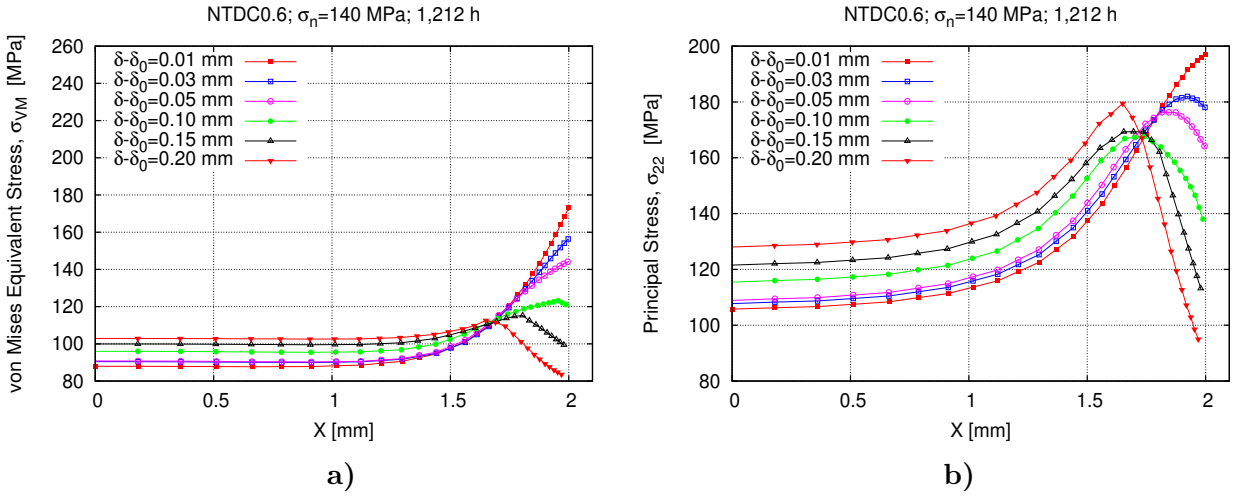

Figure VI.15 : Distribution of σ_{VM} (a) and σ_{22} (b) in the NTDC0.6 notched specimen as a function of the notch opening (δ), $\sigma_n = 140$MPa, $t_r = 1,212$h

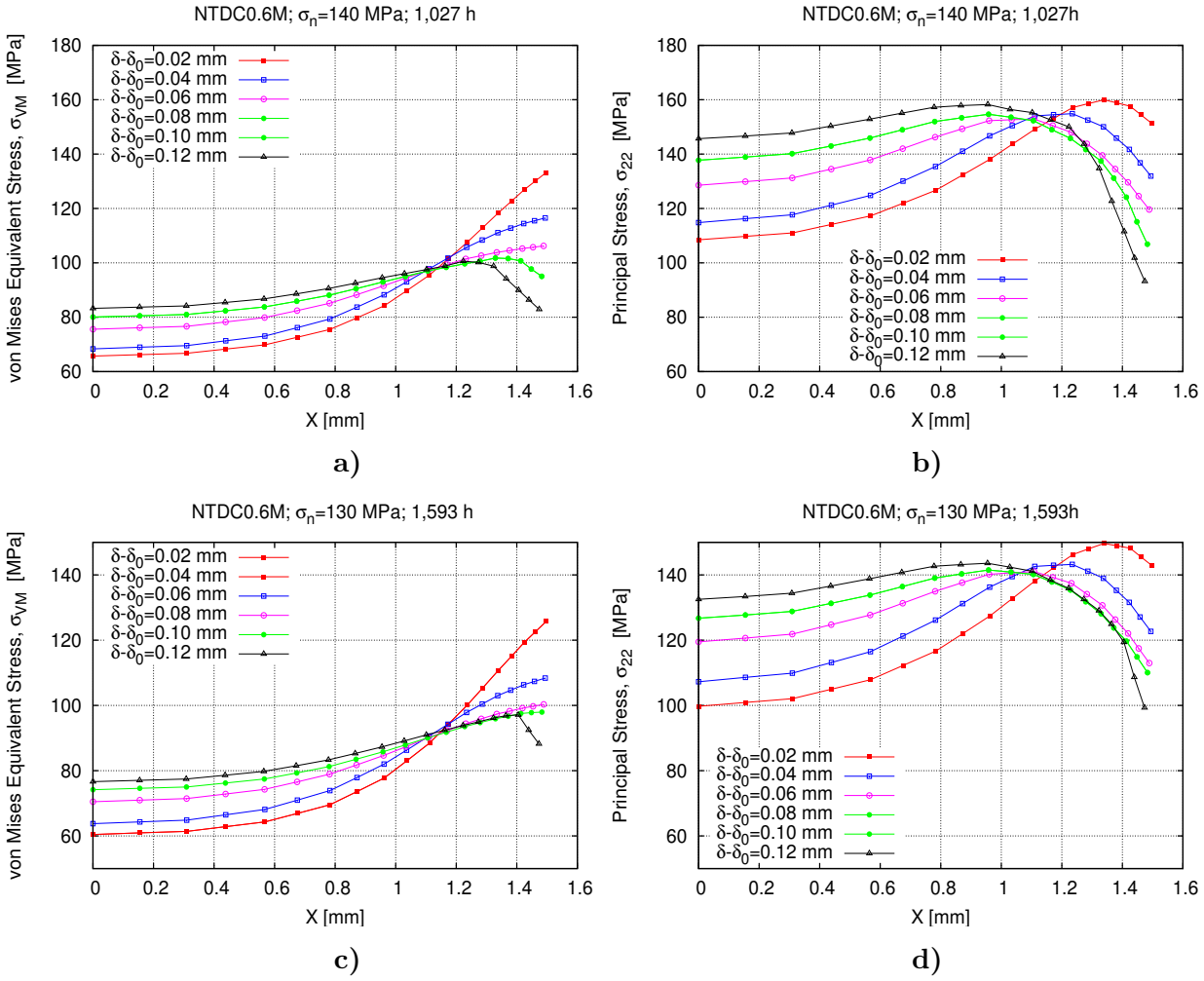

Figure VI.16 : Distribution of σ_{VM} and σ_{22} in the NTDC0.6M specimens as a function of the notch opening (δ); a), b) $\sigma_n = 140$MPa, $t_r = 1,027$h; c), d) $\sigma_n = 130$MPa, $t_r = 1,593$h

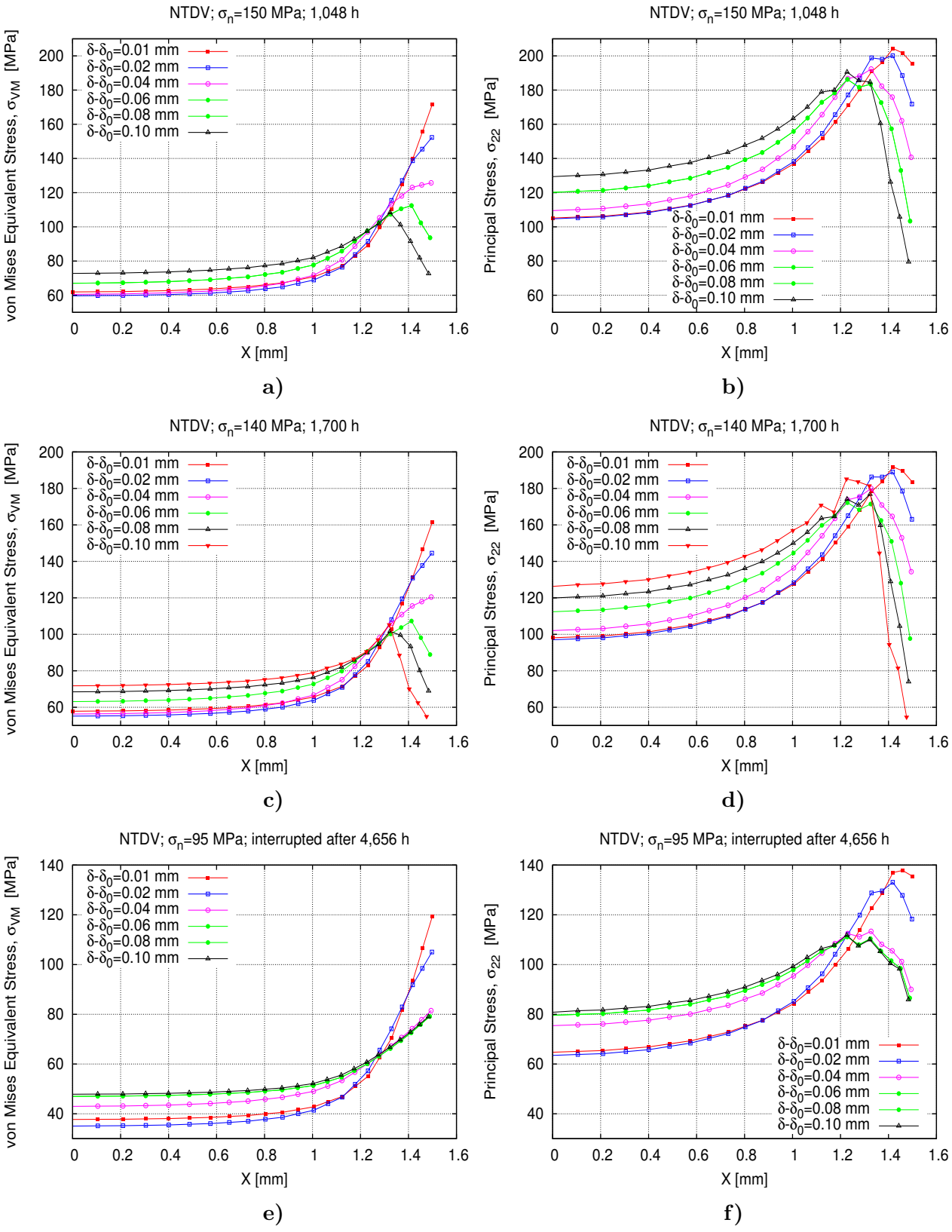

Figure VI.17 : Distribution of von Mises equivalent stress (σ_{VM}) and principal stress (σ_{22}) in the NTDV notched specimens as a function of the notch opening (δ); a), b) $\sigma_n = 150$MPa, $t_r = 1,048$h; c), d)$\sigma_n = 140$MPa, $t_r = 1,700$h; e), f)$\sigma_n = 95$MPa, interrupted after 4,656h

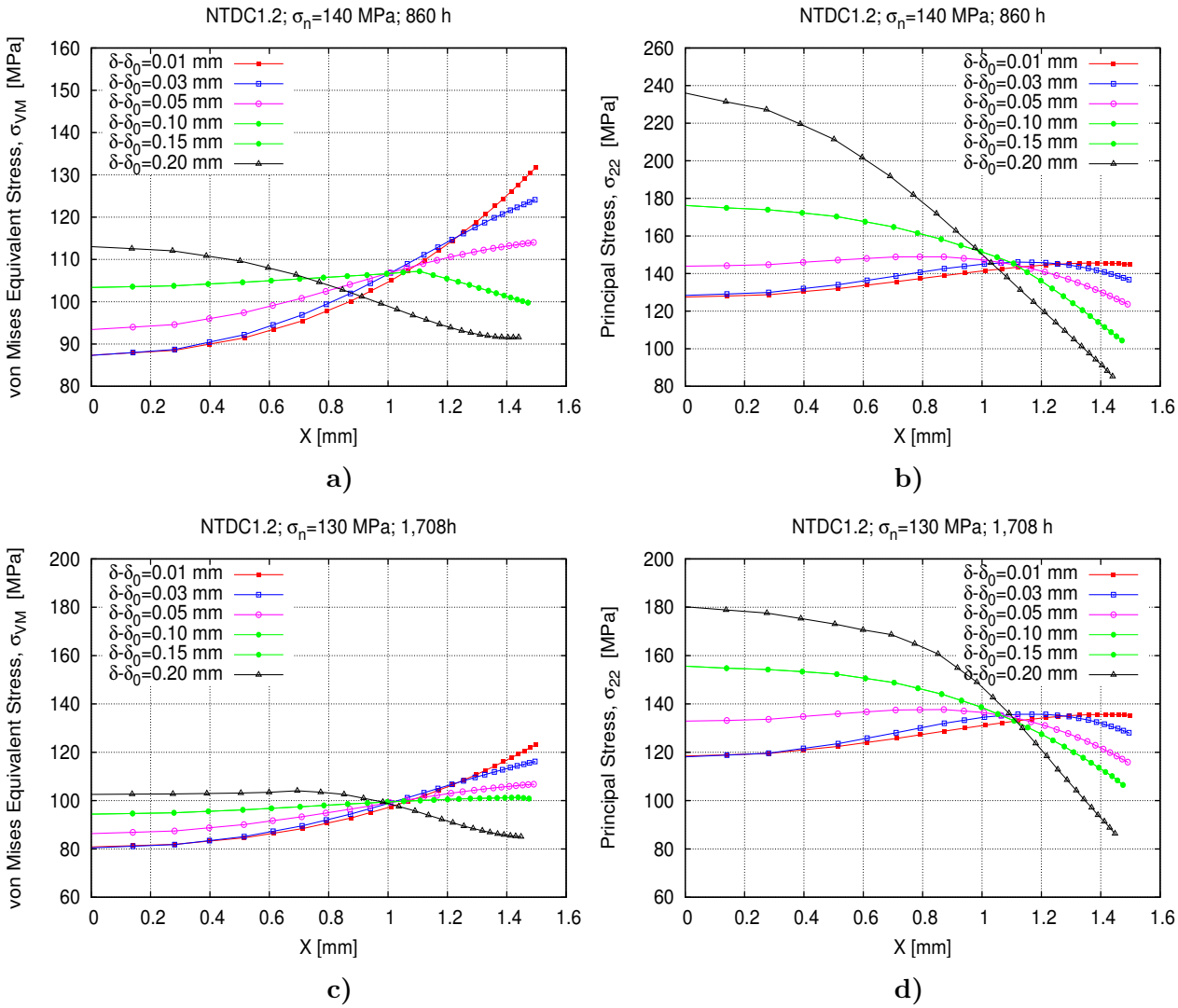

Figure VI.18 : Distribution of von Mises equivalent stress (σ_{VM}) and principal stress (σ_{22}) in the NTDC1.2 notched specimens during testing; a), b) $\sigma_n = 140$MPa; c), d) $\sigma_n = 130$MPa

In figure VI.19 are represented the lifetime of smooth specimens and notched specimens versus engineering stress (σ_n). In figure VI.20 the values of von Mises equivalent stress (σ_{VM}) corespond to the maximum value of σ_{VM} in figures VI.15, VI.16, VI.17 and VI.18 in the second part of the test. For the same levels of σ_n a higher t_r is observed on notched specimens compared to smooth ones while for the same levels of σ_{VM} the values of t_r of smooth and notched specimens are similar.

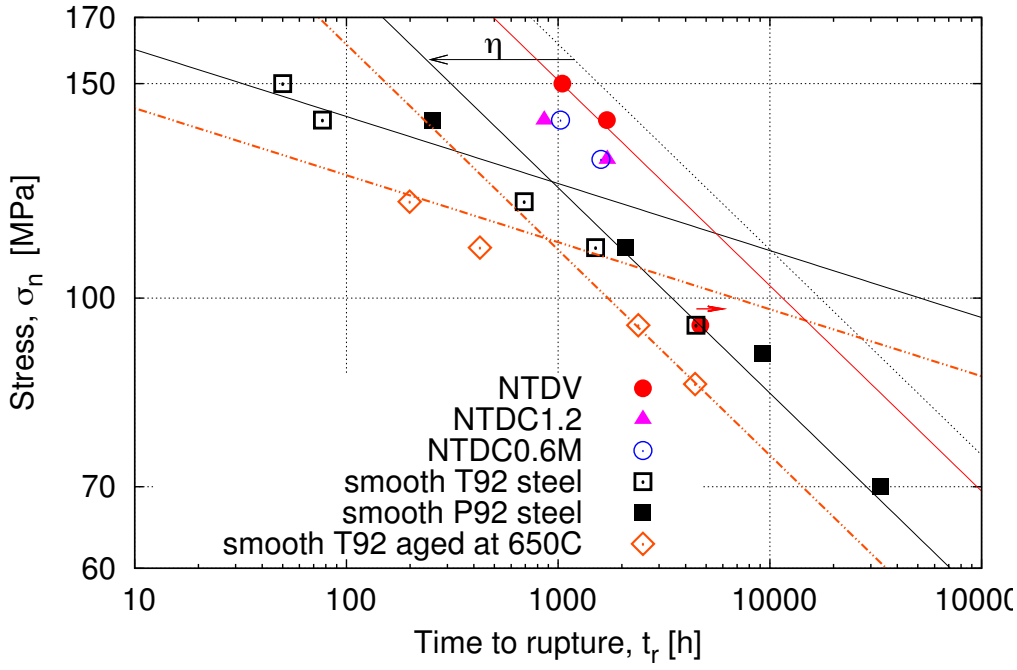

Figure VI.19 : Creep rupture data of the smooth (as-received T92 steel, P92 steel and T92 steel thermally aged at 650°C for 10^4h) and notched specimens as a function of engineering stress, σ_n

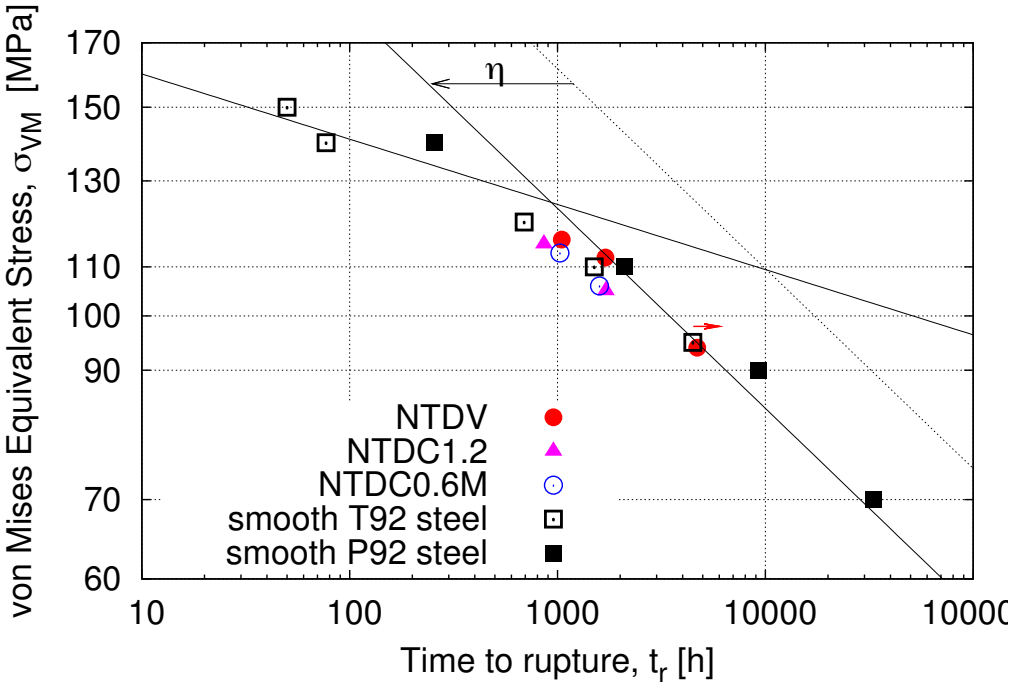

Figure VI.20 : Creep rupture data of the smooth and notched specimens as a function of von Mises equivalent stress, σ_{VM}

VI.5 Summary

All the creep tests conducted at 650°C on smooth, thermally aged, thermo-mechanically prepared and notched specimens are summarized in table VI.5. The results of these tests are plotted on figure VI.19. For visibility reasons the results obtained on NTDC0.6 notched specimen and thermo-mechanically prepared specimens are not represented in figure VI.19.

Table VI.5 : Summary of all creep tests conducted at 650°C

Creep specimen	Levels of stress σ, σ_n [MPa]	Nb. of tests	Accumulated time testing machine [h]	Observations
T92 steel, smooth	95-150	5	6,790	
P92 steel, smooth	70-140	4	44,867	data delivred by SZMF
T92 steel thermally aged	85-120	4	7,452	
(600°C, 10^4h)	70	1	(5,000)	in progress
thermo-mechanically	95	1	4,659	thermo-mech.prepared at 550°C
prepared	95	1	3,210	thermo-mech.prepared at 600°C
NTDC0.6	140	1	1,212	
NTDC0.6M	130-140	2	2,620	
NTDC1.2	130-140	2	2,568	
NTDV	95-150	3	7,228	one test interrupted before rupture
TOTAL	-	24	40,736	lifetime of the P92 crept specimens was not added

A slope change is observed in $\dot{\varepsilon}_{ss}$ for levels of stress 100-110MPa both in as-received T92 steel and aged T92 steel creep tested at 650°C. This slope change is often associated with a change in the dominant creep deformation mechanism.

A Norton power equation (i.e. $\dot{\varepsilon}_{ss} = A\left(\frac{\sigma}{\sigma_0}\right)^n$) was adjusted to creep results at 650°C and the values of the exponent n was found to be 18 in the high stress region ($\sigma > 110$MPa) and 6 in the low stress region ($\sigma > 110$MPa). Same values of the exponent n were found for the creep results on thermally aged specimens.

The lifetime of short-term creep tests ($\sigma > 110$MPa) can be estimated from the flow behavior of the specimens, whereas the same relationship overestimate the lifetime of long-term crept specimens ($\sigma < 110$MPa), see figure VI.12.

After a thermal aging at 650°C for 10^4h the T92 steel shows a higher secondary creep rate and a lower t_r compared to the as received T92 steel for a given level of stress. The effect of thermal aging on the creep behavior seems to depend on the level of the applied stress: in the high stress region, $\dot{\varepsilon}_{ss}$ is four times higher (respectively t_r four times lower) on a thermally aged specimen compared to that of an as-received one; in the low stress region, the $\dot{\varepsilon}_{ss}$ of a thermally aged specimen is only twice higher (respectively t_r twice lower) compared to that of a specimen in T92 steel. This loss of creep strength after thermal aging can be due to a significant precipitation of Laves phases during aging heat treatment (as shown in chapter III).

Monkman-Grant relationship gives a good representation of the creep results at 650°C both on the as-received T92 and the T92 steel thermally aged at 650°C for 10^4h, see figure VI.11.

For a given σ_n the lifetime of a notched specimen is higher compared to that of a smooth one. This is due to a lower von Mises equivalent stress on the notched specimen, see figure VI.19. On the other hand, for a given level of the von Mises equivalent stress at rupture the lifetime of a notched specimen is similar to that of a smooth one, see figure VI.20. The slope of the stress versus lifetime curves is the same for the notched and the smooth specimens tested for long-term creep, see figure VI.19.

The geometry of notch seems to have a different influence on the lifetime of notched specimens at 650°C compared to that at 650°C. The creep results at 600°C reveals that for a given σ_n the lifetime of the NTDV specimens is higher than that of the NTDC0.6M specimens, see figure V.22. At 650°C the lifetime of the NTDC0.6M specimens is higher than that of the NTDV specimens for a given σ_n, see figure VI.19. However, the low number of the creep tests on the NTDC0.6M specimens both at 600°C and 650°C, does not allow to conclude on this issue.

Two creep tests were conducted at 650°C under σ = 95MPa on thermo-mechanically prepared specimens. No significant change was observed in the values of $\dot{\varepsilon}_{ss}$ of the thermo-mechanically prepared specimens compared to that of as-received T92 steel. The results of these tests as well as the investigations of the specimens after creep testing are gathered in *Appendix A*. The results of these tests does not allow to conclude on a possible effect of the matrix substructure on the creep strength.

The creep tests conducted under a load of 95MPa on creep specimens with various microstructures before testing revealed the following results:

- t_r=4,480h on smooth specimen with an as-received T92 steel microstructure before testing;
- t_r=2,392h on thermally aged (650°C for 10^4h) specimen. This lifetime, twice lower than that of the as-received T92 steel, is corelated to a $\dot{\varepsilon}_{ss}$ twice higher after aging. However, in the high stress region the lifetime is four times lower on a thermally aged specimen compared to that of the as received T92 steel.
- t_r= 4,656h on the specimen thermo-mechanically prepared at 550°C (see *Appendix A*). Recovery of the substructure matrix after 330 creep-fatigue cycles at 550°C did not seem to have a significant influence on the $\dot{\varepsilon}_{ss}$. This could not be confirmed for creep tests conducted at higher stresses.
- t_r= 3,210h on the specimen thermo-mechanically prepared at 600°C (see *Appendix A*). This specimen showed a similar $\dot{\varepsilon}_{ss}$ to that of the specimen thermo-mechanically prepared at 550°C, see figures A.14 and A.15.

Résumé

Les essais de fluage réalisés à 650°C sur différents type d'éprouvettes sont reportés dans le tableau VI.5. Les résultats de ces essais sont représentés sur la figure VI.19. Pour des raisons de visibilité les résultats de l'éprouvette entaillée NTDC0.6 et les éprouvettes pré-fatiguées n'y figurent pas.

Un changement de pente est observé dans la vitesse de fluage secondaire des éprouvettes lisses et éprouvettes pré-vieillies pour des niveaux de contraintes de 100-110MPa. Ce changement de pente est souvent associé à un changement dans le mécanisme de déformation dominant.

Une loi de type Norton ($\dot{\varepsilon}_{ss} = A\left(\frac{\sigma}{\sigma_0}\right)^n$) a été ajustée sur les résultats des essais sur les éprouvettes lisses à 650°C. Un exposant n égal à 18 a été trouvé pour des contraintes élevées (égal à 6 pour les faibles contraintes). On obtient les mêmes valeurs pour les éprouvettes pré-vieillies.

La durée de vie des éprouvettes testées pendant des temps courts peut être estimée à partir de la vitesse de déformation en utilisant l'équation VI.3, cependant la même équation surestime la durée de vie des éprouvettes testées pendant de temps prolongés, figure VI.12b.

Les essais de fluage sur le matériau vieilli thermiquement (650°C, 10^4h) montrent une vitesse de fluage secondaire ($\dot{\varepsilon}_{ss}$) plus élevée et un temps à rupture (t_r) plus court que les essais sur le matériau à l'état de réception. L'effet du vieillissement thermique sur le comportement en fluage semble dépendre du niveau de la contrainte appliquée: la vitesse de fluage $\dot{\varepsilon}_{ss}$ d'une éprouvette en matériau vieilli est 3-4 fois plus élevée (respectivement le t_r est 3-4 fois plus faible) pour des niveaux de contraintes élevées et n'est que deux fois plus élevée (respectivement le t_r est deux fois plus faible) pour des faibles contraintes comparée à celle d'une éprouvette en acier T92 testée dans les mêmes conditions. La perte de résistance en fluage après le vieillissement thermique peut être due à la précipitation significative des phases de Laves (voir le chapitre III).

La relation de Monkman-Grant donne une bonne représentation des résultats des essais à 650°C sur les éprouvettes lisses et sur les éprouvettes pré-vieillies, figure VI.11.

Pour une même valeur de la contrainte nominale la durée de vie d'une éprouvette entaillée est plus élevée que celle d'une éprouvette lisse, figure VI.19. Ceci est due à une contrainte de von Mises plus faible dans l'éprouvette entaillée comparée à celle dans l'éprouvette lisse. Cependant pour la même valeur de la contrainte de von Mises, la durée de vie de ces deux types d'éprouvettes est comparable, figure VI.20. La pente de la courbe temps à rupture en fonction de la contrainte appliquée des éprouvettes entaillées est la même que celle des éprouvettes lisses testées pendant des temps prolongés, figure VI.19.

La géométrie de l'entaille semble avoir une influence différente sur la durée de vie des éprouvettes entaillées testées à 650°C comparée à celles testées à 600°C. Les résultats des essais à 600°C montrent que pour une contrainte nominale donnée la durée de vie des éprouvettes NTDV est plus élevée que celles des éprouvettes NTDC0.6M (voir la figure V.22). Les résultats des essais à 650°C montrent le contraire. En effet, pour la même contrainte nominale la durée de vie des éprouvettes NTDC0.6M est plus élevée que celles des éprouvettes NTDV (voir la figure VI.19). Néanmoins, il faut noter que le nombre très limité des essais de fluage sur éprouvettes NTDC0.6M réalisés à 600°C et 650°C ne nous permet pas de conclure définitivement sur ce sujet.

Deux essais de fluage ont été réalisés à 650°C, σ =95MPa sur éprouvettes pré-fatiguées (Annexe A). Les résultats de ces deux essais ne permettent pas de se prononcer sur un éventuel effet de l'état de la matrice sur le comportement en fluage de l'acier T92.

Les résultats des essais réalisés à 650°C, σ =95MPa sur des éprouvettes avec différents état de la microstructure avant le fluage sont comparés ci-dessous:

- *t_r=4480h sur une éprouvette lisse en acier T92 à l'état de réception;*
- *t_r=2392h sur une éprouvette lisse en acier T92 vieilli thermiquement à 650°C pendant 10^4h. Ce temps à rupture est deux fois plus faible que celui du matériau à l'état de réception. Ceci est lié à une vitesse de fluage secondaire deux fois plus élevée pour le matériau vieilli;*
- *t_r= 4656h sur une éprouvette pré-fatiguée à 550°C. La restauration de la matrice après 330 cycles de fatigue-fluage à 550°C ne semble pas avoir une influence significative sur la vitesse de fluage secondaire. Ceci n'a pas pu être confirmé par des essais sous des contraintes plus élevées*

- *t_r = 3210h sur une éprouvette pré-fatiguée à 600°C. Cette éprouvette a montré la même vitesse de fluage secondaire que celle pré-fatiguée à 550°C, voir les figures A.14 et A.15.*

Chapter -VII-

Investigation of crept specimens

Contents

Introduction

Chapter V and VI presented the results of the creep tests conducted at 600°C and 650°C using specimens with an as-received T92 steel microstructure before testing (smooth and notched specimens) and specimens with a *modified* T92 steel microstructure before creep testing (thermally aged and thermo-mechanically prepared specimens). Specimens after creep testing both at 600°C and 650°C were investigated to better understand the effect of the microstructural state on creep flow and the effect of stress triaxiality on creep damage development. The crept specimens were investigated with regard to their microstructure (matrix and precipitates) and creep damage. Investigations of the crept specimens was intended to allow deeper understanding and better interpretation of creep results.

Creep tests on smooth specimens were reference tests to get reference specimens. Some differences were observed on the specimens tested for short-term creep (t_r<10^4h at 600°C and t_r<10^3h at 650°C) compared to long-term crept specimens. The short-term crept specimens show a relatively high values of elongation of area (A) and reduction of area (Z) compared to those of the long-term crept specimens. The lifetime of the short-term crept specimens can be estimated from the secondary creep rate of tests, the same method overestimates the lifetime of long-term crept specimens. This overestimation was suggested to be due to creep damage development.

Smooth crept specimens were investigated in order to build a reference database in both short-term and long-term specimens concerning what happened during the creep test. These investigations will enable to differentiate between physical mechanisms dominant for short-term versus long-term crept specimens. Localization of creep damage was investigated at a macroscopic scale and at a microscopic scale. The purpose of investigating creep damage in the long-term creep specimens was to establish physical mechanisms linked to metallurgical evolution and creep damage development, knowing that the purpose of tests in other kinds of specimens was to reproduce such mechanisms within a shorter time. Metallurgical evolution with regard to hardness, matrix substructure and precipitates was investigated especially in long-term crept specimens (P92 steel), both in the gauge part (exposed to creep) and in the ends (assumed to be exposed to thermal aging only).

The interest of notched creep specimens consists in promoting creep damage development due to stress triaxiality. The stress triaxiality varies with the notch geometry, thus notched specimens were investigated after creep testing to see whether higher stress traixiality modify or accelerate metallurgical evolution or/and creep damage development. These investigations enable to decide whether a geometry provides more interesting information from this point of view. This could be useful for further alloy development purposes.

The thermally aged T92 specimens showed a higher secondary creep rate and a lower lifetime (t_r) compared to these of the as-received T92 steel for same testing conditions. Thermally aged creep specimens were investigated after testing to study the effect of large Laves phases on the creep damage development. Creep damage might also develop more significantly in the aged T92 steels than in the as-received T92 steel. The duration of aging heat treatments was fixed to 10^4h, because published data on the precipitation and growth of Laves phases revealed a significant increases in their mean diameter in the first 10^4h of thermal exposure at 600°C and 650°C. Precipitation and/or growth of Laves phases continue during creep exposure of the aged T92 steels. A more significant recovery of the matrix could also occurr in the aged steels due to a lower amount of Mo and W atoms in solid solution compared to as received T92 steel. Thus the microstructure of the thermally aged specimens was investigated after creep testing with regard to the initial (i.e. before creep)

matrix substructure and Laves phases.

The thermo-mechanically prepared specimens were investigated after creep testing to study the effect of a recovered matrix on the creep damage development and/or precipitation of Laves phases during creep exposure.

Table VII.1 : Investigated crept specimens tested at 600°C

Specimen	Load σ_n [MPa]	Lifetime t_r [h]	Z [%]	Investigation techniques	Feature of the microstructure
smooth, P92 steel	180	2,399	74	TEM, SEM-BSE, hardness	quantification of creep damage; size of Laves phases and $M_{23}C_6$; chemical composition of $M_{23}C_6$; Z-phases; microtexture
	160	9,497	68	TEM, SEM-BSE, hardness	
	140	22,547	27	TEM, SEM-BSE, hardness	
	120	49,721	16	TEM, SEM-BSE, EBSD	
smooth, T92 steel	180	1,642	84	SEM-BSE, hardness	
	170	2,867	78	SEM-BSE, hardness	
smooth, T92 aged at 600°C	190	169	87	SEM-BSE, hardness	
	160	2,016	82		
NTDV	310	598	27	SEM-BSE, hardness	creep damage
	260	1,568	22	SEM-BSE, hardness	
	210	4,063	8	SEM-BSE, hardness	quantification of creep damage
	190	8,199	3	SEM-BSE, EBSD	quantification of creep damage; microtexture
NTDC1.2	230	842	57	SEM-BSE, hardness	
	210	2,957	24	SEM-BSE, hardness	quantification of creep damage
	170	(14,137)	-	SEM-BSE, EBSD	quantification of creep damage; microtexture
NTDC0.6M	240	2,202	16	SEM-BSE, hardness	creep damage
	230	4,843	19	SEM-BSE, hardness	creep damage
ther-mec. prep. at 550°C	170	1,129	72	SEM-BSE, EBSD	microtexture

ther-mec. prep.-thermo-mechanically prepared

Table VII.2 : Investigated crept specimens tested at 650°C

Specimen	Load σ_n [MPa]	Lifetime t_r [h]	Z [%]	Investigation techniques	Feature of the microstructure
smooth, P92 steel	140	256	74	TEM, SEM-BSE, hardness	quantification of creep damage; size of Laves phases and $M_{23}C_6$ chemical composition of $M_{23}C_6$ Z-phases; hardness
	110	2,092	74	TEM, SEM-BSE, hardness	
	90	9,211	43	TEM, SEM-BSE, hardness	
	70	33,308	20	TEM, SEM-BSE, EBSD	
smooth, T92 aged at 650°C	110	427	80	hardness, SEM-BSE	
	95	2,392	65		creep damage
	85	4,434	43	hardness, SEM-BSE, EBSD	quantification of creep damage, microtexture
NTDV	140	1,700	6	hardness, SEM-BSE	hardness, creep damage
NTDC1.2	140	860	24	hardness, SEM-BSE	creep damage
	130	1,708	25		
ther-mec. prep. at 550°C	95	4,656	17	hardness, SEM-BSE, EBSD	quantification of creep damage; microtexture

ther-mec. prep.-thermo-mechanically prepared

In this study almost fifty creep tests were conducted at 600°C and 650°C on several kinds of specimens and eight long-term crept specimens in P92 steel were provided by SZMF, Germany. Only a few specimens were investigated after creep testing. For each

kind of specimens, investigations were conducted preferentially on the specimens with higher testing times, which was thought to be more representative for the long-term microstructural evolution and its influence on the loss of the creep strength. In tables VII.1 and VII.2 are summarized the investigated crept specimens, investigation techniques and the investigated features of the microstructure. The experimental procedure is detailed in the following section.

General remarks:

- Except when is precised, in all SEM images of specimens after creep testing (whatever notched or smooth) the **loading direction** is always horizontal
- **Bright precipitates** in all SEM-BSE images are Laves phases. Because Laves phases are enriched in W, they appear as bright precipitates in a dark matrix du to their high average atomic number.
- **Hardness measurements** were conducted with a step size of 0.25mm and a 500g load in all specimens after creep testing
- All microstructural investigations were conducted on the longitudinal section of the crept specimens after a **final** mechanical-chemical **polishing** with colloidal silica slurry.

VII.1 Experimental procedure

The microstructure of the crept specimens was investigated using TEM on extractive replicas of precipitates, SEM-BSE and EBSD. Hardness measurements were also conducted in the crept specimens.

All SEM and EBSD investigations were conducted on longitudinal cross sections of crept specimens after a final mechanical-chemical polishing with colloidal silica to reveal cavities without opening them, as chemical etching could have done. One broken part of the creep specimens was asymmetrically cut into two halves (i.e. quarters of complete specimens) by spark erosion and the half containing the specimen axis was used for metallographic examinations.

VII.1.1 Scanning Electron Microscope (SEM) investigations

VII.1.1.1 Quantification of Laves phases

SEM investigations for the quantification of Laves phases and observation of creep damage were performed using a LEO 1450 VP Scanning Electron Microscope.

Size distributions of Laves phases were determined by image analysis of SEM images in backscattered electron mode (BSE) with a magnification of $\times 2000$. Figure VII.1b represents a typical SEM-BSE image used for quantification of Laves phases and figure VII.1c shows the same SEM-BSE image after image analysis. For comparison in figure VII.1a) is also given a SEM-BSE image of the as-received P92 steel after a final colloidal silica polishing. Precipitation of Laves phases occurs during creep and/or thermal exposure, in the as-received P92 steel there are no Laves phase, thus no bright precipitates are revealed in the SEM-BSE image of the as-received P92 steel, figure VII.1a).

The BSE mode is highly sensitive to the crystallographic orientation and to the average atomic number (Z) of the probe volume. Laves phases, bright precipitates in figure VII.1b,

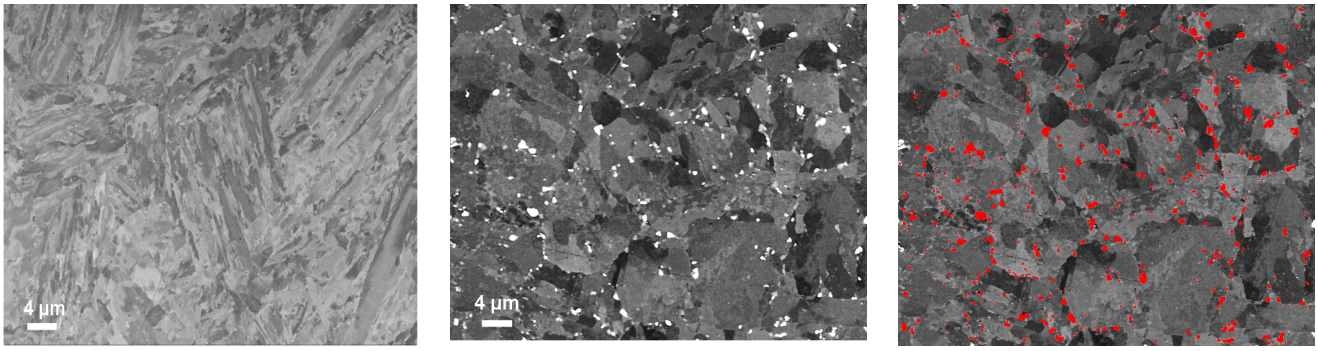

a) b) c)

Figure VII.1 : Images SEM-BSE after colloidal silica polishing showing a) microstructure of the as received P92 steel; b) microstructure of P92 steel after 33,308h of creep at 650°C, showing Laves phases as brigth precipitates; c) same as b) after image analysis, Laves phases in red

are enriched in W and clearly visible thanks to their high Z using BSE mode. $M_{23}C_6$ carbides, enriched in Cr, show a value of Z similar to that of the matrix so discrimination between Laves phases and $M_{23}C_6$ carbides was made possible using BSE mode (Dimmler et al., 2003).

Measurements of Laves phase in the gauge and head portions of crept specimens revealed no obvious difference in particles size between the two portions (Seung et al., 2006), (Panait et al., 2009). In this study SEM-BSE images for Laves phase quantification were taken only from the gauge portion.

Laves phases are relatively large particles, average diameter larger than 250 nm and for a correct evaluation of their size, SEM techniques were recommended because it allows to sample larger area, obtain more particles per image and a better statistic of measured values compared to TEM techniques (Korcakova et al., 2001).

Image analysis was performed using Matlab image processing toolbox in which an image processing treatment was implemented. For each creep specimens approximately 40 SEM-BSE images were used and thousands of particles were quantified. All the SEM-BSE images were acquired in the same operating conditions (accelerating voltage: 15kV and working distance WD=10mm). Following this procedure the minimum size of particle taken into account is of about 100nm. A lognormal distribution was adjusted to the values of the equivalent circle diameters determined from binarized images.

VII.1.1.2 Quantification of creep damage

Creep damage was quantified by analysis of SEM images in backscattered electron mode (BSE) with a magnification of ×400. Creep damage is heterogeneously distributed in the gauge part of the specimens after creep testing. Moreover the size of observed cavities varies from a few hundreds of nanometers to few micrometers. Some tests were realized in order to decide the optimum magnification of the analyzed SEM-BSE image for creep damage quantification. A magnification of ×400 was considered to reveal enough features of the creep damage and it allows to sample large areas of the investigated crept specimen.

In figure VII.2 are represented typical SEM-BSE images used for quantification of creep damage. Cavities are traps for electrons from the incident electron beam and thus they appear in black in the SEM-BSE images. Therefore an automated analysis of these images is made possible. The minimum size of cavities quantified using this procedure was of about 250 µm

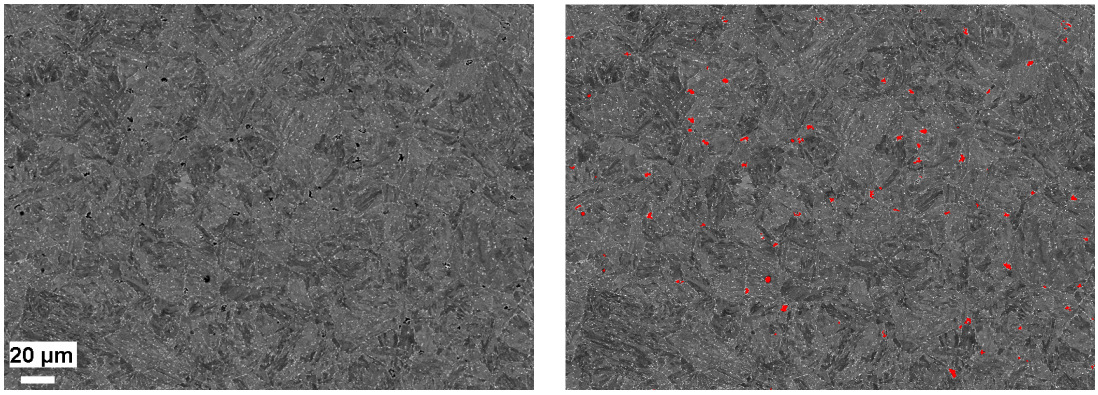

600°C; 140MPa; 22,547h (10 mm from fracture surface)

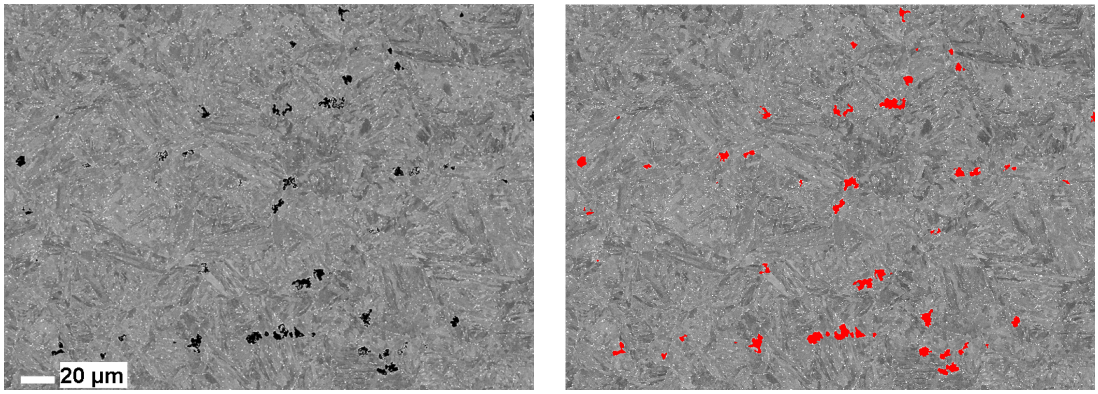

600°C 1420MPa; 49,721h (10 mm from fracture surface)

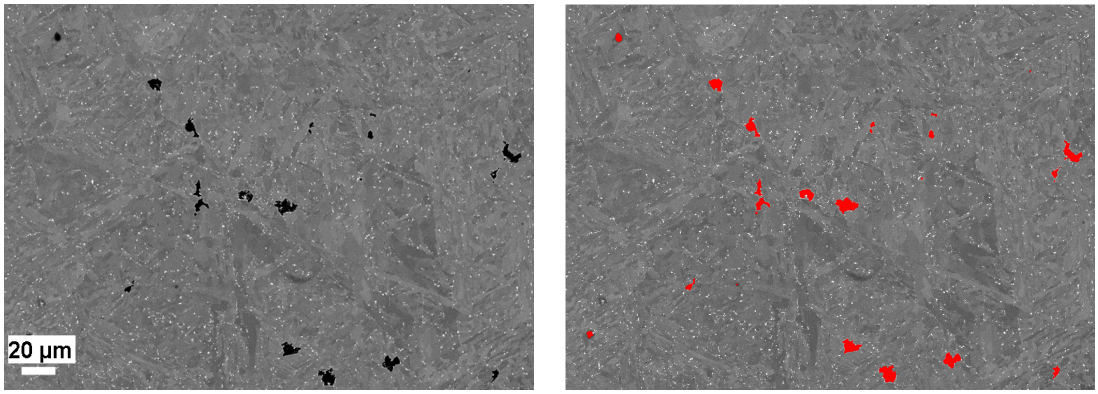

650°C; 90MPa; 9,211h (10 mm from fracture surface)

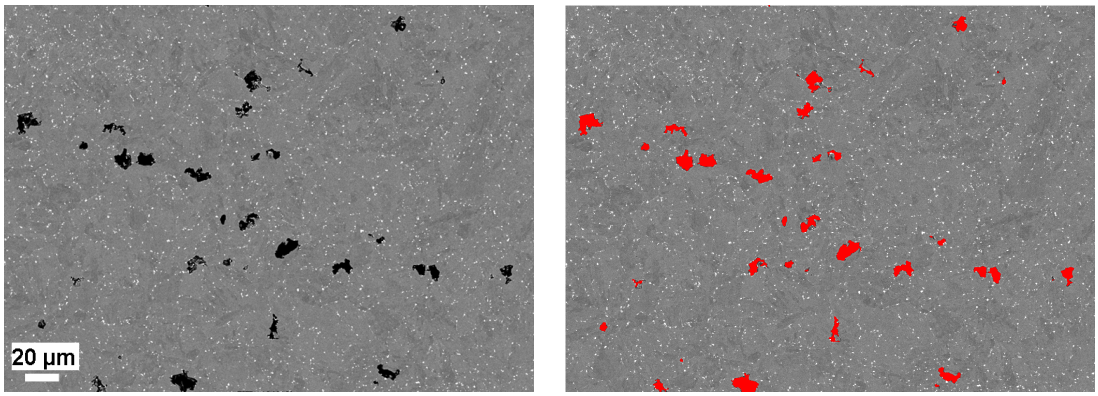

650°C; 70MPa; 33,308h (7 mm from fracture surface)

Figure VII.2 : Typical SEM-BSE images used for quantification of creep damage (left); same images after image analysis (right)

VII.1.2 Electron Backscatter Diffraction (EBSD) investigations *Characterization of the matrix substructure*

EBSD investigations were performed using a ZEISS DSM982 Gemini Scanning Electron Microscope operating with a field emission gun and equipped with an orientation imaging system (from OIM-TSL). The electron gun consists of a Shottky filament.

EBSD investigations were conducted under the following conditions: accelerating voltage 20kV, working distance 19mm, aperture 120μm, a sample tilt angle of 70°, probe current between 0.1 and 1nA.

Dedicated software allow acquisition of diffraction patterns (NORDIF 1.3.0) and their indexation (TSL OIM Data Collection 5.2). The EBSD data were then processed with TSL OIM Analysis 5.

The first map to be obtained is the *image quality* map, which reports, for each analysis, the ability of the software to detect the diffraction bands. The brighter the gray level in that map, the better the diffraction conditions. Image quality is sensitive to the crystal orientation, as well as to the *channelling effect* that yields the BSE image contrast. In addition, image quality is very sensitive to crystal defects such as dislocations. As soon as dislocations are clustered somewhere, the EBSD pattern quality decreases. Thus, the image quality map is very sensitive to the presence of boundaries, even for very low angle boundaries ($LABs$). (Tak et al., 2009) investigated the microtexture evolution of a X20 steel after long-term exposure considering a minimum misorientation angle of 1°. In our investigated samples the density of $LABs$ with a misorientation of $\sim 1°$ was so high that we were not able to distinguish *true* $LABs$ from measurements artefacts. Thus, a minimum misorientation angle of 2° was considered to process the EBSD data.

The inverse pole figure (IPF) map is colour-coded according to the orientation of a given direction of the sample in the crystal frame. The color key is recalled next to each IPF map. Note that the color is not sensitive to any rotation about that given direction of the sample, so that two IPF maps are generally needed to discriminate between grains.

In addition to IPF, one may calculate the misorientation between neighboring pixels and assign a color code to any pair of pixels whose misorientation meets a given criterion. This helps investigations whether a *boundary* imaged in the image quality maps corresponds to a high or to a low misorientation, or even to negligible misorientation between neighboring crystals. This is particularly useful to investigate subgrain boundaries. In all maps, the color code for boundaries is recalled according to the misorientation angles.

VII.1.3 Transmission Electron Microscope (TEM) investigations *Characterization of $M_{23}C_6$ carbides and modified Z phase*

TEM investigations were carried out with a FEI Tecnai F20 ST operated at 200kV, equipped with energy-dispersive X-Ray spectrometry (EDX). TEM investigations were conducted on single extractive replicas of precipitates from the homogeneusly deformed part of specimen during creep testing.

The carbon extractive replicas of precipitates were prepared by carbon coating the polished and Villela etched samples. A 1% HCl solution in ethanol was used to remove the carbon layer from the Villela etched specimens. The carbon replicas were then deposited on copper round grids.

The chemical composition of each precipitate was determined by EDX analysis in conjunction with TEM and identified as follows: $M_{23}C_6$ (enriched in Cr), Laves phase (enriched in W), modified Z phase (~50 at.% (Cr + Fe) and ~50 at.% (V+Nb)) and MX (enriched in V and/or Nb). Typical EDX-TEM spectra of $M_{23}C_6$ carbides, NbC, VN

precipitates and Laves phases were given in figures II.12 and III.5 respectively. In figure VII.3 is given a typical EDX-TEM spectrum for modified Z-phase.

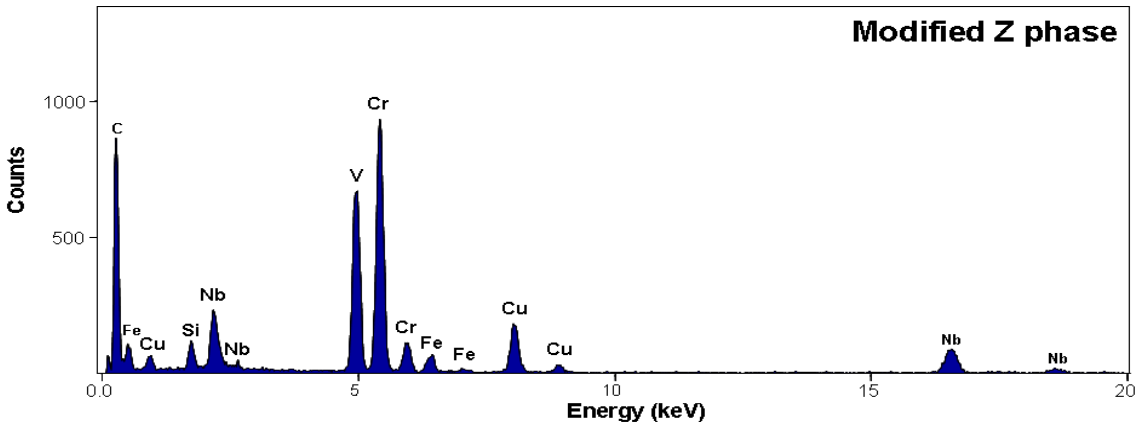

Figure VII.3 : Typical TEM-EDX spectrum for modified Z-phase obtain on an extractive replica of precipitates (P92 steel after 49,721h of creep at 600°C, 120MPa)

To get information about precipitation of modified Z phase after long term creep, TEM investigations were focused on the specimen with the longest testing time i.e. P92 steel after 49,721h of creep at 600°C and P92 steel after 33,308h of creep at 650°C.

The chemical composition of the modified Z phases in metal elements is $\sim$ 50 at.% (Fe+Cr) and $\sim$ 50 at.% (V+Nb). TEM techniques allow a high spatial resolution and a precise determination of the chemical composition of the precipitates.

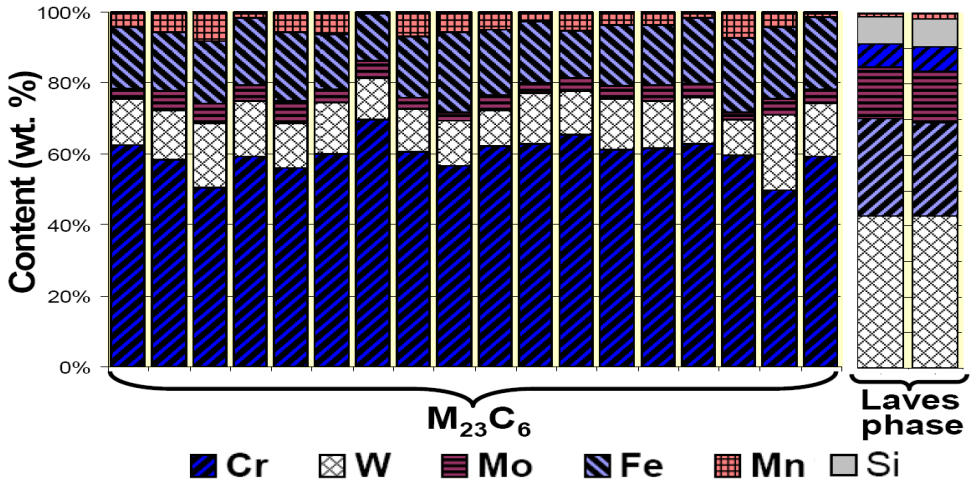

Figure VII.4 : Chemical composition of some $M_{23}C_6$ carbides and Laves phases in the P92 steel after 49,721h of creep at 600°C determined by EDX analysis coupled with TEM micrographs on extractive replicas of precipitates

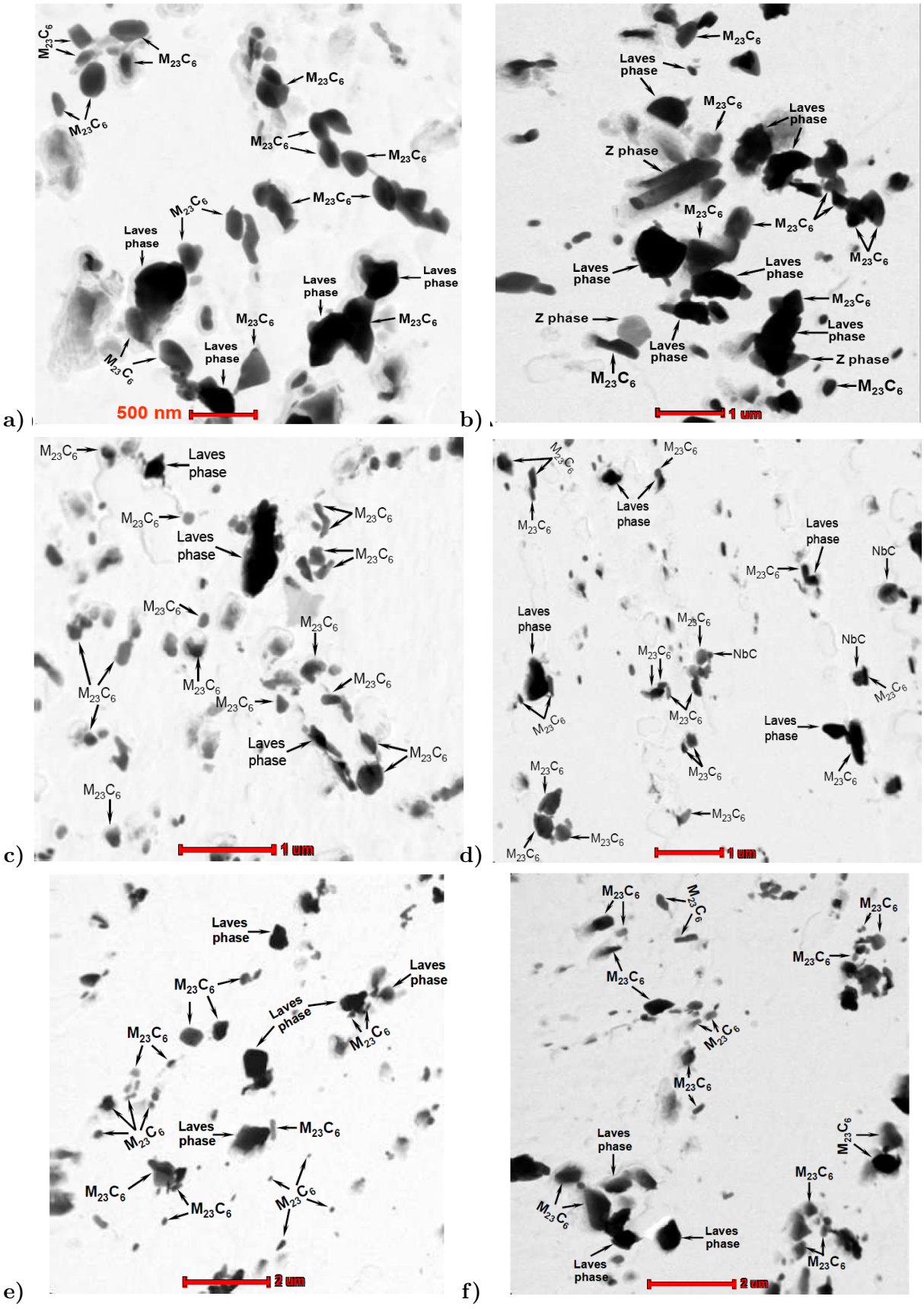

Figure VII.5 : Microstructure of P92 steel creep tested at 600°C for 49,721h (TEM micrographs on extractive replicas of precipitates)

Due to their small size (average equivalent diameter of about $\sim$ 90nm in the as-received P92 steel (Ennis et al., 1997)) TEM is best suited technique to characterize $M_{23}C_6$ carbides.

The chemical composition of precipitates in figure VII.5 was identified by EDX analysis in conjunction with TEM and identified as presentated in section VII.1.

Figure VII.4 shows the chemical composition ofsome of the precipitates corresponding to the figure VII.5 identified by EDX-TEM analysis.

VII.2 Smooth creep specimens

VII.2.1 Hardness and diameter measurements

Hardness measurements with a load of 500g were conducted along the specimen axis (of the longitudinal cross section of specimens) and the results are plotted in figures VII.6a and VII.7a. The hardness was measured both on gauge and head portion after creep rupture.

Fracture of the creep specimens does not occur in the middle of the gauge length. Only one half of specimen after fracture was provided by SZMF, Germany and the length of these P92 steel specimens was not the same for the various specimens. The diameter of the P92 steel crept specimens was measured by Laser Scan Micrometre techniques (profilometric methods) and the profile of these specimens is given in figures VII.6b and VII.7b.

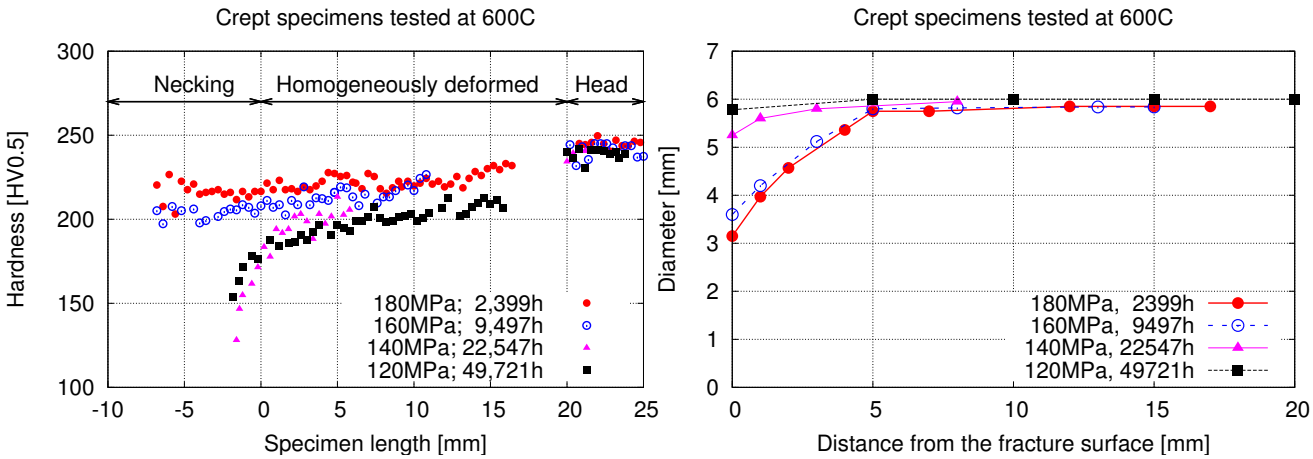

Figure VII.6 : a) Hardness along the specimen axis of creep specimens tested at 600°C; b) diameter of these half specimens

The hardness of the crept specimens is represented with respect to the necking area and the homogeneously deformed part of the specimens during creep testing, figures VII.6a and VII.7a.

Compared to the hardness of the as received P92 steel i.e. $237\pm5HV_{0.5}$, the hardness of homogeneously deformed part decreases with the increase of exposure time to creep. The decrease in hardness is higher for specimens tested at 650°C than for those tested at 600°C. This decrease in hardness can be an indication of a microstructural evolution during creep or of damage development. It was reported that recovery of the dislocation density in tempered martensitic steel during creep deformation can lead to a decrease in hardness (Sawada et al., 2005).

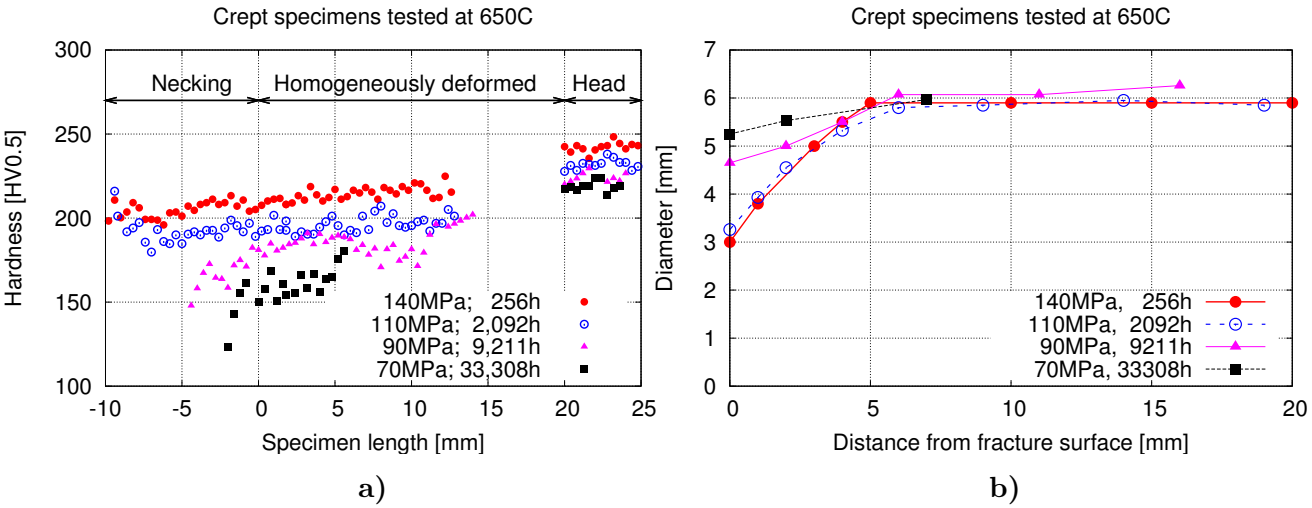

Figure VII.7 : a) Hardness along the specimen axis of specimens creep tested at 650°C; b) diameter of these half specimens

A significant decrease in hardness is observed close to fracture surface of specimens tested for long term (time higher than 10^4h) compared to that of the homogeneously deformed. This is probably due to the accelerated creep damage development under increasing stress triaxiality (i.e. after the onset of necking) during tertiary creep stage.

The head of specimens tested at 600°C show no change in hardness. A decrease in hardness is observed for the head of specimens tested for times higher than 2,000h at 650°C. This could be an indication of static recovery of the matrix and/or softening due to the precipitation of Laves phases during long-term exposure at 650°C in view the fact that heads of the specimens are not subject to significant deformation during creep testing.

This decrease in hardness for non-loaded parts of the creep specimens seems to saturate between 9,211h and 33,308h. Compared to the thermally aged T92 steel (10^4h at 600°C and 650°C) results on specimens heads of P92 steel are not surprising at 600°C (no evolution) but at 650°C the behavior of the two kinds of specimens is different (no evolution for the T92 steel, decrease by $sim15\mathrm{HV}_{0.5}$ (out of $sim40$) for P92). However, comparison between blanks thermally aged in a furnace and heads of creep specimens aged in a creep machine maybe not so obvious. Unfortunately, no specimen T92 steel creep for more than 4,480h was available. No published data concerning the hardness of tempered martensitic steel thermally aged at 650°C could be found.

In figure VII.2.1 are represented the average hardness in the homogeneously deformed part of crept specimens as a function of lifetime (t_r). The error bars represents the minimum and the maximum values of hardness corresponding to the homogeneously deformed part of various crept specimens. The following relationship could be established to describe the evolution of the average hardness during creep exposure

$$F_H(t) = h_0 - dh\left(1 - \exp\left(\frac{t}{\tau}\right)\right) \tag{VII.1}$$

where h_0 represented the hardness of the steel before creep testing ($h_0 = 235$), t is the time in hours and dh is fitting parameter. Under the assumption that creep damage decrease the

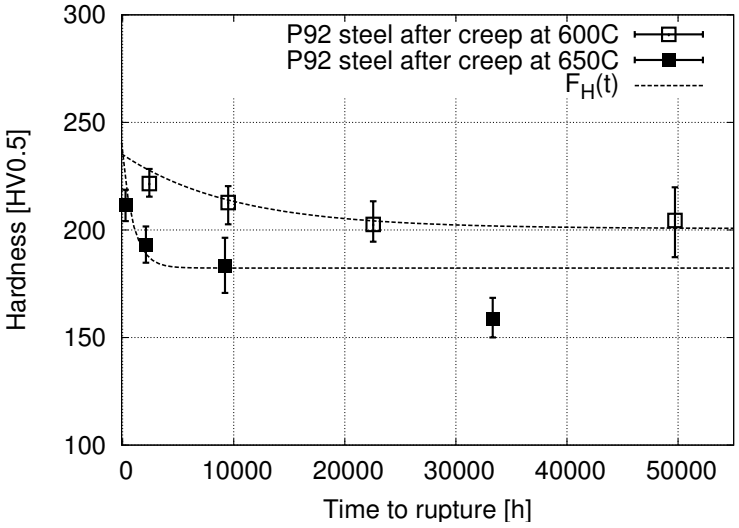

Figure VII.8 : Average hardness in the homogeneously deformed part of P92 steel crept specimens as a function of their lifetime

hardness the values of τ were set to 10,000h at 600°C and to at 650°C corresponding to the times after which creep damage is observed in crept specimens.

After adjusting the equation VII.1 to the experimental results it was found $dh = 34$ and $dh = 53$ at 600°C and 650°C, respectively.

(Masuyama, 2006) established the following relationship to describe the evolution of hardness with the creep lifetime fraction (exposure time (t) divided by the fracture time (t_r)) from interrupted creep tests :

$$\frac{H}{H_0} = 0.98 - 0.15\left(\frac{t}{t_r}\right) \tag{VII.2}$$

were H is the hardness of the crept material state and H_0 is the hardness of the initial.

The equation VII.2 could not be applied for the results obtained in this study, however this relationship was successfully applied for interrupted creep tests, see for instance (Aghajani et al., 2009b).

VII.2.2 Creep damage

VII.2.2.1 Specimens tested for short-term creep

Figure VII.9 shows SEM-SE images of the longitudinal cross section of the P92 steel specimen creep tested at 600°C under 180MPa for 2,399h. Figure VII.9 shows typical damage observed in the specimens tested for short-term creep ($t_r < 10^4$h at 600°C and $t_r < 10^3$h at 650°C). In these specimens cavities were observed only whithin the necking area close to the specimen axis. Cavities had an elongated shape along the loading direction, as can be seen in figure VII.9b,c. Cavities were not observed far from the fracture surface, more precisely whithin the homogeneously deformed part of the crept specimen.

Cavities in the short-term crept specimen appeared probably because of localized plastic deformation (necking) during the tertiary state of creep. These cavities are probably the consequence of structure instability (necking) without no effect on the creep flow of the

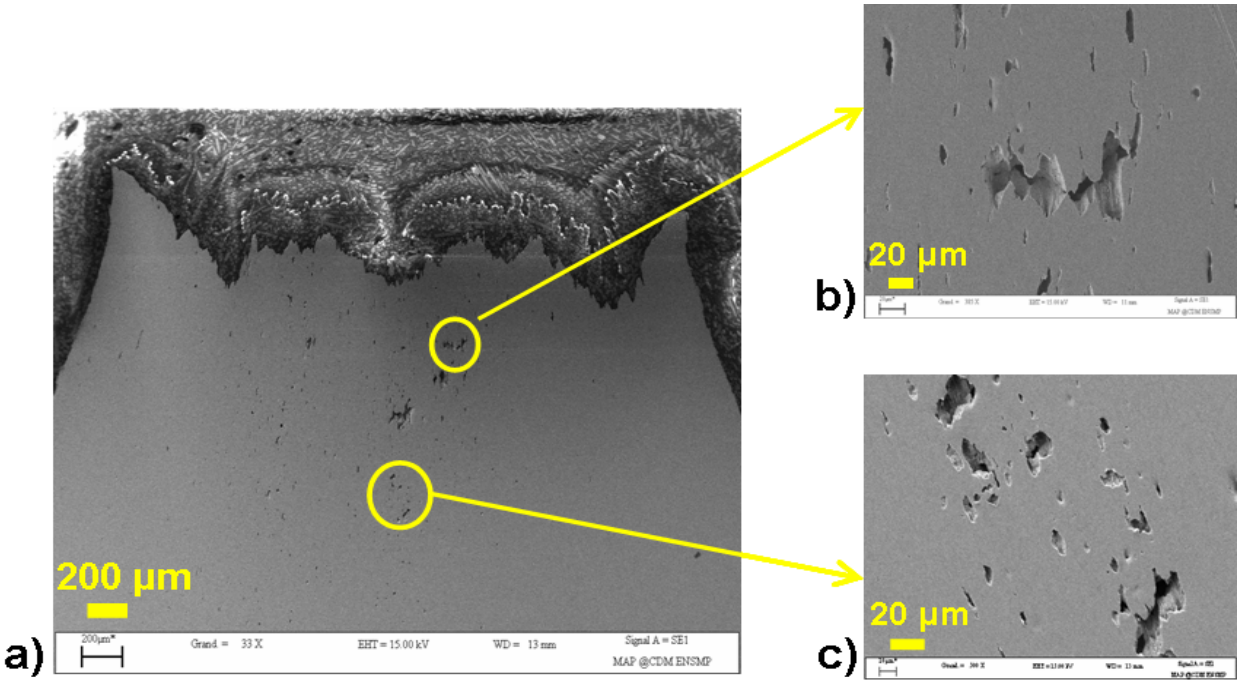

Figure VII.9 : SEM images of longitudinal cross section of P92 crept specimen tested at 600°C, 180MPa for 2,399h. The loading axis is vertical

specimen. Thus cavities in the short-term crept specimens could not really be considered as *creep damage*, but result from ductile damage processes occuring at the very end of the test.

VII.2.2.2 Specimens tested for long-term creep

The SEM images of the longitudinal cross section of P92 steel specimen tested at 600°C under 120MPa for 49,721h, in figure VII.10 are representative for the long-term creep damage.

Cavities were observed throughout the gauge portion of the specimens tested for times higher than 10^4h at 600°C and higher than 10^3h at 650°C, i.e. creep specimens showing a Norton exponent n=6, in figure V.14a and VI.12a. In figure VII.2 (left) were given SEM-BSE images showing cavities observed in the gauge portion of these specimens. As can be seen in figure VII.2 cavities are located mainly at boundaries and their size increases with testing time both at 600°C and 650°C. At higher magnification (i.e. $\times$1000, $\times$2000) small cavities of a few hundreds of nanometres in size can be observed close to some Laves phases, see figure VII.10c. However, this only observation does not prove whether if Laves phases precipitation have an influence on the creep damage development. Probably cavities nucleate at boundaries as well as Laves phases do. Because of their large size (an average diameter of about 400nm) Laves phases could enhance nucleation of cavities at boundaries. Investigation of creep damage both in a Grade 92 steel with large Laves phases before creep testing (i.e. a Grade 92 steel thermally aged for times high enough to precipitate large Laves phases) and an as-received Grade 92 steel specimen, both creep tested under same level of load and temperature could enable to study the influence of Laves phases on creep damage development.

Close to fracture surface there is a coalescence of cavities, see figure VII.10a. Far from fracture surface (i.e. homogeneously deformed part) creep damage is represented by isolated cavities located at boundaries as shown in figure VII.10c and figure VII.2.

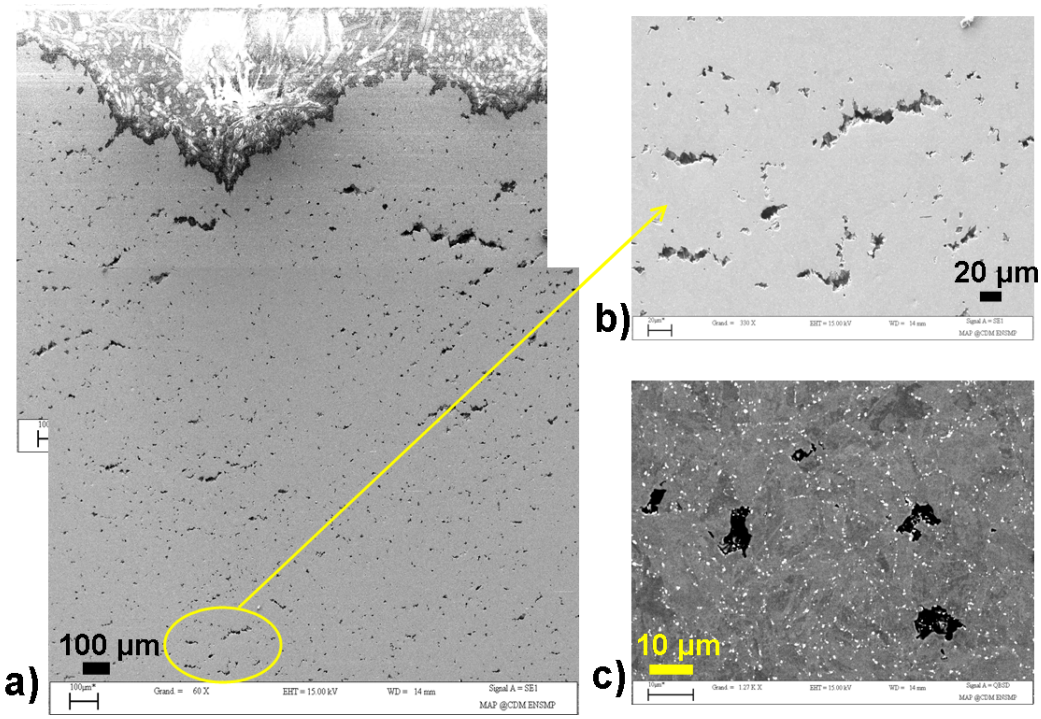

Figure VII.10 : Longitudinal cross section of P92 crept specimen tested at 600°C, 120MPa for 49,721h after a final colloidal polishing. The loading axis is vertical. a), b) SEM-SE images; c) SEM-BSE image

VII.2.2.3 Quantification of creep damage

Creep damage was quantified as the number of cavities and the area fraction of cavities in all above mentioned P92 steel specimens after creep testing at 600°C and 650°C. The experimental procedure of creep damage quantification was presented in section VII.1.

In figures VII.11a and VII.12a are represented the average number of cavities determined on areas of 270 µm × 210 µm on each P92 steel crept specimens at several distances from fracture surface. Error bars in figures VII.11a and VII.12a correspond to the lowest and the highest number of cavities on areas of 270 µm × 210 µm.

Figures VII.11b and VII.12b show the porosity, i.e. area fraction of cavities in the P92 steel specimens creep tested. The porosity was estimated as the ratio between the surface area of cavities and the size of investigated area (i.e. 270 µm × 210 µm).

In figures VII.11 and VII.12 zero specimen length means the beginning of the homogeneously deformed part of the crept specimens; negative values indicate the necking part of the specimen. For the specimens tested for short-term creep ($t_r < 10^4$h) the necking part is clearly visible; for specimens tested for long-term ($t_r > 10^4$h) creep, which show a low reduction of area (see tables V.2 and VI.2) the necking part was chosen arbitrary as up to 1 mm away from fracture surface, which is much larger than the length observed on the specimen section by light microscopy and by profilometric measurements.

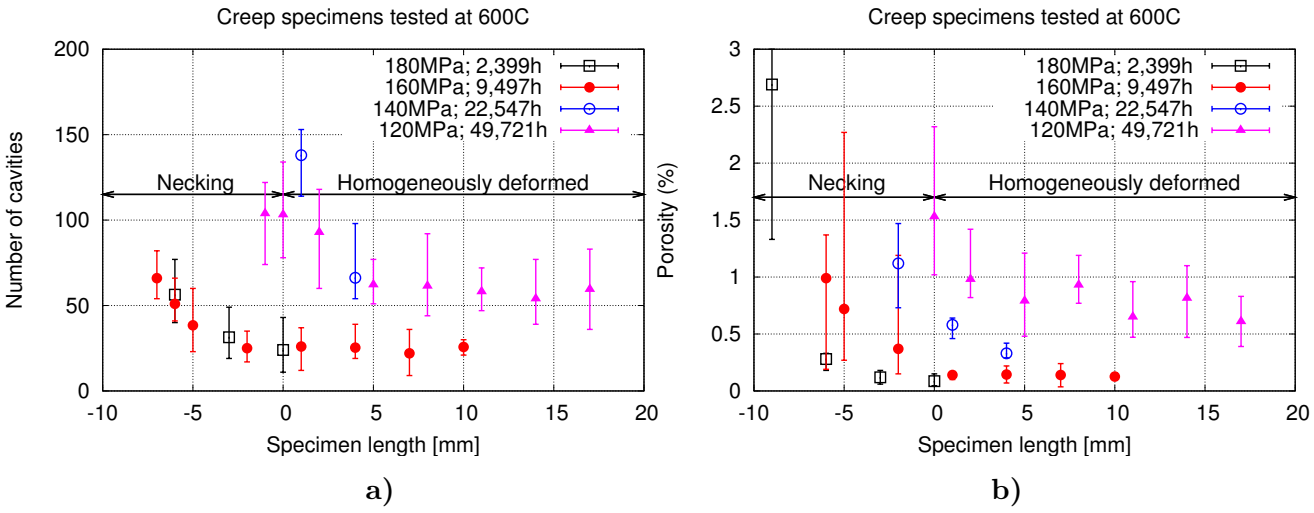

Figure VII.11 : Number (a) and area fraction (b) of cavities measured on areas of 270 µm × 210 µm by image analysis of SEM-BSE micrographs on creep specimens tested at 600°C

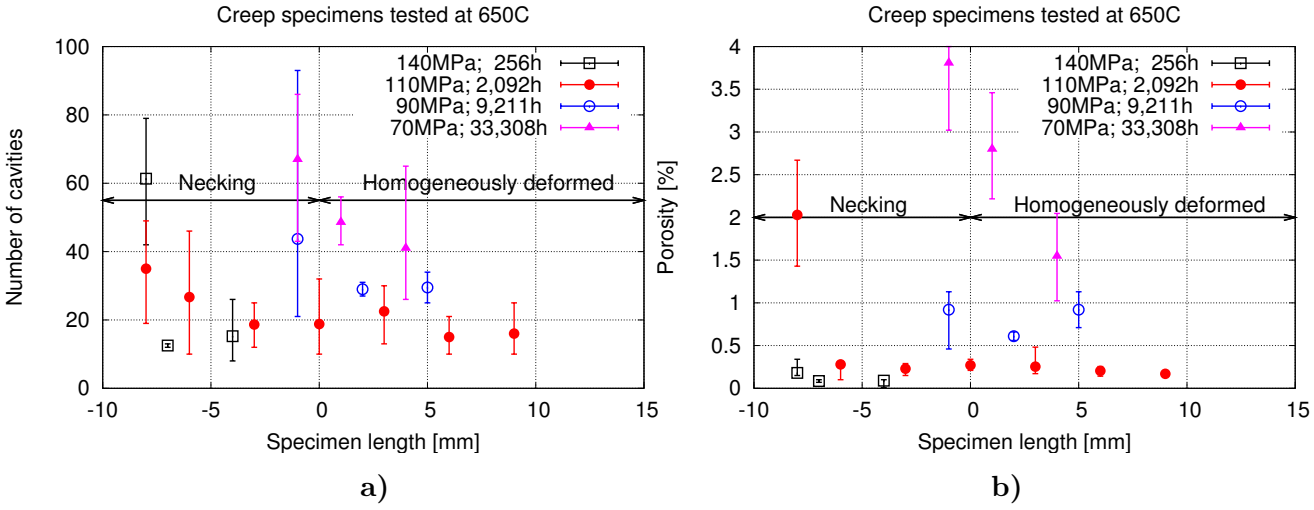

Figure VII.12 : Number (a) and area fraction (b) of cavities measured on areas of 270 µm × 210 µm by image analysis of SEM-BSE micrographs on creep specimens tested at 650°C

Fracture of the crept specimens does not occur in the middle of their gauge length, thus the length of the crept specimens available for microstructural investigations is variable. The profile (diameter along the specimens length) of these specimens was given in figures VII.6b and VII.7b. This is why in figures VII.11 and VII.12 experimental results for some specimens are given on a smaller length compared to the other specimens.

No cavitie was observed at a magnification of ×400 and higher on the gauge length of the creep specimens tested at 600°C for 2,399h and tested at 650°C for 256h. Cavities in the necking area of these specimens were quantified and the results are represented in figures VII.11 and VII.12.

As can be seen in figures VII.11a and VII.12a, the number of cavities increases with exposure time to creep both at 600°C and 650°C. This may suggest that nucleation of cavities

could have occured by diffusion-assisted mechanisms, which are enhanced by high temperature and involve long-term exposition to significantly affect the creep strength. Moreover, the number of cavities in the creep specimen tested for almost 10^4h at 600°C is similar to that of the specimen tested for almost 10^4h at 650°C. In this case, temperature seems not to have a significant influence on the early developement of cavities for a given creep lifetime.

On the homogeneously deformed part of the specimens the number of cavities and porosity is almost constant. Close to fracture surface, more precisely on the necking area of the specimens the number of cavities and the porosity are higher then in homogeneously deformed part, indicating that stress triaxiality due to necking of the specimens in the tertiary creep stage enhance nucleation and growth of cavities.

The area fraction of cavities (i.e. porosity) is higher in the creep specimens tested at 650°C compared to those tested at 600°C for similar times, indicating that temperature enhance growth of cavities for a given creep lifetime.

In the homogeneously deformed part of the specimens tested for long-term creep, the size of observed cavities goes from a few hundred nanometers to 5μm. The presence of small cavities in all the long-term crept specimens could be an indication of a continuous nucleation of cavities. An average equivalent diameter (EqD) of cavities was estimated on areas of 270 µm × 210 µm and revealed values from 1.2 µm to 2 µm in the specimens tested at 600°C for 9,497h and 22,547h and values between 2 µm to 3.2 µm in the specimen tested for 49,721h at 600°C. Higher values were found in specimens tested at 650°C. The average EqD of cavities varies from 2 µm to 3 µm in the specimen tested for 2,092h; from 3 µm to 4 µm in the specimen tested for 9,211h and from 3 µm to 5 µm in the specimen tested for 33,308h.

Nucleation and growth of cavities observed in long-term crept specimens could cause a premature failure of these specimens. This explains why the lifetime of the long-term crept specimens is surestimated using the same methods as for short-term crept specimens. Thus creep damage development should be integrated in models to better estimate the creep strength after long-term creep exposure.

VII.2.3 Microstructural evolution after long term creep exposure at 600°C and 650°C

During creep due to thermal exposure at high temperatures there is a microstructural evolution of the steel which could degrade its mechanical properties such as creep strength. Precipitation of new phases such as Laves phases and modified Z phases, growth of precipitates and recovery of the matrix are the main microstructural evolution mechanisms in the 9-12% Cr tempred martensitic steels during creep/thermal exposure at 600°C and 650°C.

VII.2.3.1 $M_{23}C_6$ carbides (TEM investigations)

a) Size of $M_{23}C_6$ carbides after creep at 600°C and 650°C

Figure VII.13 shows the size distribution of carbides identified using EDX analysis coupled with TEM on extractive replicas of precipitates. The equivalent circle diameter (E_qD) was measured from TEM micrographs using the $ImageJ$ software.

For each crept specimen an average E_qD of $M_{23}C_6$ carbides was calculated and reported in table VII.3. The measurement errors in table VII.3 were estimated using the formula VII.3 which corresponds to 95% confidence interval for an expected normal distribution. The formula VII.3 was already used in quantitative microstructural studies by (Gustafson and Hättestrand, 2002), (Korcakova et al., 2001).

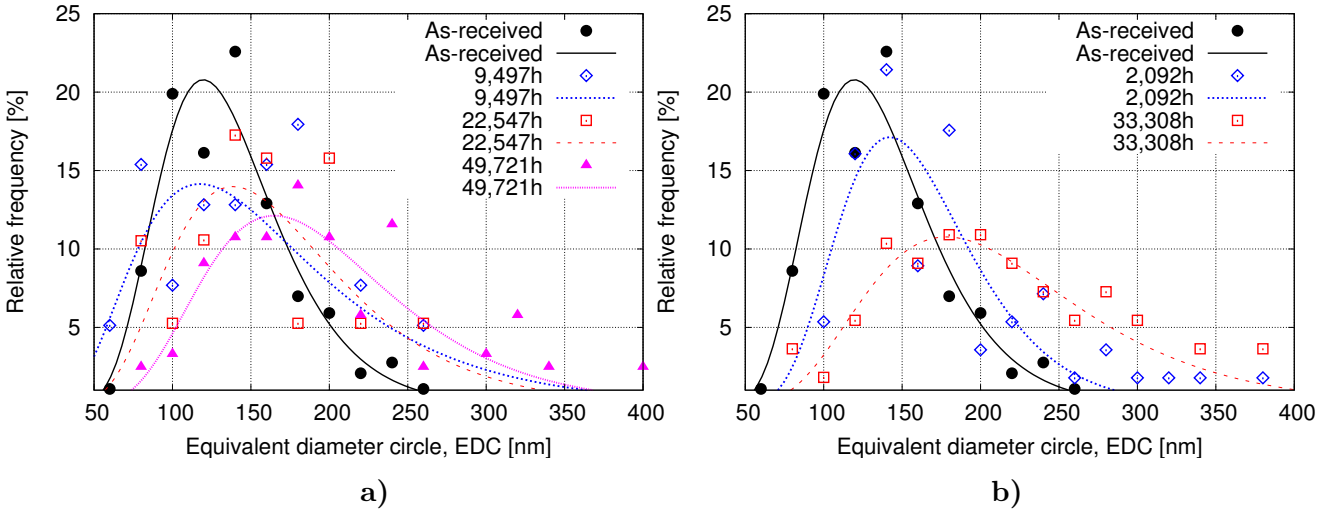

Figure VII.13 : Size distribution of $M_{23}C_6$ carbides after creep exposure at 600°C (a) and 650°C (b). Experimental results (symbols) compared with a lognormal fit (lines)

$$d \pm k_1 s \tag{VII.3}$$

where d is the diameter, $k_1 = 1.96\sqrt{n}$ with n the number of particles and s is the standard deviation.

Table VII.3 : Equivalent diameter of $M_{23}C_6$ carbides after creep exposure at 600°C and 650°C

Temp. [°C]	Time t_r[h]	Diameter [nm]	Number of precipitates
As-received		127±6	185
600	9,497	134±15	43
600	22,547	141±20	23
600	49,721	208±16	124
650	2,092	187±23	59
650	33,308	207±22	58

The average E_qD of $M_{23}C_6$ carbides increases from 127 nm in the as received conditions up to about 208 nm after almost 50,000h of creep exposure at 600°C. Similar E_qD of $M_{23}C_6$ carbides is observed after 33,308h of creep exposure at 650°C.

The growth of $M_{23}C_6$ carbides during creep exposure was modeled on the basis of the Ostwald ripening equation (Ostwald, 1896), (Ratke and Voorhees, 2002):

$$d^3 = d_0^3 + K_d t \tag{VII.4}$$

where d is the diameter; d_0 is the initial diameter; K_d is a growth rate and t is time.

The symbols and error bars in figure VII.14 correspond to the results given in table VII.3 and the curves represents the adjusted Ostwald equation (VII.4). It was found $K_d =$

0.94×10^{-29} m^3/s and $K_d = 5.89 \times 10^{-29}$ m^3/s for the growth of $M_{23}C_6$ carbides at 600°C and 650°C respectively.

The Ostwald equation (VII.4) is often used to model the growth of precipitates during creep/thermal exposure. (Aghajani et al., 2009b) found a $K_d = 1.37 \times 10^{-29}$ m^3/s for the growth of $M_{23}C_6$ carbides in a 12%Cr steel (German grade X20) during almost 140,000h of creep exposure at 550°C.

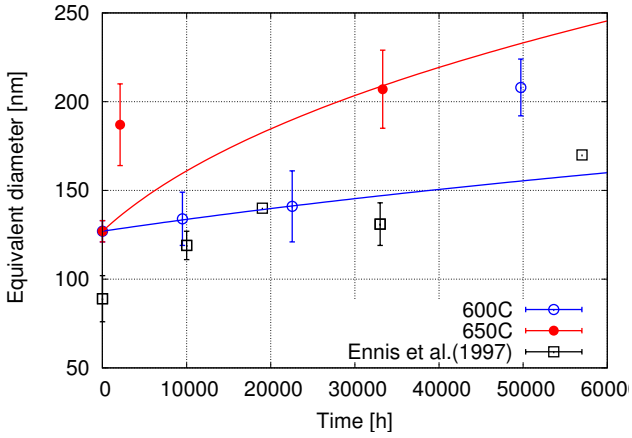

Figure VII.14 : Average equivalent diameter of $M_{23}C_6$ carbides during creep exposure at 600°C and 650°C

In figure VII.14 are also represented the values of E_qD of $M_{23}C_6$ carbides in a P92 steel during creep exposure at 600°C, published by Ennis in several studies (Ennis et al., 1997), (Ennis and Czyrska-Filemonowicz, 2002). The chemical composition and the heat treatment of the P92 steel studied by Ennis were (wt.%) 0.124C-0.02Si-0.47Mn-0.011P-0.006P-9.07Cr-0.46Mo-1.78W-0.19V-0.063Nb-0.003B-0.043N-0.06Ni-0.002Al; 2h/1070°C+12h/775°C air cooling.

The sizes of $M_{23}C_6$ carbides during exposure at 600°C found in this study are higher than those published by (Ennis et al., 1997). This is probably due to a sampling effect. The main purpose of TEM investigations was to study the modified Z phase precipitation in the P92 steel during long-term creep exposure at 600°C and 650°C. Thus the EDX-TEM analysis were focused on large precipitates (equivalent diameter higher than 100nm). This could have lead to overestimate the size of $M_{23}C_6$ carbides after creep.

b) Chemical composition of $M_{23}C_6$ carbides after creep at 600°C and 650°C

TEM investigations revealed a change in the average chemical composition of $M_{23}C_6$ carbides. The Cr content increases from about 60 at.% in the as received conditions to 70 at.% after 49,721h of creep exposure at 600°C and the Fe content decreases from about 30 at.% to 20 at.% after 49,721h at 600°C. Similar change in the average chemical composition of $M_{23}C_6$ carbides is observed after exposure at 650°C. Table VII.4 summarizes the results of EDX analysis conducted on $M_{23}C_6$ carbides after several times exposure to creep at 600°C and 650°C.

In figure VII.15 are represented the results corresponding to table VII.4. The error bars in figure VII.15 represents the minimum and the maximum values from table VII.4.

Table VII.4 : Average chemical composition of $M_{23}C_6$ carbides (EDX-STEM analysis of single carbon replicas)

Creep conditions		Cr [at.%]	W [at.%]	Mo [at.%]	Fe [at.%]	Mn [at.%]	V [at.%]	Number of precipitates
P92 steel as received	min	42.87	1.34	0	21.62	0	0	185
	average	**61.84**	**3.85**	**2.24**	**27.98**	**3.79**	**0.30**	
	max	70.75	7.63	5.47	46.278	8.28	1.03	
	st. deviation	4.58	1.12	1.15	3.09	2.76	0.29	
9,497h; 160MPa; 600°C	min	56.27	2.74	0	16.29	0	0	43
	average	**64.34**	**4.68**	**2.48**	**23.52**	**4.43**	**0.56**	
	max	72.94	6.61	7.12	34.75	7.83	4.00	
	st. deviation	3.26	0.90	1.41	3.34	2.53	0.67	
22,547h; 140MPa; 600°C	min	59,.1	2.85	0.79	16.67	0	0	23
	average	**67.65**	**4.20**	**2.45**	**21.01**	**4.25**	**0.45**	
	max	75,25	5,76	5,71	25,61	7,64	1,46	
	st. deviation	4,54	0,82	1,16	2,08	2,80	0,45	
49,721h; 120MPa; 600°C	min	61.01	1.94	0	11.04	0	0	124
	average	**72.33**	**4.04**	**2.30**	**17.42**	**3.79**	**0.11**	
	max	80.91	7.66	6.75	23.98	9.33	1.04	
	st. deviation	4.36	0.94	0.98	2.52	2.81	0.21	
2,092h; 110MPa; 650°C	min	59.10	1.25	0	15.46	0.17	0	59
	average	**68.29**	**3.82**	**2.08**	**20.95**	**4.54**	**0.32**	
	max	75.26	7.50	6.19	28.58	9.78	1.39	
	st. deviation	3.66	1.13	1.23	2.74	2.91	0.36	
33,308h; 70MPa; 650°C	min	65.56	1.85	1.23	16.08	0.33	0	58
	average	**71.68**	**3.85**	**2.24**	**17.83**	**4.01**	**0.39**	
	max	77.92	6.27	4.14	22.97	7.71	5.39	
	st. deviation	3.13	0.84	0.70	1.58	2.36	0.90	

In this study TEM investigations were conducted on extractive replicas of precipitates from the homogeneously deformed part of the specimen during creep testing. The same change in the average chemical composition of $M_{23}C_6$ carbides might have occurred during thermal exposure. An increase in the Cr content from about 65 at. % to about 70 at.% was reported by (Ghassemi-Armaki et al., 2009) after 10^4h of thermal ageing at 650°C in a 9% Cr tempered martensitic steel (wt.% 0.097C-0.25Si-0.52Mn-0.010P-0.87Cu-0.31Ni-9Cr-0.39Mo-0.2-1.87W-0.052Nb-0.054N) with a similar chemical composition as the Grade 92 steel.

The change in the average chemical composition of $M_{23}C_6$ carbides probably does not have a direct consequence on the loss of creep strength. This is an indication of the microstructural instability of P92 steel during exposure at 600°C and 650°C.

VII.2.3.2 Laves phases (SEM investigations)

Figure VII.16 shows the size distribution of Laves phases after creep exposure at 600°C (a) and 650°C (b) determined by image analysis of SEM-BSE images.

An average equivalent diameter (E_qD) of about 200 nm is observed after almost 10^4h of creep exposure at 600°C. For higher exposure times at 600°C the average E_qD increases slightly, see figure VII.16a. After 10^4h of exposure at 600°C, the frequency of large Laves

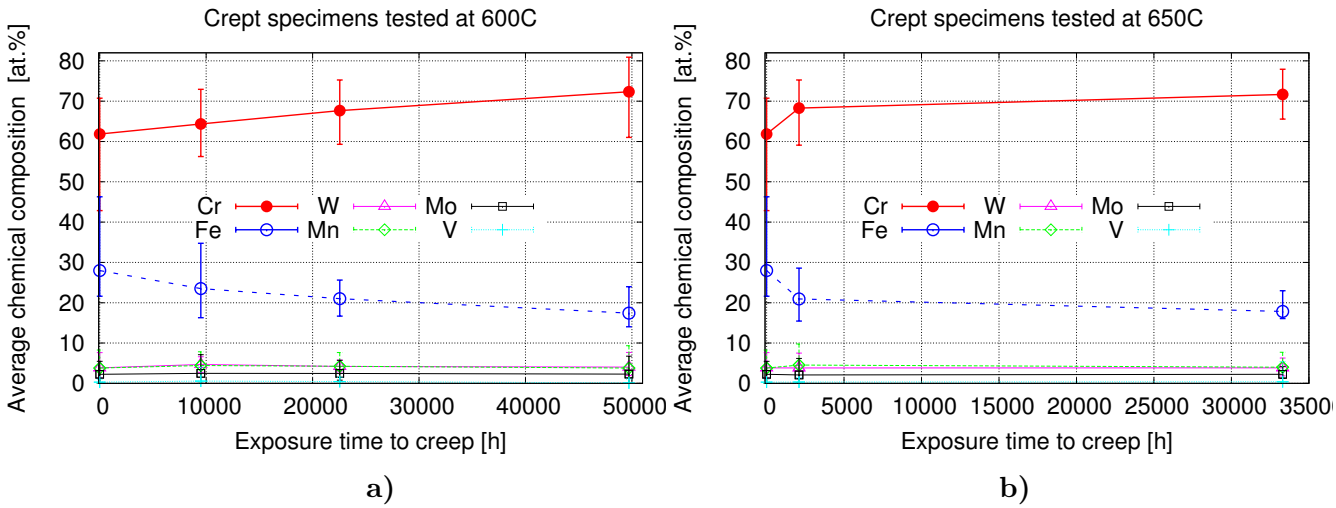

Figure VII.15 : Average chemical composition of $M_{23}C_6$ carbides in the P92 steel during creep exposure at 600°C (a) and 650°C (b)

phases increases. Image analysis was processed on about forty SEM-BSE images for each specimen, the number of Laves phases decreases significantly in the specimen tested for 49,721h which may probably suggest a coalescence of these phases.

Temperature enhances precipitation of Laves phases. An average E_qD of about 250 nm is observed after only 2,000h of creep exposure at 650°C. The average E_qD increases to 350 nm after almost 10^4h creep exposure at 650°C and no significant evolution occurs for longer exposure times.

The significant precipitation and growth of Laves phases in the first 10^4h of exposure both at 600°C and 650°C, followed by a slight growth for longer exposure times were also reported by previous studies (Dimmler et al., 2003), (Korcakova et al., 2001).

In figure VII.17 is represented the evolution of the average equivalent diameter (EqD) of Laves phases in the P92 steel during creep exposure at 600°C and 650°C. For each crept specimens the diameter of Laves phases with the highest frequency in figure VII.16 was considered as the average EqD in figure VII.17.

Considering $d_0 = 0$ in the Ostwald ripening equation (VII.4) a growth rate $K_d = 15.44 \times 10^{-29}\text{m}^3/\text{s}$ is found for the growth of Laves phases during exposure at 600°C. This growth rate is more than ten times higher than that found for the growth of $M_{23}C_6$ carbides (i.e. $K_d = 0.89 \times 10^{-29}\text{m}^3/\text{s}$) during exposure at 600°C.

Considering $d_0 = 0$, the growth of Laves phases during exposure at 650°C can be modeled using Ostwald ripening equation. It is to be mentioned that the Ostwald ripening equation describes the growth of precipitates prior existing in the material before thermal exposure. There are no Laves phases in the P92 steel before creep/thermal exposure (i.e. in the as-received conditions). A relatively good adjustment is found for the growth of Laves phases during exposure at 650°C using the Ostwald ripening equation in the form (VII.5)

$$d^3 = d_0^3 + K_d\,(t - t_0) \tag{VII.5}$$

where d and d_0 are respectively the average diameters at time t and t_0; K_d is a growth rate.

Considering $d_0 = 275$ nm which corresponds to the average equivalent diameter of Laves phases in the P92 steel creep tested for 2,092h and $t_0 = 2,092$h in the equation VII.5 a

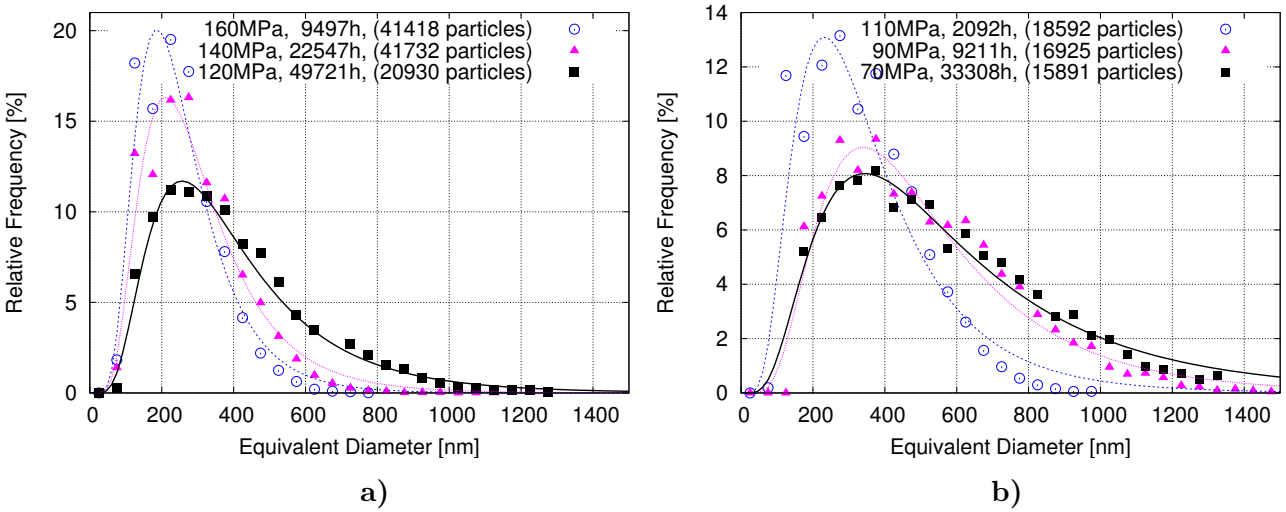

Figure VII.16 : Equivalent diameter of Laves phases after creep exposure at 600°C (a) and 650°C (b). Symbols-experimental results; lines-lognormal fit

$K_d = 34.28 \times 10^{-29}\mathrm{m}^3/\mathrm{s}$ is found. Thus, this K_d can be interpreted as the growth rate of Laves phases during exposure at 650°C after a prior exposure time of about 2,000h. The growth rate of Laves phases during exposure at 650°C is found to be almost six times higher than that found for the growth of $M_{23}C_6$ carbides (i.e. $K_d = 5.89 \times 10^{-29}\mathrm{m}^3/\mathrm{s}$) during exposure at same temperature.

An average area fraction of Laves phases was considered as the fraction between the number of pixels representing Laves phases and the total number of pixels of the number of pixels of the binarized SEM-BSE image. Nevertheless the values of area fraction estimated in this manner should be regarded with caution because they depend on the magnification of the SEM-BSE image. For example (Dimmler et al., 2003) reported an area fraction of Laves phases of 1% for the NF616 steel (Japanese denomination of Grade 92 steel) after 10^4h of creep exposure at 650°C, estimated by images analysis of SEM-BSE with a magnification of ×25000. In this study the quantification of Laves phases was determined from SEM-BSE images with a magnification of ×2000 only.

(Gustafson and Hättestrand, 2002) estimated an area fraction of Laves phases from the amount of W still in the matrix (measured by APFIM techniques) after thermal exposure at 600°C and 650°C. This should be more reliable for the estimation of area fraction of Laves phases. The results of (Gustafson and Hättestrand, 2002) were given in chapter I of this thesis.

The symbols in figure VII.18 represent the average area fraction of Laves phases and the errors bars represent the minimum and the maximum values of the area fraction of Laves phases estimated on areas of 54 µm × 40 µm.

A Johnson-Mehl-Avrami (JMA) (Avrami, 1939), (Avrami, 1940), (Avrami, 1941) equation type (VII.6) was used to describe the time dependence of the area fraction of Laves phases after creep exposure.

$$f(t) = C_{JMA}\left(1 - \exp\left(-\left(\frac{t}{t_0}\right)^n\right)\right) \tag{VII.6}$$

where $f(t)$ is the area fraction; t is the time; t_0 and n are constants depending on temperature.

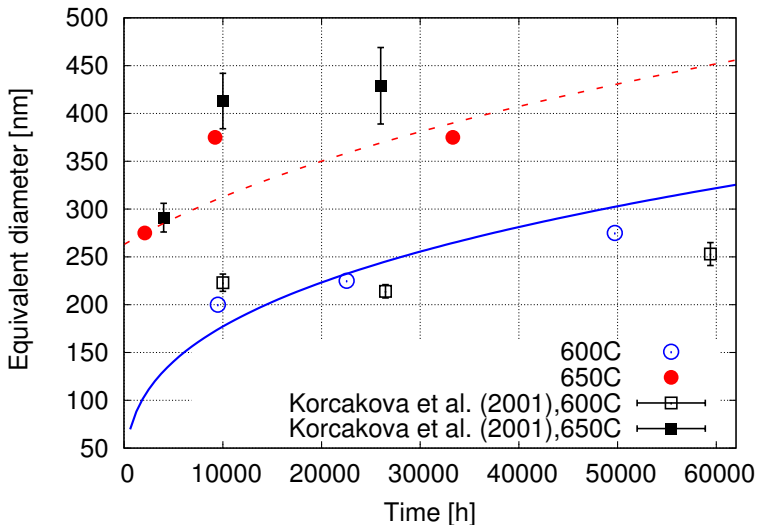

Figure VII.17 : Average equivalent diameter of Laves phases in the P92 steel during creep exposure at 600°C. Experimental results (symbols) adjusted with a Ostwald ripening equation (lines)

A time exponent $n = 3/2$ is often interpreted as describing an one-time nucleation process followed by growth of a constant number of precipitates (Dimmler et al., 2003). Based on the study of (Dimmler et al., 2003), the time exponent in equation VII.6 was set to 3/2. Adjusting the equation VII.6 to experimental results in figure VII.18, a $t_0 = 7,107$h ($C_{JMA} = 2.4$) and $t_0 = 1,946$h ($C_{JMA} = 3.1$) were found for the surface fraction evolution of Laves phases during exposure at 600°C and 650°C, respectively.

VII.2.3.3 Modified Z-phase (TEM investigations)

As precised previously, the main purpose of the TEM investigations, conducted on carbon extractive replicas, was to study the precipitation of Z-phase during long-term creep exposure in 9% Cr tempered martensitic steels.

Previous studies reported that the precipitation of Z-phase is lower in the 9% Cr steel compared to that in 12% Cr steels (Danielsen and Hald, 2007), (Sawada et al., 2007), (Yoshizawa et al., 2009). Nevertheless the precipitation of this phase in 9% Cr steel was only investigated for testing times lower than 50,000h and only few quantitative data were reported. Thus TEM investigations were focused on the 9% Cr steel creep specimens with the longest testing times, namely, P92 steel, 49,721h of creep at 600°C. Low amounts of Z-phase were observed in this specimen with respect to the total number of the investigated precipitates or to the size of the investigated area. Amongs 600 investigated precipitates only 6 particles were identified to be modified Z-phases. The observed modified Z-phases are widelly spaced particles; thus, a density number i.e. a ratio between number of Z-phases reported to the size of the investigated area could not be relevant. The observed Z-phases have an average equivalent diameter of about 400 nm.

VII.2.3.4 Matrix substructure evolution (EBSD investigations)

The degradation of tempered martensite features (i.e. sugrains size, lath width) during long-term creep as well as their impact on the creep strength are not fully understood. During creep exposure there is an interaction between the mobile dislocations inside lath subgrains and

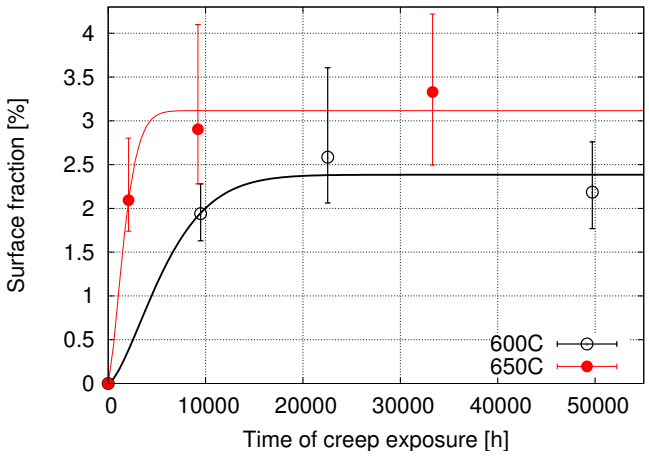

Figure VII.18 : Area fraction of Laves phases after creep exposure at 600°C and 650°C. Experimental results (symbols) compared with an adjusted Johnson-Mehl-Avrami (JMA) equation VII.6

subgrains boundaries leading to an increase in subgrains size. A decrease in the initial high dislocation density inside subgrains occurs during creep exposure at 550°C-650°C (Aghajani et al., 2009b), (Pešička et al., 2010), (Blum and Götz, 1999).

However data on the matrix substructure of the Grade 92 steel after long-term creep exposure at 600°C and 650°C is scarcely. Thus the matrix substructure of the P92 steel specimens creep tested at 600°C for 49,721h and at 650°C for 33,308h were characterized using EBSD techniques.

EBSD investigations conducted on the as-received P92 steel (from the same pipe as the P92 steel crept specimens) revealed similar EBSD maps and similar histogram of misorientation angles of boundaries to those for the as-received T92 steel. In the following the EBSD maps of the as-received T92 steel, given in figure II.9, were considered for comparisons with EBSD results obtained in the specimens creep tested.

An extensive study of the microtexture before and after creep exposure both at 600°C and 650°C was conducted using EBSD techniques. Various EBSD maps were acquired with various step size and at various distances from fracture surface of crept specimens.

It is to be mentioned that comparing EBSD maps, the changes in the microtexture during creep can be only qualitatively evaluated. In order to study any onset of recrystallization an advanced processing of EBSD data was realized to identify the boundaries respecting the well-known orientation relationships between austenite and martensite (i.e Kurdjumov and Sachs (K-S) relationships (Kurdjumov and Khachaturyan, 1975), Greninger-Troiano (G-T) relations). A good identification of boundaries respecting the K-S relationships or G-T relationships could reveal new grains formed during creep deformation. Note that N-W or G-T relationships does not allow a full characterisation of boundaries, combined models allow a higher accuracy description of boundaries, because they are not strictly obeyed in martensitic stell microstructures.

a) P92 steel after 49,721h of creep at 600°C

EBSD maps

The EBSD-IQ maps and the corresponding SEM-BSE image in figure VII.19 taken at

2 mm away from the fracture surface in the P92 steel specimen creep tested for 49,721h at 600°C reveals some small round-shaped grains (arrowed in figure VII.19a and c) which are not clearly observed in the EBSD maps of the as-received steel (figure II.9). These grains do not have a specific crystal orientation in the corresponding EBSD-IPF map. Thus they cannot be considered as an indication of a possible recrystallization process during creep. These features could be i) martensite packets cut by sample preparation or ii) subgrains inside martensite laths.

The EBSD map of figure VII.19 were acquired at 2 mm from the fracture surface of the crept specimen, thus the stress triaxiality or accelerated creep damage development preceding specimen fracture could have enhached evolution of the microtexture. In order to get representative data on the microtexture of the P92 steel during long-term creep at 600°C, EBSD maps were acquired at 15 mm from fracture surface of this crept specimen.

EBSD maps acquired at 15 mm from the fracture surface and on the head of the 49,721h crept specimen revealed no significant difference compared to the EBSD maps of the as-received P/T92 steel. The corresponding histograms of misorientation angles of boundaries of these EBSD maps show a typical distribution between martensite variants.

High angle boundaries

Figure VII.21 shows that G-T relationships describe a higher amount of boundaries (i.e. block, some packet and former austenite grain boundaries) compared to the K-S relationships considering the same EBSD map.

Table VII.5 summarizes the analysis of boundaries coresponding to the K-S and the G-T relationships in various EBSD maps of the as-received steel and the P92 steel specimen crept for 49,721h. No significant change was observed in the area fraction of boundaries coresponding to the K-S and the G-T relationships after long-term creep exposure at 600°C (i.e 15mm from the fracture surface and head of the crept specimen) compared to that of the as-received steel, see table VII.5.

In table VII.6 are represented the fraction of boundaries revealed on various EBSD maps of P92 steel after 49,721h of creep at 600°C. The EBSD maps given in figures VII.19 and VII.20 are representative for the EBSD maps considered in table VII.6.

EBSD maps acquired at 2 mm from the fracture surface of the crept specimen for 49,721h revealed a decrease in the fraction of boundaries with a rotation angle 2°-5° and an increase in the boundaries of 15°-180°, compared to these of the as-received steel. The EBSD maps acquired at 15 mm from fracture surface of this specimen revealed a slight increase of boundaries of 2°-5° and a slight decrease in fraction of boundaries of 15°-180°, table VII.6.

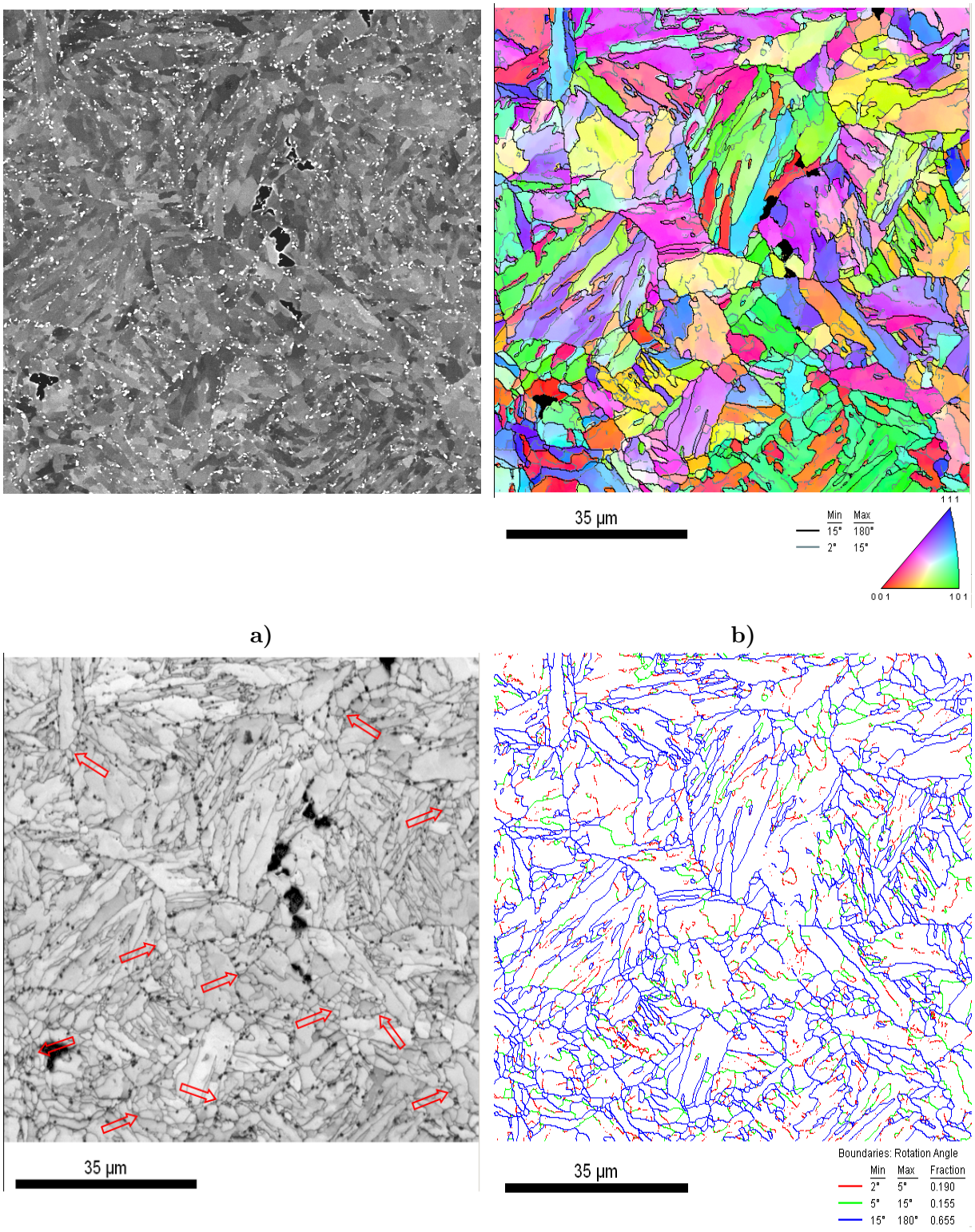

Figure VII.19 : Microtexture of P92 steel creep tested at 600°C for 49,721h (2mm from the fracture surface). SEM-BSE image (a); Inverse Pole Figure (IPF) map with orientation of sample normal in the crystal frame as color key (b); EBSD Image Quality (IQ) map (c); EBSD boundary map (d)

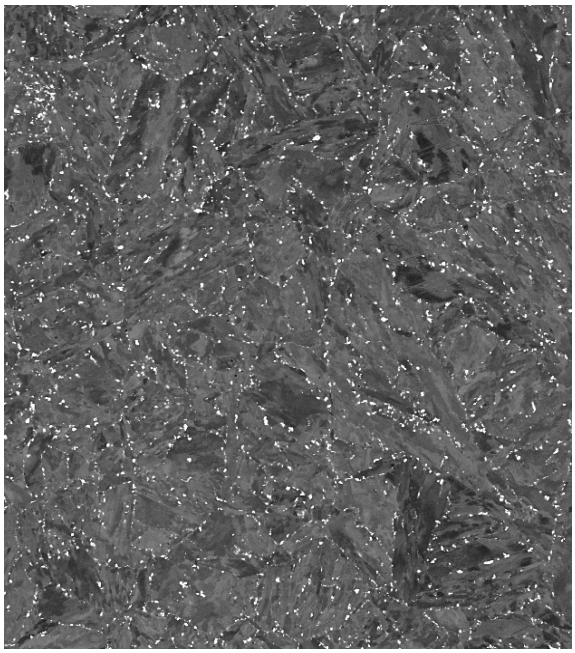

a)

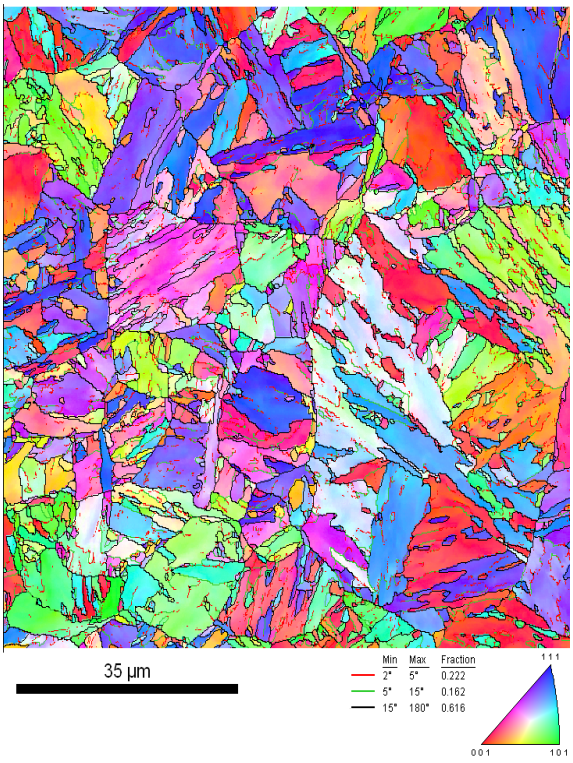

b)

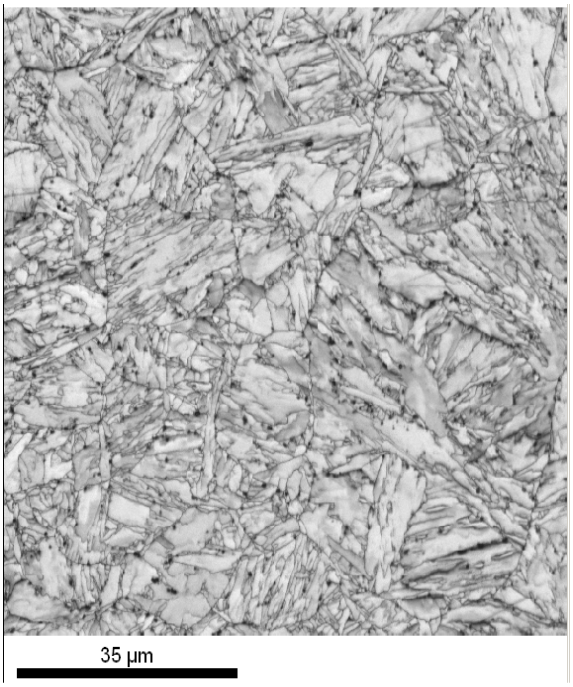

c)

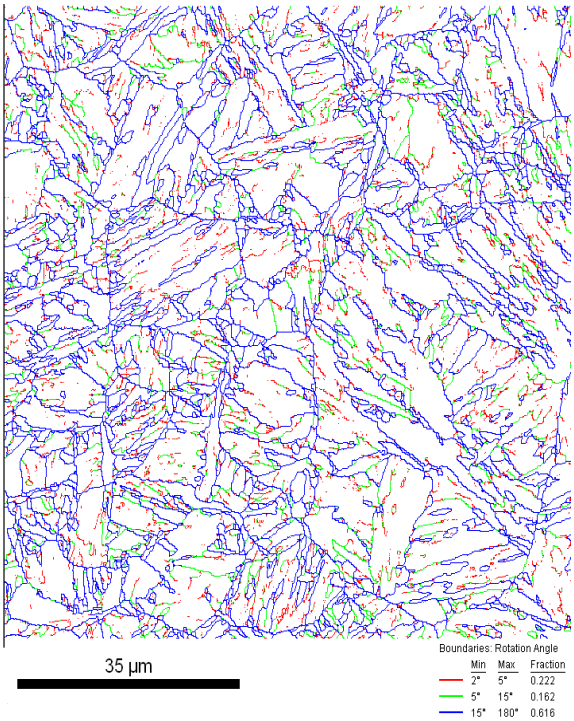

d)

Figure VII.20 : Microtexture of P92 steel creep tested at 600°C for 49,721h (head of the specimen). Inverse Pole Figure (IPF) map with orientation of sample normal in the crystal frame as color key (b); EBSD Image Quality (IQ) map (c); EBSD boundary map (d)

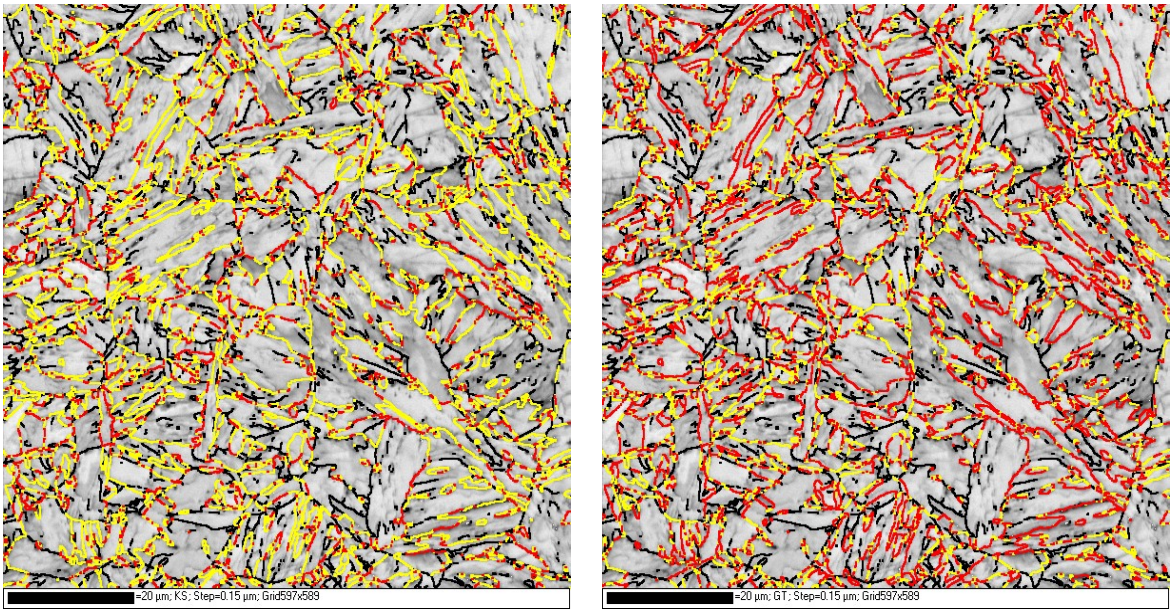

a) **b)**

Figure VII.21 : EBSD-IQ maps (same area as in figure VII.20) showing in red boundaries coresponding to K-S relationships (a) and G-T relationships (b). Other boundaries with a misorientation higher than 40° are represented in yellow and boundaries with a misorientation between 5°-40° are represented in black.

Table VII.5 : Analysis of boundaries respecting the K-S and G-T relationships in EBSD map

EBSD map	**T92** As-received	**P92** As-received	**49,721h; 600°C** (head)
Size of area	71 µm × 77 µm	75 µm × 80 µm	89.5 µm × 88.4 µm
Step size	0.15 µm	0.15 µm	0.15 µm
Observations			figure VII.21
Fraction of G-T (K-S) boundaries in EBSD maps			
G-T type boundary			
⟨433⟩ 60.2 G-T	26.4	23.4	23.3
⟨111⟩ 49.6 G-T	1.16	1.11	0.91
⟨331⟩ 50. G-T	2.16	3.40	2.43
⟨433⟩ 50.2 G-T	1.72	2.03	2.20
⟨332⟩ 50.8 G-T	3.87	3.63	3.77
⟨110⟩ 60. G-T	5.06	4.25	4.26
⟨331⟩ 51.9 G-T	3.61	4.80	3.77
⟨110⟩ 54.3 G-T	4.94	4.62	4.62
⟨331⟩ 55.6 G-T	3.58	3.78	3.49
⟨441⟩ 57.5 G-T	4.02	4.08	4.12
K-S type boundary			
⟨111⟩ 60. K-S	1.49		1.89
⟨432⟩ 57.2 K-S	2.1		2.31
⟨331⟩ 57.2 K-S	4.79		5.09
⟨221⟩ 51.7 K-S	3.39		3.42
⟨322⟩ 50.5 K-S	0.9		1.44
⟨431⟩ 50.5 K-S	0.62	0.79	0.85
⟨111⟩ 49.5 K-S	0.04	0.14	0.04
⟨221⟩ 47. K-S	0.8	0.99	0.79
⟨110⟩ 49.5 K-S	0.1	0.14	0.23
⟨110⟩ 60. K-S	5.06	4.25	4.26

in paranthesis is indicated where the EBSD map was realized

Table VII.6 : Analysis of boundaries in EBSD maps

	T92 as-received					P92 as-received		
Map size [µm × µm]	70 × 74	71 × 68	71 × 77	80 × 80	76 × 80	75 × 79	26 × 29	30 × 31
Step size	0.15 µm	0.15 µm	0.15 µm	0.15 µm	0.15 µm	0.15 µm	0.15 µm	0.15 µm
Obs.								
Boundary	Fraction of length boundaries							
2°-5°	0.293	0.274	0.287	0.322	0.256	0.303	0.425	0.240
5°-15°	0.155	0.160	0.151	0.140	0.156	0.151	0.129	0.145
15°-180°	0.553	0.567	0.562	0.539	0.588	0.546	0.445	0.616
P92 steel after 49,721h of creep at 600°C								
Map size	(2 mm)	(2 mm)	(2 mm)	(15 mm)	(15 mm)	(15 mm)	(head)	(head)
[µm × µm]	89 × 79	92 × 80	88 × 84	86 × 86	90 × 88	89 × 90	86 × 88	88 × 84
Step size	0.15 µm	0.15 µm	0.15 µm	0.15 µm	0.15 µm	0.15 µm	0.15 µm	0.15 µm
Obs.		fig. VII.19						fig. VII.20
Boundary	Fraction of length boundaries							
2°-5°	0.174	0.190	0.180	0.328	0.337	0.296	0.235	0.222
5°-15°	0.145	0.155	0.160	0.144	0.153	0.148	0.149	0.162
15°-180°	0.681	0.655	0.660	0.528	0.510	0.555	0.616	0.616

in paranthesis is indicated the distance from fracture surface of crept specimens where the EBSD map was acquired

Low-angle boundaries

The histograms of misorientation angles between grains corresponding to the EBSD maps in figure VII.19 and figure VII.23 (P92 steel after 49,721h of creep at 600°C) shows a typical distribution between martensite invariants, see figure VII.22 and figure VII.23.

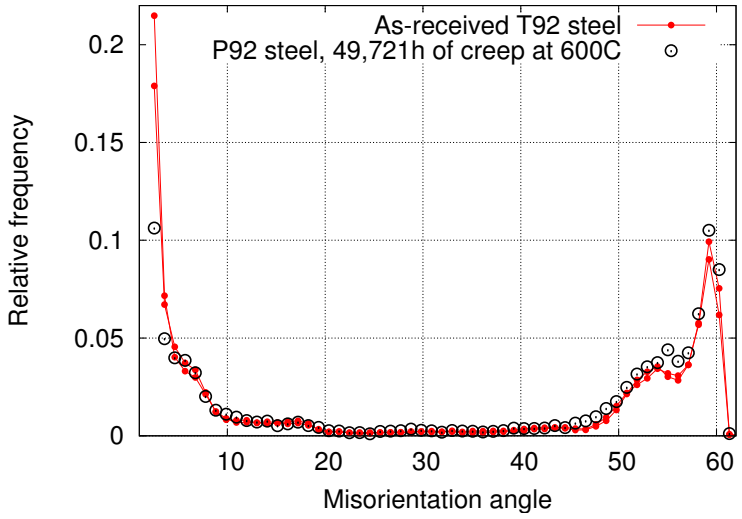

Figure VII.22 : Misorientation angles (°) between grains corresponding to the as-received material and to the EBSD map in figure VII.19

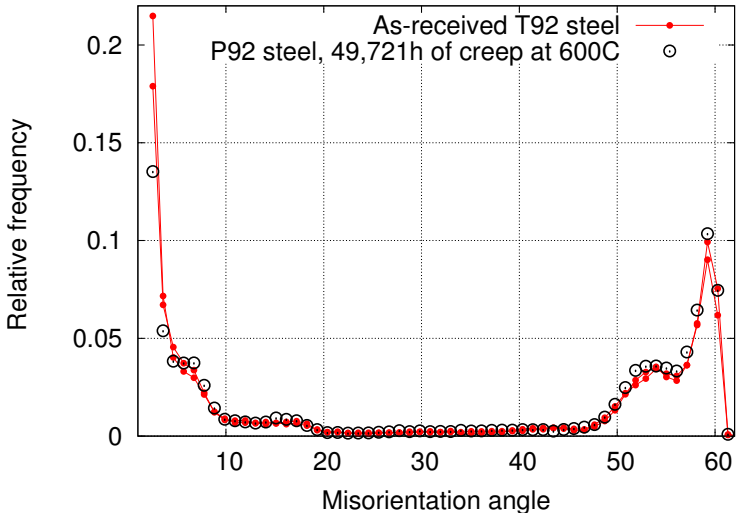

Figure VII.23 : Misorientation angles (°) between grains corresponding to the as-received material and to the EBSD map in figure VII.20

Table VII.7 : Analysis of boundaries in EBSD maps

	T92 as-received			**P92 as-rec.**		
Map size [µm × µm]	71 × 77	80 × 80	76 × 80	75 × 79		
Step size	0.15 µm	0.15 µm	0.15 µm	0.15 µm		
Observations						
Boundary	Fraction of length boundaries					
1°-2°	0.542	0.570	0.517	0.553		
2°-10°	0.184	0.185	0.185	0.186		
10°-180°	0.274	0.246	0.298	0.244		
P92 steel after 49,721h of creep at 600°C						
Map size	(2 mm)	(2 mm)	(2 mm)	(15 mm)	(head)	(head)
[µm × µm]	89 × 79	92 × 80	88 × 84	89 × 90	86 × 88	88 × 84
Step size	0.15 µm	0.15 µm	0.15 µm	0.15 µm	0.15 µm	0.15 µm
Obs.		figure VII.19				figure VII.20
Boundary	Fraction of length boundaries					
1°-2°	0.340	0.339	0.339	0.538	0.481	0.469
2°-10°	0.186	0.203	0.201	0.189	0.182	0.185
10°-180°	0.474	0.458	0.460	0.272	0.337	0.346

(Tak et al., 2009) studied the microtexture evolution of a 12%Cr steel (German grade X20) during large creep deformation and during thermal aging at 550°C. (Tak et al., 2009) reported an increase in the frequency of boundaries with a misorientation angle $\sim 1°$ and a slight decrease in the frequency of boundaries angles between 2°-5° during creep/thermal exposure. In this study, the minimum misorientation angle was set to 2° for the processing of the EBSD data. A slight decrease in the frequency of boundaries angles of about 2° is observed after both thermal (head of the specimen) and creep exposure at 600°C (see figures VII.22, VII.23) compared to that of the as-received T92 steel. This is consistent with the

results of (Tak et al., 2009).

Given the results reported by (Tak et al., 2009) a second processing of EBSD data was realized considering a minimum misorientation angle of 1° and the fraction of boundaries obtained in this case is given given in table VII.7. A slight decrease in frequency of boundaries with a misorientation angle ∼1°-2° is observed after long term exposure at 600°C compared to that in the as-received steel, see table VII.7. This is more significant for the EBSD maps acquired at 2 mm from the fracture surface.

b) P92 steel after 33,308h at 650°C

EBSD maps

EBSD maps acquired at 5 mm from fracture surface (i.e. in the homogeneously deformed part during creep testing) of the specimen tested for 33,308h at 650°C revealed a significant change in the microtexture of the steel (figure VII.24 and VII.25) compared to that of the as-received steel (figure II.9). The lath substructure organized in packets and block can not be roughly be distinguished after long-term creep exposure at 650°C, see figures VII.24 and VII.25 compared to figure II.9.

Moreover, the EBSD-IQ maps revels what seems to be small size round shaped grains close to the prior austenite grains and/or packets boundaries. Some of such grains are arrowed in the IQ maps (figures VII.24c and VII.25c) These grains are probably delimited by low angle boundaries because the boundaries of such grains are not revealed in the corresponding EBSD boundary maps. In order to get more precise data on the microtexture of the P92 steel after long-term creep exposure at 650°C, EBSD investigations were conducted with a smaller step size (i.e. 0.07 µm and 0.04 µm), see figures VII.26 and VII.27. The EBSD maps in figures VII.27, VII.26 reveal similar features of microtexture as the EBSD maps in figures VII.24 and VII.25.

High-angle boundaries

In figure VII.28 are represented the grain boundaries respecting the K-S and G-T relationships corresponding to the EBSD maps in figure VII.24. A lower fraction of boundaries are recognized respecting the K-S and G-T relationships in the EBSD map of the specimen creep tested for 33,308h at 650°C compared to that of the specimen tested for 49,721h at 600°C, see figure VII.28 compared to figure VII.21.

In table VII.8 are summarized the analysis of of boundaries respecting the K-S and the G-T relationships in various EBSD maps of the as-received steel and of the steel creep tested at 650°C. The frequency of some G-T grain boundaries recognized after long-term creep exposure at 650°C decreases compared to that of the as received steel (table VII.8). The frequency of some K-S boundaries increases slightly after long-term creep exposure at 650°C.

The EBSD investigations conducted on the P92 steel specimen tested for 33,308h at 650°C reveal also a significant increase in the fraction of boundaries with a misorientation of 2°-5° and a decrease in the fraction of boundaries of 15°-180°, compared to those of the as-received steel, table VII.9.

It is to be mentioned that EBSD investigations conducted with step sizes of 0.04 µm in the P92 steel tested for 33,308h at 650°C allow to sample only small areas of the crept specimen which probably does not cover one prior austenite grain. This may explain the large variations in the fraction of boundaries in the EBSD maps of this specimen, see table VII.9.

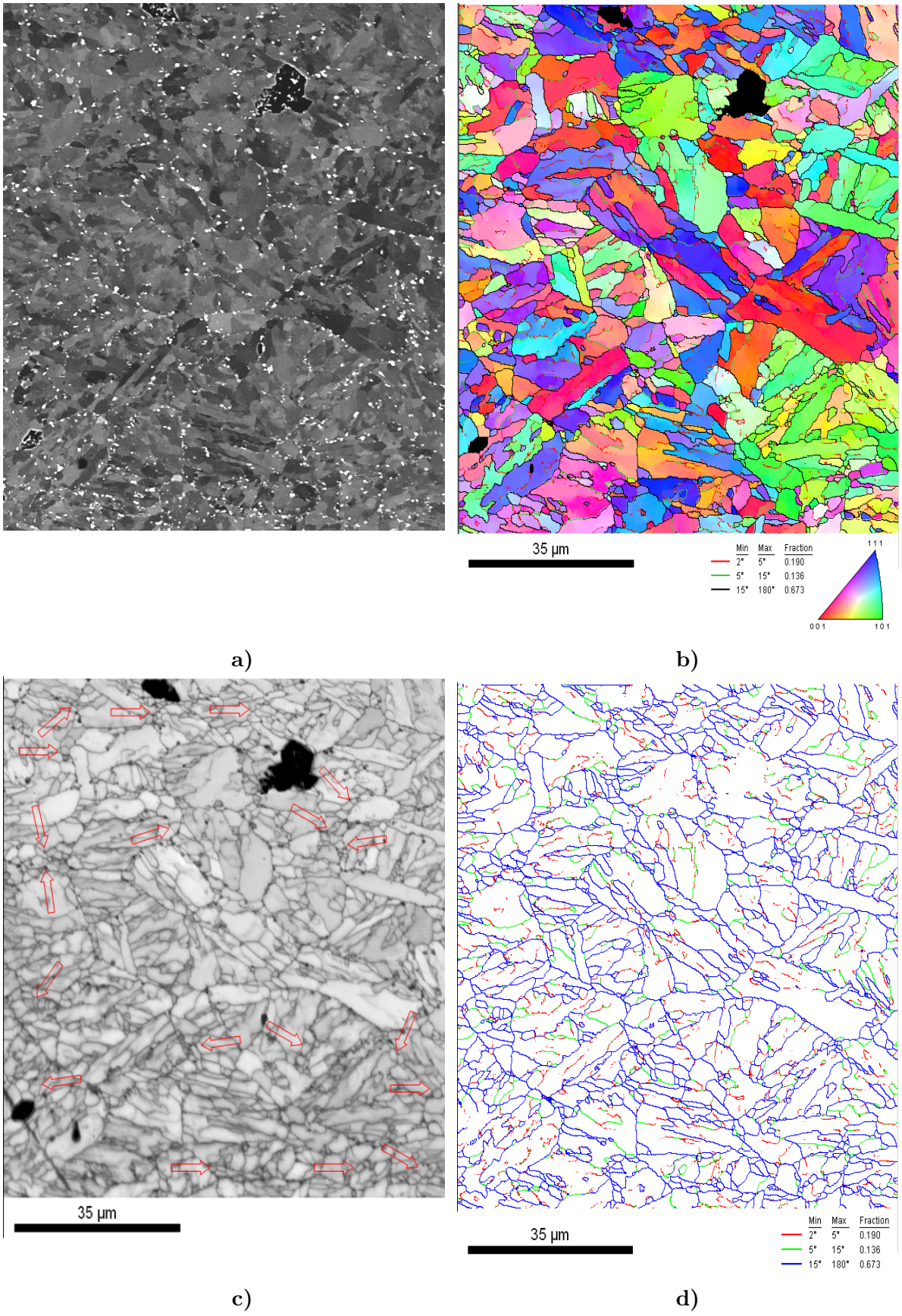

Figure VII.24 : Microtexture of the P92 steel creep tested at 650°C for 33,308h (5mm from the fracture surface). SEM-BSE image (a); EBSD-IPF map with orientation of sample normal in the crystal frame as color key (b); EBSD-IQ map (c); EBSD boundary map (d)

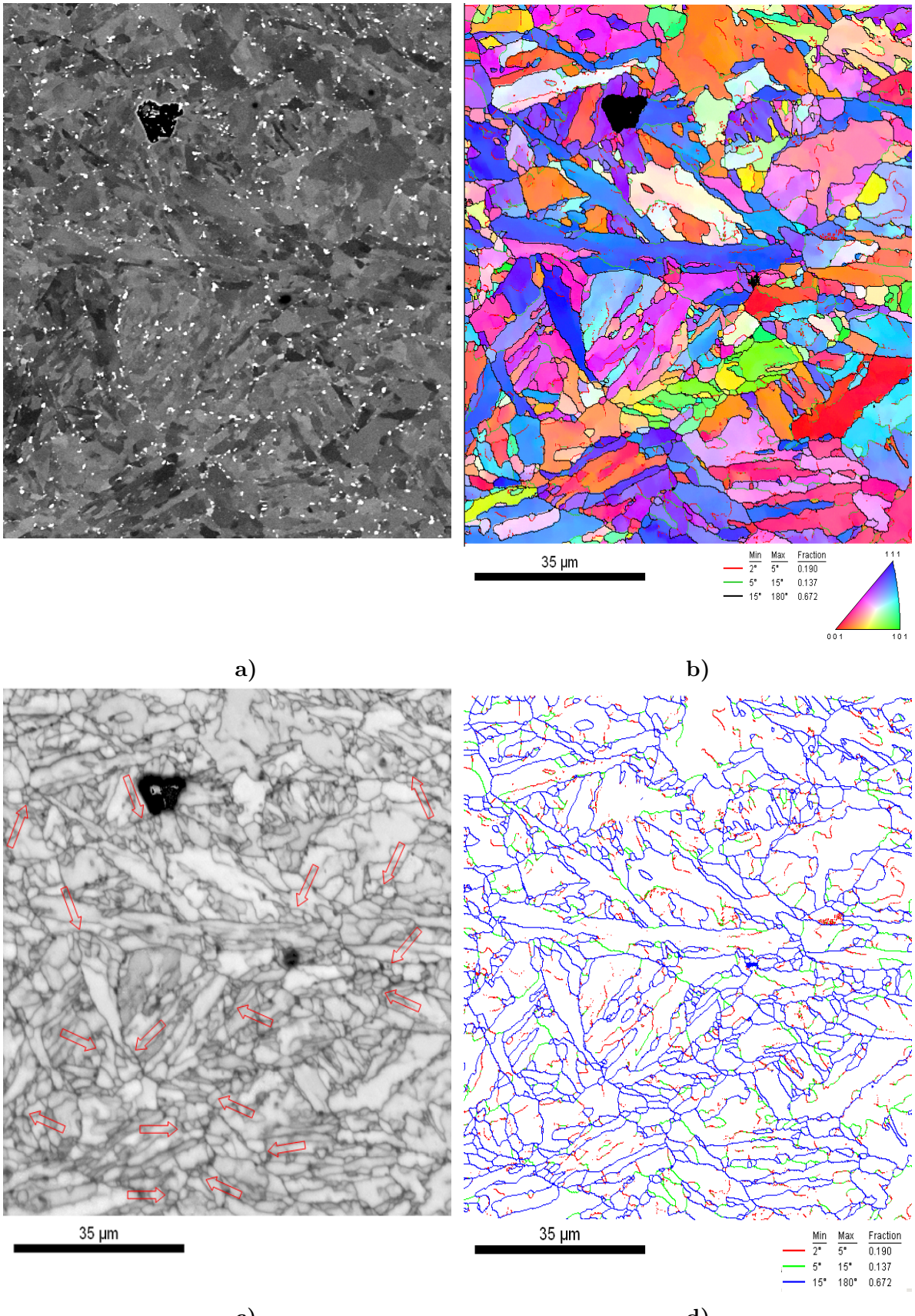

Figure VII.25 : Microtexture of the P92 steel creep tested at 650°C for 33,308h (5mm from the fracture surface). SEM-BSE image (a); EBSD-IPF map with orientation of sample normal in the crystal frame as color key (b); EBSD-IQ map (c); EBSD boundary map (d)

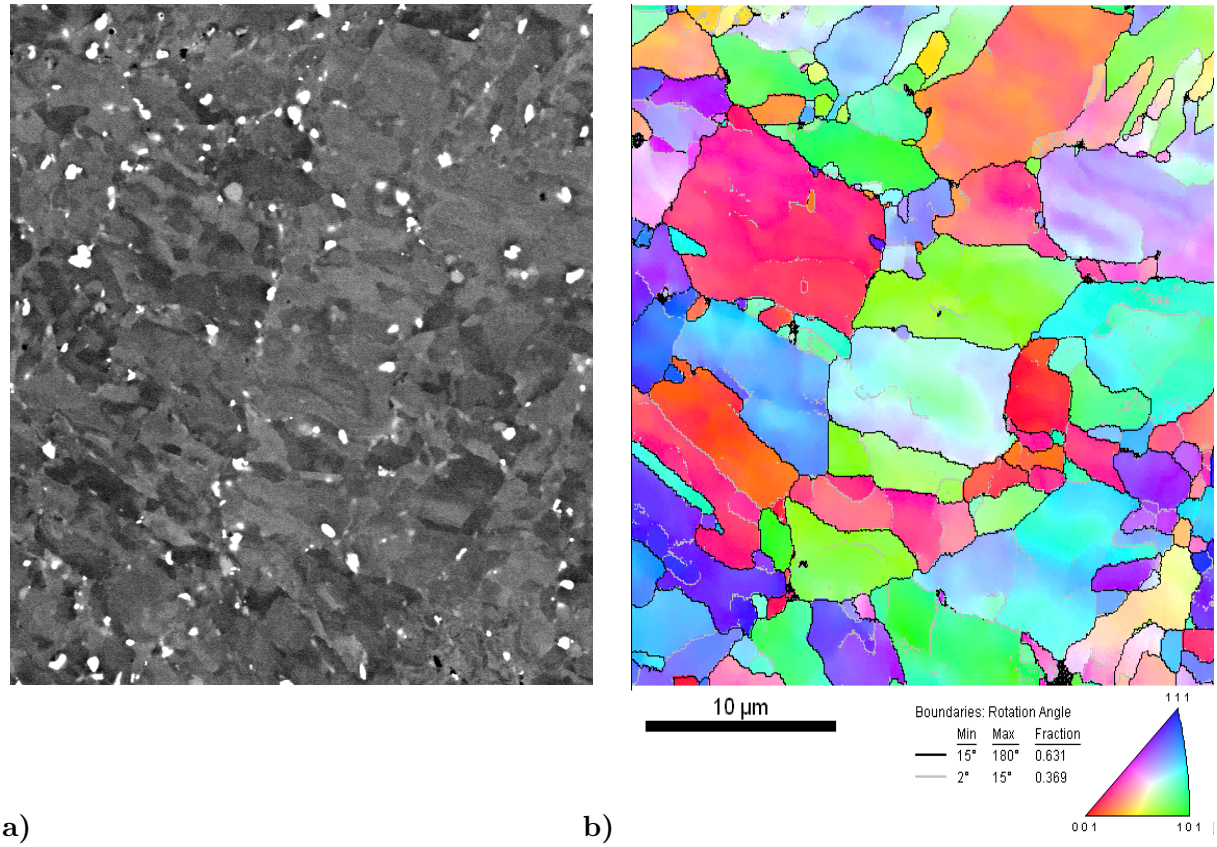

a) b)

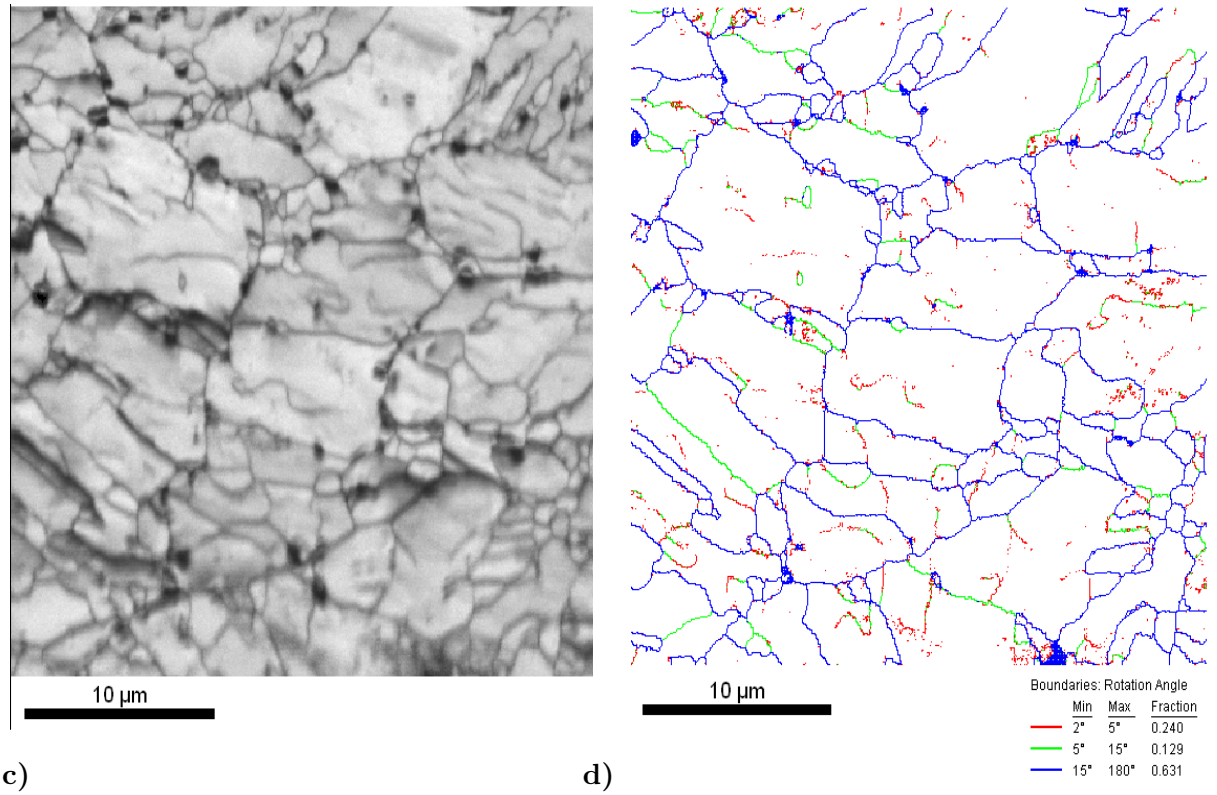

c) d)

Figure VII.26 : Microtexture of the P92 steel creep tested at 650°C for 33,308h (5mm from the fracture surface, step size of 0.07 µm). SEM-BSE image (a); Inverse Pole Figure (IPF) map with orientation of sample normal in the crystal frame as color key (b); EBSD Image Quality (IQ) map (c); EBSD boundary map (d)

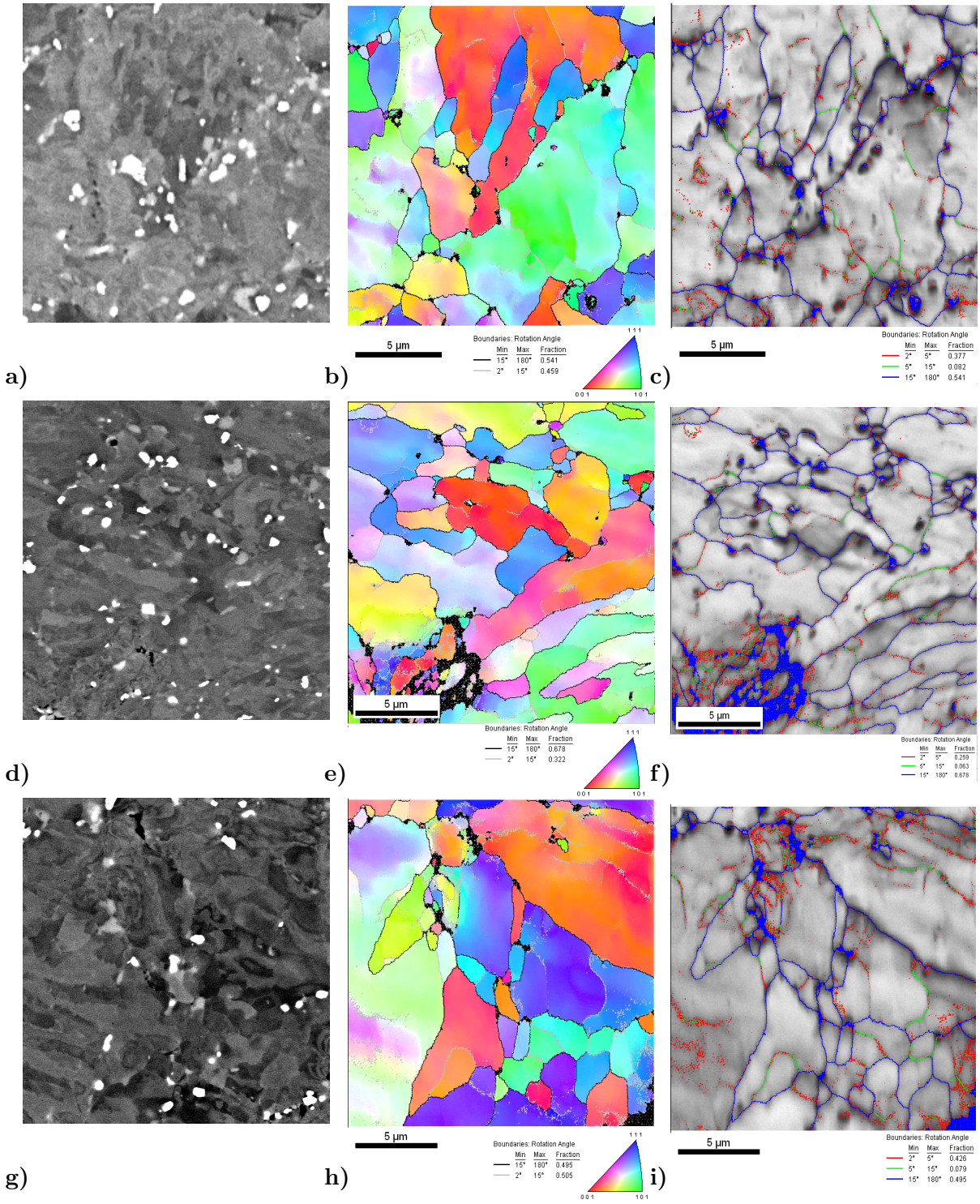

Figure VII.27 : EBSD maps of P92 steel creep tested at 650°C for 33,308h (5mm from the fracture surface, step size 0.04 µm). SEM-BSE images (a, d, g); EBSD-IPF map with orientation of sample normal in the crystal frame as color key (b, e, h); EBSD-IQ overlapped with EBSD boundary map (c, f, i)

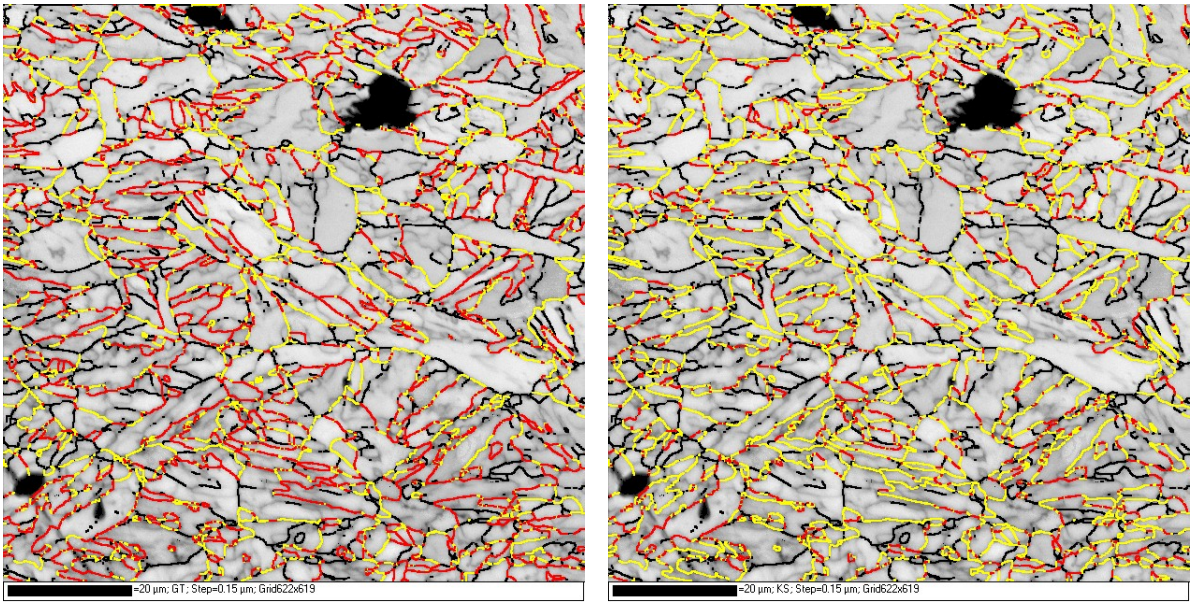

a) **b)**

Figure VII.28 : EBSD-IQ maps (same area as in figure VII.24) showing in red boundaries coresponding to K-S relationships (a) and G-T relationships (b). Other boundaries with a misorientation higher than 40° are represented in yellow and boundaries with a misorientation between 5°-40° are represented in black

Table VII.8 : Analysis of boundaries respecting the K-S and G-T relationships in EBSD map

EBSD map	**T92** As-received	**P92** As-received	**33,308h; 650°C** (5mm)	**33,308h; 650°C** (5mm)
Size of area	71 µm × 77 µm	75 µm × 80 µm	93 µm × 93 µm	92 µm × 93 µm
Step size	0.15 µm	0.15 µm	0.15 µm	0.15 µm
Observations			figure VII.28	figure VII.29
Fraction of G-T (K-S) boundaries in EBSD maps				
G-T type boundary				
⟨433⟩ 60.2 G-T	26.4	23.4	20.3	22.1
⟨111⟩ 49.6 G-T	1.16	1.11	0.81	0.42
⟨331⟩ 50. G-T	2.16	3.40	2.72	3.05
⟨433⟩ 50.2 G-T	1.72	2.03	1.57	1.69
⟨332⟩ 50.8 G-T	3.87	3.63	2.98	3.42
⟨110⟩ 60. G-T	5.06	4.25	4.47	5.15
⟨331⟩ 51.9 G-T	3.61	4.80	4.80	5.11
⟨110⟩ 54.3 G-T	4.94	4.62	5.81	7.68
⟨331⟩ 55.6 G-T	3.58	3.78	4.41	4.71
⟨441⟩ 57.5 G-T	4.02	4.08	4.48	4.46
K-S type boundary				
⟨111⟩ 60. K-S	1.49		1.12	1.28
⟨432⟩ 57.2 K-S	2.1		1.95	1.85
⟨331⟩ 57.2 K-S	4.79		5.76	6.19
⟨221⟩ 51.7 K-S	3.39		2.8	4.64
⟨322⟩ 50.5 K-S	0.9		0.85	1.12
⟨431⟩ 50.5 K-S	0.62	0.79	1.47	1.12
⟨111⟩ 49.5 K-S	0.04	0.14	0.01	0.05
⟨221⟩ 47. K-S	0.8	0.99	1.28	0.67
⟨110⟩ 49.5 K-S	0.1	0.14	0.11	0.13
⟨110⟩ 60. K-S	5.06	4.25	4.47	5.15

in paranthesis is indicated the distance from fracture surface where the EBSD map was acquired

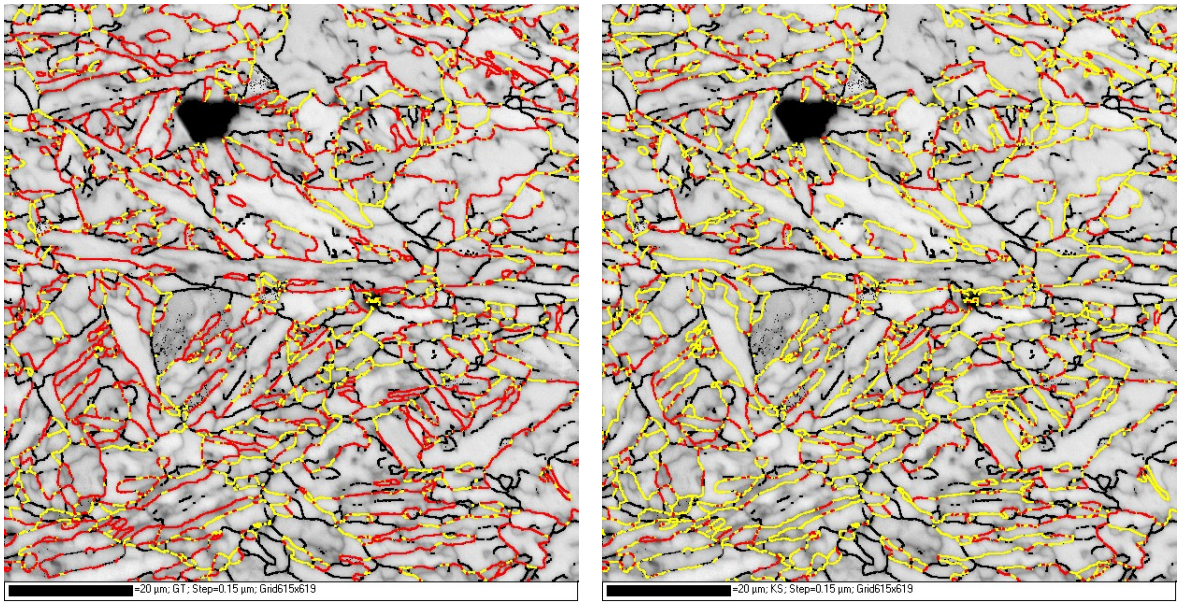

a) **b)**

Figure VII.29 : EBSD-IQ maps (same area as in figure VII.25) showing in red boundaries coresponding to K-S relationships (a) and G-T relationships (b). Other boundaries with a misorientation higher than 40° are represented in yellow and boundaries with a misorientation between 5°-40° are represented in black

Table VII.9 : Analysis of boundaries in EBSD maps

	T92 as-received					**P92 as-received**		
Map size [µm × µm]	70 × 74	71 × 68	71 × 77	80 × 80	76 × 80	75 × 79	26 × 29	30 × 31
Step size	0.15 µm	0.15 µm	0.15 µm	0.15 µm	0.15 µm	0.15 µm	0.15 µm	0.15 µm
Obs. Boundary	Fraction of length boundaries							
2°-5°	0.293	0.274	0.287	0.322	0.256	0.303	0.425	0.240
5°-15°	0.155	0.160	0.151	0.140	0.156	0.151	0.129	0.145
15°-180°	0.553	0.567	0.562	0.539	0.588	0.546	0.445	0.616
P92 steel after 33,308h of creep at 650°C								
Map size [µm × µm]	(5 mm) 17 × 17	(5 mm) 46 × 46	(5 mm) 93 × 93	(5 mm) 92 × 93	(5 mm) 18 × 18	(5 mm) 19 × 19	(5 mm) 19 × 19	(5 mm) 31 × 31
Step size	0.05 µm	0.10 µm	0.15 µm	0.15 µm	0.035 µm	0.04 µm	0.04 µm	0.07 µm
Obs.			fig. VII.24d	fig. VII.25d	fig. VII.27c	fig. VII.27f	fig. VII.27i	fig. VII.26
Boundary	Fraction of length boundaries							
2°-5°	0.516	0.481	0.190	0.190	0.377	0.259	0.426	0.240
5°-15°	0.127	0.161	0.136	0.137	0.082	0.063	0.079	0.129
15°-180°	0.358	0.358	0.673	0.672	0.541	0.678	0.495	0.631

in paranthesis is indicated the distance from the fracture surface of crept specimens where the EBSD map was acquired

It is also to be mentioned that the fraction of boundaries in the EBSD maps of the specimen tested for 33,308h is affected by the creep damage and by the presence of large Laves phase. As can be seen in figures VII.26, VII.27 the creep damaged areas (or large

Laves phases) corresponds in the EBSD maps with areas with high amount of boundaries of 15°-180°, which are not real grain boundaries. These boundaries could not be correctly removed by *clean up* methods used for EBSD data processing.

Low- angle boundaries

As observed from the EBSD data of the crept specimen tested at 600°C (i.e. 49,721h), the frequency of the misorientation angle of ∼2° between grains decreases after long-term creep exposure at 650°C compared to that of the as-received steel, see figure VII.30a and VII.31a.

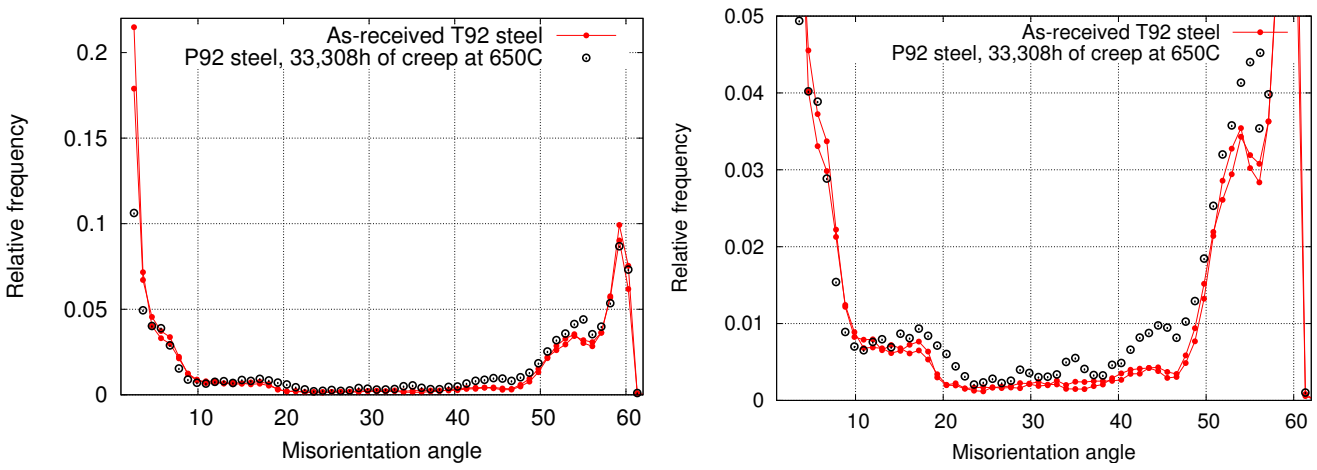

Figure VII.30 : a) Misorientation angles (°) between grains corresponding to as-received material and the EBSD map in figure VII.24; b) same as a) close-up view

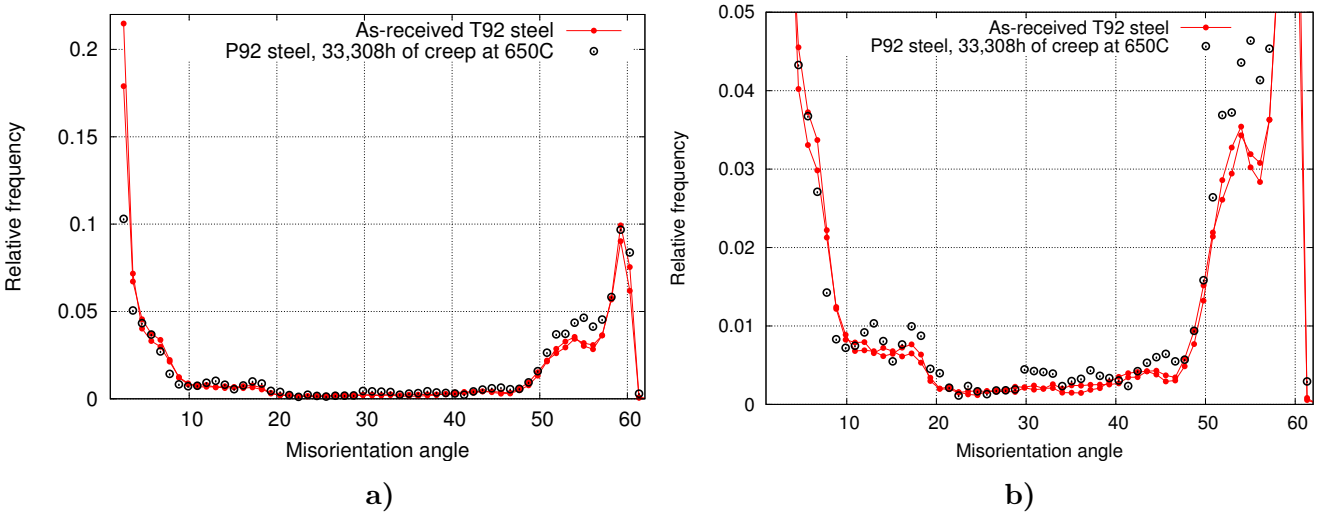

Figure VII.31 : a) Misorientation angles (°) between grains corresponding to as-received material and the EBSD map in figure VII.25; b) same as a) close-up view

The histograms in figures VII.30 and VII.31 shows also that the frequency of boundaries with a misorientation angle of 50°-60° increases after long-term creep exposure at 650°C compared to that of the as-received steel. This is not observed in the histogram of misorientation angles coresponding to the EBSD maps of the creep specimen tested for long-

term creep at 600°C. It is to be mentioned that 650°C is close to the tempering temperature of the Grade 92 steel (i.e. 770°C), this might probably explain why more significant changes are observed on the EBSD maps of the specimen tested at 650°C compared to these of the specimen tested at 600°C.

Based on the work of (Tak et al., 2009), (Aghajani et al., 2009b) which reports an increase in the frequency of boundaries of ∼1° after long-term creep exposure at 550°C of a 12%Cr steel, a second processing of EBSD data was realized considering a minimum misorientation angle of 1°.

In table VII.10 are given the fraction of boundaries in these EBSD maps after the second data processing. It is to be mentioned that considering a minimum misorientation angle of 1°, grain boundaries of 1°-2° in the EBSD maps could not be precisely distinguished from what could probably be a noise signal.

The frequency of boundaries of 1°-2° increases after long-term creep exposure at 650°C, which is consistent to the results reported by (Tak et al., 2009), (Aghajani et al., 2009b). As already mentioned the frequency of boundaries of 1°-2° could be affected by the creep damaged areas in the P92 steel crept specimen tested at 650°C for 33,308h as explained previously. It cannot be clearly decided whether grain boundaries of 1°-2° are real boundaries or signal noise or artefacts from sample preparation.

Table VII.10 : Analysis of boundaries in EBSD maps

	T92 as-received			**P92 as-rec.**	
Map size [µm × µm]	71 × 77	80 × 80	76 × 80	75 × 79	
Step size	0.15 µm	0.15 µm	0.15 µm	0.15 µm	
Boundary	Fraction of length boundaries				
1°-2°	0.542	0.570	0.517	0.553	
2°-10°	0.184	0.185	0.185	0.186	
10°-180°	0.274	0.246	0.298	0.244	
P92 steel after 33,308h of creep at 650°C					
Map size	(5 mm)	(5 mm)	(5 mm)	(5 mm)	(5 mm)
[µm × µm]	93 × 93	92 × 93	18 × 18	18 × 18	30 × 30
Step size	0.15 µm	0.15 µm	0.035 µm	0.04 µm	0.07 µm
Obs.	fig. VII.24	fig. VII.25	fig. VII.27c	fig. VII.27f	fig. VII.26
Boundary	Fraction of length boundaries				
1°-2°	0.378	0.380	0.639	0.499	0.548
2°-10°	0.182	0.178	0.159	0.152	0.146
10°-180°	0.440	0.442	0.196	0.349	0.307

in () is indicated the distance from fracture surface where the EBSD map was acquired

c) Summary

The results of EBSD investigations conducted on the P92 steel specimens creep tested for long-term at 600°C ($t_r = 49,721$h) and at 650°C ($t_r = 33,308$h) were presented in this section. The purpose of these investigations was to get data on the changes occurring in the microtexture during long-term creep exposure of the P92 steel.

More obvious changes were observed in the microtexture of the specimen crept at 650°C compared to that of the as-received material. The tempered martensitic microstructure could hardly be recognized in the EBSD maps of this specimen. Moreover, the histograms of misorientation angles between grains corresponding to the EBSD maps of the crept specimen

at 650°C shows a slight increase in the frequency of high angle boundaries (see figures VII.30 and VII.30) which was not observed in these corresponding to the EBSD maps of the crept specimens at 600°C.

The EBSD maps of the crept specimens investigated in this study revealed the microtexture organized in blocks, packets inside prior austenite grains. The size of these microtexture features does not significantly evolve during creep exposure at 600°C and 650°C in the P92 steel. The changes occurring in the microtexture during creep exposure most probably concerns the size of subgrains inside martensite laths. An increase in size of subgrains during creep exposure is reported for various 9-12%Cr tempered martensitic steels (see for instance (Aghajani et al., 2009b), (Kostka et al., 2007), (Ennis et al., 2000)). TEM investigations on thin foils are needed to study the subgrains. EBSD is probably not the most appropriated technique to study the changes in the microtexture of these steels during creep.

VII.2.4 Summary

Metallographic investigations of specimens creep tested at 600°C and 650°C for various amounts of time yielded the following main results:

Creep damage

Creep damage (i.e. cavities) was observed throughout the gauge part (i.e. the homogeneously deformed part during creep testing) of the specimens tested for times higher than 10^4h at 600°C and higher than 10^3h at 650°C. The number of cavities as well as their area fraction increase with increasing testing time. Larger size of cavities are observed in specimens tested at 650°C compared to these tested at 600°C for similar testing time. A quantification of creep damage was realized by image analysis of SEM-BSE images. The presence of these cavities could cause premature failure of the specimens. This might explain the overestimation of lifetime of the long-term crept specimens ($t_r > 10^4$h at 600°C and $t_r > 10^3$h at 650°C) when considering their secondary creep rate only. Thus premature creep damage development should be considered in modeling of the long-term creep behavior of Grade 92 steel.

Cavities were observed only on the necking area of the short-term crept specimens ($t_r < 10^4$ at 600°C and $t_r < 10^3$ at 650°C) and it is believed that this is not really *creep damage*. These cavities could appeared during the localized (rapid) plastic deformation due to macroscopic necking of the specimens in tertiary creep stage.

Microstructural evolution

Microstructural investigations of the crept specimens revealed a significant precipitation and growth of Laves phases during creep exposure both at 600°C and 650°C. A quantification of Laves phases (i.e. size and area fraction) was realized by image analysis of SEM-BSE images. The precipitation of Laves phases decreases solid solution strengthening of the steel by reducing the amount of W and Mo atoms in solid solution. Thus, precipitation of Laves phases should be considered in the further models to estimate the long term creep strength. Anyway the effect of Laves phase precipitation on the creep behavior of Grade 92 steel is not fully understood. Investigations of thermally aged specimens after creep testing will enable to establish whether the precipitation of Laves phases only affects the creep deformation and/or creep damage development.

TEM investigations conducted on extractive replicas of precipitates revealed low amounts of Z-phases in the crept specimen with the longest testing time (i.e. 49,721h at 600°C). No

significant change was observed in the number density of MX-type precipitates after long-term creep exposure despite precipitation of modified Z phases. Thus, precipitation of this phase could be considered as having no significant influence on the loss of creep strength of Grade 92 steel.

TEM investigations also revealed growth of $M_{23}C_6$ carbides and a change in their average chemical composition during creep exposure both at 600°C and 650°C. The average size of $M_{23}C_6$ carbides after various exposure times is believed to be overestimated because of a sample effect. Note also the extremely low number of particles investigated. However the growth rate of $M_{23}C_6$ carbides during creep is much lower than that of Laves phases, both modeled with an Orowan ripening equation. Consequently, it was decided not to consider the growth of $M_{23}C_6$ carbides in the further model.

During creep exposure both at 600°C and 650°C there is an evolution of the matrix substructure such as an increase in subgrain size (Aghajani et al., 2009b), (Tak et al., 2009) and a decrease in dislocation density inside subgrains (Ennis and Czyrska-Filemonowicz, 2002).

The changes that might have occurred in the matrix substructure of the P92 steel specimens tested for long-term creep were investigated using EBSD techniques. A more significant change was observed after long term creep exposure at 650°C. The tempered martensitic substructure could not readily be recognized in the P92 steel specimen after 33,308h of creep at 650°C. It was rather difficult to quantify the EBSD data obtained in this study. Anyway, even in the absence of results from TEM observations on thin foils recovery of the matrix should be considered in the mechanical model for assessement of the long-term creep strength of the Grade 92 steel.

VII.3 Thermally aged specimens

Microstructural investigations were conducted on the thermally aged specimens after creep testing to study the influence of large Laves phases on the creep behaviour of the Grade 92 steel.

EBSD and SEM investigations revealed that presence of large Laves phases was the only obvious change in the microstructure of the thermally aged specimens compared to that of the as-received T92 steel.

VII.3.1 Thermally aged specimens creep tested at 600°C

Four creep tests were conducted up to rupture and one creep test is in progress (σ_n = 120MPa) at 600°C on thermally aged specimens (600°C, 10^4h). The results of these tests were summarized in table V.3.

EBSD and SEM investigations revealed that presence of large Laves phases with an average equivalent diameter of $\sim$ 200nm was the only obvious change in the microstructure of the thermally aged specimens compared to that of the as-received T92 steel.

Thermally aged specimens creep tested under levels of stress higher than 160MPa (respectively testing times lower than 2,000h) showed a $\dot{\varepsilon}_{ss}$ four times higher (respectively a lifetime four times lower) compared to that of the as-received steel creep tested under same conditions. Moreover, the $\dot{\varepsilon}_{ss}$ versus the applied stress coresponding to these specimens showed same value of slope as the as-received T92 steel creep tested for high stresses ($\sigma >$ 160MPa). Microstructural evolution and/or creep damage that might happen during creep exposure was investigated in the thermally aged specimen with longest testing time (i. e. 2,016h) to establish the influence of large Laves phase on the creep behavior of the T92 steel at 600°C for levels of stress higher than 160MPa.

VII.3.1.1 Hardness

In figure VII.32 are represented the evolution of hardness in the center along the longitudinal axis of the thermally aged specimens creep tested under 180MPa (t_r = 543h) and 160MPa (t_r = 2,016h). The part homogeneously deformed during the creep testing of these two specimens reveal a hardness of 210±5HV0.5. This value of hardness is similar to that of P92 steel specimens creep tested at 600°C for times higher than 10^4h, see figure VII.6.

Close to fracture surface, more precisely in the necking area, an increase in hardness is observed in the thermally aged specimen creep tested under 180MPa with a lifetime of 543h. This was also observed on Grade 91 steel crept specimens tested at 500°C for lifetimes lower than 4,500h (Vivier et al., 2008). This increase in hardness in the necking area of specimens might be due to localized plastic deformation and associated work hardening.

It is to be mentioned that before creep testing the hardness of the aged specimens was the same as that of the as-received T92 steel. Recovery of the matrix due to deformation or creep damage developement during creep exposure might explain the lower hardness of thermally aged specimens after creep testing. No change in hardness was observed in the head of specimens after creep testing compared to that before creep testing.

VII.3.1.2 Creep damage

No creep damage was observed on the homogeneously deformed part of the thermally aged specimen with the longest testing time (i.e. 2,016h). Thus it can be supposed that no extensive creep damage development occurs in the thermally aged specimens tested for times lower than 2,000h (i. e. under levels of stress higher than 160MPa) at 600°C.

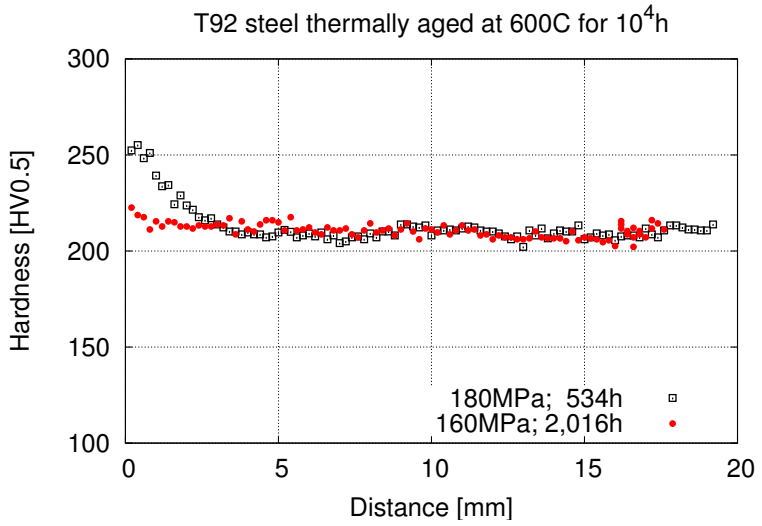

Figure VII.32 : Hardness along the axis of the specimens thermally aged at 600°C for 10^4h and then creep tested at 600°C

VII.3.2 Thermally aged specimens creep tested at 650°C

The results of creep tests conducted at 650°C on thermally aged specimens (650°C, 10^4h) were given in table VI.3. The lifetime of the thermally aged specimens tested for levels of stress higher than 110MPa was three times lower than that of the as-received T92 steel tested under same levels of stress. The lifetime of the thermally aged specimens tested for levels of stress lower than 95MPa was only twice lower than that of the as-received steel. Moreover, the value of 95MPa was found to correspond to the low stresses region for the creep flow at 650°C of the Grade 92 steel.

Creep damage was observed in all as-received P92 specimens tested at 650°C under levels of stress lower than 100MPa. Extensive creep damage was also observed in the as-received T92 specimen creep tested at 650°C under 95 MPa for 4,480h. Thus, the thermally aged specimen tested under 110MPa, 427h as well as the two thermally aged specimens tested for levels of stress lower than 100MPa (i.e. 95MPa and 85MPa) were investigated with regard to their microstructural evolution and creep damage.

VII.3.2.1 Hardness

Figure VII.33 shows the hardness along the axis of the thermally aged specimens creep tested at 650°C under 110MPa, 95MPa and 85MPa. The average hardness in the homogeneously deformed part of the aged specimen tested under 110MPa (t_r = 427h) is similar to that of the P92 steel creep tested under 110MPa ($t_r = 2,092$h), see figure VII.7b. In addition, the thermally aged specimen tested under 95MPa ($t_r = 2,392$h) shows an average hardness similar to that of the P92 steel creep tested under 90MPa ($t_r = 9,211$h), see figure VII.7b. This might indicate similar microstructural changes (i.e. creep damage development, recovery of the matrix) occurring during creep testing of the P92 steel specimens as those occurring within a shorter time in the thermally aged specimens.

Thus creep damage in the thermally aged specimens tested under 85MPa ($t_r = 4,434$h) was quantified to be further compared to that in the as-received T92 steel specimens after creep testing, see figure VII.36 and VII.38.

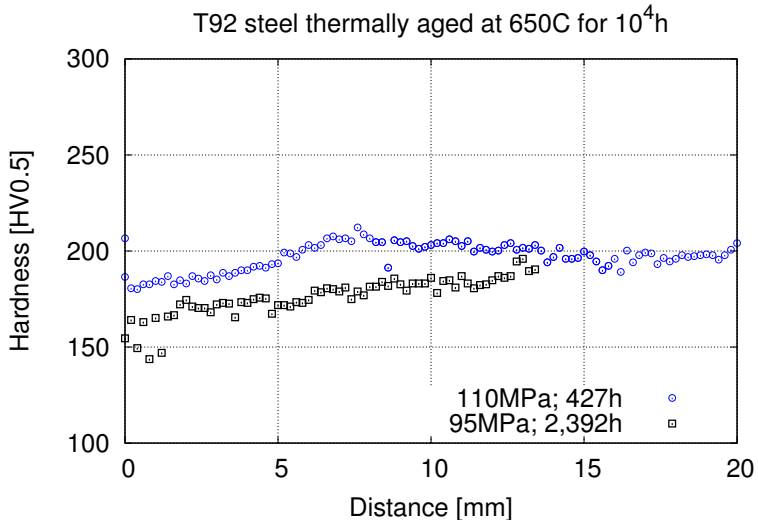

Figure VII.33 : Hardness along axis of the specimens thermally aged at 650°C for 10^4h and then creep tested at 650°C

No change in hardness was observed in the head of thermally aged specimens after creep testing at 650°C compared to that before creep testing.

VII.3.2.2 Creep damage

No creep damage was observed in the homogeneously deformed part of the thermally aged specimen tested under 110MPa for 427h. In this specimen cavities were observed only within the necking area. This specimen exhibited the same failure mode as the P92 steel specimens tested for short-term creep at 650°C (i.e. testing times lower than 1,000h).

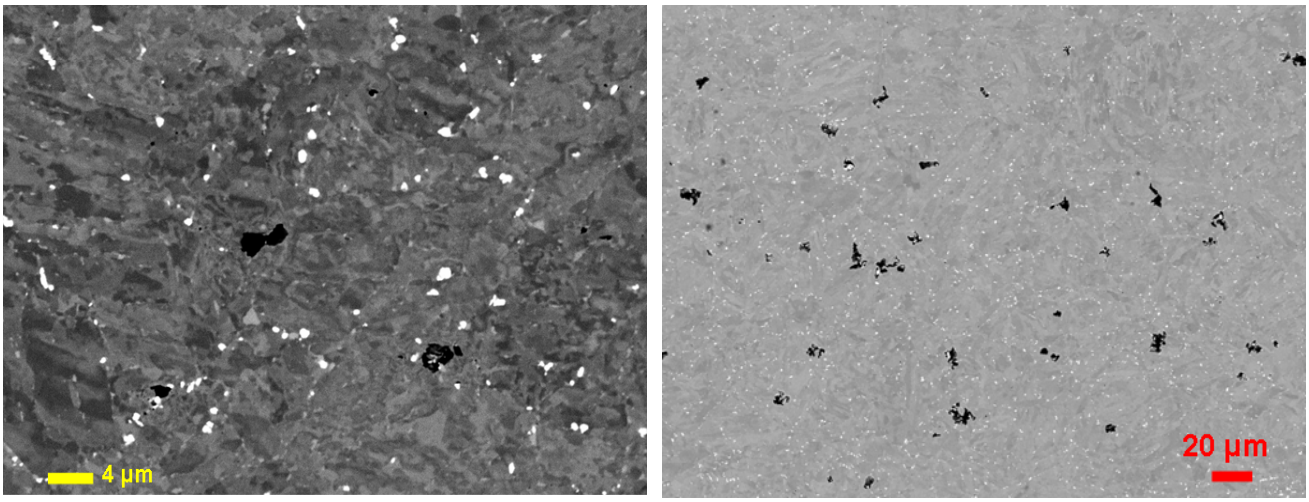

a) 95MPa, 2,392h **b)** 85MPa, 4,434h

Figure VII.34 : Typical creep damage in the thermally aged specimens creep tested at 650°C at 10 mm from fracture surface (SEM-BSE images after final colloidal silica polishing)

Creep damage was observed throughout the gauge part of the thermally aged specimens tested under 95 MPa ($t_r = 2,392$) and 85MPa ($t_r = 4,434$h). In figure VII.34 is shown

typical creep damage observed in these two specimens at 10 mm from the fracture surface. Creep damage is mainly observed at boundaries.

Small cavities are observed close to large Laves phases (figure VII.34a) indicating that these phases might be nucleation sites of creep damage. However, no significant change was observed in the amount of creep damage (number of cavities, size of cavities) in the thermally aged specimens compared to that in as-received T92 steel creep tested at 650°C for similar amounts of time.

VII.4 Influence of the initial metallurgical state on the creep strength

The following three specimens revealed similar lifetime despite a different microstructural state before creep testing. Moreover, these three specimens showed similar values of secondary creep rate ($\dot{\varepsilon}$). Thus detailed investigations were conducted on these three crept specimens in order to study whether large Laves phases or a recovered matrix substructure prior to creep testing enhanced creep damage development and/or matrix recovery during creep.

- T92 steel as-received creep tested at 650°C under **95MPa** for **4,480**h
- T92 thermally aged at 650°C for 10^4h and creep tested at 650°C under **85MPa** for **4,434**h
- T92 steel thermo-mechanically prepared at 550°C and creep tested at 650°C under **95MPa** for **4,656**h

VII.4.1 Creep damage

In order to investigate a possible effect of large Laves phases already formed prior to creep testing on the creep damage development, creep damage was quantified using the procedure detailed in section VII.1. Figure VII.34b and figure VII.35 show typical SEM-BSE images used for creep damage quantification.

No significant difference could be observed in the number or area fraction of cavities in the as-received T92 steel, T92 steel thermally aged and T92 steel thermo-mechanically prepared at 550°C creep tested at 650°C for similar times, see figure VII.36.

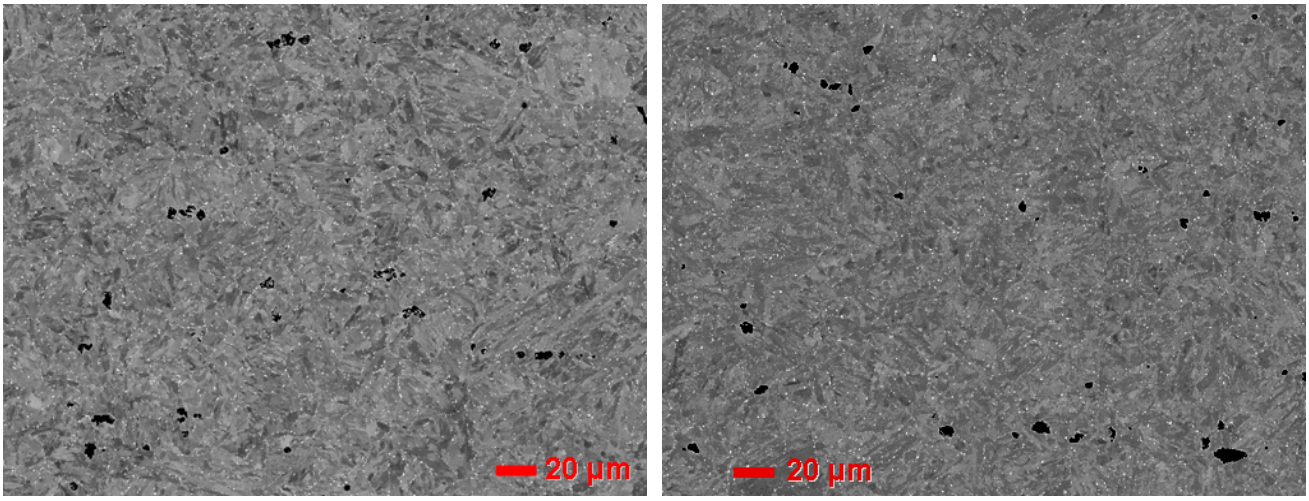

a) As-received T92 steel
650°C, 95MPa, $t_r = 4,480$h

b) T92 steel thermo-mech. prep. at 550°C
650°C, 95MPa, $t_r = 4,656$h

Figure VII.35 : Typical SEM-BSE images (×400) used for creep damage quantification (10 mm from fracture surface)

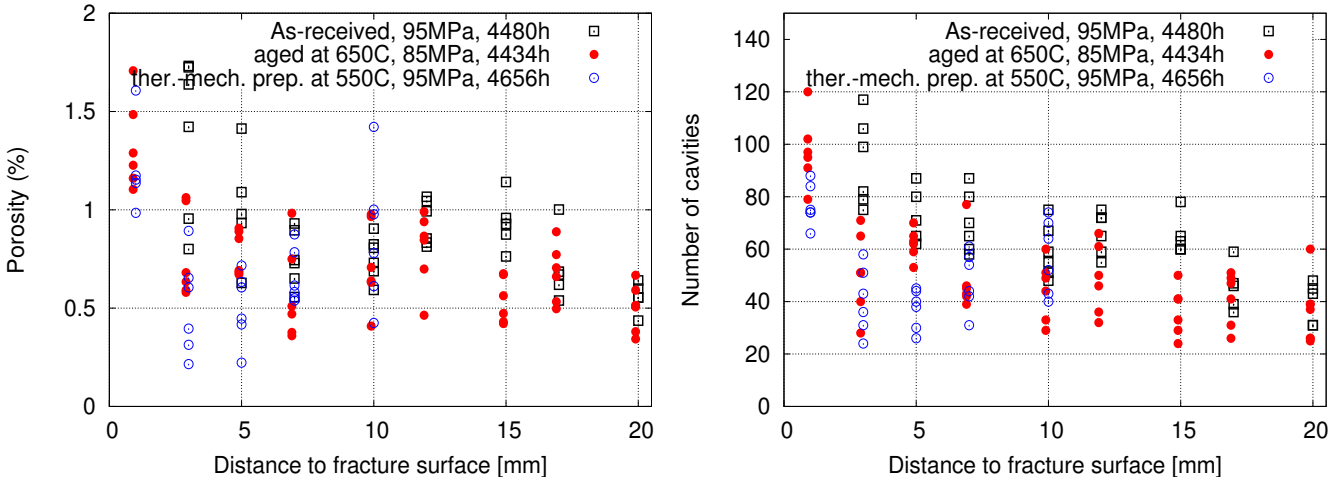

a) **b)**

Figure VII.36 : Area fraction (a) and number (b) of cavities estimated on areas of 270 µm × 210 µm in the as-received T92 steel (95MPa, 4,480h), T92 steel thermo-mechanically prepared (95MPa, 4,656h) and T92 steel thermally aged at 650°C for 10^4h (85MPa, 4,434h)

Creep damage is not homogeneously distributed in gauge part of the specimens. One might think that the scatter of data in figure VII.36 can be due to relatively small size areas which were analyzed using SEM-BSE images.

Thus, a second image analysis was conducted using light micrographs to sample larger areas of crept specimens (at the expense of smallest cavities) and get more representative data on the amount of creep damage in the as-received T92 steel and aged T92 steel both creep tested for similar amounts of time. Figure VII.37 shows such light micrographs.

For this porpose, two light micrographs from each side of the longitudinal axis were taken starting at 10 mm from fracture surfaces to avoid any coalescence of cavities due to fracture of specimens or localized plastic deformation. As can be seen in figure VII.36, close to the

fracture surface (i.e. on a distance of about 5mm) the area fraction of cavities is higher than that on the rest of the gauge length in all three investigated specimens.

Consequently, image analysis of light micrographs revealed a scatter of data and no clear difference could be identified in the amount of creep damage in as-received T92 steel compared to that in the thermally aged specimen both creep tested for 650°C for similar times.

Heterogeneously distribution of creep damage can be observed on the light micrographs in figure VII.37.

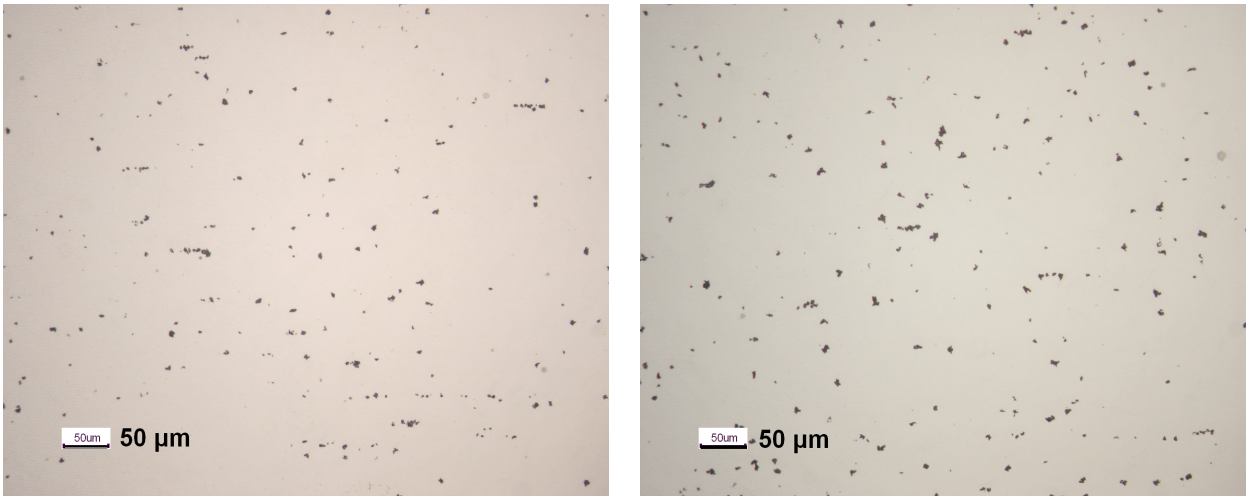

a) As-received T92 steel 650°C, 95MPa $t_r = 4,480$h

b) T92 steel thermally aged at 650°C for 10^4h 650°C, 85MPa, $t_r = 4,434$h

Figure VII.37 : Typical light micrographs used for creep damage quantification (10 mm from fracture surface, after final colloidal silica polishing)

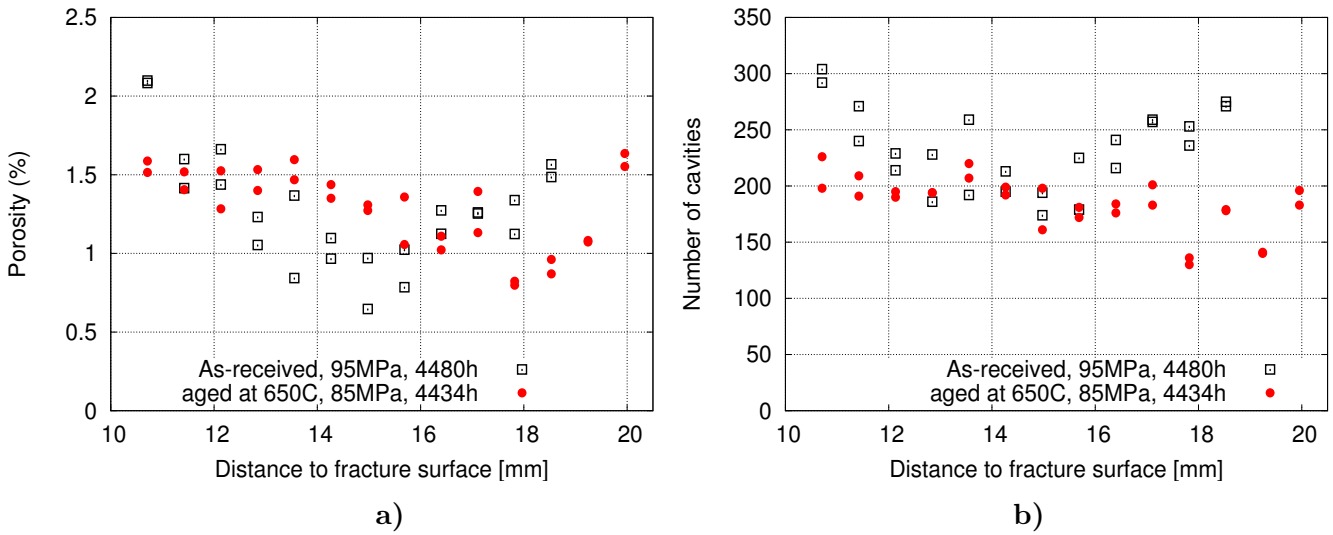

a) **b)**

Figure VII.38 : Area fraction of cavities (a) and number of cavities (b) estimated on areas of 711 µm × 489 µm in the as-received T92 steel (95MPa, 4,480h) and T92 steel thermally aged at 650°C for 10^4h (85MPa, 4,434h)

Note that the values of porosity (respectively number of cavities) in figure VII.38 were estimated on larger areas (i.e. 711 µm × 489 µm) compared to these in figure VII.36 estimated

on areas of 270 µm × 210 µm, consequently the values of porosity (respectively number of cavities) in figure VII.38 are higher compared to these in figure VII.36.

However, the values of porosity (respectively number of cavities) estimated by analysis of SEM images and light micrographs (figure VII.36 and figure VII.38) could be compared by considering the porosity (respectively number of cavities) per mm^2. Roughly from the results in figure VII.38 an average number of cavities roughly of about 200 on a light micrograph could be considered which corresponds roughly to about 600 cavities per mm^2. An average number of cavities of about 60 cavities could be considered on SEM images (see figure VII.36) which corresponds with about roughly 1200 cavities per mm^2. The number of cavities per mm^2 estimated using SEM images are roughly twice higher than that estimated using light micrographs. This could be explained by the fact that small size cavities are revealed in the SEM images which could not be revealed using the magnification of the light micrographs.

VII.4.2 Microtexture

For a given level of stress thermally aged steel shows a higher secondary creep rate ($\dot{\varepsilon}_{ss}$) compared to that of as-received steel T92. No clear evidence of a higher amount of creep damage was found in the thermally aged T92 steel specimen compared to that in the as-received steel both creep tested for similar amount of time ($\sim 4,500$h). This could be an indication of an enhanced recovery of the matrix in the thermally aged T92 steel compared to that in as-received T92 steel. In order to study this possible effect EBSD investigations were conducted on the T92 steel thermally aged at 650°C and creep tested under 85MPa for 4,434h. To further compare these results with a reference state, EBSD investigations were also conducted in the as-received T92 steel creep tested for similar lifetime, see figure VII.39.

EBSD investigations were also conducted on the T92 steel thermo-mechanically prepared at 550°C and then creep tested at 650°C, 95MPa ($t_r = 4,656$h) to study the influence of the prior recovery of the matrix on the creep creep behaviour. EBSD maps corresponding to this specimens are given in figure VII.44.

As-received T92 steel creep tested for 4,480h at 650°C, 95MPa

The microtexture of the as-received T92 steel creep tested for 4,480h at 650°C consists of both areas with small round-shaped grains and recovered areas with larger grains free of subgrains, see such grains in the corresponding EBSD boundaries map. The small grains are observed close to boundaries, some of such grains are indicated by full arrows in figure VII.39c. The recovered grains are probably prior martensite blocks. Some such grains are indicated by empty arrows in figure VII.39c. Most of boundaries of such grains are respecting the G-T relationships, see figure VII.39 compared with figure VII.40.

What seems to be small size grains (full arrows in figure VII.39c) in the EBSD-IQ map are not delimited by high angle boundaries (see such grains in the corresponding EBSD boundary map). Thus, the boundaries of such grains could not be analysed using G-T or K-S relationships.

The tempered lath martensitic microtexture could hardly be recognized after 4,480h of creep exposure at 650°C, see EBSD maps in figure VII.39 compared with EBSD maps in figure II.9. However no significant change could be observed in the histogram of misorientation angle between grains corresponding to the EBSD maps of the as-received T92 steel creep tested for 4,480h at 650°C compared to that of the as-received steel, see figure VII.41. Thus, only low-angle boundaries seem to have been affected by creep.

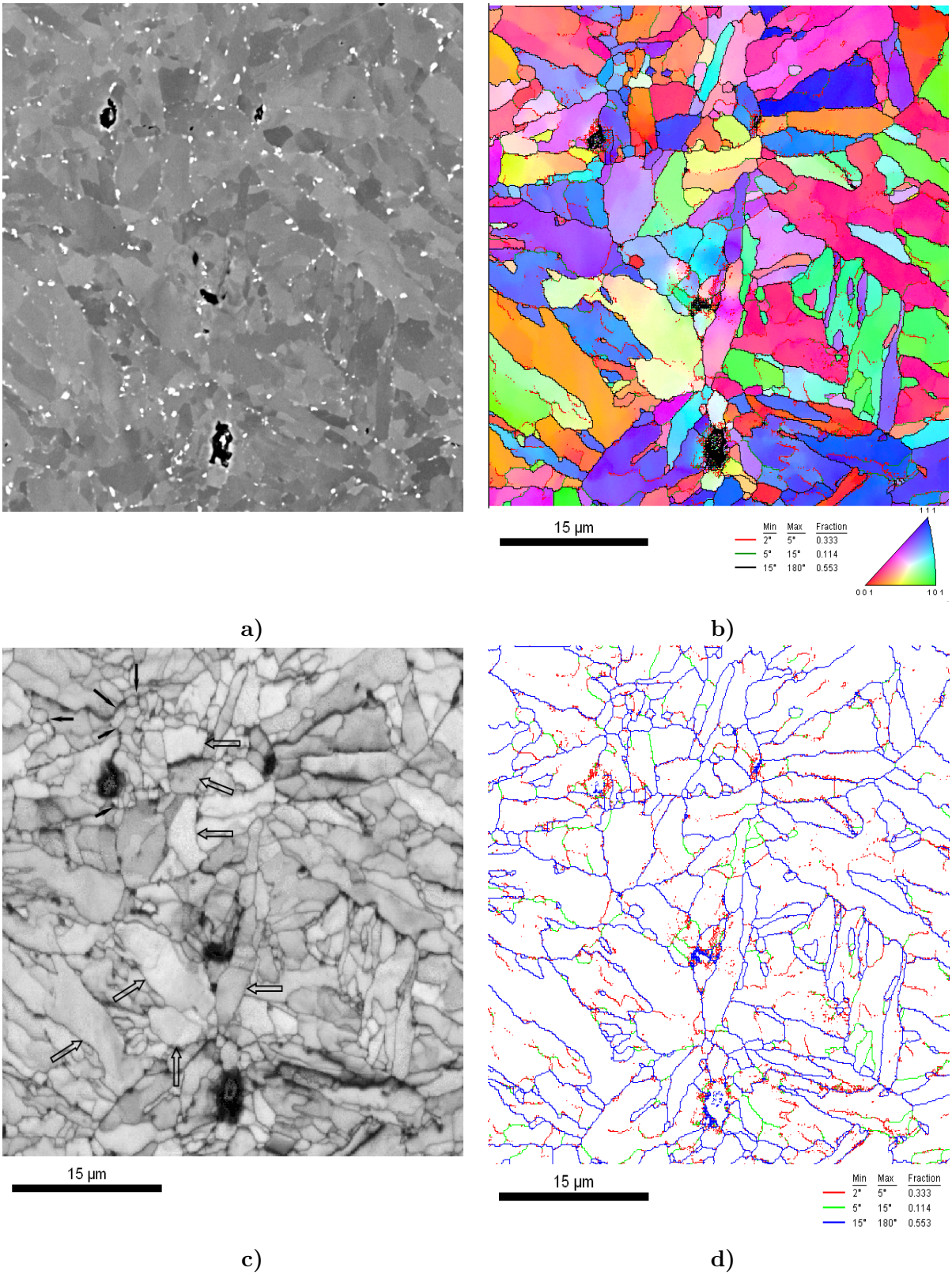

Figure VII.39 : EBSD maps of the as-received T92 steel creep tested at 650°C, 95MPa for 4,480h (at 10mm from the fracture surface). SEM-BSE image (a); EBSD-IPF map with orientation of sample normal in the crystal frame as color key (b); EBSD-IQ map (c); EBSD boundary map (d). Full arrows indicate small round-shaped grains; empty arrows indicate recovered grains

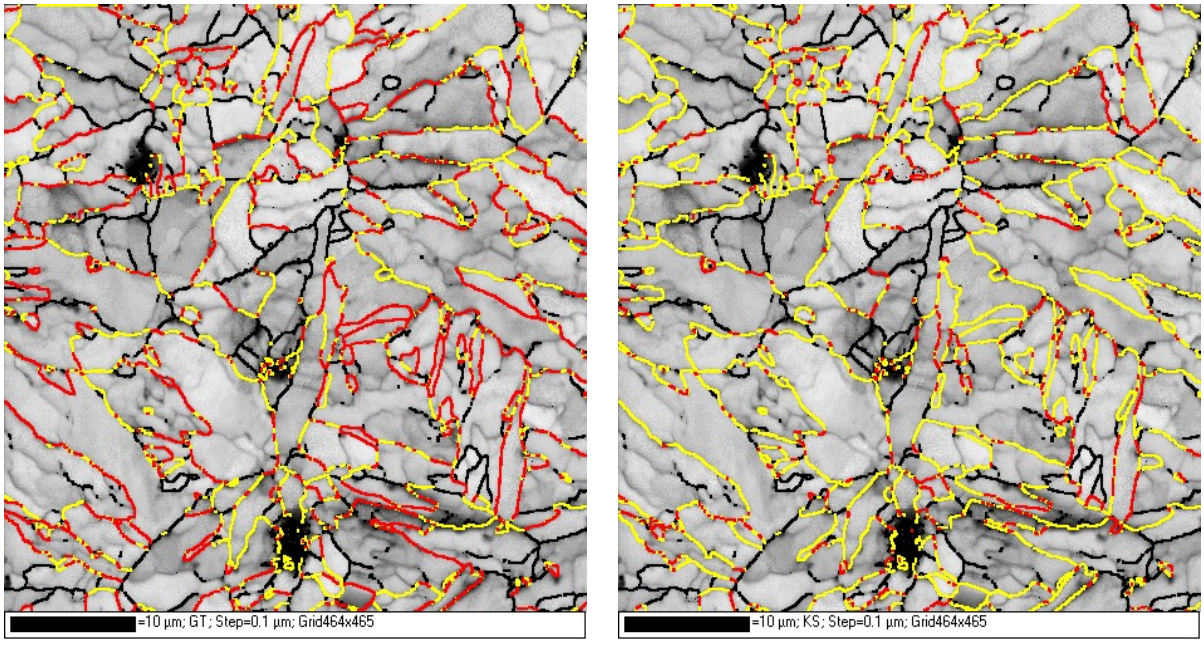

a) **b)**

Figure VII.40 : EBSD-IQ maps (same as in figure VII.39) showing in red boundaries respecting K-S relationships (a) and G-T relationships (b). Boundaries higher than 40° are represented in yellow and boundaries between 5°-40° are represented in black.

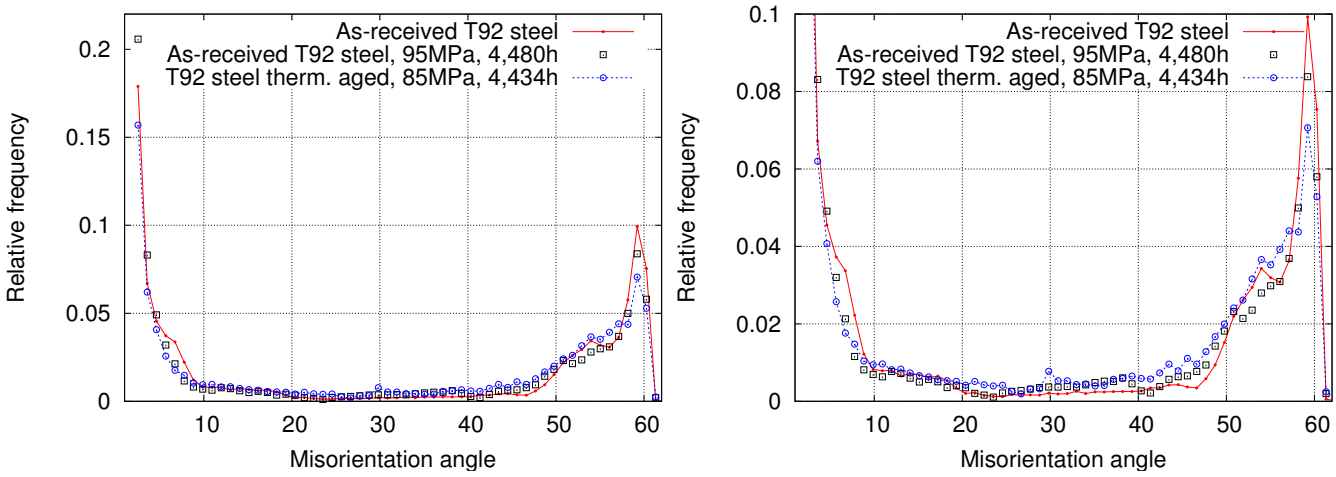

a) **b)**

Figure VII.41 : a) Distribution of misorientation angles (°) between neighboring grains corresponding to the EBSD maps in figures VII.42 and VII.39 compared to that from as-received T92 steel (corresponding to the lower EBSD map in figure II.9); b) same as a), close-up view

T92 steel thermally aged creep tested for 4,434h at 650°C, 85MPa

EBSD maps of the T92 steel thermally aged and then creep tested for 4,434h reveal a high amount of small round-shaped grains, mainly located at boundaries, see figure VII.42. It is difficult to say at which kind of boundaries these grains are located from figure VII.42. It could be prior austenite grain boundaries or packet boundaries. The amount of such small grains seems to be higher in the aged T92 steel compared to the as-received steel, both creep tested for similar times at 650°C, see figure VII.42 compared with figure VII.39.

As previously discussed, most of the boundaries of small size grains are not recognized to respect the G-T and/or K-S relationships, see figure VII.42 compared with figure VII.43. The fraction of 60.2 GT boundaries in the EBSD maps of the aged T92 steel significantly decreases after creep testing compared to that in the as-received T92 steel, see table VII.11.

The presence of large Laves phase prior to creep testing might be responsible for the formation of these small grains, probably due to a preferentially localization of strain close to the boundaries. Moreover, Laves phase precipitation during aging heat treatment had probably lead to areas depleted in W and Mo atoms close to boundaries at which they had precipitated. Thus deformation during creep could preferentially occur on these areas and lead to the formation of such smaller grains.

In order to see rather the diffusion of W had an influence on the formation of the small round-shaped grains observed in the EBSD-IQ maps, the average diffusion distance of W was estimated for an exposure time of 14,434h (10,000h of thermal aging and 4,434h of creep testing). The average diffusion distance (l) during a duration t is given by $l = \sqrt{2Dt}$, where D is the diffusion coefficient of the solute element under consideration. The values of diffusion coefficient (D) at temperature 650°C are needed to evaluated the l. Limited data are available in the literature. Using the data from the reference (Durand-Charre, 2003) the value of D at 650°C was estimated using the following formula:

$$D = D_0 \exp\left(-\frac{Q}{RT}\right) \tag{VII.7}$$

where $D_0 = 1,57 \times 10^{-4} \mathrm{m^2 s^{-1}}$, R is the universal gas constant (8,314472 $\mathrm{JK^{-1}mol^{-1}}$) and T is the temperature in K.

Thus, an average diffusion distance (l) of about 11 µm was found for an exposure time of 14,434h. This value corresponds more to the width of martensite blocks in the steel rather than the size of small round-shaped grains observed in the EBSD-IQ maps.

The microtexture of the T92 steel thermally aged crept specimens (85MPa; 4,434h) revealed by the EBSD maps in figure VII.42 seems to be comparable to that of the P92 steel creep tested for 33,308h at 650°C, 70MPa, see figure VII.24 and figure VII.25. This might suggest that microtexture evolution during long-term creep might be achieved on the thermally aged specimens whithin a shorter time.

The distribution of misorientation angles between neighbouring grains corresponding to the thermally aged T92 steel creep tested for 4,434h shows a slightly higher frequency of 30° angles compared to that in the as-received steel, see figure VII.41. Probably this is a misindexing artifact. Note that no significant difference was observed in the histogram of misorientation angles corresponding to the thermally aged T92 steel before creep testing.

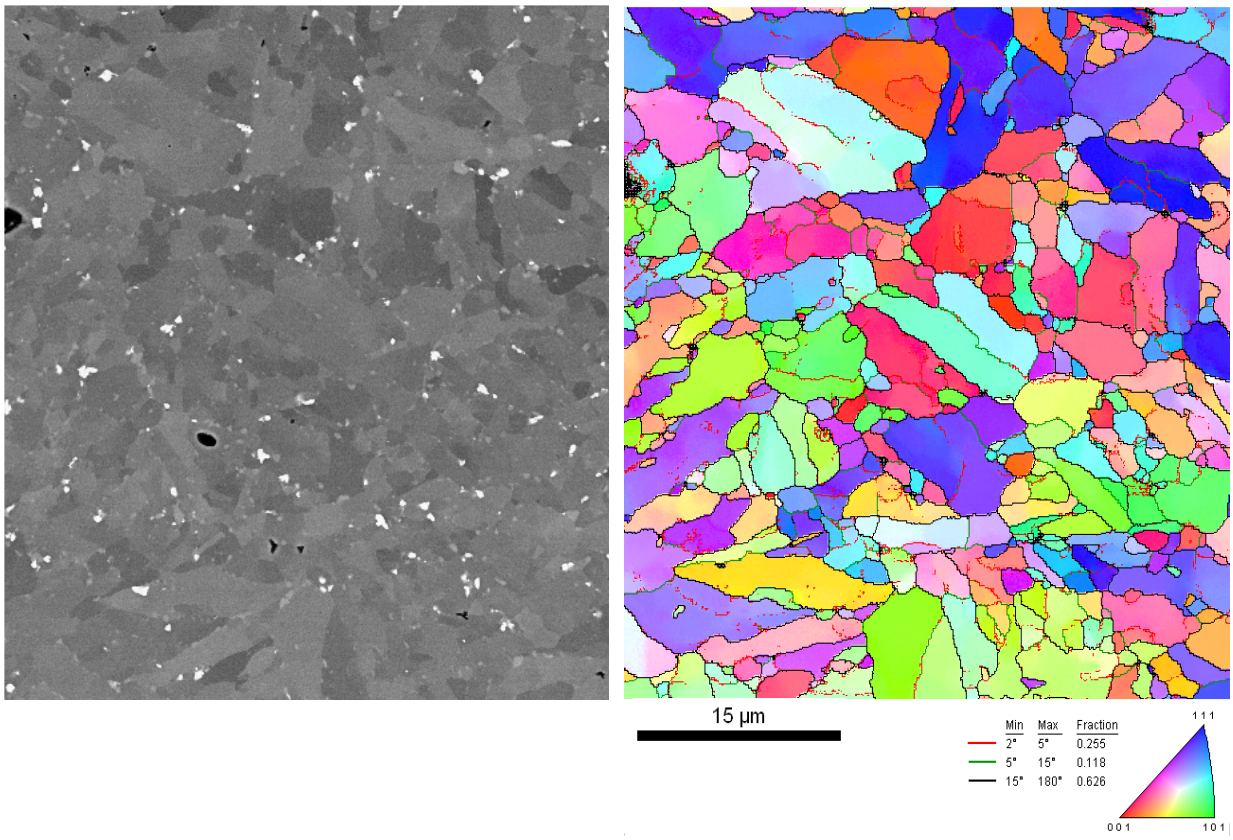

a) b)

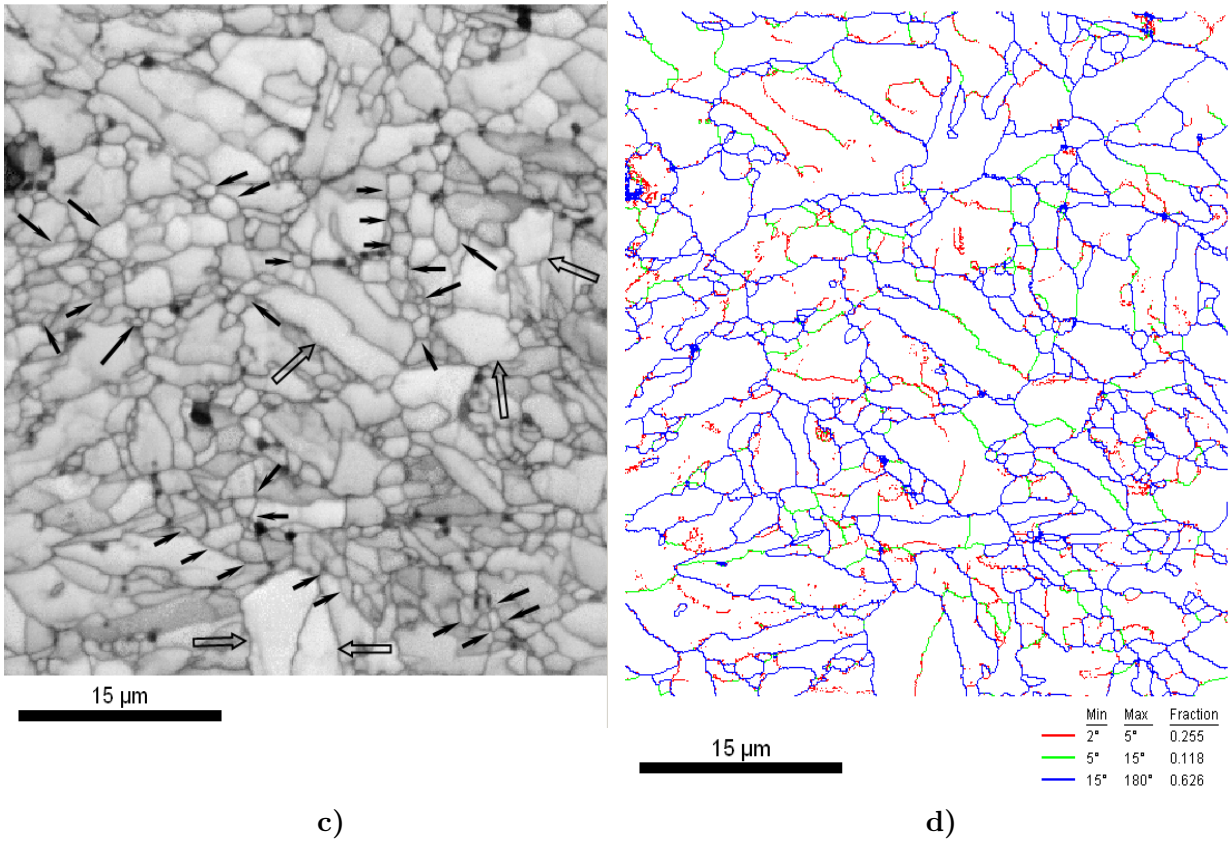

c) d)

Figure VII.42 : EBSD maps of the T92 steel thermally aged at 650°C for 10^4h and creep tested at 650°C, 85MPa for 4,434h (at 10mm from the fracture surface). SEM-BSE image (a); EBSD-IPF map with orientation of sample normal in the crystal frame as color key (b); EBSD-IQ map (c); EBSD boundary map (d). Full arrows indicate small round-shaped grains; empty arrows indicate recovered grains

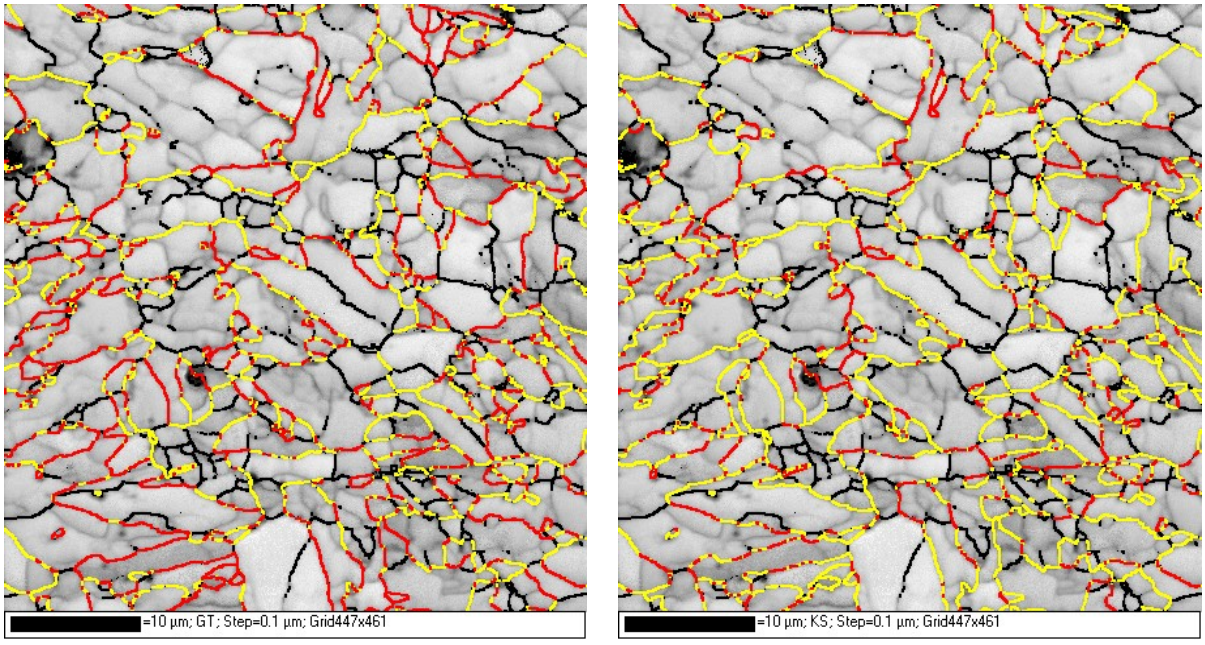

a) **b)**

Figure VII.43 : EBSD-IQ maps (same as in figure VII.42) showing in red boundaries respecting K-S relationships (a) and G-T relationships (b). Boundaries higher than 40° are represented in yellow and boundaries between 5°-40° are represented in black.

T92 steel thermo-mechanically prepared at 550°C then creep tested for 4,656h at 650°C, 95MPa

EBSD maps (figure VII.44) of the specimen thermo-mechanically prepared at 550°C then creep tested at 650°C reveals a recovered microtexture with large grains that appear to be free of sub-grains. However, the distribution of misorientation angle (figure VII.45) between neighbouring grains shows a typical shape commonly found for martensite variants from the same parent austenite grain. Compared to the as-received T92 steel a slight decrease in the frequency of low angle boundaries is observed in the thermo-mechanically prepared steel creep tested.

EBSD-IQ maps of the T92 steel thermo-mechanically prepared at 550°C revealed what seem to be small round subgrains without any particular crystal orientation in the corresponding BSD-IPF map, see figure A.11. Such subgrains are not observed after creep testing.

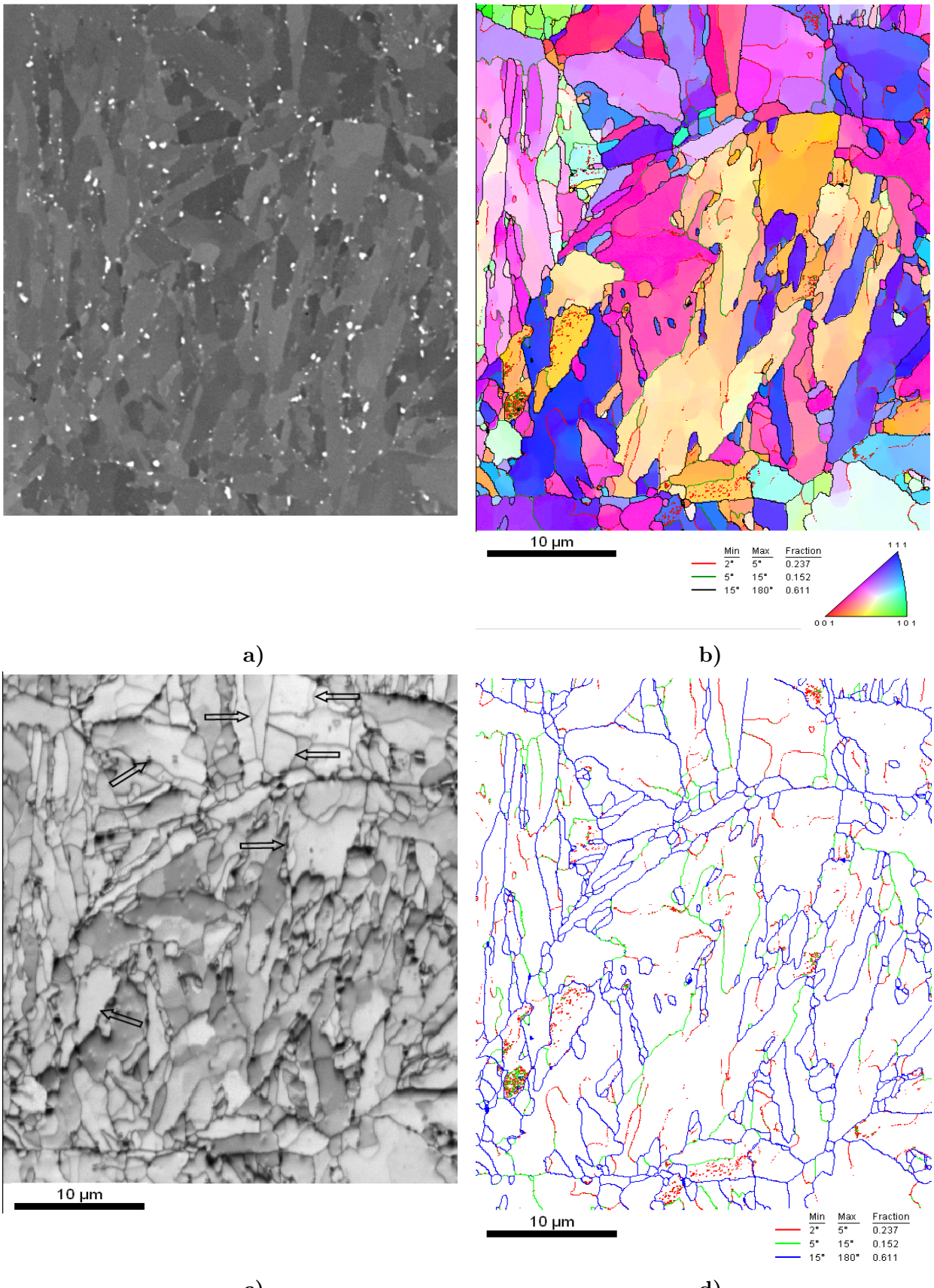

Figure VII.44 : EBSD maps of the T92 steel thermo-mechanically prepared at 550°C and creep tested at 650°C, 95MPa for 4,656h (at 10mm from the fracture surface). SEM-BSE image (a); EBSD-IPF map with orientation of sample normal in the crystal frame as color key (b); EBSD-IQ map (c); EBSD boundary map (d) Full arrows indicate small round-shaped grains; empty arrows indicate recovered grains

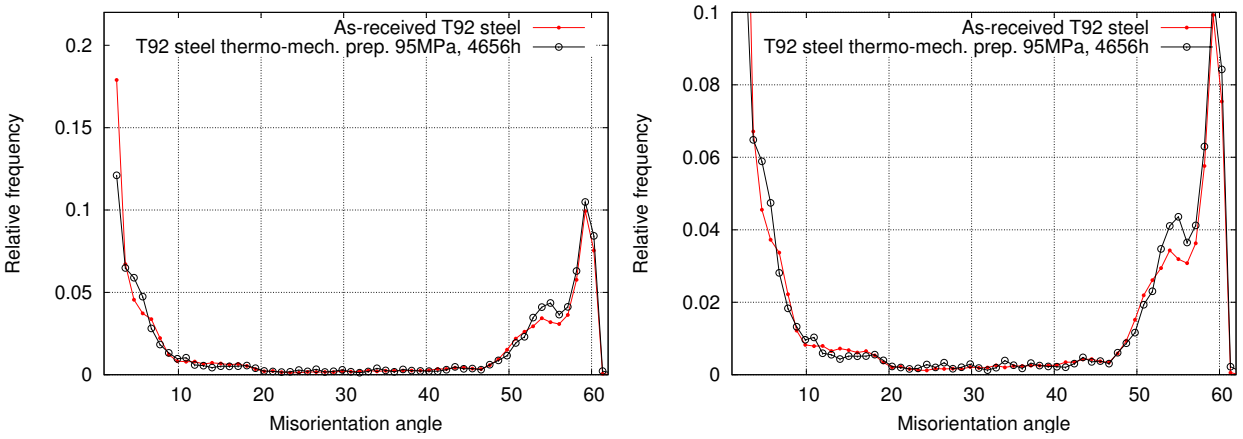

Figure VII.45 : a) Distribution of misorientation angles (°) between neighbouring grains corresponding to the EBSD map in figure VII.44 compared to that from as-received T92 steel (corresponding to the lower EBSD map in figure II.9); b) same as a), close-up view

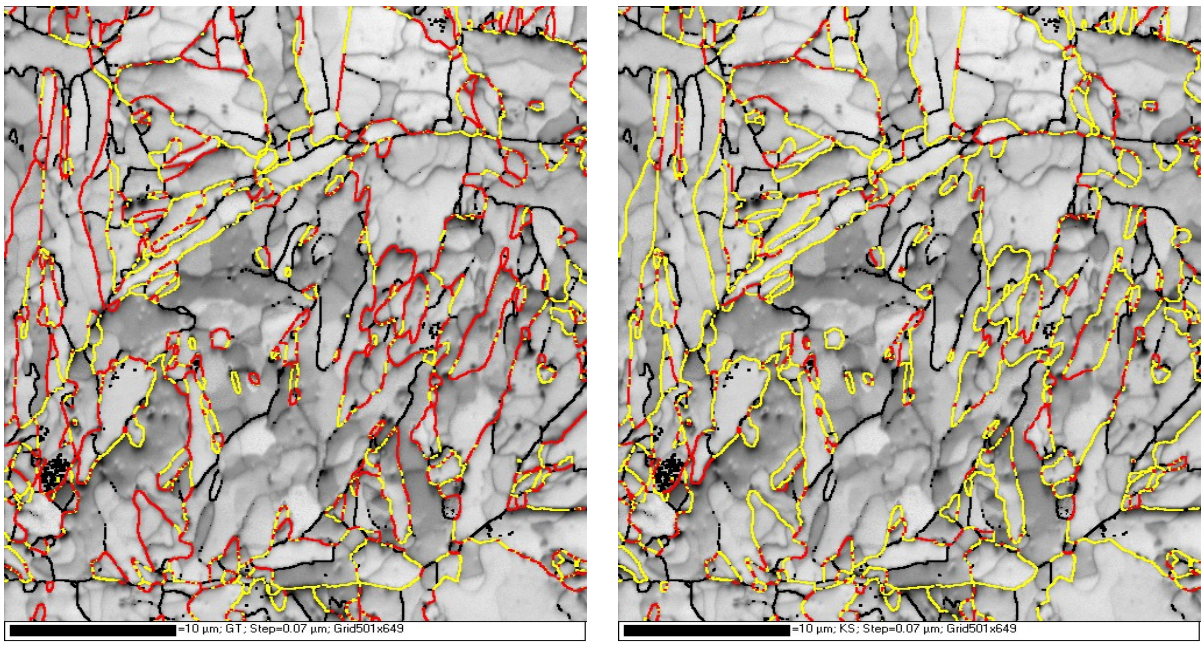

a) **b)**

Figure VII.46 : EBSD-IQ maps (same as in figure VII.44) showing in red boundaries respecting K-S relationships (a) and G-T relationships (b). Boundaries higher than 40° are represented in yellow and boundaries between 5°-40° are represented in black.

Table VII.11 : Analysis of boundaries respecting the K-S and G-T relationships in EBSD map

EBSD map	T92 steel As-received	T92 steel (95MPa; 4,480h)	T92 therm. aged (85MPa; 4,434h)	T92 th.mec.prep. at 550°C (95MPa; 4,656h)
Size of area	71 µm × 77 µm	46 µm × 46 µm	45 µm × 46 µm	35 µm × 45 µm
Step size	0.15μm	0.10 µm	0.10 µm	0.10 µm
Observations		figure VII.40	figure VII.43	figure VII.46
Fraction of G-T (K-S) boundaries in EBSD maps				
G-T type boundary				
⟨433⟩ 60.2 G-T	26.4	24.2	16.9	25.2
⟨111⟩ 49.6 G-T	1.16	0.67	0.96	0.38
⟨331⟩ 50. G-T	2.16	1.92	2.88	2.53
⟨433⟩ 50.2 G-T	1.72	1.76	2.06	1.11
⟨332⟩ 50.8 G-T	3.87	3.49	2.53	1.67
⟨110⟩ 60. G-T	5.06	3.69	4.55	4.80
⟨331⟩ 51.9 G-T	3.61	2.31	3.65	3.43
⟨110⟩ 54.3 G-T	4.94	3.56	4.11	4.60
⟨331⟩ 55.6 G-T	3.58	2.64	5.59	3.87
⟨441⟩ 57.5 G-T	4.02	2.39	4.76	4.10
K-S type boundary				
⟨111⟩ 60. K-S	1.49	1.70	2.02	2.66
⟨432⟩ 57.2 K-S	2.1	2.12	2.68	1.81
⟨331⟩ 57.2 K-S	4.79	3.32	6.27	4.85
⟨221⟩ 51.7 K-S	3.39	2.21	2.64	2.50
⟨322⟩ 50.5 K-S	0.9	1.17	1.28	0.65
⟨431⟩ 50.5 K-S	0.62	0.82	1.5	0.66
⟨111⟩ 49.5 K-S	0.04	0.11	0.06	0.01
⟨221⟩ 47. K-S	0.8	0.59	1.47	0.54
⟨110⟩ 49.5 K-S	0.1	0.32	0.41	0.23
⟨110⟩ 60. K-S	5.06	3.69	4.55	4.8

T92 th.mec.prep.: T92 steel thermo-mechanically prepared; T92 therm. aged: thermally aged at 650°C, 10^4h

in paranthesis are indicated the creep testing conditions

VII.4.3 Summary

No creep damage was observed in the homogeneously deformed part of the thermally aged specimens after creep testing under levels of stress at least equal to 160MPa at 600°C and higher than 110MPa at 650°C, i.e. for lifetimes lower than 10^4h and 10^3h, respectively. These levels of stress correspond to high stress regions in the creep flow at 600°C and 650°C of the as-received Grade 92 steel. The T92 steel and P92 steel creep tested for high stress both at 600°C and 650°C showed no creep damage in the part of the specimens homogeneously deformed during creep.

Creep damage was observed throughout the gauge part of the thermally aged specimens tested at 650°C under 95MPa for 2,016h and under 85MPa for 4,434h. No significant change was observed in the amount of creep damage in these specimens compared to that in as-

received specimens tested for similar amounts of time at 650°C.

Consequently, prior thermal ageing at the same temperature as the creep tests temperature does not seem to accelerate the development of creep damage, at least in smooth tensile specimens with respect to the as-received steel. This is consistent with the fact that the reduction of area is not affected either. Thus the reduction in creep lifetime could be attributed to an increase in the creep rate without any decrease in creep ductility.

Precipitation of Laves phases enhance creep deformation, thermally aged specimens show a higher $\dot{\varepsilon}_{ss}$ both at 600°C and 650°C compared to that of the specimens in as-received steel. Although Laves phases are frequently observed in the vicinity of creep damage cavities, the precipitation of Laves phases does not seem to enhance creep damage development. Creep damage development occurs in the thermally aged specimens for similar levels of stress and similar testing times, as in as-received T/P92 steels.

For similar amounts of creep testing time the hardness of thermally aged T92 steel is lower than that of the as-received T92 steel, both at 600°C and 650°C. This might be explained by an enhanced matrix substructure recovery during creep of the thermally aged T92 steel compared to that occurring in as-received T92 steel.

EBSD investigations revealed a microtexture of the thermally aged T92 steel creep tested for 4,434h at 650°C similar to that of the P92 steel creep tested for 33,308h at 650°C. Moreover, the EBSD-IQ maps revels what seems to be small size round shaped grains close to the prior austenite grains and/or packets boundaries. These grains are probably delimited by low angle boundaries because the boundaries of such grains are not revealed in the corresponding EBSD boundary maps. However, the amount of such grains seems to be higher in the aged T92 steel compared to the as-received T92 both creep tested at 650°C for similar amount of times, see figure VII.39 compared with figure VII.42.

VII.5 Notched specimens

The results of creep tests conducted at 600°C and 650°C on notched specimens were given in tables V.4 and VI.4 respectively. The purpose of the notched specimens was to investigate the influence of stress triaxility on creep damage development. Thus, creep damage was investigated in the unbroken notch of specimens after testing both at 600°C and 650°C. Stress triaxiality could have affected microstructural evolution during creep exposure, thus this was also investigated in notched specimens after testing.

General remarks

Hardness measurements

Hardness measurements along the longitudinal axis of all kinds of notched specimens after creep testing revealed a decrease in hardness in the notched area while the hardness of the smooth parts (i.e. outside the notches) was unchanged compared to that of the as-received T92 steel (i.e. $\sim 237 \pm 5\text{HV}_{0.5}$), see figures VII.47, VII.48, VII.55, VII.57 and VII.58. Because of the small size of notched areas, hardness measurements were also conducted in the transversal axis in the middle of notched areas in order to increase the number of hardness measurement points in the notched area. These measurements confirmed the above mentioned results.

The decrease in hardness in the notched area occurs because only the notched area was subject to creep deformation but it could also be an indication of creep damage development. The hardness in notched areas is similar to the hardness (roughtly of $\sim 200\text{HV}_{0.5}$ at 600°C and $\sim 170\text{HV}_{0.5}$ at 650°C) of smooth specimens tested for long-term creep ($t_r > 10^4$h at 600°C and $t_r > 10^3$h at 650°C), see figures VII.47, VII.48, VII.55, VII.57 and VII.58 compared with figures VII.6 and VII.7.

Creep damage development

Creep damage occurred more extensively in the notched areas of specimens compared to that in a smooth specimen creep tested for similar amounts of time. Cavities are observed throughout the notched areas of the specimens after creep testing but they are not homogeneously distributed. The localization of the most damaged area inside the unbroken notch was found to depend on the geometry of the specimen.

Investigation of creep damage and/or microstructural evolution close to the broken notch is difficult due to its small size, high damage development and artefacts of sample preparation (i.e. edge effects). Thus, microstructural investigations were conducted mainly on unbroken notches. Moreover, the unbroken notch is not affected by the acceleration of deformation preceding fracture of the specimen.

In the following are presented creep damage characteristic features that are typical to each kind of notched specimen after creep testing.

VII.5.1 NTDC1.2 notched specimen

VII.5.1.1 Hardness

The center of the notched area of the NTDC1.2 specimens creep tested under $\sigma_n = 210$MPa, $\sigma_n = 230$MPa and $\sigma_n = 170$MPa show a hardness of about 200HV0.5, see figure VII.47. This value of hardness is similar to that of the P92 steel specimens creep tested for 49,721h, see figure VII.6.

Note that the NTDC1.2 specimen under σ_n = 170MPa was interrupted after 14,137h of testing which corresponds to the onset of tertiary creep stage on the creep curve. The hardness of both unbroken notches of this specimen is similar to that of notched areas of the fractured NTDC1.2 specimens under σ_n = 210MPa, σ_n = 230MPa.

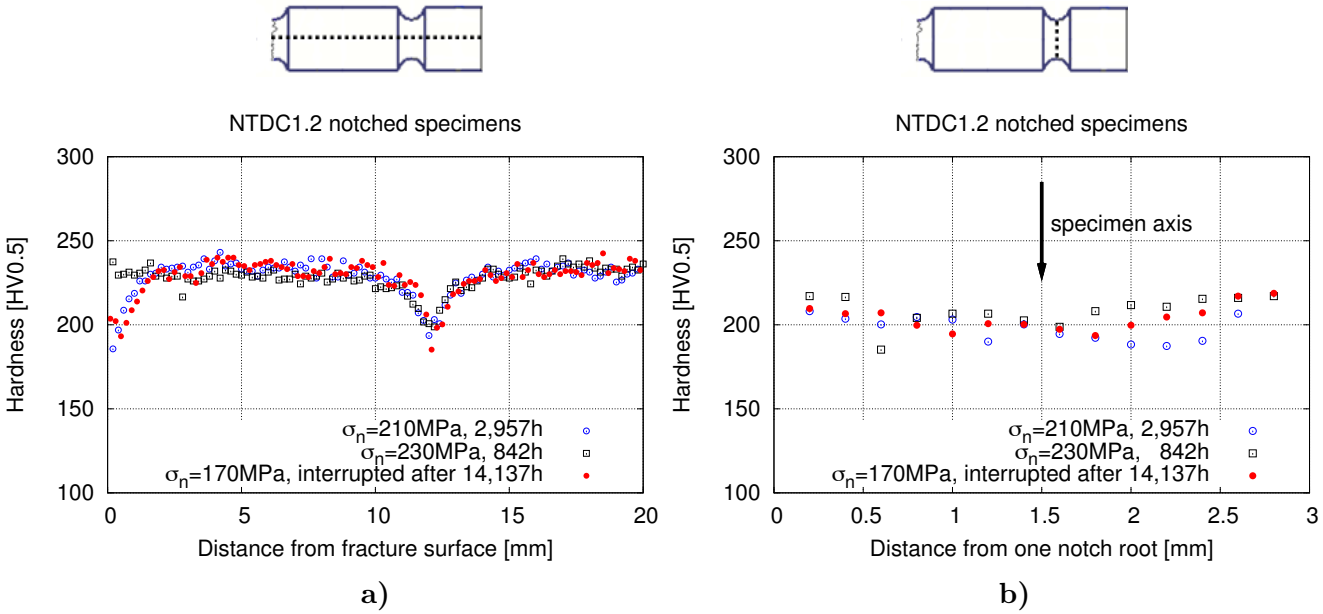

Figure VII.47 : Hardness along the longitudinal direction (a) and along radial direction of notched area (b) of NTDC1.2 specimens (dotted lines in upper drawings) after creep testing at 600°C

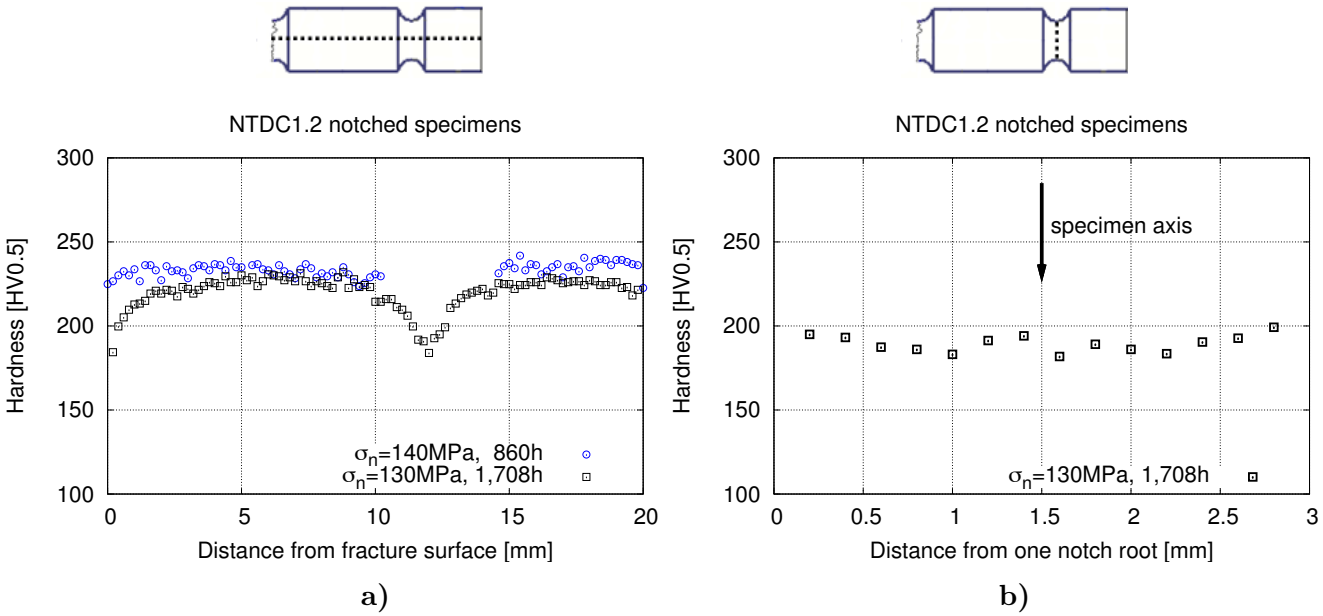

Figure VII.48 : Hardness along the longitudinal direction (a) and along radial direction in the notched area (b) of NTDC1.2 specimens (dotted lines in upper drawings) after creep testing at 650°C

The hardness in the unbroken notch of the NTDC1.2 specimen creep tested under σ_n = 130MPa for 1,708h is similar to that of P92 steel specimens creep tested for long-term creep

at 650°C, see figure VII.48 compared with figure VII.7.

The unbroken notch of the NTDC1.2 specimen tested at $\sigma_n = 140$MPa for 860h was accidentally broken during the removal of the specimen after testing, thus the hardness could not be measured in the notched area of this specimen.

VII.5.1.2 Creep damage

Figure VII.49a shows creep damage observed in the center of the notched area of the NTDC1.2 specimen tested under $\sigma_n = 210$MPa for 2,957h. No creep damage was observed in a smooth specimen creep tested for a similar amount of time at 600°C (i. e. T92 steel; 170MPa; 2,867h). Creep damage in the notched area of the NTDC1.2 specimen tested for 2,957h under $\sigma_n = 210$ MPa was quantified by image analysis and the results are given in figure VII.50. The area fraction of cavities in this specimen is maximum in the center of the notched area. This corresponds to maximum of principal stress (σ_{22}) during creep testing estimated by finite element simulations (see figures V.19 and VI.18).

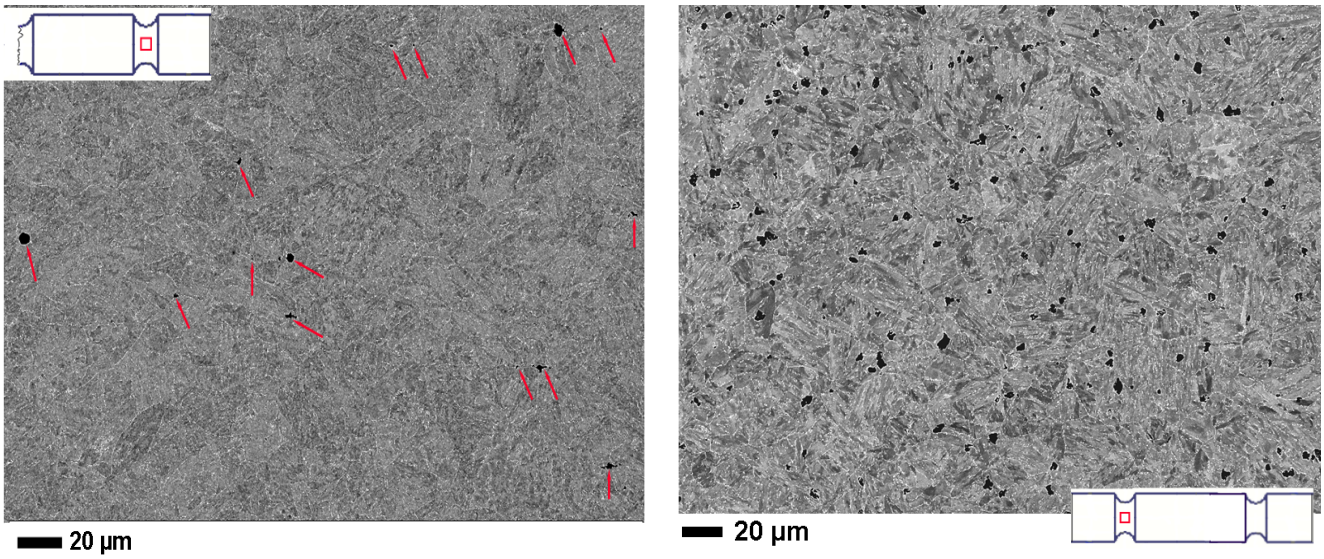

a) $\sigma_n = 210$MPa, $t_r = 2,957$h **b)** $\sigma_n = 170$MPa, interrupted after 14,137h

Figure VII.49 : Creep damage (in black) in the unbroken notch of NTDC1.2 specimens creep tested at 600°C (SEM-BSE images after colloidal silica polishing)

Extensive creep damage is observed in both unbroken notches of the NTDC1.2 specimen interrupted after 14,137h. Figure VII.52 shows the creep damage in one unbroken notch of this specimen. A high amount of cavities can be observed even using a light microscope. No significant difference was observed in the amount of creep damage between the two unbroken notches of this NTDC1.2 specimen.

Creep damage quantification in one unbroken notch of the NTDC1.2 specimen interrupted after 14,137h reveals higher number and higher area fraction of cavities compared to these in smooth P92 steel specimen creep tested for 49,721h at 600°C, 120MPa; see figure VII.51 compared with figure VII.11. Figure VII.49b shows a typical SEM-BSE image used for creep damage quantification in the NTDC1.2 specimen.

No maximum of area fraction of cavities could clearly be found in the unbroken notches of the NTDC1.2 specimen interrupted after 14,137h as was the case of the NTDC1.2 specimen creep tested at $\sigma_n = 210$MPa ($t_r = 2,957$h). As can be seen in figure VII.52 the distribution

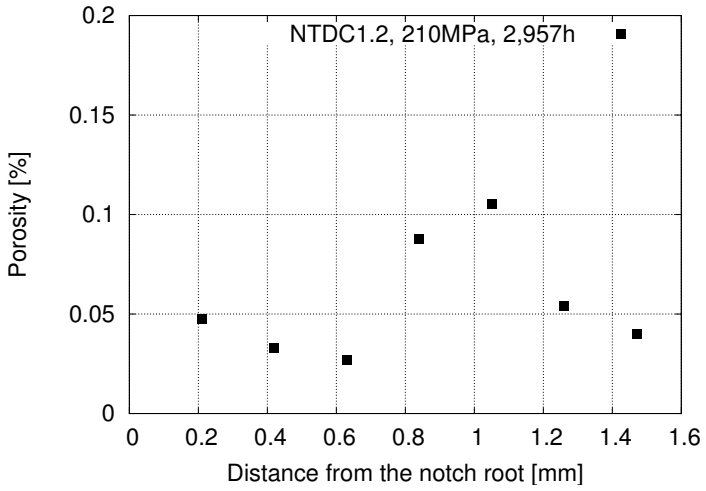

Figure VII.50 : Area of cavities estimated on areas 270 µm × 210 µm in the unbroken notch of the NTDC1.2 specimen creep tested under $\sigma_n = 210$MPa at 600°C for 2,957h

of cavities does not clearly indicate an area with highest amount of cavities. This seems to be consistent with the distribution of principal stress (σ_{22}) estimated by FE simulations for this specimen, see figure V.19. The NTDC1.2 specimen interrupted after 14,137h which corresponds to an opening of both notches of about 0.13mm, the creep curve of this specimen in figure V.17. The levels of σ_{22} corresponding to this notch opening (i.e. $\delta - \delta_0 = 0.065$mm in figure V.19) are slightly higher close to the notch root, but no significant difference could be observed in the σ_{22} distribution inside the notched area.

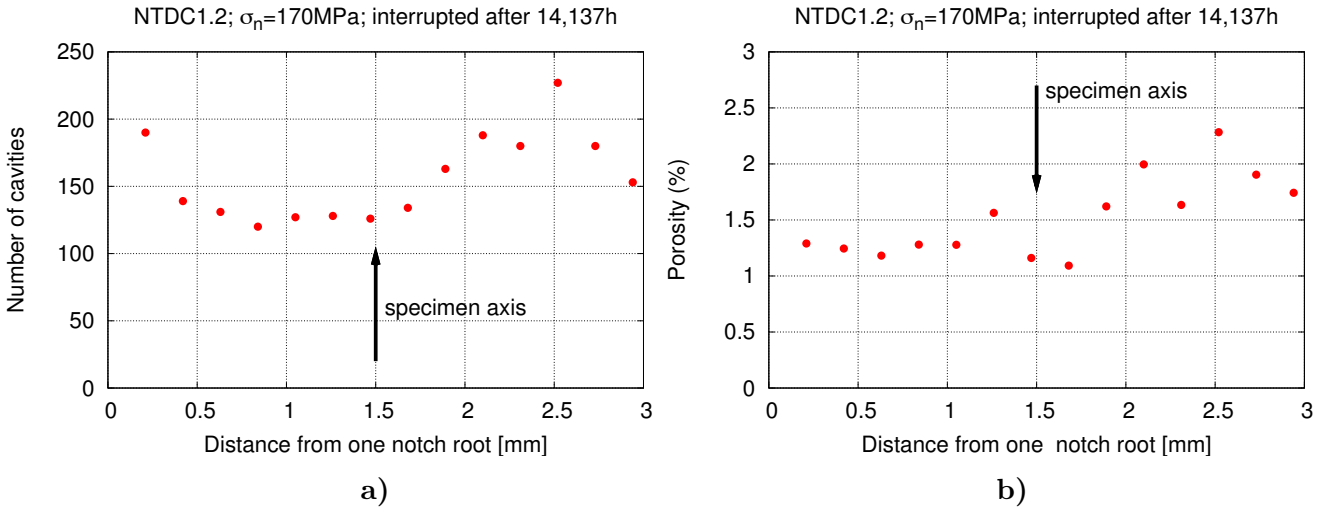

Figure VII.51 : Number (a) and area fraction (b) of cavities measured on areas of 270 µm × 210 µm in one unbroken notch of the NTDC1.2 specimen interrupted after 14,137 h of creep at 600°C, $\sigma_n = 170$MPa

The area fraction of cavities determined by image analysis of SEM-BSE images shows higher values close to the notch root, figure VII.51. This might result from the scatter of data due relatively small size of areas which can be analysed using SEM-BSE images.

EBSD investigations were conducted in the center of the notched area of the NTDC1.2

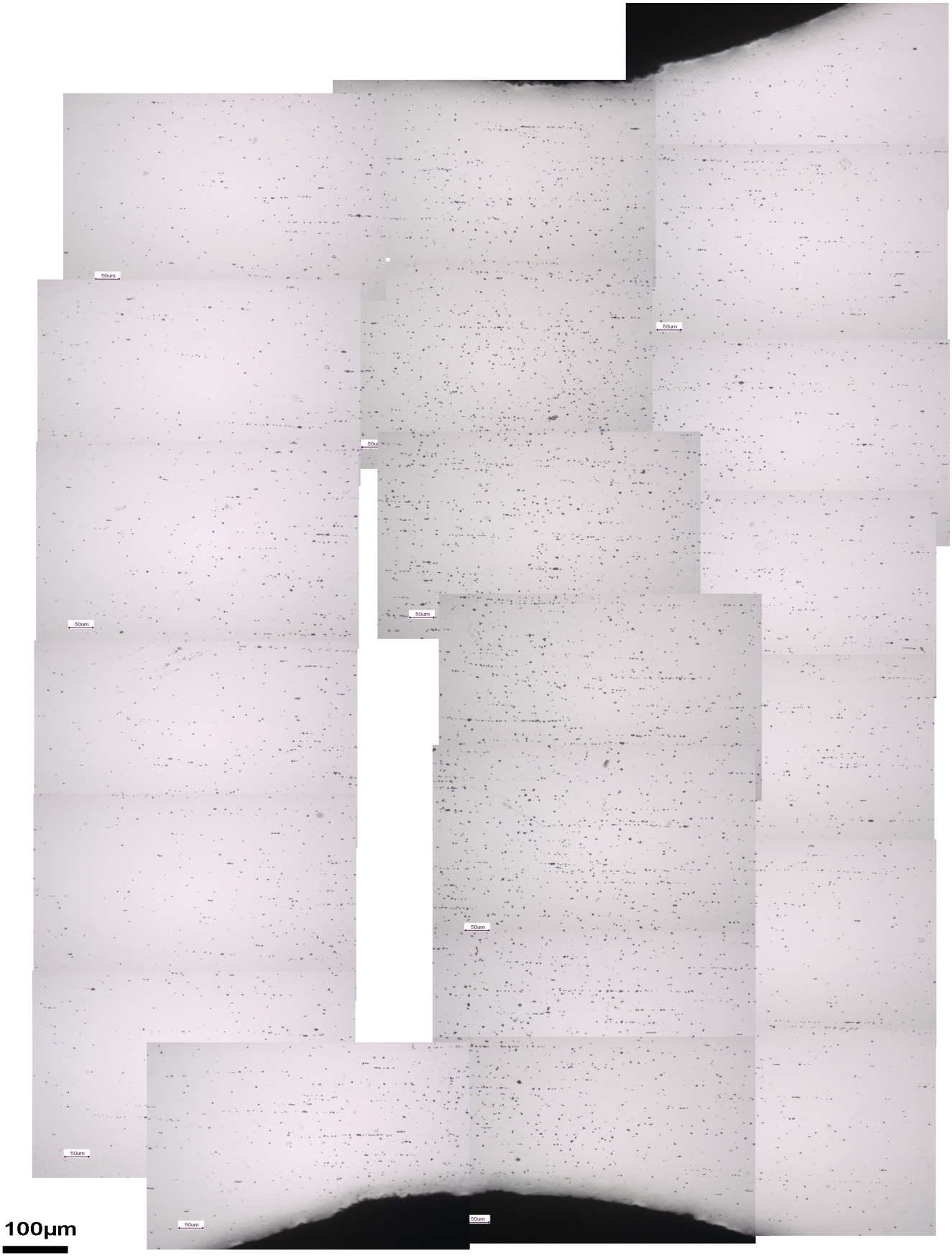

Figure VII.52 : Creep damage in one unbroken notch of the NTDC1.2 notched specimen interrupted after 14,137h of creep at $\sigma_n = 170$MPa, 600°C

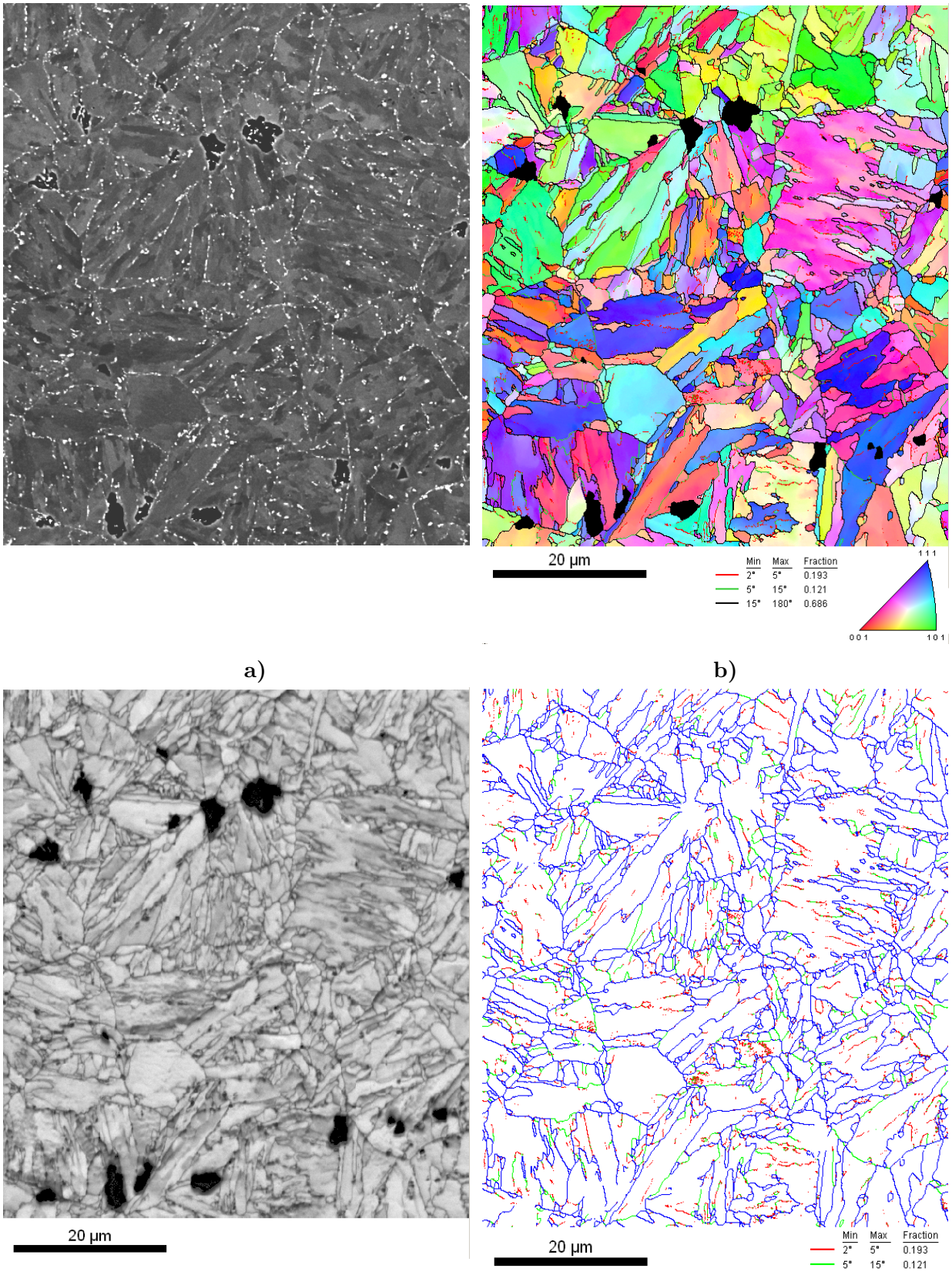

Figure VII.53 : Microstructure of NTDC1.2 notched specimen interrupted after 14,137h of creep at σ_n = 170MPa, 600°C. a) SEM-BSE image; b) Inverse Pole Figure (IPF) with orientation of sample normal in the crystal frame as color key; c) EBSD Image Quality map (IQ); d) EBSD boundary map

specimen interrupted after 14,137h to study whether stress triaxiality enhanced recovery of the matrix. No significant change could be observed between the EBSD maps (figure VII.53) of this specimens compared to that of the as-received steel (figure II.9) or that of the P92 steel creep tested for long-term creep at 600°C (figure VII.19). No significant difference was observed in the histogram of misorientation angles between grains corresponding to the EBSD maps in figure VII.53 and that of the as-received steel.

VII.5.2 NTDC0.6 notched specimen

VII.5.2.1 Hardness

No significant change in hardness was observed in the NTDC0.6 specimen interrupted after 6,193h of creep at σ_n = 170MPa, 600°C, see figure VII.54. This is probably because this specimen was not subject to a significant deformation, see the corresponding creep curve in figure V.16.

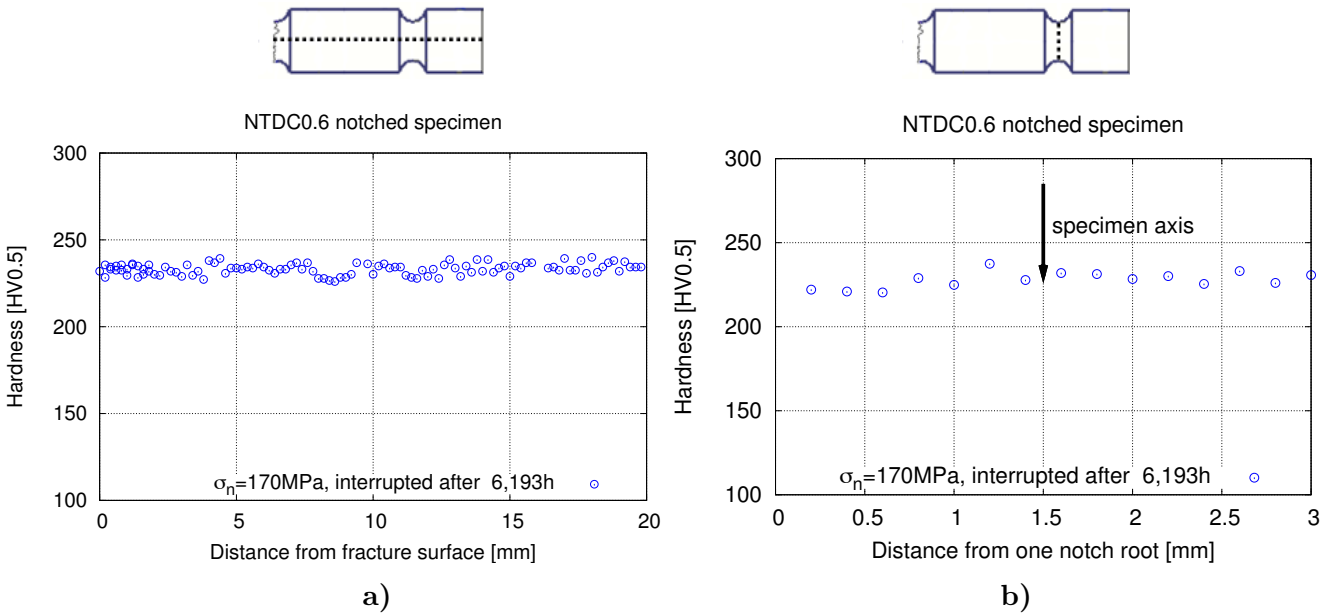

Figure VII.54 : Hardness along the longitudinal direction (a) and the radial direction of notched area (b) of NTDC0.6 specimen (dotted lines in upper drawings) interrupted after 6,193h of creep at σ_n = 170MPa, 600°C

VII.5.2.2 Creep damage

Creep damage was observed in the unbroken notch of the NTDC0.6 specimen tested for 4,074h under σ_n = 210MPa at 600°C. A maximum area fraction of cavities is observed close to the notch root. No creep damage was observed in the homogeneously deformed part of the smooth specimens tested for similar amounts of time at 600°C.

No creep damage was observed in the NTDC0.6 notched specimen interrupted after 6,193h at 600°C, σ_n = 170MPa. It is to be mentioned that this specimen was not subject to high creep deformation, as can be seen in figure V.16.

VII.5.3 NTDC0.6M notched specimen

VII.5.3.1 Hardness

Figure VII.55 shows the hardness of the NTDC0.6M specimens after creep testing at 600°C under the σ_n = 230MPa and σ_n = 240MPa. The hardness of the NTDC0.6M specimens creep tested under σ_n = 130MPa at 650°C is represented in figure VII.55. The hardness in the notched area of these specimens is similar to that of the specimens creep tested for long-term.

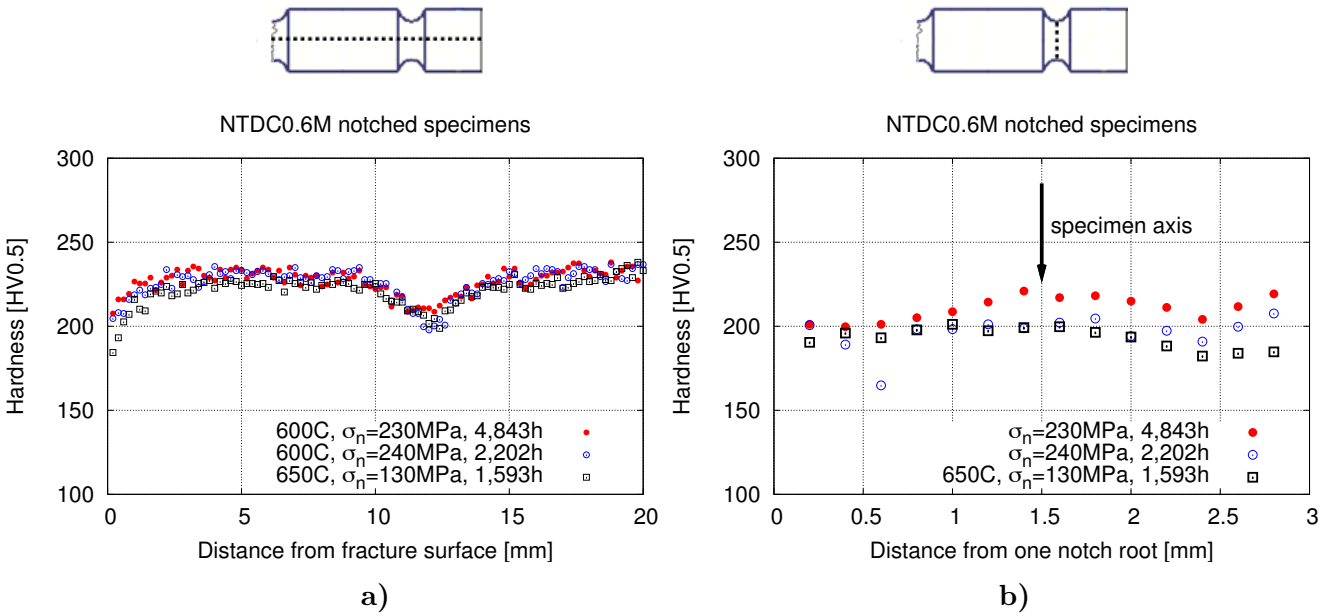

Figure VII.55 : Hardness along the longitudinal direction (a) and the radial direction of notched area (b) of NTDC0.6M specimens (dotted lines in upper drawings) after creep testing

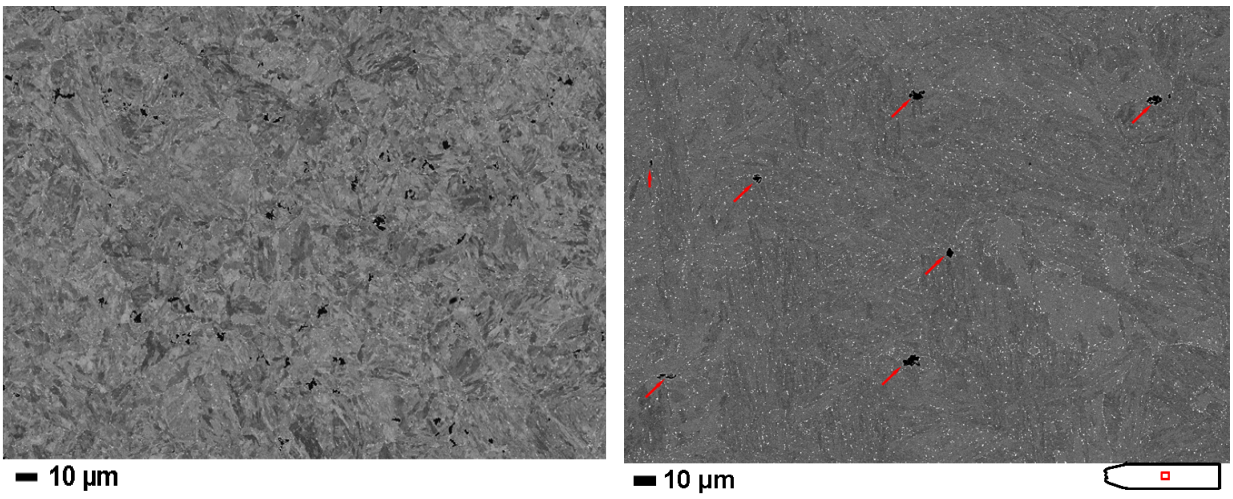

Figure VII.56 : a) Creep damage close to the notch root of the NTDC0.6M notched specimen tested at 650°C and σ_n = 130MPa for 1,593h; b) Creep damage at 10 mm from the fracture surface in the smooth P92 creep specimen tested at 650°C, 110MPa for 2,092h

VII.5.3.2 Creep damage

In figure VII.56 are compared creep damage observed close to the notch root in the NTDC0.6M notch specimen tested for 1,593h at 650°C and creep damage observed in a smooth specimen tested for a similar amount of time at 650°C. A higher number density of cavities is observed in the NTDC0.6M notched specimen compared to a smooth one both creep tested for similar amount of time at 650°C, see figure VII.56.

VII.5.4 NTDV notched specimen

VII.5.4.1 Hardness

In figure VII.57 and figure VII.58 are represented the hardness of several NTDV specimens creep tested at 600°C and 650°C, respectively. An increase in hardness is observed close to the notch roots of the NTDV specimen creep tested under σ_n310MPa at 600°C for 598h, see figure VII.57. This could be due to a hardening of the steel close to the root of notches, most probably consequence of the relatively high levels of stress during creep testing in these areas. In figure V.18 were represented the stress distribution in the radial axis of the notched area of a NTDV specimen for a σ_n = 350MPa. NTDV specimens creep tested for longer times both at 600°C and 650°C shows a decrease in hardness close to the notch roots.

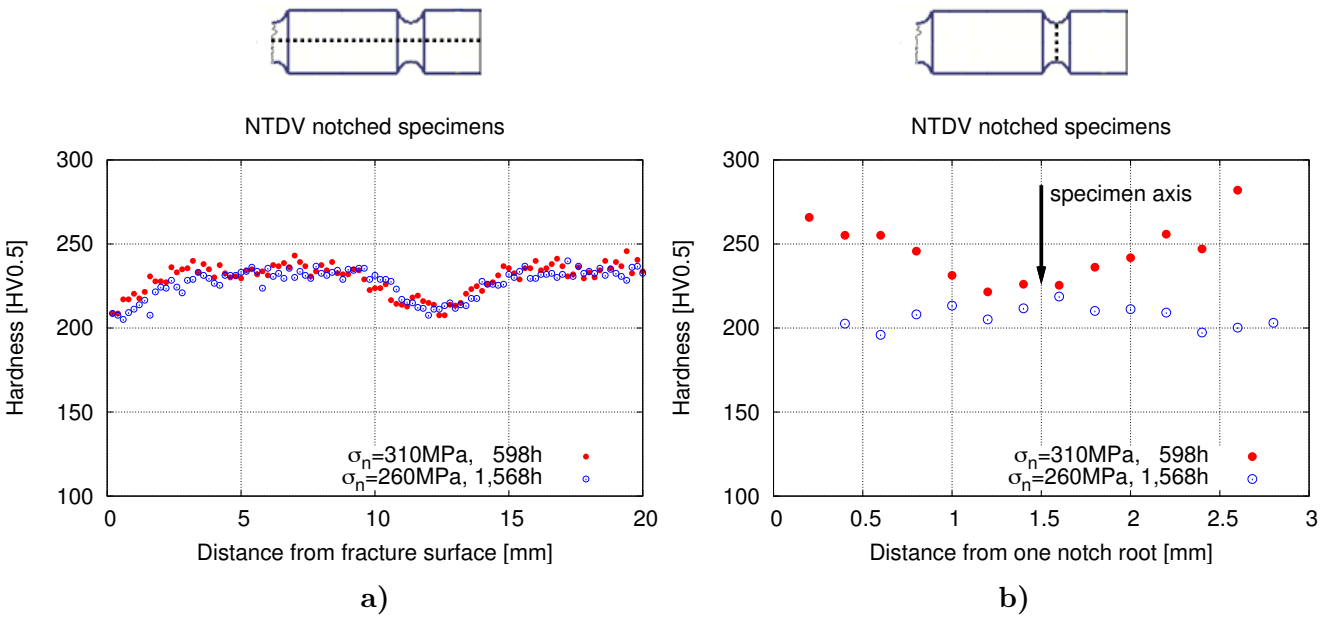

Figure VII.57 : Hardness along the longitudinal direction (a) and the radial direction of notched area (b) of NTDV specimens after creep testing at 600°C (dotted lines in upper drawings)

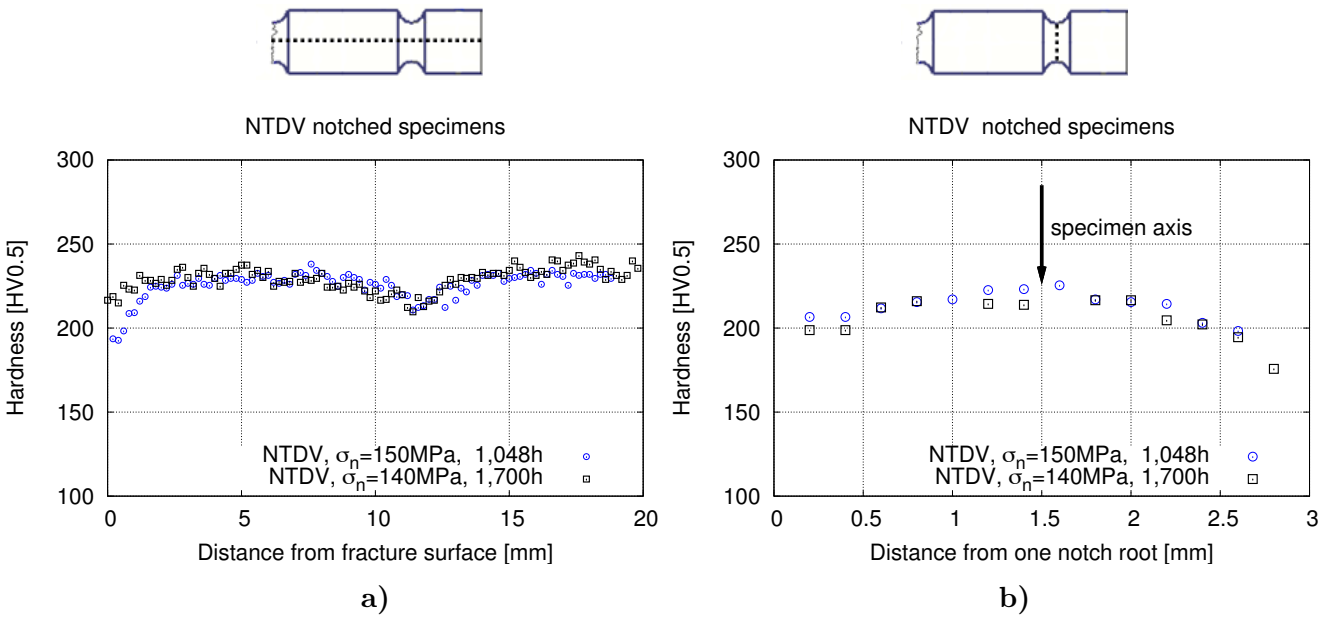

Figure VII.58 : Hardness along the longitudinal direction (a) and the radial direction of notched area (b) of NTDV specimens after creep testing at 650°C (dotted lines in upper drawings)

VII.5.4.2 Creep damage

Most of the boundaries are affected by creep damage close to the unbroken notch root of NTDV specimens after creep testing, see figure VII.59. From the distribution of precipitates creep damage cavities seem to be located at both prior autenite grain and packet boundaries, see for instance figure VII.59. To get complementary informations about the kind of boundaries at which cavities are observed EBSD investigations were conducted on the NTDV specimen creep tested under $\sigma_n = 140$MPa, 650°C for 1,700h.

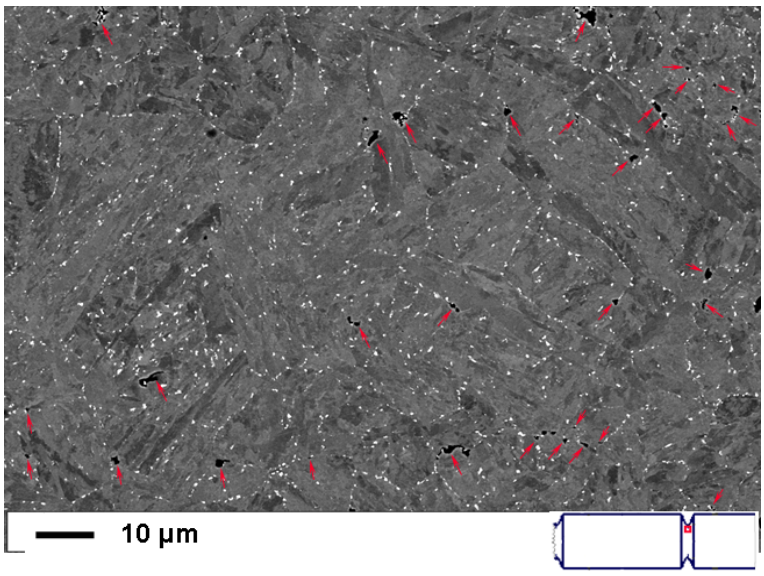

Figure VII.59 : Creep damage in the NTDV notched specimens tested at 650°C and $\sigma_n = 140$MPa for 1,700h showing cavities located at boundaries

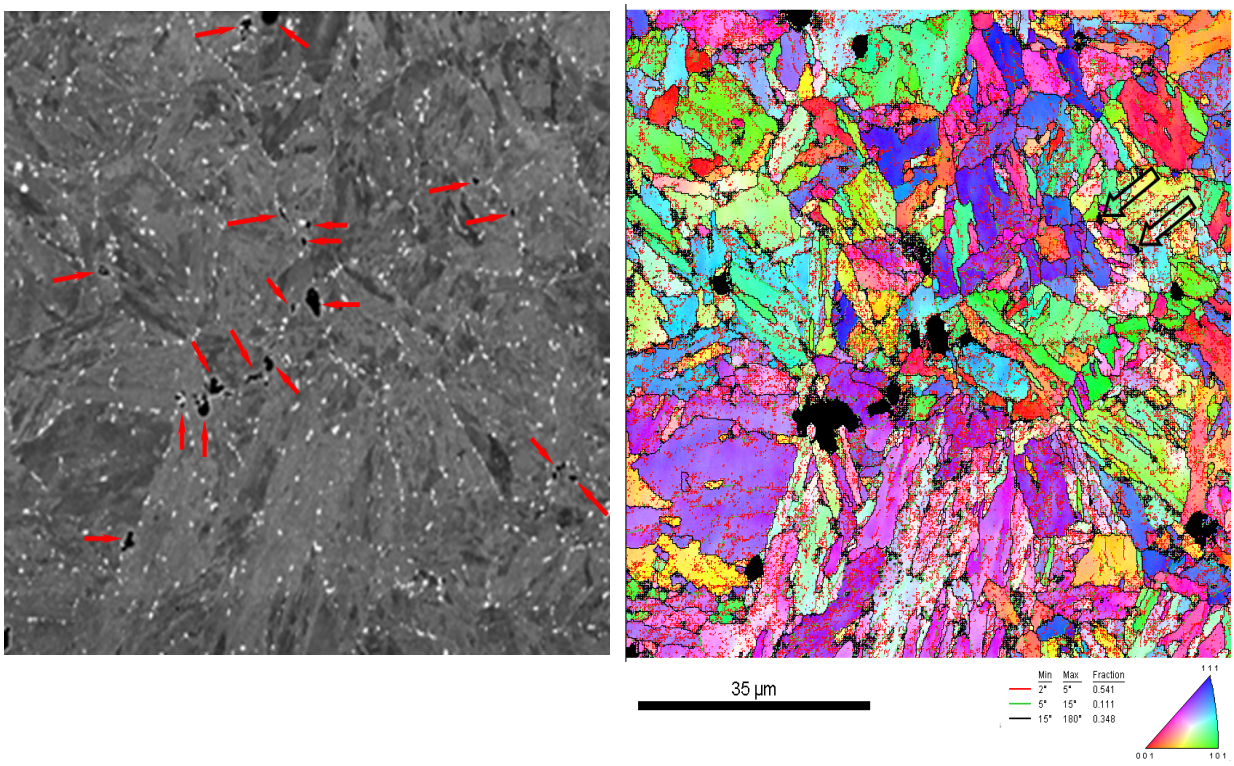

a) **b)**

Figure VII.60 : Microstructure of NTDV notched specimen creep tested at $\sigma_n = 140$MPa, 650°C for 1,700h, close to root of the unbroken notch (arrows indicate cavities). a) SEM-BSE image; b) Inverse Pole Figure (IPF) with orientation of sample normal in the crystal frame as color key

Although an area showing relatively small size cavities was selected for EBSD investigations it was difficult to get informations about the crystal structure around cavities; as can be seen in figure VII.60 around cavities diffraction patterns could hardly be detected (i.e. the size of cavities are higher in the IPF map compared to these in the corresponding SEM-BSE image). However, the IPF map reveals several cavities located at boundaries higher than 15°, see arrows in figure VII.60.

The area fraction of cavities is maximum close to the notch root in the NTDV notched specimens after creep testing. Finite element simulations suggest that the maximum principal stress (σ_{22}) is located close to the notch root in the NTDV specimens, see figures V.18, VI.17.

In figure VII.62 are compared the creep damage close to the unbroken notch root of the NTDV specimen tested for 8,199h with that in the the P92 steel tested for 49,721h at 600°C. Creep damage quantification in these two crept specimens revels a higher area fraction of cavities close to the notch root of the NTDV specimen compared to that in the homogeneously deformed part of the P92 steel crept specimen, see figure VII.61 compared with figure VII.11 compared with figure VII.61.

It is to be mentioned that no creep damage was observed in the smooth specimens creep tested for times lower than 10^4h at 600°C.

The area fraction of cavities in the notch area of crept specimen increases with testing time. Thus creep damage was quantified in the unbroken notch of two NTDV specimens after creep testing (figure VII.61).

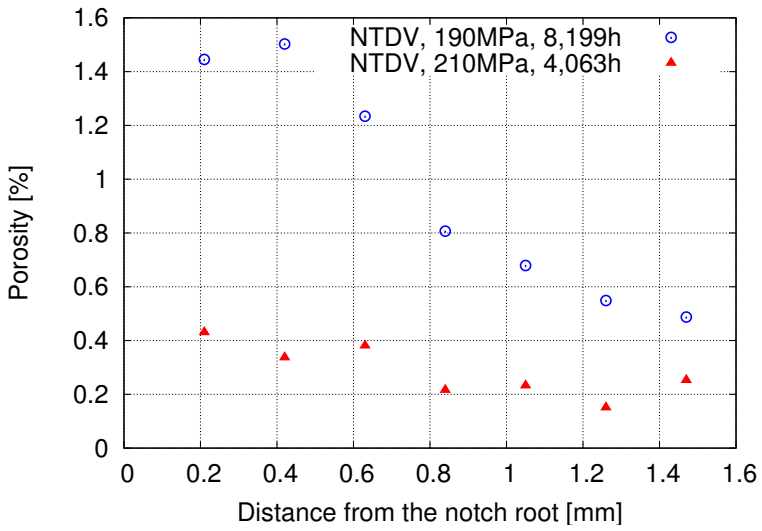

Figure VII.61 : Area fraction of cavities estimated on areas of 270 µm × 210 µm in the unbroken notches of NTDV notched specimens creep tested at 600°C

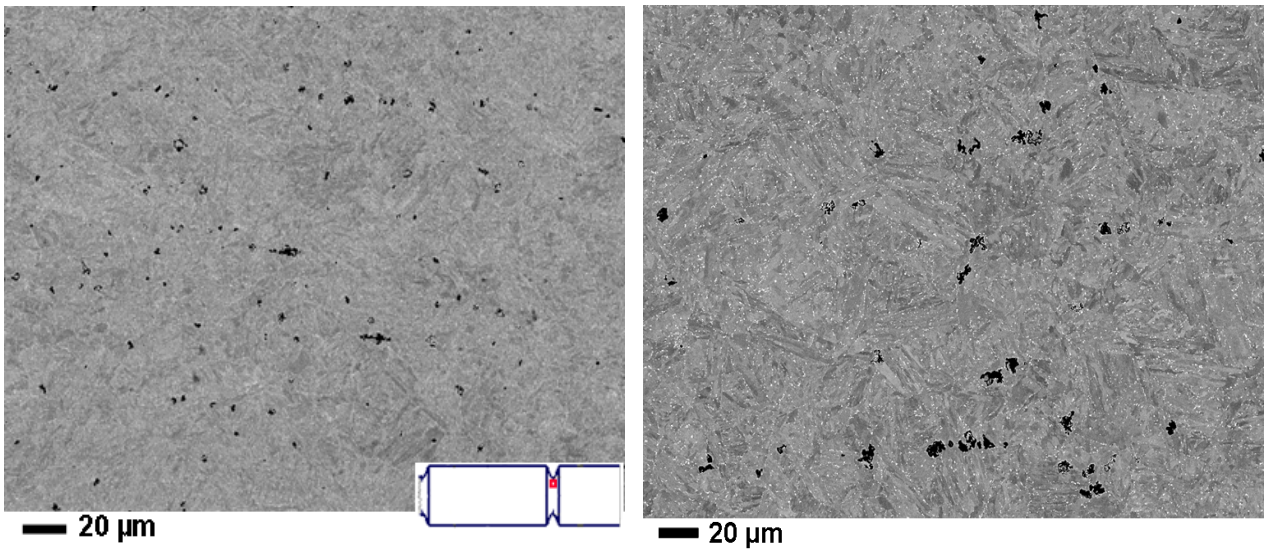

a) **b)**

Figure VII.62 : a) Creep damage in the NTDV notched specimens tested at 600°C and σ_n = 190MPa for 8,199h; b) Creep damage at 10 mm from fracture surface in the smooth P92 creep specimen tested at 600°C, 120MPa for 49,721h

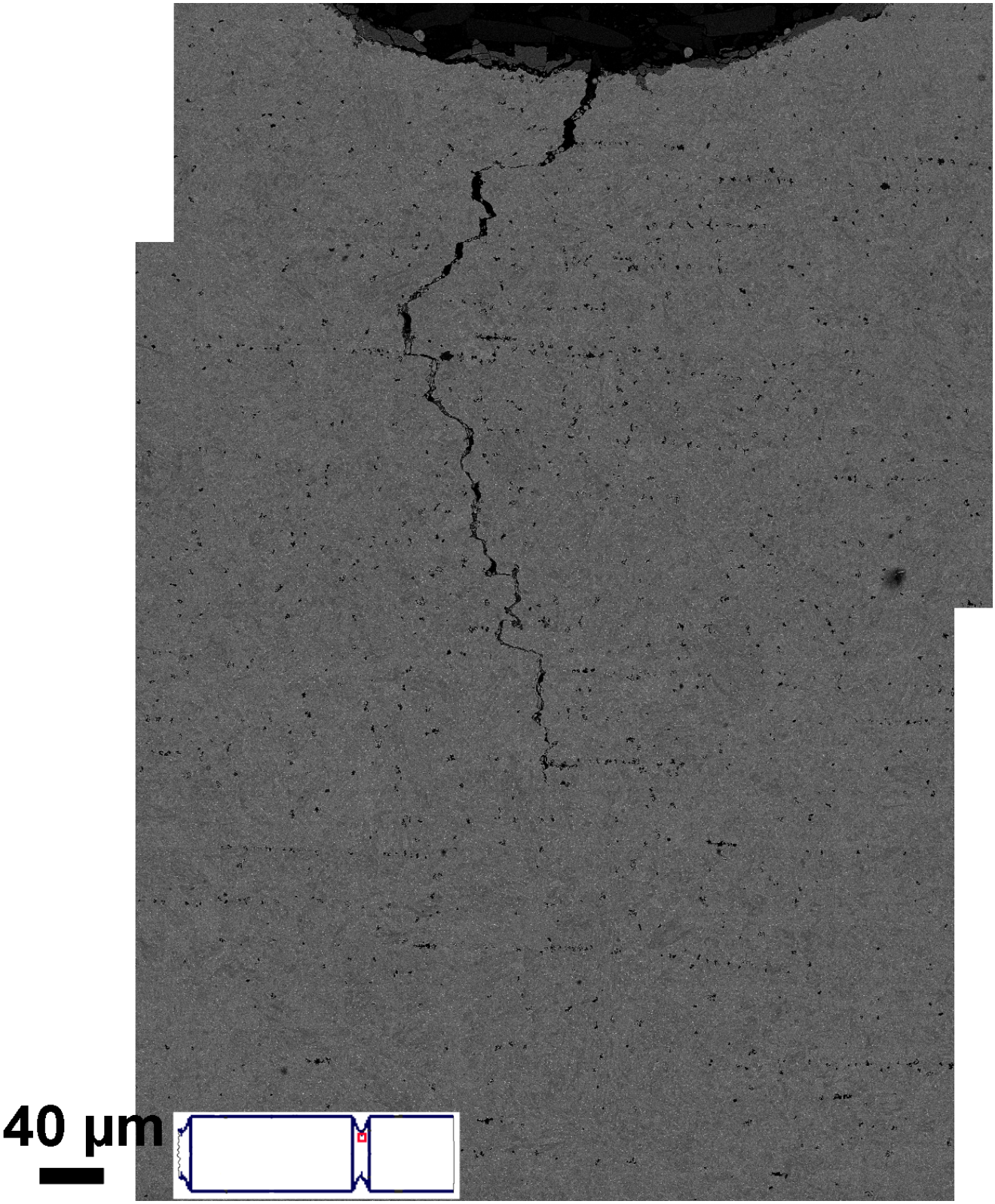

Figure VII.63 : Creep damage in the unbroken notch of the NTDV notched crept specimen tested at $\sigma_n = 190$MPa, 600℃ for 8,199h

VII.5.5 Complementary microstructural investigations

A crack connected to the unbroken notch root is observed in the NTDV notched specimens creep tested for times higher than 2,000h ($\sigma_n < 230$MPa) indicating that fracture of these specimens did not occur suddenly. This crack seems to propagate in a stable manner along boundaries as can be seen figure VII.63. Consistently, the fracture surface of the specimen appeared much more severely oxidised close to the notch root than close to the specimen axis.

In fact stable propagation of a crack initiated next to notch root could explain a longer exposition of that part of the fracture surface to oxidation. The tertiary creep stage of the NTDV specimens is well defined on the creep curves (figures V.17 and VI.14b). The tertiary creep stage could correspond to the initiation and/ or propagation of a crack. Nevertheless, the contribution of crack opening to the total elongation of the specimen is probably negligible, as shown (after unloading) in figure VII.63: the crack mouth opening does not exceed 15 µm.

The high amount of damage could be due to either purely mechanical effect (high stress triaxiality, which further increases after the onset of cracking) or to metallurgical evolution (enhanced itself by a high stress triaxiality ration) or to both.

EBSD investigations were conducted in the specimen with the longest creep testing time (i. e. NTDV; 600°C; 190MPa; 8,199h) to study whether stress triaxiality enhanced recovery of the matrix.

The EBSD maps in figure VII.65 corresponds to an area close to the notch root, but ~ 500 µm away from the crack which is outside the area in figure VII.63.

EBSD maps of that specimen revealed no significant change in the microtexture compared to that of the as-received T92 steel. In figure VII.64 are compared the histogram of misorientation angles corresponding to the EBSD map in figure VII.65 to that of the as-received T92 steel (EBSD maps given in figure II.9). Here also, no significant change was evidenced.

It is to be mentioned that it was also rather difficult to appreciate a change in the microtexture of the P92 steel specimens tested for long-term creep at 600°C using EBSD investigations. Significant changes were revealed by EBSD investigations only after long-term creep exposure at 650°C.

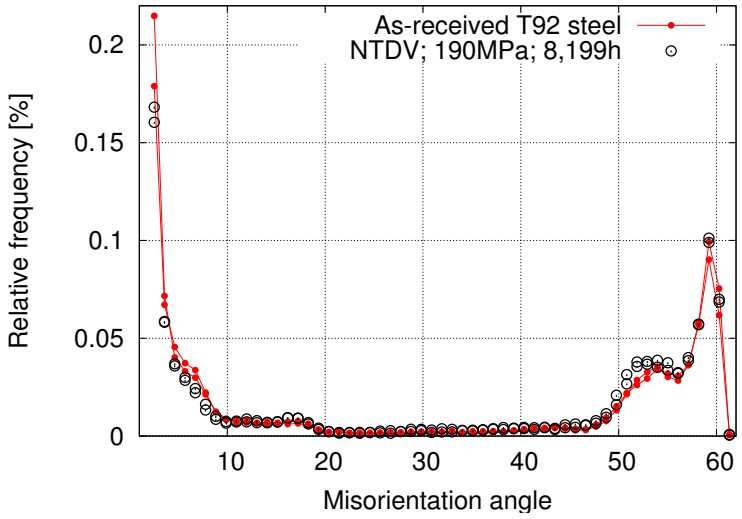

Figure VII.64 : Misorientation angles (°) between grain boundaries corresponding to the EBSD map of the NTDV notched crept specimen tested for 8,199h at 600°C (figure VII.65) compared to that in as-received T92 steel (coresponding EBSD maps of figure II.9)

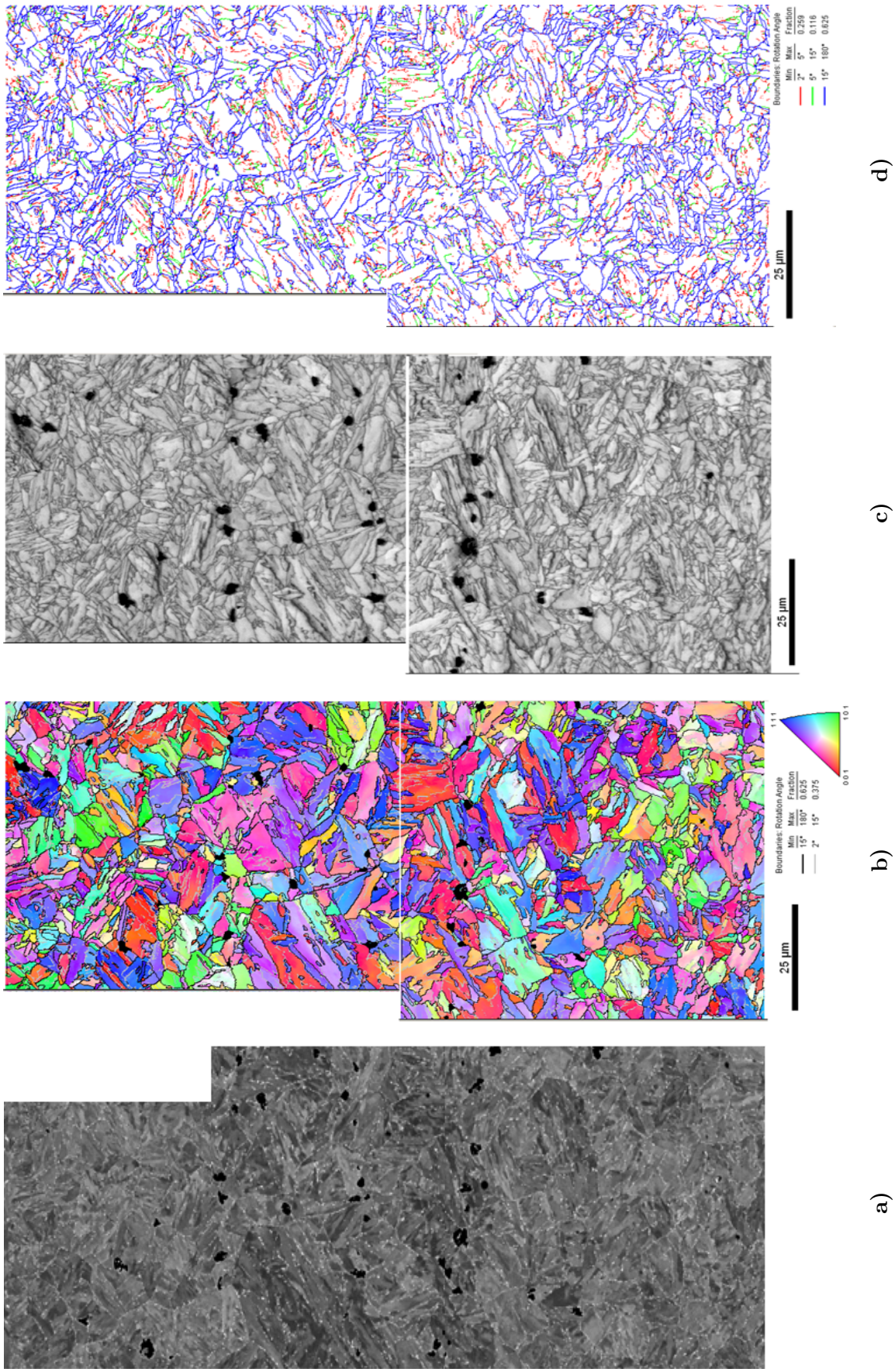

Figure VII.65 : Microstructure of NTDV notched specimen tested for 8,199h at 600°C. a) SEM-BSE image; b) Inverse Pole Figure (IPF) with orientation of sample normal in the crystal frame as color key; c) EBSD Image Quality map (IQ); d) EBSD boundary map

VII.5.6 Summary

Higher amount of creep damage (i. e. number of creep cavities, area fraction of creep cavities) is observed in the notched area of specimens compared to that in the gauge part of smooth specimens both creep tested for similar times.

Due to stress triaxiality, notched specimens promote creep damage development for a given von Mises stress (i.e. for a given creep strain rate). Significant creep damage is observed in notched specimens creep tested for times lower than 10^4h at 600°C (see figure VII.63, VII.62), while in smooth specimens creep damage is only observed for testing times higher than 10^4h at 600°C.

Higher amount of creep damage (i.e. area fraction of cavities) is observed in the NTDV specimens compared to that in the NTDC1.2 specimens both creep tested under $\sigma_n = 210$MPa for comparable lifetimes (i.e. t_r=4,064h for NTDV and t_r=2,957h for the NTDC1.2).

Creep damage is observed throughout the notched area of the NTDV specimens. Yet the amount of creep damage in the centre of the NTDV specimen could be considered as negligible compared to that close to the notch root which corresponds to the location of the highest value of the principal stress.

The area fraction of cavities in the notched area is maximum in the center of the NTDC1.2 specimens. This corresponds to location of the highest value of principal stress (σ_{22}) inside the notched area during creep testing as estimated by finite element simulations.

VII.6 Discussion and concluding remarks

In this study creep tests were conducted at 600°C and 650°C on several kinds of specimens. The results of these tests together with the creep rupture data of the P92 steel long-term crept specimens are represented in figure VII.66. The main findings corresponding to each kind of specimens as well as further use of such specimens are discussed in the following. The dashed lines in figure VII.66 separate the crept specimens without creep damage from those where creep damage was observed. The arrows in figure VII.66 indicate the crept specimens on which EBSD investigations revealed significant changes in the microstructure compared to that of the as-received T92 steel.

VII.6.1 P92 steel long-term crept specimens

P92 steel specimens creep tested at 600°C and 650°C for long-term creep were investigated using appropriate techniques such as: SEM, EBSD and TEM on extractive replicas. The purpose of these investigations was to get reference data on the microstructural evolution and creep damage after long-term creep exposure to be then further compared with the observations of different kinds of specimens creep tested in this study. To this aim quantitative data were obtained on the creep damage and size of Laves phases.

EBSD, SEM and TEM investigations in the P92 steel specimens tested for long-term creep strongly suggest that precipitation of Laves phases and recovery of the matrix substructure are the dominating microstructural evolution mechanisms of this steel during creep exposure both at 600°C and 650°C.

Thus, to separately study the impact of these two metallurgical evolution mechanisms on the loss of creep strength, creep tests were conducted on thermally aged and thermo-mechanically prepared specimens. Creep tests were also conducted on notched specimens to study the effect of stress triaxiality on creep damage development.

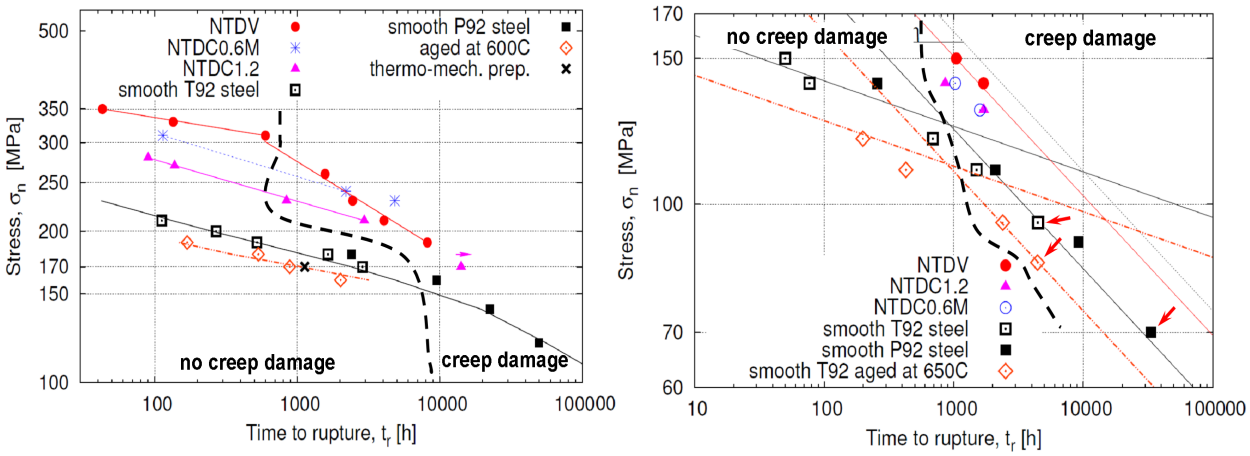

Figure VII.66 : Creep rupture data of creep tests conducted at 600°C (a) and 650°C (b). The dashed line represents the boundary between the specimens without creep damage and specimens where extensive creep damage was observed. Arrows show specimens where EBSD investigations revealed significant changes in the microtexture

VII.6.2 Notched specimens

The presence of a notch induces a stress concentration and changes the macroscopic stress state from uniaxial to multiaxial and thus promoting creep damage development due to the rather high hydrostatic stress. In order to study the influence of stress triaxiality on creep damage development three different geometries of notches were used for the creep tests.

VII.6.2.1 Creep damage

Stress triaxiality enhances creep damage development. Higher amount of creep damage are observed in a notched specimen compared to that in a smooth specimen both creep tested for similar amount of times, see for instance figure VII.56 and figure VII.62.

Moreover, the amount of creep damage in the NTDC1.2 notched specimen after 14,135h of creep at 600°C under $\sigma_n = 170$MPa was higher than that in the P92 steel creep tested for 49,721h at 600°C, 120MPa.

Consequently, notched specimens should be regraded as a method to accelerate, for a given von Mises stress, the development of creep damage cavities and thus to assess the sensitivity of a given steel to creep damage within in a shorter time.

As can be seen in figure VII.66 creep damage is observed in a notched specimen after a relatively short time of creep testing. Creep damage (i.e. cavities) is observed mainly on boundaries. Thus, notched specimens could be used in alloy design to test the sensitivity (respectively the creep strength) of new alloys to creep damage development.

Comparing the lifetime of a notched specimen cut from a new alloy to that cut from a reference steel, such as Grade 92 or Grade 91 steels, creep tested in the same conditions (same geometry of specimen, same level of stress) could already give an indication on its creep strength (or sensibility to creep damage development and microstructural evolution) compared to the reference steel. This could bring a preliminary indication whether the long-term creep properties of a new alloy were improved compared to that of a reference steel.

An arrested crack was observed in the NTDV notched specimens after creep testing for times higher than 10^3h at 600°C. Thus, these kind of notched specimens could be used to study stable crack propagation under creep.

Microstructural investigations revealed the localization of the maximum area fraction of cavities depends on the geometry of the notches. It is located close to the notch root in the NTDV and NTDC0.6M specimens and in the center of the NTDC1.2 specimens. This is consistent with the localization of the maximum of the principal stress during creep estimated by finite element simulations.

For a given testing time higher amount of creep damage (i.e. size and number of cavities) is observed close to the notch root in the NTDV specimen compared to that in the NTDC1.2 or NTDC0.6M specimens. However, the relatively small volume (less than 1 mm in size) close to the notch root were higher creep damage is observed and the crack initiation observed in some NTDV specimens could be the drawbacks of this kind of specimens. Creep damage development could be affected by crack initiation, more precisely by the highly stress triaxiality in the front of the crack. The relatively small area of interest close to the notch root could make microstructural investigations difficult.

VII.6.2.2 Microstructural evolution

The effect of hydrostatic stress (which could somehow enhance diffusion) on microstructural evolution is poorly known. Notched specimens could also be used as a complementary method to study the microstructural evolution of new alloys in alloy design.

a) Precipitates

Notched specimens could be used to study the effect of stress triaxiality on the precipitation and growth of precipitates during creep exposure at high temperature. In the present study this was not investigated. Qualitatively, no significant difference was observed in the size distribution of Laves phases in the notched area compared to that in the smooth part, however no quantification was realized to this aim. Note that the size and spatial distribution of Laves phases is heterogeneous and only a extensive quantitative study could bring more relevant data.

In this study, the size distribution of Laves phases in the head (stress-free thermally aged during creep) and in the gauge part of a P91 steel creep tested for 113,431h at 600°C was quantified and no significant difference was observed (Appendices B and C). Thus it was supposed that stress does not have an influence on the growth of Laves phases for very long exposure times. The effect of stress on the growth of Laves phases is not fully understood. There are not enough published data on this issue. The stress could probably enhance growth of Laves phases in the early stage of its precipitation and/or growth (times lower than 10^4h). Notched specimens creep tested for times lower than 5,000h at 600°C are available for microstructural investigations. They could be used to investigate the size distribution of Laves phases in the notched areas to be then further compared to that in stress-free thermally aged specimens for similar amounts of times.

It is also worth conducting similar investigations concerning the size of $M_{23}C_6$ carbides. To this aim extractive replicas of precipitates or thin foils can be taken from the notched areas to be further investigated using TEM. (Ennis and Czyrska-Filemonowicz, 2002), (Czyrska-Filemonowicz et al., 2006) reported higher average diameter of $M_{23}C_6$ carbides in the gauge part of the crept specimens compared to that in the head of crept specimens, see figure I.8. Any additional effect of hydrostatic stress could be thus investigated using notched specimens.

b) Microtexture

A significant decrease in hardness is observed in the notched area after creep testing for relatively short times (lower than 4,000h at 600°C and lower than 1,000h at 650°C). The

values of hardness in these areas are similar to that of the P92 steel creep tested for long-term (times higher than 10,000h at 600°C). Once again, this might indicate that in the notched area similar microstructural evolution occurs as in the long-term crept specimens but for much shorter times.

(Aghajani et al., 2009b) suggested that the strong decrease in hardness after long-term creep exposure is mainly governed by the increase in subgrain size. Quantification of subgrains size in the notched area after creep testing will enable to conclude rather the strong decrease in hardness is either due to a significant increase in subgrain size or to creep damage development or to both. To this aim TEM investigations of thin foils are required.

The stress distribution on the notched area during creep depends on the geometry of the notch, thus the place in the notched area where samples are taken for microstructural investigations is of great importance.

Significant changes in microtexture was revealed by EBSD investigations in the P92 steel creep tested for 33,308h at 650°C, 70MPa. Stress triaxiality could enhance recovery of the matrix, thus it will be interesting to compare the microtexture of this specimen to that in notched areas of specimens creep tested at 650°C and to see rather typical long-term microtexture could be obtained in a notched specimen within a shorter testing time. In this study EBSD investigations were conducted mainly on notched specimens after creep testing at 600°C. EBSD investigations conducted on the NTDC1.2 interrupted after 14,137h at 600°C, $\sigma_n = 170$MPa and on the NTDV notched specimen creep tested for 8,199h at 600°C, $\sigma_n = 190$MPa revealed no significant change in the matrix substructure compared to that of the as-received T92 steel. Note however than EBSD investigations did not revealed significant changes either in the P92 steel specimen creep tested for 49,721h at 600°C, 120MPa. Probably EBSD is not the appropriated technique to reveal changes occurring during creep exposure at 600°C.

VII.6.2.3 Comparison with literature data

It is rather difficult to compare the results of creep tests on notched specimens obtained in this study with published data because: i) there are very few published data and ii) in the few existent studies the geometry of notches and material are different from those used in the present study. The results reported in (Gaffard et al., 2005a), (Gaffard, 2004) seems to be the most appropriate to be compared to those obtained in this study due to comparable notch geometries, material (Grade 91 steel) and temperature.

(Gaffard, 2004) conducted creep tests on the Grade 91 steel at 625°C using notched specimens namely: NV and NC1.2. The notch geometry of the NV and NC1.2 specimens is the same as that of NTDV and NTDC1.2 specimens used in the present study. Nevertheless, the geometry of the whole specimens are slightly different in the two studies (for more details see (Gaffard, 2004)).

As the creep testing temperature is different in this study (i.e. 600°C) from that in references (Gaffard, 2004) (i.e. 625°C) and the creep behavior of the Grade 91 steel is different from that of Grade 92 steel, to be able to compare the results obtained in the two studies, the stress had to be normalized by a reference stress (σ_0) which was arbitrary chosen as the stress corresponding to a lifetime of about 1,000h on a smooth specimens at the given temperature. This reference stress was chosen because it allows to plot the creep results on smooth specimens on a single curve for the two steels, see figure VII.67.

A notch strengthening effect effect is observed for the two steels, i.e. for a given lifetime the applied axial stress is higher on the notched specimen compared to that on a smooth one, see figure VII.67. (Gaffard et al., 2005a) also reported stable crack propagation in their NV specimens and higher amount of creep damage in these specimens compared to that in a

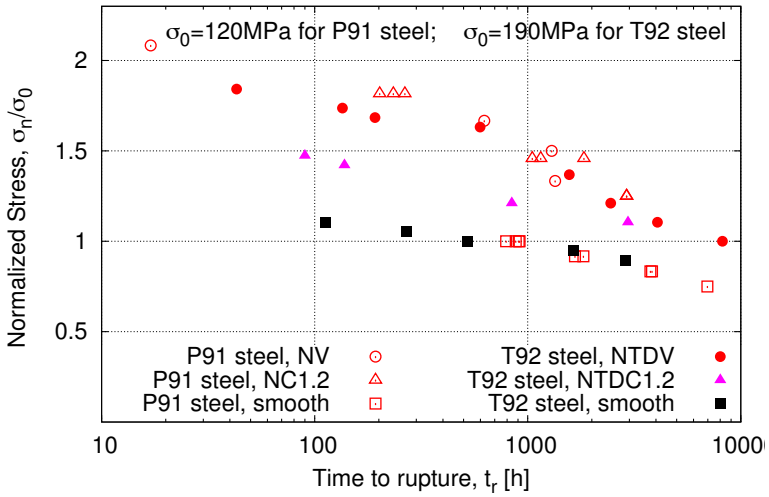

Figure VII.67 : Creep rupture data of creep tests conducted at 600°C on smooth and notched specimens (NTDV and NTDC1.2) compared to available published data (Gaffard et al., 2005a), (Gaffard, 2004), P91 steel

smooth specimens both creep tested for similar amounts of time.

The representation of creep results from the two studies in figure VII.67 shows similar lifetimes for the NV (in P91 steel) and NTDV (in T92 steel) specimens for a given level of the engineering stress. This might indicate similar creep damage mechanisms in the two steels.

VII.6.3 Thermally aged specimens

Thermally aged specimens were initially investigated after creep testing to better understand the effect of large Laves phases on the loss of creep strength and creep damage developement.

VII.6.3.1 Creep damage

No creep damage was observed in the homogeneously deformed part of the thermally aged specimens creep tested in the high stress region both at 600°C and 650°C (i.e. $t_r < 10^4$h at 600°C and $t_r < 10^3$h at 650°C), similarly to the case of the smooth specimens in as-received P/T92 steel. However, a significant increase (a factor of about four) in minimum creep rate was found in the thermally aged specimens compared to these in as-received steel.

Thermally aged specimens creep tested in the low stress region were only available at 650°C. No significant change was observed in the amount of creep damage in these specimens compared to that in as-received T92 for a given lifetime. Thus, aging does not seem to significantly influence on creep damage development, at least up to almost 4,500h at 650°C.

The running creep tests on thermally aged specimens under 120MPa at 600°C and under 70MPa at 650°C could provide complementary information on a possible effect of large Laves phase on the creep damage development.

VII.6.3.2 Microstructural evolution

a) Precipitates

SEM observations revealed no significant change in the size of Laves phases in thermally aged specimen after creep testing both at 600°C and 650°C compared to that before testing (i.e. in the free-stress thermally aged specimens), although no quantification was conducted in these crept specimens. Note, also that the testing times (t_r) are much lower than the duration of aging heat treatments and already mentioned no significant change in the size of Laves phases is expected after 10^4h of exposure at 600°C and 650°C (see chapter I).

b) Microtexture

A higher matrix recovery during creep of the thermally aged T92 steel might explain its higher creep flow rate compared to that of the as-received T92 steel for similar levels of applied stress. TEM investigations on thin foils could enable to confirm this effect. Most probably the size of subgrains (respectively dislocation density) are higher (respectively lower) in thermally aged specimen compared to that in as-received steel both creep tested for similar times.

The microtexture of the thermally aged T92 steel creep tested at 650°C, 85MPa for 4,434h revealed by the EBSD investigations shows similarities to that of the P92 steel creep tested for 33,308h at 650°C. This might suggests that microstructural changes occurring during long-term might occur in thermally aged specimens within a shorter time. Thus, thermally aged specimens could be considered as a to complementary method to accelerate microstructural evolution mechanisms usually observed during long-term creep.

A higher amount of small size round shaped grains are observed in the thermally aged T92 steel creep tested at 650°C, 85MPa for 4,434h compared to that in as-received T92 steel creep tested at 650°C, 95MPa for 4,480h. This might indicate a higher recovery process in the aged steel compared to the as-received one. Thermally aged specimens could be used in alloy design as complementary method to test the sensitivity to matrix recovery during creep of new alloys.

The results of this study seem to indicate that thermal aging for 10^4h, which corresponds to a saturation in Laves phases precipitation enhance recovery of the matrix (more obvious at 650°C). Once again, TEM investigations on thin foils are needed to confirm this. The kinetics of Laves phase precipitation (i.e. nucleation, growth) and their influence on the recovery of the matrix and/or creep flow are not fully understood. During creep, recovery of the matrix could probably be enhanced when the growth of Laves phases starts rather than during the nucleation stage of these phases. Thus, possible further work could be microstructural investigations of interrupted creep tests loaded for various times and assessment of size of Lave phases and recovery of the matrix.

VII.6.4 Thermo-mechanically prepared specimens

One specimen thermo-mechanically prepared at 550°C was creep tested at 600°C under 170MPa, which corresponds to the high stress region and revealed a lifetime almost twice lower than that of a standard specimen tested in same conditions. No creep curve was available for this test. No creep damage was observed in the homogeneusly deformed part of the specimen after creep testing. EBSD maps show large recovered areas free of subgrains, see figure A.16.

The second specimen thermo-mechanically prepared at 550°C and further creep tested at 650°C under 95MPa revealed no significant change in the $\dot{\varepsilon}_{ss}$ and lifetime compared those of as-received steel.

No significant change was observed in the amount of creep damage in this specimen after creep testing compared to that in the as-received T92 creep tested for 4,480h at 650°C, 95MPa, see figure VII.36. A higher amount of large grains free of subgrains is observed in the specimen thermo-mechanically prepared at 550°C compared to that in the as-received steel both creep tested at 95MPa for similar times, see figure VII.44 compared with figure VII.39.

One specimen thermo-mechanically prepared at 600°C was then creep tested at 650°C, 95MPa. This specimen showed a similar value of $\dot{\varepsilon}_{ss}$ to that of the as-received steel and the thermo-mechanically prepared at 550°C both creep tested at 650°C, 95MPa.

Note that the level of stress used (i.e. 95MPa) for the creep tests at 650°C on the thermo-mechanically prepared specimens corresponds to the low stress region. In the high stress region the effect of matrix substructure might be different compared to that in the low stress region, but the low stress region is of a higher importance to creep design for the the industrial applications.

Results of creep tests as well as investigations results of specimens after creep testing lead to the following main conclusions to be taken into account for the modeling of creep behavior of the Grade 92 steel at 600°C and 650°C:

1. creep deformation
    - two deformation regimes: high stress and low stress
    - enhanced by prior precipitation of Laves phases
2. creep damage development
    - appears during long-term creep exposure and affects lifetime
    - enhanced by stress triaxiality
    - Laves phases have no significant influence

Résumé et discussion

Dans cette étude, des essais de fluage ont été réalisés à 600°C et 650°C sur différents types d'éprouvettes. Les résultats de ces essais ainsi que les résultats correspondants aux éprouvettes en P92 testées pendant des temps prolongés sont représentés sur la figure VII.66. Ce chapitre a été consacré à l'expertise microstructurale des éprouvettes après fluage. Les résultats principaux de cette expertise ainsi que l'utilisation future de chaque type d'éprouvettes sont discutés dans cette section. Un endommagement significatif a été observé dans les éprouvettes localisées à la droite des lignes interrompues sur les graphes de la figure VII.66. Les flèches sur la figure VII.66 indiquent les éprouvettes pour lesquelles les investigations EBSD ont montré des changements significatifs de microtexture par rapport à l'état de réception.

VII.6.1 L'acier P92 testé pendant des temps prolongés de fluage

Une expertise des éprouvettes en acier P92 testées pendant des temps prolongés de fluage à 600°C et 650°C a été réalisée en utilisant des techniques adaptées comme le MEB et le MET sur des répliques extractives pour étudier les précipités et l'EBSD pour étudier la microtexture.

L'objectif de cette expertise était d'obtenir des données de référence sur la microstructure et l'endommagement après des temps prolongés de fluage, qui seront en suite comparées avec celles des éprouvettes pré-vieillies, entaillées et pré-fatiguées testées en fluage dans le cadre de cette étude. Pour ce faire, des données quantitatives ont été obtenues sur la taille des phases de Laves et sur l'endommagement.

Les observations MEB, MET et EBSD sur les éprouvettes testées pendant des temps prolongés indiquent que la précipitation des phases de Laves et la restauration de la matrice sont les mécanismes majeurs de l'évolution métallurgique de cet acier pendant le fluage. De ce fait, pour étudier l'impact séparé de chacun des ces mécanismes sur le comportement en fluage, des essais de fluage ont été réalisés sur éprouvettes pré-vieillies et pré-fatiguées. Des essais de fluage ont également été réalisés sur des éprouvettes entaillées pour étudier l'influence du taux de triaxialité des contraintes sur le developpement de l'endommagement par fluage.

VII.6.2 Les éprouvettes entaillées

La présence d'une entaille induit une concentration des contraintes et change l'état de contrainte d'uniaxial en triaxial ce qui pourrait favoriser l'endommagement par fluage du à une contrainte hydrostatique élevée. Trois géométries d'entaille différentes ont été utilisées pour étudier l'influence du taux de triaxialité des contraintes sur le développement de l'endommagement.

VII.6.2.1 L'endommagement par fluage

La triaxialité des contraintes favorise le développement de l'endommagement par fluage. Un endommagement plus important a été observé dans une éprouvette entaillée par rapport à celui dans une éprouvette lisse testée en fluage pour des temps comparables, (voir par exemple les figures VII.56 et VII.62.

De plus, l'endommagement dans la zone entaillée de l'éprouvette NTDC1.2 interrompue après 14137h de fluage à 600°C, $\sigma_n = 170MPa$ est plus important que celui dans l'éprouvette lisse en acier P92 testée pendant 49721h à 600°C, 120MPa. Par conséquent, l'utilisation des éprouvettes entaillées peut être considérée comme une méthode complémentaire pour accélérer (pour une contrainte de von Mises donnée) le développement des cavités par fluge et/ou tester la sensibilité à l'endommagement par fluage d'un acier dans en temps plus court.

L'endommagement par fluage est observé dans une éprouvette entaillée pour un temps relativement court (figure VII.66). Les éprouvettes entaillées peuvent être très utiles dans le développement de nouvelles nuances d'acier pour tester leur sensibilité à l'endommagement par fluage. Une indication préliminaire sur les propriétés en fluage (sensibilité à l'endommagement par fluage) d'une nouvelle nuance d'acier peut être obtenue dans un temps relativement court par la simple comparaison de la durée de vie (ou la déformation) d'une éprouvette entaillée en nouvelle nuance d'acier avec celle d'un acier de référence, comme par exemple le Grade 92 ou le Grade 91, testé dans les mêmes conditions (géométrie de l'éprouvette, contrainte appliquée).

Une fissure arrêtée a été observée dans les éprouvettes entaillées NTDV testées en fluage pour des temps supérieurs à $10^3 h$ à 600°C. De ce fait, ce type d'éprouvette pourrait être utilisé pour étudier la propagation stable des fissures en fluage.

Les observations microstructurales ont révélé que la localisation de la fraction surfacique maximale des cavités dépend de la géométrie de l'entaille. Elle est localisée près du rayon de l'entaille dans les éprouvettes NTDC0.6M et NTDV et dans le centre de l'éprouvette NTDC1.2. Ceci est cohérent avec la localisation de la contrainte principale maximale estimée par éléments finies.

Pour des temps d'exposition en fluage comparables, l'endommagement (taille et nombre de cavités) est plus important près du rayon de l'entaille de l'éprouvette NTDV comparé à celui au centre de l'éprouvette NTDC1.2. Cependant le volume très limité de la zone proche du rayon de l'entaille où l'endommagement est le plus important (taille inférieure à 1mm) et l'amorçage d'une fissure peuvent être des inconvénients de l'éprouvette NTDV. L'endommagement par fluage peut être affecté par l'amorçage de fissure, plus précisément la trixialité très élevée en pointe de fissure pourrait accélérer encore l'endommagement. La taille relativement petite de la zone d'intérêt proche du rayon de l'entaille dans cette éprouvette peut rendre difficile les observations microstructurales, comme la préparation métallographique de l'échantillon ou le prélèvement des lames minces pour observations au MET.

VII.6.2.2 Évolution microstructurale

L'effet de la pression hydrostatique (qui pourrait intensifier quelque peu les mécanismes de diffusion) sur l'évolution microstructurale est mal connu. Les éprouvettes entaillées pourraient être utilisées comme méthode complémentaire pour étudier l'évolution métallurgique pendant le fluage des nouvelles nuances d'acier.

a) ***Précipités***

Les éprouvettes entaillées pourraient être utilisées pour étudier l'influence de l'état des contraintes sur la précipitation et la croissance des précipités pendant le fluage à haute température. Ceci n'a pas été analysé dans cette étude. De manière qualitative, il n'y a pas de différence notable dans la taille de phases de Laves dans les zones entaillées des éprouvettes comparée à celle dans les parties lisses de l'éprouvette, cependant aucune étude quantitative n'a été réalisée. À noter que la taille et la distribution spatiale des phases de Laves est très hétérogène et seule une étude quantitative pourrait apporter des données fiables sur un possible effet de l'état des contraintes sur la croissance des phases de Laves.

Dans cette étude, la distribution de taille de phases de Laves a été quantifiée dans la tête (ayant subi un vieillissement thermique pendant le fluage) et dans la partie utile d'une éprouvette en P91 testée pendant 113431h a 600°C (Annexes B et C). Les distributions de taille déterminées pour les deux échantillons n'ont pas montré de différence notable. Il a donc été conclu que la contrainte n'a pas d'influence sur la croissance des phases de Laves à très long terme. Il n'y a pas beaucoup de données publiées disponibles à ce sujet. L'état de contraintes a probablement une influence sur la croissance de phases de Laves en début de précipitation (temps inférieurs à $10^4 h$). Des éprouvettes entaillées testées en fluage à 600°C pendant des temps inférieurs à 5000h sont disponibles pour des observations microstructurales. Elles pourraient être utilisées pour déterminer la taille des phases de Laves dans les zones entaillées pour être ensuite comparées à celles déterminées sur des échantillons vieillis thermiquement pendant des temps similaires et apporter une réponse sur l'effet de l'état de contraintes sur la croissance de phases de Laves.

Il serait également intéressant de mener des observations similaires concernant la taille de carbures $M_{23}C_6$. Pour ce faire, des observations MET sur des répliques extractives ou lames minces prélevées dans les zones entaillées sont nécessaires. (Ennis and Czyrska-Filemonowicz, 2002), (Czyrska-Filemonowicz et al., 2006) ont signalé un diamètre équivalent des carbures $M_{23}C_6$ plus élevée dans les parties utiles des éprouvettes de fluage comparé à ceux dans les têtes d'éprouvettes de fluage (figure I.8). Un eventuel effet additionnel de la pression hydrostatique sur la croissance des carbures $M_{23}C_6$ pourrait être évalué à l'aide des éprouvettes entaillées.

b) *Microtexture*

Une diminution significative de la dureté est observée dans les zones entaillées des éprouvettes testées en fluage pendant des temps relativement courts (i.e. inférieurs à 4000h à 600°C et inférieurs à 1000h à 650°C). Les valeurs de la dureté dans ces zones sont similaires à celles des éprouvettes en P92 testées pendant des temps prolongés (temps supérieurs à 10000h) à 600°C.

Cela pourrait indiquer, une fois encore que les zones entaillées pourraient connaître des évolution microstructurales similaires à celles observées dans les éprouvettes long-terme, mais dans des temps beaucoup plus courts.

(Aghajani et al., 2009b) ont suggéré que la diminution significative de la dureté après exposition au fluage pendant des temps prolongés est liée à une croissance significative de la taille des sous-grains. La quantification de la taille de sous-grains dans les zones entaillées après fluage permettra de savoir si l'adoucissement significatif dans ces zones est la conséquence de la croissance significative de sous-grains ou de l'endommagement par fluage ou des deux. Pour ce faire des observations MET sur lames minces sont nécessaires.

La distribution des contraintes dans les zones entaillées dépend de la géométrie de l'entaille, l'endroit où les échantillons sont prélevés pour les investigations microstructurales est donc très important.

Les investigations EBSD ont montré un changement de la microtexture de l'éprouvette en acier P92 testée pendant 33308h à 650°C, 70MPa. La contrainte hydrostatique pourrait intensifier la restauration de la matrice pendant le fluage, il serait donc intéressant de faire des observations EBSD sur les éprouvettes entaillées testées à 650°C pour chercher des similitudes avec la microtexture de l'éprouvette testée pendant des temps prolongés. Un état de la microtexture caractéristique à des temps prolongés de fluage pourrait être obtenu dans un temps plus court sur une éprouvette entaillée. Dans cette étude des observations EBSD ont été réalisées principalement sur les éprouvettes entaillées testées à 600°C. La microtexture de l'éprouvette NTDC1.2 interrompue après 14137h et de l'éprouvette NTDV testée pour 8199h ($\sigma_n = 190MPa$) n'ont pas montrée de changement significatif par rapport à l'état de réception. Il faut noter que les cartographies EBSD de l'acier P92 testé pendant 49721h à 600°C, 120MPa. n'ont pas révélé non plus de changement significatif par rapport à l'état de réception. L'EBSD n'est probablement pas l'outil le plus adapté pour révéler les changements dans la microtexture pendant le fluage à 600°C.

VII.6.2.3 *Comparaison avec des données bibliographiques*

Il est assez difficile de comparer les résultats des essais de fluage obtenus sur les éprouvettes entaillées avec des données bibliographiques parce que: i) il n'y a pas beaucoup de données publiées disponibles et ii) le peu de données existantes ont été obtenues sur des géométries et matériaux très différents de ceux utilisés dans cette étude. Les résultats obtenus par (Gaffard, 2004) sur un acier Grade 91 semblent être les plus pertinents pour être comparés à ceux de cette étude en termes de géométrie de l'entaille, de matériaux et de température d'essai.

La géométrie des entailles des éprouvettes NV et NC1.2 utilisées par (Gaffard et al., 2005a) sont les mêmes que celles des éprouvettes NTDV et NTDC1.2 utilisées dans cette étude. La géométrie entière des éprouvettes entaillées utilisées dans les deux études sont légèrement différentes (pour plus de détails, voir la référence (Gaffard, 2004)).

Comme la température d'essai (625°C) utilisée par (Gaffard et al., 2005a) est différente de celle utilisée dans cette étude (600°C) et le comportement en fluage de l'acier Grade 91 est différent de celui de l'acier Grade 92, pour pouvoir comparer les résultats obtenus dans les deux études, les contraintes des essais ont du être normalisées par une contrainte de référence. Le niveau de la contrainte de référence a été choisi d'une manière arbitraire pour

pouvoir aligner les résultats des essais de fluage sur éprouvettes lisses des deux aciers sur une même courbe. Cette contrainte correspond à un temps à rupture d'environ 1000h sur les deux nuances d'aciers, voir la figure VII.67.

Un renforcement par effet d'entaille est observé pour les deux aciers: pour une durée de vie donnée, un niveau de contrainte axiale plus élevé est nécessaire sur une éprouvette entaillée comparé à celui sur une éprouvette lisse. (Gaffard et al., 2005a) ont également observé l'amorçage d'une fissure stable sur leurs éprouvettes NV et un endommagement plus significatif dans les zones entaillées comparé à celui sur une éprouvette lisse testée pendant des temps similaires.

La représentation des résultats de fluage sur la figure VII.67 montre une durée de vie similaire sur les éprouvettes NTDV et NV pour un niveau de contrainte normalisée donné. Ceci pourrait indiquer que les mécanismes l'endommagement seraient similaires dans les deux aciers.

VII. 6.3 *Éprouvettes pré-vieillies*

Une expertise des éprouvettes pré-vieillies après fluage a été réalisée pour mieux comprendre l'influence des phases de Laves sur le comportement et l'endommagement en fluage.

VII. 6.3.1 *L'endommagement par fluage*

Les observations MEB n'ont pas révélé d'endommagement par fluage sur la partie déformée uniformément des éprouvettes pré-vieillies testées en fluage pour des contraintes élevées à 600°C et à 650°C ($t_r < 10^4 h$ à 600°C et $t_r < 10^3 h$ à 650°C). Cependant, pour une même valeur de la contrainte appliquée, la vitesse de fluage secondaire des éprouvettes pré-vieillies est trois à quatre fois plus élevée que celle d'une éprouvette à l'état de réception.

Des éprouvettes pré-vieillies testées en fluage sous basses contraintes ont été disponibles seulement à 650°C. La quantification de l'endommagement dans l'éprouvette pré-vieillie testée pendant 4434h à 85MPa et dans l'éprouvette lisse en acier T92 testée en fluage pendant 4480h à 95MPa, n'a pas révélé une différence significative par rapport à l'état de réception. Par conséquent, le vieillissement thermique ne semble pas avoir une influence significative sur le développement de l'endommagement par fluage, au moins pour des temps d'exposition inférieurs à 4500h à 650°C.

L'expertise des éprouvettes pré-vieillies testées à 70MPa, 650°C et à 120MPa, 600°C (essais en cours) pourrait apporter des informations complémentaires sur un éventuel effet de phases de Laves grossières sur l'endommagement par fluage.

VII. 6.3.2 *L'évolution microstructurale*

a) *Précipités*

La taille de phases de Laves ne semble pas évoluer significativement pendant le fluage dans les éprouvettes pré-vieillies (observations MEB). Il est à noter que la durée des essais de fluage (t_r) sur ce type d'éprouvettes est plus courte que la durée des traitements de vieillissement thermique ($10^4 h$). Comme il a été mentionné précédemment, la croissance des phases de Laves n'est très significative que dans les 10^4 premières heures d'exposition à 600°C et 650°C (voir le chapitre I).

b) *Microtexture*

Une restauration de la matrice plus importante pendant le fluage des éprouvettes pré-vieillies pourrait expliquer la vitesse de fluage secondaire plus élevée de ces éprouvettes par rapport

à celle de l'acier T92 testé pour la même valeur de contrainte. Des observations MET sur lames minces seront nécessaires pour étudier cette hypothèse. Pour une durée de vie donnée, la taille des sous-grains (respectivement la densité de dislocations) est probablement plus élevée (respectivement plus faible) sur une éprouvette pré-vieillie comparée à celle dans une éprouvette en acier T92.

La microtexture de l'éprouvette pré-vieillie testée à 650°C, 85MPa pendant 4434h montre des similitudes avec la microtexture de l'acier P92 testé pendant 33308h à 650°C. Ceci pourrait indiquer que les changements dans la matrice observés après des temps prolongés de fluage pourront être obtenus dans un temps plus court sur une éprouvette pré-vieillie. Les éprouvettes pré-vieilles pourront donc être considérées comme une méthode complémentaire pour accélérer les mécanismes de l'évolution microstructurale normalement observés après des temps prolongés d'exposition au fluage.

Les cartographies EBSD réalisées sur l'éprouvette pré-vieillie testée à 650°C, 85MPa pendant 4434h révèlent des petits grains arrondis localisés principalement près des anciens joints austenitiques. Ce type de grains est observé également dans l'éprouvette en acier T92 testée à 650°C, 95MPa pendant 4480h mais leur nombre est plus grand dans l'éprouvette pré-vieillie. Ceci pourrait être une indication d'une restauration pendant le fluage plus importante dans l'acier pré-vieilli que dans l'acier T92. Les essais de fluage sur éprouvettes pré-vieilles pourront donc être une méthode complémentaire pour étudier la sensibilité à la restauration pendant le fluage des nouvelles nuances d'aciers.

Les résultats de cette étude semblent indiquer que le vieillissement thermique pendant $10^4 h$ *intensifie la restauration de la matrice pendant le fluage (des changements plus notables sont observés à 650°C). Encore une fois, des observations MET seront nécessaires pour confirmer cette hypothèse. La cinétique (germination, croissance) de précipitation des phases de Laves et son influence sur la restauration de la matrice et/ou le comportement en fluage ne sont pas complètement compris. Pendant le fluage, la restauration de la matrice peut-être plus intense pendant la croissance des phases de Laves que pendant l'étape de germination de ces phases. Il serait donc intéressant de caractériser l'état de la matrice et la taille des phases de Laves dans les éprouvettes des essais de fluage interrompus après des temps différents.*

VII. 6.4 *Les éprouvettes pré-fatiguées*

Une éprouvette pré-fatiguée à 550°C et testée en fluage à 600°C, 170MPa a révélé une durée de vie deux fois plus faible que l'acier T92 testé dans les mêmes conditions. L'enregistrement de la courbe de fluage correspondant à cet essai n'a pas été possible. L'expertise de cette éprouvette après fluage n'a pas révélé d'endommagement sur la partie déformée uniformément pendant l'essai. Les cartographies EBSD montrent de grandes zones restaurées (i.e. zones sans sous-grains). Il est à noter que 170MPa correspond au domaine des contraintes élevées.

Une deuxième éprouvette pré-fatiguée à 550°C et testée en fluage à 650°C, 95MPa n'a pas montré un changement dans la vitesse de déformation secondaire (respectivement la durée de vie) comparée à celle de l'acier T92 testé à 650°C, 95MPa. La quantification de l'endommagement dans l'éprouvette pré-fatiguée à 550°C et dans l'éprouvette standard en acier T92 testés à 650°C, 95MPa n'a pas révélé des différence significatives entre les deux éprouvettes (figure VII.36). Un nombre plus élevé de grains restaurés est observé dans les cartographies EBSD de l'éprouvette pré-fatiguée après fluage par rapport à ceux de l'acier T92 testé dans les même conditions (contrainte, durée de vie), à voir la figure VII.44 comparée à la figure VII.39.

Une éprouvette pré-fatiguée à 600°C a été aussi testée en fluage à 650°C, 95MPa. Cette éprouvette a montré la même vitesse de fluage secondaire et une durée de vie comparable à celles de l'acier T92 et l'éprouvette pré-fatiguée à 550°C testés en fluage dans les mêmes

conditions (650°C, 95MPa).

À noter que la valeur de la contrainte utilisée pour les essais de fluage à 650°C sur éprouvettes pré-fatiguées correspond au régime des contraintes faibles pour l'acier T92 à 650°C. À des contraintes élevées, l'effet de l'état de la matrice sur le comportement en fluage pourrait être différent de celui à faibles contraintes (qui est celui adopté à l'application industrielle).

Les résultats des essais de fluage ainsi que l'expertise des éprouvettes après fluage mènent aux conclusions suivantes, qui devront être pris en compte dans la modélisation du comportement en fluage de l'acier Grade 92:

1. *la déformation par fluage*
    - *deux régimes de déformation: contraintes élevées et faibles contraintes*
    - *intensifiée par la précipitation préalable des phases de Laves*
2. *l'endommagement par fluage*
    - *observé après des temps prolongés d'exposition au fluage et affectant la durée de vie*
    - *intensifié par la triaxialité des contraintes*
    - *pas d'influence notable des phases de Laves*

Chapter -VIII-

Modelling creep behaviour and failure of the Grade 92 steel

Contents

VIII.1 Introduction

In this study, the modeling of the creep flow is based on the use of a finite element model developed by (Gaffard et al., 2005a), (Gaffard, 2004) for the creep flow and damage behavior at 625°C of the 9Cr1Mo-NbV steel (i.e. Grade 91 steel) weldments. This model had already been implemented in the finite element software Zebulon (Besson and Foerch, 1997) and integrates multiple deformation and damage mechanisms allowing a description of the creep behavior from high stresses to low stresses. The mentioned model was modified to improve the description of the mechanisms involved in the creep behavior of the Grade 92 steel such as viscoplasticity, hardening, microstructural evolution and damage developement.

The major modifications that have been brought to the existing model consisted in implementation of internal variables to describe the effect of the microstructural evolution on the creep flow of the Grade 92 steel.

The strongest metallurgical effect that was experimentally observed in this study was that of thermal aging. Although acceleration of creep deformation in aged specimens was not directly due to the precipitation of Laves phases but most probably to an acceleration in the matrix evolution under stress, it was chosen to describe this evolution with an internal variable having a kinetic evolution similar to that of the precipitation of Laves phases.

As discussed in the previous chapter the effect of both growth of $M_{23}C_6$ carbides and precipitation of modified Z phase on the loss of the creep strength of the Grade 92 steel could be considered negligible compared to that of precipitation of Laves phases. These two microstructural degradation mechanisms during creep were thus not considered in the modeling of the creep flow. Moreover, the purpose of this study was to build a mechanical model that could be further easily used in engineering software dedicated to the design of structure integrity. Thus, simple well-known constitutive equations were used and the number of internal variables was reduced as much as possible.

A review of constitutive equations able to represent damage-free materials under several deformation mechanisms can be found in references (Besson, 2009), (Chaboche, 2008).

In the following the constitutive equations of the model will be presented using similar notations as those used in references (Gaffard et al., 2005a), (Gaffard, 2004).

VIII.2 Constitutive equations

VIII.2.1 Strain partition

The model accounts for three main mechanisms which contribute to permanent creep deformation. The first one, named *quasi-plastic* (*qp*) accounts for loading and final rupture stage. Based on experimental results, two other mechanisms were considered, namely: *high stress (Hs)* and *low stress (Ls)* to describe the creep flow (*viscoplasticity*) of Grade 92 steel in two stress regime.

The *high stress* mechanism is mostly used to describe creep deformation for short-term creep tests. The *low stress* mechanism is also to describe creep deformation but its contribution to total strain keeps low (as will be shown later) even for long-term tests. On the other hand, this mechanism is used to trigger nucleation of creep cavities, which were observed after long-term creep.

This model intends to describe creep damage and to predict creep lifetime, but not to represent ductile fracture (which occurs in a very short time compared to the creep lifetime). Thus only the *Ls* mechanism contributes to nucleation of cavities. Cavity growth is due to all deformation mechanisms.

Each mechanism contributes to deformation and thus the strain rate tensor ($\underline{\dot{\varepsilon}}$) was assumed to be the sum of the elastic strain rate tensor ($\underline{\dot{\varepsilon}}_e$) and the strain rate tensors of the three mechanisms contributing on creep deformation, as follows:

$$\underline{\dot{\varepsilon}} = \underline{\dot{\varepsilon}}_e + \underline{\dot{\varepsilon}}_{qp} + \underline{\dot{\varepsilon}}_{Hs} + \underline{\dot{\varepsilon}}_{Ls} \tag{VIII.1}$$

where $\underline{\dot{\varepsilon}}_{qp}$ is the quasiplastic strain rate tensor; $\underline{\dot{\varepsilon}}_{Hs}$ is the viscoplastic strain rate tensor for high stresses and $\underline{\dot{\varepsilon}}_{Ls}$ is the viscoplastic strain rate tensor for low stresses.

$\underline{\varepsilon}_e$ obeys the Hooke's law: $\underline{\sigma} = \underline{\underline{C}} : \underline{\varepsilon}_e$, where $\underline{\underline{C}}$ is the fourth order stiffness tensor and $\underline{\sigma}$ is the stress tensor.

VIII.2.2 Viscoplastic potential

The strain rate tensor ($\underline{\dot{\varepsilon}}_m$, $m = qp, Hs, Ls$) of each mechanism contributing to creep deformation is related to the equivalent strain rate ($\dot{p}_m$) by the following normality rule:

$$\underline{\dot{\varepsilon}}_m = \dot{p}_m \frac{\partial \phi_m}{\partial \underline{\sigma}} \tag{VIII.2}$$

where ϕ_m is the viscoplastic potential coresponding to mechanism m ($m = qp, Hs, Ls$) defined as:

$$\phi_m = \sigma_m^* - R_m \tag{VIII.3}$$

where R_m is the flow stress which depends on the flow mechanism and σ_m^* is a scalar effective stress coresponding to the von Mises equivalent stress in the case of the undamaged material.

A non-elastic (i.e. permanent) deformation by mechanism "m" occurs when $\phi_m > 0$.

For the *quasiplastic* mechanism, the flow stress was assumed to be constant (i.e. $R_{qp} =$ constant). In fact it was not possible to fit hardening parameters from tensile tests because of the early decrease in load (figure II.14 and II.15). Having no such tests on notched specimens (which could have been analysed with FE simulations), it was chosen not to introduce hardening for the qp regime. This could affect (i) final rupture (which is not considered in the model) and (ii) the very beginning of primary creep. Only in very limited area of notched specimens and at the very beginning of the test was the value of the von Mises stress found to be higher than the fitted value of R_{qp} (see below and also figures V.18, V.19, V.20, V.21).

It was assumed that the Ls mechanism induces no hardening. For the *low stress* regime, there were several possible options:

- either keep the Norton exponent to 1 (i.e. assuming that this mechanism represents diffusional creep) as in (Gaffard et al., 2005a), (Gaffard, 2004), with or without introduction of a threshold (internal) stress. Note that for diffusional creep R_{Ls} should logically be set to zero.

- or let the Norton exponent to any value, with or without threshold stress; this avoids assuming that nucleation of creep cavities is only due to diffusional creep. This option was selected in the present study (in particular due to lack in published available experimental data on diffusional creep in the Grade 92 steel) and the R_{Ls} was set to 0.

A more complex definition was used for the yield flow (R_{Hs}) in the Hs mechanism, as follows:

$$R_{Hs}(\bar{p}) = R0_{Hs} + Q_{Hs}(1 - 1/exp(b_1\bar{p}) * min(1, 1/exp(b_2(\bar{p} - p_c))) \quad \text{(VIII.4)}$$

where $R0_{Hs}, Q_{Hs}, b_1, b_2, p_c$ are constants and $\bar{p}$ is the cumulated irreversible strain. $\bar{p} = \sum_m p_m$, where p_m is the irreversible strain due to mechanism m ($m = qp, Hs, Ls$)

In equation VIII.4, $Q_{Hs}(1 - 1/exp(b_1\bar{p}_{Hs}))$ accounts for the hardening of the steel in the first steps of the creep deformation (i.e. primary creep stage) and the term $min(1, 1/exp(b_2(\bar{p}_{Hs} - p_c)))$ was added in a heuristic manner to better describe the onset of tertiary creep stage. Without this term the short-term creep lifetime is overestimated by a factor of 2 to 3, which however could have been considered as acceptable. Here this term express a strain induced relaxation of the flow stress. It could be linked to some evolution in the material (i.e. matrix recovery).

Of course, as the flow stress in the Ls regime was set to nearly zero, no such term was introduced for the Ls regime.

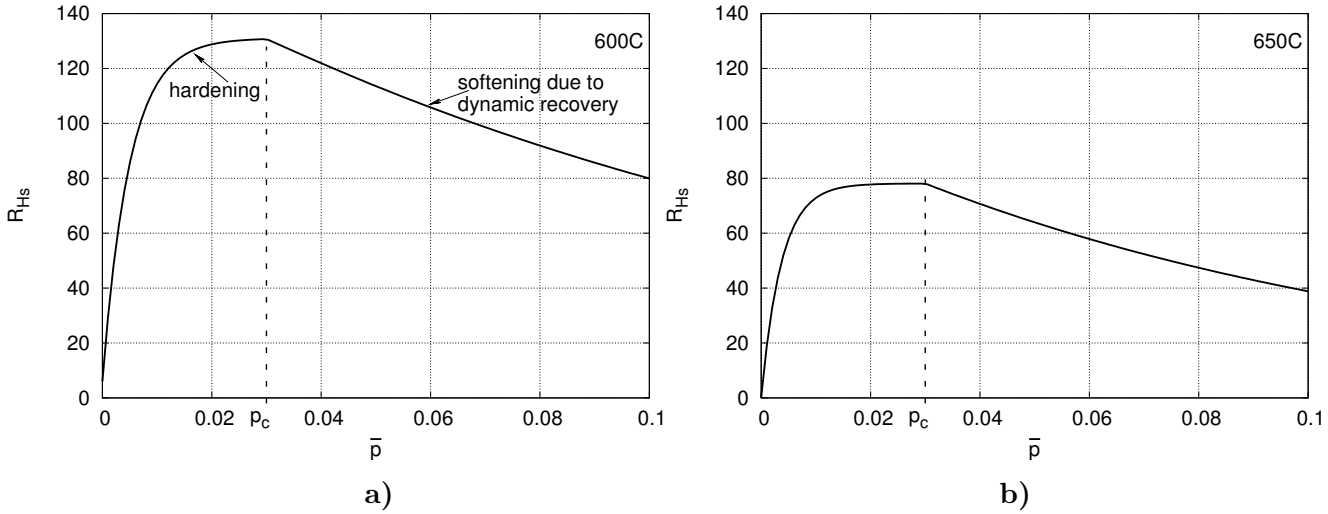

Figure VIII.1 : Representation of the function R_{Hs} adjusted for modeling the creep flow at 600°C (a) and 650°C (b)

VIII.2.3 Flow rule

It is assumed that plastic multiplier ($\dot{p}_m$) is given by a Norton power-law type. In the qp and Ls mechanism the $\dot{p}_m$ is defined as follows:

$$\dot{p}_m = K_m \left\langle \frac{\phi_m}{\sigma_{0m}} \right\rangle^{n_m} \quad \text{(VIII.5)}$$

where K_m, σ_{0m} and n_m are material constants.

The cumulated strain ($\bar{p}_m$) is defined as the time integral of $\dot{p}_m$ ($\bar{p}_m = \int_0^t \dot{p}_m dt$).

Increase in the creep rate in the high stresses region after long-term aging was attributed to metallurgical evolution. To model this effect, the strain rate associated to the Hs mechanism

is linked to the kinetics of that metallurgical evolution. In absence of thin foils TEM observations of the matrix substructure during short-term creep aged and unaged specimens, the kinetics of metallurgical evolution affecting further creep was chosen to be that of the precipitation of Laves phases (i.e. f_{Laves}) as follows:

$$\dot{p}_{Hs} = K_{Hs}\,(1+a)\left\langle \frac{\phi_m}{\sigma_{0m}} \right\rangle^{n_m} \tag{VIII.6}$$

In equation VIII.6, a is an internal variable describing the metallurgical state of the material i.e. evolution induced by thermal ageing. It was assumed that a was independent of stress (which in fact might not be really true). a is a temperature and time-dependent variable. In fact, the value of C_{JMA} was fitted from observations of Laves phase precipitation under a variety of stress levels (see figure VII.18).

As explained before, the evolution of a with time was chosen proportional to the area fraction of Laves phases:

$$a = h f_{Laves} = h\left[C_{JMA}\left(1-\exp\left(-\left(\frac{t}{t_0}\right)^n\right)\right)\right] \tag{VIII.7}$$

The proportionality coefficient, h, is a material constant which depends on temperature. It represents the mechanical effect of ageing. Thus the term $K_{Hs}\,(1+a)$ evolves between K_{Hs} (as-received material) and $K_{Hs}\,(1+hC_{JMA})$ (fully aged material). Note that the value of ϕ_{Hs} is not affected by ageing i.e. no relaxation of flow stress by metallurgical evolution is included in the model.

To represent no cross-hardening between mechanisms a new isotropic hardening variable ($\bar{p}_m$) is introduced for each mechanism:

$$\bar{p}_m = \sum_m H^p_m p_m, \qquad (m = qp, Hs, Ls) \tag{VIII.8}$$

where H^p_m is the corresponding interaction matrix, $H^p_m = \begin{bmatrix} 1 & 0 & 0 \\ 0 & 1 & 0 \\ 0 & 0 & 1 \end{bmatrix}$.

VIII.3 Damage incorporation

VIII.3.1 Effective stress (σ^*_m)

The effect of damage on creep deformation was taken into account through a new definition of σ^*_m based on extensions of models for porous materials as detailed in references (Besson et al., 2001), (Besson and Guillemer-Neel, 2003), (Besson, 2009).

In the quasi-plastic mechanism the σ^*_m was defined using the Gurson-Tvergaard-Needleman (GTN) model (Needleman and Tvergaard, 1991), as follows:

$$\frac{\sigma^2_{VM}}{\sigma^{*2}_{qp}} + 2q_1 f^*_{qp}\cosh\left(\frac{q_2}{2}\frac{\sigma_{kk}}{\sigma^*_{qp}}\right) - 1 - q_1^2 f^{*2}_{qp} = 0 \tag{VIII.9}$$

where: σ_{kk} is the trace of the stress tensor; σ_{eq} is the von Mises equivalent stress; q_1 and q_2 are model constants representing void growth and f^*_{qp} is a function of total porosity.

The generalization of the Gurson model proposed by (Leblond et al., 1994) was used for the definition of σ^*_m in the viscoplastic mechanism (i.e. H_s, L_s), as follows:

$$\frac{\sigma^2_{VM}}{\sigma^{*2}_m} + q_1 f^*_m k_m \left(\frac{1}{2} q_2 \frac{\sigma_{kk}}{\sigma^*_m}\right) - 1 - q_1^2 \frac{1 - M_m}{1 + M_m} (f^*_m)^2 = 0 \tag{VIII.10}$$

where: $k_m = h_{Mm}(x) + \dfrac{1 - M_m}{1 + M_m} \dfrac{1}{h_{Mm}(x)}$ with $h_{Mm}(x) = \left[1 + M_m x^{1+M_m}\right]^{1/M_m}$. M is a strain rate sensitivity, equal to the inverse of Norton power law exponent ($M_m = 1/n_m$).

VIII.3.2 Damage evolution

Previous studies (Wu and Sandstrom, 1995), (Wu and Sandstrom, 1996) reported that nucleation of cavities is strain controlled, thus the strain rate tensor is modified to relate the porosity to the strain rate:

$$\underline{\dot{\varepsilon}}_m = (1 - f_{tm})\, \dot{p}_m \frac{\partial \phi_m}{\partial \underline{\sigma}} \tag{VIII.11}$$

where $\phi_m = \sigma^*_m - R_m$, with the new definition of the σ^*_m given by equations VIII.9 and VIII.10 for quasiplastic and viscoplastic mechanism, respectively.

A porosity is associated to each mechanism ($m = Ls, Hs$) and two source of damage are considered (i.e. void nucleation and void growth). Thus, the total porosity (f_{tm}) is assumed to be:

$$f_{tm} = \sum_m f_{nm} + \sum_m f_{gm} = f_n + f_g \simeq f_t \tag{VIII.12}$$

where f_{nm} represents the damage nucleation due to mechanism m and f_{gm} represents porosity due to void growth caused by mechanism m.

Due to mass conservation, the evolution of porosity corresponding to each mechanism is expressed as:

$$\dot{f}_{tm} = (1 - f_{tm}) \sum_m \mathrm{trace}(\dot{\underline{\varepsilon}}_m) + \dot{f}_{nm} = \dot{f}_{gm} + \dot{f}_{nm} \tag{VIII.13}$$

The effect of stress triaxiality on creep damage development observed on notched specimens after relatively short term creep testing see section VII.5, was considered in the nucleation of voids coresponding to each mechanism as:

$$\dot{f}_{nm} = (A_m + B_m \tau)\, \dot{p}_m \qquad m = Ls \tag{VIII.14}$$

where A_m and B_m are material parameters representing nucleation rate and τ is the stress triaxiality.

$$\tau = \frac{1}{3}\frac{\sigma_{kk}}{\sigma_{VM}} \tag{VIII.15}$$

where $\sigma_{kk} = \sigma_{11} + \sigma_{22} + \sigma_{33}$ and σ_{VM} is the von Mises equivalent stress.

A_m and B_m are material parameter representing nucleation rate.

f_m^* accounts for void coalescence and it often express as:

$$f_m^* = \begin{cases} f_t & \text{if} \quad f_{gm} + f_{nm} < f_c \\ f_t + \delta\left(f_{gm} + f_{nm} - f_c\right) & \text{if} \quad f_{gm} + f_{nm} > f_c \end{cases} \tag{VIII.16}$$

where f_c represents a critical value of porosity at which the coalescence of cavities is onset.

The interaction between damage caused by each individual mechanism is represented throughout a damage variable $\bar{f}_m$ which results from interaction:

$$\bar{f}_{nm} = \sum_m H_{nm}^f f_{tm} \tag{VIII.17}$$

where H_{nm}^f is the corresponding interaction matrix. It was assumed that damage caused by one mechanism affects all deformation mechanisms thus $H_{nm}^f = 1$.

It is assumed that macroscopic viscoplastic work ($\dot{\underline{\varepsilon}}_m : \underline{\sigma}$) is equal to the microscopic viscoplastic work ($(1 - ft)\,\dot{p}_m \sigma_m^*$).

VIII.4 Identification procedure

The parameters of the model were identified based on the elongation vs. time curves from both creep and tensile tests. These parameters are given in table VIII.1.

The values of parameters counting for void interaction (q_1, q_2) in the definition of σ_m^* corresponding to each deformation mechanisms were set to the classical values i.e. 1.5 and 1 respectively. The values of δ in equation VIII.16 was set to 6. Note these values are identical to these used in references (Gaffard et al., 2005a), (Gaffard, 2004).

All FE simulations were conducted using quadratic interpolation elements together with reduced integration (i.e. 8 nodes axisymmetric or plane strain elements with 4 Gauss points).

The material was considered to be broken when f_m^* was higher than $\frac{1}{q_1} - \varepsilon$ where $\frac{1}{q_1}$ is the theoretical value for f_m^* at fracture and ε is taken equal to 0.01. Gauss points where $f_m^* > \frac{1}{q_1} - \varepsilon$ are referred as *broken Gauss points*. Elements containing two broken Gauss points were automatically removed by checking this condition after each time increment.

VIII.4.1 Parameters corresponding to the *qp* mechanism

The yield flow (Rqp) as well as the parameters of the effective strain in the $quasi - plastic$ mechanism were adjusted from the results of tensile tests conducted at 600°C and 650°C under various strain rates (i.e. $\dot{\varepsilon} = 10^{-3}\text{s}^{-1}$; $\dot{\varepsilon} = 10^{-4}\text{s}^{-1}$; $\dot{\varepsilon} = 10^{-5}\text{s}^{-1}$) up to maximum load.

VIII.4.2 Parameters corresponding to the Hs mechanism

The function f_{Laves} corresponds to the Johnson-Mehl-Avrami function adjusted to describe the evolution of surface fraction of Laves phases during creep. The constant h was set so that when time is equal to 10^4h the creep rate is higher by a factor of 4 than for time equal 0 for a given value of ϕ_{Hs} as was revealed by the creep tests conducted on thermally aged specimens both at 600°C and 650°C.

The $R0_{vp}, Q_{vp}, b_1$ constants in the yield flow (R_{Hs}) definition were designed to model primary creep stage while b_2 is to model the tertiary creep stage. The value of p_c was set to 0.03, as tertiary creep stage is onset roughly at this values of elongation in the short-term creep tests , see figures V.2, VI.2.

The parameters of the model corresponding to the Hs mechanism were identified based on microstructural investigations which revealed no creep damage in the specimens creep tested for short-term. Therefore A_m and B_m were set to zero (i.e. damage-free model) and only the Hs mechanism was first considered to identify the parameters describing the creep flow in the Hs mechanism.

The identification procedure consisted in using an optimization method (nelder-mead (Nelder and Mead, 1965) or simplex) implemented in the FE software Zebulon which adjusts the parameters to reduce the difference between the simulated creep response and the experimental creep curves. The first half of creep curves (i.e. up to 0.5 of the creep lifetime) both on smooth and notched specimens were used in the optimization procedure (i.e. lifetime was not used for this part of parameters identification).

Note that the values of the Norton exponent found after optimization (i.e. $n = 6$) is much lower than that found in the simple analysis of creep curves (i.e. $n = 18$), see section V.3. This is because the flow stress R_{Hs} is not zero as it was the case in the simple analysis.

The flow stress R_{Hs} with the optimized parameters (given in table VIII.1) are represented in figure VIII.1. A significant internal stress develops up to $p = p_c$ ($\simeq$ 120MPa at 600°C and $\simeq$ 80MPa at 650°C, see figure VIII.1), which then relaxes slowly with increasing strain. Due to the rather low values of b_2 model allows significant relaxation for the short-term tests (p up to 0.03) while little relaxation is allowed for long-term creep (small fracture strain).

VIII.4.3 Parameters corresponding to the Ls mechanism

It was assumed that the Ls mechanism does not involve internal stresses, thus the yield flow is zero.

The flow parameters corresponding to the Ls mechanism where identified to improve the description of the experimental creep curves of the long-term tests.

The model developed by (Gaffard et al., 2005a), (Gaffard, 2004) counts for a Norton exponent, $n = 1$ in the diffusional creep mechanism. Starting from this value simulations were conducted using the model developed in this study with a $n = 1$ for the Ls mechanism. This could describe the lifetime of smooth specimens (both short and long-term) but it fails describing the lifetime of notched specimens. Consequently, the Norton exponent corresponding to the Ls mechanism was set to the same values as for the Hs mechanism.

The lifetime of both long-term crept and notched specimens were used to adjust the damage nucleation parameters A_{Ls}, B_{Ls}.

The model parameter concerning the effect of the stress triaxiality on damage (B_{Ls}) was identified to preferentially describe the experimental results at 600°C on notched specimens because of a higher number of tests at this temperature compared to these at 650°C.

As it will be later discussed the value retained for B_{Ls} underestimates by a factor of about 2 the lifetime of the NTDV specimens at 650°C but fairly well describes the lifetime of the others notched specimens creep tested both at 600°C and 650°C.

Note that $\dot{f}_{nm}$ in equation VIII.14 is a linear function of stress triaxiality (τ) and not a square function of τ as in (Gaffard et al., 2005a), (Gaffard, 2004). In fact, both functions were tried and in our case the linear function was found to more accurately describe experimental results on notched specimens.

Table VIII.1 : Model parameters for Grade 92 steel

		600°C	**650°C**
Elastic properties	E (GPa)	150	150
	ν	0.3	0.3
Quasi-plastic flow	R_{qp}(MPa)	230	180
	K_{qp}	1	1
	n_{qp}	5	5
	$\sigma 0_{qp}$ (MPa)	100	70
Viscoplastic hardening	$R0_{Hs}$(MPa)	6	0.1
	Q_{Hs}(MPa)	125	78
	b_1	202	270
	b_2	7.5	10
	p_c	0.03	0.03
	$R0_{Ls}$(MPa)	0.01	0.01
Viscoplastic flow	K_{Hs} (h^{-1})	6.19×10^{-4}	2.98×10^{-3}
	K_{Ls} (h^{-1})	2.93×10^{-8}	1.79×10^{-6}
	$n_{Hs} = n_{Ls}$	6	6
	$\sigma 0_{Hs} = \sigma 0_{Ls}$(MPa)	100	100
GTN model	q_1	1.5	1.5
	q_2	1	1
	f_c	0.1	0.1
	δ	6	6
Damage nucleation	A_m	12	8
($m = Ls$)	B_m	45	45
Microstructural	f_{Laves}	$2.39\,(1-\exp(-t/7108))^{1.5}$	$2.39\,(1-\exp(-t/1946))^{1.5}$
parameters	h	1.25	0.94

VIII.5 Model validation

VIII.5.1 Smooth specimens

The model with the values of parameters given in table VIII.1 satisfactorily describes the creep elongation curves of smooth specimens both at 600°C and 650°C, as can be seen in figure VIII.2. Lifetime of smooth specimens is also fairly well predicted by the model both at 600°C and 650°C.

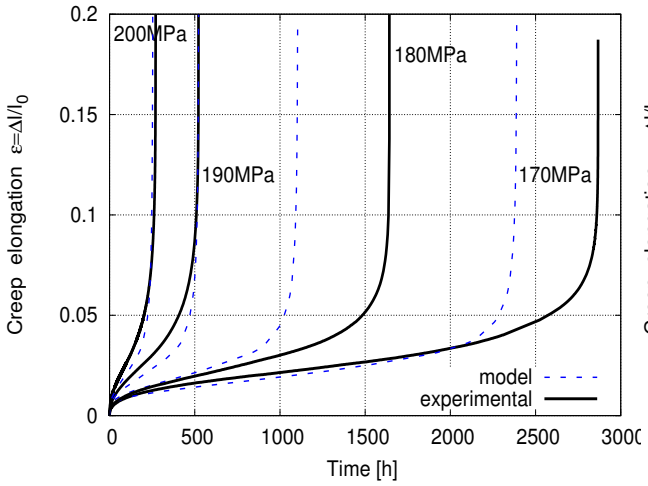

a) 600°C, T92 steel, smooth specimens

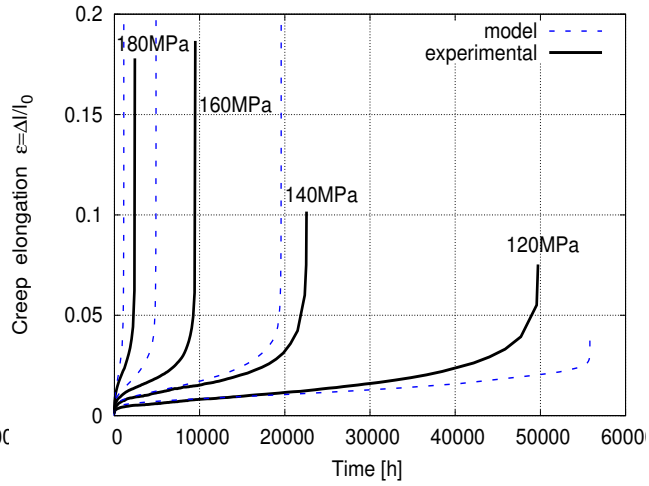

b) 600°C, P92 steel, smooth specimens

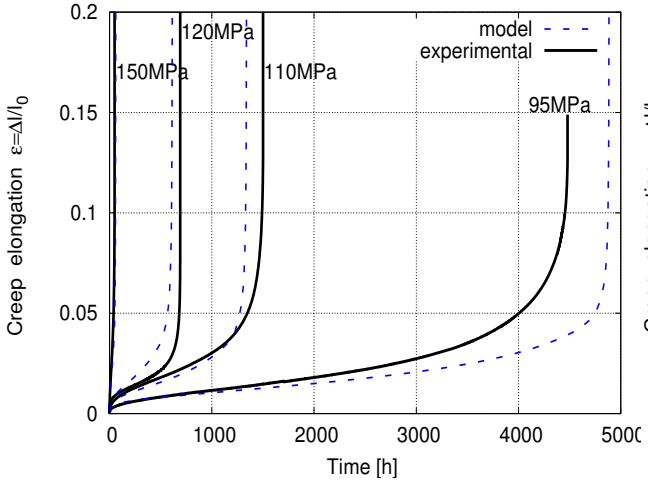

a) 650°C, T92 steel, smooth specimens

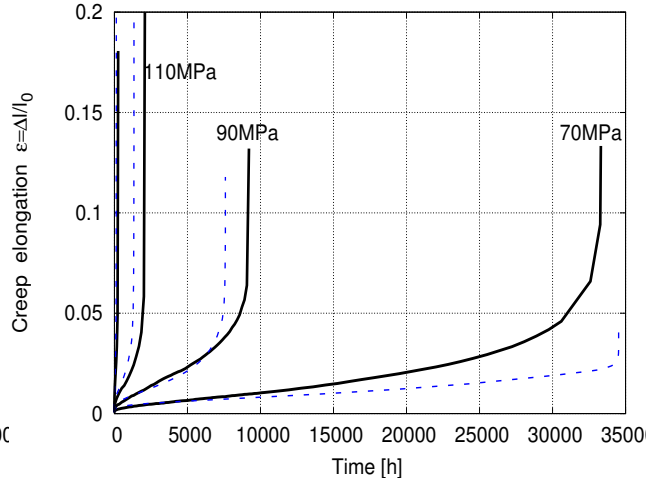

b) 650°C, P92 steel, smooth specimens

Figure VIII.2 : Comparison between simulated (dotted lines) and experimental (continuous lines) creep curves of tests conducted at 600°C (a, b) and 650°C (c,d) on smooth specimens

Tables VIII.2 and VIII.3 summarize data processing of both simulated and experimental creep curves using the procedure detailed in chapter IV. Tables VIII.2 and VIII.3 shows a more quantitative comparison between the experimental results and the simulated ones. The model fairly well predicts the onset of the tertiary creep stage $(ts_{III}, \varepsilon_{III})$ both for short-term and long-term tests.

Table VIII.2 : Comparison between the experimental and simulated creep curves at 600°C on smooth specimens (as-received material prior creep testing)

	Experimental creep curves						Simulated creep curves			
Temp. Steel	σ_n [MPa]	t_r [h]	Z [%]	ts_{III} [h]	ε_{III}	$\dot{\varepsilon}_{ss}$ [h^{-1}]	t_r [h]	ts_{III} [h]	ε_{III}	$\dot{\varepsilon}_{ss}$ [h^{-1}]
600°C T92 steel	210	112	89	60	0.036	43.77×10^{-5}	133	86	0.034	27.8×10^{-5}
	200	270	90	141	0.034	17.38×10^{-5}	253	165	0.033	13.7×10^{-5}
	190	523	85	287	0.034	8.58×10^{-5}	522	361	0.033	6.36×10^{-5}
	180	1,642	84	1,133	0.033	2.15×10^{-5}	1,103	798	0.032	2.77×10^{-5}
	170	2,867	78	1,718	0.029	1.07×10^{-5}	2,389	1631	0.028	1.15×10^{-5}
600°C P92 steel	180	2,399	74	1,637	0.031	1.22×10^{-5}	1,103	798	0.032	2.77×10^{-5}
	160	9,497	68	5,876	0.021	2.05×10^{-6}	4,883	3,307	0.026	5.00×10^{-6}
	140	22,547	27	13,258	0.018	8.37×10^{-7}	19,574	11,436	0.020	10.3×10^{-7}
	120	49,721	16	25,560	0.014	3.70×10^{-7}	55,805	40,189	0.017	2.73×10^{-7}

Table VIII.3 : Comparison between the experimental and simulated creep curves at 650°C on smooth specimens (as-received material prior creep testing)

	Experimental creep curves						Simulated creep curves			
Temp. Steel	σ_n [MPa]	t_r [h]	Z [%]	ts_{III} [h]	ε_{III}	$\dot{\varepsilon}_{ss}$ [h^{-1}]	t_r [h]	ts_{III} [h]	ε_{III}	$\dot{\varepsilon}_{ss}$ [h^{-1}]
650°C T92 steel	150	50	92	26	0.032	95.66×10^{-5}	60	35	0.030	65.75×10^{-5}
	140	67	88	33	0.036	82.78×10^{-5}	127	70	0.027	29.25×10^{-5}
	120	691	84	403	0.016	2.48×10^{-5}	613	331	0.023	4.85×10^{-5}
	110	1,502	77	782	0.024	2.11×10^{-5}	1,339	718	0.020	1.89×10^{-5}
	95	4,480	35	2,102	0.018	0.65×10^{-5}	4,885	2523	0.017	0.48×10^{-5}
650°C P92 steel	140	256	74	140	0.030	14.40×10^{-5}	127	70	0.027	29.25×10^{-5}
	110	2,092	74	1,017	0.019	1.28×10^{-5}	1,339	718	0.020	1.89×10^{-5}
	90	9,211	43	5,900	0.027	3.97×10^{-6}	7,599	4,184	0.018	3.06×10^{-6}
	70	33,308	20	14,293	0.014	0.79×10^{-6}	34,524	22,655	0.014	0.45×10^{-6}

The value of the p_c in the definition of the flow stress R_{Hs} (equation VIII.4) was set to 0.03 to describe the onset of tertiary creep stage. This corresponds to the value of elongation at which the tertiary creep stage is onset on short-term crept specimens both at 600°C and 650°C. Data processing of simulated creep curves shows that the tertiary creep stage is onset at values of elongation of about 0.03 on short-term creep tests. As can be seen in tables VIII.3 and VIII.2 the tertiary creep stage on long-term crept specimens is onset at lower values of elongation which corresponds fairly well to the values observed on the experimental creep curves. This proves the accuracy of the model.

The second part in the definition of the flow stress R_{Hs} (i.e. $min\left(1, 1/exp\left(b_2\left(\bar{p}_{Hs} - p_c\right)\right)\right)$) was defined to describe the onset of tertiary creep stage. FE simulations revealed that this term affect only the lifetime of short-term specimens without effect on the long-term lifetime. Without this term the lifetime of short-term crept specimens is overestimated by a factor of about 2.

The contributions of Hs and Ls mechanisms to the total strain versus time of a short-term and a long-term creep is illustrated in figure VIII.3. As expected the contribution of the Ls mechanism is negligible in the short-term (figures VIII.3a and VIII.3c), accordingly no creep damage is predicted by the model as experimentally observed. For long-term creep the contribution of the Ls mechanism is much more significant, see figures VIII.3b and VIII.3d.

In figure VIII.4 is represented the ratio between irreversible strain due to the Hs and that due to Ls mechanisms at 0.9 times the lifetime of the simulated creep curves. The longer the

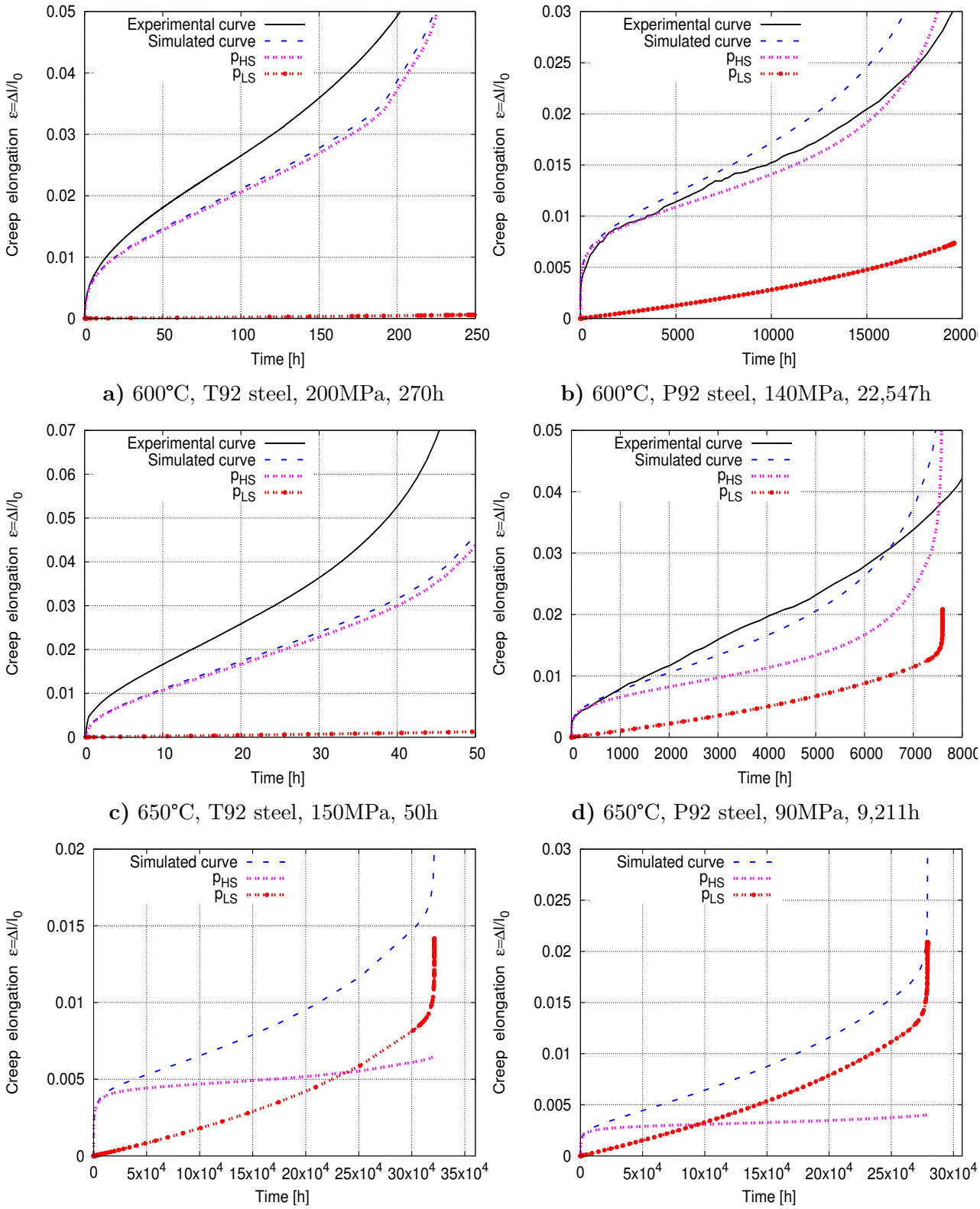

a) 600°C, T92 steel, 200MPa, 270h

b) 600°C, P92 steel, 140MPa, 22,547h

c) 650°C, T92 steel, 150MPa, 50h

d) 650°C, P92 steel, 90MPa, 9,211h

e) 600°C, 90MPa

f) 650°C, 50MPa

Figure VIII.3 : Simulated (dotted lines) and experimental (continuous lines) creep curves of tests conducted on smooth specimens at 600°C and 650°C. Contribution to strain corresponding to both Hs mechanism (p_{Hs}) and Ls mechanism (p_{Ls}) are also represented.

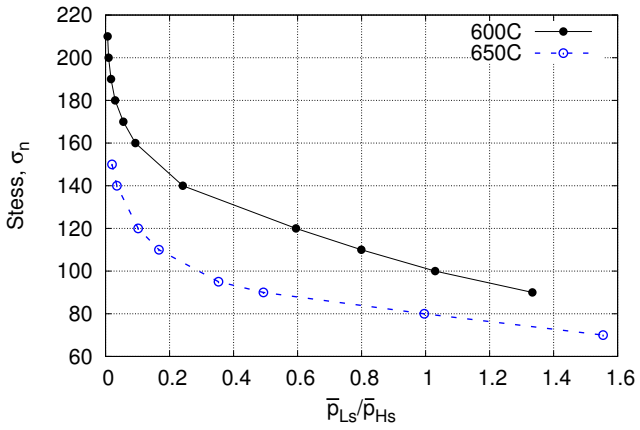

Figure VIII.4 : Contributions of the Ls and Hs mechanism to total strain at 0.9 times the simulated lifetime of smooth specimens as a function of the stress level

lifetime and the lower the applied stress, the higher the contribution of the Ls mechanism.

For levels of stress lower than 100MPa at 600°C and lower than 80MPa at 650°C, the contribution of the Ls mechanism to the overall deformation becomes higher than that of the Hs mechanism, see figures VIII.3, VIII.4. Note that there are no experimental data for the levels of stress used for simulations in figures. These levels of stress are difficult to be creep tested due to extremely long duration of tests.

VIII.5.2 Notched specimens

Model fairly well describes the creep elongation as well as lifetime of all kinds of notched specimens, see figures VIII.5, VIII.6, VIII.7 and VIII.8.

A sudden acceleration of elongation in the tertiary creep stage can be observed on the simulated creep curves of tests on NTDC1.2 and NTDC0.6M both under $\sigma_n = 130$MPa at 650°C, see figure VIII.6a,c. This might be due to a computational artefact of convergence. However the first part of these curves is well described.

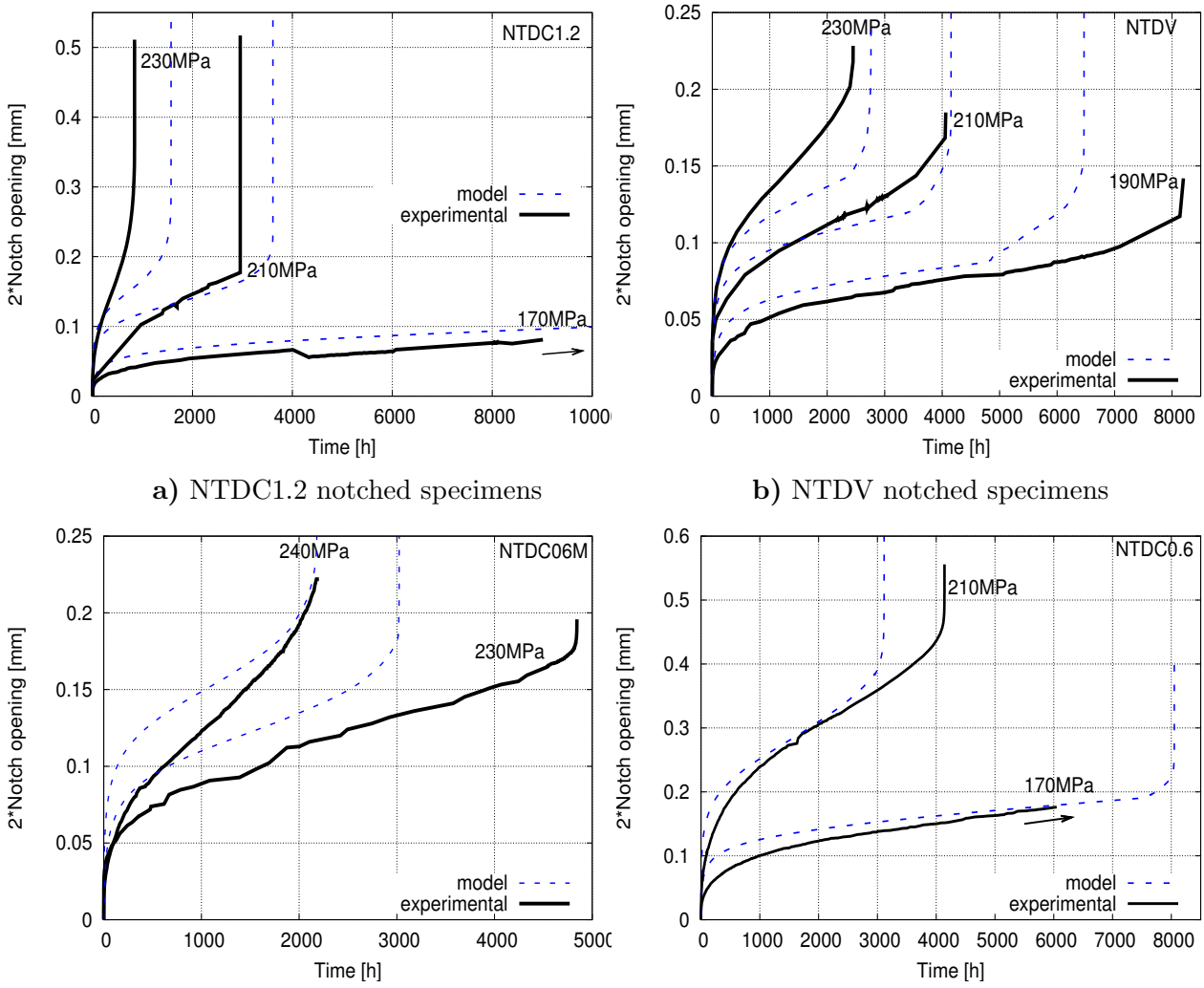

a) NTDC1.2 notched specimens

b) NTDV notched specimens

c) NTDC0.6M notched specimens

d) NTDC0.6 notched specimens

Figure VIII.5 : Comparison between simulated (dotted lines) and experimental (continuous lines) creep curves of tests conducted at 600°C on smooth specimens

The model fairly well predicts the time to failure both at 600°C and 650°C on smooth and notched specimens, as can be seen in figures VIII.7 and VIII.8 respectively.

The experimental slope of σ_n versus lifetime curves of NTDC1.2 notched specimens at 600°C has an intermediate value between that of smooth and that of the most severe notched specimens (NTDV and NTDC0.6M). The model fairly well predicts these slopes. Moreover, two slopes are predicted for the NTDV notched specimens, as experimentally observed.

The notch strengthening effect of the NTDV specimens is counterbalanced by accelerated creep damage developed for lifetimes higher than 4,000h at 600°C (i.e. the σ_n versus lifetime

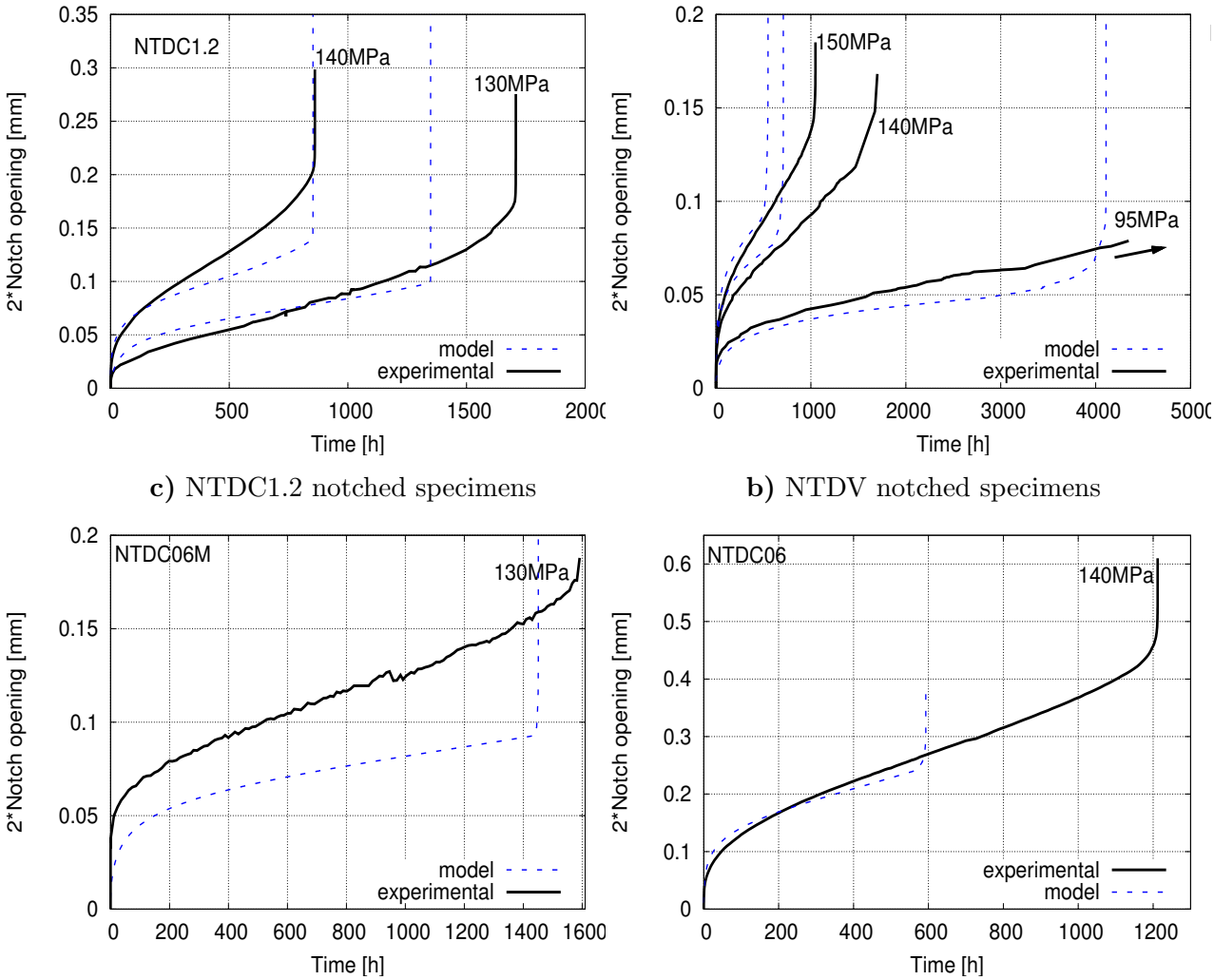

c) NTDC1.2 notched specimens

b) NTDV notched specimens

c) NTDC0.6M notched specimens

d) NTDC0.6 notched specimens

Figure VIII.6 : Comparison between simulated (dotted lines) and experimental (continuous lines) creep curves of tests conducted at 650°C on smooth and notched specimens

curves of NTDV specimens cross that of NTDC1.2 specimens), see figure VIII.7. This was also observed for Grade 91 steel using notched specimens with similar notch geometry to these used in this study (Gaffard et al., 2005a), (Gaffard, 2004).

There is a difference in the effect of notch geometry on the lifetime at 600°C compared to that at 650°C (i.e. for the same level of the σ_n at 600°C the lifetime of the NTDV specimens is higher than that of the NTDC0.6M specimens; the experimental results at 650°C show the contrary) see figure VIII.7 compared with figure VIII.8. Due to this difference, the model could not reproduce all experimental results at same time for a given set of parameters. As can be seen in figure VIII.8 the lifetime of NTDV specimens is underestimated by a factor of about 2. However, the lifetime as well as the creep curves of the other notched specimens tested at 650°C are fairly well predicted by the model with the parameters gathered in table VIII.1.

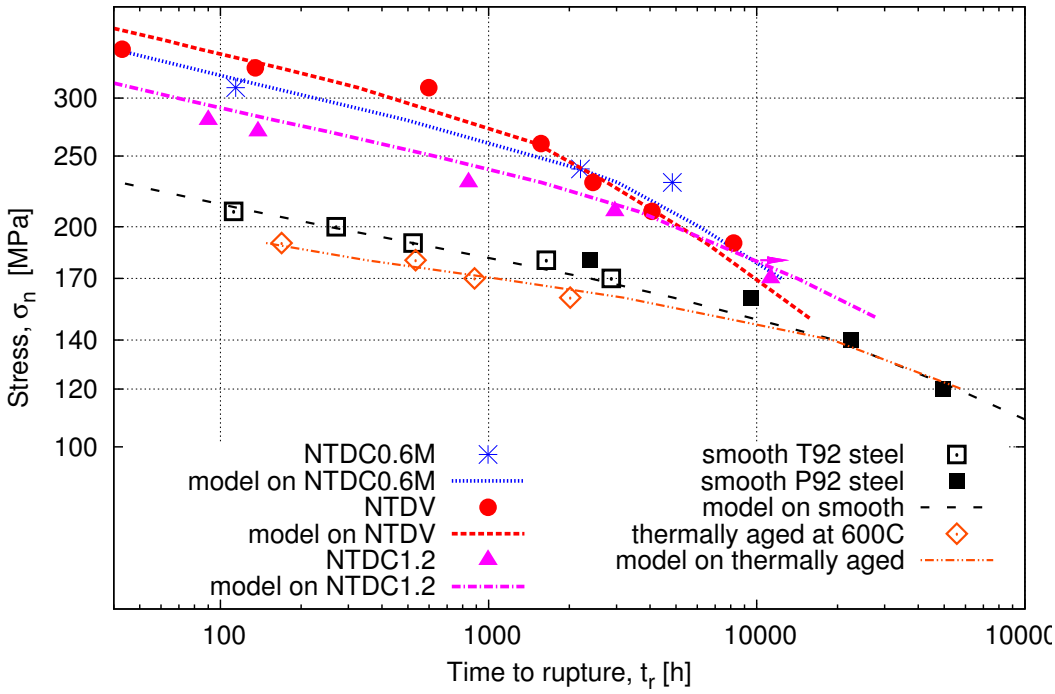

Figure VIII.7 : Creep rupture data for tests conducted at 600°C (symbols) compared with simulations results (dotted lines)

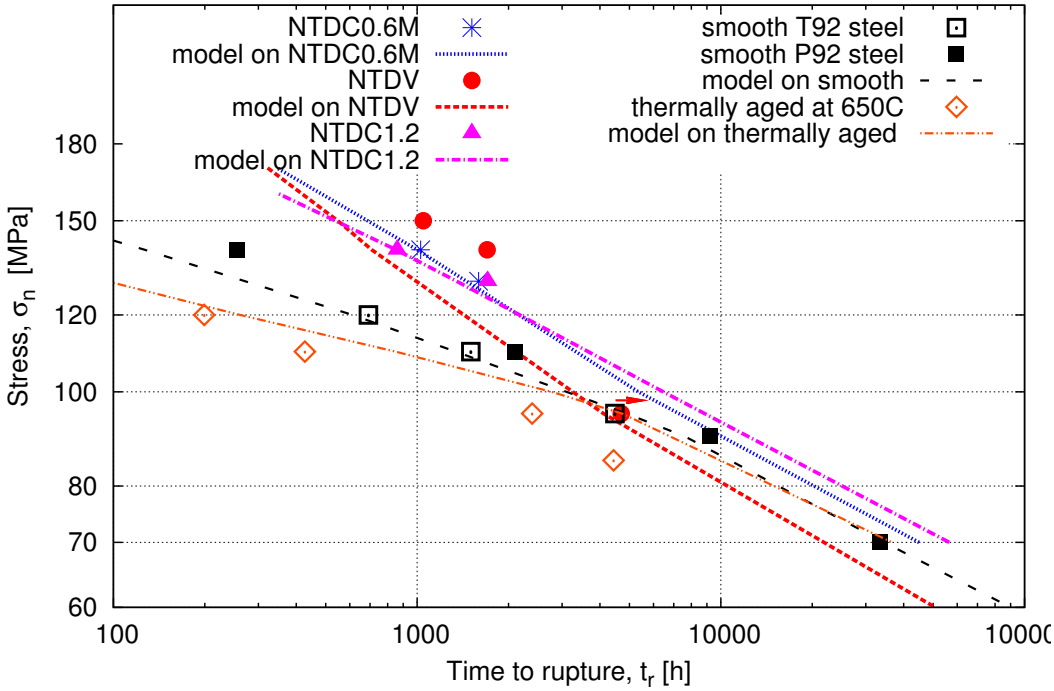

Figure VIII.8 : Creep rupture data for tests conducted at 650°C (symbols) compared with simulations results (dotted lines)

The function of total porosity (f_t) at the end of simulated lifetime of notched specimens is given in figure VIII.9. The total porosity has a maximum value close to the axis of the NTDC1.2 specimen as was experimentally observed, see figure VII.61 and figure VIII.10. In figure VIII.10 are compared the location maximum values of porosity measured in the notched areas of specimens (see figures VII.50, VII.61) to that predicted by the model. In the NTDV and NTDC0.6 notched specimens the maximum of porosity is located close to the notch roots. The highest values of porosity are observed in a smaller area than in the NTDC0.6M specimen, see figure VII.61b compared to figure VII.61c. This corresponds to the microstructural observations which revealed a high area fraction of cavities close to the notch area of the NTDV specimen, figure VII.61. In the NTDC0.6M specimens high amount of creep cavities were observed throughout the notched area with higher values of area fraction close to the notch roots.

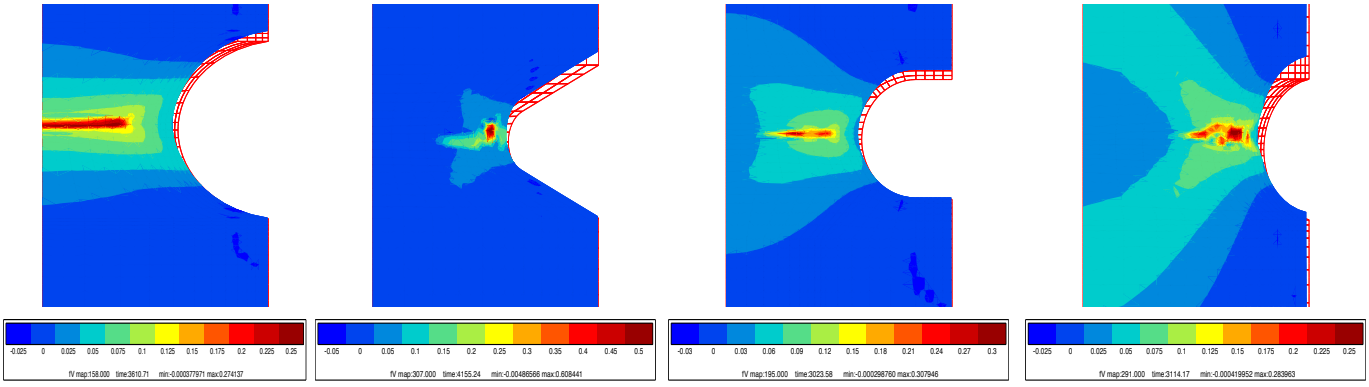

a) **b)** **c)** **d)**

Figure VIII.9 : Distribution of total porosity (f_t) on notched specimens. a) 600°C, NTDC1.2, σ_n =210MPa, 3,610h; b) 600°C, NTDV, σ_n =210MPa, 4,155h; c) 600°C, NTDC0.6M, σ_n =230MPa, 3,023; d) 600°C, NTDC0.6, σ_n =210MPa, 3,114h (simulated lifetimes)

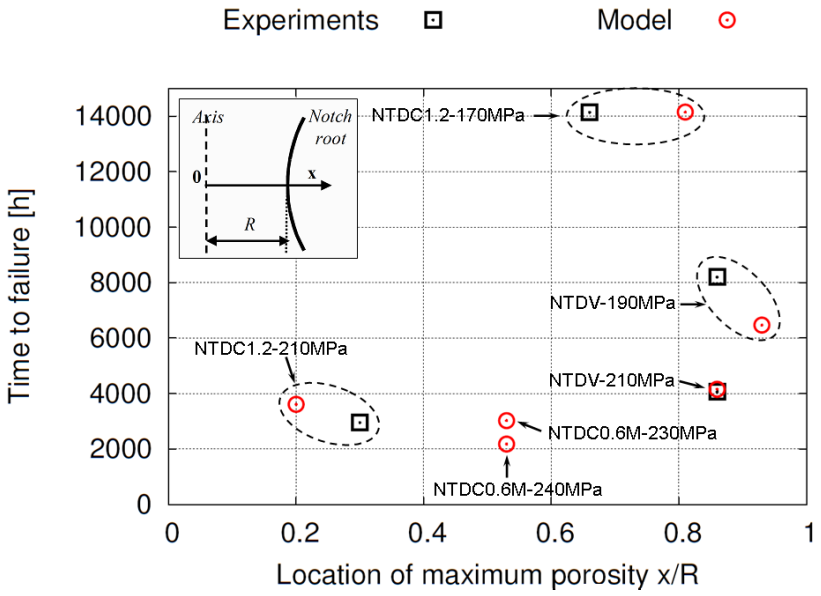

Figure VIII.10 : Location of the most damaged area in the notched areas of specimens. Comparison between model predictions and experimental observations

As it was previously indicated the notch in the NTDC0.6 specimen was not deep enough and the notch geometry is strongly deformed during creep test and consequently the strengthening effect is lost. This can be clearly be seen in figure VIII.9d. Moreover, FE simulations revealed that the strain field is not confined in the notched area of the NTDC0.6 as it is the case of the other notched specimens.

Figures VIII.11, VIII.12 and VIII.14 shows various plots of the FE simulations (σ_n = 210MPa, 600°C) results in the section of the NTDC1.2, NTDV and NTDC0.6M notched specimens at 0.9 of their predicted lifetime. The X axis in these figures is the same as that in figure IV.2.

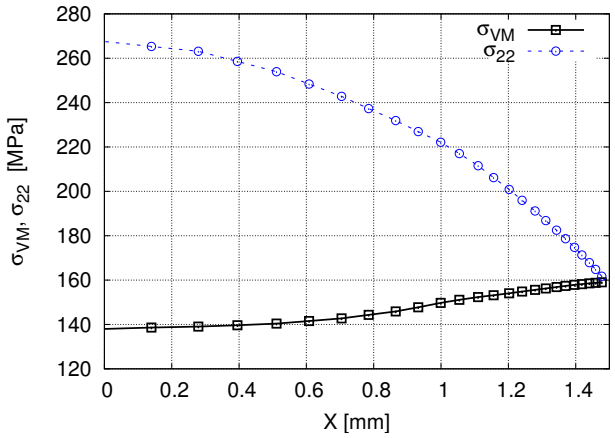

a) von Mises equivalent stress (σ_{VM}) and principal stress (σ_{22})

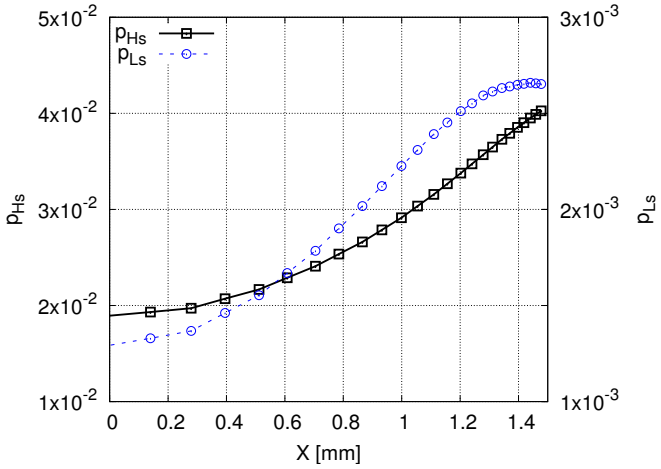

b) irreversible strain due to Hs ($\bar{p}_{Hs}$) and Ls ($\bar{p}_{Ls}$) mechanism

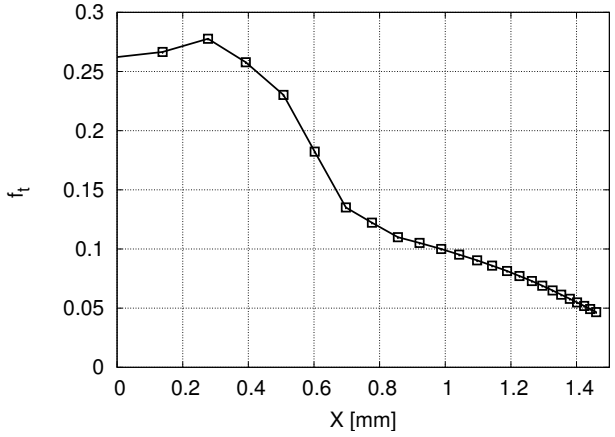

c) total porosity (f_t)

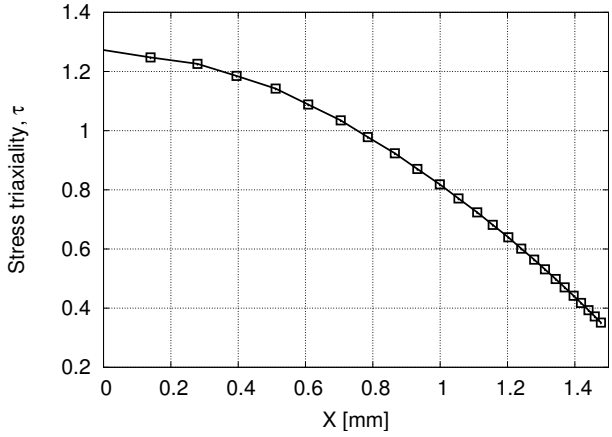

d) stress triaxiality ratio (τ)

Figure VIII.11 : Results of FE simulations at 0.9 times (i.e. at 3,249h) the simulated lifetime of NTDC1.2 specimen at 600°C, $\sigma_n = 210$MPa, $t_r = 3,611$h (simulated)

Lifetimes of 2,957h and of 4,063h were experimentally found for the NTDC1.2 and NTDV specimens both creep tested under σ_n = 210MPa at 600°C. For these testing conditions the model predicts a lifetime of 3,610h and of 4,155h on NTDC1.2 and NTDV specimens, respectively.

The stress distribution in the notched area during creep varies with the notch geometry and consequently creep flow and creep damage development is different from one notched type of specimen to the other.

The maximum principal stress (σ_{22}) is highest in the centre of the NTDC1.2 specimen, see figure VIII.11a. This induces high values of stress triaxiality along the axis of the NTDC1.2 specimen, see figure VIII.11d. The model takes the effect of stress triaxiality (equation VIII.14) into account and thus predicts a maximum of area fraction of cavities close to the axis of the NTDC1.2 specimen over a radius of about 0.4mm, see figure VIII.11c. This corresponds to microstructural observations of creep damage in the NTDC1.2 specimen (see figure VII.61).

In the NTDV specimen σ_{22} shows a maximum value close to the notch root (figure VIII.12a) which induces a maximum value of stress triaxiality close to the notch root (figure VIII.12d). Accordingly, the model predicts a maximum value of total porosity close to the notch root, see figure VIII.12c. In the centre of the NTDV specimen the total porosity is negligible.

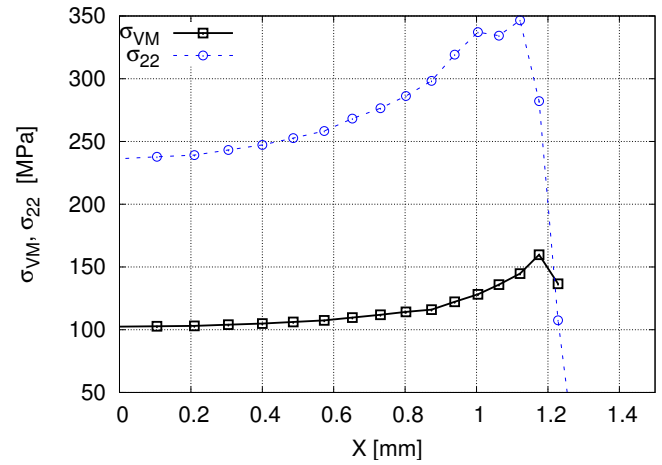

a) von Mises equivalent stress (σ_{VM}) and principal stress (σ_{22})

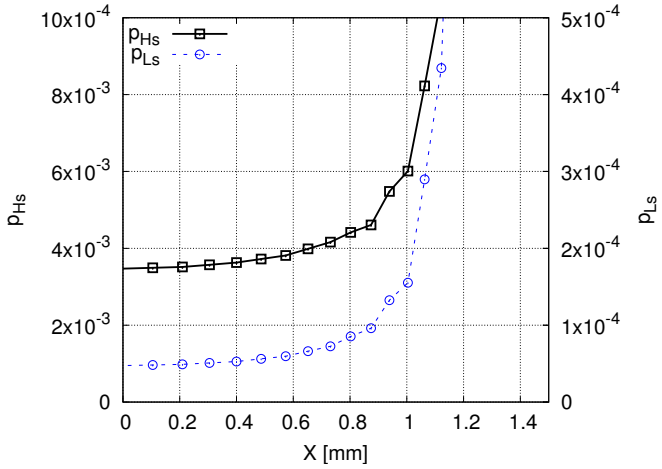

b) irreversible strain due to Hs ($\bar{p}_{Hs}$) and Ls ($\bar{p}_{Ls}$) mechanism

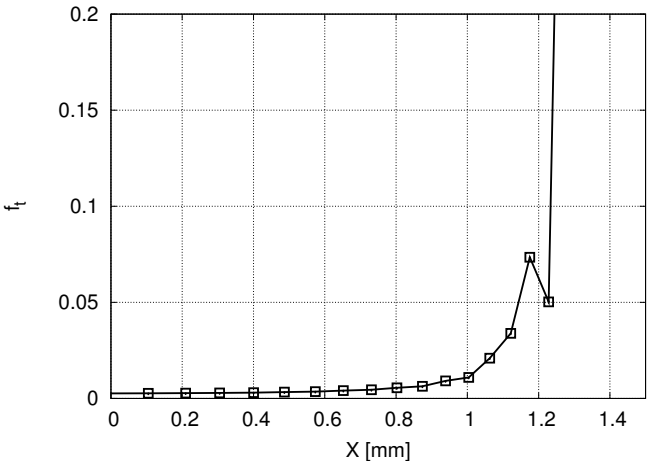

c) total porosity (f_t)

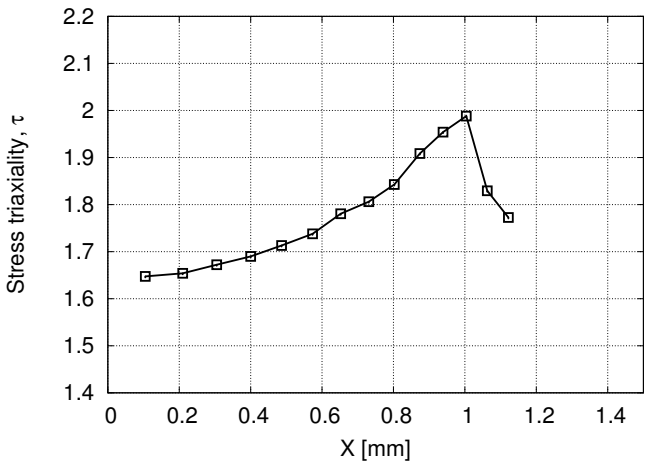

d) stress triaxiality ratio (τ)

Figure VIII.12 : Results of FE simulations at 0.9 times (i.e. 3,739h) the simulated lifetime of NTDV specimen at 600°C, $\sigma_n = 210$MPa, $t_r = 4,155h$ (simulated)

The plots of figure VIII.12 show no values for radius (i.e. X) higher than 1.2mm while the radius in the notched area of the NTDV specimen before creep testing is 1.5mm. This is because the FE elements close to the notch root are *broken*. An element is considered to

be broken when total porosity in two Gauss points is higher than $\frac{1}{q_1} - 0.01$. The first *broken* element is the second one away from the notch root and the elements close to it *broke* with increasing testing time up to distance of about 0.5mm from the notch root. This is ilustrated in figure VIII.13. The testing time of the first *broken* element corresponds to the onset of the tertiary creep stage on the simulated creep curves of the NTDV specimens. Note that possible effects of the mesh size on these results were not investigated.

This could be experimentally confirmed by interrupted creep tests on NTDV notched specimens at the onset of the tertiary creep stage. However, the outer borders of the fracture surface (i.e. close to the notch root) of the NTDV specimens seem to have been exposed to oxidation for longer times than their centre which might confirm the FE simulations.

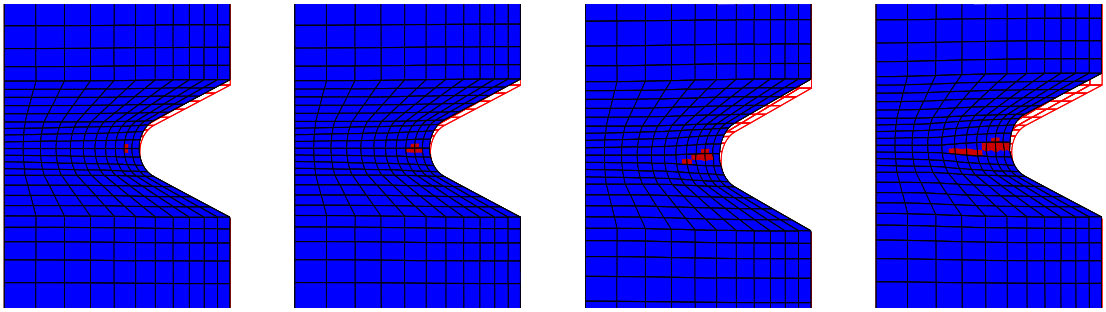

a) 3,480h **b) 3,789h** **c) 4,151h** **d) 4,155h**

Figure VIII.13 : Broken elements during simulated creep test on NTDV σ_n =210MPa, 600°C. (simulated lifetime of 4,155h and a experimentally lifetime of 4,074h)

Note that a relatively high time is needed between the time corresponding to the first FE element broken and the failure of the NTDV specimens tested under $\sigma_n < 280$MPa, see figure VIII.13. This is might indicate a stable crack propagation. The time between the first broken element and failure of NTDC1.2 and NTDC0.6M specimens is less than 1-2 hours. The first broken element is located close to the axis specimen in the NTDC1.2 and at a distance of about 0.6 mm from the the notch root of the NTDC0.6M specimen.

A *crack* connected to the unbroken notch root and following grains boundaries is observed in all NTDV specimens tested under σ_n lower than 250MPa which might indicated stable crack propagation.

The FE simulation results of figure VIII.13 could be explained by the stress distribution in the notched area of the NTDV specimen (see figures V.18, VI.17, VIII.12a). The σ_{22} (stress triaxiality) is maximum close to the notch root on a relatively limited area, thus creep damage (porosity) will develop faster in this area than in the rest of specimen. When the elements corresponding to this area will broke, they will be removed and the σ_{22} will be maximum on a relatively limited area close to broken elements and so on until failure of the specimen.

The observation of first broken element (FE simulations) corresponds to the failure of the NTDV specimens tested for $\sigma_n > 300$MPa. Note that a slope change is observed at this level of stress in the stress versus lifetime curves of NTDV specimens creep tested at 600°C.

As expected the maximum stress triaxiality is higher in the NTDV specimens compared to that in the NTDC1.2 specimen for a given level of the σ_n, see figure VIII.12 compared with figure VIII.11. Accordingly the model predicts higher values of total porosity (cavities) in the NTDV specimen compared to that in NTDC1.2 specimen for a given level of the σ_n, see figures VIII.12c and VIII.11c.

From figures VIII.11, VIII.12 and VIII.14 it can be concluded that the NTDV specimen geometry provides the most favourable stress state for creep damage development. The drawback of these specimens is that principal stresses (respectively stress triaxiality) are very

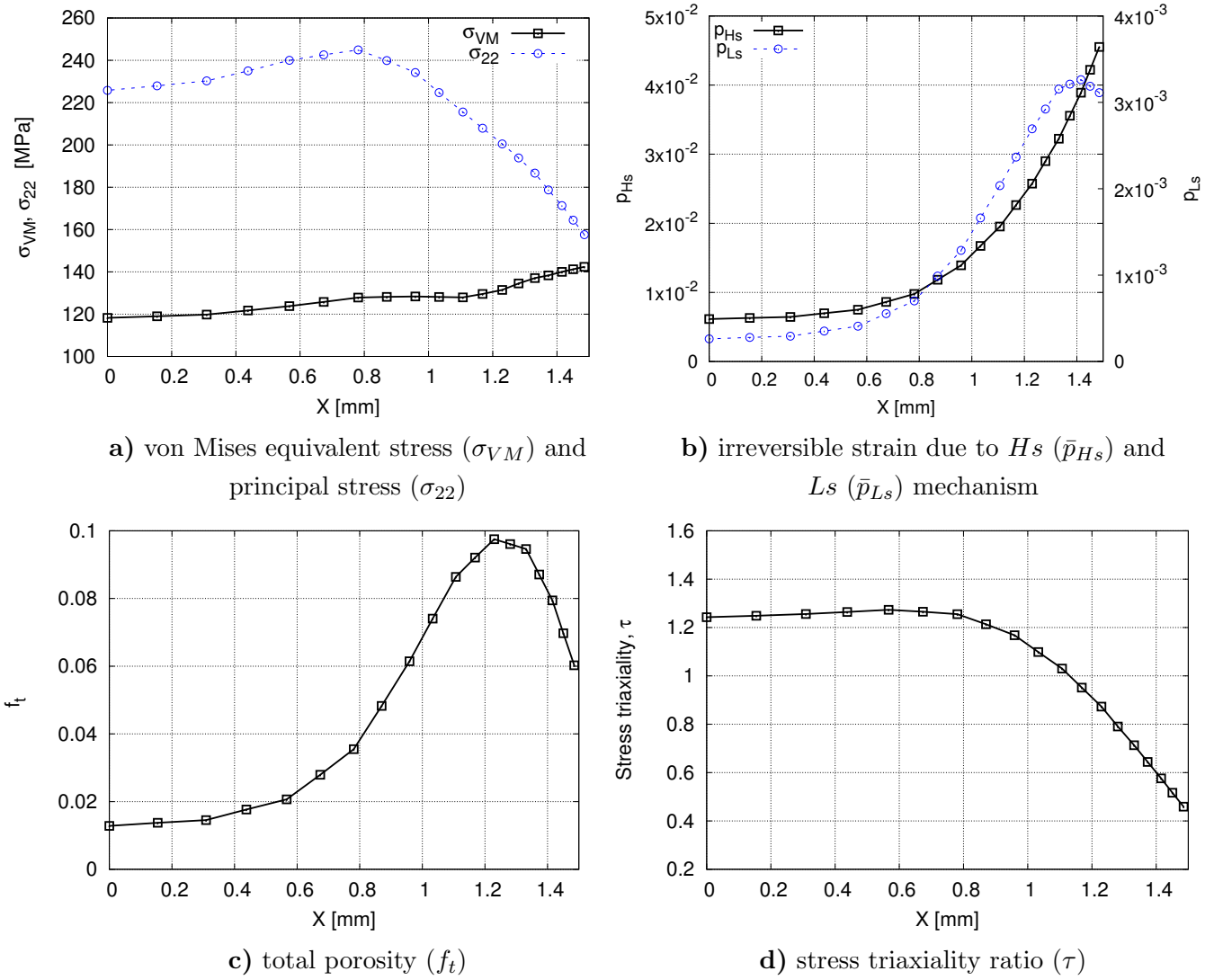

a) von Mises equivalent stress (σ_{VM}) and principal stress (σ_{22})

b) irreversible strain due to Hs ($\bar{p}_{Hs}$) and Ls ($\bar{p}_{Ls}$) mechanism

c) total porosity (f_t)

d) stress triaxiality ratio (τ)

Figure VIII.14 : Results of FE simulations at 0.9 times (i.e. 4,448h) simulated lifetime of NTDC0.6M specimen at 600°C, $\sigma_n = 210$MPa, $t_r = 4,973$h (simulated)

high only in a relatively reduced area located close to the notch root (figure VIII.12a,d) and thus limited area is available for microstructural investigations such as quantification of creep damage or precipitates. For example, the effect of stress on the growth of precipitates could be rather difficult to study using this kind of specimens due to relatively reduced area for sample preparation. In addition, stable crack propagation must be tracked to quantitatively interpret creep curves.

Creep damage significantly develops on a larger area of NTDC1.2 notched specimens compared to the NTDV specimens, see figure VIII.12c compared with figure VIII.11c. However, levels of the σ_{22}, stress triaxiality and total porosity are lower than those in the NTDV specimens for a given level of σ_n.

NTDC0.6M specimens could be a good comprise between the advantages and drawbacks of the NTDV and NTDC1.2 notched specimens. NTDC0.6M allows both levels of σ_{22} and stress triaxiality comparable to these in the NTDV specimens (see figures VIII.12a,d and VIII.14a,d) and significant creep damage development on a larger area than that in a NTDV specimen (see figures VIII.12c and VIII.14c) for a given level of σ_n.

VIII.5.3 Thermally aged specimens

After validation on notched and smooth specimens, the model was tested on thermally aged specimens by setting the time (t) to 10^4h in the function f_{Laves} (equation VIII.7), which corresponds to duration of aging heat treatments.

Model thus modified overestimates systematically the lifetime of thermally aged specimens. This is more pronounced for levels of stress lower than 95 MPa at 650°C.

In the low stress region model predicts lifetime of thermally aged specimens similar to that of smooth ones, see figures VIII.7 and figure VIII.8. This may not be true given the experimental results on thermally aged specimens tested under levels of stress lower than 95MPa. These tests revealed a lifetime almost twice lower on thermally aged compared to that of smooth ones under same load.

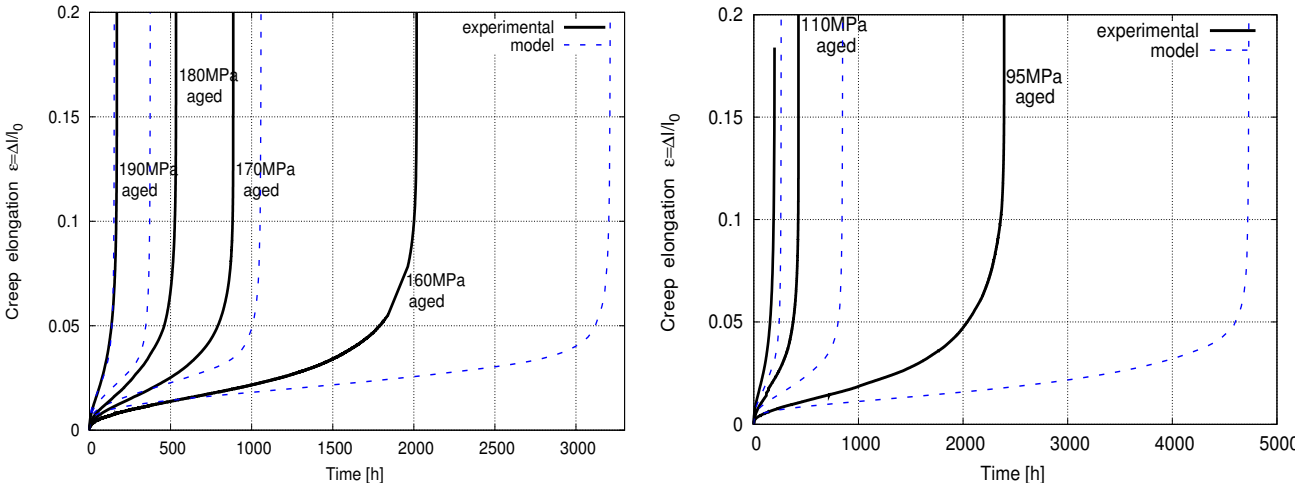

a) T92 steel thermally aged at 600°C for 10^4h **b)** T92 steel thermally aged at 650°C for 10^4h

Figure VIII.15 : Comparison between simulated (dotted lines) and experimental (continuous lines) creep curves of tests conducted thermally aged specimens at 600°C (a) and 650°C (b)

Note that creep damage development occurs in the low stress region both at 600°C at 650°C. Probably creep damage development is enhanced in a aged microstructure prior creep testing compared to that in a standard smooth specimen (i.e. with an as-received microstructure prior creep testing) and the values of model damage parameters are not able to predict correctly the lifetime of thermally aged specimens.

The mechanisms involved in creep of aged microstructure prior creep testing might be different from these in an as-received microstructure prior creep testing. For example higher number of precipitates in the aged microstructure prior creep testing could increase the nucleation sites of cavities and thus enhance creep damage development compared to that in an as-received microstructure. Also recovery of the matrix might be enhanced in an aged microstructure due to lower solution strengthening (in our case) compared to that in an as-received microstructure under same testing conditions.

Mechanisms involved in creep of aged microstructure prior creep testing should be further investigated before establishing a model. The model developed in this study was not aimed for this purpose. Note also that the model parameters were identified based on experimental results on smooth and notch specimens.

Table VIII.4 : Comparison between the experimental and simulated creep curves at 600°C and at 650°C on thermally aged specimens

	Experimental creep curves						Simulated creep curves			
Temp. Steel	σ_n [MPa]	t_r [h]	Z [%]	ts_{III} [h]	ε_{III}	$\dot{\varepsilon}_{ss}$ [h^{-1}]	t_r [h]	ts_{III} [h]	ε_{III}	$\dot{\varepsilon}_{ss}$ [h^{-1}]
Aged T92 steel* 600°C	190	169	87		0.026	$25{,}3\times10^{-5}$	153	96	0.031	$21{,}5\times10^{-5}$
	180	534	87	251	0.023	7.33×10^{-5}	374	257	0.31	8.40×10^{-5}
	170	886	82	474	0.024	$3{,}95\times10^{-5}$	1,058	838	0.033	2.75×10^{-5}
	160	2016	82	1,060	0.023	1.60×10^{-5}	3,212	2,487	0.032	0.81×10^{-5}
Aged T92 steel** 650°C	120	199	88	94	0.026	$21{,}1\times10^{-5}$	261	155	0.027	12.5×10^{-5}
	110	427	80	270	0.030	9.43×10^{-5}	848	501	0.25	3.59×10^{-5}
	95	2,392	65	1,098	0.020	1.45×10^{-5}	4,731	2,527	0.20	0.50×10^{-5}
	85	4,434		2,074	0.017	0.73×10^{-5}	10,928	6,384	0.017	0.17×10^{-5}

*T92 steel thermally aged at 600°C for 10^4h and creep tested at 600°C

**T92 steel thermally aged at 650°C for 10^4h and creep tested at 650°C

Given the FE simulations results given in figures VIII.7 and VIII.8 one can say that lifetime of thermally aged specimens for times up to 5,000h at 600°C and up to 2,000h at 650°C could fairly well be predicted. Data processing of the simulated creep curves on thermally aged specimens shows that the model fails predicting the onset of tertiary creep stage (table VIII.4) as it was the case of smooth specimens.

VIII.6 Summary and discussion

A mechanical model coupling damage, multiple deformation mechanism and microstructural evolution was developed to describe the creep flow of the Grade 92 steel both at 600°C and 650°C. The design of this model is similar to that developed by V. Gaffard in his PhD. thesis for the creep flow of the Grade 91 steel (Gaffard et al., 2005a), (Gaffard, 2004). A new definition of the deformation mechanisms was assumed and internal variables were incorporated to describe the effect of microstructural evolution on the creep flow compared to the model designed by (Gaffard et al., 2005a), (Gaffard, 2004).

The model was developed on the basis of experimental results (i.e. creep tests and microstructural observations).

The model takes three flow and damage mechanisms into consideration, contributing to the overall deformation and damage accumulation. A quasi-plastic (qp) mechanism and two viscoplastic mechanisms respectively corresponding to the high stresses (Hs) and low stresses (Ls) regions were defined to model the creep deformation.

The viscoplastic mechanisms were designed in such a way that deformation corresponding to the Hs mechanism is higher than that corresponding to the Ls mechanism and damage development corresponding to the Ls mechanism is much higher than that corresponding to Hs mechanism.

Creep damage has a significant influence on the lifetime of the long-term creep specimens. In figures VIII.16 and VIII.17 are represented the lifetimes of the various specimens predicted by the model without damage. As can be seen in figures VIII.16 and VIII.17 the lifetimes of specimens tested for short term creep could be predicted without taking damage development into account (the lifetime of specimens is given by structure instability (necking)).

Damage is described throughout a new definition of the effective stress (σ^*_{eq}) which considers the effect of both porosity (i.e. cavities) and engineering stress on the deformation.

The general description of Gurson model proposed by (Leblond et al., 1994) was used for the definition of σ^*_{eq} in the Ls and Hs mechanisms.

Internal variables account for the effect of metallurgical evolution of the steel on the creep flow. Precipitation and significant growth of Laves phases was considered as the preponderant microstructural evolution during creep exposure both at 600°C and 650°C. Thus internal variables implementated in the model follow kinetics of Laves phase precipitation.

The model thus defined fairly well describes the creep elongation of both smooth (see figure VIII.2) and notched (see figure VIII.5 and VIII.6) specimens as well as their lifetime (see figures VIII.7 and VIII.8).

Data processing of simulated creep curves on smooth specimens showed that the tertiary creep stage is onset at similar values of elongation as these observed on experimental creep curves, see table VIII.2. This proves the accuracy of the model in predicting viscoplastic strain for a given level of stress.

The accuracy of the model is also proved in prediction of creep damage development for a given geometry of specimen. The model predicts a maximum area fraction of cavities (porosity) close to the axis in the NTDC1.2 specimens and close to the notch root in the NTDV and NTDC0.6M specimens. This corresponds to microstructural observations of notched specimens after creep testing. Moreover, the size of the most damaged area estimated by FE simulations is comparable to that observed in the crept notched specimens.

Two slopes can be observed on the stress versus lifetime of the NTDV specimens. Model is able to predict these two slopes as well as the slopes of stress versus lifetime curves of NTDC1.2 and NTDC0.6M specimens.

The model predicts a stable crack propagation in the NTDV specimens for $\sigma_n < 280$MPa. This is indicated by a relatively high testing time between the first FE element broken and final failure of specimen (figure VIII.13). This is not observed in the NTDC1.2 and NTDC0.6M specimens. Observations of fracture surface of NTDV specimens after creep testing together with existence of a *crack* starting from the unbroken notch root and following the grain boundaries might suggest a stable crack propagation. However the model was not designed to simulate stable crack propagation.

Promising results are obtained on the thermally aged specimens by setting the t=10^4h in the function of the metallurgical evolution (f_{Laves}). However the aging effect prior creep testing is underestimated, this is more pronounced for low stress region.

Note that mechanisms involved in creep of an aged microstructure prior creep testing might be different from these occurring in an as-received microstructure prior creep testing. Creep damage development as well as recovery of the matrix should be investigated in thermally aged specimens after creep testing.

The model could be further developed to improve the description of mechanisms involved in the creep behavior of the Grade 92 steel. For example, internal variables could be implemented to describe the growth of $M_{23}C_6$ carbides during creep exposure. In this study, the effect of $M_{23}C_6$ carbides growth on the creep strength loss was considered to be negligible compared to that of Laves phases. Moreover, it is difficult to evaluate the effect of $M_{23}C_6$ carbides growth on the creep strength. Little improvements of model predictions would such be expected.

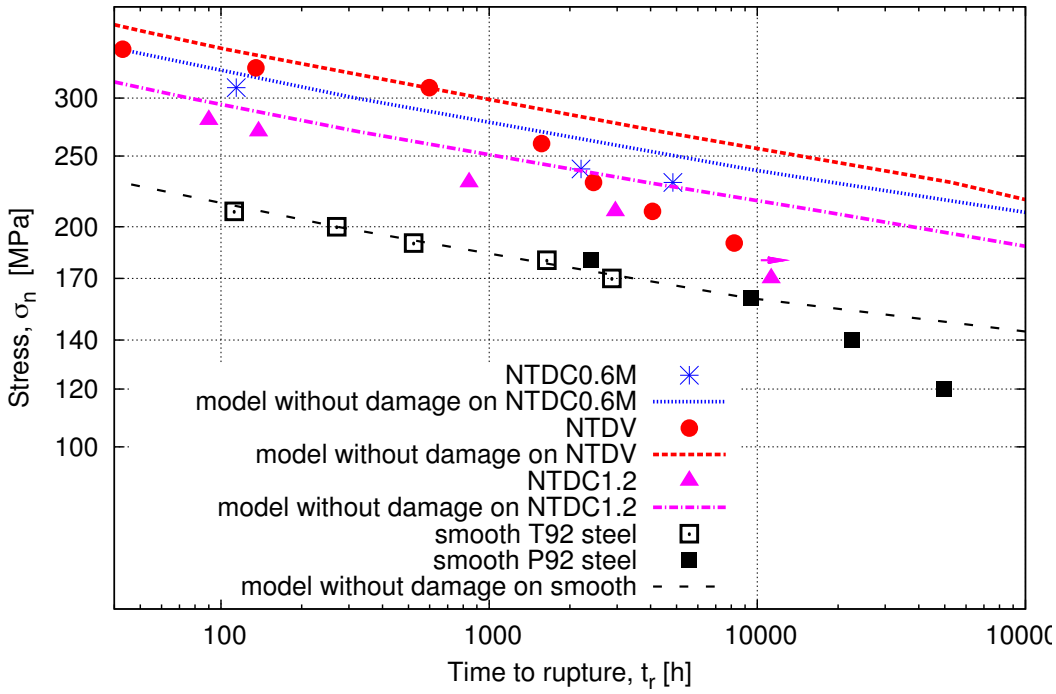

Figure VIII.16 : Creep rupture data for tests conducted at 600°C (symbols) compared with results predicted by the model without damage (dotted lines)

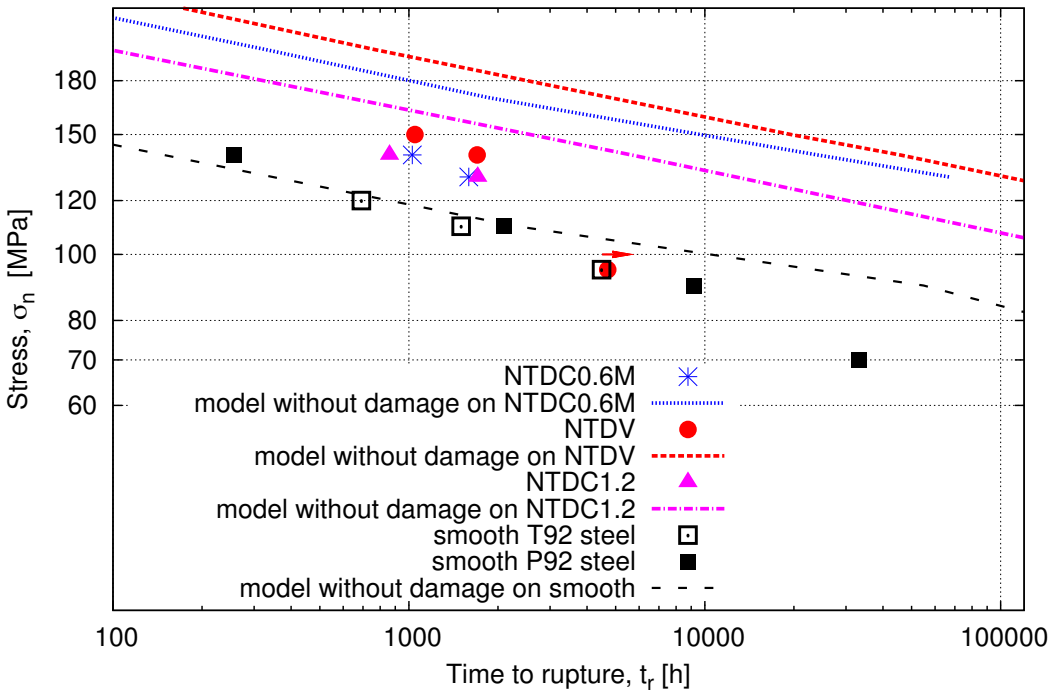

Figure VIII.17 : Creep rupture data for tests conducted at 650°C (symbols) compared with results predicted by the model without damage (dotted lines)

In the present model the precipitation and growth of Laves phases is not related to damage. Growth of Laves phases could enhance damage development. In this study the investigations of thermally aged specimens after creep testing were not relevant for this issue. This was probably because the creep testing time of thermally aged specimens was relatively low (times lower than 5,000h) compared to the lifetime of long-term specimens which revealed significant amount of damage. This should be further investigated.

The model does not accounts for the effect of the matrix recovery on the creep strength loss. In this study it was unsuccessfully tried to evaluate this effect. This should be also further investigated.

Résumé

Un modèle mécanique intégrant l'endommagement, plusieurs mécanismes de déformation et l'évolution microstructurale a été développé pour décrire le comportement en fluage de l'acier Grade 92 à 600°C et 650°C. L'architecture de ce modèle est similaire à celle du modèle développé par V. Gaffard dans sa thèse pour décrire le comportement en fluage de l'acier Grade 91 (Gaffard et al., 2005a), (Gaffard, 2004). Une nouvelle définition de mécanismes de déformation a été utilisée et des variables internes ont été intégrées pour modéliser l'influence de l'évolution métallurgique sur la déformation en fluage. Ce sont ici les différences majeures par rapport au modèle développé par V. Gaffard (Gaffard et al., 2005a), (Gaffard, 2004).

Le modèle prend en compte trois mécanismes de déformation qui contribuent à la déformation totale en fluage. Un mécanisme quasi-plastique (qp) et deux mécanismes viscoplastiques qui correspondent respectivement au régime de contrainte élevées (Hs) et au régime de contraintes faibles (Ls).

Les mécanismes viscoplastiques ont été définis de façon à ce que la contribution du mécanisme Hs à la déformation totale soit plus importante que celle du mécanisme Ls et la contribution du mécanisme Ls sur l'endommagement soit plus importante que celle du mécanisme Hs.

L'endommagement par fluage a une influence significative sur la durée des vie des éprouvettes long terme. Les durées de vie prédites par le modèle sans endommagement sont comparées avec les résultats expérimentaux sur les figures VIII.16 et VIII.17. Dans ce cas, les durées de vie des éprouvettes testées pendant des temps courts sont assez bien estimées, par contre celle des éprouvettes testées pendant des temps prolongés est surestimée notamment sur les éprouvettes entaillées, voir les figures VIII.16 et VIII.17.

L'endommagement est modélisé à l'aide d'une nouvelle définition de la contrainte effective (σ^*_{eq}) qui prend en compte l'effet de la porosité (cavités) et de la contrainte appliquée sur la déformation. La description générale du modèle de Gurson proposée par (Leblond et al., 1994) a été utilisée pour la définition de σ^*_{eq} correspondant aux mécanismes de déformation Hs et Ls.

Des variables internes ont été définies pour prendre en compte l'influence de l'évolution microstructurale sur la déformation en fluage. La précipitation et la croissance de phases de Laves ont été considérés comme les indicateurs majeurs de l'évolution microstructurale pendant le fluage à 600°C et 650°C.

Le modèle décrit assez bien la déformation en fluage des éprouvettes lisses et entaillées ainsi que leur durée de vie. De plus, le dépouillement des courbes de fluage simulées a montré que le début de stage tertiaire correspond à des valeurs d'allongement similaires à

celles observées sur les courbe expérimentales. Ce qui prouve la précision du modèle dans la description de la déformation viscoplastique pour une valeur donnée de la contrainte.

La précision du modèle est confirmée pour la prédiction du développement de l'endommagement. Le modèle prévoit la localisation du maximum de la porosité proche du rayon de l'entaille dans les éprouvettes NTDV et NTDC0.6M et près de l'axe de l'éprouvette NTDC1.2, voir la figure VIII.9, ce qui correspond bien aux observations métallographiques, voir la figure VIII.10.

Deux pentes sont observées sur les courbes contraintes en fonction du temps à rupture des éprouvettes NTDV. Le modèle est capable de décrire ces deux pentes. De plus, le modèle prédit aussi deux pentes pour les éprouvettes NTDC1.2 et NTDC0.6M. Le modèle prédit la propagation d'une fissure stable dans les éprouvettes NTDV pour des contraintes σ_n <280MPa à 600°C. Ceci est indiqué par un temps assez élevé entre l'apparition du premier élément cassé et la rupture finale de l'éprouvette, voir la figure VIII.13. Ceci n'est pas observé pour les éprouvettes NTDC1.2 et NTDC0.6M. L'observation des faciès de rupture ainsi que l'observation d'une fissure intergranulaire connectée au rayon des entailles des éprouvettes NTDV qui n'ont pas rompus pendant l'essai suggèrent la propagation stable d'une fissure. Il est à noter que le modèle n'a pas été défini pour simuler la propagation des fissures.

Une bonne estimation de la durée de vie et de la déformation des éprouvettes pré-vieillies est obtenue en mettant le temps (t) à $10^4 h$ dans la fonction de l'évolution métallurgique (f_{Laves}). Cependant l'influence du vieillissement thermique avant le fluage est sous-estimée par le modèle, plus particulièrement pour les contraintes faibles.

À noter que les mécanismes impliqués dans le fluage d'un acier vieilli thermiquement peuvent être différents de ceux impliqués dans le même acier non-vieilli. Une étude plus détaillée de l'endommagement et de la restauration de la matrice des éprouvettes pré-vieillies testées en fluage serait nécessaire pour mieux comprendre les mécanismes impliqués dans le fluage de l'acier vieilli.

Le modèle pourrait être encore amélioré pour mieux décrire les mécanismes microstructuraux impliqués dans le fluage de l'acier Grade 92. Par exemple, des variables internes pourraient être implémentées pour décrire la croissance des carbures $M_{23}C_6$ pendant le fluage. Dans cette étude l'effet de la croissance des carbures $M_{23}C_6$ sur le comportement en fluage a été considéré comme négligeable par rapport à celui de la croissance des phases de Laves. De plus, il est assez difficile d'évaluer l'effet de la croissance de carbures $M_{23}C_6$ sur la résistance en fluage. L'amélioration attendue d'une telle prise en compte serait donc minime.

Dans le modèle développé dans cette étude, la précipitation et la croissance des phases de Laves ne sont pas liées à l'endommagement. La croissance des ces phases pourrait intensifier l'endommagement par fluage. Les observations métallographiques des éprouvettes pré-vieillies testées en fluage n'ont pas apporté de réponse concernant ce sujet. Ceci pourrait être due au fait que la durée des essais de fluage sur ces éprouvettes est relativement courte (temps inférieurs à 5000h) par rapport à celle des éprouvettes ayant révélé un endommagement par fluage significatif.

Le modèle ne prend pas en compte l'influence de la restauration de la matrice sur le comportement en fluage. Dans cette étude il a été essayé d'étudier et d'évaluer cet effet sans beaucoup de succès.

Chapter -IX-

General conclusions

This study aimed at a better understanding of the microstructural evolution during long-term creep exposure and of its influence on the creep behavior. The approach of this study was based on coupling of creep tests results with microstructural investigations. Grade 92 steel was chosen as the material under study, because of its good creep strength and of existing long term creep rupture data at 600°C and 650°C. Complementary methods were used in this study to further investigate the creep behavior of this steel such as notched, thermally aged or thermo-mechanically prepared specimens. The interest of using such specimens was first to study the influence of the microstructure state and stress triaxility on the creep behavior and creep damage development.

Microstructural investigations of specimens after creep testing reveled that the complementary methods used in this study could bring an indication on the long term creep behavior whithin a relatively short time. This could be very useful in alloy design to study the sensitivity of a new alloy to matrix recovery or to creep damage development.

The main results of microstructural investigations conducted on crept specimens as well as possible further use of such specimens are discussed in detail at the end of chapter VII.

P92 steel specimens (provided by SZMF, Germany) that have been creep tested for times up to 50,000h at 600°C and 650°C were investigated in order to have reference data on the microstructure and creep damage of the Grade 92 steel after long term exposure to creep at 600°C and 650°C. The following main results were found:

- extensive creep damage is observed on the homogeneously deformed part of specimens after exposure times higher than 10^4h at 600°C and 10^3h at 650°C. Creep damage was quantified in these crept specimens as the number and area fraction of cavities;
- significant precipitation of Laves phases was observed after creep exposure. A size distribution of Laves phases was realized by image analysis of SEM-BSE images;
- the precipitation of modified Z phase seems to be very slow in the P92 steel during creep exposure at 600°C, at least for exposure times lower than 50,000h;
- a change in the average chemical composition of $M_{23}C_6$ carbides was observed. The average content of Cr increases from about 60 wt.% (in the as-received conditions) to about 70 wt.% after creep exposure at both 600°C and 650°C and the average iron

content decreases from about 30 wt.% (as-received) to about 20 wt.% after creep. A growth of $M_{23}C_6$ carbides during creep was observed. Note that the average size of $M_{23}C_6$ carbides determined in this study might be overestimated due to a sampling effect;

- a recovery of the matrix substructure occurs during creep exposure. EBSD investigations were conducted on the crept specimens with the longest testing times at 600°C (49,721h) and 650°C (33,308h). EBSD maps revealed a significant change in the microtexture of the specimen crept for 33,308h at 650°C, 70MPa.

The results of microstructural investigations conducted on these crept specimens complete the scarcely published data on microstructure and creep damage of the the Grade 92 steel after long term creep exposure at 600°C and 650°C.

Creep tests were conducted at 600°C and 650°C on **smooth specimens** in order to compare the creep behavior of the T92 steel, material under study, to available creep data for Grade 92 steel. The results of creep tests conducted on smooth specimens in T92 steel together with the creep data corresponding to the crept specimens provided by SZMF were analyzed and the following conclusions can be given:

- the creep rupture data of the T92 steel (material studied here) are on the mean line established by the ECCC for the Grade 92 steel at 600°C and 650°C. The creep behavior of the T92 steel is similar to that of the P92 steel;

- a slope change is observed in the secondary creep rate in the stress range of 140-160MPa at 600°C and of 100-110MPa at 650°C. This divides the levels of applied stress in two regions: high stresses ($\sigma > 160$MPa at 600°C and $\sigma > 110$MPa at 650°C) and low stresses ($\sigma < 160$MPa at 600°C and $\sigma < 110$MPa at 650°C). A value of 18 (respectively 6) was found for the Norton exponent n in the high stresses region (respectively low stresses region). These values correspond to values already reported for Grade 92 steel in previous studies (Ennis et al., 1997), (Sklenička et al., 2003), (Dimmler et al., 2008);

- the lifetime of specimens tested for short-term creep can be estimated using a simple equation derived from both Norton power law and Monkman-Grant equation. The same equation overestimates the lifetime of specimens creep tested for long term (times higher than 10^4h at 600°C and higher than 10^3h at 650°C);

- specimens creep tested for long-term creep (low stress region) show relatively low values of reduction of area at rupture compared to these of specimens creep tested for short-term (high stress region).

Creep tests were conducted on **thermally aged specimens** to better understand the effect of large Laves phases (i.e. thermal aging) on the creep flow and creep damage development. These tests lead to the following main results:

- the slope change in the secondary creep rate of the thermally aged specimens is observed for the same levels of stress as for the as-received T92 steel;

- in the high stresses region for a given level of stress the secondary creep rate (respectively lifetime) of a thermally aged specimen is about 3-4 times higher (respectively lower)

than that of an as-received specimen; in the low stresses region for a given level of stress the secondary creep rate (respectively lifetime) of thermally aged specimen is about twice higher (respectively lower) than that of an as-received specimen;

- no significant change was observed in the values of reduction of area at rupture of thermally aged specimens compared to these of as-received specimens creep tested for same levels of stress;

- the Monkman-Grant relationship still gives a good description of the creep results on thermally aged specimens. Same values of the Norton exponent were found for the thermally aged steels as for the as-received steel;

- two creep tests are still running on thermally aged specimens: 600°C, 120MPa and at 650°C, 70MPa.

The following main conclusions can be drawn from the microstructural investigations conducted on the thermally aged specimens after creep testing:

- for a given testing time the hardness of the thermally aged specimens is slightly lower than that of an as-received specimen;

- for a given testing time no significant change in the amount of creep damage was observed in thermally aged specimen compared to that in an as-received one, at least for testing times lower than 4,500h at 650°C;

- EBSD maps realized of the thermally aged specimen crept for 4,434h at 650°C, 85MPa showed similar microtexture to that of the P92 steel creep tested for 33,308h at 650°C, 70MPa.

The results of creep tests together with the microstructural investigations seems to indicate a higher recovery of the matrix in the thermally aged specimens compared to that in the as-received steel both creep tested in similar conditions. Thus, thermally aged specimens could be used as a complementary method to study the sensitivity of new alloys to matrix recovery.

Notched specimens were used to study the influence of stress triaxiality on creep damage development. Creep tests and investigations of notched specimens after creep testing lead to the following results:

- for a given level of engineering stress (σ_n) a higher lifetime is obtained on a notched specimen compared to a smooth one. For similar values of von Mises equivalent stress, the lifetime of the two kinds of specimens is similar;

- two slopes can be observed on the engineering stress versus lifetime of the NTDV specimens;

- for a given testing time, higher amount of creep damage is observed in the notched area compared to that in a smooth specimen;

- creep damage is observed after relatively short testing times, less than 1,000h both at 600°C and 650°C. Thus, notched specimens could be used to study the sensitivity of new alloys to creep damage developement in alloy design;

- location of the most damaged area in notched specimens depends on the geometry of the notch. It is located close to the notch root in the NTDV and NTDC0.6M specimens and in the center of the NTDC1.2 specimen;
- higher amount of creep damage was observed in the notched area of the NTDC1.2 specimen interrupted after 14,137h (beginning of the tertiary creep stage) of creep at 600°C, σ_n = 170MPa compared to that in the P92 steel creep tested for 49,721h at 600°C, 120MPa (smooth specimen);
- indications of stable crack propagation were observed in the NTDV specimens. This might affect the creep damage development during creep. Anyway this kind of notch geometry could be used to study the stable crack propagation under creep conditions;
- NTDC0.6M specimen could be a good compromise between the advantages and drawbacks of the NTDC1.2 and NTDV specimens;
- the values of hardness in the notched areas after creep testing are similar to these in the smooth specimens creep tested for long-term creep both at 600°C and 650°C;
- EBSD investigations revealed no significant change in the microtexture of the notched areas of NTDC1.2 specimen interrupted after 14,137h of creep at 600°C, σ_n =170MPa and of the NTDV specimen creep tested for 8,199h at σ_n =190MPa compared to that of the as-received steel.

Notched specimens could be also used as a complementary method to study the effect of stress triaxiality on the microstructural evolution during creep.

Creep tests were carried out on **thermo-mechanically prepared specimens** to study the influence of matrix substructure on the creep behavior. Due to experimental difficulties in preparation of this kind of specimens only three creep tests were performed on such specimens. The limited number of this kind of tests does not allow to conclude on a possible influence of the matrix substructure on the creep behavior. The results of these tests are summarized in the following:

- a lifetime (t_r) of 1,129h was obtained on a specimen thermo-mechanically prepared at 550°C and then creep tested 170MPa, 600°C. This value of lifetime is about 2.5 times lower than of the as-received T92 steel creep tested in the same conditions;
- a lifetime (t_r) of 4,656h was obtained on the specimen thermo-mechanically prepared at 550°C and then creep tested at 650°C, 95MPa. This lifetime is similar to that of the T92 steel creep tested in the same conditions. this might indicate that recovery of the substructure matrix after 330 creep-fatigue cycles at 550°C did not seem to have a significant influence on the $\dot{\varepsilon}_{ss}$. This could not be confirmed for creep tests conducted at higher stresses;
- a lifetime (t_r) of 3,210h was obtained on a specimen thermo-mechanically prepared at 600°C and then creep tested at 650°C, 95MPa. This specimen showed a similar $\dot{\varepsilon}_{ss}$ to that of the specimen thermo-mechanically prepared at 550°C, see figures A.14 and A.15.

Based on the experimental results, a **mechanical model** was proposed to describe the creep behavior at 600°C and 650°C of the Grade 92 steel. The model was design in the

framework of the mechanics of porous media. The design of the model is similar to that of the model developed by (Gaffard et al., 2005a) in his thesis. The main elements of the model are:

- three deformation mechanisms are considered: a quasi-plastic mechanism to account the primary and tertiary creep stage and two viscoplastic mechanisms, namely: *high stress (Hs)* and *low stress (Ls)*;
- creep damage (cavity nucleation, growth and coalescence) are considered throughout a new definition of the effective stress (σ^*_{eq}). The general description of Gurson model proposed by (Leblond et al., 1994) was used for the definition of σ^*_{eq} in the Ls and Hs mechanisms;
- internal variables count for the effect of metallurgical evolution (growth of Laves phase) of the steel on the creep flow;
- the model gives a good description of the creep curves and lifetime of all kinds of specimens creep tested in this study;
- the accuracy of model is also proved in predicting the location of the most damaged areas in the notched specimens.

Conclusions générales

Cette étude a porté sur une meilleure compréhension de l'évolution métallurgique pendant l'exposition prolongée au fluage et sur son influence sur le comportement en fluage. La démarche de l'étude consiste principalement à expertiser des différentes éprouvettes testées en fluage pour mieux comprendre le comportement en fluage. L'acier Grade 92 a été choisi comme matériau d'étude pour sa bonne résistance au fluage et pour l'existence de données publiées sur son comportement à long terme. Des méthodes complémentaires ont été utilisées pour tester le comportement en fluage de cet acier, à savoir des éprouvettes entaillées, des éprouvettes pré-vieillies et des éprouvettes pré-fatiguées. L'objectif de ces essais a été à priori d'étudier l'influence de l'état de la microstructure et de l'état de contrainte sur le comportement en fluage et l'endommagement par fluage, respectivement.

L'expertise des différentes éprouvettes après fluage a montré que ces méthodes complémentaires peuvent apporter des indications sur le comportement à long-terme dans un temps relativement plus court. Ces méthodes peuvent être très utiles dans le développement de nouvelles nuances d'acier pour étudier la sensibilité d'un nouvel alliage à la restauration de la matrice ou à l'endommagement par fluage.

Les résultats principaux de l'expertise des éprouvettes ainsi que les possibilités d'utilisation de ces type d'éprouvettes ont été discutés à la fin du chapitre VII.

Des ***éprouvettes de fluage en acier P92*** *testées pendant des temps allant jusqu'à 50000h à 600°C et 650°C ont été expertisées pour obtenir des données de référence sur la*

microstructure et l'endommagement par fluage après des temps prolongés d'exposition au fluage. Les résultats principaux de cette expertise sont synthétisés ci-dessous:

- *de l'endommagement par fluage a été observé sur la partie déformée uniformément des éprouvettes testées pendant des temps supérieurs à $10^4 h$ à 600°C et supérieurs à $10^3 h$ à 650°C. L'endommagement par fluage à été quantifié dans ces éprouvettes comme le nombre et la fraction surfacique des cavités;*
- *une précipitation significative des phases de Laves a été observée après exposition au fluage. Une distribution de taille de phases de Laves a été déterminée par des techniques d'analyse d'images;*
- *la précipitation de la phase Z modifiée semble être très faible dans l'acier Grade 92 pendant l'exposition au fluage à 600°C, au moins pour des temps d'exposition inférieurs à 50000h;*
- *un changement dans la composition chimique des carbures $M_{23}C_6$ a été observé. La teneur en Cr augmente de 60 wt.% (à l'état de réception) à 70 wt.% après exposition au fluage à 600°C et 650°C et la teneur en Fe diminue de 30 wt.% (à l'état de réception) à 20 wt.% après fluage. Une croissance des carbures $M_{23}C_6$ est également observée pendant le fluage. À noter que les diamètres des carbures $M_{23}C_6$ déterminés dans cette étude peuvent être surestimés dû à un effet d'échantillonnage;*
- *pendant le fluage il y a une restauration de la matrice. Des cartographies EBSD ont été réalisées sur les éprouvettes avec des durées de vie les plus longues à 600°C (49721h) et à 650°C (33308h). Les cartographies EBSD de l'éprouvette testée pendant 33308h à 650°C, 70MPa montrent un changement significatif dans la microtexture par rapport à l'état de réception.*

Les résultats de l'expertise de ces éprouvettes enrichirent le peu des données existantes dans la littérature sur la microstructure et l'endommagement de l'acier Grade 92 après exposition au fluage à 600°C et 650°C.

Des essais de fluage ont été réalisés sur des ***éprouvettes lisses en acier T92*** *pour comparer le comportement en fluage de l'acier T92, le matériau de l'étude, avec des données disponibles dans la littérature sur le comportement en fluage de l'acier Grade 92. Les résultats des essais de fluage réalisés sur l'acier T92 ainsi que les résultats correspondants aux éprouvettes en acier P92 fournies par SZMF sont résumés ci-dessous:*

- *les résultats des essais (contrainte, temps à rupture) réalisés sur l'acier T92 (le matériau de l'étude) sont localisés sur la courbe moyenne établie par l'ECCC pour l'acier Grade 92 à 600°C et 650°C. Le comportement en fluage de l'acier T92 est similaire à celui de l'acier P92;*
- *la vitesse de fluage secondaire en fonction de la contrainte nominale montre un changement de pente pour de niveaux de contrainte de 140-160MPa à 600°C et de 100-110MPa à 650°C. Ceci sépare les niveaux des contrainte appliquées dans deux domaines: contraintes élevées (σ >160MPa à 600°C et σ >110MPa à 650°C) et contraintes faibles (σ <160MPa à 600°C et σ <110MPa à 650°C). Une valeur de 18 (respectivement 6) a été trouvée pour l'exposant de la loi de Norton dans le domaine des contraintes élevées (respectivement dans le domaine des contraintes faibles); Ces valeurs correspondent aux valeurs trouvées dans des études précédentes telles que (Ennis et al., 1997), (Skleničkа et al., 2003), (Dimmler et al., 2008);*

- *les durées de vie des éprouvettes testées pendant des temps courts peuvent être estimées en utilisant une équation simple dérivée de la loi de Norton et la relation de Monkman-Grant. La même équation surestime la durée de vie des éprouvettes testées pendant des temps prolongés;*

- *les éprouvettes testées pendant des temps prolongés (contraintes faibles) montrent des valeurs relativement faibles de la réduction de l'aire à rupture comparées à celles des éprouvettes testées pendant des temps courts (contraintes élevées)*

Des essais de fluage ont également été réalisés sur des ***éprouvettes pré-vieillies*** *pour étudier l'influence des phases de Laves grossières (i.e. vieillissement thermique) sur le comportement en fluage et l'endommagement par fluage. Ces essais ont révélés les résultats suivants:*

- *le changement de pente dans la vitesse de fluage secondaire en fonction de la contrainte nominale est observé pour les mêmes niveaux de contraintes que pour l'acier T92 à l'état de réception;*

- *pour une valeur de la contrainte donnée dans le domaine des contraintes élevées, la vitesse de fluage secondaire (respectivement la durée de vie) d'une éprouvette pré-vieille est 3-4 fois plus élevée (respectivement plus faible) que celle d'une éprouvette en acier T92; pour une valeur de la contrainte donnée dans le domaine de contraintes faibles la vitesse de fluage secondaire (respectivement la durée de vie) d'une éprouvette pré-vieille n'est que 2 fois plus élevée (respectivement plus faible) que celle d'une éprouvette en acier T92;*

- *les valeurs de la réduction de l'aire à rupture des éprouvettes pré-vieillies n'ont pas montrées des changements significatifs par rapport aux éprouvettes en acier T92 testées en fluage pour les mêmes valeurs de la contrainte appliquée;*

- *la relation du Monkman-Grant donne une bonne description des résultats des essais de fluage sur éprouvettes pré-vieilles. Les valeurs de l'exposant de la loi de Norton trouvées pour ces éprouvettes sont les mêmes que pour les éprouvettes en acier T92;*

- *deux essais de fluage sont encore en cours sur des éprouvettes pré-vieilles: 600°C, 120MPa et 650°C, 70MPa.*

L'expertise des éprouvettes pré-vieillies testées en fluage a mené vers les conclusions suivantes:

- *pour une même durée de vie, la dureté d'une éprouvette pré-vieillie est légèrement plus faible que celle d'une éprouvette en acier T92;*

- *l'endommagement par fluage d'une éprouvette pré-vieillie ne montre pas de changement significatif comparé a celui dans une éprouvette en acier T92 testé en fluage pour une durée de vie comparable, au moins pour des durées de vie inférieures à 4500h;*

- *les cartographies EBSD de l'éprouvette pré-vieillie testée pendant 4434h à 650°C, 85MPa montrent une microtexture similaire à celle de l'éprouvette en acier P92 testée pendant 33308h à 70MPa, 650°C.*

Les résultats des essais de fluage sur éprouvettes pré-vieillies ainsi que l'expertise de ces éprouvettes après fluage semble indiquer une restauration de la matrice plus importante dans l'acier T92 pré-vieilli que dans l'acier T92 testé dans les mêmes conditions. Par conséquent les éprouvettes pré-vieillies pourraient être utilisées comme une méthode complémentaire pour étudier la sensibilité à la restauration de la matrice de nouveaux alliages.

L'objectif des essais de fluage sur les ***éprouvettes entaillées*** *était d'étudier l'influence du taux de triaxialité des contraintes sur l'endommagement par fluage. Les résultats des essais de fluage sur les éprouvettes entaillées ainsi que l'expertise de ces éprouvettes après fluage sont résumés ci-dessous:*

- *pour une contrainte nominale donnée (σ_n), la durée de vie d'une éprouvette entaillée est plus élevée que celle d'une éprouvette lisse. Pour une valeur donnée de la contrainte équivalente de von Mises, les durées de vie des deux types d'éprouvettes sont comparables;*

- *la contrainte nominale en fonction de la durée de vie des éprouvettes NTDV montre deux pentes;*

- *pour une durée de vie donnée, un endommagement par fluage plus important est observé dans la zone entaillée des éprouvettes comparé à celui dans une éprouvette lisse;*

- *l'endommagement par fluage est observé dans une éprouvette entaillée après un temps d'exposition au fluage relativement court, moins de 1000h à 600°C et 650°C. Par conséquent, ce type d'éprouvette pourrait être utilisé pour étudier la sensibilité de nouveaux alliages à l'endommagement par fluage;*

- *la location de la zone la plus endommagée dans les éprouvettes entaillées dépend de la géométrie de l'entaille. Elle est localisée proche du rayon de l'entaille dans les éprouvettes NTDV et NTDC0.6M et dans le centre de la zone entaillée de l'éprouvette NTDC1.2;*

- *l'endommagement par fluage dans l'éprouvette NTDC1.2 interrompue après 14137h de fluage à 600°C, σ_n =170MPa (début du stage tertiaire) est plus important que dans l'éprouvette lisse en acier P92 testée en fluage pendant 49721h à 600°C, 120MPa;*

- *les observations métallographiques des éprouvettes NTDV ont indiqué une propagation stable d'une fissure pendant le fluage. L'amorçage de la fissure pourrait encore favoriser l'endommagement par fluage. Néanmoins ce type d'éprouvette pourrait être utilisée pour étudier la propagation de fissures sous des sollicitations en fluage;*

- *l'éprouvette NTDC0.6M pourrait être un bon compromis entre les avantages et les inconvenients des éprouvettes NTDC1.2 et NTDV;*

- *les valeurs de la dureté dans les zones entaillées des éprouvettes après fluage sont similaires à celles dans les éprouvettes lisses testées pendant des temps prolongés;*

- *les cartographies EBSD n'ont pas révélé des changements significatifs dans la microtexture de l'éprouvette NTDC1.2 interrompue après 14137h de fluage à 600°C, σ_n =170MPa et de l'éprouvette NTDV testées pendant 8199h à 600°C, σ_n =190MPa par rapport à celle de l'état de réception.*

Les éprouvettes entaillée pourraient également être utilisées comme méthode complémentaire pour étudier l'effet de la triaxialité des contraintes sur l'évolution métallurgique pendant le fluage.

Des essais de fluage ont été réalisés sur des ***éprouvettes pré-fatiguées*** *pour étudier l'influence de l'état de la matrice sur le comportement en fluage. A cause des difficultés expérimentales due à la préparation de ces éprouvettes seulement trois essais de fluage ont été réalisés sur des éprouvettes pré-fatiguées. Le nombre limité de ces essais ne permet pas de conclure sur un possible influence de l'état de la matrice sur le comportement en fluage. Les résultats de ces essais sont résumés ci-dessous:*

- *une durée de vie de 1129h a été obtenue sur une éprouvette pré-fatiguée à 550°C et testée en fluage à 600°C, 170MPa. Cette durée de vie est presque 2.5 fois plus faible que celle d'une éprouvette en acier T92 testée à 600°C, 170MPa;*
- *une durée de vie de 4656h a été obtenue sur une éprouvette pré-fatiguée à 550°C et testée en fluage à 650°C, 95MPa. Cette durée de vie est similaire à celle d'une éprouvette en acier T92 testée dans les mêmes conditions;*
- *une éprouvette pré-fatiguée à 600°C et testée en fluage à 650°C, 95MPa a révélé une durée de vie de 3210h. Cette éprouvette a montré une vitesse de fluage secondaire similaire à celle de l'éprouvette pré-fatiguée à 550°C et testée à 650°C, 95MPa (figures A.14 et A.15).*

À partir des résultats expérimentaux un modèle mécanique a été proposé pour décrire le comportement en fluage à 600°C et 650°C de l'acier Grade 92. L'architecture de ce modèle est similaire à celle du modèle développé par V. Gaffard dans sa thèse (Gaffard, 2004). Les éléments principaux du modèle sont:

- *trois mécanismes de déformation sont pris en compte: un mécanisme quasi-plastique (qp) pour décrire le stage primaire et tertiaire de fluage et deux mécanismes viscoplastiques qui correspondent respectivement au régime de contraintes élevées (Hs) et au régime de contraintes faible (Ls);*
- *l'endommagement par fluage (germination, croissance et coalescence des cavités) est modélisé à l'aide d'une nouvelle définition de la contrainte effective (σ^*_{eq}). La description générale du modèle de Gurson proposé par (Leblond et al., 1994) a été utilisé pour la définition du σ^*_{eq} dans les mécanismes Hs et Ls;*
- *des variables internes ont été définies pour prendre en compte l'influence de l'évolution métallurgique (la croissance de phases de Laves) de l'acier sur la déformation en fluage;*
- *le modèle décrit assez bien la déformation en fluage et la durée de vie de tous les type d'éprouvettes;*
- *la précision du modèle est également prouvée aussi dans la prédiction de la zone la plus endommagée dans les éprouvettes entaillées.*

Bibliography

Abd El-Azim, M., Nasreldin, A. M., Zies, G., and Klenk, A. (2005). Microstructural instability of a welded joint in P91 steel during creep at 600°c. *Materials Science and Technology*, 21:779–790.

Abe, F. (2004). Bainitic and martensitic creep-resistant steels. *Current Opinion in Solid State & Materials Science*, 8:305–311.

Abe, F. (2006). Acier à 9%Cr stabilisé par bore pour résistance au fluage à 650°C dans les centrales thermiques à haut rendement et faible émissions. *La revue de Metallurgie-CIT*, mai:247–256.

Abe, F. (2009). Analysis of creep rate of tempered martensitic 9%Cr steel based on microstructure evolution. *Materials Science and Engineering: A*, 510-511:64–69.

Abe, F., Taneike, M., and Sawada, K. (2007). Alloy design of creep resistant 9Cr steel using a dispersion of nano-sized carbonitrides. *International Journal of Pressure Vessels and Piping*, 84:3–12.

Aghajani, A., Richter, F., Somsen, C., Fries, S., Steinbach, I., and Eggeler, G. (2009a). On the formation and growth of Mo-rich Laves particles during long-term creep of a 12% chromium tempered martesitic ferritic steel. *Scripta Materialia*, 61:1068–1071.

Aghajani, A., Somsen, C., and Eggeler, G. (2009b). On the effect of long-term creep on the microstructure of a 12% chromium tempered martensite ferritic steel. *Acta Materialia*, 57:5093–5106.

Agren, J., Clavaguera-Mora, M., Golczewski, J., Inden, G., Kumar, H., and Sigli, C. (2000). Application of computational thermodynamics. *Computer Coupling of Phase Diagrams and Thermochemistry (Calphad)*, 24:41–54.

Andrén, H.-O. (2001). Combining TEM and APFIM techniques to study the microstructure of steels and hardmetals. *Micron*, 32:713–719.

Avrami, M. (1939). Kinetics of phase change. I. General Theory . *Journal of Chemical Physics*, 7:1103–1112.

Avrami, M. (1940). Kinetics of phase change. II. Transformation-Time Relations for Random Distribution of Nuclei. *Journal of Chemical Physics*, 8:212–224.

Avrami, M. (1941). Kinetics of phase change. III. Granulation, Phase Change, and Microstructure. *Journal of Chemical Physics*, 9:177–184.

Beer, J. (2007). High efficiency electric power generation: The environmental role. *Progress in Energy and Combustion Science*, 33:107–134.

Bendick, W. and Gabrel, J. (2005). Assessment of creep rupture strength for the new martensitic 9%Cr steels E911 and T/P92. In *Creep & fracture in high temperature components: Design & life assessment issues ; ECCC Creep Conference*, pages 406–427, London, UK. Lancaster, Pa: DEStech Publ. ISBN 1-932078-49-5.

Besson, J. (2009). Damage of ductile materials deforming under multiple plastic or viscoplastic mechanisms. *International Journal of Plasticity*, 25:2204–2221.

Besson, J., Cailletaud, G., Chaboche, J. L., and Forest, S. (2001). In *Mécanique non linéaire des matériaux*, volume in french. Hermes-Paris, ISBN: 2-7462-0268-9.

Besson, J. and Foerch, R. (1997). Large scale object-oriented finite element code design. *Computer Methods in Applied Mechanics and Engineering*, 142:165–187.

Besson, J. and Guillemer-Neel, C. (2003). An extension of the Green and Gurson models to kinematic hardening. *Mechanics of Materials*, 35:1–18.

Bhadeshia, H. (2001). Design of ferritic creep-resistant steels. *ISIJ International*, 41:626–640.

Binder, W. (1950). Symposium on sigma phases. *ASTM*, pages 147–164.

Blum, W. and Götz, G. (1999). Subgrain structure during annealing and creep of the cast martensitic Cr-steel G-X12CrMoWVNbN 10-1-1. *Steel Research*, 70:274–278.

Cadek, J., Sustek, V., and Pahutova, M. (1997). An analysis of a set of creep data for a 9Cr1Mo0.2V (P91 type) steel. *Materials Science and Engineering: A*, 225:22–28.

Cermak, J., Ruzickova, J., and Pokorna, A. (1995). Grain boundary diffusion of W in Fe-Cr ferritic alloys. *Scripta Metallurgica et Materialia*, 33:289–294.

Chaboche, J. L. (2008). A review of some plasticity and viscoplasticity constitutive theories. *International Journal of Plasticity*, 24:1642–1693.

Cipolla, L., Danielsen, H., DiNuzio, P. E., Venditti, D., Hald, J., and Marcel A.J. Somers (2010a). On the role of Nb in Z-phase formation in a 12% Cr steel. *Scripta Materialia*, 63:324–327.

Cipolla, L., Danielsen, H., Venditti, D., DiNuzio, P. E., Hald, J., and Marcel A.J. Somers (2010b). Conversion of MX nitrides to Z-phase in a martensitic 12% Cr steel. *Acta Materialia*, 58:669–679.

Cipolla, L., DiGianfrancesco, A., Cumino, G., and Caminada, S. (2005). Long term creep behaviour and microstructural evolution of E911 steel. In *I.A. Shibli, S.R. Holdsworth (Eds.), Proc. of Creep & fracture in high temperature components: Design & life assessment issues ; ECCC Creep Conference*, pages 288–299, Lancaster, U.S.A. DEStech Publ. ISBN 1-932078-49-5.

Cui, J., Kim, I., Kang, C., and Miyahara, K. (2001). Creep stress effect on precipitation behaviour of Laves phase in Fe-10%Cr-6%W alloys. *ISIJ International*, 41:368–371.

Czyperek, M., Zapp, P., Bouwmeesler, H., Modigell, M., Peinemann, K.-V., Voigt, I., Meulenberg, W. A., Singheiser, L., and Stöver, D. (2009). MEM-BRAIN gas separation membranes for zero-emission fossil power plants. *Energy Procedia*, 1:303–310.

Czyrska-Filemonowicz, A., Zielińska-Lipiec, A., and Ennis, P. (2006). Modified 9% Cr steels for advanced power generation: microstructure and properties. *Journal of Achievements in Materials and Manufacturing Engineering*, 19:43–46.

Danielsen, H. and Hald, J. (2006). Behaviour of Z phase in 9-12%Cr steels. *Energy Materials*, 1:49–57.

Danielsen, H. and Hald, J. (2007). A thermodynamic model of the Z-phase Cr(V, Nb)N. *Computer coupling of phase diagrams and thermochemistry (Calphad)*, 31:505–514.

Danielsen, H. K. (2007). *Z-phase in 9-12%Cr steels*. PhD thesis, Technical University of Denmark.

Danielsen, H. K. and Hald, J. (2009). On the nucleation and dissolution process of Z-phase Cr(V,Nb)N in martensitic 12%Cr steels. *Materials Science and Engineering: A*, 505:169–177.

Danielsen, H. K., Hald, J., Flemming B. Grumsen, and Marcel A.J. Somers (2006). On the crystal structure of Z-phase Cr(V,Nb)N. *Metallurgical and Materials Transactions A*, 37:2633–2640.

Dimmler, G., Weinert, P., and Cerjak, H. (2008). Extrapolation of short-term creep rupture data-The potential risk of over-estimation. *International Journal of Pressure Vessels and Piping*, 85:55–62.

Dimmler, G., Weinert, P., Kozeschnik, E., and Cerjaket, H. (2003). Quantification of Laves phase in advanced 9-12%Cr steels using a standard SEM. *Materials Characterization*, 51:341–352.

Durand-Charre, M. (2003). La microstructure des aciers et des fontes: genèse et interprétation. Paris.

Dyson, B. (2000). Use of CDM in materials modeling and component creep life prediction. *Journal of Pressure Vessel Technology*, 122:281–296.

Ennis, P. and Czyrska-Filemonowicz, A. (2002). Recent advances in creep resistant steels for power plant applications. OMMI, 1:1-27. `http://www.ommi.co.uk/PDF/Articles/32.pdf`.

Ennis, P., Zielińska-Lipiec, A., and Czyrska-Filemonowicz, A. (2000). Influence of heat treatments on microstructural parameters and mechanical properties of P92 steel. *Materials Science and Technology*, 16:1226–1232.

Ennis, P., Zielińska-Lipiec, A., Wachter, O., and Czyrska-Filemonowicz, A. (1997). Microstructural stability and creep rupture strength of the martensitic steel P92 for advanced power plant. *Acta Materialia*, 45:4901–4907.

Foldyna, V., Purmensky, J., and Kubon, Z. (2001). Development of advanced chromium steels with respect to microstructure and structural stability. *ISIJ International*, 41:Supplement, S81–S85.

Fournier, B. (2007). *Fatigue-fluage des aciers martensitiques à 9-12%Cr:Comportement et endommagement*. PhD thesis, Ecole des Mines de Paris.

Fournier, B., Sauzay, M., Barcelo, F., Rauch, E., Renault, A., Cozzika, T., Dupuy, L., and Pineau, A. (2009a). Creep-fatigue interactions in a 9 Pct Cr-1Pct. Mo martensitic steel: Part II. Microstructural evolution. *Metallurgical and Materials Transactions A*, 40:330–341.

Fournier, B., Sauzay, M., Caes, C., Noblecourt, M., Mottot, M., Allais, L., Tournie, I., and Pineau, A. (2009b). Creep-fatigue interactions in a 9 Pct Cr-1Pct Mo martensitic steel: Part I. mechanical test results. *Metallurgical and Materials Transactions A*, 40:321–329.

Fujiyama, K., Mori, K., Kaneko, D., Kimachi, H., Saito, T., Ishii, R., and Hino, T. (2009). Creep damage assessment of 10Cr-1Mo-1W-VNbN steel forging through EBSD observation. *International Journal of Pressure Vessels and Piping*, 86:570–577.

Gaffard, V. (2004). *Experimental study and modelling of high temperature creep flow and damage behaviour of 9Cr1Mo-NbV steel weldments*. PhD thesis, Ecole des Mines de Paris.

Gaffard, V., Besson, J., and Gourgues-Lorenzon, A. (2005a). Creep failure model of a tempered martensitic stainless steel integrating multiple deformation and damage mechanisms. *International Journal of Fracture*, 133:139–166.

Gaffard, V., Gourgues-Lorenzon, A., and Besson, J. (2005b). High temperature creep flow and damage properties of 9Cr1MoNbV steels: Base metal and weldment. *Nuclear Engineering and Design*, 235:2547–2562.

Ghassemi-Armaki, H., Chen, R., Maruyama, K.and Yoshizawa, M., and Igarashi, M. (2009). Static recovery of tempered lath martensite microstructures during long-term aging in 9-12% Cr heat resistant steels. *Materials Letters*, 63:2423–2425.

Golpayegani, A. and Andrén, H. (2006). An EFTEM study on Z-phase nucleation in martensitic chromium steels. In *Proceedings of the 8th Conference on "Alloy Development for Critical Components of Environmentally Friendly Steam Power Plants & on "High Temperature Plant lifetime Extension"*, pages 1267–1273, Belgium, Liége. Grafische Medien.

Golpayegani, A., Andrén, H., Danielsen, H., and Hald, J. (2008). A study on Z-phase nucleation in martensitic chromium steels. *Materials Science and Engineering: A*, 489:310–318.

Gourgues, A.-F., Flower, H. M., and Lindley, T. (2000). Electron backscattering diffraction study of acicular ferrite, bainite and martensite microstructures. *Materials Science and Technology*, 16:26–40.

Graus, W. and Worrell, E. (2009). Trend in efficiency and capacity of fossil power generation in the EU. *Energy Policy*, 37:2147–2160.

Gustafson, A. and Hättestrand, M. (2002). Coarsening of precipitates in an advanced creep resistant 9% chromium steel-quantitative microscopy and simulations. *Materials Science and Engineering: A*, 333:279–286.

Hald, J. (1996). Metallurgy and creep properties of new 9-12% Cr steels. *Steel Research*, 67:369–374.

Hald, J. (2004). Creep strength and ductility of 9 to 12% chromium steels. *Materials at high temperatures*, 21:41–46.

Hald, J. (2006). Materials development for advanced steam boilers. In *Proceedings of the 8th Conference on "Alloy Development for Critical Components of Environmentally Friendly Steam Power Plants & on "High Temperature Plant lifetime Extension"*, pages 917–930, Belgium, Liége. Grafische Medien.

Hald, J. (2008). Microstructure and long-term creep properties of 9-12% Cr steels. *International Journal of Pressure Vessels and Piping*, 85:30–37.

Hald, J. and Korcakova, L. (2003). Precipitate stability in creep resistant ferritic steels-experimental investigations and modelling. *ISIJ International*, 43:420–427.

Hald, J. and Straub, S. (1998). Microstructural stability of 9-12%CrMo(W)VNbN-steels. In *Materials for Advanced Power Engineering*, pages 155–170, Belgium, Liége. J. Lecomte-Beckers, M. Carton, F. Schubert, P.J. Ennis (Editors), Forschungszentrum Jülich GmbH; ISBN 3-89336-228-2.

Hamada, K., Tokuno, K., Tomita, Y., Mabuchi, H., and Okamoto, K. (1995). Effects of precipitate shape on high temperature strength of modified 9Cr-1Mo steels. *ISIJ International*, 35:86–91.

Haney, E. M., Dalle, F., Sauzay, M., Vincent, L., Tournie, I., Allais, L., and Fournier, B. (2009). Macroscopic results of long-term creep on a modified 9Cr-1Mo steel (T91). *Materials Science and Engineering: A*, 510-511:99–103.

Hasegawa, T., Abe, Y. R., Tomita, Y., Maruyama, N., and Sugiyama, M. (2001a). Microstructural evolution during creep test in 9Cr-2W-V-Ta steels and 9Cr-1Mo-V-Nb steels. *ISIJ International*, 41:922–929.

Hasegawa, Y., Muraki, T., Ohgami, M., and Mimura, H. (2001b). Optimization of tungsten content of ASME Gr. 92 for the high creep rupture strength. In *Proceedings of the 3rd Conference on Advances in Material Technology for Fossil Power Plants*, pages 447–455, Swansea. Edited by: R. Viswanathan, W.T. Bakker, J.D. Parker, ISBN 1-86125-145-9.

Hättestrand, M. and Andrén, H.-O. (1999). Boron distribution in 9-12% chromium steels. *Materials Science and Engineering: A*, 270:33–37.

Hättestrand, M. and Andrén, H.-O. (2001). Evaluation of particle size distributions of precipitates in a 9% chromium steel using energy filtered transmission electron microscopy. *Micron*, 32:789–797.

Hättestrand, M., Schwind, M., and Andrén, H.-O. (1998). Microanalysis of two creep resistant 9-12% chromium steels. *Materials Science and Engineering: A*, 250:27–36.

Hayhurst, D., Lin, J., and Hayhurst, R. (2008). Failure in notched tension bars due to high-temperature creep: Interaction between nucleation controlled cavity growth and continuum cavity growth. *International Journal of Solids and Structures*, 45:2233–2250.

Hofer, P., Miller, M., Babu, S., David, S., and Cerjak, H. (2002). Investigation of boron distribution in martensitic 9% Cr creep resistant steel. *ISIJ International*, 42:Supplement, S62–S66.

Hoff, N. (1953). The necking and the rupture of rods subjected to constant tensile loads. *Journal of applied mechanics-Transactions of the ASME*, 20:105–108.

Horiuchi, T., Igarashi, M., and Abe, F. (2002). Improved utilization of added B in 9Cr heat-resistant steels containing W. *ISIJ International*, 42:Supplement, S67–S71.

Hosoi, Y., Wade, N., Kunimitsu, S., and Urita, T. (1986). Precipitation behaviour of Laves phases and its effect on toughness of 9Cr-2Mo ferritic martensitic steel. *Journal of nuclear materials*, 141-143:461–467.

Jack, D. and Jack, K. (1972). Structure of Z-phase, NbCrN. *Journal of the Iron and Steel Institute*, 210:790.

Janovec, J., Richarz, B., and Grabke, H. (1994). Phase transformations and microstructure changes in 12%Cr-steel during tempering at 1053K. *Steel Research*, 65:438–443.

Jayaram, R. and Klueh, R. (1998). Microstructural characterization of 5-9% Cr-2%W-V-Ta martensitic steels. *Metallurgical and Materials Transactions A*, 29:1551–1558.

Jiang, Y., Guo, W., Yue, Z., and Wang, J. (2006). On the study of the effects of notch shape on creep damage development under constant loading. *Materials Science and Engineering: A*, 437:340–347.

Kager, F., Böck, N., Spiradek-Hahn, K., Höfinger, S., Brabetz, M., and Zeiler, G. (2006). Superior long-term behaviour and microstructural evolution of 9%Cr steels with boron. In *Proceedings of the Conference on the "Materials for Advanced Power Engineering"*, pages 1031–1040, Belgium, Liege. Eds. J. Lecomte-Beckers et al., Forschungszentrum Jülich ISBN.

Kaneko, K., Matsumura, S., Sadakata, A., Fujita, K., Moon, W. J., Ozaki, S., Nishimura, N., and Tomokyio, Y. (2004). Characterization of carbides at different boundaries of 9Cr-steel. *Materials Science and Engineering: A*, 374:82–89.

Karlsson, L. and Nordén, H. (1988a). Non-equilibrium grain boundary segregation of boron in austenitic stainless steels - II. Fine scale segregation behaviour. *Acta Metallurgica*, 36:13–24.

Karlsson, L. and Nordén, H. (1988b). Non-equilibrium grain boundary segregation of boron in austenitic stainless steels -IV. Precipitation behaviour and distribution of elements at grain boundaries. *Acta Metallurgica*, 36:35–48.

Kauffmann, F. and et al. (2006). Microstructural characterization of modern boron containing 9-11%Cr steels developed in the framework of the COST program. In *Proceedings of the Conference on the "Materials for Advanced Power Engineering"*, pages 1041–1051, Belgium, Liege. Eds. J. Lecomte-Beckers et al., Forschungszentrum Jülich ISBN.

Kimura, K., Kushima, H., Abe, F., Suzuki, K., Kumai, S., and Satoh, A. (2000). Microstructural change and degradation behaviour of 9Cr-1Mo-V-Nb steel in the long term. In *Proceedings of the 5th International Charles Parsons Conference*, pages 590–602, Cambridge, UK. A. Strang et al. (Editors), ISBN 1-86125-113-0.

Kimura, K., Kushima, H., and Sawada, K. (2009). Long-term creep deformation property of modified 9Cr-1Mo steel. *Materials Science and Engineering: A*, 510-511:58–63.

Kimura, K., Suzuki, K., Toda, Y., Kushima, H., and Abe, F. (2002). Precipitation of Z-phase and degradation behaviour of mod. 9Cr-1Mo steel. In *Proceedings of the* 7^{th} *Liége Conference on the "Materials for Advanced Power Engineering"*, pages 1171–1180, Belgium, Liege. J. Lecomte-Beckers, M. Carton, F. Schubert, P.J. Ennis (Editors), Forschungszentrum Jülich GmbH; ISBN 3-89336-312-2.

Kloc, L. and Sklenička, V. (1997). Transition from power-law to viscous creep behaviour of p-91 type heat-resistant steel. *Materials Science and Engineering: A*, 234-236:962–965.

Kloc, L. and Sklenička, V. (2004). Confirmation of low stress creep regime in 9% chromium steel by stress change creep experiments. *Materials Science and Engineering: A*, 387-389:633–638.

Klueh, R., Alexander, D., and Sokolov, M. (2002). Effect of chromium, tungsten, tantalum and boron on mechanical properties of 5-9Cr-WVTaB steels. *Journal of Nuclear Materials*, 304:139–152.

Korcakova, L., Hald, J., and Marcel, A.J. Somers (2001). Quantification of Laves phase particle size in 9CrW steel. *Materials Characterization*, 47:111–117.

Kostka, A., Tak, K.-G., Hellmig, R., Estrin, Y., and Eggeler, G. (2007). On the contribution of carbides and micrograin boundaries to the creep strength of tempered martensite ferritic steels. *Acta Materialia*, 55:539–550.

Koukouzas, N. and Typou, I. (2009). An assessment of CO_2 transportation cost from the power plants to geological formations suitable for storage in North Greece. *Energy Procedia*, 1:1657–1663.

Kurdjumov, G. and Khachaturyan, A. (1975). Nature of axial ratio anomalies of the martensite lattice and mechanism of diffusionless $\gamma \rightarrow \alpha$ transformation. *Acta Metallurgica*, 23:1077–1088.

Kushima, H., Kimura, K., and Abe, F. (1999). Degradation of Mod.9Cr-1Mo steel during long-term creep deformation. *Tetsu-to-Hagane*, 85:841–847.

Leblond, J. B., Perrin, G., and Suquet, P. (1994). Exact results and approximate models for porous viscoplastic solids. *International Journal of Plasticity*, 10:213–235.

Letofsky, E., Cerjak, H., Papst, I., and Warbichler, P. (2001). The use of light and electron-microscopic investigations to characterise the creep bhaviour of welded joints in modern power station materials. In *Proceedings of the 3rd Conference on Advances in Material technology for fossil power plants*, Swansea. Edited by: R. Viswanathan, W.T. Bakker, J.D. Parker, ISBN 1-86125-145-9.

Lifshitz, I. and Slyozov, V. (1961). The kinetics of precipitation from supersaturated solid solutions. *Journal of Physics and Chemistry of Solids*, 19:35–50.

Liu, X. Y. and Fujita, T. (1989). Effect of chromium content on creep rupture properties of a high chromium ferritic heat resisting steel. *ISIJ International*, 29:680–686.

Lundin, L. (1996). Direct measurement of carbon solubility in the intermetallic $(Fe,Cr)_2(Mo,W)$ Laves phases using atom-probe field-ion microscopy. *Scripta Materialia*, 34:741–747.

Lundin, L., Fällman, S., and Andrén, H.-O. (1997). Microstructure and mechanical properties of a 10% chromium steel with improved creep resistance at 600°C. *Materials Science and Technology*, 13:233–242.

Lundin, L. and Richarz, B. (1995). Atom-probe study of phosphorus segregation to the carbide/matrix interface in an aged 9% chromium steel. *Applied Surface Science*, 87-88:194–199.

Maruyama, K., Sawada, K., and Koike, J. (2001). Strengthening mechanisms of creep resistant tempered martensitic steel. *ISIJ International*, 41:641–653.

Massabki, e. a., editor (1986). *Binary alloy phase diagrams*. ASM, American Society for Metals, ISBN (vol.1): 0-87170-262-2.

Masuyama, F. (1998). Steam plant material developments in Japan. In *Materials for Advanced Power Engineering*, page 1807, Belgium, Liége. J. Lecomte-Beckers, M. Carton, F. Schubert, P.J. Ennis (Editors), Forschungszentrum Jülich GmbH; ISBN 3-1807-1823-228-2.

Masuyama, F. (2001). History of power plants and progress in heat resistant steels. *ISIJ International*, 41:612–625.

Masuyama, F. (2006). Creep degradation in welds of Mod.9Cr-1Mo steel. *International Journal of Pressure Vessels and Piping*, 83:819–825.

Mathis, K. and Rauch, E. (2007). Microstructural characterization of a fine-grained ultra low carbon steel. *Materials Science and Engineering: A*, 462:248–252.

Merckling, G. (2008). Long-term creep rupture strength assessment: Developement of the european collaborative creep committee post assessment tests. *International Journal of Pressure Vessels and Piping*, 85:2–13.

Millich, E., Ferrero, G., and Kotronaros, A. (1994). Major achievements of the thermie programme in the field of renewable energies. *Renewable Energy*, 5:12–21.

Miyata, K. and Sawaragi, Y. (2001). Effect of Mo and W on the phase stability of precipitates in low Cr heat resistant steels. *ISIJ International*, 41:281–289.

Miyata, K., Sawaragi, Y., Okada, H., Masuyama, F., Yokoyama, T., and Komai, N. (2000). Microstructural evolution of a 12Cr-2W-Cu-V-Nb steel during three year service exposure. *ISIJ International*, 40:1156–1163.

Morito, S., Huang, X., Furuhara, T., Maki, T., and Hansen, N. (2006). The morphology and crystallography of lath martensite in alloy steels. *Acta Materialia*, 54:5323–5331.

Morito, S., Tanaka, H., Konishi, R., Furuhara, T., and Maki, T. (2003). The morphology and crystallography of lath martensite in Fe-C alloys. *Acta Materialia*, 51:1789–1799.

Murata, Y., Kamiya, M., Kunieda, T., Abdel-Daiem, A., Koyama, T., Morinaga, M., and Hashizume, R. (2005). Dependence of solvus temperature of the Laves phase on (Mo+W+Re) contents in high Cr ferritic steels. *ISIJ International*, 45:101–106.

Needleman, A. and Tvergaard, V. (1991). An analysis of dynamic, ductile crack growth in a double edge cracked specimen. *International Journal of Fracture*, 49:41–67.

Nelder, J. and Mead, R. (1965). A simplex method for fonction minimization. *Computer Journal*, 7:308–313.

Nowakowski, P. (2000). PhD thesis, TU Wien.

Okubo, Muneki, S., and Abe, F. (2004). Effects of a new thermo-mechanical magnetic heat treatment process on creep properties of highCr- ferritic heat resistant steels. In *Proceedings from the Fourth International Conference on Advances in Materials Technology for Fossil Power Plants*, Hilton Heat Island, South Carolina.

Oliver, T. (2008). Clean fossil-fuelled power generation. *Energy policy*, 36:4310–4316.

Ostwald, W. (1896). *Lehrbuch der Allgemeinen Chemie*, 2:Leipzig, Germany.

Panait, C., Bendick, W., Fuchsmann, A., Gourgues-Lorenzon, A.-F., and Besson, J. (2009). Study of the microstructure of the Grade 91 steel after more than 100,000h of creep exposure at 600°C. In *I.A. Shibli, S.R. Holdsworth (Eds.), Creep & fracture in high temperature components: Design & life assessment issues ; ECCC Creep Conference*, pages 877–888, Lancaster, U.S.A. DEStech Publ. ISBN 978-1-60595-005-1.

Panait, C., Bendick, W., Fuchsmann, A., Gourgues-Lorenzon, A.-F., and Besson, J. (2010a). Study of the microstructure of the Grade 91 steel after more than 100,000h of creep exposure at 600°C. *International Journal of Pressure Vessels and Piping*, 87:326–335.

Panait, C., Zielińska-Lipiec, A., Koziel, T., Czyrska-Filemonowicz, A., Gourgues-Lorenzon, A.-F., and Bendick, W. (2010b). Evolution of dislocation density, size of subgrains and MX-type precipitates in a P91 steel during creep and during thermal ageing at 600°C for more than 100,000h. *Materials Science and Engineering: A*, 527:4062–4069.

Perrin, I. and Fishburn, J. (2008). A perspective on the design of high temperature boiler components. *International Journal of Pressure Vessels and Piping*, 85:14–21.

Petry, C. and Lindet, G. (2009). Modelling creep behaviour and failure of 9Cr-0.5Mo-1.8W-VNb. *International Journal of Pressure Vessels and Piping*, 86:486–494.

Pešička, J. Aghajani, A., Somsen, C., Hartmaier, A., and Eggeler, G. (2010). How dislocation substructures evolve during long-term creep of a 12% Cr tempered martensitic ferritic steel. *Scripta Materialia*, 62:353–356.

Pešička, J., Kuzel, R., Dronhofer, A., and Eggeler, G. (2003). The evolution of dislocation density during heat treatment and creep of tempered martensite ferritic steels. *Acta Materialia*, 51:4847–4862.

Qin, Y., Götz, G., and Blum, W. (2003). Subgrain structure during annealing and creep of the cast martensitic Cr-steel G-X12CrMoWVNbN 10-1-1. *Materials Science and Engineering: A*, 341:211–215.

Ratke, L. and Voorhees, P. W. (2002). Growth and coarsening: Ostwald ripening in materials processing. Springer. `http://books.google.com/books?id=baKRnEuSBXkC&dq=ostwald+ripening&printsec=frontcover&source=web&ots=kBeZYYJtTO&sig=ITeiJwNfKgXfQ7WzyiVR3YnMOx4#PPA117,M1`.

Rubin, E. S., Chen, C., and Rao, A. B. (2007). Cost and performance of fossil fuel power plants with CO_2 capture and storage. *Energy policy*, 35:4444–4454.

Rukes, B. and Taud, R. (2004). Status and perspectives of fossil power generation. *Energy*, 29:1853–1874.

Sakuraya, K., Okada, H., and Abe, F. (2004). Coarse size BN type inclusions formed in boron bearing high Cr ferritic heat resistant steel. In *Proceedings from the Fourth International Conference on Advances in Materials Technology for Fossil Power Plants*, pages 1270–1279, Hilton Heat Island, South Carolina.

Sauzay, M., Fournier, B., Mottot, M., Pineau, A., and Monnet, I. (2008). Cyclic softening of martensitic steels at high temperature-Experimental and physically based modelling. *Materials Science and Engineering: A*, 483-484:410–414.

Sawada, K., Bauer, M., Kauffmann, F., Mayr, P., and Klenk, A. (2010). Microstructural change of 9%Cr-welded joints after long-term creep. *Materials Science and Engineering: A*, 527:1417–1426.

Sawada, K., Kubo, K., and Abe, F. (2001). Creep behavior and stability of MX precipitates at high temperature in 9Cr-0.5Mo-1.8W-VNb steel. *Materials Science and Engineering: A*, 319-321:784–787.

Sawada, K., Kubo, K., and Abe, F. (2003). Contribution of coarsening of MX carbonitrides to creep strength degradation in high chromium ferritic steel. *Materials Science and Technology*, 19:732–738.

Sawada, K., Kushima, H., and Kimura, K. (2006). Z-phase formation during creep and aging in 9-12% Cr heat resistant steels. *ISIJ International*, 46:769–775.

Sawada, K., Kushima, H., Kimura, K., and Tabuchi, M. (2007). TTP diagrams of Z phase in 9-12% Cr heat-resistant steels. *ISIJ International*, 47:733–739.

Sawada, K., Miyahara, K., Kushima, H., Kimura, K., and Matsuoka, S. (2005). Contribution of microstructutal factors to hardness change during creep exposure in Mod.9Cr-1Mo steel. *ISIJ International*, 45:1934–1939.

Sawada, K., Takeda, M., Maruyama, K., Ishii, R., Yamada, M., Kamine, R., and Nagae, Y. (1998a). Residual creep life assessment by change of martensitic lath structure in modified 9Cr-1Mo steels. *Tetsu-to-Hagané*, 84:580–585.

Sawada, K., Takeda, M., Maruyama, K., Ishii, R., Yamada, M., Nagae, Y., and Kamine, R. (1998b). Dislocation substructure degradation during creep of martensitic heat resistant steels with and without W. In *Materials for Advanced Power Engineering*, pages 575–583, Belgium, Liége. J. Lecomte-Beckers, F. Schubert, P.J. Ennis (Editors), Forschungszentrum Jülich GmbH; ISBN 3-89336-228-2.

Sawada, K., Takeda, M., Maruyama, K., Ishii, R., Yamada, M., Nagae, Y., and Komine, R. (1999). Effect of W on recovery of lath structure during creep of high chromium martensitic steels. *Materials Science and Engineering: A*, A267:19–25.

Sawada, K., Taneike, M., Kimura, K., and Abe, F. (2004). Effect of nitrogen content on microstructural aspects and creep behavior in extremely low carbon 9Cr heat-resistant steel. *ISIJ International*, 44:1243–1249.

Scarlin, B., Kern, T.-U., and Staubli, M. (2004). The European efforts in material development for 650°C USC power plants-COST552. In *Proceedings from the Fourth International Conference on Advances in Materials Technology for Fossil Power Plants*, pages 80–99, Hilton Heat Island, South Carolina.

Seung, L. J., Armaki, H. G., Maruyama, K., Muraki, T., and Asahi, H. (2006). Causes of breakdown of creep strength in 9Cr-1.8W-0.5Mo-VNb steel. *Materials Science and Engineering: A*, 428:270–275.

Shigesato, G. and Rauch, E. (2007). Dislocation structure misorientation measured with an automated electron diffraction patten indexing tool. *Materials Science and Engineering: A*, 462:402–406.

Sklenička, V., Kuchařova, K., Svoboda, M., Kloc, L., Buršik, J., and Kroupa, A. (2003). Long-term creep behavior of 9-12% Cr power plant steels. *Materials Characterization*, 51:35–48.

Sonderegger, B., Mitsche, S., and Cerjak, H. (2007). Martensite laths in creep resistant martensitic 9-12% Cr steels-calculation and measurements of misorientations. *Materials characterization*, 58:874–882.

Sonderegger, B., Mitsche, S., and Cerjak, H. (2008). Microstructural analysis on a creep resistant martensitic 9-12% Cr steel using the EBSD method. *Materials Science and Engineering: A*, 481-482:466–470.

Soumail, T. (2001). Precipitation in creep resistant austenitic stainless steels. *Materials Science and Technology*, 17:1–14.

Strang, A. and Vodarek, V. (1996). Z-phase formation in martensitic 12CrMoVNb steel. *Materials Science and Technology*, 12:552–556.

Strang, A. and Vodarek, V. (1998). Microstructural degradation of martensitic 12%Cr power plant steels during prolonged high temperature creep exposure. In *Proceedings of the Conference on the "Materials for Advanced Power Engineering"*, pages 603–614, Belgium, Liege. Eds. J. Lecomte-Beckers et al., Forschungszentrum Jülich ISBN 3-89336-228-2.

Suzuki, K., Kumai, S., Toda, Y., Kushima, H., and Kimura, K. (2003). Two-phase separation of primary MX carbonitride during tempering in creep resistant 9Cr1MoVNb steel. *ISIJ International*, 43:1089–1094.

Tak, K.-G., Schulz, U., and Eggeler, G. (2009). On the effect of micrograin crystallography on creep of FeCr alloys. *Materials Science and Engineering: A*, 510-511:121–129.

Tamura, M., Ikeda, K., Esaka, H., and Shinouzuka, K. (2001). Precipitation behavior of NbC in 9%Cr1%Mo0.2%VNb steel. *ISIJ International*, 41:908–914.

Tamura, M., Ilda, T., Kusuyama, H., Shinozuka, K., and Esaka, H. (2004). Re-dissolution of VN during tempering in high chromium heat resistant martensitic steel. *ISIJ International*, 44:153–161.

Tamura, M., Shinozuka, K., Esaka, H., Sugimoto, S., Ishizawa, K., and Masamura, K. (2000). Mechanical properties of 8Cr-2WVTa aged for 30 000 h. *Journal of Nuclear Materials*, 283-287:667–671.

Taneike, M., Kondo, M., and Morimoto, T. (2001). Accelerated coarsening of MX carbonitrides in 12%Cr steels during creep deformation. *ISIJ International*, 41:Supplement, S111–S115.

Terada, D., Yoshida, F., Nakashima, H., Abe, H., and Kadoya, Y. (2002). In-situ observation of dislocation motion and its mobility in Fe-Mo and Fe-W solid solutions at high temperatures. *ISIJ International*, 42:1546–1552.

Tokuno, K., Hamada, K., Uemori, R., Takeda, T., and Itoh, K. (1991). Role of a complex carbonitride of niobium and vanadium in creep strength of 9% Cr ferritic steels. *Scripta Metalurgica et Materialia*, 25:1763–1768.

V & M (2000). *Vallourec & Mannesmann Tubes, The T92/P92 Book*.

V & M (2002). *Vallourec & Mannesmann Tubes, The T91/P91 Book*.

Vaillant, J., Vandenberghe, B., Hahn, B., Heuser, H., and Jochum, C. (2008). T/P23, 24, 911 and 92: New grades for advanced coal-fired power plants-properties and experience. *International Journal of Pressure Vessels and Piping*, 85:38–46.

Vangkilde-Pedersen, T., Anthonsen, K., Smith, N., Kirk, K., Neele, F., van der Meer, B., Le Gallo, Y., Bossie-Codreanu, D., Wojcicki, A., Le Nindre, Y.-M., Hendriks, C., Dalhoff, F., and Christensen, N. P. (2009). Assessing of European capacity for geological storage of carbon dioxide-the EU GeoCapacity project. *Energy Procedia*, 1:2663–2670.

Vivier, F. (2009). *Fluage à 500°C d'un joint soudé d'un acier 9Cr-1Mo modifié. Evolution de la microstructure & comportement mécanique*. PhD thesis, Ecole des Mines de Paris.

Vivier, F., Panait, C., Gourgues-Lorenzon, A., and Besson, J. (2008). Microstructure evolution in base metal and welded joint of Grade 91 steel martensitic steels after creep at 500-600°C. In 17^{th} *European conference on fracture ECF17*, pages 1095–1102, 2-5 septembre 2008, Brno Tchèque, République.

Vodarek, V., Danielsen, H. K., Flemming B. Grumsen, Hald, J., and Strang, A. (2006). Electron diffraction studies on (Nb,V)CrN particles in 12CrMoVNbN steels. In *Proceedings of the 8th Conference on "Alloy Development for Critical Components of Environmentally Friendly Steam Power Plants & on "High Temperature Plant lifetime Extension"*, pages 1251–1265, Belgium, Liége. Grafische Medien.

Vodarek, V. and Strang, A. (1998). Effect of nickel on the precipitation processes in 12CrMoV steels during creep at 550°C. *Scripta Materialia*, 38:101–106.

Vodarek, V. and Strang, A. (2000). Compositional changes in minor phases present in 12CrMoVNb, during thermal exposure at 550°C and 600°C. *Materials Science and Technology*, 16:1207–1213.

Vodarek, V. and Strang, A. (2006). Z-phase characteristics in martensitic 12CrMoVNb steels. In *Proceedings of the 8th Conference on "Alloy Development for Critical Components of Environmentally Friendly Steam Power Plants & on "High Temperature Plant lifetime Extension"*, pages 1223–1229, Belgium, Liége. Grafische Medien ISBN 1-86125-145-9.

Weinert, P. (2002). Microstructural physically based creep modelling on 9-12% Cr steels. In *Proceedings of the Conference on the "Materials for Advanced Power Engineering"*, Belgium, Liege. Eds. J. Lecomte-Beckers et al., Forschungszentrum Jülich ISBN 1-1211-1221-145-9.

Wu, R. and Sandstrom, R. (1995). Creep cavity nucleation and growth in a 12Cr-Mo-V steel. *Materials Science and Technology*, 11:579–588.

Wu, R. and Sandstrom, R. (1996). Strain dependence of creep cavity nucleation in low alloy and 12%Cr steels. *Materials Science and Technology*, 12:405–415.

Yamada, K., Igarashi, M., Muneki, S., and Abe, F. (2001). Creep properties affected by morphology of MX in high-Cr ferritic steels. *ISIJ International*, 41 Supplement:S116–S120.

Yescas, M. and Morris, P. (2005). Improved creep resistance of steel 92 by the use of modified heat treatments. In *Creep & fracture in high temperature components: Design & life assessment issues*, pages 143–152, Lancaster, U.S.A. I.A. Shibli, S.R. Holdsworth, G. Merckling (Eds). DEStech Publ. ISBN 1-932078-49-5.

Yin, Y. and Faulkner, R. (2005). Creep damage and grain boundary precipitation in power plant metals. *Materials Science and Technology*, 21:1239–1246.

Yin, Y. and Faulkner, R. (2006). Continuum damage mechanics modelling based on simulations of microstructural evolution kinetics. *Materials Science and Technology*, 22:929–936.

Yoshino, M., Mishima, Y., Toda, Y., Kushima, H., Sawada, K., and Kimura, K. (2005). Phase equilibrium between austenite and MX carbonitride in a 9Cr-1Mo-V-Nb steel. *ISIJ International*, 45:107–115.

Yoshizawa, M., Igarashi, M., Moriguchi, K., Iseda, A., Armaki, H. G., and Maruyama, K. (2009). Effect of precipitates on long-term creep deformation properties of P92 and P122 type advanced ferritic steels for USC power plants. *Materials Science and Engineering: A*, 510-511:162–168.

Zielińska-Lipiec, A., Czyrska-Filemonowicz, A., Ennis, P., and Wachter, O. (1997). The influence of heat treatments on the microstructure of 9% chromium steels containing tungsten. *Journal of Materials Processing Technology*, 64:397–405.

Appendices

Introduction

The loss of the long-term creep strength can be partially due to a metallurgical evolution of the steel such as recovery of the tempered martesitic matrix, growth of precipitates and precipitation of new phases. In order to study the effect of the matrix substructure on the loss of the creep strength, on original method was explored. It consists in using creep specimens with a tempered martensitic matrix modified by creep-fatigue cycling.

The *Appendix A* regroups details about thermo-mechanical preparation of creep specimens, results of creep tests conducted in this kind of specimens and investigations of the thermo-mechanically prepared specimens after creep testing.

An exceptionally P91 steel specimen that have been creep tested for 113,431h at 600°C was investigated using TEM, SEM, EBSD to better understand the creep strength loss during long-term exposure of the 9%Cr tempered martensitic steels. Moreover, the investigations results of this P91 steel crept specimen complete the expertise of the P92 steel crept specimens as the two steels have similar chemical composition.

The results of investigations conducted in the P91 steel tested for 113,431h at 600°C are summarized in the forme of two published articles included in *Appendix B* and *Appendix C* of this manuscript. The title of these two articles as well as details about their publication are given here below:

1. Microstructure of the Grade 91 steel after more than 10^5h of creep at 600°C

   C.G. Panait, W. Bendick, A. Fuchsmann, A.-F. Gourgues-Lorenzon, J. Besson

   - article presented in *Creep & fracture in high temperature components: Design & life assessment; ECCC Creep Conference, 21-23 April, Dübendorf (Zurich) Switzerland.* Proceedings published by *I.A. Shibli, S.R. Holdsworth (Eds.), DEStech Publications, Lancaster USA, ISBN 978-1-60595-005-1*
   - article published in *International Journal of Pressure, Vessels and Piping, vol. 87 (2010) pages 326-335*, (Panait et al., 2010a),

2. Evolution of dislocation density, size of subgrains and MX-type precipitates in a P91 steel during creep and during thermal ageing at 600°C for more than 100,000h

   Clara Gabriela Panait, Anna Zielińska-Lipiec, Tomasz Koziel, Aleksandra Czyrska-Filemonowicz, Anne-Françoise Gourgues-Lorenzon, Walter Bendick

   - article published in *Materials Science and Engineering: A, vol. 527 (2010) pages 4064-4069*, (Panait et al., 2010b)

After 113,431h of creep exposure at 600°C the hardness of the P91 steel is with 20 units lower than that of the as-received P91 steel. Quantification of creep damage and size of Laves phases were realized by image analysis of SEM images of this P91 crept specimen. These results are presented in the *Appendix B*.

MX-type precipitates were observed on extractive replicas of precipitates in P91 steel after 113,431h of creep. To get complementary information about the evolution of MX-type precipitates during long-term exposure, TEM investigations were conducted on thin foils at AGH-University (Krakow, Poland). The results of this study are summarized in the *Appendix C* of this manuscript. No significant change in the size or number density of MX-type precipitates was observed after 113,431h of creep compared to that of the as-received P91 steel. A quantification of dislocation density and subgrain size before and after 113,431h of creep at 600°C was also realized by image analysis of TEM images on thin foils. A significant growth of subgrains and a twice lower dislocation density were observed after long-term creep exposure, for more details see *Appendix C*.

At the end of *Appendix B* and *Appendix C* are given complementary results and details which could not be included in the mentioned articles.

Contributions to the following articles were brought during this phd. work, but have not been included in this manuscript because of partial overlap with results already presented in the manuscript:

1. Microstructure evolution in base metal and welded joint of Grade 91 martensitic steels after creep at 500-600°C

   F. Vivier, C. Panait, A.-F. Gourgues-Lorenzon, J. Besson

   - article presented at *17th European Conference on Fracture (ECF17), 2-5 September 2008, Brno, Czech Republic*, (Vivier et al., 2008)

2. Long-term aging effect on the creep strength of the T92 steel

   C. Panait, A.-F. Gourgues-Lorenzon, J. Besson, A. Fuchsmann, W. Bendick, J. Gabrel, M. Piette

   - article presented at *9th Liège Conference on Materials for Advanced Power Engineering, 27-29 September 2010, Liège, Belgium*

3. Creep strength and microstructural evolution of 9-12% Cr heat resistant steels during creep exposure at 600°C and 650°C

   Francisca Mendez Martin, Clara Gabriela Panait, Walter Bendick, Mihaela Albu, Bernhard Sonderegger, Gerald Kothleitner, Christof Sommitsch, Anne-Françoise Gourgues-Lorenzon, Jacques Besson, Arno Fuchsmann

   - article presented at *9th Liège Conference on Materials for Advanced Power Engineering, 27-29 September 2010, Liège, Belgium*

Appendix -A-

Thermo-mechanically prepared creep specimens

Contents

A.1 Introduction

This section focuses on thermo-mechanical preparation of creep specimens by creep-fatigue tests conducted at 550°C.

The purpose of the fatigue-creep tests at 550°C is to create a microstructure for T92 steel with a recovered matrix and to test it in creep at 600°C and 650°C in order to quantify the effect of matrix recovery during creep on the loss of creep strength. The temperature of 550°C was chosen because (i) experimental data are already available on creep-fatigue behaviour of P/T91 steels (Fournier, 2007), which can be used both to design the creep-fatigue test and for comparison purposes, and, (ii) it is low enough to prevent from major evolution concerning precipitates (MX, $M_{23}C_6$ coarsening and precipitation of Laves phases). There is no growth of precipitates reported in the literature for this temperature and for the duration of the test, $260 \pm 20h$. This was checked using SEM and EBSD.

A.2 Preparation

In order to study the contribution of the matrix substructure on the creep strength, creep specimens were thermo-mechanically prepared by creep-fatigue tests at 550°C.

A minimum fatigue strain $\varepsilon_{min} = -0.35\%$ and a maximum fatigue strain $\varepsilon_{max} = 0.35\%$ were imposed for the fatigue sequence of the cycle, leading to a total fatigue strain amplitude of $\Delta\varepsilon_{fatigue} = 0.7\%$ on loading (resp. 1.2% on unloading). A creep strain $\varepsilon_{creep} = 0.5\%$ under tension was imposed for the creep sequence.

Figure A.1 shows the cycle shape and the symbols used for these tests.

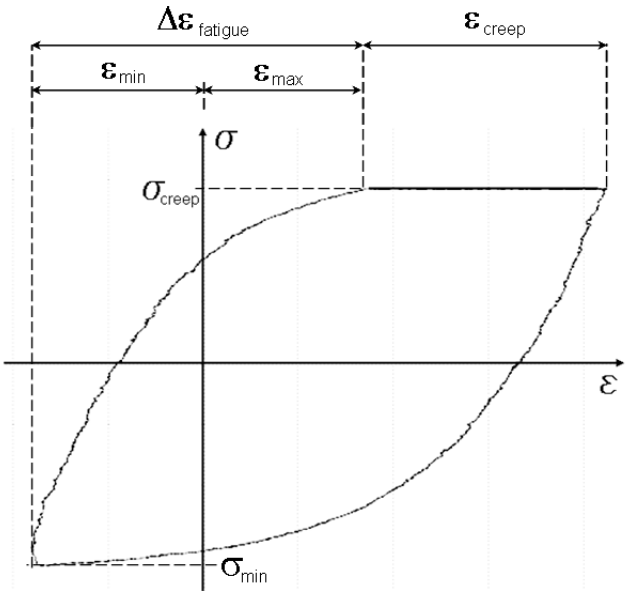

Figure A.1 : Cycle shape used for creep-fatigue tests conducted in this study

The testing conditions are believed to be severe for T92 steel and able to generate a recovered matrix within a relatively short time, e.g. a few hundreds of hours but at significant stress amplitudes. Tests conducted in identical conditions on a P91 steel, having a chemical composition not so different from that of the steel studied here, revealed a significant growth of subgrains in these conditions (Fournier et al., 2009a), (Sauzay et al., 2008).

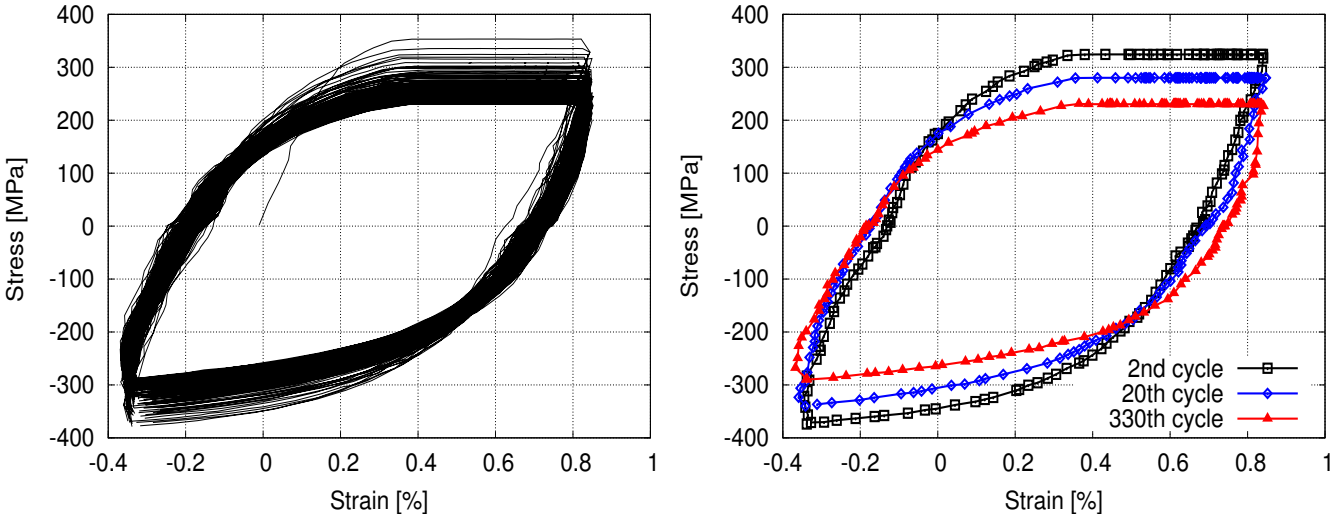

a) b)

Figure A.2 : a) 330 creep-fatigue cycles conducted at 550°C on thermo-mechanically prepared specimens; b) same as a), only the 2^{nd}, 20^{th} and 330^{th} cycles are represented

All creep-fatigue tests at 550°C were conducted with a fatigue strain rate of 10^{-3} s^{-1} and stopped well before rupture of the specimen. The fatigue-creep test was interupted after the compression half cycle and under a stress close to zero.

Thermo-mecanically prepared creep specimens were further machined from creep-fatigue specimens with 6.5 mm in gauge diameter, which had been subjected to 330 such creep-fatigue cycles at 550°C. Based on reference (Fournier, 2007), it was belived that 330 cycles of creep-fatigue were enough to considerably change the substructure of the matrix without damage initiation.

The 330 creep-fatigue cycles are represented in figure A.2a), for visibility reasons in figure A.2b) are represented only the 2^{nd}, 20^{th} and the last cycle of the test, the 330^{th} one. In figure A.2a) the first cycle starts from zero stress, this corresponds to the first loading of creep-fatigue sequence of the test.

For each cycle the creep stress is the level of stress for which a 0.35% strain of the specimen is achieved. Due to a softening of the material after some cycles a lower level of stress is necessary to achieve 0.35% strain, as can be seen in figure A.2 the creep stress corresponding to 330^{th} creep-fatigue cycle is lower than that corresponding to the 2^{nd} or 20^{th} cycle.

The geometry of the thermo-mecanically prepared creep specimens is given in figure A.3 and a sketch of both the parent creep-fatigue specimen and the daughter creep specimen is represented in figure A.4. The gauge length of thermo-mechanically prepared creep specimens was reduced and their gauge diameter further slightly reduced to localise loading within the part of the creep-fatigue specimen subjected to cyclic loading (e.g. belonging to the gauge part of the creep-fatigue parent specimen), see figure A.4.

A.3 Creep-fatigue results at 550°C

In figure A.5 are given the maximum (tensile) stress, σ_{creep}, coresponding to the creep sequence and the minimum stress in compression loading, σ_{min} of each creep-fatigue cycle. A softening of the T92 steel is noticed under cyclic loading, leading to a decrease in σ_{creep} and in the absolute value of σ_{min} with increasing the number of cycles.

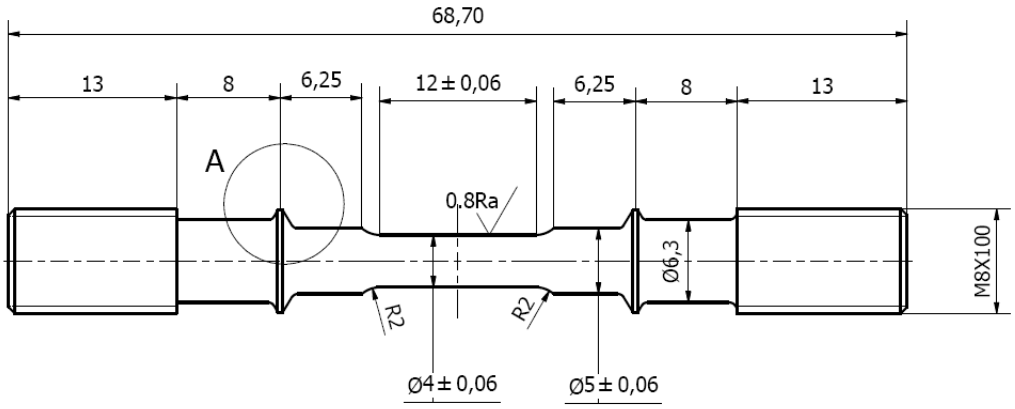

Figure A.3 : Geometry of the thermo-mecanically prepared creep specimen

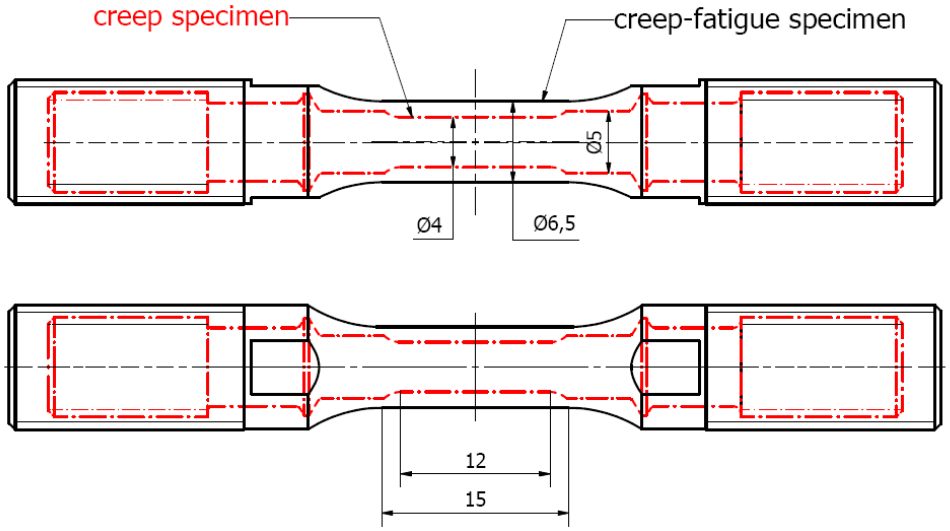

Figure A.4 : Machining of a creep specimen (in red, dotted lines) from a creep-fatigue specimen (black, full lines) after 330 creep-fatigue cycles at 550°C

Three creep-fatigue tests were conducted at 550°C and the results of these tests are comparable e.g. similar values of σ_{creep} and σ_{min} are obtained for the three tests.

The creep sequence duration was on average about 20 to 30 minutes, except for the first 5 cycles where the duration was about 5 to 10 minutes due to the higher stress level.

Strain evolution versus time corresponding to the 2^{nd}, 20^{th}, 100^{th} and 330^{th} creep-fatigue cycles are represented in figure A.6. The strain in the creep stage of each cycles evolves from 0.35% to 0.85% under a constant load. The strain time curve in figure A.6 show a typical creep curve shape with a primary stage and possibly the beginning of a secondary stage.

From the curves in figure A.6 a final creep rate ($\dot{\varepsilon}_{ss}$) was estimated as the slope of linear parts of curves. The $\dot{\varepsilon}_{ss}$ was determined using the procedure detailed in chapter IV, but taking whole creep curve into account.

In the first one hundred creep-fatigue cycles a decrease in $\dot{\varepsilon}_{ss}$ is observed, this is due to cyclic softening of the material. For the last cycles $\dot{\varepsilon}_{ss}$ seems to increase without a significant change in level of σ_{creep}.

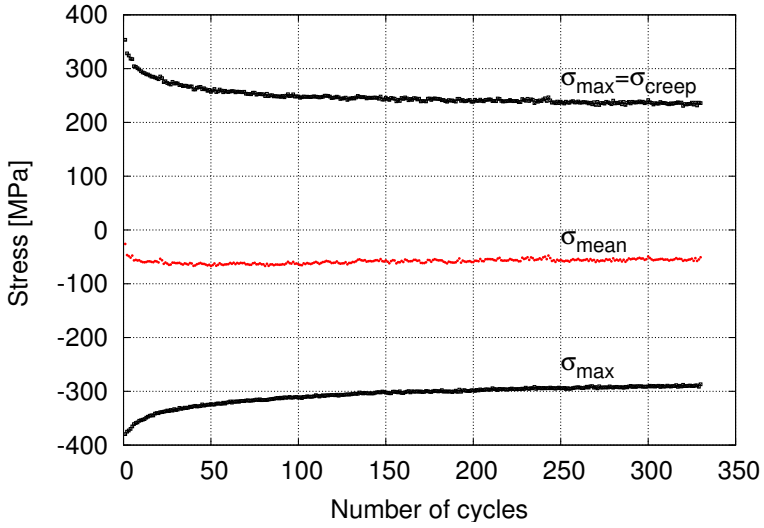

Figure A.5 : Stress corresponding to the creep sequence (σ_{creep}), upper curve and minimum stress (σ_{min}) in compression loading of each creep-fatigue cycle. The middle curve indicates the mean stress

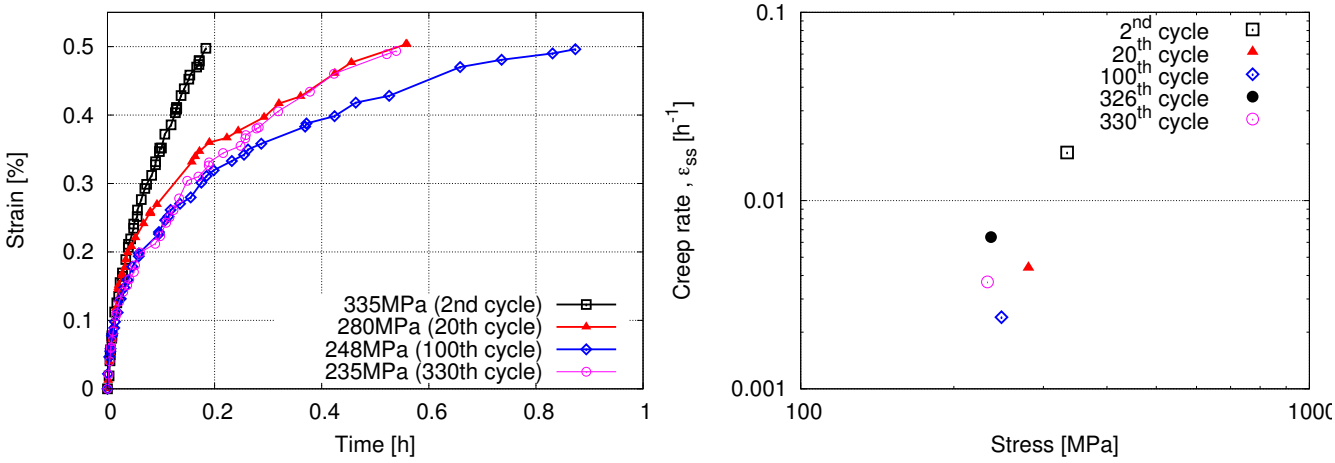

Figure A.6 : a) Strain evolution during the creep sequence corresponding to the 2^{nd}, 20^{th}, 100^{th} and 330^{th} creep-fatigue cycles conducted at 550°C; b) Final creep rate ($\dot{\varepsilon}_{ss}$) estimated from the curves in a)

A.4 Creep-fatigue results at 600°C

Figure A.7 shows the maximum (σ_{creep}) and the minimum (σ_{min}) stresses corresponding to each creep-fatigue cycle for the test conducted at 600°C on as-received T92 steel. The values of σ_{creep} are in average 20% lower compared to those for tests conducted at 550°C.

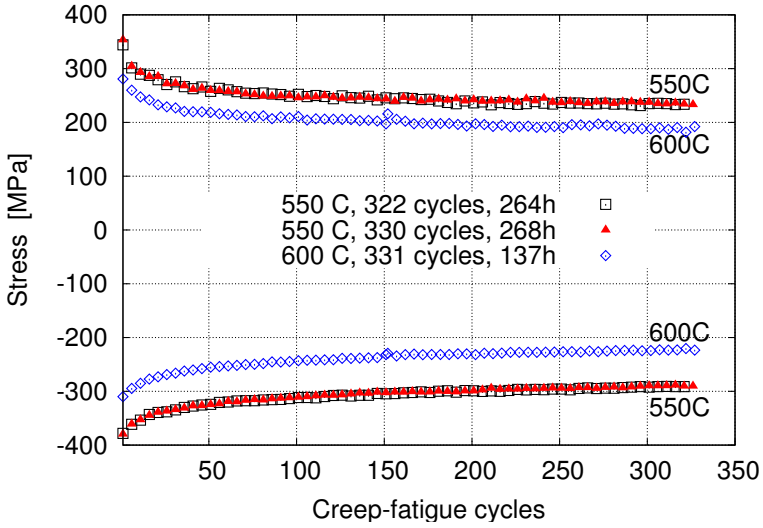

Figure A.7 : Stresses corresponding to the creep sequence (σ_{creep}), upper curves, and minimum stresses (σ_{min}) in compression loading, lower curves, for each creep-fatigue cycle from tests conducted at 550°C and 600°C

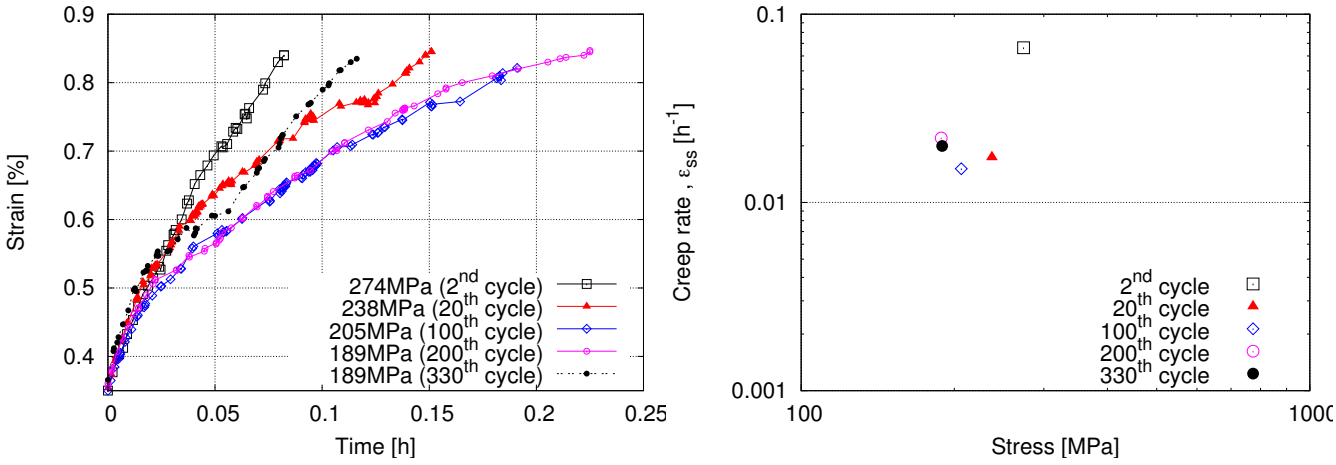

a) b)

Figure A.8 : a) Strain evolution during the creep sequence corresponding to the 2^{nd}, 20^{th}, 100^{th}, 200^{th} and 330^{th} creep-fatigue cycles conducted at 600°C; b) Final creep rate estimated from the curves in a)

In figure A.8a are represented the strain evolution during the creep sequence of the 2^{nd}, 20^{th}, 100^{th}, 200^{th} and 330^{th} cycles and in figure A.8b are given the final creep rate estimated from the curves in figure A.8a. The $\dot{\varepsilon}_{ss}$ was determinate using the procedure detailed in chapter IV. The values of $\dot{\varepsilon}_{ss}$ estimated from the creep stage of the creep-fatigue cycles conducted at 600°C is almost one hundred times higher than the values of $\dot{\varepsilon}_{ss}$ estimated from standard creep tests conducted at 600°C for same levels of stress (i.e. 170MPa-210MPa), see table V.1 and figure A.8b.

A.5 Microstructural investigations of T92 steel thermo-mechanically prepared at 550°C

Three specimens were creep-fatigue tested at 550°C as described previously. Two of these specimens were creep tested after machining as sketched in figure A.4. One of the creep-fatigue specimens tested at 550°C without further creep testing was used for metallographic investigations.

As the three specimens were subjected to the same testing conditions and the results are comparable the microstructural characterization of one specimen is considered to be representative for all the three specimens.

Due to the lack of time and availability of the testing machine, preparation of a second specimen creep-fatigue loaded at 600°C for metallographic investigations was not possible.

A.5.1 Hardness

Vickers hardness measurements with a 500g load were conducted along the axis of the longitudinal cross-section of the investigated fatigue-creep tested specimen. Results are given in table A.1. The measured hardness of the thermo-mechanically prepared T92 steel is 10 % lower then that of the as-received T92 steel. This decrease after creep-fatigue at 550°C can be an indication of either damage or microstructural evolution during the test.

Table A.1 : Hardness measurements of thermo-mechanically prepared T92 steel

Hardness $[HV0.5]$	As-received T92 steel	Thermo-mechanically prepared T92 steel
Minimum	221	201
Average	231	209
Maximum	236	215
Standard deviation	3.3	3.3
Number of measurements	60	40

A.5.2 Scanning Electron Microscopy investigations

No cracks or any other type of damage was observed on the specimen side surfaces after creep-fatigue testing. The oxide layer of the tested specimens was very thin. The creep-fatigue tests were too short and the temperature relatively low for a significant oxidation given the high oxidation resistance of the T92 steel due to its chromium content. A fragmentation of the oxide layer was observed due to cyclic loading, see figure A.9.

Creep-fatigue specimen dedicated to metallographic investigations was cut longitudinally by spark erosion machining. One half containing the specimen axis was prepared for microstructural investigations by grinding with various SiC papers and then polishing with a diamond paste down to $1\mu m$. A final colloidal silica polishing was realized.

A modification of the substructure of T92 steel without any damage initiation such as fatigue-like cracks, cavities, permanent plastic deformation was desired in the fatigue-creep specimens tested at 550°C. No damage was observed on the cross section of the investigated specimen using a light microscope and a SEM. A very small area fraction of isolated round pores was observed in the specimen after testing. It could not be established whether these pores appeared during testing or they were present in the steel before test since a similar fraction surface of pores was also observed in the as-received T92 steel.

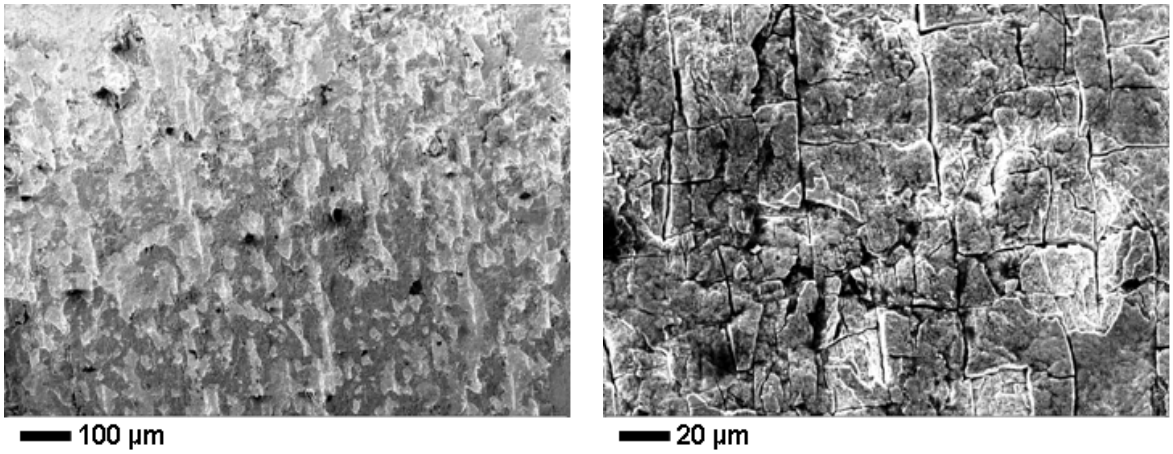

Figure A.9 : Oxide layer on fatigue-creep specimens after testing at 550°C. The loading direction is horizontal

As BSE images are highly sensitive to the crystal orientation of the sample, the BSE image in figure A.10a) shows entities with a polygonal shape in the thermo-mechanically prepared T92 steel. The lath structure of tempered martensite could not be as readily recognized as in the as received T92 steel (figure A.10a).

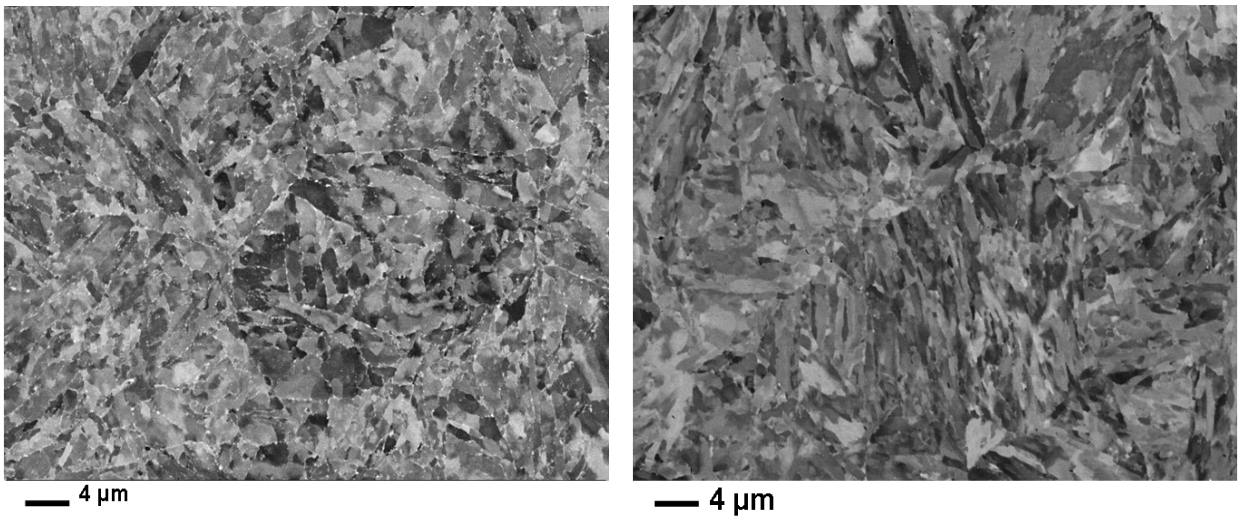

a) **b)**

Figure A.10 : Microstructure of thermo-mechanically prepared T92 steel (a), the loading direction is horizontal and of as-received T92 steel (b) (BSE-SEM images, colloidal silica polishing)

A.5.3 Electron Backscatter Diffraction (EBSD) investigations

Sample preparation for EBSD investigations is the same as for SEM investigations.

Figure A.10 shows a significant change in the substructure of the steel after creep-fatigue testing at 550°C. EBSD investigations were thus conducted on the creep-fatigue specimen to get further information on the change in the substructure of T92 steel after testing.

In figure A.11 are represented EBSD maps acquired with a step size of $0.2\mu m$. The IQ map shows many small equiaxed subgrains after creep-fatigue test. These small subgrains are not so clearly seen in the IPF orientation map, only some of them are delimited by low-angle boundaries in the IPF map.

IQ maps represent the quality of the diffraction pattern, which is very sensitive to crystal defects such as: dislocations, boundaries. Most probably the IQ map shows the boundaries of subgrains with a very low dislocation density inside. Such boundaries cannot be seen on the IQ maps of the as-received T92 steel, probably due to the higher dislocation density inside subgrains and a large amount of subgrain boundaries present in the as-received conditions. It can be concluded that during the fatigue-creep test there might be some subgrain growth caused by the disappearance of some subgrain boundaries due to their interaction with mobile dislocations, but these subgrains do not change significantly their crystal orientation.

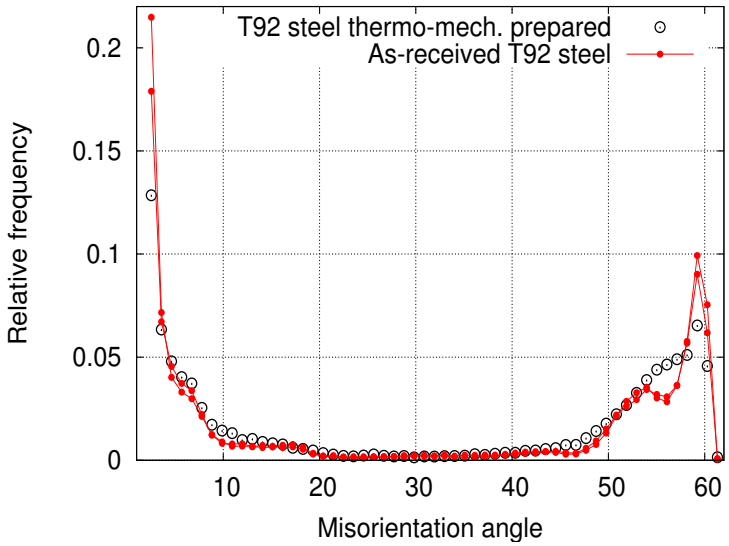

Figure A.12 : Misorientation angles (°) between grains coresponding to the EBSD map in figure A.11

Figure A.12 shows histograms of misorientation angles between grains corresponding to the EBSD map of figure A.11. This histogram shows a typical distribution of boundaries between martensite variants which indicates that after creep-fatigue test the microtexture is still inherited from the martensitic phase transformation.

The only difference is (i) that the plateau observed between 10 and $\sim 17°$ in the as-received and thermally aged materials is not so clearly observed after creep-fatigue and (ii) that the peak at $\sim 58°$ is not so high, whereas the local minimum at $\sim 56°$ has disappeared after creep-fatigue. However, it was not checked that such differences were not due to sampling effect.

High resolution EBSD maps with a step size of 40 nm were acquired from the creep-fatigue specimen to get more accurate information on the substructure of the matrix after testing, see figure A.13. EBSD maps of figure A.13 confirm previous EBSD observations: a microstructure with polygonal shaped subgrains is observed after 330 creep-fatigue cycles at 550°C.

Arrows in figure A.13b) and A.13d) indicate what seems to be subgrain boundaries. What seems to be a clear boundary in the EBSD-IQ map does not correspond to a boundary in the IPF map, i.e. misorientation angle is lower than 2°.

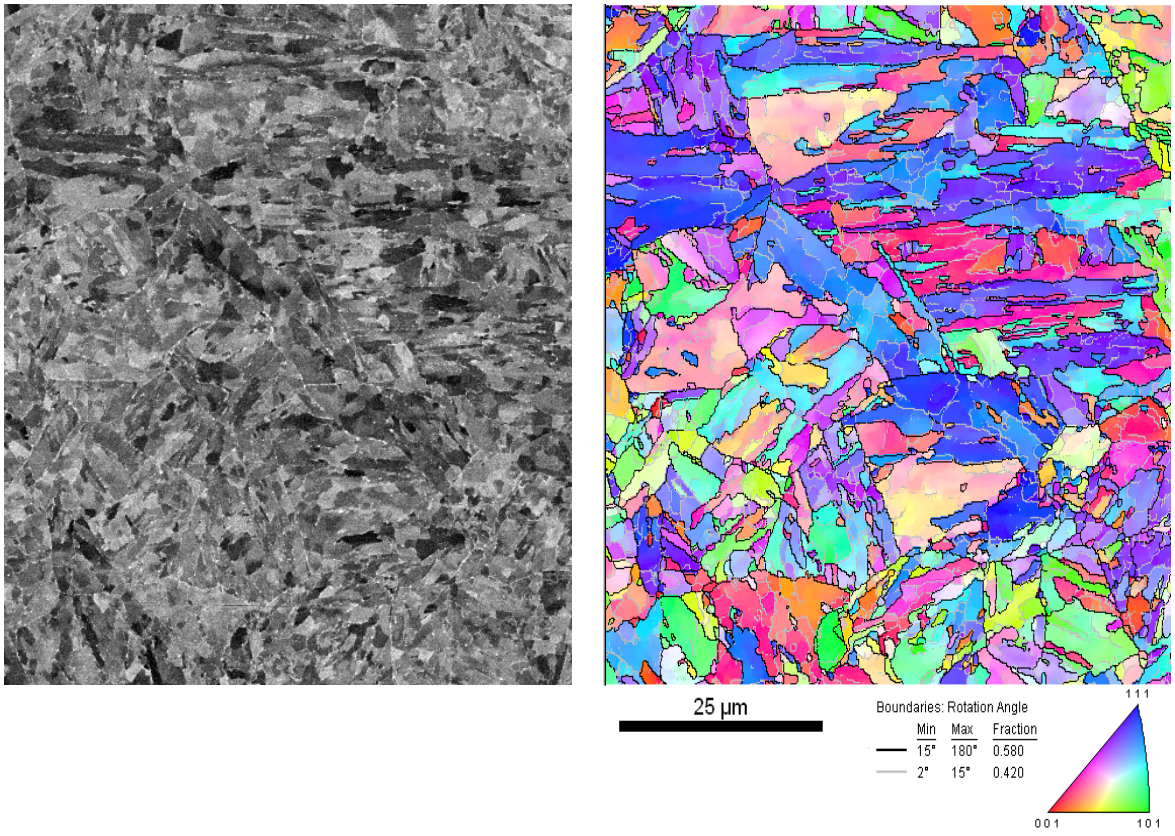

a) b)

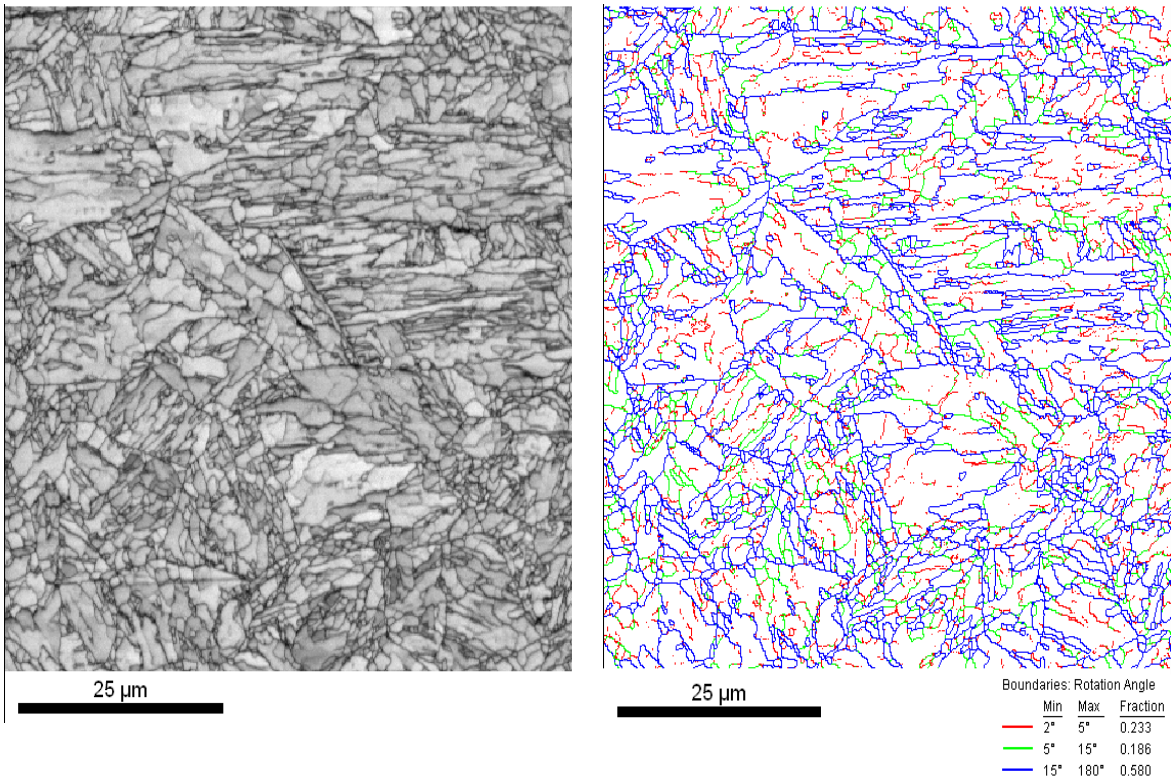

c) d)

Figure A.11 : Microstructure of thermo-mecanically prepared T92 steel.
a) SEM-BSE image; b) Inverse Pole Figure (IPF) map with orientation of sample normal in the crystal frame as key color; c) EBSD Image Quality (IQ) map showing what appears to be subgrain boundaries; d) EBSD boundary map

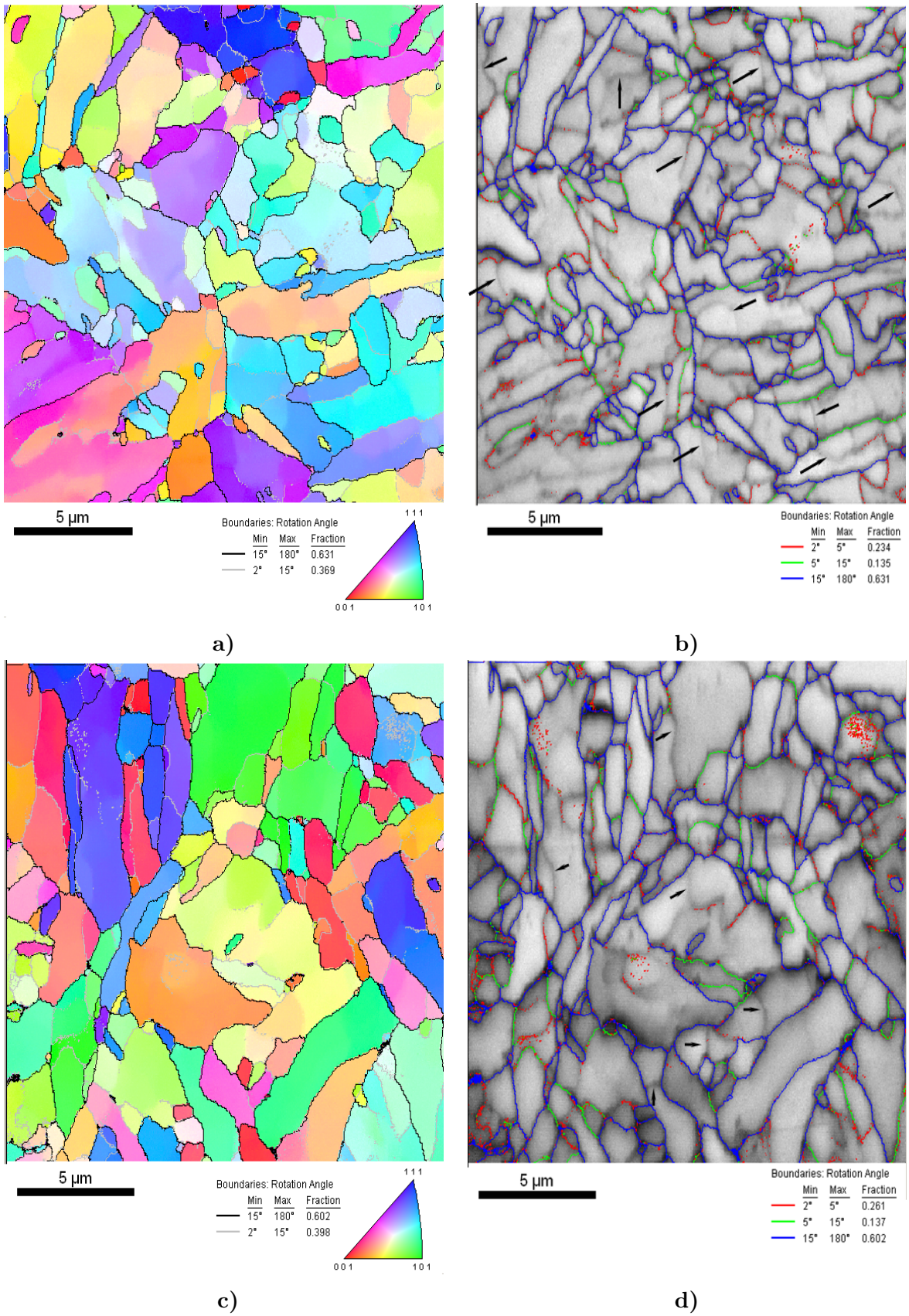

Figure A.13 : Microstructure of thermo-mecanically prepared T92 steel.
Inverse Pole Figure (IPF) map with orientation of sample normal in the crystal frame as key color (a, c); EBSD Image Quality (IQ) map (b,d)

As a further study to better understand the origin of these "boundaries" in the EBSD-IQ maps, it would be interesting to do EBSD investigations coupled with SEM, crystal orientation investigations coupled with TEM (Shigesato and Rauch, 2007), (Mathis and Rauch, 2007) and TEM bright field imaging of the same area of the sample and to compare the features revealed by each technique.

These crossed investigations (EBSD-SEM, BSE-SEM, TEM) will be able to valid the most suitable investigation technique for matrix substructure of martensitic steels. TEM is the most advanced investigation technique able to reveal the individual martensite laths and subgrains inside laths, but the drawback of this technique is the small area of the sample which can be investigated. All TEM results should be regarded with caution for the representativity of the investigated area reported to the entire steel microstructure. Generally the martensitic steels have a heterogeneous microstructure with an average prior austenitic grain of 20-40μm, subdivided in packets, blocks and precipitates located mainly on boundaries. Usually on TEM, areas of about 10μm$\times$10μm can be observed.

SEM investigations allow to sample larger areas and get more representative data of the steel microstructure. The drawback of this technique is the lower spatial resolution compared with TEM.

The crossed TEM and SEM investigations would enable to see how TEM brings complementary data on the matrix substructure compared to SEM. It is to be noted the EBSD investigations (in SEM) on a 12%Cr tempered martensitic steel with a step size of 10nm of (Tak et al., 2009) which revealed microstructural features usually observed using MET.

A.6 Summary

This section presented the results of creep-fatigue tests conducted at 550°C and 600°C. The purpose of these tests was to change the matrix substructure of the T92 steel and to study the effect of matrix substructure state on the creep strength loss.

The microstructure of one creep-fatigue specimen tested at 550°C was characterized using SEM and EBSD. The following observations can be made about the microstructure of the T92 steel after 330 cycles of creep-fatigue at 550°C.

- The hardness of the T92 steel after 330 cycles of creep-fatigue at 550°C was by 20 units lower than the hardness of T92 steel in the as-received condition.
- EBSD and SEM investigations revealed a change in the substructure of the T92 steel creep-fatigue tested, but the microtexture is still that of tempered martensite. Moreover, polygonized subgrains were observed after creep-fatigue. These subgrains are mainly revealed in EBSD-IQ maps.
- TEM observations on thin foils are needed to quantify the size of subgrains. This could not be realized during this study.
- More advanced investigations are needed to better understand the nature of boundaries revealed on EBSD-IQ maps.

The decrease in hardness and the slight acceleration of creep at the end of the creep-fatigue tests indicate that softening should be related to microstructural evolution. In fact round-shaped subgrains and microstructural features observed by SEM indicate that matrix recovery has occurred during creep-fatigue. However, the effect on creep at higher temperature (600°C

and 650°C) could be modified by the loading and primary creep stage of the creep test itself, which could again modify the matrix microstructure of both as-received and thermo-mechanically prepared specimens.

In conclusion, two specimens were thermo-mechanically prepared by creep-fatigue cycling at 550°C and one specimen by creep-fatigue cycling at 600°C.

In order to study and quantify the effect of matrix substructure on the loss of creep strength, the levels of stress applied on the thermo-mechanically prepared at 550°C correspond to the applied on both specimens with an as-received T92 steel prior testing and specimens with an thermally aged T92 steel microstructure. More precisely, one creep test was realized at 600°C under 170MPa and one test was conducted at 650°C under 95MPa both on thermo-mechanically prepared at 550°C. The specimen thermo-mechanically prepared at 600°C was creep tested at 650°C under 95MPa.

Due to machining difficulties, creep curve was available only for the creep tests conducted at 650°C under 95MPa.

A.7 Result of the creep test conducted at 600°C on thermo-mechanically prepared specimen

A microstructural characterization of the thermo-mechanically prepared specimen before testing was given in section A.2. Details about its preparation were also given in section A.2.

Due to experimental difficulties and availability of creep testing machines only 1 creep test was conducted at 600°C on thermo-mechanically prepared specimen. The result of this test is given in table A.2.

Due to the deformation of specimen after creep-fatigue test at 550°C, machining of the thermo-mechanically prepared creep specimen was difficult and recording of the creep curve for the test conducted at 170MPa was not possible.

Table A.2 : Result of creep test conducted at 600°C on specimen thermo-mechanically prepared at 550°C

Temp.	σ_n [MPa]	t_r [h]	A [%]	Z [%]	E_0	Q	τ [h]	$\dot{\varepsilon}_{ss}$ [h^{-1}]
600°C	170	1129	11.2	72	no creep curve available			

Without the record of elongation during this creep test there is no information about the secondary creep rate for this test. However for a given engineering stress (i.e. σ_n =170MPa), a t_r almost three times lower is observed on the specimen thermo-mechanically prepared at 550°C and then creep tested at 600°C compared to that of the as-received T92 steel (see table V.1 compared to table A.2).

A similar result was reported for a P91 steel creep tested at 550°C. Creep tests conducted at 230MPa, 550°C revealed $t_r \sim$ 1,200h on a standard creep specimen and ∼500h was obtained on creep specimen which has been subject to 100 creep-fatigue cycles similar to our specimen ($\Delta\varepsilon_{fatigue} = 0.7\%$ and $\varepsilon_{creep} = 0.5\%$, (Fournier et al., 2009b)).

For a given level of stress (i.e. σ_n =170MPa) the lifetime (t_r) of the thermo-mechanically prepared T92 steel is similar to that of the T92 steel thermally aged at 600°C for 10^4h, indicating that precipitation of Laves phases and recovery of the matrix during creep test could have a similar effect on the creep strength for such creep lifetimes. This hypothesis should be confirmed by complementary creep tests (including long-term creep) on thermo-mechanically prepared specimens.

It is to be mentioned that without a creep curve from the creep test conducted on the thermo-mechanically prepared specimen, it is difficult to compare the result of this test to tests conducted on thermally aged or standard creep tests.

A.8 Results of creep tests conducted at 650°C on thermo-mechanically prepared specimens

Due to experimental difficulties and availability of testing machines only two creep tests were conducted at 650°C on thermo-mechanically prepared specimens. One specimen was thermo-mechanically prepared at 550°C (TMP550) and another one at 600°C (TMP600) in same strain conditions. Both specimens were creep tested under the same load (i.e. 95MPa) in order to quantify the effect of matrix substructure on the creep strength. Creep-fatigue tests conducted at 600°C are believed to induce a more significant recovery of the matrix compared to creep-fatigue cycles conducted at 550°C.

A microstructural characterization of the TMP550 specimen before creep testing was given in section A.2. Because only one specimen thermo-mechanically prepared at 600°C (TMP600) was available, a characterization of its microstructure was not possible. It can be assumed that the effect of the 330 creep-fatigue cycles on the T92 steel microstructure are both decrease in dislocation density and an increase in subgrain size.

The results of creep tests conducted at 650°C on thermo-mechanically prepared specimens are given in table A.3. The creep rate of these two specimens are represented in figure A.14. The creep rate of the TMP600 specimen is slightly lower than that of the TMP550 specimen. Note that the difference in creep rate between the two specimens is equivalent to the scatter of data. Moreover, there is no significant difference between the secondary creep rate s of the two specimens.

The elongation at rupture (A) of the TMP550 specimen could not be correctly measured. Demounting of this specimens after creep testing was difficult and had lead to deformation of one broken part (i.e. half of the entire TMP550 specimen). The broken part of the TMP550 specimen which have been correctly demounted was used for metallographic investigations and measurement of the reduction of area (Z). The reduction of area of the TMP600C specimen is higher than that of the TMP550C specimen, this could be explained by a higher recovery in the TMP600C specimen compared to that in TMP550C specimen.

Table A.3 : Results of creep tests conducted at 650°C on thermo-mechanically prepared specimen

Temp. of creep-fatigue test	σ_n [MPa]	t_r [h]	A [%]	Z [%]	E_0	Q	τ [h]	ts_{III} [h]	ε_{III}	$\dot{\varepsilon}_{ss}$ [h^{-1}]
550°C (TMP550)	95	4,656	-	17	0.00018	0.0012	18	2,171	0.013	4.71×10^{-6}
600°C (TMP600)	95	3,210	34	46	0.00014	0.0019	0.56	1,528	0.010	4.73×10^{-6}

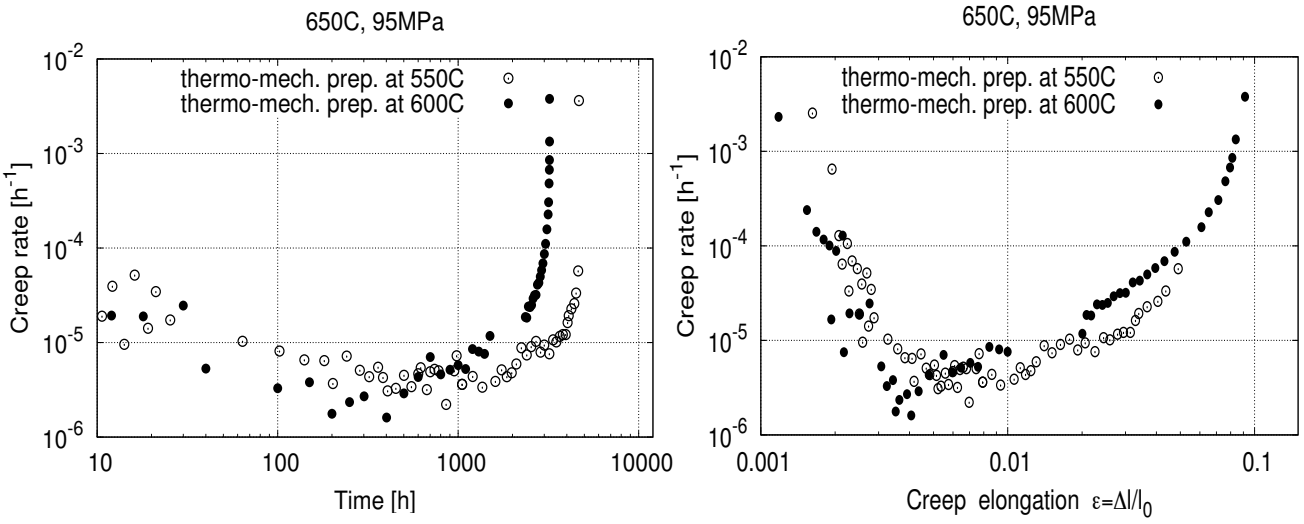

a) **b)**

Figure A.14 : Creep rate of specimens thermo-mechanically prepared at 550°C and 600°C, both creep tested under 95MPa at 650°C

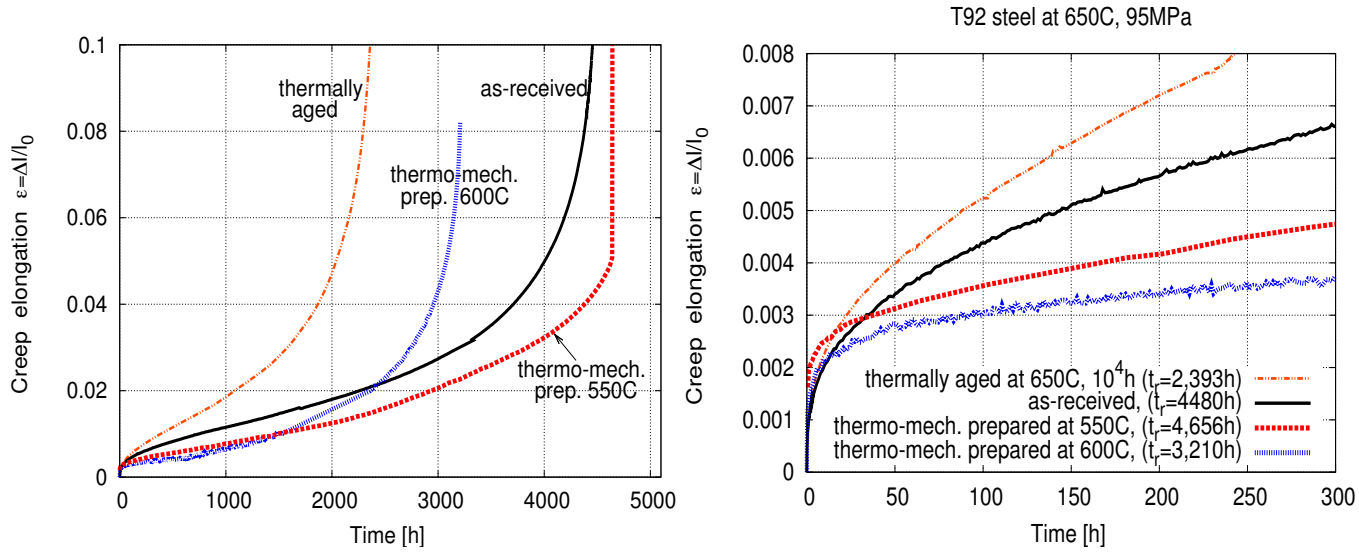

a) **b)**

Figure A.15 : Creep curves for tests conducted at 95MPa on standard (as-received T92 steel microstructure), thermally aged (650°C, 10^4h) and thermo-mechanically prepared specimens

There is no significant difference between the $\dot{\varepsilon}_{ss}$ and t_r of the as-received T92 steel and T92 steel thermo-mechanically prepared at 550°C both creep tested under 95MPa. This may indicate that matrix substructure state does not have a significant influence on the creep deformation mechanisms at low stresses.

Because of the softening of the T92 steel after creep-fatigue cycles at 550°C, during the primary creep stage the deformation of thermo-mechanically prepared T92 steel is higher

than the deformation of the as-received T92 steel, see figure A.14b. The secondary creep stage is onset at lower values of elongation (the sum of E_0 and Q in table A.3) on the T92 steel thermo-mechanically prepared compare to the as-received T92 steel creep tested under $\sigma = 95$MPa.

A.9 Investigations of the thermo-mechanically prepared specimens after creep testing

A.9.1 Hardness

Before creep testing the specimen thermo-mechanically prepared at 550°C revealed a hardness of $\sim$ 210HV0.5. In table A.4 are given the results of hardness measurements conducted with a load of 500g and a step size of 0.25 mm on the longitudinal axis of the thermo-mechanically prepared specimens after creep testing. The hardness measurements were conducted on the homogeneously deformed part of the specimens after creep testing.

Table A.4 : Hardness measurements of thermo-mechanically prepared specimens after creep testing

Hardness	As-received	Thermo-mechanically prepared			
$[HV0.5]$	T92 steel	before creep	600°C; 1,129h	650°C; 4,656h	650°C, 3210h
Minimum	221	201	196	186	168
Average	231	209	206	196	186
Maximum	236	215	214	208	197
St. dev.	3.3	3.3	5.1	4.6	7.2
Numb. meas.	60	40	35	30	30

Numb. meas. - number of measurements; St. dev - standard deviation

The specimen thermo-mechanically prepared at 550°C and than creep tested at 600°C, 170MPa shows no significant change in hardness compared to that before creep testing. Lower values of hardness are observed in the TMP550C and TMP600C specimens after creep, see table A.4.

A.9.2 Creep damage

A.9.2.1 Thermo-mechanically prepared specimen creep tested for 1,129h at 600°C, 170MPa

No creep damage was observed in the homogeneously deformed part of thermo-mechanically prepared specimen creep tested for 1,129h at 600°C, 170MPa.

A.9.2.2 Thermo-mechanically prepared specimen creep tested for 4,656h at 650°C, 95MPa

Creep damage was quantified in this crept specimen and then compared to that in the as-received steel creep tested for 4,480h at 650°C, 95MPa, see figure VII.36. No significant change was observed in the amount of creep damage in the two crept specimens. Typical creep damage in the thermo-mechanically prepared specimen at 550°C (TMP550) and then creep tested at 650°C, 95MPa for 4,656h were given in figure VII.35.

A.9.3 Matrix substructure

Blocks completely recovered are observed in the thermo-mechanically prepared specimen after 1129h of creep exposure at 170MPa, 600°C, figure A.16. Before creep testing, EBSD-IQ maps revealed boundaries which were believed to be subgrain boundaries in the thermo-mechanically prepared specimen. These boundaries are no longer revealed by EBSD-IQ maps; probably they disappear due to creep deformation. Bright precipitates in the SEM-BSE images in figure A.16a are Laves phases which precipitated during creep exposure. Before creep testing no Laves phases was observed in the thermo-mechanically prepared specimen.

EBSD maps of the specimen thermo-mechanically prepared at 550°C then creep tested at 650°C, 95MPa for 4,656h were given in figure VII.44. These maps reveals a recovered microtexture with large grains that appear to be free of sub-grains. However, the distribution of misorientation angle (figure VII.45) between neighbouring grains shows a typical shape commonly found for martensite variants from the same parent austenite grain.

A.10 Summary

The purpose of thermo-mechanically prepared creep specimens was to study the effect of matrix substructure on the loss of creep strength. These specimens were prepared by 330 creep-fatigue cycles at 550°C. EBSD-IQ maps of the thermo-mechanically prepared specimen revealed some round-shape features that could be subgrains inside martensite laths.

One thermo-mechanically specimen creep tested at 600°C under 170MPa revealed a lifetime of 1129h, which was almost twice lower than the lifetime of a standard specimen (i. e. with an as-received T92 steel microstructure before testing) creep tested under same conditions. No creep curve (i. e. deformation in time) was available for the creep test conducted at 600°C, 170MPa on thermo-mechanically prepared specimen.

No significant change was observed in the creep deformation (respectively lifetime) of the specimen thermo-mechanically at 550°C and a standard specimen both creep tested under 95MPa at 650°C.

It is to be mentioned that 170MPa corresponds to the high stresses region of the creep flow of the Grade 92 steel at 600°C and 95MPa was found to correspond to the low stresses region of the creep flow of the Grade 92 steel at 650°C. Probably this is the reason why the two specimens thermo-mechanically prepared at 550°C show different creep behavior. Moreover, the reduction of area and elongation at rupture of the two thermo-mechanically specimens was different (see table A.2 and table A.3).

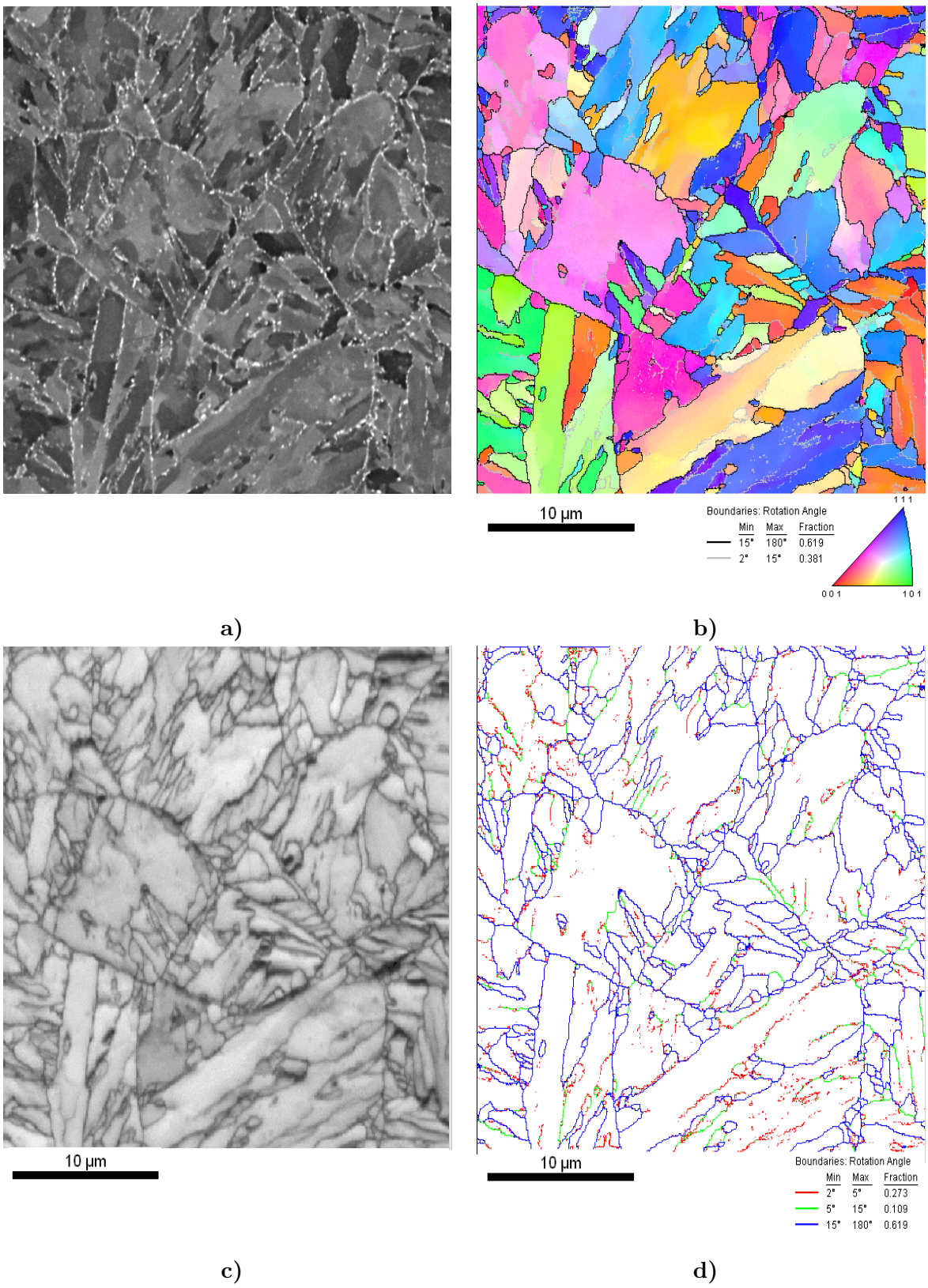

Figure A.16 : Microstructure of specimen thermo-mecanically prepared at 550°C and creep tested for 1,129h at 600°C, 170MPa. a) SEM-BSE image; b) Inverse Pole Figure (IPF) map with orientation of sample normal in the crystal frame as key color; c) EBSD Image Quality (IQ) map showing what appears to be subgrain boundaries; d) EBSD boundaries map

Appendix -B-

Study of the microstructure of the Grade 91 steel after more than 100,000h of creep exposure at 600°C

The present appendix reproduces an article presented in the conference *Creep & fracture in high temperature components: Design & life assessment; ECCC Creep Conference, 21-23 April 2009, Dübendorf (Zurich) Switzerland*. The proceedings of the conference were published by *I.A. Shibli, S.R. Holdsworth (Eds.), DEStech Publications, Lancaster USA, ISBN 978-1-60595-005-1* (Panait et al., 2009).

This article was also published in *International Journal of Pressure, Vessels and Piping*, vol. 87 (2010) pages 326-335 (Panait et al., 2010a).

International Journal of Pressure Vessels and Piping 87 (2010) 326–335

Contents lists available at ScienceDirect

International Journal of Pressure Vessels and Piping

journal homepage: www.elsevier.com/locate/ijpvp

Study of the microstructure of the Grade 91 steel after more than 100,000 h of creep exposure at 600 °C

C.G. Panait [a,b,*], W. Bendick [c], A. Fuchsmann [b], A.-F. Gourgues-Lorenzon [a], J. Besson [a]

[a] Centre des Matériaux, MINES ParisTech, UMR CNRS 7633, B.P. 87, 91003 Evry Cedex, France
[b] Vallourec Research Aulnoye, Route de Leval, B.P. 20149, 59620 Aulnoye-Aymeries, France
[c] Salzgitter Mannesmann Forschung GmbH, Ehinger Straße 200, D-47259 Duisburg, Germany

ARTICLE INFO

Article history:
Received 30 November 2008
Accepted 14 January 2010

Keywords:
P91 steel
Creep
Microstructure
Laves phases
Modified Z-phase
SEM
TEM

ABSTRACT

This paper presents results on the evolution of microstructure (both matrix and precipitates) of an ASME Grade 91 steel that has been creep tested for 113,431 h at 600 °C under a load of 80 MPa.

The microstructure was investigated using transmission electron microscopy (TEM) and revealed chromium rich $M_{23}C_6$ carbides, MX-type precipitates, Laves phases and modified Z-phases. Only a small amount of modified Z-phase was found. In order to quantify coarsening of precipitates and growth of new phases during creep, the size distributions of the identified precipitates were determined by analysis of TEM images. In addition to this, the size distribution of Laves phases was determined by image analysis of scanning electron micrographs.

Substructure modifications and creep damage were investigated on cross sections of the creep specimen using Electron Backscatter Diffraction and Scanning Electron Microscopy.

1. Introduction

There are few published data available on the microstructure of 9–12% chromium heat resistant steels after nearly 100,000 h of exposure to creep. Further development of new heat resistant steels such as ASME Grade 91 steel, presently successfully used for components in fossil power plants operating at temperatures around 550–600 °C [1] rely on a better understanding of their long-term microstructural evolution. Previous works [2–4] presented data on the microstructure of the ASME P91 steel after long-term creep exposure, but for exposure times lower than 100,000 h.

It has been shown that extrapolation of short-term creep data (e.g. for lifetime lower than 10,000 h) can lead to an overestimation of the creep strength after long-term creep [5–7]. This overestimation is probably due to the metallurgical evolution of the steel during creep or damage development. This paper presents data on the microstructure of the Grade 91 after more than 100,000 h of creep exposure, which will be useful for a better understanding of the loss of long-term creep strength.

2. Literature data on precipitate evolution in 9–12%Cr steels during creep

The microstructure of the as-received ASME Grade 91 steel consists of a tempered martensite matrix with high dislocation density and precipitates. There are two kinds of precipitates: $M_{23}C_6$ (M = Cr, Fe, Mo) carbides located at prior austenite grain boundaries (PAGBs) and at other (packet, block, martensite lath) boundaries and finely dispersed MX-type (M = V, Nb and X = C, N) carbonitrides within laths. Carbides of type MC, M_2C [8] can be also identified in Grade 91 steels, but most of the precipitates present at boundaries (PAGBs, laths, blocks, packets) are $M_{23}C_6$ carbides.

There is a microstructural evolution of the ASME Grade 91 steel during creep exposure: precipitation of new phases (Laves phases, modified Z-phases), coarsening of precipitates (primarily $M_{23}C_6$ carbides) and recovery of tempered martensitic lath structure.

Intermetallic Laves phases precipitate during creep or aging. Their precipitation is observed after relatively short-term creep exposure at 600 °C, for times shorter than 4,000 h [9]. Laves phase precipitation decreases the amount of Mo dissolved in the matrix, reducing solid solution strengthening. Quantitative studies on the evolution of the size of Laves phases during creep or aging have revealed a significant growth rate during the first 10,000 h of exposure [10].

Modified Z-phase is a complex (Cr,Fe)(Nb,V)N nitride. Its composition for metal elements is 50 at.% (Cr + Fe) and 50 at.%

* Corresponding author. Centre des Matériaux, MINES ParisTech, UMR CNRS 7633, B.P. 87, 91003 Evry Cedex, France.
E-mail address: clara.panait@ensmp.fr (C.G. Panait).

0308-0161/$ – see front matter © 2010 Elsevier Ltd. All rights reserved.
doi:10.1016/j.ijpvp.2010.03.017

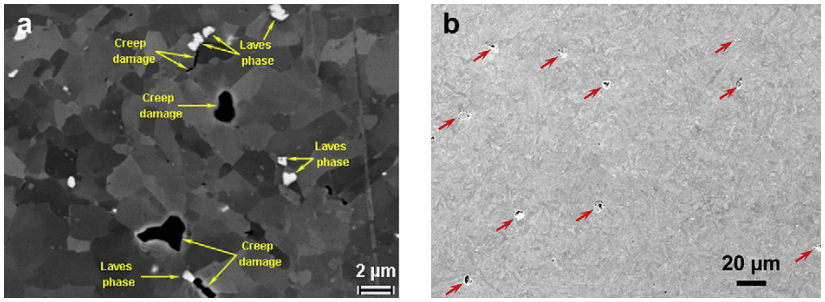

Fig. 1. Creep damage in the P91 steel after creep at 600 °C for 113,431 h 7 mm from fracture surface, SEM images, BSE-mode (a) and SE-mode (b).

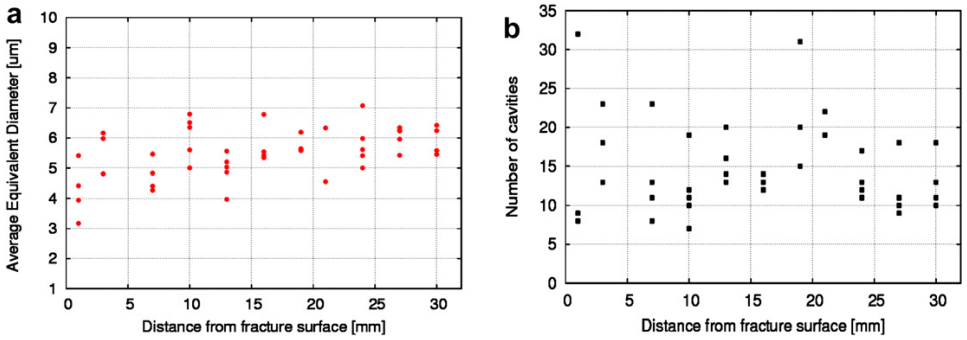

Fig. 2. Average equivalent diameter (a) and number of cavities (b) calculated on areas of 342 μm × 214 μm along the creep specimen axis.

(Nb + V) [11]. In the ASME Grade 91 steel, modified Z-phase formation is observed after very long-term creep, for example after 34,141 h, at 600 °C, under a load of 100 MPa [12]. The precipitation of modified Z-phases is also reported in the heat-affected zone (HAZ) of welded joints [13,14]. The modified Z-phase precipitation occurs at the expense of MX precipitates, possibly leading to partial or complete disappearance of those precipitates and suppression of MX-induced strengthening. For this reason, the modified Z-phase precipitation could be detrimental to service life of 9–12% Cr ferritic–martensitic steels. In fact, it was suggested to be the major cause of premature loss of creep strength of some 11–12% Cr heat resistant steels after relatively short term (<15,000 h) creep [15]. It is more intense in the 11–12% Cr steels content than in 9% Cr steels [11]; for the ASME Grade 91 steel, the effect of precipitation of modified Z-phase on creep strength is not fully understood.

3. Experimental procedure

3.1. Materials

A broken P91 steel creep specimen with a rupture time of 113,431 h at 600 °C under a constant load corresponding to an initial tensile stress of 80 MPa and a sample from the same pipe in the as-received conditions (no thermal or creep ageing) were provided by Salzgitter Mannesmann Forschung GmbH, Germany. The pipe was 121 mm in outside diameter and 20 mm in wall thickness. Its chemical composition was (wt.%): 0.1C–0.36Si–0.41Mn–0.015P–0.003S–0.059N–0.022Al–8.43Cr–0.92Mo–0.04Cu–0.068Nb–0.11Ni–0.20V. The pipe had been given the following heat treatment: 1050 °C for 60 min, air cooling followed by 730 °C for 60 min and 750 °C for 60 min, air cooling. The investigated creep specimen with a rupture time of 113,431 h at 600 °C (80 MPa) exhibited an elongation of 7.3% and a reduction of area of 37%. During creep the specimen showed a minimum creep rate of 1.1×10^{-7} (h^{-1}).

3.2. Transmission electron microscopy (TEM) investigations

TEM investigations were performed with a Tecnai F20 transmission electron microscope. TEM investigations were carried out on single carbon extractive replicas and thin foils. The carbon replicas of precipitates were prepared as follows. First, the creep sample was polished and Villela etched. Then, a carbon coating was evaporated onto the polished and etched surface; after that the sample was immersed in a 1% HCl solution in methanol to detach the carbon layer from the specimen. The carbon replicas were

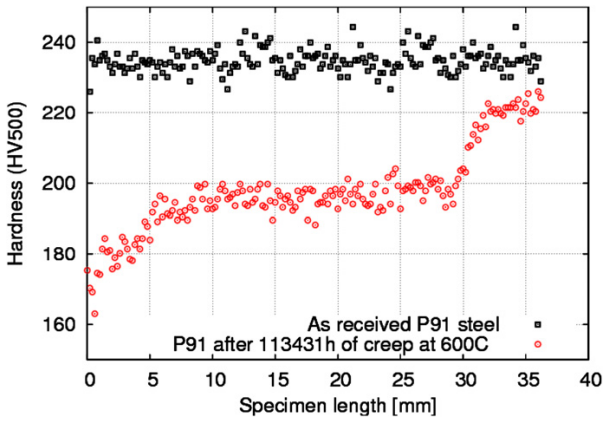

Fig. 3. Evolution of hardness along the tensile direction of investigated creep specimen (circles) compared to that of a similar piece of as-received steel from the same pipe (squares).

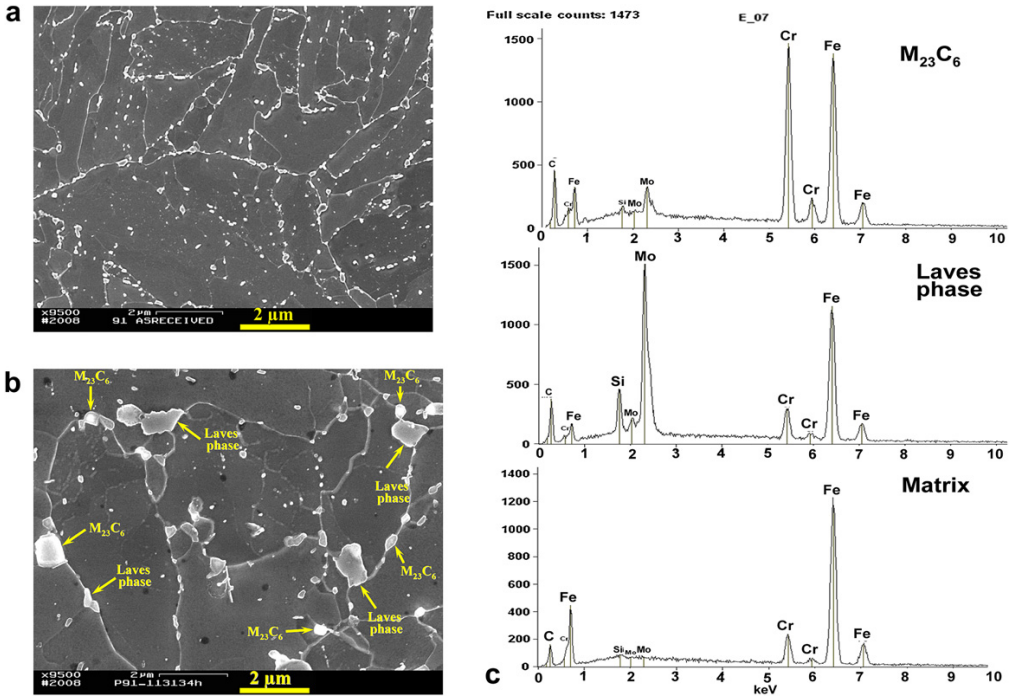

Fig. 4. Microstructure of the a) as-received P91, b) after creep at 600 °C for 113,431 h (gauge); c) typical EDS (FEG-SEM) spectra for $M_{23}C_6$ carbides, Laves phases and matrix, respectively.

recovered on round copper grids. Thin foils from the gauge part of the creep specimen were prepared combining electropolishing and ion beam milling. An acid solution (45% acetic acid, 10% perchloric acid, 45% Butoxyethanol) cooled down to −1 °C was used for electropolishing. The electropolished foils were further thinned by ion beam milling for a few minutes at low angle using a Gatan Precision Ion Polishing System (PIPS).

The chemical composition of each precipitate was determined by Energy dispersive X-ray spectrometry (EDX) in conjunction with TEM. The identification was done using the following criteria: $M_{23}C_6$ carbides are enriched in Cr, Laves phases are enriched in Mo, modified Z-phase are made out of ~50 at.% (Cr + Fe) and ~50 at.% (V + Nb) and MX are enriched in V and Nb. More than 600 precipitates were investigated on several extractive replicas.

It is not sure that all precipitates are extracted on the carbon replica. As a consequence, special attention was paid to select an investigation area that was representative of the microstructure of the steel after etching.

Literature reports an average diameter of MX precipitates of 20–40 nm [16]. MX-type precipitates were identified on investigated extractive replicas; nevertheless, attention was focused to identify only larger precipitates after long-term creep, which could have a significant influence on the loss of creep strength. Thus, EDS analyses were mainly conducted on precipitates with an average diameter higher than 90 nm. MX–type precipitates were observed on thin foils.

3.3. Scanning electron microscopy (SEM) investigations

Creep damage was investigated using a Scanning Electron Microscope (Leo 1450 VP, with a tungsten filament) on longitudinal cross sections. One broken half of the creep specimen was cut into

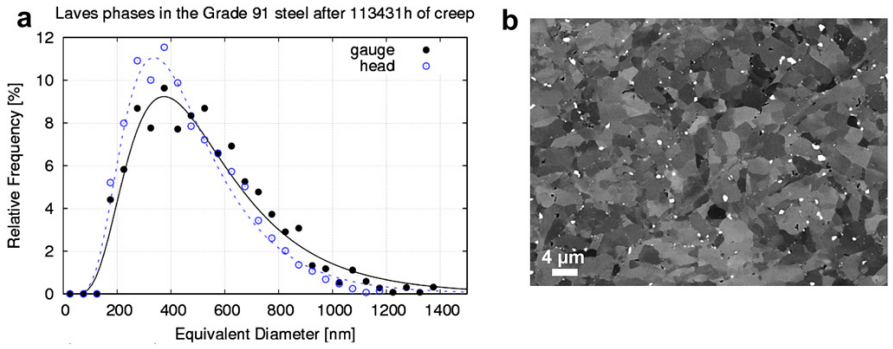

Fig. 5. a) Size distribution of Laves phases in the P91 steel in the head (□) and in the gauge portion (•) of the creep specimen; b) Microstructure of the P91 steel after creep, showing Laves phases (white).

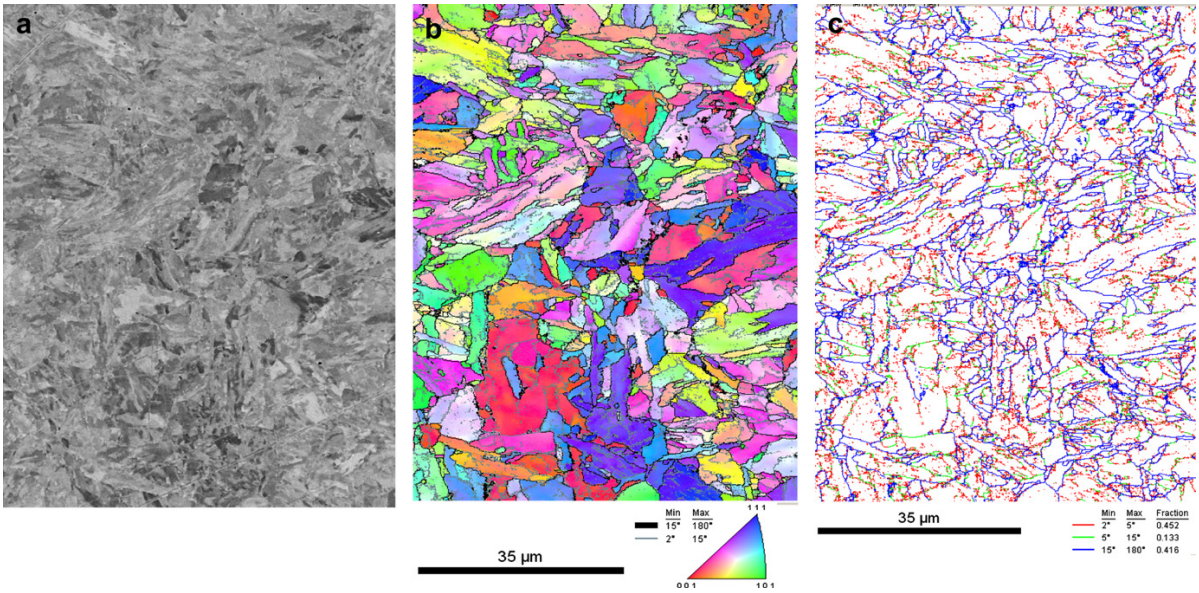

Fig. 6. Microstructure of the as-received P91 steel. a) SEM-BSE micrograph; b) Inverse Pole Figure (IPF) with orientation of sample normal in the crystal frame as key colour; c) EBSD Boundary map.

two halves (i.e. quarters of "complete" specimens) by spark erosion. The half containing the specimen axis was used for metallographic examinations. A final mechanical-chemical polishing with colloidal silica was then carried out to reveal cavities without opening them, as chemical etching could have done. The creep damage was quantified as a fraction of porosity determined by image analysis of SEM images with a magnification of $\times$400.

3.4. Electron backscatter diffraction (EBSD) investigations

Electron backscatter diffraction (EBSD) maps were acquired from the same cross section with a Zeiss DSM 982 Gemini field emission gun (FEG) SEM equipped with a Shottky filament, a Hjelen-type camera and TSL OIM facilities. The specimen for EBSD maps was also polished with colloidal silica. All EBSD measurements were conducted with a step size of 0.15 μm at 20 kV, working distance 19 mm, aperture 120 μm, probe current between 0.1 and 1 nA.

The EBSD maps were acquired together with a backscattered electron (BSE) image (taken at 0° specimen tilt), where the contrast is highly sensitive to the crystallographic orientation of the sample normal (i.e., of the primary electron beam). Laves phases, enriched in Mo, are also clearly visible thanks to their high average atomic number.

The first map built after EBSD data processing is the "image quality" map, which reports, for each analysed point, the ability of the software to detect the diffraction bands. The brighter the grey level, the better the diffraction conditions. Image quality is sensitive to the crystal orientation, as well as to the "channelling effect" that yields the BSE image contrast. In addition, image quality is very sensitive to crystal defects such as dislocations. As soon as dislocations are clustered somewhere, the EBSD pattern quality decreases. Thus, the image quality map is very sensitive to the presence of boundaries, *even for very low angle boundaries.*

Inverse pole figure (IPF) maps were colour-coded according to the orientation of a given direction of the sample in the crystal frame. The colour key is recalled next to each IPF map.

In addition to IPF mapping, one may calculate the misorientation between neighbouring pixels and assign a colour code to any

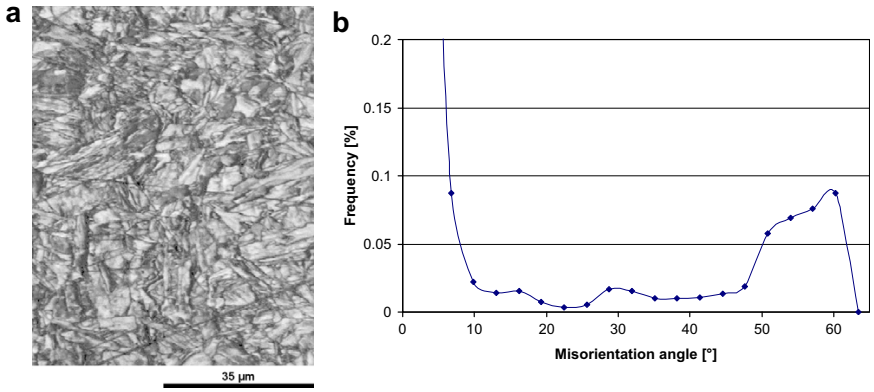

Fig. 7. EBSD Image Quality map (a) and misorientation angles for EBSD maps in Fig. 6.

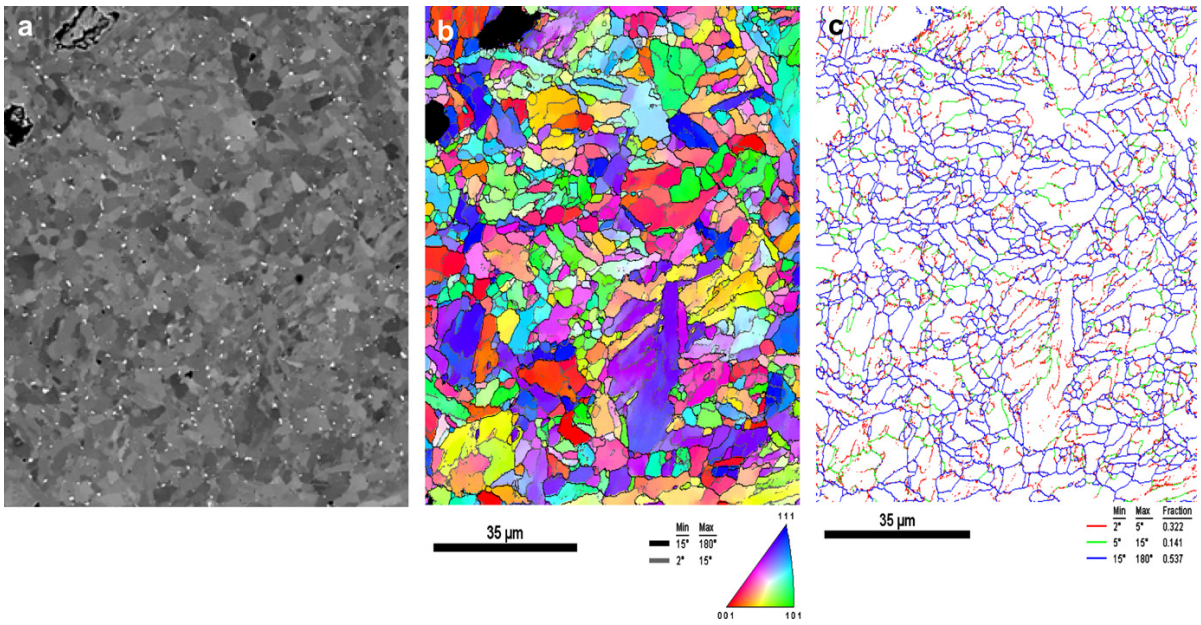

Fig. 8. Microstructure of P91 steel after 113,431 h of creep at 600 °C (2 mm from fracture surface) a) SEM-BSE micrograph; b) Inverse Pole Figure (IPF) with orientation of sample normal in the crystal frame as key colour; c) EBSD Boundary map.

pair of pixels whose misorientation meets a given criterion. This helps investigations whether a "boundary" imaged in the image quality maps corresponds to a high or to a low misorientation angle, or even to negligible misorientation between neighbouring crystals. This is particularly useful to investigate subgrain boundaries. In all maps, the colour code for boundaries is recalled according to the misorientation angles.

4. Creep damage

A high number density of cavities was observed throughout the specimen section even far from the fracture surface, using either backscatter electron (BSE) or secondary electron (SE) imaging (Fig. 1). Many cavities can even be observed using a light microscope.

Fig. 2 reports data on the average equivalent diameter of cavities and number of cavities observed at a magnification of ×400. At this magnification cavities with a minimum equivalent diameter of 0.7 μm can be revealed. Creep damage was quantified on areas of 342 μm × 214 μm. In Fig. 1b is represented a typical SEM image used for creep damage quantification, arrows show creep cavities. Cavities seem to nucleate at boundaries next to large particles such as Laves phases (Fig. 1a). At a distance lower than about 0.5 mm from the fracture surface, coalescence of cavities was observed.

5. Hardness

The gauge portion of the investigated creep specimen exhibits hardness with about fifty units lower than in the as-received P91 steel. This decrease in hardness can be due to both the presence of cavities and microstructural evolution of the steel during creep. Close to the fracture surface, one observes a slight decrease in hardness compared to that of the rest of the gauge portion of the specimen. This can be related to creep damage development. The head of the creep specimen shows a lower decrease in hardness,

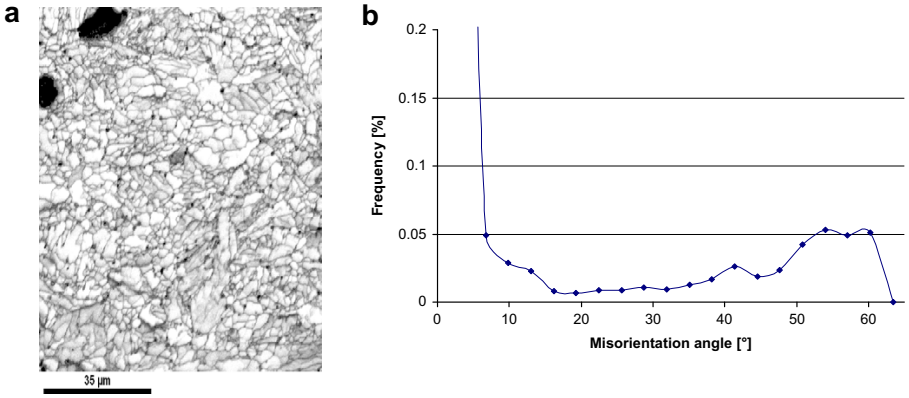

Fig. 9. EBSD Image Quality map (a) and misorientation angles (b) for EBSD maps in Fig. 8.

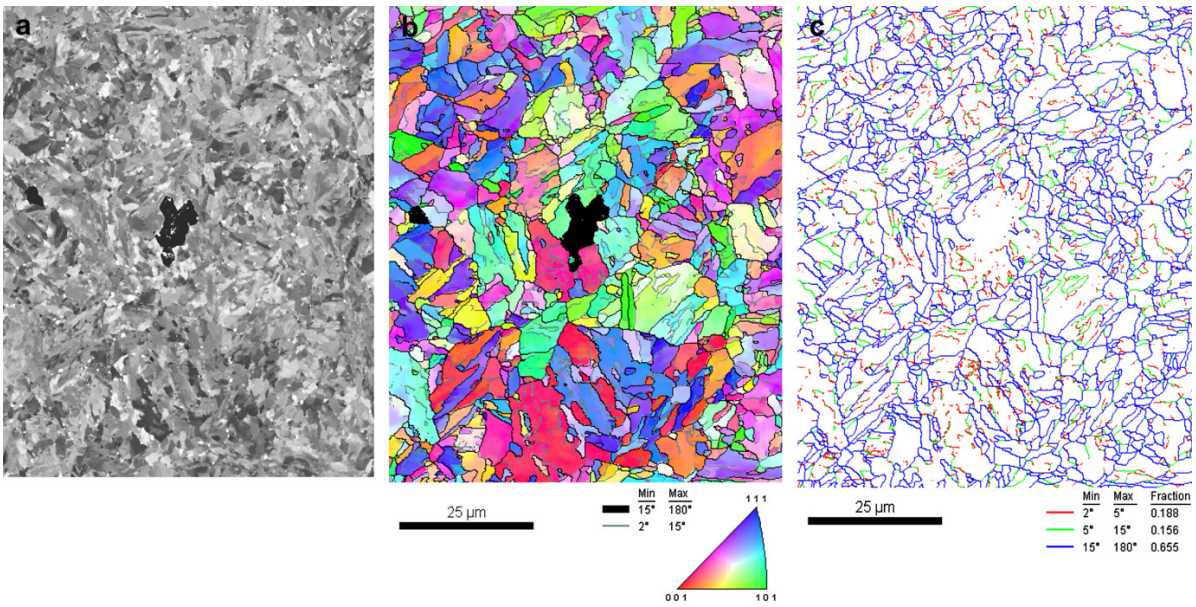

Fig. 10. Microstructure of P91 steel after 113,431 h of creep at 600 °C (25 mm from fracture surface). a) SEM-BSE micrograph; b) Inverse Pole Figure (IPF) with orientation of sample normal in the crystal frame as key colour; c) EBSD Boundary map.

about twenty units lower than the as-received P91 steel. This small decrease is probably due to microstructural evolution (Fig. 3).

The difference in hardness between gauge and specimen head could be due to either the effect of stress on microstructural evolution or damage development, or both. Thus, three states of the microstructure of the P91 steel were investigated:

- the as-received state,
- the head of the creep specimen (stress-free thermal ageing),
- the gauge portion far from fracture surface (microstructural evolution under stress/strain).

6. Microstructural evolution during creep

6.1. Scanning electron microscopy results (Laves phases)

In the as-received state, precipitates are too small to be analysed using SEM. The precipitates that can be seen in Fig. 4a are $M_{23}C_6$ carbides mainly located at boundaries. There are also small MX-type precipitates finely distributed within the martensite laths and Mo atoms in solid solution in the matrix.

After long-term creep, $M_{23}C_6$ carbides have obviously grown (Fig. 4). FEG-SEM investigations revealed precipitation of Laves phases. Small-size precipitates (~40 nm) finely distributed was also observed by FEG-SEM in the crept specimen. They were too small to be identified by FEG-SEM; they could be MX-type precipitates. To study this kind of precipitates, TEM investigations are needed.

The precipitates indicated in Fig. 4b were identified by EDS analysis coupled with FEG-SEM. The large size of some precipitates after long-term creep allowed their chemical identification by EDS analysis (Fig. 4c).

Fig. 5a shows the size distribution of Laves phases after creep. Because Laves phases are enriched in Mo, they can be easily evidenced using BSE images, which are sensitive to the mean atomic number of the probe area. Fig. 5b shows a typical BSE image used for quantification of Laves phases, white spots

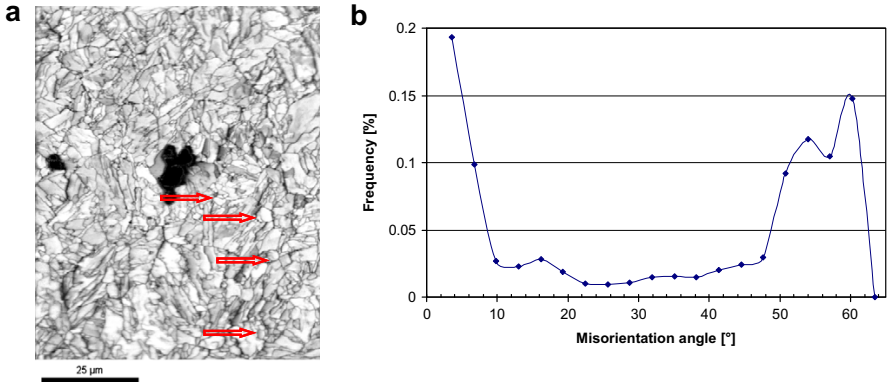

Fig. 11. a) EBSD Image Quality map some equiaxed subgrains are arrowed; b) misorientation angles (b) for EBSD maps in Fig. 10.

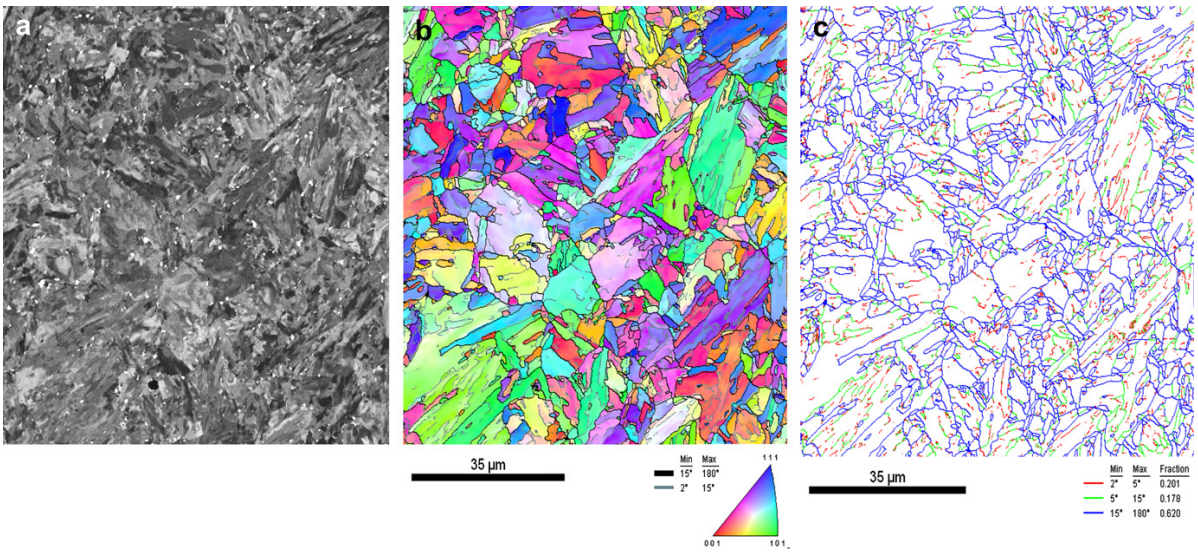

Fig. 12. Microstructure of the P91 steel after 113,431 h of creep at 600 °C (head of the specimen) a) EBSD IPF (same colour key as in Fig. 6a); b) BSE image; c) EBSD Image Quality map.

being Laves phase particles. The precipitation of Laves phases occurs during high-temperature exposure; in the as-received state there are no Laves phases, as can be seen in the micrograph of Fig. 6a.

There is no significant difference between the size of Laves phases in the gauge portion compared to the head portion. The slight difference between curves of Fig. 5a could be due to the scatter of measurements.

6.2. Electron backscatter diffraction results (grain/subgrain structure)

SEM–BSE investigations revealed a significant change in the substructure of the steel after long-term creep, as can be seen from Fig. 6 compared to Figs. 8, 10 and 12.

EBSD maps of the steel in as-received state revealed a typical martensitic matrix with blocks and packets. After creep, EBSD measurements revealed a matrix with more or less equiaxed subgrains (Figs. 8b, 10b and 12b). These subgrains are revealed by both BSE imaging and EBSD mapping. The shape of these subgrains is very elongated in the as-received state (Fig. 7a) and less elongated in the specimen head (Fig. 13a). In the specimen gauge, at 25 mm from the fracture surface, equiaxed subgrains are readily found (arrows in Fig. 11a). Next to the fracture surface, most subgrains are round shaped (Fig. 8).

Subgrain evolution occurred both upon thermal aging (head) and creep deformation (gauge) but probably mostly during fast deformation immediately proceeding fracture. To assess the metallurgical evolution of the creep specimen it is necessary to separately study what occurred during creep deformation (homogeneously deformed area, Fig. 10) and what is due to fast "quasi-plastic" deformation at the end of lifetime (next to fracture area, Fig. 8). First of all, as creep cavities are uniformly distributed along the gauge length (see Fig. 2), it can be concluded that extensive recovery leading to round-shaped subgrains is not necessary to induce premature creep failure.

In addition, small equiaxed grains (a few microns in size) delimited by high-angle boundaries (>15°) were revealed in the EBSD maps (Figs. 8b, 10b and 12b) although they could not be clearly identified by BSE imaging. Such grains were not so obviously detected in the as-received state (Fig. 6) and must have appeared during creep.

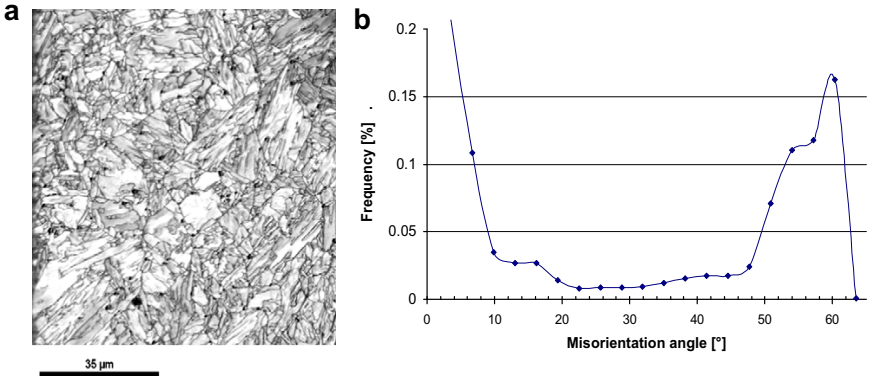

Fig. 13. EBSD Image Quality map (a) and misorientation angles (b) for EBSD maps in Fig. 12.

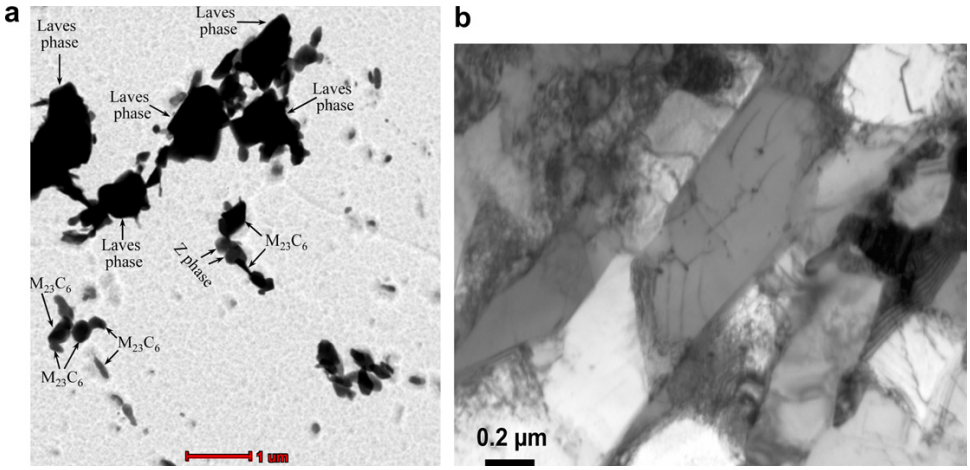

Fig. 14. Microstructure of the steel after creep; a) extractive replica; b) thin foil.

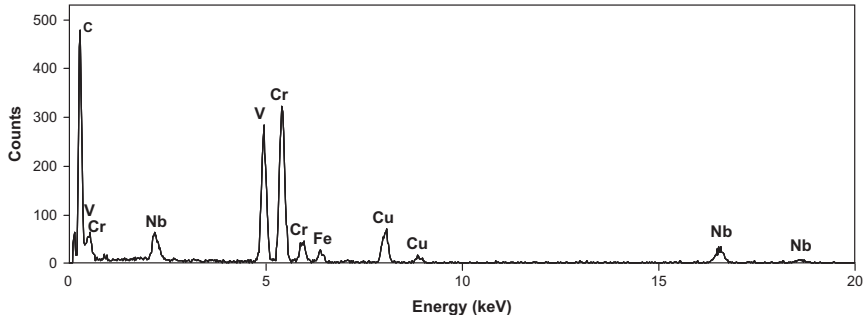

Fig. 15. Typical EDX-TEM spectra for modified Z phase.

Misorientation angle histograms of Figs. 7b, 9b and 11b, 13b showed that while in Figs. 7b, 11b and 13b boundaries between small grains have misorientation angles typical of those between martensite variants from the same parent austenite grain [17,18], this might be not so clearly the case 2 mm from the fracture surface (Fig. 9b). This suggests that some continuous recrystallisation might have occurred close to the fracture surface. This is consistent with dynamic recrystallisation occurring in another P91 steel fractured in tension (10^{-3} s^{-1}) at 625 °C [19]. Getting more information about this phenomenon requires more detailed EBSD data processing that is beyond the scope of this paper.

Note that this phenomenon occurs just before failure and does not influence lifetime.

6.3. Transmission electron microscopy results (modified Z-phase and $M_{23}C_6$ carbides)

The main purpose of TEM investigations was to determine the size and number density of modified Z-phase particles in order to decide how to take into account the influence of this phase on the creep strength of the ASME Grade 91 steel.

As Laves phases are large and relatively scarcely distributed, more representative data on the size of Laves phases can be obtained using SEM (see Fig. 5a). Thus, to determinate the sizes of relative large precipitates such as Laves phases, SEM is better suited [22] because of the possibility of a higher number of precipitates per image, which allows better statistics compared to TEM images.

Table 1
Average chemical composition of modified Z-phase found in the P91 steel after 113,431 h of creep at 600 °C.

	Cr		Fe		V		Nb	
	at.%	wt.%	at.%	wt.%	at.%	wt.%	at.%	wt.%
Min	41.1	34.9	2.1	2.1	30.9	26.4	4.2	7.3
Max	50	47.6	7.7	8.0	45.2	42.5	23.3	35.3
Average	46.5	42.9	3.8	3.8	38.2	34.7	11.3	18.4
Standard deviation	2.2	2.9	1.1	1.1	4.1	4.6	4.6	6.9
Danielsen and Hald [19]	45		5		40		10	

Number of EDX analysis (modified Z-phase particles): 33

Table 2
Synthesis of EDX analysis of $M_{23}C_6$ carbides on single extractive replicas (at.%).

	As received					After 113,431 h of creep at 600 °C				
	Cr	Mo	Fe	Mn	V	Cr	Mo	Fe	Mn	V
Minimum	55.2	0	21.4	0	0	61.4	4.0	11.6	1.0	0
Maximum	67.9	10.7	39.7	7.8	5.6	77.6	11.9	21.4	10.9	1.3
Average	61.2	5.7	27.7	4.8	0.1	70.5	6.8	17.0	5.3	0.1
Standard deviation	2.8	1.6	2.1	2.0	0.6	3.6	1.5	2.0	2.3	0.2

Number of investigated carbides: 128. (as-received) and 120 (after creep).

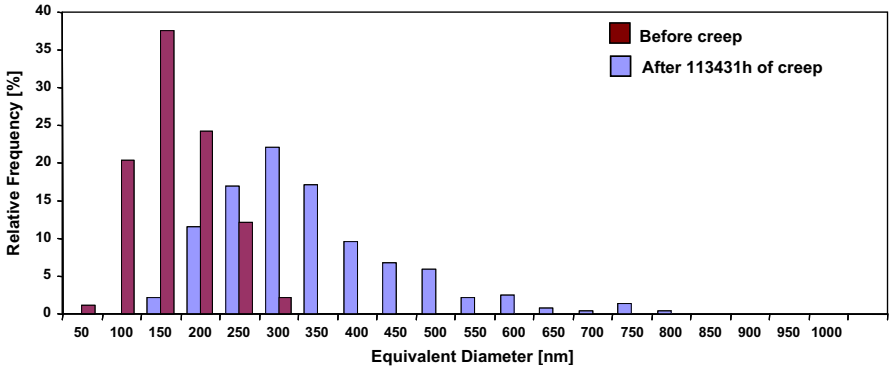

Fig. 16. Size distribution of $M_{23}C_6$ carbides in the as-received P91 steel and after 113,431 h of creep at 600 °C (carbides identified on extractive replicas of precipitates).

However, TEM is better suited to investigation of modified Z-phases, which are frequently located very close to other particles, so that good spatial resolution is needed to analyse them.

TEM is also better suited for the characterization of $M_{23}C_6$ carbides, due to their small size (an average equivalent diameter of 90–100 nm in as-received Grade 91 steel).

6.3.1. Modified Z-phase

Fig. 14a shows typical precipitates in the P91 steel after long-term creep exposure. TEM investigations revealed a low number of modified Z-phase particles compared to the size of the investigated area or the number of investigated precipitates. Only 41 precipitates out of 640 identified precipitates were found to be modified Z-phases. The observed modified Z-phases are large and widely spaced particles with a mean diameter going from 250 nm to 750 nm.

Precipitation of modified Z-phase can put the MX-type precipitates into solution. However, TEM investigations on thin foils of the crept portion revealed dislocations still pinned by MX-type precipitates as shown in Fig. 14b. This suggests that precipitation of modified Z-phase did not have a significant influence on the number density of MX-type precipitates; nevertheless, no quantification of MX-type precipitates was done in this study.

As mentioned above, the identification of modified Z-phase was based mainly on its chemical composition of about ~50 at.% (Cr + Fe) and ~50 at.% (V + Nb) (metal elements only). Fig. 15 shows a typical EDX-TEM spectrum for modified Z-phases. Table 1 summarizes EDX results on modified Z-phases identified on extractive replicas of the creep specimen (gauge portion). The Cr/Fe ratio was uniform with around 46 at.% Cr and 4 at.%. Fe. The V and Nb contents showed large scatter. Danielsen and Hald [20] found similar variations of Cr/Fe ratio and Nb/V ratio in chemical composition of modified Z-phases of various 9–12% Cr martensitic steels.

6.3.2. $M_{23}C_6$ carbides.

Table 2 summarizes EDX results on $M_{23}C_6$ carbides in the as-received state and after long-term creep. A change in average chemical composition of the $M_{23}C_6$ particles after creep can be observed. For metal elements, an increase in Cr content from about 60 at.% to 70 at.% and a decrease in Fe content from about 30 at.% to 20 at.% are observed in the crept specimen.

K. Kimura et al. [21] found the same change in chemical composition of the $M_{23}C_6$ in a Grade 91 steel with an exposure time to creep of 34,000 h at 600 °C. In the as-received state, the chemical composition of the $M_{23}C_6$ determined in this study is similar to those determined in a similar steel [21].

Fig. 16 shows the size distribution of $M_{23}C_6$ carbides identified on extractive replicas by EDX-TEM in the as-received P91 steel and after creep at 600 °C. A growth in size of $M_{23}C_6$ carbides is observed after creep. The average equivalent diameter of $M_{23}C_6$ carbides increases from about 150 to 180 nm to about 300 nm.

7. Conclusions

Quantitative data on the microstructure (both matrix and precipitate) of P91 steel after long-term creep were obtained in this study. After creep for 113,431 h at 600 °C, significant coarsening of existing $M_{23}C_6$ carbides, as well as intensive precipitation of coarse Laves phases and a low amount of modified Z-phases were observed.

The investigated creep specimens showed a significant decrease in hardness on the gauge area and a reduced decrease in the head. Creep damage was observed throughout the gauge area, next to coarse Laves phases.

A significant change in the substructure of the matrix was revealed by EBSD measurements. It was accelerated by creep compared to thermal ageing, but no extensive recrystallisation occurred prior to necking. Dislocation pinning by MX precipitates was still observed in the crept area.

This paper suggests that loss of creep strength is probably mainly due to coarsening of $M_{23}C_6$ carbides, significant precipitation and coarsening of Laves phases and significant recovery of the matrix, rather than to extensive precipitation of modified Z-phase and significant MX dissolution.

Acknowledgments

Authors would like to thank Dr. Ing. Frédéric Delabrouille, from EDF, Renardières for TEM observations on thin foils. Authors will also like to thank Dr. Ing. Mohamed Sennour from Centre des Matériaux for his precious advises with carrying on TEM investigations. Dr. Ing. Francois Grillon from Centre des Matériaux is also acknowledged for kind technical support with conducting EBSD investigations.

References

[1] Rukes B, Taud R. Status and perspectives of fossil power generation. Energy 2004;29:1853–74.
[2] Hald J, Korcakova L. Precipitate stability in creep resistant ferritic steels–experimental investigations and modelling. ISIJ International 2003;43:420–7.
[3] Sawada K, Miyahara K, Kushima H, Kimura K, Matsuoka S. Contribution of microstructural factors to hardness change during creep exposure in mod.9-Cr–1Mo steel. ISIJ International 2005;45:1934–9.

B.1 Complementary data

In this section are given complementary results and details which were not included in the previous article.

The precipitates indicated in TEM images of extractive replicas of precipitates (P91 steel, 113,431h, 600°C) in figure B.2 were identified by EDX-TEM analysis as explained in section VII.1. In figure B.1 are represented the chemical composition of some precipitates in figure B.2d.

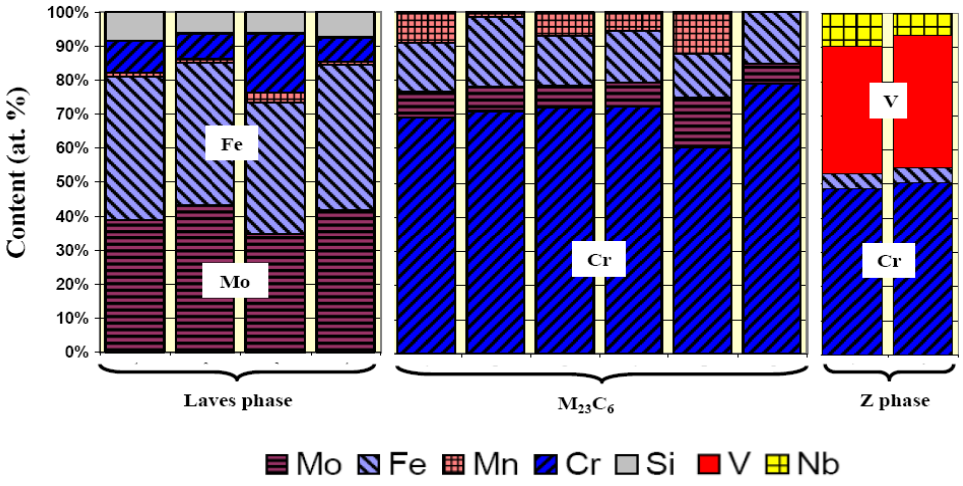

Figure B.1 : Chemical compositions (metallic elements only) of some precipitates corresponding to TEM micrographs of figure B.2d determined using EDX-TEM analysis

Figure B.3a shows an extractive replica of precipitates observed with SEM-FEG and figure B.3b shows the same area of the extractive replicas observed with TEM, bright field. Precipitates in figure B.3b were identified by EDX-TEM analysis. Identification of chemical composition of precipitates by EDX analysis coupled with SEM-FEG could not be possible due to their small size and overlapping of some precipitates on extractive replicas.

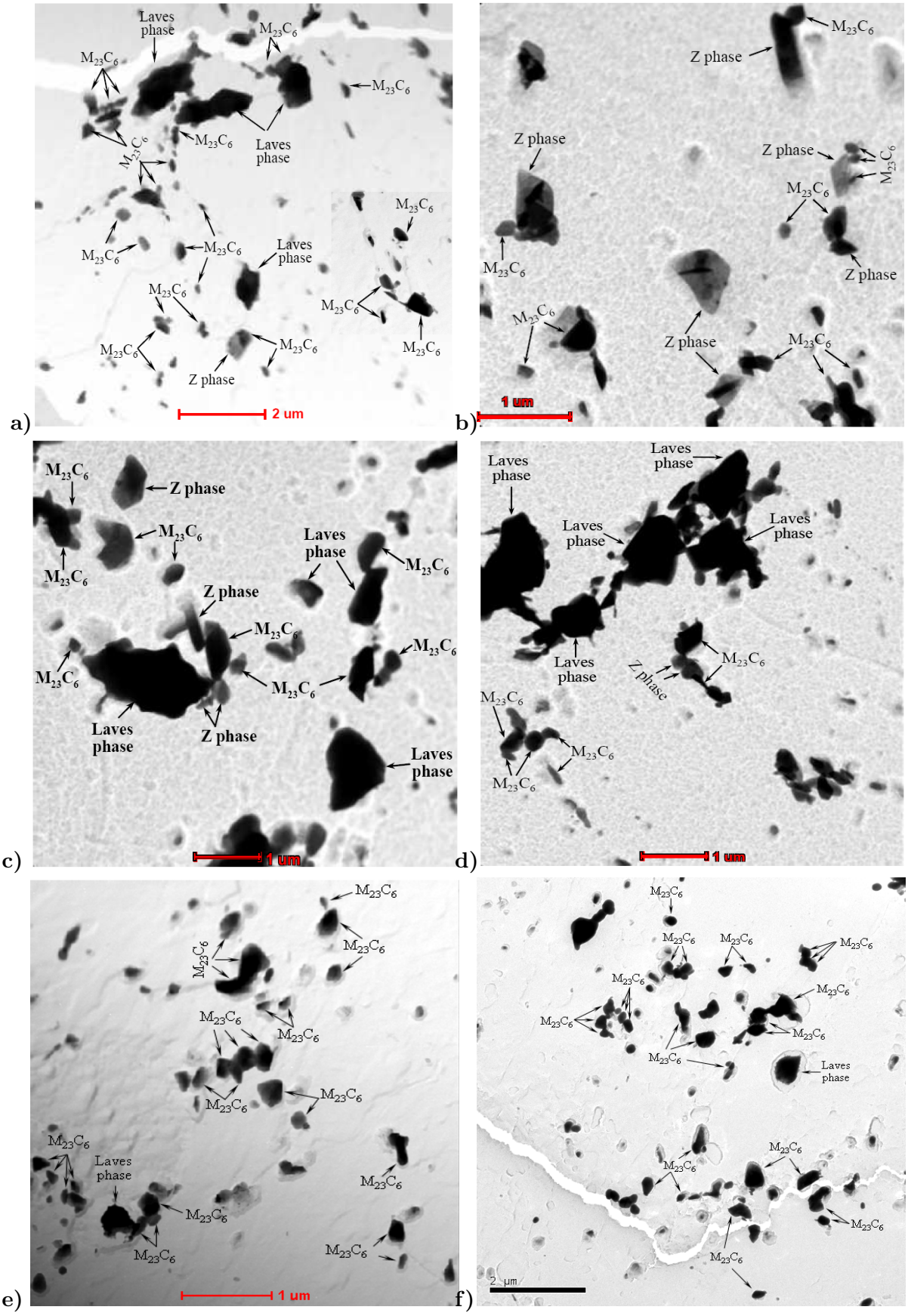

Figure B.2 : Microstructure of the P91 steel creep tested at 600°C for 113,431h (TEM micrographs on extractive replicas of precipitates

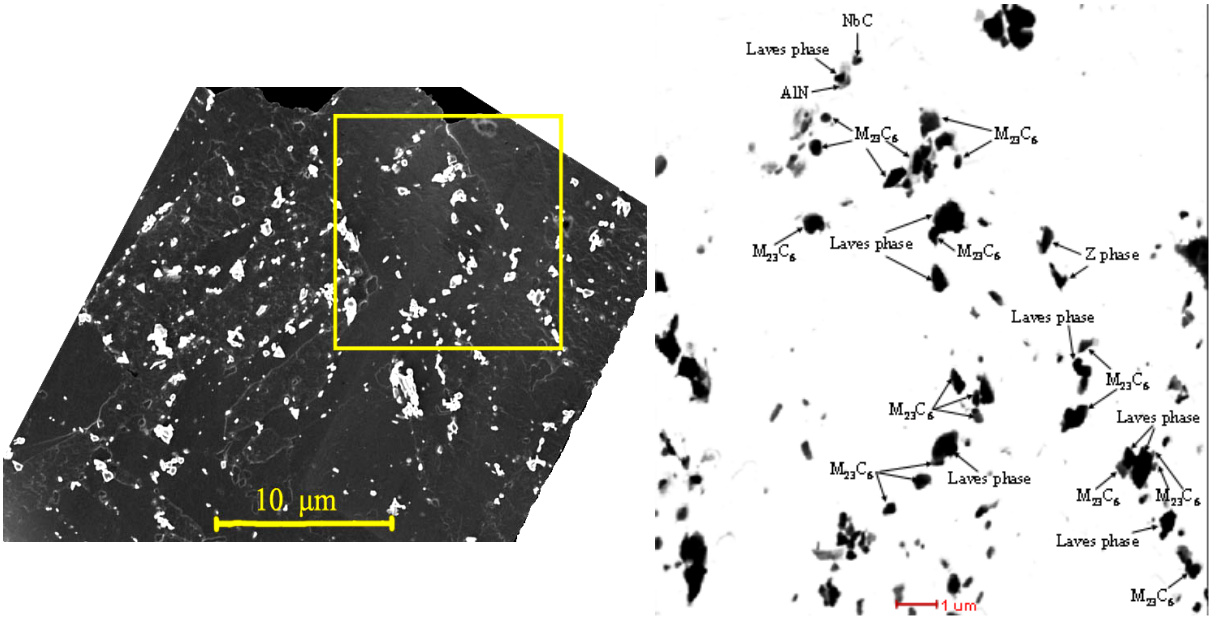

Figure B.3 : Extractive replica of precipitates in P91 steel after 113,431h of creep at 600°C, 80MPa; a) FEG-SEM micrograph; b) TEM micrograph, bright field, same area as that indicated by yellow rectangle in a)

B.1.1 Modified Z-phase (TEM investigations)

The main purpose of TEM investigations was to investigate the modified Z-phase precipitation in the P91 steel after long-time exposure to creep at 600°C and to decide how to take into account the precipitation of this phase on the creep strength loss of the P91 steel.

Low amount of modified Z phase were found in the P91 steel after 113,431h of creep at 600°C. Table B.1 summarizes the size of the investigated area of extractive replicas and number of identified modified Z phase. NPT in table B.1 indicates the number of all precipitates in the investigated area of extractive replicas. EDX analyses were focused on large precipitates (averange diameter higher than 100nm). NPT takes into account small precipitates also.

The equivalent diameter of identified modified Z phase was 200-700 nm. It is to be mentioned that in this crept specimen the equivalent diameters of Laves phases determined by image analysis of SEM-BSE was 200-1200nm. The effect of modified Z phase precipitation on the creep strength loss is probably extremely low compared to that of the significant precipitation of Laves phases (size and number).

Table B.1 : Synthesis of EDX-TEM investigations on the P91 steel creep sample after 113,431h of creep exposure at 600°C, 80MPa

Size of investigated area (μm^2)	Number of identified precipitates (NP)	NP/NPT	Number of EDX analyses	Number of modified Z phase
∼166	∼ 54	54/117	∼210	2
∼196	∼29	29/∼150	36	1
∼50	∼18	18/48	29	1
∼12.5	∼12	12/25	19	1
∼28	∼19	19/44	23	0
∼26.5	∼19	19/34	19	0
∼6.5	∼12	12/28	28	2
∼26	∼31	31/52	53	0
∼26	∼43	43/67	68	2
∼68	∼34	34/76	126	0
∼5.6	8	8/26	12	1
∼95	∼44	44/119	46	1
∼193	∼85	85/217	93	3
∼47	∼36	36/65	50	4
∼49	∼15	15/97	17	2
∼22	∼28	28/32	38	3
∼28	∼26	26/37	47	6
∼41	∼22	22/50	31	4
∼44	∼17	17/66	20	0
∼90	∼41	41/97	79	5
∼43	∼34	34/71	42	3
∼45	∼16	16/81	16	0
TOTAL	**∼643**			**41**

B.1.2 Matrix substructure (EBSD investigations)

An analysis of boundaries between grains respecting K-S and G-T relationships was carried out from the EBSD data of the P91 steel after 113,431h of creep and the results are given in table B.2.

In table B.3 are summarized the fraction of boundaries in several EBSD maps. EBSD investigations revealed a significant decrease in the fraction of boundaries with a rotation angle between 2°-5° in the P91 steel after long-term creep exposure at 600°C compared to that in the as-received P91 steel, see table B.3.

(Aghajani et al., 2009b), (Tak et al., 2009) reported an increase in the fraction of boundaries of ∼ 1° in a 12%Cr steel (grade X20) after creep exposure at 550°C for times higher than 10^5h. Thus, a second processing of EBSD data acquired on the P91 steel creep tested for 113,431h was realized considering a minimum misorientation angle of 1° and the fraction of boundaries corresponding to EBSD maps is reported in table B.4. For this second data processing only the EBSD maps conducted with a step size of 0.15μm were considered to be assure that representative areas of the crept specimens are analyzed. A decrease in the fraction of boundaries of ∼ 1° is observed after long-term creep exposure of the P91 steel. This result is different from that reported by (Aghajani et al., 2009b), (Tak et al., 2009).

Table B.2 : Analysis of boundaries respecting the K-S and G-T relationships in EBSD map

EBSD map	**P91** As-received	**113,431h; 600°C** (15 mm)	**113,431h; 600°C** (25 mm)	**113,431h; 600°C** (2 mm)
Size of area	83.5μm×70.2μm	30.6μm×31μm	73.6μm×86.2μm	91.6μm×88.5μm
Step size	0.15 µm	0.07 µm	0.15 µm	0.15 µm
Observations	figure **??**	figure C.2	figure **??**	figure **??**
Fraction of G-T (K-S) boundaries in EBSD maps				
⟨433⟩ 60.2G-T	19.4	13.4	19.6	12.9
⟨111⟩ 49.6G-T	0.85	1.7	1.06	0.80
⟨331⟩ 50G-T	2.71	4.65	3.88	3.46
⟨433⟩ 50.2G-T	1.92	2.54	2.36	1.88
⟨332⟩ 50.8G-T	4.78	3.96	4.38	2.64
⟨110⟩ 60G-T	3.14	3.49	3.84	1.98
⟨331⟩ 51.9G-T	4.11	7.53	6.56	4.43
⟨110⟩ 54.3G-T	3.33	3.05	4.76	3.55
⟨331⟩ 55.6G-T	4.56	5.81	4.25	4.41
⟨441⟩ 57.5G-T	4.29	4.62	4.13	4.17
K-S type boundary				
⟨111⟩ 60K-S	2.11	0.99	0.86	1.65
⟨432⟩ 57.2K-S	2.39	1.34	2.03	2.55
⟨331⟩ 57.2K-S	6.06	6.48	5.54	5.39
⟨221⟩ 51.7K-S	4.11	5.94	5.15	3.35
⟨322⟩ 50.5K-S	1.14	1.93	1.81	1.14
⟨431⟩ 50.5K-S	1.16	-	1.44	1.76
⟨111⟩ 49.5K-S	0.12	-	0.12	0.06
⟨221⟩ 47K-S	1.12	-	0.94	1.45
⟨110⟩ 49.5K-S	0.17	-	0.08	0.26
⟨110⟩ 60K-S	3.14	-	3.84	1.98

Table B.3 : Analysis of boundaries in EBSD maps

Creep testing conditions	Size of EBSD maps Step size	Boundaries rotation angle	Total length (Fraction)	Observations
P91 steel As-received	90μm×66μm 0.15μm	2°-5°	0.452	
		5°-15°	0.133	
		15°-180°	0.416	
P91 steel As-received	90μm×84μm 0.15μm	2°-5°	0.410	
		5°-15°	0.128	
		15°-180°	0.462	
P91 steel As-received	83μm×70μm 0.15μm	2°-5°	0.453	
		5°-15°	0.132	
		15°-180°	0.416	
P91 steel 113,431h;600°C (25 mm)	77μm×84μm 0.15μm	2°-5°	0.210	figure **??**
		5°-15°	0.162	
		15°-180°	0.627	
P91 steel 113,431h;600°C (head)	77μm×77μm 0.15μm	2°-5°	0.193	
		5°-15°	0.166	
		15°-180°	0.641	
P91 steel 113,431h;600°C (head)	78μm×84μm 0.15μm	2°-5°	0.210	
		5°-15°	0.162	
		15°-180°	0.627	

Table B.4 : Analysis of boundaries in EBSD maps

P91 steel as-received

Map size [μm×μm]	83 × 70	90 × 84	90 × 66	
Step size	0.15μm	0.15μm	0.15μm	
Boundary	Fraction of length boundaries			
1°-2°	0.557	0.555	0.529	
2°-10°	0.258	0.248	0.242	
10°-180°	0.195	0.197	0.229	

P91 steel after 113,431h of creep at 600°C

Map size	(2 mm)	(2 mm)	(25 mm)	(25 mm)	(25 mm)	(head)	(head)	(head)
[μm×μm]	92×83	91×88	73 × 86	70 × 90	77 × 83	77×77	78 ×80	88×81
Step size	0.15 µm	0.15 µm	0.15 µm	0.15 µm	0.15 µm	0.15 µmm		
Obs.								
Boundary	Fraction of length boundaries							
1°-2°	0.472	0.505	0.369	0.360	0.405	0.392	0.405	0.403
2°-10°	0.214	0.212	0.195	0.197	0.196	0.192	0.196	0.201
10°-180°	0.314	0.283	0.436	0.443	0.399	0.416	0.399	0.396

Appendix -C-

Evolution of dislocation density, size of subgrains and MX-type precipitates in a P91 steel during creep and during thermal ageing at 600°C for more than 100,000h

This appendix reproduces an article published in *Materials Science and Engineering: A, vol. 527 (2010) pages 4062-4069*, (Panait et al., 2010b).

This article deals with TEM investigations conducted on thin foils of the P91 steel creep tested for 113,431h at 600°C. TEM investigations were realized at AGH-Krakow (University of Mining and Metallurgy, Krakow Poland).

Complementary data which were not included in the article are given at the end of this appendix.

Materials Science and Engineering A 527 (2010) 4062–4069

Contents lists available at ScienceDirect

Materials Science and Engineering A

journal homepage: www.elsevier.com/locate/msea

Evolution of dislocation density, size of subgrains and MX-type precipitates in a P91 steel during creep and during thermal ageing at 600 °C for more than 100,000 h

Clara Gabriela Panait[b,c,*], Anna Zielińska-Lipiec[a], Tomasz Koziel[a], Aleksandra Czyrska-Filemonowicz[a], Anne-Françoise Gourgues-Lorenzon[b], Walter Bendick[d]

[a] AGH University of Science and Technology, Al. Mickiewicza 30, 30-059 Krakow, Poland
[b] MINES ParisTech, Centre des Matériaux, CNRS UMR 7633, BP 87 91003 Evry Cedex, France
[c] Vallourec Research Aulnoye, Route de Leval, B.P. 20149, 59620 Aulnoye-Aymeries, France
[d] Salzgitter Mannesmann Forschung GmbH, Ehinger Straße 200, D-47259 Duisburg, Germany

ARTICLE INFO

Article history:
Received 26 September 2009
Received in revised form 1 March 2010
Accepted 2 March 2010

Keywords:
Dislocation density
MX-type precipitates
P91 steel
Subgrains
Creep

ABSTRACT

There are rather few quantitative data on the microstructure of the 9–12%Cr heat resistant steels after long-term creep. This paper presents results of the quantitative measurement of the size of MX precipitates, subgrain size and dislocation density in a P91 steel that had been creep tested for 113,431 h at 600 °C. The same measurements were conducted in the same P91 steel in the as received conditions.

Transmission electron microscopy investigations were conducted using thin foils and revealed a decrease in dislocation density and an increase in subgrain size after creep exposure. MX carbonitrides are very stable during thermal and creep exposure of P91 steel at 600 °C up to 113,431 h.

Electron backscatter diffraction (EBSD) investigations also revealed a significant change in the substructure of the steel after creep exposure.

1. Introduction

9–12% chromium heat resistant steels are used for high temperature applications, in particular in fossil and nuclear power plants. In service, under high temperature (500–600 °C) there is a microstructural evolution of these steels such as precipitation of new secondary phases (Laves phase, modified Z-phase), growth of precipitates and recovery of the tempered martensite matrix. After long-term exposure this may impair the mechanical properties, including creep strength. A better understanding of the long-term microstructural evolution under creep or thermal exposure can be a key for the improvement of these heat resistant steels.

The creep strength of P91 steel combines some solid solution strengthening by Mo atoms as well as precipitation strengthening by MX precipitates and $M_{23}C_6$ carbides. In the 9–12%Cr tempered martensitic steels, including P91 steel, carbide-stabilised substructure strengthening is considered as the most significant creep strengthening mechanism [1,2].

There are rather few quantitative data [3,4] on the size of precipitates ($M_{23}C_6$ carbides, Laves phase, MX) for the Grade 91 steel after long-term creep exposure at 600 °C. Cipolla et al. [4] reported an increase in the diameter of $M_{23}C_6$ carbides from about 100 nm to 120 nm in the as received steel to about 250 nm, as well as a mean diameter of about 400 nm for the Laves phases after creep exposure at 600 °C for almost 60,000 h. The growth rate of Laves phases is very high in the first 10^4 h [4,5]. The evolution of the matrix substructure (subgrains, dislocation density) during creep of this steel was scarcely investigated [6–8]. A preferential recovery of the microstructure in the vicinity of prior austenite grain boundaries was reported after 34,141 h at 600 °C [6,9,10]. To the authors' knowledge there are no quantitative data on the size of subgrains, dislocation density and MX-type precipitates in the Grade 91 steel after more than 10^5 h of creep or thermal aging exposure at 600 °C.

P91 steel belongs to the family of 9–12%Cr tempered martensitic steels and similar evolution of subgrains, dislocation density are expected to happen during long-term creep exposure. The purpose of this paper is to report quantitative data on the microstructural evolution of this steel during long-term creep exposure and thus to enrich the scarcely published data on this issue.

Microstructural evolution of a 12%Cr tempered martensite steel (German Grade X20) during long-term aging and creep was investigated using interrupted creep tests loaded for 12,456 h,

* Corresponding author. Tel.: +33 0 1 60 76 30 49; fax: +33 0 1 60 76 31 50.
E-mail address: clara.panait@ensmp.fr (C.G. Panait).

0921-5093/$ – see front matter © 2010 Elsevier B.V. All rights reserved.
doi:10.1016/j.msea.2010.03.010

51,072 h, 81,984 h and 139,971 h (ruptured) at 550 °C under 120 MPa [11–13]. Coarsening of subgrains, loss of the correlation between carbides and subgrain boundaries and an increase in the fraction of low-angle boundaries were reported recently [11–13]. The interaction between the free dislocations with particles and subgrain boundaries was described for instance in refs. [14,15].

The present study is a part of a comprehensive characterization of a P91 steel specimen crept at 600 °C, 80 MPa for 113,431 h including evaluation of precipitation, subgrain and dislocation density. $M_{23}C_6$ carbides, Laves phases and Z-phase precipitation as well as creep damage in that specimen were already investigated using transmission electron microscopy on extractive replicas and scanning electron microscopy [16]. The equivalent diameter of $M_{23}C_6$ carbides increases from about 150 nm in the as-received state up to 300 nm after creep. The size distribution of Laves phases after creep exposure was measured and a mean diameter of 400 nm was observed. Only a few particles of the modified Z-phase after 113,431 h of creep at 600 °C were reported [16]. Creep damage was observed throughout the gauge area of the specimen, quantitative data on the size and number of cavities along specimen axis are given in Ref. [16]. Compared to the as-received steel (230 HV0.5), the crept specimen showed a lower hardness of 200 HV0.5 in the gauge area and 220 HV0.5 in the head of the specimen. The decrease in hardness during both long-term exposure to creep and to thermal aging is an indication of microstructural evolution and creep damage development.

To complete the characterization of microstructural evolution and deformation mechanisms in that specimen, the present study is devoted to both MX precipitates and recovery (change in dislocation density and/or in subgrain size) of the tempered martensite matrix, as well as their impact on the creep deformation resistance.

2. Experimental procedure

2.1. Materials and creep behavior

The P91 steel was delivered by Salzgitter Mannesmann Forschung GmbH as a pipe, 121 mm in outer diameter and 20 mm in wall thickness. The chemical composition (wt.%) is as follows: 0.1C; 0.36Si; 0.41Mn; 0.015P; 0.003S; 0.059N; 0.022Al; 8.43Cr; 0.92Mo; 0.04Cu; 0.068Nb; 0.11Ni; 0.20V. The pipe was subjected to the following heat treatment: austenitisation at 1050 °C/1 h/air cooling followed by tempering at 730 °C/1 h and 750 °C/1 h/ air cooling.

The creep test was carried out at 600 °C under constant load corresponding to an initial tensile stress of 80 MPa. The investigated crept specimen exhibited an elongation of 7.3%, reduction of area of 37% and a rupture time of 113,431 h.

Creep data in Fig. 1 show that the minimum strain rate, e.g. 1.1×10^{-5}%/h (i.e. $3.06 \times 10^{-11} s^{-1}$) is achieved after almost 30,000 h (Fig. 1b) and corresponds to a strain of ~0.8% (Fig. 1c). Thus, this specimen shows similar minimum creep rate at similar strain and creep time compared to that investigated in Ref. [12] (i.e. X20 steel, 550 °C, 120 MPa, fracture time almost 140,000 h, minimum creep rate of $3 \times 10^{-11} s^{-1}$ at a strain of ~1% , creep time ~30,000 h). Less than 4% of strain was measured after 10^5 h. Due to the difference in test temperature and chemical composition the underlying microstructural evolution of the two steels is different (e.g. size distribution of Laves phases at least [12,16]).

Fig. 2 shows the microstructure of the as received P91 steel, which consists of tempered martensite with carbides and carbonitrides precipitates. Boundaries between prior austenite grains, packets, blocks, laths are mainly decorated with $M_{23}C_6$ carbides (M = Cr, Fe, Mo); some of them are underlined with arrows in Fig. 2a. The MX carbonitrides (M = V, Nb and X = C, N) precipitated finely

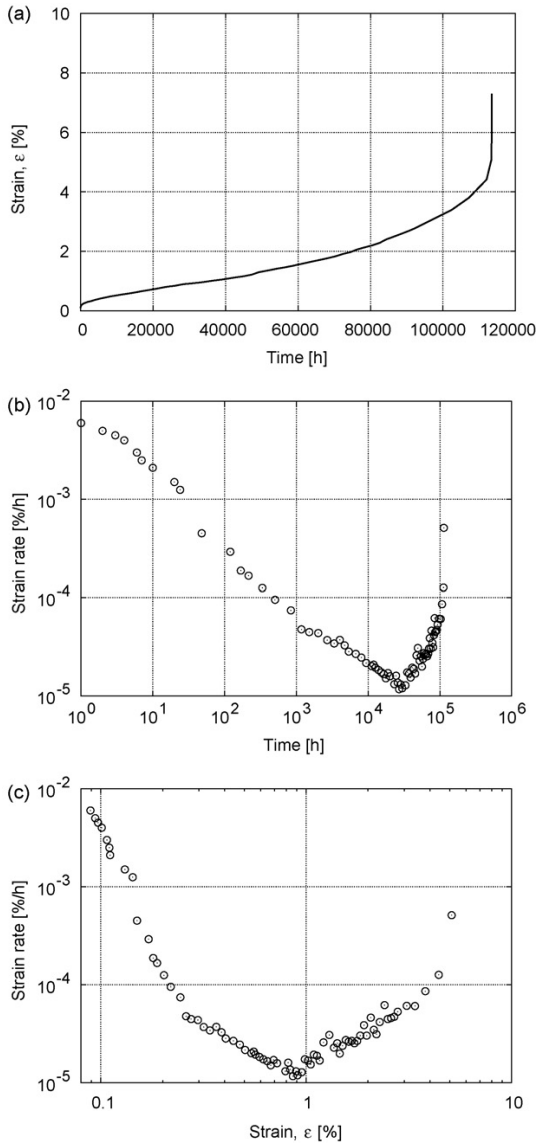

Fig. 1. Long-term creep data for the investigated P91 steel specimen (80 MPa, 600 °C). (a) Creep strain as a function of time; (b) strain rate as a function of time; (c) strain rate as a function of strain.

and with a high number density within the laths. A high dislocation density is observed inside subgrains (Fig. 2b).

2.2. Transmission electron microscopy (TEM) investigations

The TEM investigations were performed using a JEOL JEM 200CX equipped with an energy dispersive X-ray spectrometer (EDS). Thin foils for microstructural investigations after creep test were taken from the head (examined as a thermal exposed steel) and from the gauge length (examined as a creep deformed steel) of the specimen at a distance of 20 mm from the fracture surface, well within the homogeneously deformed part of the specimen. They were electrolytically thinned in a solution of 95% acetic acid and 5% perchloric acid.

Quantitative microstructural characterization was realized using the ImageJ 1.38X commercial software. The MX precipitates

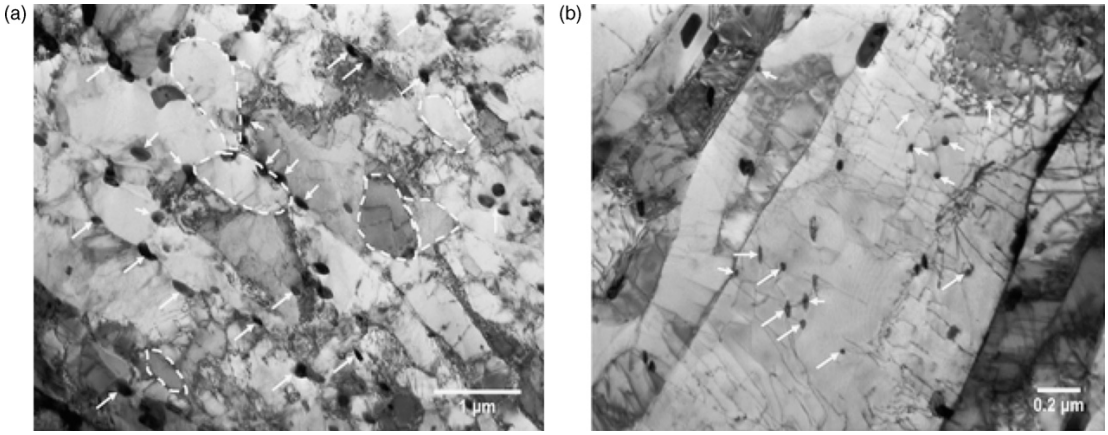

Fig. 2. Bright-field transmission electron micrographs of the as received P91 steel. Arrows indicate $M_{23}C_6$ carbides (a) and MX precipitates (b). Some subgrains are underlined with dotted lines in (a).

and subgrains were manually indicated on TEM bright field images. For illustration some subgrains are indicated with dotted lines in Fig. 2a. Two values of parameters of the MX precipitates (resp. subgrains) were determined namely the equivalent circle diameter (*ECD*) and the mean diameter (*D*) of precipitates (resp. subgrains) by using the following formulas:

$$ECD = 2\sqrt{\frac{A}{\pi}}; \qquad D = \frac{P}{\pi} \tag{1}$$

where *A* is the precipitate (or subgrain) area and *P* is the precipitate (or subgrain) perimeter. A shape coefficient (*f*) was also calculated for the MX-type precipitates and subgrains:

$$f = 4\pi\frac{A}{P^2} \tag{2}$$

A value of 1 for the shape coefficient indicates a circular shape. For each kind of measurements, about ten TEM images were used at several magnifications going from 7000× and 10,000× (for subgrain microstructural characterization) to 37,000× and 50,000× (for quantification of MX-type precipitates and dislocations). The MX-type precipitates were identified using both selected area electron diffraction and EDS. For the acquisition of TEM images used for subgrain characterization, the bright-field image contrast was optimized to reveal subgrain boundaries instead of revealing dislocations or MX-type precipitates.

The average dislocation density (ρ) within the subgrains (i.e. so-called free dislocations), was determined using a mean linear intercept method (recommended and first used by [17]) on TEM images with optimized contrast using the following equation:

$$\rho = \frac{2X\sum_i n_i}{e\sum_i l_i} \tag{3}$$

with *e* the measured thickness of the thin foil, n_i the number of intersections between segment number *i* and a dislocation, *X* a factor introducing the proportion of invisible dislocations of $(a/2)\langle 1\ 1\ 1\rangle$ Burgers vectors in various reflection conditions (its value was estimated to be 2 for all the TEM images) and l_i the length of segment *i*.

The mean linear intercept method consists in overlapping a grid of horizontal and vertical lines on subgrains and counting the intersections of dislocations with grid lines. The number of vertical and horizontal grid lines is adjusted in relation with the size and shape of subgrains in such a way to keep a constant grid spacing while avoiding including boundaries. This method has already been used to evaluate dislocation density, see for instance Refs. [8,15,18,19].

2.3. Electron backscatter diffraction (EBSD) investigations

Electron backscatter diffraction (EBSD) maps were acquired from the longitudinal cross-section of the creep specimen at 20 mm from the fracture surface and from the steel in the as-received condition with a ZEISS DSM 982 Gemini Shottky field emission gun (FEG) SEM equipped with a Hjelen-type camera and TSL OIM facilities. Acquisition and indexation of diffraction patterns were realized using dedicated softwares such as NORDIF 1.3.0 and TSL OIM Data Collection 5.2, respectively. EBSD measurements were conducted with step size of 40 nm and 150 nm at 20 kV, working distance 19 mm, tilt angle 70°, aperture 120 μm, probe current between 0.1 nA and 1 nA.

The EBSD maps were acquired together with a backscattered electron (BSE) image (taken at 0° specimen tilt), where the contrast is highly sensitive to the crystallographic orientation of the sample normal (i.e. of the primary electron beam). Laves phases, enriched in Mo, are also clearly visible in the BSE mode as bright precipitates in a dark matrix thanks to their high average atomic number.

The first map to be obtained is the *image quality* map, which reports, for each analysis, the ability of the software to detect the diffraction bands. The brighter the gray level in that map, the better the diffraction conditions. Image quality is sensitive to the crystal orientation, as well as to the *channelling effect* that yields the BSE image contrast. In addition, image quality is very sensitive to crystal defects such as dislocations. As soon as dislocations are clustered somewhere, the EBSD pattern quality decreases. Thus, the image quality map is very sensitive to the presence of boundaries, even for very low angle boundaries (*LABs*). Tak et al. [13] investigated the microtexture evolution of a X20 steel after long-term exposure considering a minimum misorientation angle of 1°. In our investigated samples the density of *LABs* with a misorientation of ∼1° was so high that we were not able to distinguish *true LABs* from measurements artefacts. Thus, a minimum misorientation angle of 2° was considered to process the EBSD data.

The inverse pole figure (IPF) map is color-coded according to the orientation of a given direction of the sample in the crystal frame. The color key is recalled next to each IPF map. Note that the color is not sensitive to any rotation about that given direction of the sample, so that two IPF maps are generally needed to discriminate between grains.

In addition to IPF, one may calculate the misorientation between neighboring pixels and assign a color code to any pair of pixels whose misorientation meets a given criterion. This helps investigations whether a *boundary* imaged in the image quality maps corresponds to a high or to a low misorientation, or even to negligible misorientation between neighboring crystals. This is particularly useful to investigate subgrain boundaries. In all maps, the color code for boundaries is recalled according to the misorientation angles.

3. Experimental results

3.1. Transmission electron microscopy investigations

3.1.1. Dislocation density

The dislocation density measured after thermal exposure and after creep deformation is shown in Table 1. The values are higher than those found for tempered P91 steel in Ref. [8]. Nevertheless, in the crept material, the dislocation density is about twice lower than that of the as received material (Table 1). Still a rather high dislocation density can be observed after such a thermal exposure, Fig. 3.

The dislocation density measured in the crept material is almost 10 times higher than that predicted by the well-known relation of material science ($\rho < (\sigma/bG)^2 \approx 2.5 \times 10^{13}\ \mathrm{m}^{-2}$) but corresponds to values of dislocation density reported for the 9–12%Cr tempered martensitic steel after creep exposure at 600–625 °C [20,21].

The dislocation density of the specimen after thermal exposure is almost the same as in the creep deformed sample. This suggests that creep deformation in the case of dislocation creep and static recovery during thermal exposure influenced in the same manner the dislocation density whithin subgrains. This results strongly differs from that of Ref. [12], were a 2-fold decrease in dislocation density was found after thermal exposure and a more than 10-fold after creep. Note, however, that the initial dislocation density ($\cong 10^{14}\,\mathrm{m}^{-2}$) was lower and the test temperature also lower than in the present study.

Dislocations whithin subgrains (i.e. mobile dislocations) are carriers of plastic deformation under creep conditions and the creep rate ($\dot{\varepsilon}$) is a function of the mean dislocation velocity (v) and the density of mobile dislocations (ρ) as follows [22]:

$$\dot{\varepsilon} = \frac{\rho b v}{M} \tag{4}$$

where b is the Burgers vector and M is a Taylor factor. Considering the minimum creep rate of the specimen, e.g. $1.1 \times 10^{-7}\ \mathrm{h}^{-1}$, the measured dislocation density in the gauge part and $b = 0.254$nm, $M = 3$ from Ref. [22], a mean dislocation velocity of 2×10^{-15} m/s is obtained. This value is much lower than the dislocation velocity of 2.3×10^{-3} m/s evaluated by in-situ TEM observations in a Fe–Mo alloy (0.001C–1.2Mo–0.02N–0.4Si, wt.%) at 738 °C, under a stress actiong on dislocations of 5.3 MPa [23]. This is probably mainly due to different testing temperatures and different levels of stress.

The density of mobile dislocations was also used to assess the solid solution strengthening effect of Mo atoms, by using the formula given in [22]

$$\sigma^* = \frac{M\dot{\varepsilon}}{\rho b B} \tag{5}$$

where σ^* is the backstress due to solid solution strengthening; $\dot{\varepsilon}$ is the minimum creep rate and B is the dislocation mobility. There are several possibilities for assigning a value to B based on the work of Terada et al. [23] on Fe–Mo alloys. By using their Fig. 10 for $T = 600$ °C and a Mo content of 0.53 at.% one gets $B = 10^{-16}\ \mathrm{mPa}^{-1}\ \mathrm{s}^{-1}$ (with the curves corresponding to 0.5 at.%Mo and their numerical simulation) and $B = 4 \times 10^{-17}\ \mathrm{mPa}^{-1}\ \mathrm{s}^{-1}$ (if following the curve corresponding to 2.0 at.%Mo and the experimental value found for 0.7 at.%Mo). These values can reasonably be taken as two extreme possible values for B after Terada et al. [23]. This is much higher than the value taken by Hald [22] in his calculations for a P92 steel.

By taking $M = 3$, $\rho = 1.8 \times 10^{14}\ \mathrm{m}^{-2}$, $b = 2.54 \times 10^{-10}$ m and $\dot{\varepsilon} = 3.06 \times 10^{-11}\ \mathrm{s}^{-1}$ and the extreme values of B one finds that σ^* should range between 2×10^{-5} MPa and 5×10^{-5} MPa. Note that taking for B the same value as Hald did yields a value of 8×10^{-3} MPa. Thus if following Hald's approach [22], whatever the value taken for the density of mobile dislocations (experimental values or above mentioned theoretical value of $2.5 \times 10^{13}\,\mathrm{m}^{-2}$) within the range used here, solid solution strengthening by Mo is found to be negligible and Mo depletion due to precipitation of Laves phases should not be considered as the major microstructural evolution affecting creep strength.

However, one must keep in mind that short-term thermal aging (about 10^4 h) is known to decrease the creep strength of this family of steels [24], while mainly affected by precipitation of dissolved W into Laves phases [25]. Thus the role of W in the creep resistance is not fully understood. Nevertheless, one has also to consider two other possibilities for material softening i.e. loss of pining effect by MX precipitates and subgrains size evolution.

3.1.2. MX-type precipitates

The MX carbonitrides (M = Nb, V, Cr; X = C, N) are homogeneously distributed within the martensite laths. The MX

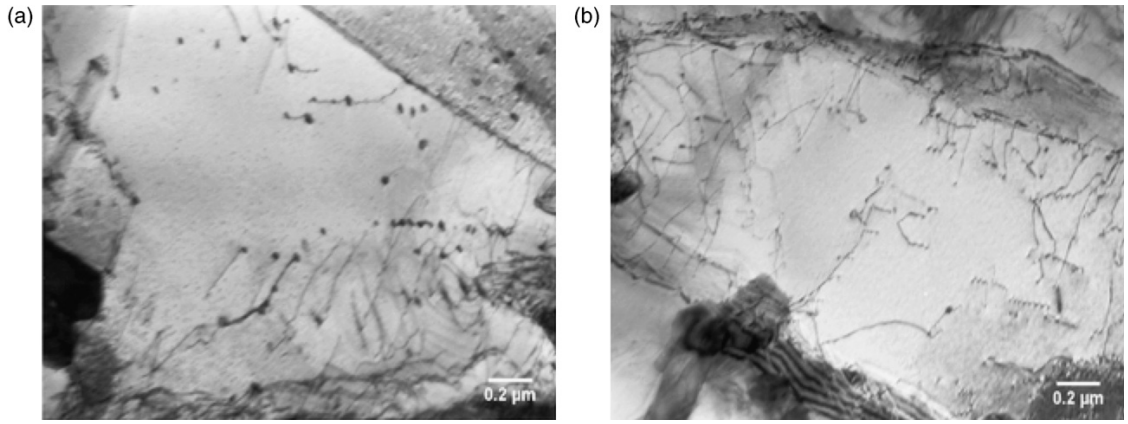

Fig. 3. Microstructure of (a) the gauge length (creep tested) and (b) the head (thermal exposure) showing dislocations pinned by MX-type precipitates.

Table 1
Dislocation density measured on TEM thin foils

	As-received	After 113,431 h of creep at 600 °C	
		Head	Gauge length
Dislocation density	$4.5 \pm 1.9 \times 10^{14}$ m^{-2}	$2.2 \pm 1.3 \times 10^{14}$ m^{-2}	$1.8 \pm 1.7 \times 10^{14}$ m^{-2}

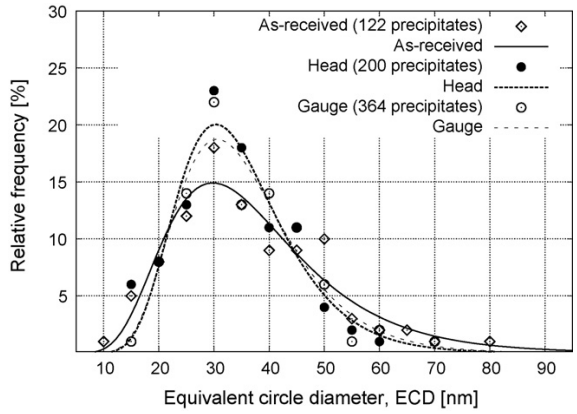

Fig. 4. Size distribution of MX precipitates in all three materials from TEM image analysis experimental results (symbols) compared with a lognormal fit (lines).

carbonitride precipitation only occurs during tempering. The size of MX carbonitrides is of about 20–40 nm. These precipitates are very stable against coarsening at temperatures below 650 °C [22,26–28], yet for exposure time lower than 10^5 h.

In the 9–12%Cr tempered martensite steels there are generally two types of MX precipitates: MX enriched in Nb with a spherical shape, MX enriched in V with a plate-like shape [18]. Low amount of the MX particles with a more complex *V-wings* shape (a Nb-rich particle with V-rich *wings*) are also observed. The MX precipitates enriched in Nb (mainly NbC) are very stable at high temperature. It was reported that in P91 steel the number of these precipitates that are not dissolved after austenitisation decreases with an increase in the austenitisation temperature [29]. In this study all three types of MX-type precipitates were quantified together.

No significant effect of either thermal or creep exposure at 600 °C for 113,413 h was detected on the size distribution of MX-type precipitates (Fig. 3). The three distributions of particles size were in good agreement with lognormal curves. The small difference between the three histograms of Fig. 4 is the lack of very fine particles (the lowest *ECD* value) after creep or thermal exposure. It might be caused by coarsening of these particles during thermal and creep exposure or by the presence of low amount of modified Z-phase which was reported in Refs. [16,30]. Modified Z-phase precipitation may put into solution smaller MX precipitates [20,31,32], this could be a reason why MX precipitates with an equivalent diameter lower than 15 nm were not observed after creep or thermal exposure. However, in the as received condition the number density of these MX precipitates is extremely low and after creep exposure the modified Z-phase was observed in low amounts [16] so that the apparent difference between the three histograms could also be due to sampling effects. This is also the case for the upper end of the size distribution. Thus, as already found in literature [16], it can be concluded that modified Z-phase precipitation does not have a significant influence on the distribution of MX precipitates.

No significant change in the shape coefficient of MX precipitates was detected either after long-term creep or thermal exposition. The shape coefficient is almost constant, indicating elongated precipitates. In summary, no significant evolution of MX precipitates was evidenced after long-term creep at 600 °C for this P91 steel specimen.

3.1.3. Subgrain size

After creep, most subgrains have a polygonal shape as shown in Fig. 5. Significant growth of subgrains is observed in the gauge part of the specimen (Figs. 5b and 6). In the head of the specimen, some growth was also observed, but not as pronounced as in the gauge part (Fig. 6). The size distribution of subgrains in the as-received steel, in thermally exposed and in creep deformed steel shows that the most significant growth of subgrains took place in the crept material, which indicates that deformation during the creep test has a significant influence on the growth of subgrains. This is confirmed by other studies [33,34].

No preferential recovery of the matrix (growth of subgrains) was observed in the vicinity of prior austenite grains boundaries as reported in Ref. [6]. It is to be mentioned that using TEM techniques it is rather difficult to distinguish prior austenite grain boundaries from block or packets martensite boundaries.

Good agreement was found when comparing the experimental results (*ECD*) with the evolution law of subgrain sizes in the same

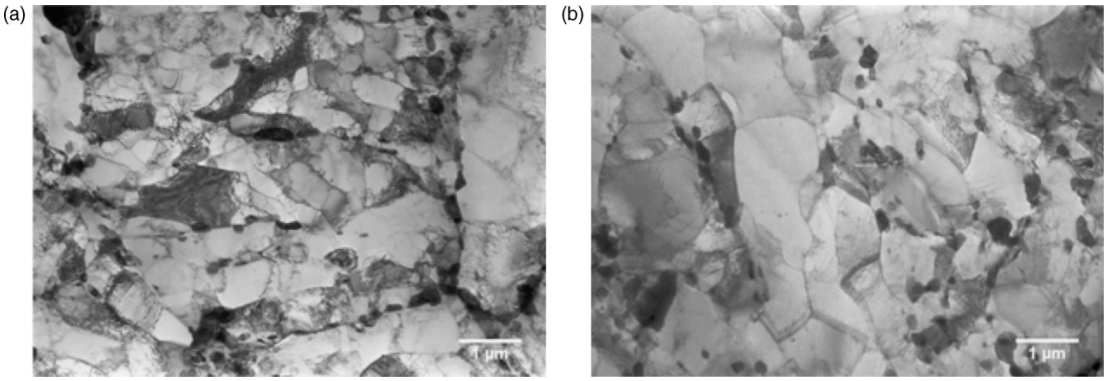

Fig. 5. Microstructure of the P91 steel after creep at 600 °C showing polygonised subgrains a) head and b) gauge length.

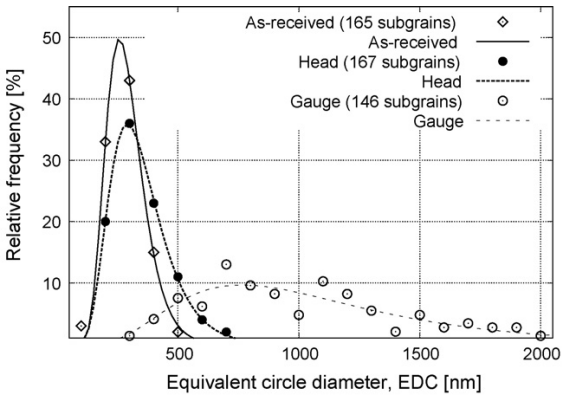

Fig. 6. Size distribution of subgrains in the as received, thermally aged and crept materials (TEM image analysis). Experimental results (symbols) compared with a lognormal fit (lines).

manner as done by Qin et al. [35]:

$$\log\ \lambda = \log\ \lambda_\infty + \log\left(\frac{\lambda_0}{\lambda_\infty}\right)\exp\left(\frac{-\varepsilon}{k(\sigma)}\right) \quad (6)$$

where λ represents the subgrain size, λ_0 is the subgrain size before creep exposure, $\lambda_\infty = 10\left[Gb/\sigma\right]$ is the steady-state subgrain size [35,36] where G is the shear modulus, b is the Burgers vector, σ is the applied stress), ε is the accumulated strain and $k(\sigma) \approx 0.12$ is a growth constant.

Eq. 6 suggests that subgrain growth requires strain and this is in agreement with results presented in Figs. 5 and 6 where subgrain size increases during long-term creep exposure while it is slightly affected by the long-term aging. Eq. 6 was applied in previous studies on the size evolution of subgrains during creep of 9–12%Cr tempered martensitic steels [3,12,37,38].

Note that only average values of λ and ε are used together with the macroscopically applied stress, although local values of ε and σ may strongly differ from average ones. With $\lambda_0 = 320$ nm, $G = 65$ GPa [12], $b = 0.254$ nm, $\sigma = 80$ MPa, one finds $\lambda_\infty = 2.06$ μm. As the amount of strain in the homogeneously deformed part is not known, it has to be bounded by (upper bound) the fracture strain ($\varepsilon_f = 0.07$) and (lower bound) the strain corresponding to the minimum creep rate $\varepsilon_{min} = 0.01$. A typical value could be the strain at onset of final acceleration of creep (about 0.04 from Fig. 1a). By taking these three values one finds $\lambda = 0.729$ μm ($\varepsilon = 0.07$), $\lambda = 0.543$ μm ($\varepsilon = 0.04$) and $\lambda = 0.371$ μm ($\varepsilon = 0.01$), respectively. These values have to be compared to the experimental data of Fig. 6 and the mean value of subgrain size in that part of the crept specimen, namely, about 1 μm for *ECD* and 1.26 μm for *D*. Thus, Eq. (6) leads to an underestimation of the average subgrain size after long-term creep of our specimen.

The sugrain size, λ, in Eq. (6) represents the mean linear subgrain intercept [35] which differs from the subgrain diameter by a geometrical factor <1 which can be approximated from $\pi(D/2)^2 = D\lambda$, thus $\lambda = 0.785D$. This last relation could explain the difference between the subgrain size, λ, corresponding to $\varepsilon = 0.07$, predicted by Eq. (6) and the subgrain size experimentally evaluated (i.e. $ECD = 1$ μm).

3.2. Electron backscatter diffraction (EBSD) investigations

Besides TEM image analysis, SEM-BSE investigations also revealed, in a much wider field of view, a change in the substructure of the matrix. Fig. 7a compared to Fig. 7b. Fig. 7a and the corresponding inverse pole figure (IPF), Fig. 8a, show a typical tempered martensite matrix with blocks and packets in the as received P91 steel. The BSE image and the corresponding IPF image in Figs. 7b and 8b reveal a microstructure with polygonal shaped subgrains after creep.

In this study orientation imaging microscopy (OIM) with a step size of 40 nm was conducted on the as received steel and on the longitudinal cross-section of creep specimens, at 20 mm from fracture surface to get information about the crystal orientation of subgrains similar to those observed in TEM micrographs. Tak et al. [13] showed that high resolution OIM with a step size of 10 nm can reveal features that are usually only observed using TEM. Indeed, image quality (IQ) maps show close resemblance with TEM micrographs. Contrast of IQ image is very sensitive to the defects in the crystal such as dislocations, boundaries. IQ images in Fig. 8c and d reveal the existence of some subgrains with a very low misorientation angle. For illustration the subgrains arrowed on the IQ images of Figs. 8c and d are not recognized as individual subgrains with a specific orientation in the IPF map, this is due to a misorientation between the subgrain and the neighboring crystal that was lower

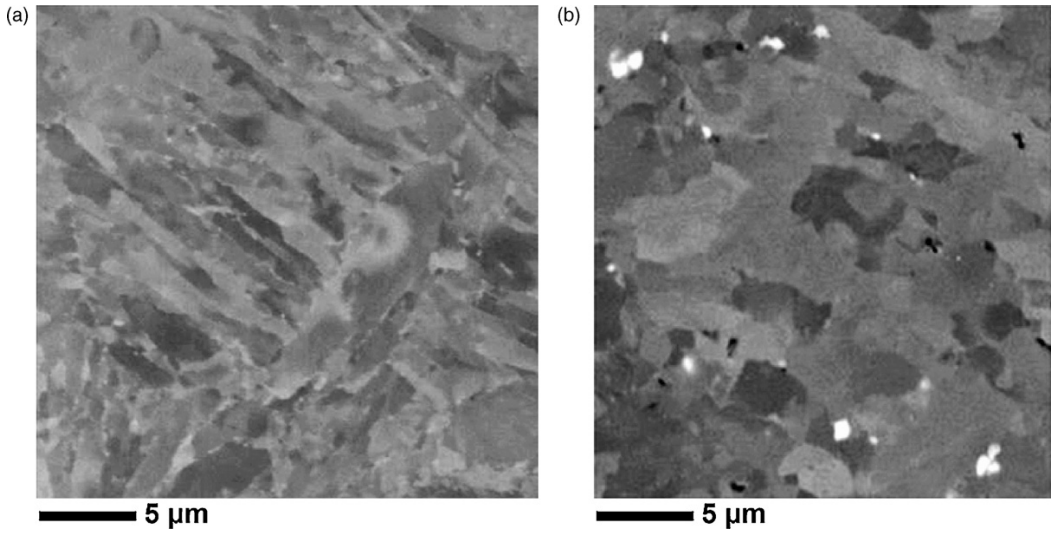

Fig. 7. Microstructure of the as received P91 steel (left) and after creep (right), BSE images, colloidal silica polishing.

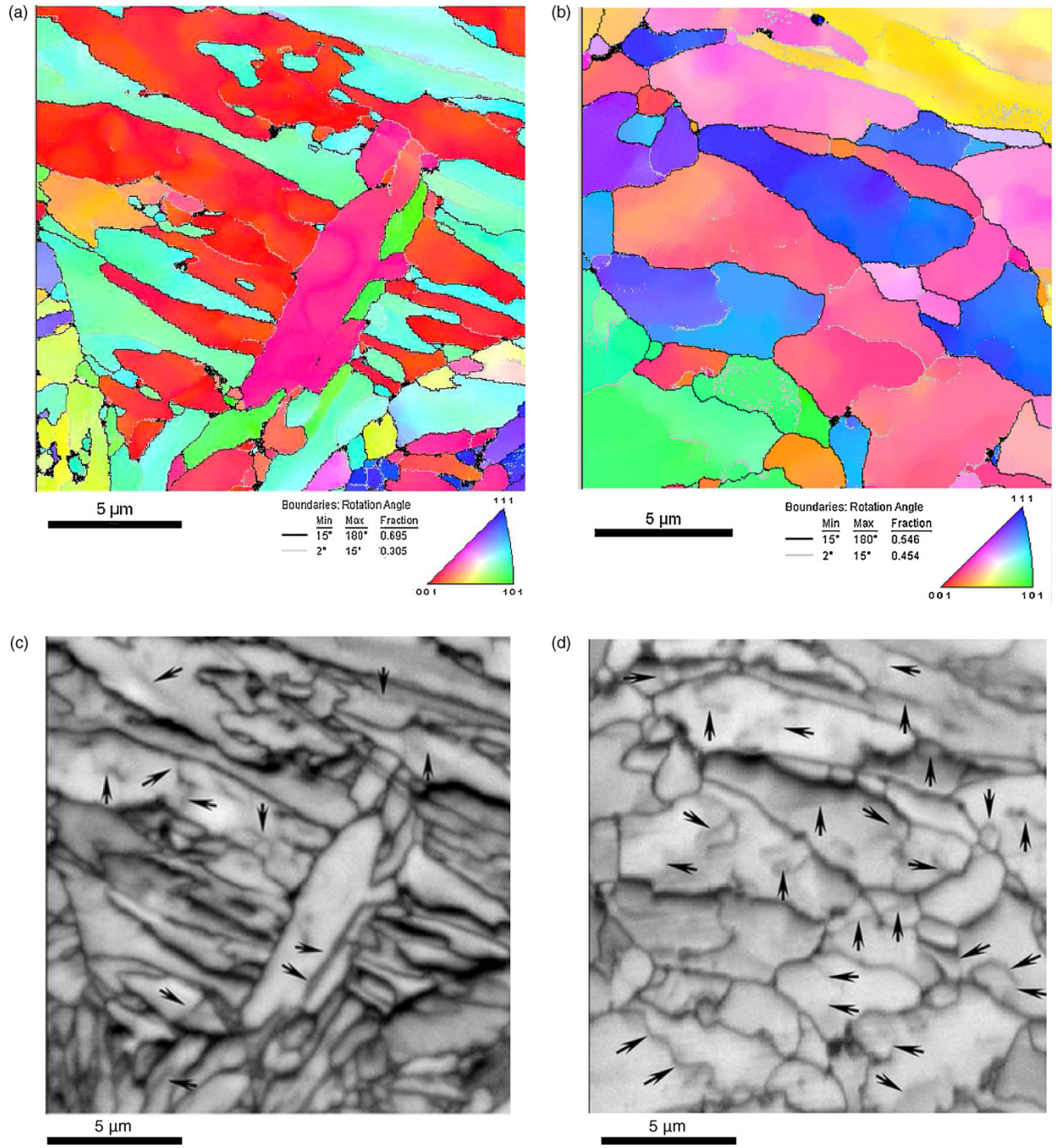

Fig. 8. Orientation imaging microscopy (OIM) images corresponding to the images of Fig. 7. (a) and (b) Inverse pole figure (IPF) maps with orientation of sample normal in the crystal frame as key color. (c) and (d) EBSD image quality map; (a) and (c) same area as in Fig. 7a; (b) and (d) same area as in Fig. 7b.

than 2°. This suggests that subgrains within a given martensite lath measured on TEM images have very close crystal orientations.

Crystal orientation mapping implemented in TEM is not expected to give more accurate information about the crystal orientation of subgrains revealed in bright field micrographs. In fact such investigations with a step size of ~40 nm conducted on a creep-fatigued specimen revealed subgrains in bright field micrograph which were not revealed in the IPF map as having a different orientation reported to the neighboring crystals [39], i.e. results similar to those presented here.

4. Discussion

From the above observations, one may conclude that (i) MX precipitates did not evolve during creep or thermal exposure, (ii) significant, but not extensive recovery occurred essentially due to

temperature effect, and (iii) subgrain growth occurred during thermal exposure but was strongly enhanced by creep.

The solid solution strengthening effect by Mo atoms was found to be negligible using Hald's approach, so that precipitation of Laves phases should not strongly affect *resistance* of this steel to creep deformation. Note, however, that damage cavities were found (often next to Laves phases) throughout the gauge part of the specimen [16], so that Laves phases could affect the resistance of that steel to creep *fracture*.

The present results also confirmed that the evolution of subgrains size is heterogeneous. The density of mobile dislocations is hardly affected by creep; however, during thermal exposure recovery is only driven by existing dislocations (i.e. those formed in the austenite to martensite phase transformation), whereas during creep dislocations are continuously created and annihilated in a dynamic way.

As also found in other steels of the same family [12,11] after quantitative study of both precipitation and matrix evolution during long-term creep, the present study suggests that the major contribution to the decrease in creep resistance during long-term creep exposure is subgrain growth/coarsening. Only a study involving interrupted tests as in [12,11,15] could provide experimental data to separately study growth and coarsening of Laves phases and of subgrains.

5. Conclusions

TEM results on thin foils of a P91 steel specimen crept for 113,431 h at 600 °C compared to as received and to thermally exposed samples showed that:

- No significant change occurred in the size, shape and spatial distribution of MX-type precipitates,
- The dislocation density within subgrains was reduced by about 50% after thermal exposition, and by about 60% after creep deformation,
- Some sub-grain growth occurred during thermal aging, much more significant and heterogeneous subgrain growth occurred after creep as shown both by TEM image analysis and EBSD mapping.

References

[1] G. Eggeler, N. Nilsvang, B. Ilschner, Steel Res. 58 (1987) 97–103.
[2] A. Kostka, K.-G. Tak, G. Eggeler, Mater. Sci. Eng. A 481–482 (2008) 723–726.
[3] J. Hald, L. Korcakova, ISIJ Int. 43 (2003) 420–427.
[4] L. Cipolla, A. DiGiafrancesco, G. Cumino, S. Caminada, in: I.A. Shibli, S.R. Holdsworth (Eds.), Proc. Creep & Fracture in High Temperature Components: Design & Life Assessment Issues, Lancaster, U.S.A., DEStech Publication, ISBN 1-932078-49-5, 2005, pp. 288–299.
[5] G. Dimmler, P. Weinert, E. Kozeschnik, H. Cerjaket, Mater. Charact. 51 (2003) 341–352.
[6] F. Abe, Curr. Opin. Solid State Mater. Sci. 8 (2004) 305–311.
[7] J. Sanchez-Hanton, R. Thomson, Mater. Sci. Eng. A 460–461 (2007) 261–267.
[8] J. Pešička, R. Kuzel, A. Dronhofer, G. Eggeler, Acta Mater. 51 (2003) 4847–4862.
[9] H. Kushima, K. Kimura, F. Abe, Tetsu-to-Hagane 85 (1999) 841–847.
[10] H. Kushima, K. Kimura, F. Abe, in: A. Strang, R.D. Conroy, G.M. McColvin, J.C. Neal, S. Simpson (Eds.), Proc. of the 5th Inter. Charles Parsons Turbine Conference, OIM Communications Ltd., Cambridge, UK, ISBN 1-86125-113-0, 2000, pp. 590–602.
[11] A. Aghajani, F. Richter, C. Somsen, S. Fries, I. Steinbach, G. Eggeler, Scripta Mater. 61 (2009) 1068–1071.
[12] A. Aghajani, C. Somsen, G. Eggeler, Acta Mater. 57 (2009) 5093–5106.
[13] K.-G. Tak, U. Schulz, G. Eggeler, Mater. Sci. Eng. A 510–511 (2009) 121–129.
[14] A. Kostka, K.-G. Tak, R. Hellmig, Y. Estrin, G. Eggeler, Acta Mater. 55 (2007) 539–550.
[15] A. Pešička, C. Aghajani, A. Somsen, G. Hartmaier, Eggeler, Scripta Mater. 62 (2010) 353–356.
[16] C. Panait, W. Bendick, A. Fuchsmann, A.-F. Gourgues-Lorenzon, J. Besson, in: I.A. Shibli, S.R. Holdsworth (Eds.), Proc. Creep & Fracture in High Temperature Components: Design & Life Assessment Issues, Lancaster, U.S.A., DEStech Publications, ISBN 978-1-60595-005-1, 2009, pp. 877–888.
[17] H.J. Klaar, P. Schwaab, W. Osterle, Prakt. Metallogr. 29 (1992) 3–25.
[18] P.J. Ennis, A. Zielińska-Lipiec, O. Wachter, A. Czyrska-Filemonowicz, Acta Mater. 45 (1997) 4901–4907.
[19] A. Zielińska-Lipiec, A. Czyrska-Filemonowicz, P. Ennis, O. Wachter, J. Mater. Process. Technol. 64 (1997) 397–405.
[20] A. Zielińska-Lipiec, W. Bendick, T. Koziel, B. Hahn, A. Czyrska-Filemonowicz, in: I.A. Shibli, S.R. Holdsworth (Eds.), Proc. Creep & Fracture in High Temperature Components: Design & Life Assessment Issues, Lancaster, U.S.A, DEStech Publication, ISBN 978-1-60595-005-1, 2009, pp. 1067–1075.
[21] P.J. Ennis, A. Zielińska-Lipiec, A. Czyrska-Filemonowicz, Mater. Sci. Technol. 16 (2000) 1226–1232.
[22] J. Hald, Int. J. Press. Vess. Pip. 85 (2008) 30–37.
[23] D. Terada, F. Yoshida, H. Nakashima, H. Abe, Y. Kadoya, ISIJ Int. 42 (2002) 1546–1552.
[24] V. Sklenička, K. Kuchařova, M. Svoboda, L. Kloc, J. Buršik, A. Kroupa, Mater. Charact. 51 (2003) 35–48.
[25] L.J. Seung, H.G. Armaki, K. Maruyama, T. Muraki, H. Asahi, Mater. Sci. Eng. A 428 (2006) 270–275.
[26] A. Gustafson, M. Hattestrand, Mater. Sci. Eng. A 333 (2002) 279–286.
[27] K. Sawada, K. Kubo, F. Abe, Mater. Sci. Eng. A 319–321 (2001) 784–787.
[28] K. Sawada, K. Kubo, F. Abe, Mater. Sci. Technol. 19 (2003) 732–738.
[29] M. Yoshino, Y. Mishima, Y. Toda, H. Kushima, K. Sawada, K. Kimura, ISIJ Int. 45 (2005) 107–115.
[30] K. Sawada, H. Kushima, K. Kimura, M. Tabuchi, ISIJ Int. 47 (2007) 733–739.
[31] A. Golpayegani, H. Andren, H. Danielsen, J. Hald, Mater. Sci. Eng. A 489 (2008) 310–318.
[32] H.K. Danielsen, J. Hald, Mater. Sci. Eng. A 505 (2009) 169–177.
[33] B. Sonderegger, S. Mitsche, H. Cerjak, Mater. Sci. Eng. A 481–482 (2008) 466–470.
[34] A. Orlová, J. Buršík, K. Kuchařová, V. Sklenička, Mater. Sci. Eng. A 245 (1998) 39–48.
[35] Y. Qin, G. Götz, W. Blum, Mater. Sci. Eng. A 341 (2003) 211–215.
[36] W. Blum, G. Götz, Steel Res. 70 (1999) 274–278.
[37] K. Maruyama, K. Sawada, J. Koike, ISIJ Int. 41 (2001) 641–653.
[38] P. Polcik, T. Sailer, W. Blum, S. Straub, J. Buršík, A. Orlová, Mater. Sci. Eng. A 260 (1999) 252–259.
[39] B. Fournier, Ph.D. thesis, Ecole des Mines de Paris, Paris, France, 2007 (in French).

C.1 Complementary data

C.1.1 TEM investigations on thin foils

Table C.1 summarizes the sizes of MX-type precipitates determined on thin foils following the experimental procedure presented previous article. The size distribution of MX-type precipitates was given in figure 4 of the previous article.

In table C.2 are summarized the results of subgrains size quantification, corresponding to the size distribution given in figure 6 of previous article.

The dislocation density was evaluated using the mean linear intercept which consists in overlapping a grid of horizontal and vertical lines on subgrains and counting the intersections of dislocations with grid lines. The number of vertical and horizontal grid lines is adjusted in relation with the size and shape of subgrains in a such way to keep a constant grid spacing as illustrated in figure C.1. Note that, the number on lines in figure C.1 do not represent the number of intersections with dislocations.

This method is generally used to evaluate dislocations density, see for instance ref. (Pešička et al., 2003), (Pešička et al., 2010), (Ennis et al., 1997), (Zielińska-Lipiec et al., 1997).

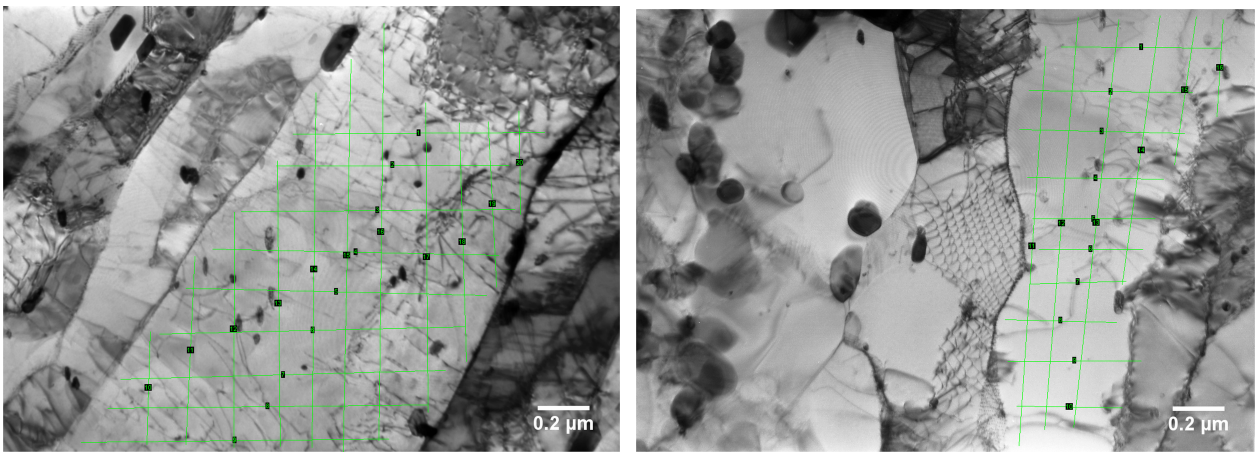

a) **b)**

Figure C.1 : Illustration of the intercept linear method used for evaluation of dislocation density a) As-received P91 steel; b) P91 steel after 113,431h of creep at 600°C (head of the specimen)

C.1.2 Matrix substructure (EBSD investigations)

EBSD maps acquired with a step size of 0.15μm at various distances from fracture surface of the P91 steel crept specimen are given in *AppendixB* of this manuscript. In order to get more precise data on the microtexture of the P91 steel after long-term creep exposure, EBSD investigations were conducted with a step size of 0.07μm and 0.04μm at 15 mm from fracture surface. Typical (representative) EBSD maps of such investigations are given in figure C.2 and C.3, respectively.

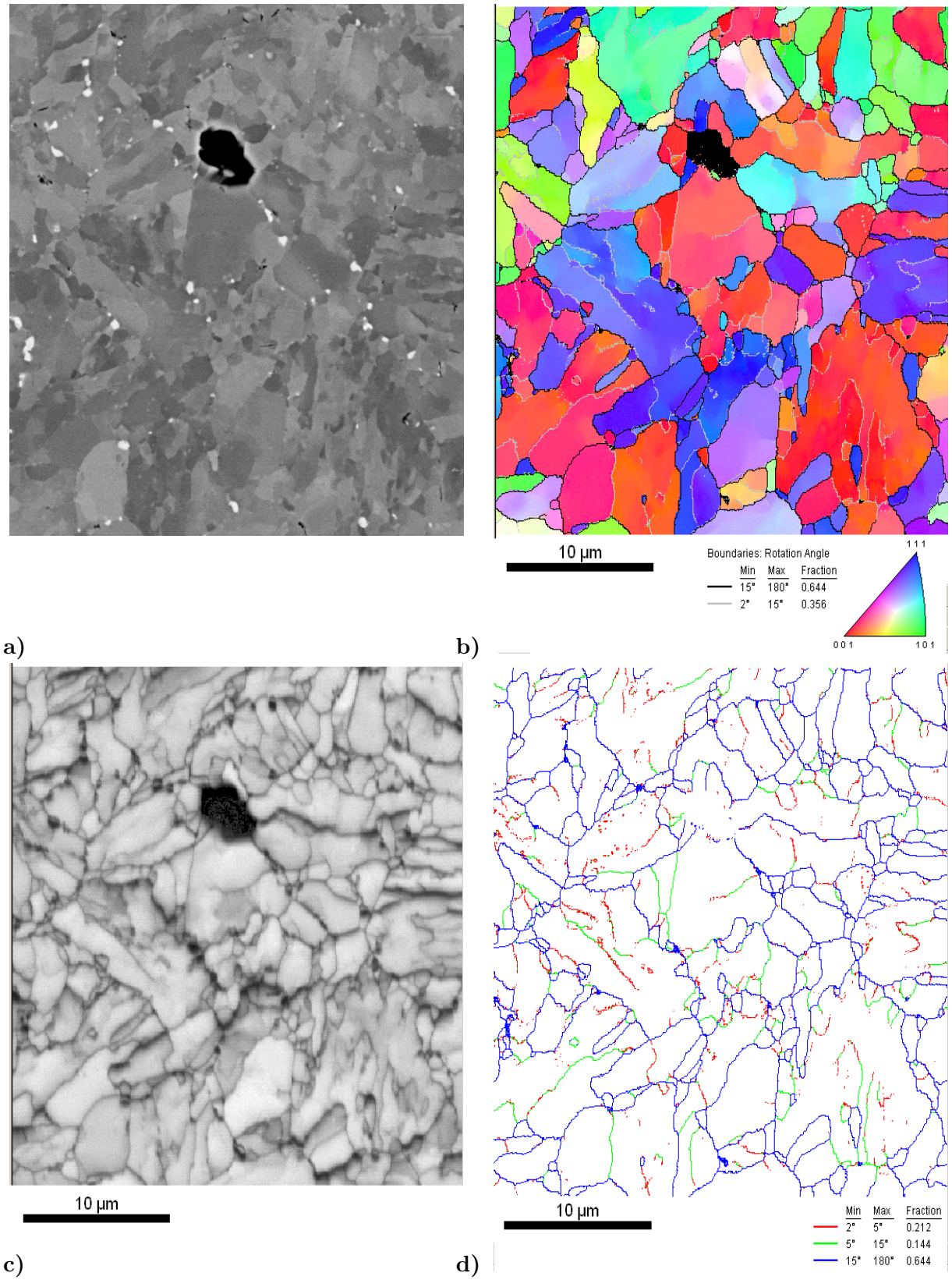

Figure C.2 : EBSD maps of the P91 steel creep tested at 600°C for 113,431h (15mm from fracture surface, step size of 0.07μm). SEM-BSE image (a); Inverse Pole Figure (IPF) map with orientation of sample normal in the crystal frame as key color (b); EBSD-IQ map (c); EBSD boundaries map (d)

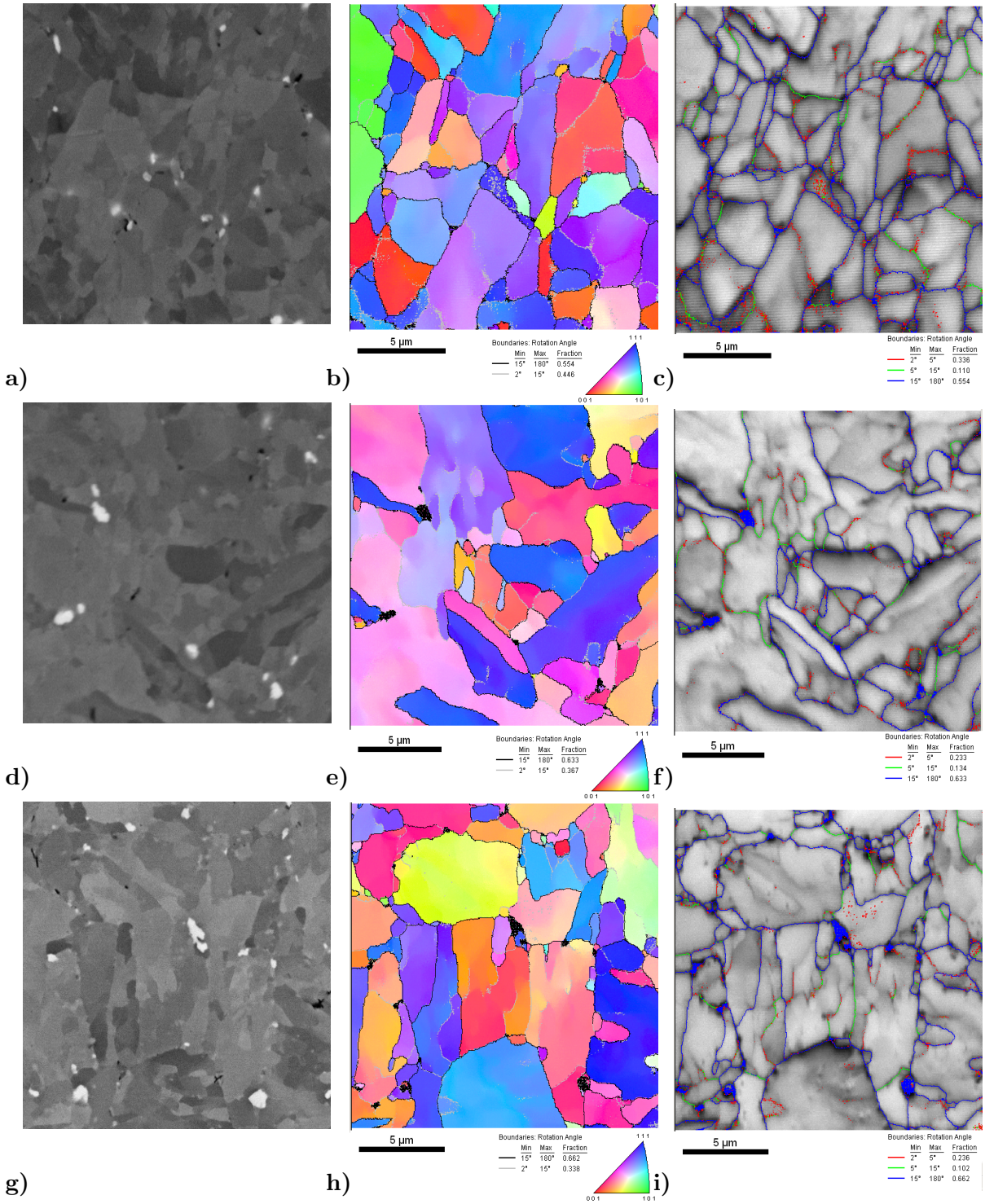

Figure C.3 : EBSD maps of P91 steel creep tested at 600°C for 113,431h (15mm from fracture surface, step size 0.04μm). SEM-BSE images (a, d, g); EBSD-IPF map with orientation of sample normal in the crystal frame as key color (b, e, h); EBSD-IQ overlapped with EBSD boundaries map (c, f, i)

Table C.1 : MX-type precipitates

	As-received				After 113431h of creep at 600°C							
					Head				Gauge length			
	Min	Mean	Max	Stand. dev.	Min	Mean	Max	Stand. dev.	Min	Mean	Max	Stand. dev.
EDC [μm]	9	34	76	14	11	31	83	10	9	33	84	12
D [μm]	11	43	106	20	12	37	111	13	13	39	103	15
S.C.	0.36	0.65	0.94	0.13	0.34	0.74	0.95	0.13	0.30	0.73	0.95	0.13
Number of investigated precipitates:				122				200				364

Table C.2 : Subgrain size in as received and crept P91 steel

	As-received				After 113431h of creep at 600°C							
					Gauge length				Head			
	Min	Mean	Max	Stand. deviation	Min	Mean	Max	Stand. dev.	Min	Mean	Max	Stand. dev.
EDC [μm]	0.07	0.23	0.67	0.09	0.20	1.01	2.60	0.49	0.10	0.30	0.72	0.12
D [μm]	0.08	0.32	0.97	0.15	0.23	1.26	3.44	0.67	0.12	0.41	1.10	0.20
S.C.	0.23	0.58	0.94	0.16	0.31	0.69	0.91	0.14	0.27	0.59	0.89	0.16
Number of investigated subgrains:				165				167				146

Table C.3 : Analysis of boundaries in EBSD maps

Creep testing conditions	Size of EBSD maps Step size	Boundaries rotation angle	Total length (Fraction)	Observations
P91 steel 113,431h;600°C (25 mm)	77μm×84μm 0.15μm	2°-5° 5°-15° 15°-180°	0.210 0.162 0.627	figure **??**
P91 steel 113,431h;600°C (head)	77μm×77μm 0.15μm	2°-5° 5°-15° 15°-180°	0.193 0.166 0.641	
P91 steel 113,431h;600°C (15 mm)	17μm×18μm 0.04μm	2°-5° 5°-15° 15°-180°	0.234 0.147 0.619	
P91 steel 113,431h;600°C (15 mm)	17μm×18μm 0.04μm	2°-5° 5°-15° 15°-180°	0.336 0.110 0.554	figure C.3c
P91 steel 113,431h;600°C (15 mm)	18μm×19μm 0.04μm	2°-5° 5°-15° 15°-180°	0.233 0.134 0.633	figure C.3f
P91 steel 113,431h;600°C (15 mm)	18μm×19μm 0.04μm	2°-5° 5°-15° 15°-180°	0.236 0.102 0.662	figure C.3i
P91 steel 113,431h;600°C (15 mm)	31μm×31μm 0.07μm	2°-5° 5°-15° 15°-180°	0.212 0.144 0.644	figure C.2

Evolution métallurgique et résistance au fluage à 600 °C et 650 °C d'aciers à 9-12%Cr

Résumé: Les aciers martensitiques à 9-12% Cr sont utilisés pour applications à haute température notamment comme composants dans des centrales thermiques de production de l'électricité. Ces composants sont soumis à des phénomènes de fluage, vieillissement thermique, fatigue, oxydation, corrosion. Cette étude vise une meilleure compréhension de l'évolution métallurgique à long terme des aciers martensitiques à 9-12% Cr, ainsi que de son influence sur la résistance en fluage à 600 et 650 °C. Le matériau de l'étude est l'acier Grade 92.

La littérature manque de données quantitatives sur la microstructure de l'acier Grade 92 après des temps prolongés d'exposition au fluage ou au vieillissement thermique (temps supérieurs à 10000h) à 600 °C et 650 °C. Par conséquent, dans un premier temps une expertise d'éprouvettes de fluage testées à 600 °C et 650 °C pendant des temps allant jusqu'à 50000h a été réalisée par microscopie électronique en transmission (MET) sur des répliques extractives, microscopie électronique à balayage (MEB) et par diffraction des électrons rétrodiffusés. Cette expertise a révélé une précipitation significative de phase de Laves, une restauration de la matrice et une très faible précipitation de la phase Z-modifiée. Une quantification de l'endommagement et des phases de Laves a été réalisée à partir des micrographies MEB.

La précipitation significative des phases de Laves et la restauration de la matrice semblent être les mécanismes prédominants de l'évolution métallurgique à 600 °C et 650 °C de l'acier Grade 92. Afin d'étudier séparément l'influence de chacun de ces deux mécanismes sur la résistance au fluage, des essais de fluage ont été réalisés sur des éprouvettes pré-vieillies et sur des éprouvettes pré-fatiguées. Des éprouvettes entaillées ont été également utilisées.

- L'intérêt des éprouvettes pré-vieillies est d'étudier l'influence de grosses phases de Laves sur la résistance au fluage. Le temps à rupture des éprouvettes pré-vieillies est quatre fois plus faible que celui des éprouvettes standard pour les mêmes niveaux de contraintes. Ceci n'est toutefois pas confirmé pour les contraintes les plus faibles.

- Deux essais de fluage ont été réalisés sur des éprouvettes pré-fatiguées à 550 °C pour étudier l'effet de l'état de la matrice sur la résistance au fluage. Un temps à rupture deux fois plus faible a été observé à 600 °C sur une éprouvette pré-fatiguée comparée à une éprouvette standard pour le même niveau de contrainte. Cet effet n'a pas été observé à 650 °C pour les contraintes faibles.

- Des éprouvettes entaillées ont été également utilisées pour étudier l'influence du taux de triaxialité des contraintes sur le développement de l'endommagement par fluage. Pour des temps de fluage comparables, l'endommagement est plus développé dans une éprouvette entaillée que dans une éprouvette lisse.

Un modèle mécanique qui prend en compte l'évolution métallurgique de l'acier a été développé pour estimer la résistance au fluage *à long terme*. Le modèle prend également en compte le taux de triaxialité des contraintes. A ce titre, il peut être utilisé pour estimer la durée de vie des composants en service ou pour analyser les composants avec une géométrie complexe qui serait plus sensible au développement de l'endommagement par fluage, du fait d'une triaxialité des contraintes plus élevée.

Mots clés: fluage, vieillissement thermique, acier Grade 92, phase de Laves, EBSD, éléments finis

Metallurgical evolution and creep strength of 9-12% Cr heat resistant steels at 600 and 650 °C

Abstract: 9-12%Cr tempered martensite steels are used for high temperature (400-600 °C) especially applications in components of fossil power plants, such as tubes, pipes, heaters. These components are exposed to creep, thermal aging, fatigue, oxidation, corrosion. The development of advanced heat resistant steels with improved long-term creep strength relies on a better understanding of the long-term microstructural evolution and of its influence on the creep strength. This study aims at better understanding of the effect of microstructural evolution on long-term creep strength at 600 °C and 650 °C of a Grade 92 steel.

There are rather few published data on the microstructure of the Grade 92 steel after long-term creep or thermal aging exposure (times higher than 10,000h) both at 600 °C and 650 °C. Thus, in a first part, P92 steel specimens that had been creep tested for times up to 50,000h at 600 °C and 650 °C were investigated using transmission electron microscopy on extractive replicas of precipitates, scanning electron microscopy and electron backscatter diffraction to get data on the microstructure of the Grade 92 steel after long-term exposure. These investigations revealed significant precipitation of Laves phases, recovery of the matrix and little precipitation of modified Z-phase. A quantification of the Laves phases and creep damage were realized by image analysis of scanning electron micrographs.

Significant precipitation of Laves phase and recovery of the matrix seem to be the most prominent microstructural degradation mechanisms. To separately investigate the effect of each of these two mechanisms on creep strength, creep tests were conducted on thermally aged and thermo-mechanically prepared creep specimens. Creep tests were also conducted on notched specimens.

- Thermally aged creep specimens enable to study the effect of large Laves phases on the creep strength. A time to rupture four times lower was observed on the aged creep specimens compared to a standard creep test for same testing conditions. This seems not be confirmed, however, at low stresses.

- Two creep specimens thermo-mechanically prepared by creep-fatigue prestraining at 550 °C were used to study the effect of the matrix substructure on the creep strength. A time to rupture twice lower was observed at 600 °C (short-term creep) on a thermo-mechanically prepared creep specimen compared to a standard one for the same testing conditions. No such effect was detected at 650 °C in the low stress regime.

- Creep tests were also conducted on notched specimens with various notch shapes to study the effect of stress triaxiality on creep damage. In notched specimens higher amounts of creep damage were observed compared to smooth specimens for similar testing time.

A finite element mechanical model coupling microstructural evolution and creep damage was proposed to estimate the long-term creep strength of the Grade 92 steel at 600 °C and 650 °C. The model taking stress triaxiality into account might also be used to estimate the remaining life of service components and to analyze service components with complex geometry more sensitive to creep damage due to stress triaxiality.

Keywords: creep, thermal aging, Grade 92, Laves phases, EBSD, finite elements

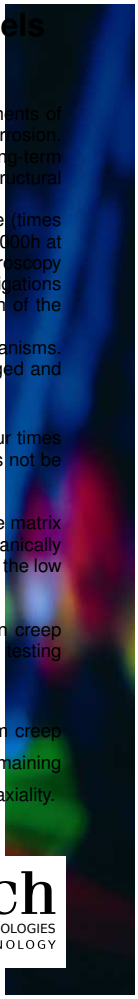

MINES ParisTech

ParisTech
INSTITUT DES SCIENCES ET TECHNOLOGIES
PARIS INSTITUTE OF TECHNOLOGY